



# THÈSE

**En vue de l'obtention du  
DOCTORAT DE L'UNIVERSITÉ DE TOULOUSE**

**Délivré par l'Université Toulouse 3 - Paul Sabatier**

**Cotutelle internationale: Université autonome de Barcelone**

---

**Présentée et soutenue par**

**Laura MALLÓN PERNIA**

Le 28 septembre 2021

**Nanocatalyseurs hybrides fonctionnalisés en surface pour le  
fractionnement de l'eau**

---

Ecole doctorale : **SDM - SCIENCES DE LA MATIERE - Toulouse**

Spécialité : **Chimie Organométallique et de Coordination**

Unité de recherche :

**LCC - Laboratoire de Chimie de Coordination**

Thèse dirigée par

**Karine PHILIPPOT et Xavier SALA**

Jury

**Mme Sara CAVALIERE**, Rapporteur

**M. Pierluca GALLONI**, Rapporteur

**M. Andrea SARTOREL**, Examineur

**M. Romuald POTEAU**, Examineur

**Mme Karine PHILIPPOT**, Directrice de thèse



*This PhD thesis has been performed in the frame of a cotutelle agreement under the supervision of Dr. Xavier Sala and Dr. Roger Bofill from the Universitat Autònoma de Barcelona (UAB), and of Dr. Karine Philippot from the Laboratoire de Chimie de Coordination (LCC-CNRS) and Université Toulouse III- Paul Sabatier (UT3 –UPS).*





## **ACKNOWLEDGMENTS**

Primerament, vull agrair en Dr. Xavier Sala i en Dr. Roger Bofill per confiar en mi per realitzar el doctorat al grup i permetre'm guanyar experiència en el camp durant aquests anys. Gràcies per compartir el vostre coneixement científic amb mi i guiar-me durant aquests quatre anys. Merci également au Dr. Karine Philippot pour avoir accepté de faire la convention de cotutelle et de me laisser faire partie de l'équipe L au LCC. I am glad to have had the opportunity of being part of both research groups and being able to discuss with you all about chemistry. Even the almost 400 km distance between us and the COVID-19, we managed to overcome all the issues encountered during my PhD travel. Thus, I want to heartily thank you all for your patience, your advises and for making me feel so comfortable in the groups from the very beginning.

I would like to thank Prof. Sara Cavaliere, Dr. Pierluca Galloni, Dr. Andrea Sartorel and Prof. Romuald Poteau for accepting being the jury members of my PhD thesis.

Furthermore, I want to thank the technicians that have made their contribution to this project, adding even more value to the obtained results. I want to thank the staff at “Servei de microscòpia UAB”, specially to Martí and Emma who have been always willing to solve any encountered problems during the characterization of the nanomaterials. I would like to thank also the “Servei d'Anàlisi Química UAB”, specially Ignasi, for his support in ICP analysis. From ICN2, thanks to Dr. Guillaume Sauthier for XPS analyses and fittings. Going to Toulouse, I am very grateful to Prof. Pierre Lecante for WAXS analyses and discussions and to Dr. Vincent Collière for helpful advises and courses on how to use the TEM apparatus.

In addition, I want to thank my collaborators. Au Prof. Romuald Poteau (LPCNO, Université de Toulouse, CNRS, INSA, UPS) pour avoir accepté que je fasse un séjour d'un mois dans son groupe de recherche à Toulouse. Je remercie également le Dr. Iker del Rosal qui, avec Romuald, m'a permis d'acquérir des connaissances sur les calculs théoriques DFT pendant mon séjour et d'effectuer des calculs spécifiques sur des nanoparticules de ruthénium fonctionnalisés en surface. Je tiens également à remercier les étudiants en doctorat et en master qui étaient présents dans le groupe pendant mon séjour, qui m'ont aidé à résoudre des problèmes de calcul et ont rendu ce séjour agréable.

Trasladándome a Valencia, quiero agradecer al Dr. Luis Miguel Martínez (ITQ, Instituto de Tecnología Química, Universitat Politècnica de València (UPV)) por compartir sus materiales de NPs de Ru soportados en óxido de grafeno reducido para su estudio electrocatalítico. Gracias por todas las discusiones y consejos. Gracias también al Dr. Rubén Mas-Ballesté (Departamento de Química Inorgánica, Facultad de Ciencias, Universidad Autónoma de Madrid) por proporcionarnos las fibras de carbono para su utilización como soporte de nanopartículas.

Now is time to thank all the people in the groups. Empezando en Barcelona, me gustaría dar las gracias al Dr. Jordi García-Antón, que me animó a unirme al grupo por primera vez durante mi proyecto de final de grado. Desde entonces, siempre ha estado ahí para ayudar, y divertirse, por supuesto. Además, gracias al Dr. Lluís Escriche, aunque no hemos compartido muchos momentos, siempre ha estado dispuesto a ayudar. También me gustaría dar las gracias a todos los estudiantes que han compartido algún momento en SelOxCat, concretamente a Bing (que siempre estaba dispuesto a ayudar), Rosa (la veterana del grupo), Marcos (por sus bromas), Jonathan (por enseñarme durante mi proyecto de final de Grado), Jordi Creus (por compartir sus conocimientos en electroquímica y su paciencia con las fibras de carbono durante mi proyecto de Máster), Nacho (por todas las vivencias compartidas en el laboratorio durante estos años), Heting (por nuestros problemas compartidos con las NPs sobre el rGO y su amable introducción a la cultura china) y a Gerard (nuestro físico-químico, por su ayuda en cuestiones físicas y conversaciones compartidas en momentos de estrés). También quiero agradecer a todos los estudiantes de TFG/TFM (Álvaro, Ariadna, David, Laia, Manel, Pau, Sergi, etc.) con los que he compartido agradables momentos. Muchas gracias a la Dra. Laia Francás que, aunque se ha incorporado a la UAB en el último año, ha estado siempre dispuesta a ayudarme en cualquier ámbito. Por compartir conmigo sus conocimientos electroquímicos, y su paciencia y consejos durante los experimentos. Por último, quiero agradecer especialmente a Nuria, sin ella nada hubiera sido igual. Por sus soluciones "creativas" para arreglar material/equipos de laboratorio, por cuidar la caja seca, por su motivación, por las discusiones científicas (y de la vida) y por su ayuda incondicional. Gracias por los momentos divertidos compartidos durante la última etapa de mi doctorado (invitarme al concierto de "la oreja" y al monólogo de Latre). Te echaremos de menos en el grupo, te deseo todo lo mejor en tu nueva etapa.

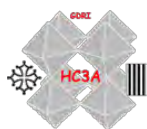
En ce qui concerne Toulouse, je voudrais remercier le Dr. Catherine Amiens qui a toujours été là pour les discussions sur la chimie. Tout d'abord je veux remercier Roberto et Elena, qui m'ont beaucoup aidé lors de mon premier séjour au LCC (en m'aidant aussi avec la langue). Je veux remercier tous les compagnons de laboratoire de l'équipe L, François (pour m'avoir mis à l'aise à Toulouse et pour nos conversations de football "Allez L'OL"), Laurent (pour ton aide inconditionnelle et nos discussions partagées sur les systèmes bimétalliques), Lorraine (pour ton aide et les moments partagés au bureau), Miquel (pour ta gentille aide avec la langue, nos discussions scientifiques et de vie et tous les moments drôles partagés à Toulouse), Quyen (pour notre expérience partagée dans un endroit étranger et tous les moments drôles partagés) et Sam (pour tes connaissances partagées en chimie et électrochimie). Merci à vous tous d'avoir rendu mon expérience à Toulouse inoubliable. J'espère que nos chemins se croiseront à nouveau.

Por último, quiero agradecer a toda mi familia su apoyo a lo largo de toda mi vida y especialmente durante este cuatrienio. A mis padres, Rosi y Juan, por ayudarme y animarme durante toda mi carrera académica. También por soportar todos los momentos de estrés. Quiero agradecer especialmente a José, mi compañero de vida, que como doctor ha podido entender todos los sentimientos que he experimentado durante el doctorado. Gracias por tu comprensión y amor incondicional en los momentos más duros.

Last, I would like to thank Universitat Autònoma de Barcelona for the pre-doctoral PIF-UAB grant, the CNRS funding and the GDRI-HC3A for internship financial support:



CTQ2015-64261-R



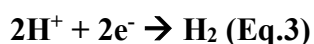
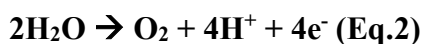
International Research Network  
**Heteroelements and Coordination Chemistry:  
from Concepts to Applications**

## RÉSUMÉ DE THÈSE

Une solution pour obtenir une source d'énergie décarbonée est la photoproduction d'H<sub>2</sub> par fractionnement catalytique de l'eau (WS, Eq.1) en utilisant l'énergie solaire.



Le fractionnement de l'eau est un processus en deux étapes : à l'anode l'eau est oxydée en O<sub>2</sub> (réaction d'évolution de l'oxygène, OER, Eq.2), libérant des électrons pour la réduction des protons en H<sub>2</sub> à la cathode (réaction d'évolution de l'hydrogène, HER, Eq.3).



Le développement de catalyseurs OER et HER performants est essentiel pour avoir une cinétique adéquate entre ces réactions. Les nanoparticules (NPs) sont des catalyseurs intéressants en raison de leur rapport surface/volume élevé, exposant un grand nombre de sites actifs. Dans cette thèse, différents nanoélectrocatalyseurs (Ru, Co et systèmes bimétalliques) ont été synthétisés via l'approche organométallique. Cette méthode permet de disposer de NPs de surface propre comparativement à d'autres méthodologies.

Pour comprendre les facteurs affectant l'activité électrocatalytique des NPs, des calculs théoriques DFT ont été effectués sur la base de concepts avancés (énergie libre d'adsorption de l'hydrogène,  $\Delta\text{GH}^*$ , et diagrammes de Volcan). Les ligands présents à la surface des NPs métalliques affectant l'activité électrocatalytique, des calculs DFT ont permis d'étudier les modes de coordination les plus favorables et d'obtenir les valeurs  $\Delta\text{GH}^*$  des NPs résultantes. De bonnes corrélations entre les données expérimentales et celles de la DFT ont été obtenues.

Les supports conducteurs carbonés sont connus pour améliorer l'activité électrocatalytique des nanocatalyseurs, limitant l'agrégation et favorisant le transfert d'électrons des sites actifs vers l'électrode. Dans cette thèse, deux matériaux carbonés ont été utilisés comme supports des NPs métalliques, un oxyde de graphène réduit (rGO) et des microfibrilles de carbone (CF). En outre, l'effet du dopage du rGO (N et P) a été étudié en HER. Un effet synergique positif a été observé entre les hétéroatomes du rGO dopé et

les RuNPs. Contrairement au graphène, les CF sont plus faciles à manipuler et sont utilisables directement comme électrodes, évitant ainsi les difficultés liées au dépôt sur des électrodes macroscopiques (GC, FTO). Des NPs de Ru et Co ont été synthétisées avec deux CF différents, présentant ou non de groupements -COOH à la surface. Deux méthodologies différentes, in-situ et ex-situ, ont été suivies pour régler l'interface entre les NPs et le support en présence d'un solvant seulement (THF ou 1-heptanol) pour les NPs de Co ou d'un ligand (4-phenylpyridine, 4PP) pour les RuNPs. Il a ainsi été montré qu'une interaction appropriée entre les NPs et la surface des CF est primordiale pour obtenir une activité catalytique accrue. Les systèmes où des interactions  $\pi$ - $\pi$  entre les structures Ru-4PP NPs/C ou des liaisons H entre  $\text{Co}(\text{OH})_2$  et les -COOH des CF existent ont donné les meilleurs résultats.

Ajouter un second métal est une autre stratégie vers des effets électroniques synergiques par modification de l'environnement chimique des sites métalliques et diminution de l'énergie d'adsorption des réactifs. A cet effet, des systèmes bimétalliques Ru@Ni-foam et RuCo NPs ont été synthétisés. Pour les systèmes Ru@Ni-foam, l'influence du dopage au Ru sur l'activité catalytique en OER a été étudiée comparativement à une mousse de Ni, en fonction du taux de dopage. Des NPs RuCo ont été synthétisés avec trois ligands différents, 4'-(4-méthylphényl)-2,2':6',2''-terpyridine, 4-PP et 1-heptanol. L'influence du ligand et du ratio métallique Ru/Co sur la taille et la morphologie des NPs a été déterminée. Des tests électrocatalytiques préliminaires ont été réalisés, ouvrant une nouvelle voie de recherche vers la détermination de l'intérêt des nanocatalyseurs bimétalliques pour l'électrolyse de l'eau et la production d'hydrogène.

## **THESIS SUMMARY**

One solution to achieve a carbon free energy source is the photoproduction of H<sub>2</sub> by the catalytic water splitting (WS, Eq. 1) using sunlight.



WS is a process in which water is oxidized to dioxygen in the anode (oxygen evolution reaction, OER, Eq. 2), thus constituting the source of electrons to reduce protons to H<sub>2</sub> in the cathode (hydrogen evolution reaction, HER, Eq. 3).



Developing highly efficient and active WS catalysts is essential for the proper kinetics of these two reactions. Nanoparticles (NPs) are true potential catalysts due to their high stability and surface per volume ratio, exposing high amounts of active sites. In this PhD, different nanoelectrocatalysts have been synthesized by following the organometallic approach which is advantageous for obtaining clean-surface nanomaterials compared to other synthesis methodologies.

To understand the factors affecting the electrocatalytic activity of the nanomaterials, theoretical DFT calculations have been performed on the basis of well accepted concepts (hydrogen adsorption free energy,  $\Delta G_{\text{H}^*}$ , and volcano plots). Given that the ligands present on the surface of metal NPs can influence the electrocatalytic activity, DFT calculations were performed to determine the most favorable coordination modes of different ligands and to obtain the  $\Delta G_{\text{H}^*}$  values of the resulting NPs. Successful correlations between experimental and DFT data have been obtained.

Conductive C-based supports are known to enhance the electrocatalytic activity by restraining the aggregation of the nanocatalysts and improving the electron transfer from the metal nanocatalyst to the electrode. In this PhD, two different carbon materials, reduced graphene oxide (rGO) and carbon microfibers (CF) have been used as supports for metal NPs. Furthermore, the effect of N and P doping onto rGO has been studied towards the HER, obtaining a positive synergistic effect between the heteroatoms and Ru NPs. In contrast to graphene, CF are easier to handle and can be directly used as electrodes, thus avoiding the issues related to the NPs deposition onto macroscopic

electrodes (GC, FTO). Thus, Ru and Co NPs have been synthesized on top of two different CF, differing in the presence or not of –COOH moieties onto the surface. Two different methodologies, *in-situ* and *ex-situ*, have been employed in order to tune the interface between the NPs and the C support by adding different solvents (THF or 1-heptanol) for Co NPs or ligands (4-phenylpyridine, 4PP) for Ru NPs. The results evidence that a proper interaction between the NPs and the support surface is key for an improved catalytic activity of the hybrid materials, obtaining better results in the systems where  $\pi$ - $\pi$  interactions between Ru-4PP NPs/C structures or H-bonds between Co(OH)<sub>2</sub> and COOH moieties in the CF take place.

Another promising strategy is the addition of another metal onto a metallic nanostructure, leading to beneficial synergistic electronic effects by changing the chemical environment of the metal centers and decreasing the adsorption energy of the reactants. In this sense, bimetallic Ru@Ni-foam and RuCo NPs systems were synthesized. The influence on the catalytic activity towards OER of different percentages of Ru-doping in Ru@Ni-foam systems has been studied. Finally, RuCo bimetallic systems were synthesized by using three different ligands, 4'-(4-methylphenyl)-2,2':6',2''-terpyridine, 4-PP and 1-heptanol. The influence of the ligand and the Ru/Co metal ratio on the size and morphology of the NPs has been determined. Preliminary electrocatalytic tests have been performed, opening a new door to explore the interest of bimetallic nanocatalysts for the water-splitting and the production of hydrogen.

## **ABBREVIATIONS**

Abs	Absorbance (a.u.)
AFM	Atomic Force Microscopy
b	Tafel Slope (mV/dec)
CA	Chronoamperometry
C <sub>DL</sub>	Double-Layer Capacitance (mF)
CF	Carbon Fibers
CNT	(Multi-Walled) Carbon Nanotubes
COD	1,5-Cyclooctadiene
COE	Cyclooctadienyl
COT	1,3,5-Cyclooctatriene
CP	Chronopotentiometry
C <sub>s</sub>	Specific Capacitance
CV	Cyclic Voltammetry
CVD	Chemical Vapor Deposition
d <sub>mean</sub>	Mean Diameter of Nanoparticles
DFT	Density Functional Theory
EA	Elemental Analysis
ECSA	Electrochemically Active Surface Area
EDX	Energy Dispersive X-ray Spectroscopy
EIS	Electrochemical Impedance Spectroscopy
Eq.	Equation
fcc	Face Centered Cubic
FT-IR	Fourier Transform – Infrared Spectroscopy
FTO	Fluorine-doped Tin Oxide
GC-RDE	Glassy Carbon – Rotating Disk Electrode
HAADF	High-Angle Annular Dark Field
hcp	Hexagonal close packed
HEC	Hydrogen Evolution Catalyst
HER	Hydrogen Evolution Reaction



$i$	Intensity
ICP-AES	Inductively Coupled Plasma Atomic Emission Spectroscopy
ICP-OES	Inductively Coupled Plasma Optical Emission Spectroscopy
$j$	Current Density (mA/cm <sup>2</sup> )
$j_s$	Specific Current Density (mA/cm <sup>2</sup> )
$j_0$	Exchange Current Density (mA/cm <sup>2</sup> )
LSV	Linear Sweep Voltammetry
M	Metal Site
MAS	Magic Angle Spinning
M-H	Metal-Hydride
NADP <sup>+</sup>	Nicotinamide Adenine Dinucleotide Phosphate
NHE	Normal Hydrogen Electrode
N/NH <sub>2</sub> -rGO	N-doped Reduced Graphene Oxide
NMR	Nuclear Magnetic Resonance
NPs	Nanoparticles
OER	Oxygen Evolution Reaction
OCP	Open Circuit Potential
PAW	Projector Augmented Waves
PBE	Perdew-Burke-Ernzerhof
PEM	Proton-Exchange Membrane
PET	Proton-Electron Transfer
P-G/P-rGO	Phosphorus-doped Reduced Graphene Oxide
PSI	Photosystem I
PSII	Photosystem II
PVD	Physical Vapor Deposition
rds	Rate-determining Step
RF	Roughness Factor
rGO	Reduced Graphene Oxide
RHE	Reversible Hydrogen Electrode
RRDE	Rotating Ring Disk Electrode

r.t.	Room Temperature
S	Geometrical Surface Area
SCE	Saturated Calomel Electrode
SCF	Supercritical Fluid
SEM	Scanning Electron Microscopy
THF	Tetrahydrofuran
STEM	Scanning Transmission Electron Microscopy
STM	Scanning Tunneling Microscopy
(HR)TEM	(High Resolution) Transmission Electron Microscopy
tpy	4'-(4-methylphenyl)-2,2':6',2''-terpyridine
UV-vis	Ultraviolet-visible Spectroscopy
WAXS	Wide-Angle X-ray Scattering
WOC	Water Oxidation Catalyst
WS	Water Splitting
XPS	X-ray Photoelectron Spectroscopy
XRD	X-ray Diffraction Analysis
$\eta$	Overpotential
$\eta_0$	Onset Overpotential
$\eta_{10}$	Overpotential at $ j  = 10 \text{ mA/cm}^2$
$\Delta G_{\text{H}^*}$	Hydrogen Adsorption Gibbs Free Energy
2PP	2-phenylpyridine
3PP	3-phenylpyridine
4PP	4-phenylpyridine

## **TABLE OF CONTENTS**

<b>Chapter 1. Introduction</b> .....	1
<b>Chapter 2. Objectives</b> .....	43
<b>Chapter 3. DFT calculations on ligand-capped Ru NPs</b> .....	47
<b>Chapter 4. Ruthenium nanoparticles supported on reduced graphene oxide as electrocatalysts towards the hydrogen evolution reaction</b> .....	67
<b>Chapter 4A. Ru nanoparticles supported on rGO (Hummers) as HER catalysts</b> .....	79
<b>Chapter 4B. Ru nanoparticles supported on rGO (Alginate) as HER catalysts</b> .....	105
<b>Chapter 5. Metallic nanoparticles supported on carbon microfibers as water splitting catalysts</b> .....	133
<b>Chapter 5A. Ru/RuO<sub>2</sub> nanoparticles supported on carbon microfibers for the hydrogen evolution reaction</b> .....	143
<b>Chapter 5B. Oxygen evolution anodes based on Co(OH)<sub>2</sub> nanoparticles supported on carbon microfibers</b> .....	161
<b>Chapter 6. Bimetallic nanomaterials for electrocatalytic water splitting</b> .....	207
<b>Chapter 6A. Ru@Ni-foam samples for electrocatalytic water splitting</b> .....	211
<b>Chapter 6B. Ligand-capped RuCo bimetallic nanoparticles</b> .....	255
<b>Chapter 7. General conclusions</b> .....	285
<b>Résumé de la Thèse</b> .....	293



# 1

## Chapter 1. Introduction

---

*Chapter 1* aims at introducing the research topic of this PhD thesis. Due to the climate change and its consequences on our planet, new technologies are urgently needed in order to access clean and renewable energy sources and decrease the CO<sub>2</sub> emissions from fossil fuels combustion. In this context, our group develops research activities focusing on the water splitting (WS) reaction activated by sunlight, which is an attractive alternative method to obtain H<sub>2</sub>, a clean energy carrier that only forms water after combustion. Development of active and robust catalysts is required to be able to implement practical WS technologies. Thus, my PhD work has been focused on the development of new nanoparticulated systems to catalyze the two WS half-reactions, namely the hydrogen evolution reaction (HER) and the oxygen evolution reaction (OER). In this first chapter, the interest of nanoparticles (NPs) in catalysis and their synthetic and stabilization methods will be introduced. The most used parameters in order to compare their activity and stability under catalytic WS conditions will be also described.

---



---

## **TABLE OF CONTENTS**

<b>1.1 Energy outlook</b> .....	5
<b>1.2 Natural vs. artificial photosynthesis and water splitting</b> .....	7
<b>1.3 Nanoparticles</b> .....	9
<b>1.3.1 The important role of the surface at the nanoscale</b> .....	9
<b>1.3.2 Stabilization of NPs</b> .....	10
<b>1.3.3 Synthesis of NPs</b> .....	11
<b>1.3.3.1 Organometallic synthesis</b> .....	16
<b>1.3.4 NPs for electrocatalysis</b> .....	18
<b>1.4 Water splitting reaction</b> .....	21
<b>1.4.1 Benchmarking of electrocatalytic activity</b> .....	21
<b>1.4.2 Hydrogen evolution reaction (HER)</b> .....	24
<b>1.4.3 Oxygen evolution reaction (OER)</b> .....	27
<b>1.4.4 Surface-functionalized NPs for WS</b> .....	29
<b>1.5 References</b> .....	35





## 1.1 Energy outlook

In 2018, the world population was increasing with a growth rate of 1.12 percent. Nowadays, the world population is almost 7.9 billion and by 2030 it will exceed 8 billion, being expected to rise to over 10 billion in 2055.<sup>1</sup> The increasing world population, jointly with the increased human activity, has been interfering with the energy balance of the planet, mainly by burning excessive fossil fuels (*i.e.* coal, natural gas and petroleum) for obtaining energy, giving rise to the release of additional carbon dioxide into the atmosphere (in fact the CO<sub>2</sub> concentration has increased by 47 percent since the industrial revolution began).<sup>2</sup> Although CO<sub>2</sub> absorbs less heat per molecule than other greenhouse gases (*i.e.* methane or nitrous oxide), which jointly with water vapour are contributing also to the greenhouse effect, CO<sub>2</sub> is the most long-lived greenhouse gas in the atmosphere. The increasing level of CO<sub>2</sub> in the Earth's atmosphere traps extra heat near the surface of the Earth, releasing it gradually over time and causing an increase in the global temperature (Fig. 1).<sup>3</sup> However, the increased global temperature is not the only effect of the global climate change. Thus, substantial changes in precipitation patterns, more frequent droughts and heat waves, stronger and more intense hurricanes, a rising of the sea level, the arctic likely to become ice-free, new diseases, reduced nutritional value of most food crops, etc. are also occurring.<sup>4</sup>

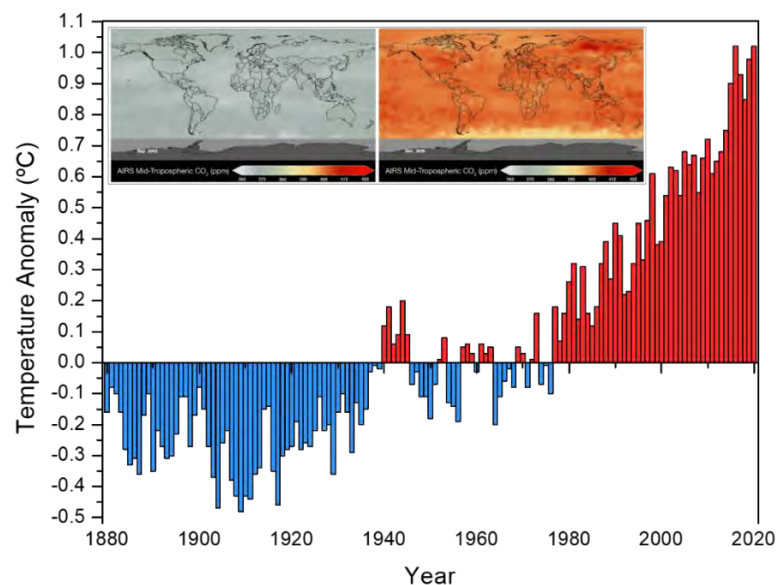


**Figure 1.** Temperature anomaly over the last 140 years. Data source: NASA's Goddard Institute for Space Studies (GISS), Credit: NASA/GISS. Inset, coloured views of world mid-tropospheric CO<sub>2</sub> (from 365 ppm, in grey, to 425 ppm, in orange) from year 2002 (left) to year 2016 (right). Data source: Atmospheric Infrared Sounder "AIRS", Credit: NASA.

At this point, it is not an exaggeration to say that finding solutions to at least mitigate the energy crisis is urgently needed. In fact, in December 2015, *The Paris Agreement*, the first-ever universal legally binding global climate change agreement, was adopted at the Paris climate conference (COP21). This agreement sets out a global framework to avoid dangerous climate change by limiting the global warming to well below 2 °C above pre-industrial levels and pursuing efforts to limit it to 1.5 °C. In addition, it states to limit, in between years 2050-2100, the amount of greenhouse gases emitted by human activity to a level equal to what trees, soil and oceans can absorb naturally.

Going in that direction, two main alternatives can be considered to reduce CO<sub>2</sub> emissions and overcome the climate change: replacing fossil fuels by renewable energy sources and improving energy efficiency by developing new technologies. In this regard, even the renewable energy supply is continuously increasing as a lot of investment is done in the research of new technologies to obtain energy from renewable sources and to produce them in a more cost-effective way, in 2018 around 85 percent of the obtained energy still came from fossil fuels consumption (Fig. 2).<sup>5</sup> In addition, one of the most attractive and possible solutions to this challenge is the production of H<sub>2</sub>, considered as a versatile energy carrier,<sup>6</sup> with the highest energy density per unit weight and producing only water under combustion. However, today hydrogen production is carried out from oil fossil fuels, with significant associated CO<sub>2</sub> emissions. Thus, a promising direction is the H<sub>2</sub> production through the water splitting (WS) process photo activated by sunlight, a process also called artificial photosynthesis.<sup>7,8,9</sup>

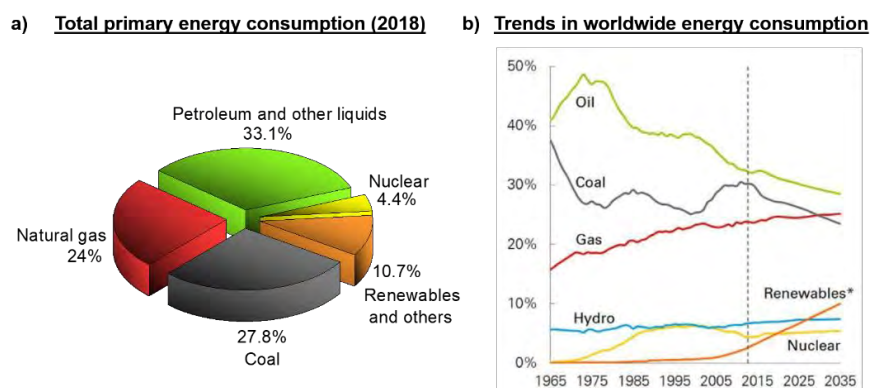


**Figure 2.** Total primary energy consumption in 2018. Source: <https://www.eia.gov/international/data/world> (a). Trends in worldwide energy consumption from 1965 to 2035. \*Renewables includes wind, solar, geothermal, biomass and biofuels. Source: <https://www.ogj.com/general-interest/article/17288577/bp-energy-outlook-global-energy-demand-to-grow-30-to-2035> (b).

## 1.2 Natural vs. artificial photosynthesis and water splitting

Natural photosynthesis is a process used by green plants, algae and cyanobacteria to convert sunlight energy into chemical energy (*i.e.* chemical bonds). The penta-oxygen tetramanganese-calcium cofactor ( $\text{Mn}_4\text{O}_5\text{Ca}$ ), with a  $[\text{Mn}_4\text{O}_4]$  cubic unit core, is the real active water oxidizing catalyst in the nature. It is embedded in a unique pigment-protein supercomplex, PSII, acting as a photosensitizer. In that way, solar energy can be absorbed by the outer light harvesting complexes (*i.e.* chlorophyll and other pigments, constituting the “antenna complex”), starting chain reactions and shuttling the absorbed energy by resonance energy transfer to the reaction centre of PSII (*chlorophyll a*), where charge separation takes place. When *chlorophyll a* absorbs photons, electrons and holes are generated, leading to the primary oxidant  $\text{P680}^+$ . The photochemically generated electrons are transferred to pheophytin and then to plastoquinone, before arriving to the next photosynthetic supercomplex, cytochrome  $\text{b}_6\text{f}$ , and finally ending in plastocyanin (Fig. 3). This process allows increasing the electron-hole distances, stabilizing the charge separated states. In addition, this creates a proton gradient across the chloroplast membrane (*i.e.* a chemiosmotic potential), which is used by ATP synthase in the synthesis of ATP.  $\text{P680}^+$  recovers its initial state by accepting  $\text{e}^-$  resulting from the oxidation of water into  $\text{O}_2$ , in a reaction catalyzed by the water oxidizing centre (*i.e.*  $\text{Mn}_4\text{O}_5\text{Ca}$  binds to two water molecules and contains the four oxidizing equivalents to drive the water oxidation reaction). Simultaneously, P700 (PSI) absorbs light and loses an electron to reduce  $\text{H}^+$  and convert  $\text{NADP}^+$  (nicotinamide adenine dinucleotide phosphate) to NADPH, generating  $\text{P700}^+$ . The electron coming from PSII is used up by  $\text{P700}^+$  to recover its initial state. The NADPH is the reducing power for the later biosynthetic reactions in the Calvin cycle, where the fixation of  $\text{CO}_2$  takes place to obtain sugars. As the generation of  $\text{O}_2$  from water is a  $4\text{-e}^-$  reaction, four successive charge-separation reactions by photosystem II are needed (Fig. 3).

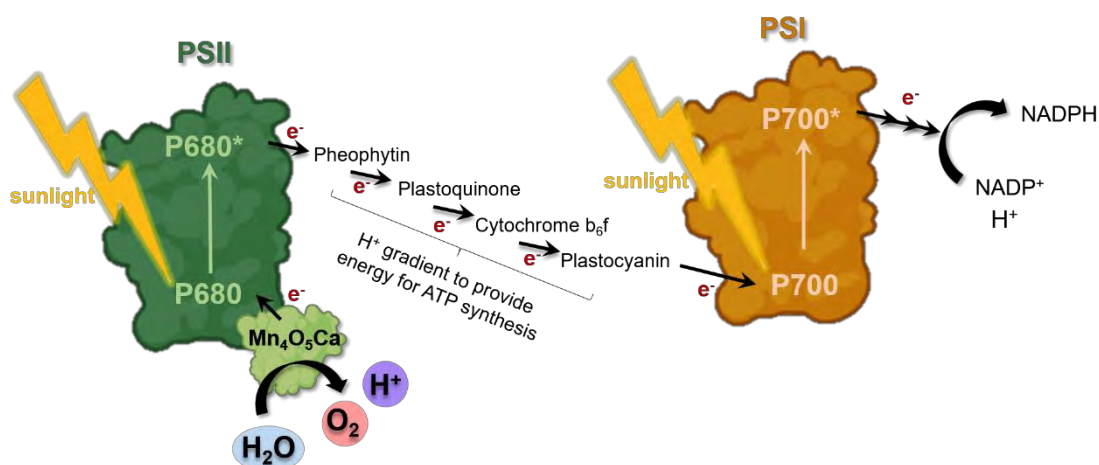


**Figure 3.** Schematic view of the natural photosynthetic electron transport chain.

At present, the technology to carry out this complex process in a commercial large-scale device is not available despite the numerous efforts have been made in recent years to understand and mimic the natural photosynthesis for being able to use solar energy to produce energy-rich molecules (*i.e.* solar fuels). One approach consists in artificial photosynthesis, that is, the use of synthetic catalysts and sunlight to drive WS into hydrogen and oxygen (Eq. 1) or to reduce CO<sub>2</sub> into synthetic carbon fuels.



Photocatalytic WS is simple in design. It is a redox process based on two half reactions in which water is oxidized to dioxygen at the anode (oxygen evolution reaction, OER, Eq. 2), constituting the source of electrons to reduce protons to dihydrogen at the cathode (hydrogen evolution reaction, HER, Eq. 3).



However, the WS process can be kinetically slow because of the difficulty of evolving gases from a liquid phase. The water oxidation reaction is the bottle neck reaction since it is highly endergonic and mechanistically complex, as a four-electron process is needed to break four O-H bonds from two water molecules to form an O=O molecule. Therefore, developing highly efficient and active water splitting catalysts<sup>10</sup> is essential for the proper kinetics of the overall WS process.

In order to simplify the systems, electrochemical cells are employed using an applied potential as energy source instead of solar light to drive the WS. In these systems, the energy to carry out WS can still come from a renewable source such as solar energy, for example by using a photovoltaic solar cell.<sup>11</sup> These simplified cells facilitate the finding of highly efficient water oxidation catalysts (WOCs) and hydrogen evolution catalysts (HECs), yielding high rates and low overpotentials needed for each half-reaction to occur (see section 1.3.4 for catalyst engineering). For such purpose, each half-reaction is usually studied in a separate manner. In this context, nanoparticles (NPs) have emerged in the last years as very promising catalysts<sup>12,13</sup> due to their high stability compared to molecular complexes and their high surface per volume ratio, exposing a high number of active catalytic sites.

## 1.3 Nanoparticles

### 1.3.1 The important role of the surface at the nanoscale

It is well known that chemical and physical properties of solid materials are strongly related to the nature and state of the surface. When decreasing the size of a solid material toward the nanoscale regime (1-100 nm), the number of surface atoms increases with respect to the total number of atoms, increasing the surface/volume ratio (Fig. 4, top).<sup>14</sup> Thus, surface phenomena gain even more importance at the nanoscale, pointing to the need of having a good control of the surface state and a well-stabilized nanomaterial. When talking about the stability of NPs, we have to consider not only the electronic configuration but also the geometric configuration (*i.e.* the presence of edges or corners). When the size decreases, small clusters can have different stabilities and one more atom or less can make the difference between a stable, metastable or unstable cluster. The stability of a system at the nanoscale regime is more dependent on its geometric configuration than its electronic configuration. Those clusters with a face centred cubic crystalline structure have closed shells with minimum volume, making them very stable. In this case, the atoms are packed in such a way that all the neighbourhood places are full, forming a complete shell around the central atom or shell. It is said that the cluster contains a “magic” number of atoms (Fig. 4, bottom).<sup>15</sup>

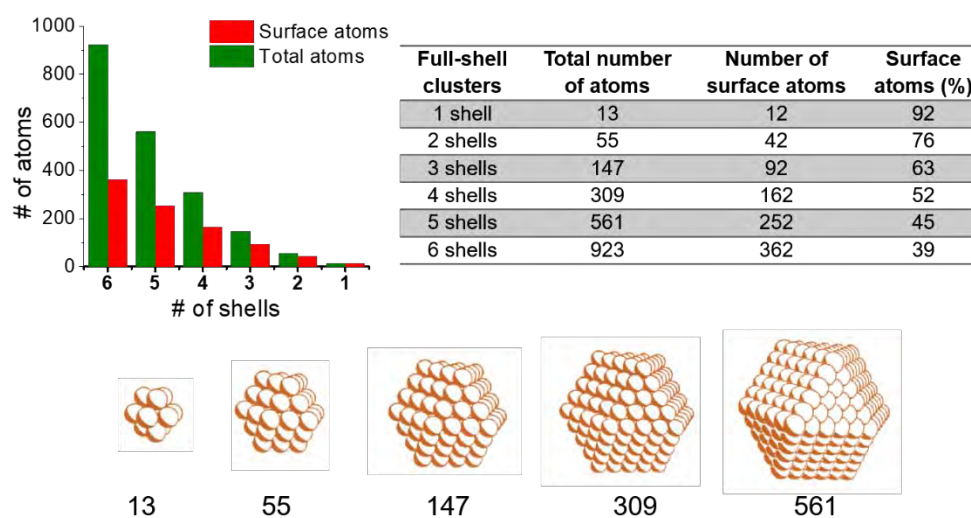


**Figure 4.** Graphical representation of the increased importance of the surface when the size is decreased, jointly with tabulated values (top). Adapted from ref. 12. Idealized representation of hexagonal close-packed full-shell “magic number” clusters (bottom). Adapted from ref. 15. The number of atoms in the  $n^{\text{th}}$  shell is  $10n^2 + 2$ . The number of atoms in the total cluster is  $(5/3)n(n + 1)(2n + 1) + 2n + 1$ .

### 1.3.2 Stabilization of NPs

The surface of NPs is the place where the interactions or bonds between atoms are interrupted.<sup>14</sup> Atoms at the surface have fewer neighbouring atoms than the atoms in the bulk of the material, so they have higher energy and less stability. It is said that surface atoms show dangling bonds (unsaturated), which have to be compensated by chemical or physical processes. The higher the surface/volume ratio, the more important becomes the surface energy. This surface energy can be decreased by reaction of the NPs with other species or molecules or even by accommodating adsorbed species. Therefore, one of the key points in the synthesis of NPs is to get sufficient stabilization to avoid aggregation, coalescence, sedimentation, etc., which lead to a decrease in the exposed surface of the material, lowering its surface reactivity. There are different ways to stabilize colloidal systems (Fig. 5):

- Stabilization by electrostatic interactions: NPs presenting charges on the surface can incorporate a layer of counterions from the solvent molecules around (electronic double layer), leading to a repulsion between NPs that limits their aggregation. It is worth mentioning that the addition of salts may decrease the

width of this double layer, so NPs can approach more one another at such an extent to lose the stability by coalescence.<sup>16,17,18,19</sup>

- Stabilization by steric hindrance: diverse molecules (*i.e.* polymers,<sup>20</sup> surfactants,<sup>21</sup> ligands,<sup>20,22</sup> dendrimers<sup>23</sup> or ionic liquids<sup>24</sup>) can be anchored to the surface of the NPs to create a protective layer and avoid the coalescence between individual NPs.
- Electrosteric stabilization: this method combines both electrostatic interactions and steric hindrance, being an efficient way to stabilize NPs.<sup>25</sup>

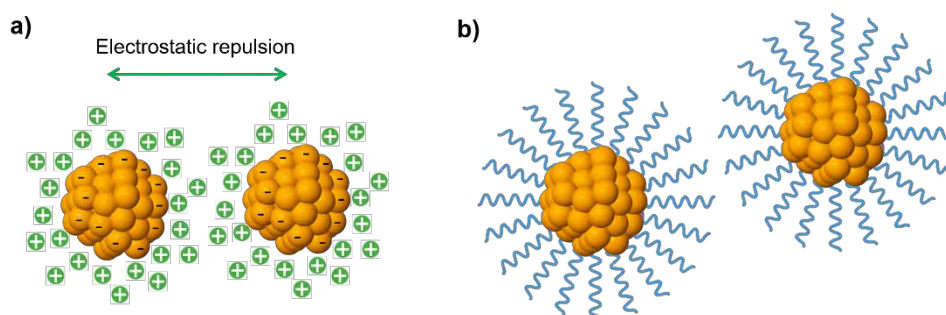


**Figure 5.** Schematic representation of the stabilization of NPs by electrostatic interactions (a) and steric hindrance (b).

However, it is important to take into account that the addition of ligands to stabilize NPs can have key effects on their catalytic activity (*i.e.* ligands should stabilize the NPs enough to avoid aggregation but not too much, to avoid totally killing their surface reactivity). The different role of the ligands on the catalytic activity of NPs towards WS will be discussed in Section 1.4.4.

### 1.3.3 Synthesis of NPs

The synthetic methodologies to obtain nanomaterials can be divided in two different approaches: the top-down (*i.e.* physical methods) and the bottom-up (*i.e.* chemical methods) approaches (Fig. 6). The top-down approach consists in the synthesis of nanomaterials starting from a bulk material and going down in size. In the bottom-up approach, the nanomaterials are synthesized from the assembly of individual metal atoms coming from single-metal atom species (like metal salts or complexes).



The bottom-up approach allows higher molecular or atomic precision. Contrarily, the precise control over the size and shape is not easy when using the top-down approach, which is normally more used for large scale production as it is a faster method.

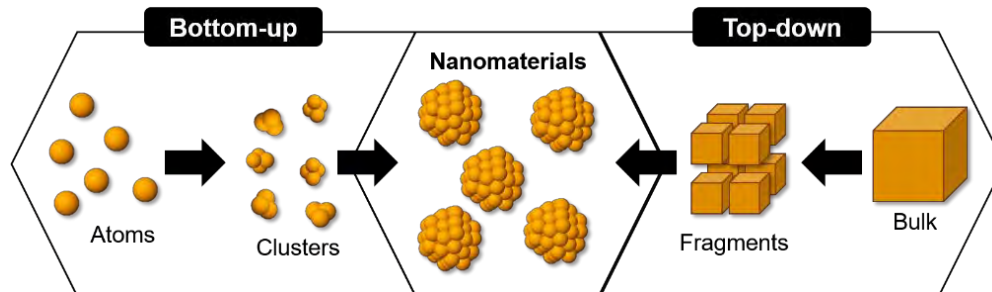


**Figure 6.** Schematic overview of the top-down and bottom-up approaches for synthesizing nanomaterials.

Among the top-down methods, we can find mechanical milling, laser ablation and ion sputtering (Fig. 7). In mechanical milling we can find ball milling,<sup>26</sup> consisting in the reduction of the particle size of a bulk powder by using a high energy rolling ball impacting the powder. In the laser ablation method,<sup>27</sup> a solid material dispersed in solution is exposed to a laser irradiation to reduce the particle size to the nano-regime, providing a colloidal suspension surrounding the original material. Ion sputtering consists in the vaporization of a solid through sputtering with a beam of inert gas ions, obtaining atom clouds from the target material, which will deposit on substrates like silicon.<sup>28</sup> Lithographic methods using photons, electrons or AFM/STM tips to nanostructure moulds to stamp the nanopattern on surfaces are also considered in this classification. However, the lithographic techniques are more widely used in optical and electronic devices and (bio)sensors.<sup>29,30,31,32,33</sup>

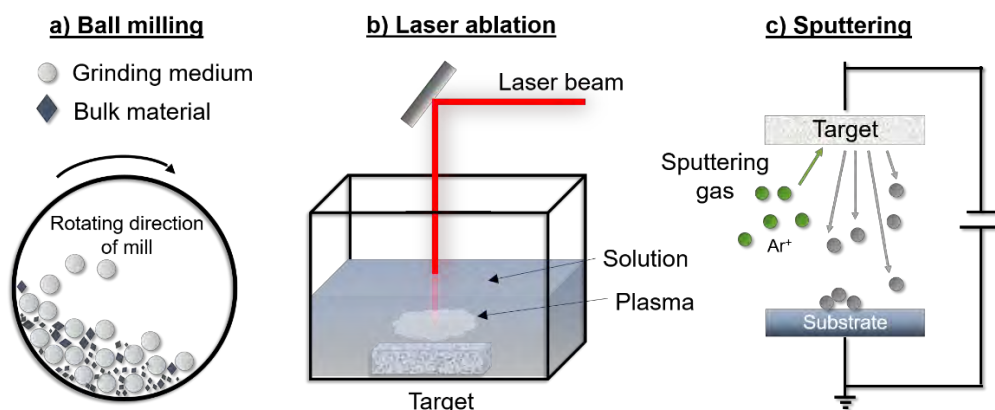


**Figure 7.** Top-down approaches to obtain nanomaterials.



Concerning the bottom-up approach, it is not an obvious task to classify the different synthetic methods and only the most used methodologies are explained below. These can be classified as chemical reactions or energy-assisted reactions.

Among the chemical reactions, one can find:

- Sol-gel method: it consists in the formation of a stable colloidal solution (sol) which becomes a network in a continuous liquid phase (gel) after hydrolysis and condensation reactions (Fig. 8a). The ions of metal alkoxides and alkoxy silanes are used as precursors for the synthesis of colloids. It is most particularly used to obtain metal oxide nanomaterials.<sup>34,35</sup>
- Chemical reduction: it is one of the most commonly used methodologies due to its simplicity and availability. Metal salts are chemically reduced by chemicals such as aluminohydrides, borohydrides, hypophosphites, formaldehyde or salts of oxalic and tartaric acids to form zerovalent metal atoms (Fig. 8b). The nature of the reducing agent is a key factor affecting the size, shape and particle size distribution. Nowadays, processes using a reducer also as stabilizer are widely developed.<sup>36,37,38,39</sup>
- Microemulsion synthesis: this synthetic method is assisted by micelles, normally reverse micelles (*i.e.* hydrophobic tail outside and hydrophilic head in the core) acting as microreactors in an oil phase. Aqueous solutions of metal salts, reducing agents and stabilizers can be encapsulated inside the micelles. When two micelles are mixed by collision, the synthetic reaction takes place (Fig. 8c).<sup>40,41,42</sup>
- Precipitation: it is one of the most ancient techniques to synthesize NPs, in which the reactants are dissolved before adding a precipitating agent to obtain the nanoparticles (Fig. 8d).<sup>43,44</sup>
- Supercritical fluid technology: physicochemical properties of supercritical fluids (SCFs) can be modified between gaseous and liquid states by simply altering the pressure or temperature close to the critical point, providing the opportunity to change the reaction environment like the density, viscosity, diffusivity or surface tension. The most commonly used SCFs are carbon dioxide, nitrous oxide, water, methanol, ethanol, ethane, propane, n-hexane and ammonia. In addition, supercritical fluids rapidly allow exceeding the saturation point of a solute, faster than in liquids, promoting nucleation over crystal growth, yielding to small and narrow distribution

NPs, which can be recovered either as a powder material or in the form of a suspension.<sup>45,46,47,48</sup>

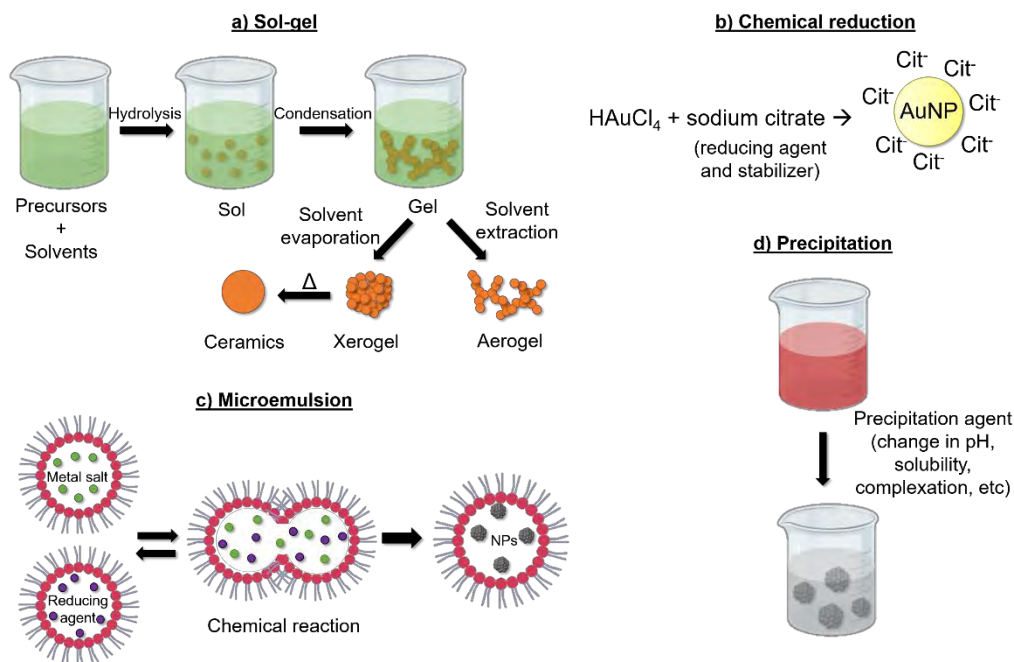


**Figure 8.** Schematic processes for the most used chemical reactions following the bottom-up approach.

Among the energy-assisted synthesis reactions, one can find:

- Physical vapour deposition (PVD) and chemical vapour deposition (CVD) techniques: they consist in the vaporization of a solid or a liquid target material (*e.g.* thermal evaporation) and its further condensation (sputtered deposition) on a substrate. These methods are usually used to produce thin films and coatings. Both methods differ in the sense that in CVD volatile molecules from the target suffer chemical reactions before deposition,<sup>49,50</sup> whereas for PVD do not.<sup>51</sup>
- Hydrothermal/solvothermal methods: a hydrothermal process consists in a chemical reaction in the presence of water at a temperature higher than its boiling temperature (Fig. 9a). The aqueous solution vapours react with the solid material at high pressure and temperature, leading to deposition of small particles.<sup>52,53</sup> The solvothermal method is similar to the hydrothermal one but normally takes place in a non-aqueous solution at relatively high temperatures (*i.e.* above their boiling point, Fig. 9a).<sup>54,55,56</sup>

The polyol process can be classified as a solvothermal reaction in which a high-boiling point polyol (*i.e.* 1,2-hexadecanediol) is used at the same time as solvent, reductant of the metal precursors and stabilizer of the NPs.<sup>57</sup>

- Electrochemical deposition: it consists in inducing chemical reactions in an electrolyte solution by applying voltage (Fig. 9b). Electrochemical deposition is a process where the metallic ions can become a solid metal coating deposited onto the cathode surface if a sufficient amount of electric current passes through the electrolyte solution.<sup>58,59</sup>
- Spray pyrolysis: in spray pyrolysis NP precursors in the vapour form (*i.e.* small droplets) are delivered into a hot reactor by using a nebulizer, where reactions take place before collecting the NPs in a precipitator (Fig. 9c).<sup>60</sup> Other types of spray pyrolysis are the ultrasonic spray pyrolysis, in which ultrasounds are used to produce atomized droplets from the precursor solution, forming aerosol droplets which are transported from the atomizer to the reactor furnace by a carrier gas for the formation of the NPs, which are finally collected by a collection system;<sup>61</sup> and the laser pyrolysis, in which the application of laser energy allows the preparation of the NPs upon absorption of the laser energy by the precursor, thereby inducing homogeneous nucleation reactions.<sup>62</sup> A similar process happens in flame pyrolysis, in which gas, liquid or solid precursors are exposed to the flame and allowed to form NPs.<sup>63,64</sup>
- Microwave assisted NPs preparation: a microwave frequency range from 300 MHz to 300 GHz is applied to precursors, homogeneously heating up the solution and leading to the synthesis of NPs.<sup>65,66,67</sup>
- Ultrasound techniques: exposure of liquids to ultrasounds produces alternating expansive and compressive acoustic waves that form oscillating bubbles that hold the ultrasounds energy. At certain conditions the bubbles overgrow, collapsing and releasing concentrated energy immediately, leading to light emission, known as sonoluminescence. The main working principle is that every cavitation bubble serves as a plasma chemical microreactor and offers a highly energetic environment at almost room temperature of the bulk solution.<sup>68,69</sup>
- Photochemical and radiation-chemical reduction: the reactants are irradiated with high energies, leading to the generation of highly active strong reducers (*i.e.* electrons, radicals and excited species). Photochemical synthesis uses lower energies than radiation-chemical processes. The photochemical and radiation-chemical reduction

processes allow obtaining higher purity NPs than the chemical reduction methods.<sup>70,71,72,73,74</sup> In addition, NPs can be obtained in solid-state conditions and low temperatures.

- Thermal decomposition: it consists in the thermal decomposition of metal precursors in boiling organic solvents containing stabilizing surfactants able to stabilize the NPs.<sup>75,76</sup>

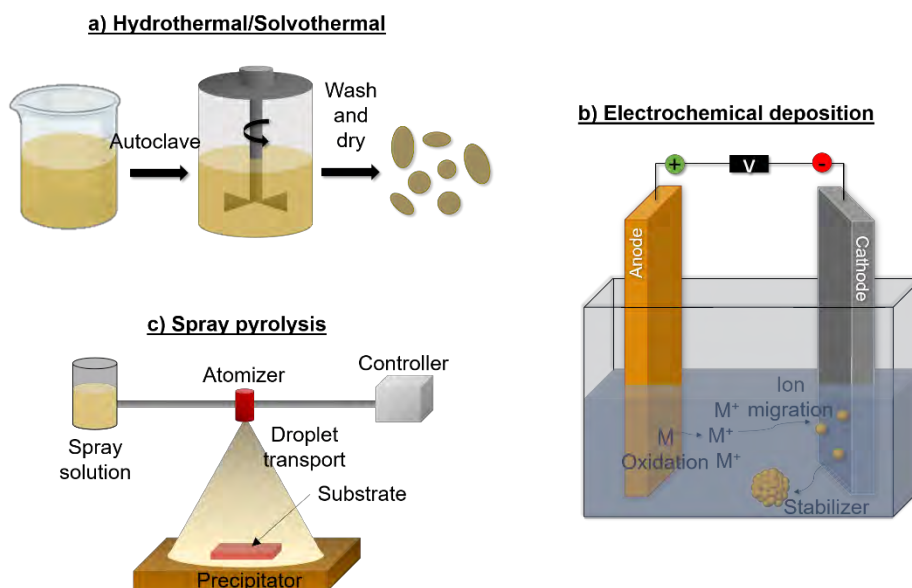


**Figure 9.** Schematic processes for the most used energy-assisted reactions following the bottom-up approach.

Given that the organometallic approach is the method used to prepare the metallic NPs described in this PhD manuscript, this methodology will be explained in detail thereafter.

### 1.3.3.1 Organometallic synthesis

The organometallic method is an efficient and versatile synthetic pathway to obtain well-controlled metal nanostructures from the decomposition of an organometallic complex.<sup>77,78,79</sup> An organometallic complex is constituted by a metal centre and organic molecules (ligands) that are linked to the metal centre through at least one direct metal-carbon bond. An advantage of these complexes is that the metal can be already in the

zero-valent state (like in olefinic complexes) or it can be easily reduced due to high reactivity with dihydrogen.

Organometallic complexes containing diene and triene ligands can be easily decomposed under  $H_2$  at room temperature to generate “naked” metal atoms in the reaction media as well as saturated alkanes, which are not able to bind to metal surfaces and can be easily eliminated under vacuum (step 1, Fig. 10). Then, metal atoms start nucleating, forming small clusters that further grow and form NPs. The formation of NPs from “naked” atoms through the growth of small clusters is controlled by the addition of stabilizers (*i.e.* ligands,<sup>80,81,82,83</sup> polymers,<sup>84,85</sup> supports,<sup>86</sup> ionic liquids<sup>87</sup>) (steps 2 and 3 in Fig. 10, respectively). The stabilizers play a major role during the NP formation process from the early stages by interacting with the metal precursor and defining the nature and relative concentration of the species composing the metal “reservoir” in the reaction media. The organometallic method allows to obtain clean and flawless surface NPs, since only solvent molecules,<sup>88</sup> stabilizing agents<sup>10,89,90,91</sup> and/or hydrides<sup>92</sup> can be present on their surface, which constitutes an advantage to study the influence of the stabilizing agents on their morphology, surface chemistry and related catalytic performance.

Another advantage of this method is that mild conditions are needed, allowing a good control of the NPs formation, obtaining reproducible small and homogeneous sizes. Furthermore, the organometallic precursors can be used in clean procedures, avoiding the presence of possible contaminants in the final nanomaterials surface (*i.e.* salts, halides, main group oxides). In addition, this procedure allows to introduce a support in the reaction media from the beginning of the synthesis, so the NPs can be directly grown on the surface of a heterogeneous support (see *Chapter 4* and *Chapter 5*). However, this methodology has also some disadvantages, such as the difficulty in the synthesis of some of the organometallic precursors and most often their sensitivity to both air and moisture, which makes the organometallic synthesis sometimes difficult to handle.

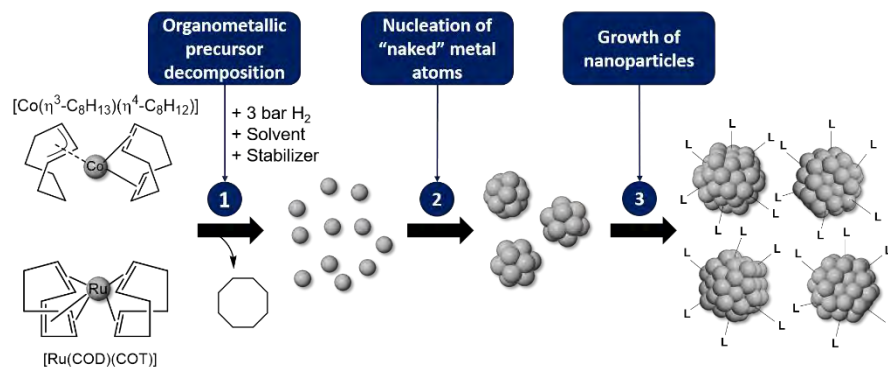


**Figure 10.** Schematic representation of the organometallic method for the synthesis of metal nanoparticles. The stabilizer can be a ligand, a polymer, a dendrimer, a support, etc. Ruthenium and cobalt precursors shown here are the ones used in this work, which can be added in independent reactions to obtain monometallic NPs or together to obtain bimetallic NPs. Numerous other analogous organometallic complexes can be also used.

### 1.3.4 NPs for electrocatalysis

The application of nanomaterials in electrocatalysis is a research field which has been exponentially growing in recent years, as evidenced by the rapid increase in the number of publications on this subject. Numerous studies concern the engineering of electrocatalysts to obtain high catalytic activities and/or to improve the reaction rate.<sup>93,94</sup>

As previously explained, electrochemical cells are used to study WS in a simplified manner. These cells consist of a set of components that have to work in a harmonized manner: a water oxidation catalyst (WOC) in the anode, a hydrogen evolution catalyst (HEC) in the cathode and a proton-exchange membrane (PEM) to physically separate the two half reactions and safely produce and store  $\text{O}_2$  and  $\text{H}_2$  in independent compartments (Fig. 11).

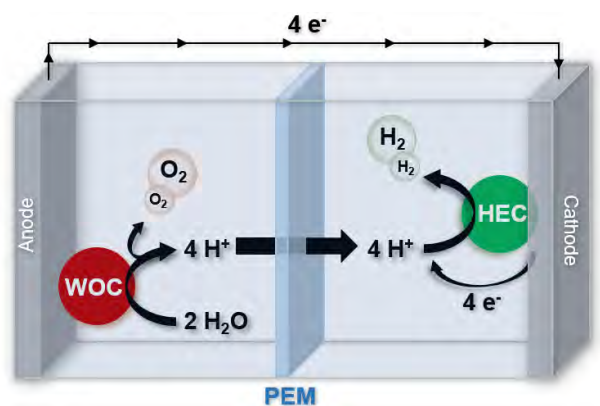


**Figure 11.** Schematic representation of an electrochemical cell for studying water splitting.

The implementation of highly active and robust WOCs and HECs is essential to decrease the energy barrier of the overall WS reaction. Although WOCs and HECs can be molecular complexes or nanostructured materials, due to the scope of this PhD work we will focus only in the engineering of nanomaterials to access highly active and robust electrocatalysts. Two major approaches have been used to improve the performance of electrocatalysts: first, the increase of the number of exposed active sites both by increasing the catalyst loading or the nanostructuring degree of the materials, and second, by increasing the intrinsic activity of the active sites. However, there is a limit when the catalyst loading is too high because it negatively affects mass transport and/or charge transfer between the catalyst and the supporting electrode (*i.e.* many catalyst units are not in direct contact with the electrode, hampering their mutual electronic communication). Consequently, there is always an intermediate loading that results in the best performance. In addition, reducing the catalyst loading is interesting from an economic viewpoint to decrease the overall cost of the system.

A list of the most useful approaches followed to increase the performance of nanostructured electrocatalytic materials can be found below (Fig. 12):

- Increase the nanostructuring degree of the materials: as explained previously, the surface of the catalytic materials becomes more prominent when their size decreases, presenting higher surface/volume ratios. One commonly used approach to increase the number of exposed active sites in catalytic materials is therefore by increasing their nanostructuring degree in order to obtain a high number of surface atoms and defects (such as edges, corners, etc). Interestingly, a high nanostructuring degree allows to decrease the total amount of catalyst used, thus diminishing the overall cost. Beside the advantages provided by the size decrease of the catalyst, the control of the shape is also important, as it can affect the number and nature of exposed active sites for electrocatalysis.<sup>95</sup>
- Use supports: another approach in electrocatalyst development is the use of supports with high surface area. It allows to improve the NP dispersion and reduce their aggregation, thus leading to higher number of exposed active sites.<sup>96,97,98,99,100</sup> The use of conductive supports is an interesting way to improve the charge transfer processes between a nanocatalyst and an electrode.<sup>97,98,99,100</sup> Moreover, from an engineering point of view, supported catalysts that can act



themselves as electrode materials are advantageous systems, since they avoid catalyst deposition onto macroscopic electrodes (*i.e.* glassy carbon, FTO). However, this last approach is still challenging.<sup>101,102</sup>

- Confinement of catalysts in a matrix: the energy levels become discretized when confinement effects are present in nanomaterials, in contrast with continuous energetic bands shown by bulk materials. These changes in energetic levels can also positively affect the catalytic behaviour of the final materials by the formation of unique microenvironments for the active sites.<sup>103,104</sup>
- Use bimetallic catalytic systems: the addition of a second metal can have beneficial electronic effects, since chemical environment changes of the metal centres in NPs lead to enhanced catalytic performances. Furthermore, alloying can decrease the adsorption energy of the reactants on top of the nanomaterials, thus facilitating the catalytic reaction. Core-shell systems can also display more favourable energetic levels and provide improved electrocatalysts.<sup>105,106,107,108</sup>

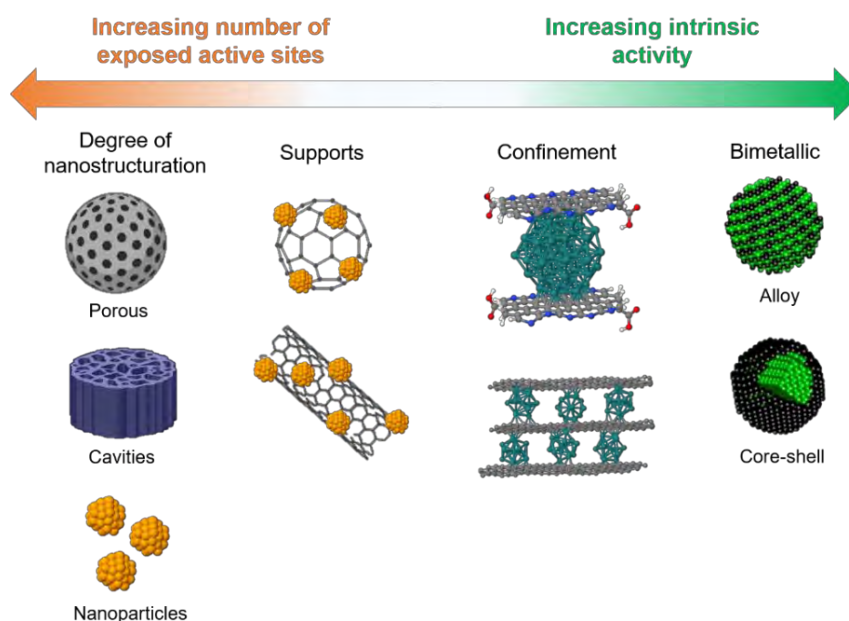


**Figure 12.** Catalyst engineering approaches to obtain increased electrocatalytic activities.

In recent years, the combination of complementary theoretical and experimental studies has led to breakthrough approaches to predict/study the catalytic activity of nanomaterials.<sup>109</sup> In this sense, theoretical calculations allow an atomic-scale description, usually provided by first-principle methods such as density functional theory (DFT). These calculations follow the idea of the Sabatier Principle, which states that the best



reaction rate corresponds to an optimal adsorption strength onto a certain surface. However, it is still difficult to accurately describe ligand-stabilized NPs to explore their surface chemistry. This difficulty arises from the partial mobility and/or lability of surface ligands stabilizing the nanosized metal core, which is even difficult to define by experimental techniques. However, some theoretical concepts such as adsorption free energy, microkinetic models, volcano plots and “d-band centres” have been recently accepted for (semi)quantitative evaluation/description of the performance of synthesized electrocatalysts, especially for HER.<sup>110</sup> In fact, the hydrogen adsorption Gibbs free energy ( $\Delta G_{H^*}$ ) is a well-accepted descriptor to theoretically predict the catalytic activity for HER in solid electrodes. Analogously, standard free energy of HO\* oxidation ( $\Delta G_{O^*} - \Delta G_{HO^*}$ ) is considered for OER. All the theoretical descriptors offer a deeper view on how the electronic structure (metal d-orbital levels) influences the adsorption strength of reactants/intermediates/products on the surface of a given electrode, leading to an approximate overview of the electrocatalytic activity trends (*i.e.* active sites, feasible reaction intermediates), therefore allowing the design and synthesis of improved electrocatalysts.

## 1.4 Water splitting reaction

### 1.4.1 Benchmarking of electrocatalytic activity

Owing to the previous lack of standardised methodologies to compare the activity and stability of different electrocatalysts, Jaramillo *et al.* reported in 2013 a protocol for evaluating the electrochemically active surface area, catalytic activity, stability and faradaic efficiency of different electrocatalysts.<sup>111,112</sup> The most relevant key parameters to take into account according to these authors are stated below:

- X-ray photoelectron spectroscopy (XPS) is the suitable technique for surface analysis in order to explore the elemental composition of the catalysts to relate composition and catalytic performance.
- Electrochemically active surface area (ECSA) calculation. The ECSA can be estimated by two different methods (*i.e.* from cyclic voltammetry (CV) or from electrochemical impedance (EIS) measurements), which can be seen as complementary for achieving more accurate results. The double-layer charge ( $C_{DL}$ )

can be calculated through CV by choosing a potential range in which no faradaic processes occur (typically a 0.1 V potential window centred at the open-circuit potential (OCP)). By this way, all the current in this non-faradaic region is assumed to be due to double-layer charging. The charge current,  $i_c$ , is measured at half potential from CVs at different scan rates. The working electrode should be held at each potential vertex for 10 s prior the next scan. The double-layer charge current is equal to the product of the scan rate,  $v$ , by the electrochemical double-layer capacitance,  $C_{DL}$  (Eq. 4):

$$i_c = vC_{DL} \quad \text{Eq. 4}$$

Plotting  $i_c$  as a function of  $v$  yields a straight line with slope equal to  $C_{DL}$ . The double-layer capacitance can also be measured by EIS in the same non-faradaic region. A sinusoidal potential is applied to the system and the frequency-dependent complex impedance is measured between 100 Hz and 100 kHz, obtaining a Nyquist plot of the real and imaginary components of the electrochemical impedance.

The ECSA is then obtained by dividing the calculated capacitance ( $C_{DL}$ ) by a tabulated value (Eq. 5,  $C_s$  = specific capacitance) that depends on the material and solution used:

$$\text{ECSA [cm}^2\text{]} = \frac{C_{DL}}{C_s} \quad \text{Eq. 5}$$

Finally, the so-called roughness factor (RF) is calculated by dividing the ECSA by the geometrical surface area ( $S$ ) of the electrode (Eq. 6):

$$\text{RF} = \frac{\text{ECSA}}{S} \quad \text{Eq. 6}$$

- Electrocatalytic activity determination: the catalytic performance of each system is measured by CV in a three-electrode electrochemical configuration cell normally at a scan rate of 10 mV/s. Glassy carbon (GC) is generally chosen as the working electrode due to its relative inactivity towards HER and OER at moderate overpotentials. The key figure of merit is the overpotential required to achieve an absolute current density of 10 mA/cm<sup>2</sup> ( $\eta_{10}$ ), which is the approximated value at 10 % solar-to-fuel efficiency for an integrated solar water-splitting device under 1 sun illumination (Eq. 7 and 8):

$$\eta_{10 \text{ (NHE)}} = E_{\text{ref.}} + E_{\text{ref.}}^0 - (0 - 0.059 \times \text{pH}) \text{ for HER} \quad \text{Eq. 7}$$

$$\eta_{10(\text{NHE})} = E_{\text{ref}} + E_{\text{ref}}^0 - (1.23 - 0.059 \times \text{pH}) \text{ for OER} \quad \text{Eq. 8}$$

where  $E_{\text{ref}}$  is the experimental potential obtained to achieve a current density of  $|10 \text{ mA/cm}^2|$ ,  $E_{\text{ref}}^0$  is a tabulated value of each reference electrode vs. NHE and the  $(0 - 0.059 \times \text{pH})$  term is the thermodynamic potential at which each reaction takes place (Fig. 13).

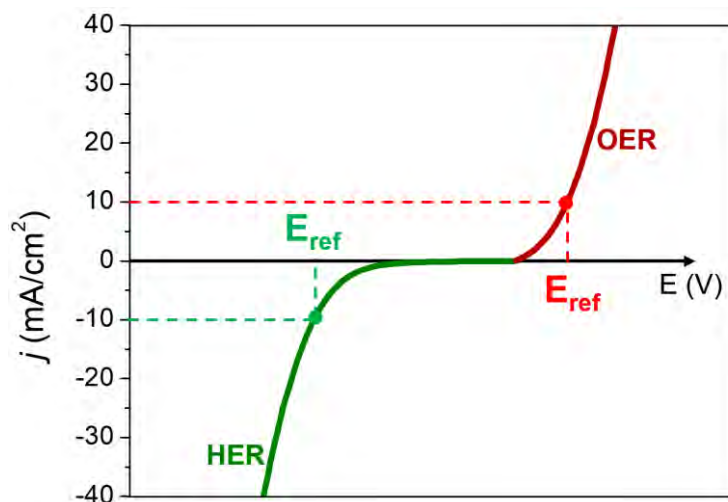


**Figure 13.** Schematic catalytic curves for both HER and OER showing the  $E_{\text{ref}}$  parameter to determine  $\eta_{10}$ .

Another illustrative parameter is the specific current density,  $j_s$ , which can be calculated by dividing the current density per geometric area (S) at a given overpotential,  $j_\eta$ , by the RF (Eq. 9):

$$j_s = \frac{j_\eta}{RF} = \frac{\left(\frac{i_\eta}{S}\right)}{\left(\frac{ECSA}{S}\right)} = \frac{i_\eta}{ECSA} \quad \text{Eq. 9}$$

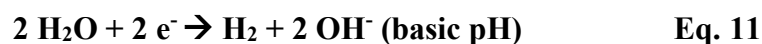
However, due to inaccuracies in determining the ECSA and RF,  $j_s$  is considered only as an approximate guide for comparing specific activities but not to replace  $\eta_{10}$ .

- Electrocatalytic stability assessment: short-term stability is determined by current-controlled electrolysis (*i.e.* chronopotentiometry, CP) at a constant current density of  $|10 \text{ mA/cm}^2|$  for 2 h. If  $\eta_{10 \text{ t}=0 \text{ s}} = \eta_{10 \text{ t}=2 \text{ h}}$ , the catalyst is stable under catalytic conditions for at least 2 h. In contrast, if  $\eta_{10 \text{ t}=0 \text{ s}} < \eta_{10 \text{ t}=2 \text{ h}}$ , it is confirmed that the catalyst is deactivating. Short-term stability (2 h) can be extended to long-term stability (24 h or 48 h) to test the most promising catalysts.

- Faradaic efficiency ( $\epsilon$ ) determination: Jaramillo *et al.* reported the determination of the faradaic efficiency by two different methods, either by using a rotating ring-disk electrode (RRDE) or by using a Clark-type electrode. In the next parts of this work, an oxygen or hydrogen selective Clark electrode has been used for OER and HER catalytic studies, respectively. The Clark probe allows to quantify in the gas phase the amount of O<sub>2</sub> or H<sub>2</sub> generated by the system during a bulk electrolysis, and the faradaic efficiency is obtained by dividing this amount by the maximum theoretical generated amount of H<sub>2</sub> or O<sub>2</sub>, calculated from the total charge passed through the electrode according to the Faraday law.

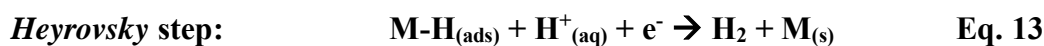
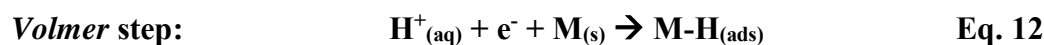
### 1.4.2 Hydrogen evolution reaction (HER)

The HER is the cathodic half-reaction of the overall redox WS reaction in which protons are reduced to dihydrogen. The reaction is stated as follows both at neutral/acidic (Eq. 10) and basic (Eq. 11) pH, respectively:



The hydrogen evolution reaction (HER) on various metal surfaces (M) is conventionally described by the sequence of three elementary steps, as shown in Fig. 14 and equations 12-14. These steps are known as the *Volmer* (electrochemical hydrogen ion adsorption), *Heyrovsky* (electrochemical desorption by protonation of an adsorbed hydrogen atom coupled with an electron transfer) and *Tafel* (chemical desorption by recombination of two adsorbed hydrogen atoms) steps:

**M = surface empty site on catalyst**



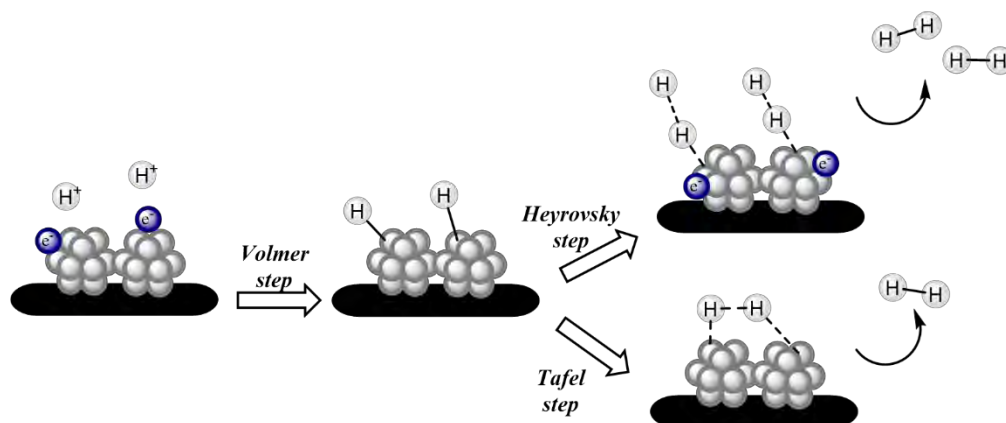


**Figure 14.** Representation of the three steps involved in the HER mechanism on a material surface.

The mechanism of the HER is discussed in terms of kinetic parameters such as the Tafel slope, which is experimentally obtained by plotting the overpotential vs. the logarithm of the absolute value of the current density,  $|j|$ , obtaining the following Tafel equation (Eq. 15):<sup>113,114,115</sup>

$$\eta = b \log |j| + a \quad \text{Eq. 15}$$

The Tafel slope ( $b$ ) allows defining the rate determining step (rds) of the catalytic reaction. Three different rds are possible for HER: Volmer, Heyrovsky and Tafel. A specific Tafel slope value can be attributed to each rds independently of the magnitude of the catalytic current. Thus, according to the literature,<sup>116</sup> Tafel slopes  $\approx 120$  mV/dec are attributed to catalysts with the *Volmer* step as the rds, whereas Tafel slopes  $\approx 40$  and  $\approx 30$  mV/dec are attributed to *Heyrovsky* and *Tafel* steps as rds, respectively. In addition, another parameter related to the intrinsic kinetic activity of each catalyst could be extracted from the Tafel equation. This value is the exchange current density ( $j_0$ ), which is defined as the current density in the absence of net electrolysis and at  $\eta = 0$  V.

Using the experimental  $j_0$  and the free energy of hydrogen adsorption values ( $\Delta G_{H^*}$ ), Parsons demonstrated a clear relationship between  $\log j_0$  and  $\Delta G_{H^*}$  in the form of a “volcano” curve (Fig. 15).<sup>117</sup> This volcano relationship reflects the Sabatier principle, according to which it is assumed that optimal surfaces are those exhibiting moderate binding energies of reaction intermediates, that is,  $\Delta G_{H^*} = 0$ . In this way, the two branches of the volcano can be interpreted as follows. In the left branch, the M-H\* binding is relatively strong ( $\Delta G_{H^*} < 0$ ), so the desorption (Heyrovsky/Tafel) step will limit the

reaction rate. Contrarily, in the right branch, the M-H\* binding is relatively weak ( $\Delta G_{H^*} > 0$ ), being in this case the adsorption (Volmer) step the rds. In other words, if the interaction between the NPs surface and H is too weak, the hydrogen atom will fail to bind to the catalyst and the proton reduction reaction won't take place. On the other hand, if the interaction is too strong, the H<sub>2</sub> product won't be easily dissociated from the surface.

An example of volcano plot for HER<sup>118</sup> on the surface of different metals,<sup>119,120</sup> alloy compounds<sup>121</sup> and non-metallic materials<sup>122</sup> is shown in Fig. 15. Materials showing a behaviour close to the top of the plot are potentially the ones showing higher activity and efficiency. As expected, platinum is located near the top, as it is the state-of-the-art metal for HER in acidic media. However, catalysts consisting of pseudomorphic Pd monolayers on a single-crystal PtRu substrate have shown even better HER catalytic activity than pure Pt catalysts.<sup>121</sup>

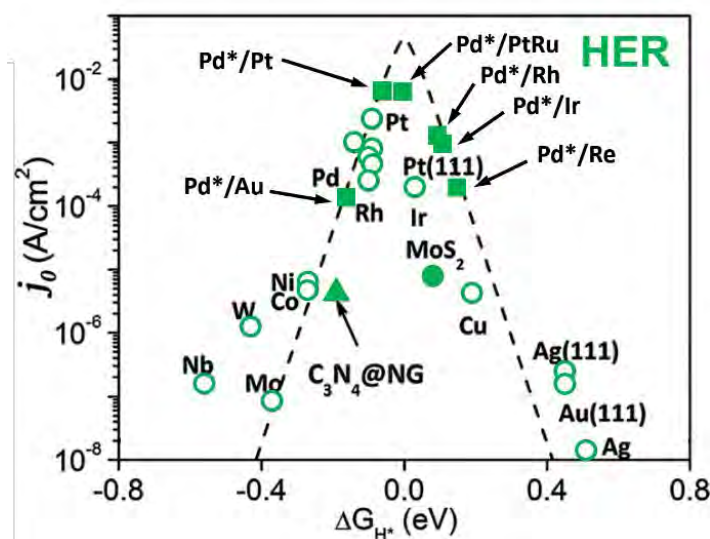
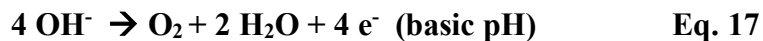
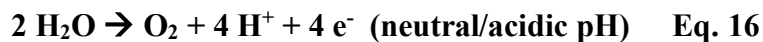


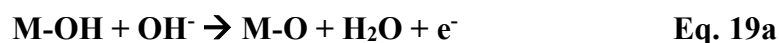
**Figure 15.** Volcano-like behaviour of experimental  $j_0$  as a function of hydrogen adsorption Gibbs free energy ( $\Delta G_{H^*}$ ) for HER on the surface of various metals, alloy compounds and non-metallic materials. Adapted from ref. 118. Data collected from refs. (119, 120, 121, 122).

### 1.4.3 Oxygen evolution reaction (OER)

The OER is the anodic half-reaction of the overall redox WS reaction in which water is oxidized to molecular oxygen. The reaction is stated as follows both at neutral/acidic (Eq. 16) and basic (Eq. 17) pH, respectively:



The OER is considered as the bottle neck reaction of WS as it is a highly endergonic and mechanistically complex reaction because it requires the breaking of four O-H bonds and the formation of a double O=O. Taking profit of the mechanistic knowledge accumulated from molecular catalysis, different mechanisms have been proposed for OER happening at the surface of solid materials under alkaline conditions (Fig. 16 and Eq. 18-20b.2). A common first step is the water coordination ( $\text{OH}^-$ ) to a surface metal centre to form a M-OH species (Eq. 18). The following step is the formation of a M-O species either by an  $\text{OH}^-$  attack (Eq. 19a), by disproportionation of two M-OH species (Eq. 19b) or by a proton-coupled oxidation of the active site (Eq. 19c). Then, the M-O species can decompose either in a bimolecular process to directly release an  $\text{O}_2$  molecule (Eq. 20a) or by a larger pathway in which the M-O species suffer an  $\text{OH}^-$  attack (Eq. 20b), forming a MOOH species, which will be then also attacked by an  $\text{OH}^-$  to form a  $\text{MOO}^-$  species (Eq. 20b.1) before the final release of an  $\text{O}_2$  molecule (Eq. 20b.2).



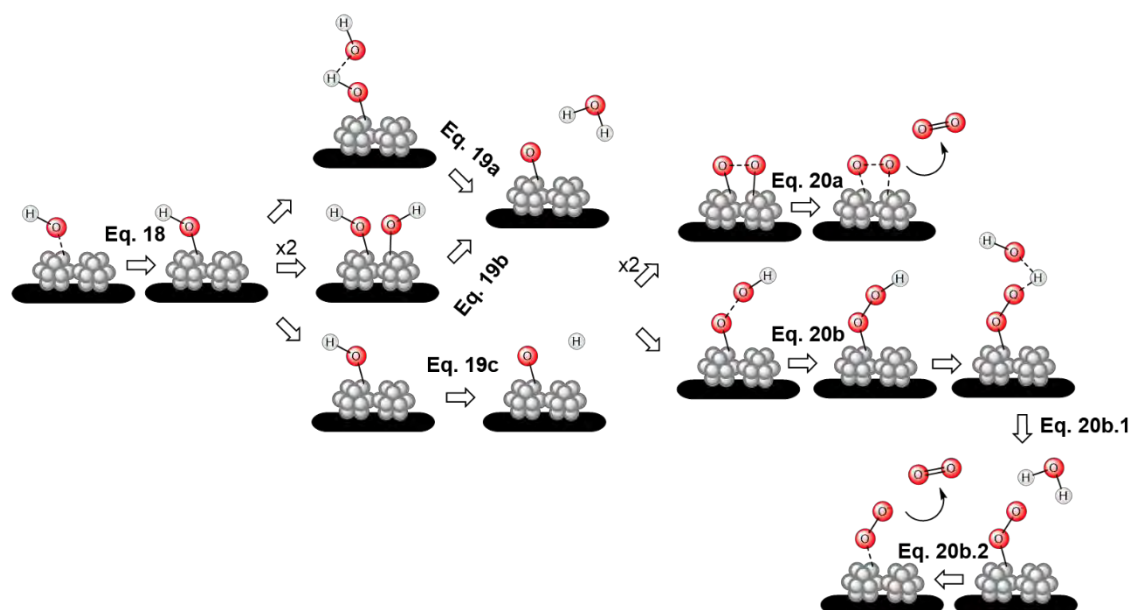


**Figure 16.** Representation of the possible steps involved in the OER mechanism on a material surface at basic pH.

In contrast to the HER, in the OER the relation between Tafel slopes and the rds is not as obvious. However, according to the literature,<sup>115</sup> Tafel slopes  $\approx 120$  mV/dec are attributed to catalysts with the formation of  $\text{M-OH}$  species (Eq. 18) as the rds. In addition, when the formation of  $\text{M-O}$  species by an  $\text{OH}^-$  attack (Eq. 19a) or the formation of  $\text{MOO}^-$  species (Eq. 20b.1) are the rds, Tafel slopes of 30 mV/dec are observed. Finally, when the formation of  $\text{MOOH}$  species from an  $\text{OH}^-$  attack (Eq. 20b) and the release of  $\text{O}_2$  molecules from a  $\text{MOO}^-$  species (Eq. 20b.2) are the rds, Tafel slopes of 40 mV/dec and 22-40 mV/dec are found, respectively.

As stated above for the HER, electrocatalytic trends are also visible in volcano-type plots for OER by using the standard free energy of  $\text{HO}^*$  oxidation ( $\Delta G_{\text{O}^*} - \Delta G_{\text{HO}^*}$ ) as the universal descriptor instead of  $\Delta G_{\text{H}^*}$  and the negative value of the theoretical  $\eta$  value instead of  $j_0$ .<sup>123</sup> Examples of volcano-like plots for perovskites are shown in Fig. 17a, whereas rutiles, anatase,  $\text{Co}_3\text{O}_4$  and  $\text{Mn}_x\text{O}_y$  oxides are shown in Fig. 17b. For perovskites, the theoretical overpotential trends are in agreement with experimental overpotentials at  $10 \text{ mA/cm}^2$  obtained by Bockris *et al.*<sup>124</sup> and Y. Matsumoto *et al.*<sup>125</sup> Similar trends have also been found comparing theoretical and experimental values of overpotentials for oxides other than perovskites (Fig. 17b).<sup>125</sup>



In this way, even though obtaining relationships between experimental and theoretical values is still a challenge due to a lot of parameters affecting the system in the experimental set-ups, it is possible to compare general trends in OER activities for different oxides, being again the most active materials the ones standing on-top of the volcano plots.

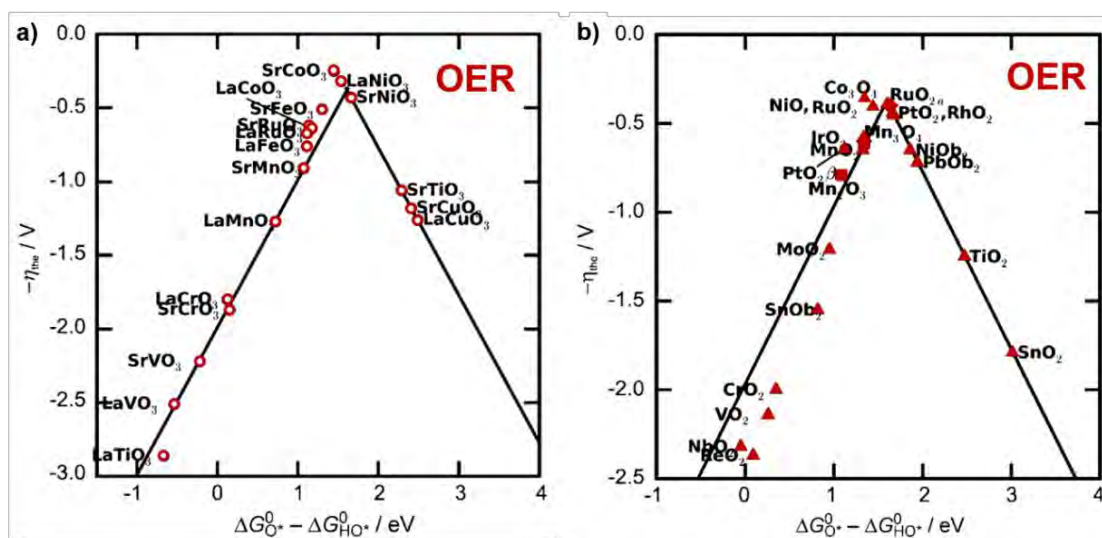


**Figure 17.** Volcano-like behaviour of the negative values of theoretical overpotentials for OER as a function of the standard free energy of  $HO^*$  oxidation ( $\Delta G_{O^*}^0 - \Delta G_{HO^*}^0$ ) for perovskites (a) and rutiles, anatase,  $Co_3O_4$  and  $Mn_xO_y$  oxides (b). Adapted from ref. 118. Data collected from refs. (124, 125).

#### 1.4.4 Surface-functionalized NPs for WS

In addition to the previous approaches to improve the activity of the nanocatalysts (section 1.3.4), the ligands used as stabilizers can coordinate at the metal surface and thus influence the electroactivity and stability of the nanocatalysts. The ligand effect can be achieved by different ways, as exposed below.

To begin with, the role of dangling non-coordinated free carboxylate groups (second coordination sphere) as proton transfer relays near the catalytic centres was first demonstrated in molecular complexes towards OER.<sup>126</sup> This second coordination effect is based on the ability of carboxylate ligands to shuttle protons from the catalyst surface, thereby accelerating the necessary deprotonation process of water/hydroxide ligands to achieve  $O_2$  formation. A very interesting example of such an effect can be found in a recent work by Sun and collaborators using as catalyst a Fe/Ni 1:9 terephthalate

coordination polymer electrochemically deposited as an amorphous film on top of nickel foam (NiFeCP/NF).<sup>127</sup> This work reports on the crucial role of free carboxylate ligands from terephthalic acid (TPA) in efficiently driving the rds of OER at basic pH, a concerted proton-electron transfer process (c-PET) and the assistance of the TPA ligands in deprotonating water and hydroxide substrates bonded to the metal active sites. In contrast, an analogous catalytic system without TPA ligands, namely NiFe layered double hydroxide (NiFe LDH), led to a poorer OER performance due to the lack of assisting deprotonated TPA ligands, this catalyst requiring the addition of an external base such as phosphate to remove protons from coordinated water or hydroxide substrates on the metal active sites. Thus, in NiFeCP/NF the TPA ligands serve as proton transfer relays to the external base added in the medium, such as phosphate. Furthermore, XPS, IR and Raman data confirm the decoordination of some TPA ligands from the metals during OER, thus providing additional free uncoordinated carboxylate groups that play the role of an internal base and allow creating new available metal hydroxide sites.

Proton transfer second coordination effects have also been proposed recently by the same group for covalently modified 1-4 nm NiO NPs through an O-C bond with the strong electron withdrawing pentafluorophenyl ( $-C_6F_5$ ) substituent.<sup>128</sup> Apart from the direct electronic effects imparted by the introduced  $C_6F_5$  ligand (first coordination effects), the outstanding OER performance of the NiO- $C_6F_5$  catalyst has also been assigned to the specific proton affinity of the  $C_6F_5$  group, which promotes proton shuttling, accelerating the deprotonation of water in the formation of the NiOOH starting key intermediate species needed for effective  $O_2$  evolution.

On the other hand, the presence of ligands on the NP surface may also lead to electronic changes in the metal core, affecting the electrocatalytic activity of the overall nanomaterial. In fact, the effect of ligands present onto the surface of metal NPs in the M-H bond energy has been described for HER in several works. However, inverse correlations have been proposed between the M-H bond energy and the HER activity of the L-modified NP system. Thus, for face-coordinated porphyrin-modified Au nanoclusters (Au NCs) through an acetylthio bridge ( $CH_3-CO-S-$ ), the HER activity is enhanced thanks to the strengthening of the M-H bond upon S-Au binding as the result of a charge migration from the  $5d_{5/2}$  state of the Au core to the Fermi level, which empties the antibonding state.<sup>129</sup> Also, the beneficial electronic effects in terms of HER activity

of the porphyrin was found to decrease as the distance between the S atoms and the porphyrin ring increases from 3.4 Å (CH<sub>2</sub> bridge between the phenyl ring and the acetylthio functional group) to 4.9 Å (CH<sub>2</sub>-CH<sub>2</sub> bridge). In contrast, for a colloidal dodecylamine-stabilized WSe<sub>2</sub> catalyst, the stronger M-H bond due to the existence of fewer filled antibonding states in presence of the amine was stated to be detrimental for the HER activity, since a stripped sample after treatment with Meerwein's reagent (triethyloxonium tetrafluoroborate) showed an improvement of the HER activity due to a decrease in  $\Delta G_{H^*}$  during the rds.<sup>130</sup>

The beneficial effect of the weakened binding of M-H intermediates towards the HER activity has also been reported for Ir NPs functionalized with 4-ethylphenylacetylene (EPA) in comparison with the same NPs functionalized with 4-ethylphenylthiol (EPT) or with 4-dodecylbenzenesulfonyl azide (DBSA).<sup>131</sup> The authors relate this M-H bond weakening with the intraparticle charge delocalization induced by the conjugated interfacial Ir-C≡C- linkages within the acetylene-bridged system (Ir-C≡), which allows a more effective charge transfer from the Ir core to the acetylene moieties (which elongate from *ca.* 1.20 Å to 1.38 Å) than in the case of the nitrene (Ir=N) and specially mercapto (Ir-S) bridged systems. Analogously, for OER, during its rds water molecules approach the Ir surface and become dissociated into \*H and \*OH adsorbed intermediates in a vertical configuration onto two neighbouring Ir atoms, for whom again the Ir-C≡ system exhibits the lowest energy barriers of all three systems. This explains that the acetylene bridged Ir system is the most active both at alkaline and acidic pH in HER and OER in terms of reduced overpotential ( $\eta$ ), Tafel slope ( $b$ ) and charge transfer resistance, and is also stable at pH 14 (for 20 h) and pH 0 (for 8 h). Concerning the induced electronic effects by the ligands covalently grafted at the NP surface, inverse effects are obviously seen for HER and OER.

Another interesting aspect is the effect of the electron donating/withdrawing capacity of ligands towards the metal activity. In an example by Miller *et al.*, the HER catalytic activity increases with the electron donating ability of the ligands, as can be seen in the progressive diminution of the impedance, the  $\eta_{10}$  and the Tafel slope, and the progressive increase of the TOF at acidic pH along the Cl<sub>2</sub>Ph, BrPh, MeOPh and Et<sub>2</sub>NPh-modified MoS<sub>2</sub> nanosheets series through S-C covalent bonds<sup>132</sup> (from lower to higher electron donating abilities of the substituents), since electron rich metal atoms are needed

for fulfilling the reduction of protons into hydrogen. On the contrary, electron withdrawing substituents are preferred for performing water oxidation, as demonstrated in the MeOPh, HCO<sub>2</sub>Ph, Cl<sub>2</sub>Ph, NO<sub>2</sub>Ph series and C<sub>6</sub>F<sub>5</sub>-modified NiO NPs,<sup>128</sup> with a progressive increase in TOF and current density (*j*) and decrease in overpotential and Tafel slope. Furthermore, apart from direct electronic effects, the C<sub>6</sub>F<sub>5</sub> substituent improves the charge transfer kinetics (diminished resistance) and accelerates the catalyst surface reconstruction through the generation of abundant  $\gamma$ -NiOOH active phases at pH 14, since the more electrophilic Ni sites show a higher tendency to experiment a water nucleophilic attack and subsequent deprotonation. Finally, a work dealing with oxidized CNTs decorated with C=O and C-O functional groups to covalently bind Ru NPs through their oxygen atom has proven that the ketonic C=O groups enable the transfer of more electrons to the CNTs than the epoxide C-O groups because of the higher polarity of the double bond.<sup>133</sup> This accelerated heterointerface charge transfer is beneficial for the HER catalytic activity at pH 14. Furthermore, according to the DFT calculations, the hydrogen adsorption energy for the C=O ligands is optimally closer to 0 eV (-0.10 eV) than in the case of C-O (-0.22 eV), indicating that adsorbed hydrogen atoms can more easily escape from the surface to generate H<sub>2</sub> gas in the case of the C=O functionalization.

Also, as expected, a high electrocatalytic activity of a nanocatalyst should be related to the ability of the reactants (H<sup>+</sup>/H<sub>2</sub>O) to come into contact with the metal surface active sites. Thus, if the reactants meet difficulties to reach the active sites, the reaction will be blocked. This was exemplified using acetate, octanoate and oleate capped CoP NPs.<sup>134</sup> It was reported that the catalytic HER overpotential increased up to 250 mV from acetate to oleate capped CoP NPs because surface ligands prevent catalysis by inhibiting access to surface active sites rather than poisoning the active sites. If the latter were the case, all carboxylates would have been expected to have similar activity regardless of their chain length. A similar study with primary alkyl amines shows a different trend, since the overpotentials for HER do not significantly vary with the increase of the alkyl chain. In this case, proved by ECSA and TGA measurements, the ligand density onto the surface of the NPs is much lower than with the carboxylate analogues, so increasing the carbon chain length of these amines does not significantly impede the protons in the solution from interacting with the surface, since there is still a large amount of bare surface available. In fact, when secondary and tertiary amines are used (dioctyl- and

trioctylamine), the overpotential increases likely because a steric effect due to the increased cone angle appears. In another example, WSe<sub>2</sub> NPs have been prepared using dodecylamine as stabilizing surface ligand.<sup>130</sup> Their HER activity was then compared to that of the same NPs whose surface ligands have been removed by treatment with Meerwein's reagent to generate ligand-free NPs. The removal of the dodecylamine ligands provoked an increase of the ECSA values (from 17.6 to 40.8 cm<sup>2</sup>) and a reduction of the overpotential in HER electrocatalysis in 62 mV, hinting that the coverage of the surface of the NPs with the ligands is blocking the H<sup>+</sup>/H<sub>2</sub>O substrates to reach the active catalytic centres due to steric hindrance effects. Nevertheless, it cannot be discarded that changes in the electronic structure of the NPs also affect the overall catalytic output.

Finally, it is well known that there is an equilibrium between all the surface species in NPs, and therefore the metal-ligand bond strength will affect the quantity of hydrides present at the NP surface, which is a key-factor for the HER activity, observing higher HER activity with increasing number of hydrides. This has been exemplified on Ru NPs prepared through the organometallic approach and stabilized with 4PP,<sup>10</sup> or just methanol and THF used as solvent.<sup>135</sup> For the MeOH/THF stabilized Ru NPs, their porous character together with the weakly coordinating stabilizing agents are claimed to provide a highly accessible metal surface, as demonstrated by the high ECSA values and outstanding HER activity. For the 4PP ligand, experimental and DFT studies show that 4PP does not significantly alter the electronic structure of the catalyst as a result of the moderate adsorption strength of this ligand onto the NP surface. This allows the NPs to have a large number of surface hydrides and, again, an outstanding HER activity. In addition, in a work by Poteau and co-workers, the  $\Delta G_{\text{H}^*}$  values obtained by DFT confirmed that some sites in 4PP-protected RuNPs could be very active towards the HER.<sup>136</sup>

Also, in another work, citrate-capped Au NPs showed an outstanding performance in HER electrocatalysis.<sup>137</sup> In this case, small citrate ligands also present a weak surface bonding energy and provoke a high negative surface charge density. These parameters are described as key factors for the high activity in HER, increasing the number of hydronium ions at the electrochemical interface and, thus, decreasing the activation energy for HER electrocatalysis. Finally, studies on carboxylate- and alkylamine-stabilized CoP NPs<sup>134</sup> have shed some light on the importance of the metal–ligand bond strength in nanostructured HER electrocatalysts. Carboxylate-capped CoP NPs present

higher overpotentials than alkylamine analogues with similar chain lengths. This is attributed to the weaker binding energy of neutral alkylamine ligands, that can move and provoke a lower surface ligand density, and thus a larger number of active sites available for HER electrocatalysis.

In conclusion, nanoparticulated metal-based systems are very promising frameworks for performing the HER and the OER electrocatalytic reactions. Thus, the objectives of this PhD thesis, mainly centred on the applicability of different strategies to tune the interactions between ligands/support/functionalities and metal NPs and the study of their effect towards the HER and the OER electroactivity, will be stated in the following chapter.

## **1.5 References**

- <sup>1</sup> <https://worldpopulationreview.com/es>
- <sup>2</sup> Global Climate Change: Vital signs of the planet. Retrieved May, **2021**, from <https://climate.nasa.gov/causes/>
- <sup>3</sup> NOAA Climate.gov
- <sup>4</sup> Global Climate Change: Vital signs of the planet. Retrieved May, **2021**, from <http://climate.nasa.gov/evidence/>
- <sup>5</sup> U.S. Energy Information Administration (Oct 2008)
- <sup>6</sup> M.A. Rosen and S. Koochi-Fayegh, *Energ. Ecol. Environ.* **2016**, 1, 10–29.
- <sup>7</sup> R.L. House, N.Y.M. Iha, R.L. Coppo, L. Alibabaei, B.D. Sherman, P. Kang, M.K. Brennman, P.G. Hoertz and T.J. Meyer, *J. Photochem. Photobiol. C* **2015**, 32–45.
- <sup>8</sup> N. Cox, D.A. Pantazis, F. Neese and W. Lubitz, *Interface Focus* **5** **2015**, 20150009.
- <sup>9</sup> U. Maitra, S.R. Lingampalli and C.N.R. Rao, *Current Science* **2014**, 106, 4, 518-527.
- <sup>10</sup> J. Creus, J. De Tovar, N. Romero, J. García-Antón, K. Philippot, R. Bofill and X. Sala, *ChemSusChem* **2019**, 12, 2493.
- <sup>11</sup> X. Elias, Q. Liu, C. Gimbert-Suriñach, R. Matheu, P. Mantilla-Perez, A. Martinez-Otero, X. Sala, J. Martorell and A. Llobet, *ACS Catal.* **2016**, 6(5), 3310-3316.
- <sup>12</sup> K. Philippot and Philippe Serp, *Nanomaterials in Catalysis* 2013 Wiley VCH Verlag GmbH & Co. kGaA, Boschstr. 12, 2013. ePDF ISBN: 978-3-527-65690-5
- <sup>13</sup> D. Astruc, *Nanoparticles and Catalysis*, Wiley-VCH Verlag GmbH & Co. KGaA. ISBN: 978-3-527-31572-7
- <sup>14</sup> R. Pool, *Science* **1990**, 248, 1186-1188.
- <sup>15</sup> G. Schmid, *Endeavour* **1990**, 14, 172–178.
- <sup>16</sup> S. Kumar, K.S. Gandhi and R. Kumar, *Ind. Eng. Chem. Res.* **2007**, 46, 3128-3136.
- <sup>17</sup> V. Merk, C. Rehbock, F. Becker, U. Hagemann, H. Nienhaus and S. Barcikowski, *Langmuir* **2014**, 30, 4213-4222.
- <sup>18</sup> G. Viau, P. Toneguzzo, A. Pierrard, O. Acher, F. Fiévet-Vincent and F. Fiévet, *Scr. Mater.* **2001**, 44, 2263.
- <sup>19</sup> S. Roux, B. Garcia, J.L. Bridot, M. Salome, C. Marquette, L. Lemelle, P. Gillet, L. Blum, P. Perriat and O. Tillement, *Langmuir* **2005**, 21, 2526–2536.
- <sup>20</sup> T. Ayvali, P. Lecante, P.F. Fazzini, A. Gillet, K. Philippot and B. Chaudret, *Chem. Commun.* **2014**, 50, 10809.
- <sup>21</sup> E. Guyonnet Bilé, E. Cortelazzo-Polisini, A. Denicourt-Nowicki, R. Sassine, F. Launay and A. Roucoux, *ChemSusChem* **2012**, 5, 91.



- <sup>22</sup> K. Pelzer, O. Vidoni, K. Philippot, B. Chaudret and V. Collière, *Adv. Funct. Mater.* **2003**, 13, 118.
- <sup>23</sup> C. Ornelas, L. Salmon, J. Ruiz Aranzaes and D. Astruc. *Chem. Commun.* **2007**, 46, 4946.
- <sup>24</sup> T. Gutel, C. Santini, K. Philippot, A. Padua, K. Pelzer, B. Chaudret, Y. Chauvin and J.M. Basset, *Mater. Chem.* **2009**, 19, 3624–3631.
- <sup>25</sup> G. Schmid and A. Lehnert, *Angew. Chem., Int. Ed. Engl.* **1989**, 28, 780–781.
- <sup>26</sup> M. Ullah, M.E. Ali and S.B.A. Hamid, *Rev. Adv. Mater. Sci.* **2014**, 37, 1-14
- <sup>27</sup> T. Wang, Y. Song, C. Liu, X. Wang, L. Lin, W. Liu and N. Zhang, *Opt. Laser Technol.* **2021**, 134, 106651.
- <sup>28</sup> Y.K. Mishra, S. Mohapatra, D. Kabiraj, B. Mohanta, N.P. Lalla, J.C. Pivin and D.K. Avasthi, *Scr. Mater.* **2007**, 56, 629-632.
- <sup>29</sup> L. Chen, X. Wei, X. Zhou, Z. Xie, K. Li, Q. Ruan, C. Chen, J. Wang, C.A. Mirkin and Z. Zheng, *Small* **2017**, 1702003.
- <sup>30</sup> L. Zhang, X. Zhong, E. Pavlica, S. Li, A. Klekachev, G. Bratina, T.W. Ebbesen, E. Orgiu and P. Samorì, *Nat. Nanotechnol.* **2016**, 11, 900-906.
- <sup>31</sup> H. Hillmer, C. Woidt, A. Istock, A. Kobylenskiy, D.T. Nguyen, N. Ahmed, R. Brunner and T. Kusserow, *Nanomaterials* **2021**, 11, 164.
- <sup>32</sup> L. Petti, R. Capasso, M. Rippa, M. Pannico, P. La Manna, G. Peluso, A. Calarco, E. Bobeico and P. Musto, *Vib. Spectrosc.* **2016**, 82, 22-30
- <sup>33</sup> M. Beck, F. Persson, P. Carlberg, M. Graczyk, I. Maximov, T.G.I. Ling and L. Montelius, *Microelectron. Eng.* **2004**, 73-74, 837-842.
- <sup>34</sup> S. S. Owoeye, S. M. Abegunde and B. Oji, *Nano-struct. Nano-Objects*, **2021**, 25, 100625.
- <sup>35</sup> I.M. Factori, J.M. Amaral, P.H. Camani, D.S. Rosa, B. A. Lima, M. Brocchi, E.R. da Silva and J. S. Souza, *ACS Appl. Nano Mater.* **2021**, 4, 7371-7383.
- <sup>36</sup> C.D. De Souza, B.R. Nogueira, M.E.C. M. Rostelato, *J. Alloys Compd.* **2019**, 798, 714-740.
- <sup>37</sup> M. Harada, M. Yamamoto and M. Sakata, *J. Mol. Liq.* **2020**, 311, 113255.
- <sup>38</sup> Z. Arif, A.B. Soni, S.N. Victoria and R. Manivannan, *J. Inst. Eng. India Ser. E* **2019**, 100(1):101-109.
- <sup>39</sup> K. Kusada, H. Kobayashi, T. Yamamoto, S. Matsumura, N. Sumi, K. Sato, K. Nagaoka, Y. Kubota and H. Kitagawa, *J. Am. Chem. Soc.* **2013**, 135, 5496-5496.
- <sup>40</sup> M. Sanchez-Dominguez, K. Pemartin and M. Boutonnet, *Curr. Opin. Colloid Interface Sci.* **2012**, 17, 297-305.
- <sup>41</sup> M. Wen, Q.Y. Liu, Y.F. Wang, Y.Z. Zhu and Q.S. Wu, *Colloids Surf. A Physicochem. Eng. Asp.* **2008**, 318, 238-244.
- <sup>42</sup> M. Sanchez-Dominguez, M. Boutonnet and C. Solans, *J. Nanopart. Res.* **2009**, 11 :1823-1829.



- 
- <sup>43</sup> T. Thilagavathi, D. Venugopal, D. Thangaraju, R. Marnadu, B. Palanivel, M. Imran, M. Shkir, M. Ubaidullah and S. AlFaify, *Mater. Sci. Semicond. Process.* **2021**, 133, 105970.
- <sup>44</sup> L. Mohan, A.V. Avani, P. Kathirvel, R. Marnadu, R. Packiaraj, J. R. Joshua, N. Nallamuthu, M. Shkir and S. Saravanakumar. *J. Alloys Compd.* **2021**, 882, 160670.
- <sup>45</sup> C. Slotowski, S. Marre, O. Babot, T. Toupance and C. Aymonier, *Langmuir* **2012**, 28, 16656-16663.
- <sup>46</sup> X. Ye and C.M. Wai, *J. Chem. Educ.* **2003**, 80, 2, 198.
- <sup>47</sup> K. Byrappa, S. Ohara and T. Adschiri, *Adv. Drug Deliv. Rev.* **2008**, 60, 299-327.
- <sup>48</sup> X.R. Ye, Y. Lin, C. Wang, M.H. Engelhard, Y. Wang and C.M. Wai, *J. Mater. Chem.* **2004**, 14, 908-913.
- <sup>49</sup> X. Li, M. Chi, S.M. Mahurin, R. Liu, Y.J. Chuang, S. Dai and Z. Pan, *Carbon* **2016**, 101, 57-61.
- <sup>50</sup> C. Liang, W. Xia, H. Soltani-Ahmadi, O. Schlüter, R.A. Fischer and M. Muhler, *Chem. Commun.* **2005**, 282-284.
- <sup>51</sup> P.A. Pandey, G.R. Bell, J.P. Rourke, A.M. Sanchez, M.D. Elkin, B.J. Hickey and N.R. Wilson, *Small* **2011**, 7, 22, 3202-3210.
- <sup>52</sup> G. Kesavan, N. Nataraj, S.M. Chen and L.H. Lin, *New. J. Chem.* **2020**, 44, 7698.
- <sup>53</sup> J.A. Darr, J. Zhank, N.M. Makwana and X. Weng, *Chem. Rev.* **2017**, 117, 11125-11238.
- <sup>54</sup> M.K. Carpenter, T.E. Moylan, R.S. Kukreja, M.H. Atwan and M.M. Tessema, *J. Am. Chem. Soc.* **2012**, 134, 8535-8542.
- <sup>55</sup> I. Ahmad, S. Shukrullah, M. Ahmad, E. Ahmed, M.Y. Naz, M.S. Akhtar, N.R. Khalid, A. Hussain and I. Hussain, *Mat. Sci. Semicond. Process.* **2021**, 123, 105584.
- <sup>56</sup> Y. Xie, Y. Qian, W. Wang, S. Zhang and Y. Zhang, *Science* **1996**, 272, 1926-1927.
- <sup>57</sup> F. Fiévet, S. Ammar-Merah, R. Brayner, F. Chau, M. Giraud, F. Mammeri, J. Peron, J.Y. Piquemal, L. Sicard and G. Viau, *Chem. Soc. Rev.* **2018**, 47, 5187-5233.
- <sup>58</sup> L. Jiang, I. Santiago and J. Foord, *Langmuir* **2020**, 36, 6089-6094.
- <sup>59</sup> M. Helen, M. Fichtner and M.A. Reddy, *Electrochem. Commun.* **2020**, 120, 106846.
- <sup>60</sup> M. Shariq, B. Friedrich, B. Budic, N. Hodnik, F. Ruiz-Zepeda, P. Majeric and R. Rudolf, *ChemistryOpen* **2018**, 7, 533-542.
- <sup>61</sup> P. Majeric and R. Rudolf, *Materials* **2020**, 13, 3485.
- <sup>62</sup> J. Sourice, A. Quinsac, Y. Leconte, O. Sublemontier, W. Porcher, C. Haon, A. Bordes, E. De Vito, A. Boulineau, S.J.S. Larbi, N. Herlin-Boime and C. Reynaud, *ACS Appl. Mater. Interfaces* **2015**, 7, 6637, 6644.
- <sup>63</sup> F. Meierhofer and U. Fritsching, *Energy Fuels* **2021**, 35, 5495-5537.
- <sup>64</sup> A.J. Gröhn, S.E. Pratsinis, A. Sánchez-Ferrer, R. Mezzenga and K. Wegner, *Ind. Eng. Chem. Res.* **2014**, 53, 10734-10742.

- <sup>65</sup> H. Jang, J.R. Lee, S.J. Kim, H. Jeong, S. Jung, J.H. Lee, J.C. Park and R.W. Kim, *J. Colloid Interface Sci.* **2021**, 599, 828-836.
- <sup>66</sup> E. Daublyte, A. Zdaniauskiene, M. Talaikis, A. Drabavicius and T. Charkova, *New. J. Chem.* **2021**, 45, 10952.
- <sup>67</sup> M. Hasanpoor, M. Aliofkhazraei and H. Delavari, *Procedia Mater. Sci.* **2015**, 11, 320-325.
- <sup>68</sup> H. Xu and K. S. Suslick, *ACS Nano* **2010**, 4, 6, 3209-3214.
- <sup>69</sup> A. P. Nagvenkar, I. Perelshtein, Y. Piuanno, P. Mantecca and A. Gedanken, *ACS Omega* **2019**, 4, 13631-13639.
- <sup>70</sup> E. Raudonyte-Svirbutaviciene, A. Neagu, V. Vickackaite, V. Jasulaitiene, A. Zarkov, C.W. Tai and A. Katelnikovas, *J. Photoch. Photobio. A* **2018**, 351, 29-41.
- <sup>71</sup> H. Gu, Y. Yang, J. Tian and G. Shi, *ACS Appl. Mater. Interfaces* **2013**, 5, 6762-6768.
- <sup>72</sup> J. D. Mangadlao, P. Cao, D. Choi and R. C. Advincula, *ACS Appl. Mater. Interfaces* **2017**, 9, 24887-24898.
- <sup>73</sup> K. Ching, T. Fang, X. Chen, S. Liu and C. Zhao, *ACS Sustainable Chem. Eng.* **2019**, 7, 4112-4118.
- <sup>74</sup> T. Okazaki, S. Seino, Y. Matsuura, H. Otake, J. Kugai, Y. Ohkubo, H. Nitani, T. Nakagawa and T.A. Yamamoto. *Radiat. Phys. Chem.* **2017**, 133, 67-71.
- <sup>75</sup> A. Lassenberger, T.A. Grünwald, P.D.J. van Oostrum, H. Rennhofer, H. Amenitsch, R. Zirbs, H.C. Lichtenegger and E. Reimhult. *Chem. Mater.* **2017**, 29, 4511-4522.
- <sup>76</sup> M. Unni, A.M. Uhl, S. Savliwala, B.H. Savitzki, R. Dhavalikar, N. Garraud, D.P. Arnold, L.F. Kourkoutis, J.S. Andrew and C. Rinaldi. *ACS Nano* **2017**, 11, 2284-2303.
- <sup>77</sup> K. Philippot and B. Chaudret, *C. R. Chimie* **2003**, 1019-1034.
- <sup>78</sup> C. Amiens, B. Chaudret, D. Ciuculescu-Pradines, V. Collière, K. Fajerweg, P. Fau, M. Kahn, A. Maisonnat, K. Soulantica and K. Philippot, *New J. Chem.* **2013**, 37, 3374-3401.
- <sup>79</sup> C. Amiens, D. Ciuculescu-Pradines and K. Philippot, *Coordination Chemistry Reviews* **2016**, 308, 409-432
- <sup>80</sup> M. Zahmarkiran, K. Philippot, S. Özkar and B. Chaudret. *Dalton Trans* **2012**, 41, 590.
- <sup>81</sup> L.M. Martínez-Prieto, C. Urbaneja, P. Palma, J. Cámpora, K. Philippot and B. Chaudret, *Chem. Commun.* **2015**, 51, 4647-4650.
- <sup>82</sup> A. Glaria, J. Cure, K. Piettre, Y. Coppel, C.O. Turrin, B. Chaudret and P. Fau, *Chem. Eur. J.* **2015**, 21, 1169-1179.
- <sup>83</sup> J. Cure, Y. Coppel, T. Dammak, P.F. Fazzini, A. Mlayah, B. Chaudret and P. Fau, *Langmuir* **2015**, 31, 1362-1367.
- <sup>84</sup> L.L.R. Vono, C. Broicher, K. Philippot and L.M. Rossi. *Catal. Today.* **2020**, <https://doi.org/10.1016/j.cattod.2020.07.078>

- 
- <sup>85</sup> T. Ayvalı, P.F. Fazzini, P. Lecante, A. Mayoral, K. Philippot and B. Chaudret, *Dalton Trans.* **2017**, 46, 15070–15079
- <sup>86</sup> R. Berthoud, P. Délichère, D. Gajan, W. Lukens, K. Pelzer, J.M. Basset, J.P. Candy and C. Coperet, *J. Catal.* **2008**, 260, 387–391.
- <sup>87</sup> J.D. Scholten, B.C. Leal and J. Dupont, *ACS Catal* **2012**, 2, 184–200.
- <sup>88</sup> R. González-Gómez, L. Cusinato, C. Bijani, Y. Coppel, P. Lecante, C. Amiens, I. del Rosal, K. Philippot and R. Poteau, *Nanoscale* **2019**, 11, 9392-9409.
- <sup>89</sup> J. Creus, S. Drouet, S. Suriñach, P. Lecante, V. Collière, R. Poteau, K. Philippot, J. García-Antón and X. Sala, *ACS Catal.* **2018**, 8, 11094–11102.
- <sup>90</sup> J. De Tovar, N. Romero, S.A. Denisov, R. Bofill, C. Gimbert-Suriñach, D. Ciuculescu-Pradines, S. Drouet, A. Llobet, P. Lecante, V. Colliere, Z. Freixa, N. McClenaghan, C. Amiens, J. García-Antón, K. Philippot and X. Sala, *Mater. Today Energy* **2018**, 9, 506–515.
- <sup>91</sup> E. Martín-Morales, Y. Coppel, P. Lecante, I. del Rosal, R. Poteau, J. Esvan, P. Sutra, K. Philippot and A. Igau, *Chem. Commun.* **2020**, 56, 4059
- <sup>92</sup> K. Pelzer, K. Philippot and B. Chaudret, *Z. Phys. Chem.* **2003**, 217, 1539-1547.
- <sup>93</sup> F. Li, G.F. Han and J.B. Baek, *Acc. Mater. Res.* **2021**, 2, 147-158.
- <sup>94</sup> Z. Xia and S. Guo, *Chem. Soc. Rev.* **2019**, 48, 3265.
- <sup>95</sup> L. Liu and A. Corma, *Chem. Rev.* **2018**, 118, 4981-5079.
- <sup>96</sup> J. Liu, K. He, W. Wu, T.B. Song and M.G. Kanatzidis, *J. Am. Chem. Soc.* **2017**, 139, 2900-2903.
- <sup>97</sup> D. Yang, W. Hou, Y. Lu, X. Wang, W. Zhang and Y. Chen, *ACS sustainable Chem. Eng.* **2019**, 7, 15, 13031-13040.
- <sup>98</sup> J. Wang W. Yang and J. Liu, *J. Mater. Chem. A* **2016**, 4, 4686.
- <sup>99</sup> M. Liu, F. Hof, M. Moro, G. Valentini, F. Paolucci and A. Pénicaud, *Nanoscale* **2020**, 12, 20165.
- <sup>100</sup> W. Zhang, X. Zhang, L. Chen, J. Dai, Y. Ding, L. Ji, J. Zhao, M. Yan, F. Yang, C.R. Chang and S. Guo, *ACS Catal.* **2018**, 8, 8092-8099.
- <sup>101</sup> J. Wang, H. Zhu, D. Yu, J. W. Chen, J.D. Chen, M. Zhang, L.N. Wang and M.L. Du, *ACS Appl. Mater. Interfaces* **2017**, 9, 19756-19765.
- <sup>102</sup> U.Y. Qazi, C.Z. Yuan, N. Ullah, Y.F. Jiang, M. Imran, A. Zeb, S.J. Zhao, R. Javaid and A. W. Xu, *ACS Appl. Mater. Interfaces* **2017**, 9, 28627-28634.
- <sup>103</sup> L. Zhang, H. Chen and Z. Wei, *ChemCatChem* **2021**, 13, 1-19.
- <sup>104</sup> X. Han, Q. Gao, Z. Yan, M. Ji, C. Long and H. Zhu, *Nanoscale* **2021**, 13, 1515-1528.
- <sup>105</sup> N.B. Halck, V. Petrykin, P. Krtil and J. Rossmeisl, *Phys. Chem. Chem. Phys.* **2014**, 16, 13682.
- <sup>106</sup> Z.K. Ghouri, A. Badreldin, K. Elsaid, D. Kumar, K. Youssef and A. Abdel-Wahab, *J. Ind. Eng. Chem.* **2021**, 96, 243-253.

- <sup>107</sup> Q. Song, J. Li, S. Wang, J. Liu, X. Liu, L. Pang, H. Li and H. Liu, *Small* **2019**, 15, 1903395.
- <sup>108</sup> Z.F. Huang, J. Song, K. Li, M. Tahir, Y.T. Wang, L. Pan, L. Wang, X. Zhang and J. J. Zou, *J. Am. Chem. Soc.* **2016**, 138, 1359-1365.
- <sup>109</sup> Z.W. She, J. Kibsgaard, C.F. Dickens, I. Chorkendorff, J.K. Nørskov and T.F. Jaramillo, *Science* **2017**, 355, 146.
- <sup>110</sup> J.K. Nørskov, T. Bligaard, J. Rossmeisl and C.H. Christensen, *Nat. Chem.* **2009**, 1, 37-46.
- <sup>111</sup> C.C.L. McCrory, S. Jung, J.C. Peters and T.F. Jaramillo, *J. Am. Chem. Soc.* **2013**, 135, 16977–16987
- <sup>112</sup> C.C.L. McCrory, S. Jung, I.M. Ferrer, S.M. Chatman, J.C. Peters and T.F. Jaramillo. *J. Am. Chem. Soc.* **2015**, 137, 13, 4347–4357
- <sup>113</sup> J. Tafel, *Zeit. Physik. Chem. 50A* **1905**, 641.
- <sup>114</sup> B.E. Conway and B.V. Tilak, *Electrochim. Acta* **2002**, 47, 3571-3594
- <sup>115</sup> T. Shinagawa, A. Garcia-Esparza and K. Takanebe, *Sci. Rep.* **2015**, 5, 13801.
- <sup>116</sup> A.P. Murthy, J. Theerthagiri and J. Madhavan, *J. Phys. Chem. C* **2018**, 122, 23943–23949.
- <sup>117</sup> R. Parsons, *Trans. Faraday Soc.* **1958**, 34, 1053.
- <sup>118</sup> Y. Zheng, Y. Jiao, M. Jaroniec and S.Z. Qiao, *Angew. Chem. Int. Ed.* **2015**, 54, 52-65.
- <sup>119</sup> J.K. Nørskov, T. Bligaard, A. Logadottir, J.R. Kitchin, J.G. Chen, S. Pandalov and U. Stimming, *J. Electrochem. Soc.* **2005**, 152, J23 – J26.
- <sup>120</sup> T.F. Jaramillo, K.P. Jørgensen, J. Bonde, J.H. Nielsen, S. Horch and I. Chorkendorff, *Science* **2007**, 317, 100 – 102.
- <sup>121</sup> J. Greeley, J.K. Nørskov, L.A. Kibler, A.M. El-Aziz and D.M. Kolb, *ChemPhysChem* **2006**, 7, 1032 – 1035
- <sup>122</sup> Y. Zheng, Y. Jiao, Y. Zhu, L.H. Li, Y. Han, Y. Chen, A. Du, M. Jaroniec and S. Z. Qiao, *Nat. Commun.* **2014**, 5, 3783
- <sup>123</sup> I.C. Man, H.Y. Su, F. Calle-Vallejo, H.A. Hansen, J.I. Martínez, N.G. Inoglu, J. Kitchin, T.F. Jaramillo, J.K. Nørskov and J. Rossmeisl, *ChemCatChem* **2011**, 3, 1159 – 1165.
- <sup>124</sup> J.O. Bockris and T. Otagawa, *J. Electrochem. Soc.* **1984**, 131, 290
- <sup>125</sup> Y. Matsumoto and E. Sato, *Mater. Chem. Phys.* **1986**, 14, 397.
- <sup>126</sup> R. Matheu, M.Z. Ertem, J. Benet-Buchholz, E. Coronado, V.S. Batista, X. Sala and A. Llobet, *J. Am. Chem. Soc.* **2015**, 137, 10786-10795.
- <sup>127</sup> W. Li, F. Li, H. Yang, X. Wu, P. Zhang, Y. Shan and L. Sun, *Nat. Commun.* **2019**, 10, 5074.
- <sup>128</sup> L. Fan, B. Zhang, Z. Qiu, N.V.R.A. Dharanipragada, B.J.J. Timmer, F. Zhang, X. Sheng, T. Liu, Q. Meng, A.K. Inge, T. Edvisson and L. Sun, *ChemSusChem* **2020**, 13, 5901–5909.
- <sup>129</sup> D. Eguchi, M. Sakamoto and T. Teranishi, *Chem. Sci.* **2017**, 9, 261–265.
- <sup>130</sup> D.A. Henckel, O. Lenz and B.M. Cossairt, *ACS Catal.* **2017**, 7, 2815–2820.

- 
- <sup>131</sup> Y. Peng, Q. Liu, B. Lu, T. He, F. Nichols, X. Hu, T. Huang, G. Huang, L. Guzman, Y. Ping and S. Chen, *ACS Catal.* **2021**, 11, 1179–1188.
- <sup>132</sup> E.E. Benson, H. Zhang, S.A. Schuman, S.U. Nanayakkara, N.D. Bronstein, S. Ferrere, J.L. Blackburn and E.M. Miller, *J. Am. Chem. Soc.* **2018**, 140, 441–450.
- <sup>133</sup> J. Yu, Y. Yang, R. Jia, K. Daasbjerg, J. Wang, M. Carraro, Z. Xin, Y. Huang and T. Skrydstrup, *T. Appl. Surf. Sci.* **2020**, 529.
- <sup>134</sup> D. Ung and B.M. Cossairt, *ACS Appl. Energy Mater.* **2019**, 2, 3, 1642–1645.
- <sup>135</sup> S. Drouet, J. Creus, V. Collière, C. Amiens, J. García-Antón, X. Sala and K. Philippot, *Chem. Commun.* **2017**, 53, 85, 11713–11716.
- <sup>136</sup> R. Poteau and I. del Rosal, *Sabatier Principle and Surface Properties of small ruthenium nanoparticles and clusters: case studies 2021* in *Nanoparticles in Catalysis: Advances in Synthesis and Applications*. Eds. K. Philippot and A. Roucoux, XIV edition. Wiley-VCH, Weinheim.
- <sup>137</sup> D. Alba-Molina, A.R. Puente Santiago, J.J. Giner-Casares, E. Rodríguez-Castellón, M.T. Martín-Romero, L. Camacho, R. Luque and M. Cano, *J. Mater. Chem. A* **2019**, 7, 35, 20425–20434.



# 2

## Chapter 2. Objectives

---

After having introduced the reader into the research field of this PhD thesis, *Chapter 2* focuses on the objectives of this work, mainly centred on the study of different strategies to obtain new efficient HER and OER nanoelectrocatalysts. The role of the interactions between ligands/support/functionalities and metal NPs will be examined. In addition, the analysis of metal-metal interactions in bimetallic nanoparticulated systems is also targeted.

---





## **2. OBJECTIVES**

As exposed in *Chapter 1*, climate change, arising from the high emission of CO<sub>2</sub> from fossil fuels combustion, is a serious global matter of concern. Therefore, there is an extreme need to develop new renewable and carbon-free energy sources. In this regard, renewable hydrogen could be considered as a clean energy vector. Mimicking natural photosynthetic processes, our research is focused on the splitting of water molecules into their constitutive elements to obtain O<sub>2</sub> and H<sub>2</sub>. The two involved reactions, the HER and the OER, are mechanistically complex processes with sluggish kinetics. Thus, catalysts are needed to facilitate both reactions. This PhD thesis will be focused on the design of new metal-based nanomaterials that could efficiently fasten the overall water splitting process, aiming at obtaining electrocatalysts with a reduced noble-metal content and better cost-efficiency. Different studies correlating structure and catalytic activity will be performed in order to rationally open new doors to find optimum catalysts to efficiently produce hydrogen in a clean and sustainable way.

In order to achieve the exposed overall goal, the guidelines of this PhD thesis are listed below:

- It is well known that capping ligands can play a key role in the electroactivity of Ru-based nanoparticles in HER. In collaboration with Prof. R. Poteau (Université Toulouse III - Paul Sabatier, Toulouse), this PhD thesis will deal with theoretical density functional theory (DFT) calculations to unravel the most favourable coordination modes of different N-donor pyridinic ligands and to obtain their corresponding hydrogen adsorption free energies ( $\Delta G_{H^*}$ ), a well-accepted descriptor for the HER activity of a catalyst under acidic conditions.
- The deposition of metal nanocatalysts into carbon-based conductive supports can have multiple advantages in HER/OER electrocatalysis such as improved long-term stability (reduced NP aggregation) and better electron-transfer kinetics. In collaboration with Dr. L. M. Martínez (Universitat de València), along this PhD thesis Ru/RuO<sub>2</sub> NPs will be deposited and characterized onto two different reduced graphene oxide supports. In addition, the use of heteroatom-doping into the carbon structures will allow to extract valuable insights about its effect into the nucleation kinetics and stabilization of the NPs during the synthetic procedures. Finally,

electrocatalytic HER studies will be performed to establish a correlation between the different physicochemical properties of the obtained systems and their electrocatalytic behaviour.

- The use of macroscopic and easy to handle carbon supports able to be directly used as an electrode in practical applications is also of interest. Therefore, we envisage the synthesis and characterization of Ru and Co-based NPs supported onto bare and functionalized carbon microfibers produced from cheap and abundant precursors. The presence of different functional groups into the carbon structure, the different synthetic procedures to obtain the metal NPs (*in situ* or *ex situ*) and the effect of different stabilizing solvents/ligands will be evaluated to determine the role of support-catalyst interactions into the final electrocatalytic activities observed.
- The incorporation of a second metal into monometallic NPs to synthesize bimetallic nanoparticulated systems is another interesting strategy to fine-tune the properties of nanomaterials. Therefore, bimetallic Ru-Ni (in collaboration with Dr. L. Peres, LCC-UPS, Toulouse) and Ru-Co nanomaterials will be synthesized and thoroughly characterized with the aim of corroborating the synergistic effects between the different metals both in the morphology and catalytic performance of the as-synthesized nanomaterials.

To achieve these objectives, the organometallic approach will be employed as the general synthetic methodology for all the metal-based electrocatalysts reported in this PhD work. The organometallic method will allow to obtain reproducible small and homogenous NPs with a clean and flawless surface under mild conditions. In addition, this methodology will allow to grow the NPs onto the surface of pre-formed supports of different nature and to combine the decomposition of different organometallic precursors to obtain bimetallic systems of different morphology. The physicochemical properties of the obtained nanomaterials will be studied by means of (HR)TEM, SEM, STEM-HAADF, WAXS, XRD, MAS NMR and ICP-AES/OES, XPS, FT-IR and Raman spectroscopies. The electrocatalytic behaviour of each nanomaterial will be examined through a three-electrode electrochemical set up by examining their HER and OER electrocatalytic behaviour in a separated manner, in order to simplify the analysis of the overall water splitting process.

# 3

## **Chapter 3. DFT calculations on ligand-capped Ru NPs**

---

*Chapter 3* describes the DFT calculations performed for diverse ligand-capped Ru NPs, namely 4'-(4-methylphenyl)-2,2':6',2''-terpyridine (RuNPs-tpy) and 2-phenylpyridine (RuNPs-2PP), to extract correlations between the experimental electrocatalytic results and a well-accepted theoretical descriptor for HER, the hydrogen adsorption Gibbs free energy ( $\Delta G_{H^*}$ ).

---



## **TABLE OF CONTENTS**

<b>Chapter 3. DFT calculations on ligand-capped Ru NPs</b> .....	47
<b>3.1 INTRODUCTION</b> .....	51
<b>3.2 DFT STUDIES</b> .....	52
<b>3.2.1 Tpy ligand coordination studies through DFT calculations</b> .....	52
<b>3.2.2 Standard free energy change calculation</b> .....	55
<b>3.2.3 DFT vs. experimental data</b> .....	58
<b>3.2.4 2PP ligand coordination studies through DFT calculations</b> .....	60
<b>3.3 CONCLUSIONS</b> .....	63
<b>3.4 PERIODIC DFT PARAMETERS</b> .....	64
<b>3.5 REFERENCES</b> .....	65



### **3.1 INTRODUCTION**

When obtained from renewable sources, hydrogen is an alternative clean energy vector of high interest in the transition our society is facing from fossil to renewable energy. Therefore, a lot of effort has been put in searching efficient electrocatalysts able to catalyze the hydrogen evolution reaction (HER). Even though Pt is the state-of-the-art HER electrocatalyst,<sup>1</sup> Ru-based nanomaterials have emerged in the last years as promising catalysts towards HER due to their high stability both in acid and alkaline media and the similar Ru-H bond strength compared to Pt-H.<sup>2</sup> In this regard, 4-phenylpyridine capped Ru NPs (Ru-4PP) have been previously synthesized and studied in our group.<sup>3</sup>

Elucidation of the catalytic mechanisms with nanoparticulate catalysts has been a challenging task despite the progress experienced in the characterization techniques at the nanoscale regime during the last years. In this sense, merging theoretical calculations with experimental results has emerged as a powerful tool to predict and/or rationalize some trends in the HER electrocatalytic activity of nanocatalysts. Thus, some theoretical concepts such as adsorption free energy, microkinetic models, volcano plots and d-band centers have been widely accepted for (semi)quantitative evaluation of the performance of HER electrocatalysts in acidic media.<sup>4</sup> It is well-known that the catalytic activity of a nanomaterial depends on its surface energy, and thus on the nature/coverage of surface species. Density functional theory (DFT) allows elucidating chemical/electronic properties of modelled metal clusters, which can be constructed based on the experimental characterization of nanocatalysts surfaces. In the particular case of HER, a good correlation between experimental exchange current density values (which reflect the intrinsic rate of electron-transfer between the analyte and the electrode) and the Gibbs adsorption free energy of hydrogen ( $\Delta G_{H^*}$ ) has been established, obtaining volcano-like dependencies.<sup>5</sup>

An ultra-small *ca.* 1.0 nm 55-atom hcp metal Ru NP (Ru<sub>55</sub>) has been widely used as a basis model to perform DFT calculations. This model has been previously reported by R. Poteau *et al.*,<sup>6</sup> confirming that it properly describes the surface properties of ultra-small Ru NPs. Thus, in previous DFT studies on 4PP-capped Ru NPs, the coordination mode of the ligand into a Ru<sub>55</sub>H<sub>53</sub> model (since surface hydrides had been confirmed by

experimental hydride titration of the real sample) has been assessed, confirming a competition between  $\sigma$ -donation of the N lone pair and an aromatic  $\pi$ -to-metal interaction, being the latest the most stable coordination mode. Taking into account these results, a final model was constructed consisting in  $\text{Ru}_{55}\text{H}_{53}(\sigma\text{-4PP}^*)_9(\pi\text{-4PP}^*)_2$ , from which  $\Delta G_{\text{H}^*}$  probing indexes have been calculated at different representative adsorption sites.<sup>7</sup> The  $\Delta G_{\text{H}^*}$  values suggested that some sites in 4PP-protected Ru NPs could be very active towards the HER, showing a  $\Delta G_{\text{H}^*} \approx 0$  kcal/mol. These computational results are in agreement with the outstanding experimental HER activity of Ru-4PP, showing a low overpotential at 10 mA/cm<sup>2</sup> ( $\eta_{10}$ ) value of 20 mV.<sup>3</sup> Thus, following this study, two new different ligand-capped Ru NPs will be studied in this chapter by DFT calculations, 4'-(4-methylphenyl)-2,2':6',2''-terpyridine (Ru-tpy) and 2-phenylpyridine-capped (Ru-2PP) Ru NPs.

## 3.2 DFT STUDIES

### 3.2.1 Tpy ligand coordination studies through DFT calculations

The coordination of the tpy ligand over the surface of a Ru NP has been studied by means of DFT in order to elucidate its most energetically favoured coordination modes. The calculations have been performed on a 1-nm hydrogenated Ru NP ( $\text{Ru}_{55}\text{H}_{35}$ , 0.8 H/ $\text{Ru}_{\text{surf}}$ ), simulating the results obtained from experimental hydride titration of the sample (see Fig. 1 for geometries of  $\text{Ru}_{55}\text{H}_{35}$  and tpy ligand).

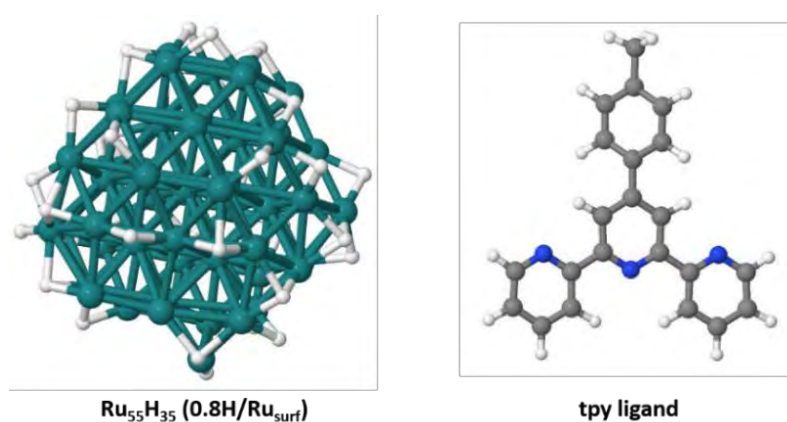


**Figure 1.** Geometry of the  $\text{Ru}_{55}\text{H}_{35}$  NP (0.8 H/ $\text{Ru}_{\text{surf}}$ ) and the 4'-(4-methylphenyl)-2,2':6',2''-terpyridine (tpy) ligand used for DFT calculations. The average adsorption energy of the 35 hydrides in  $\text{Ru}_{55}\text{H}_{53}$  is *ca.* -14.0 kcal/mol.



The three different pyridine rings of the ligand can be coordinated onto the Ru surface atoms by two different coordination modes:  $\sigma$ -donation of the nitrogen lone pair, or an aromatic  $\pi$ -metal interaction, with a flat configuration of the ring. By combining these two possibilities for all the pyridine rings, it is possible to obtain five different geometries with different coordination modes of the ligand (Fig. 2). Adsorption energies for tpy in each coordination mode are also summarized in Fig. 2.

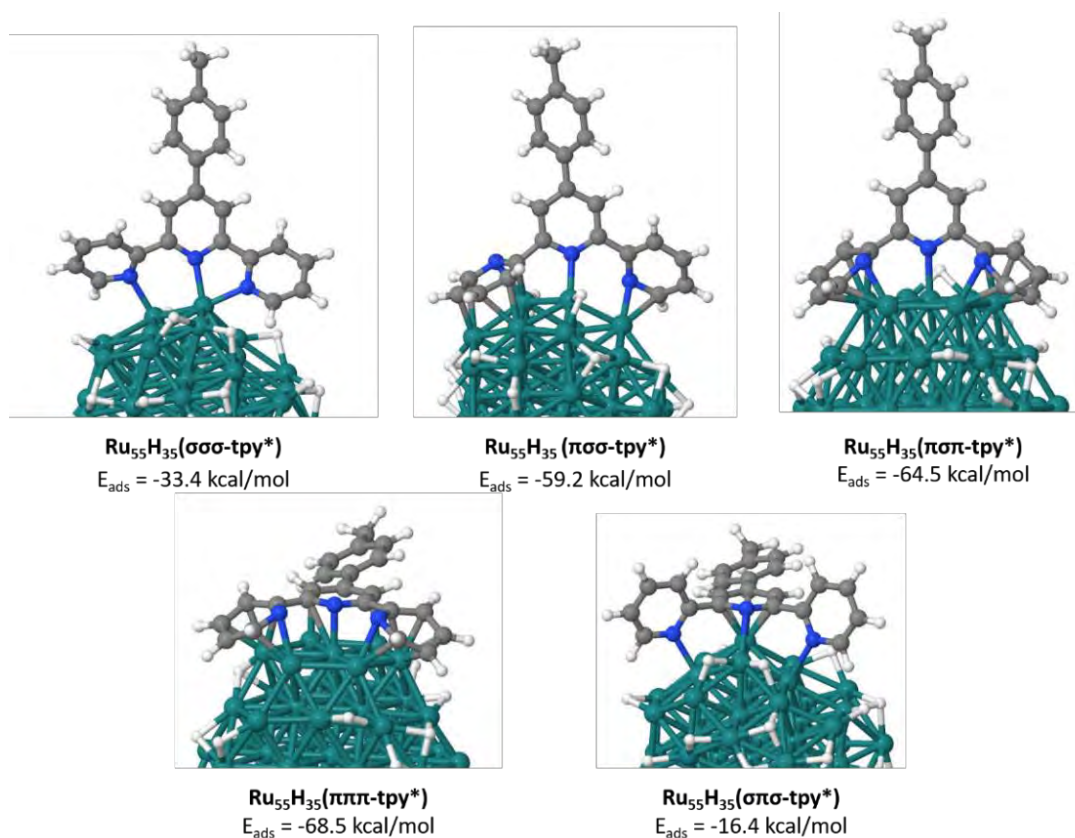


**Figure 2.** Geometry of the five different structures with different coordination modes and corresponding adsorption energies ( $E_{\text{ads}}$ ) for tpy onto Ru<sub>55</sub>H<sub>35</sub> NP (0.8 H/Ru<sub>surf</sub>).

When the three pyridine rings are all coordinated by a  $\pi$ -metal interaction, the system is stable by -68.5 kcal/mol, whereas when all the rings are coordinated by  $\sigma$ -donation, the ligand is more weakly coordinated (-33.4 kcal/mol). Whilst the geometry of the carbon atoms in the coordinated aromatic rings in  $\sigma\sigma\sigma$ -tpy is more similar to a free ligand, it is significantly distorted in the  $\pi\pi\pi$  configuration. Furthermore, in intermediate situations (hybrid  $\sigma$  and  $\pi$  coordination), a twisting of one or two of the terpyridine aromatic rings should be accomplished, which could lead to the destabilization of the final system. Among those, the  $\pi\sigma\pi$  coordination is the most stable one (-64.5 kcal/mol), since

the two twisted rings are  $\pi$ -coordinated, proportioning stability to the system and being able to counterbalance the structural changes, whereas the  $\sigma\pi\sigma$  one (-16.4 kcal/mol) is the least stable, with high twisting and only one  $\pi$ -coordinated ring. The intermediate energy hybrid case,  $\pi\sigma\sigma$  (-59.2 kcal/mol) lies in the middle because although it only contains one  $\pi$ -coordinated ring, the overall distortion is lower than in the  $\sigma\pi\sigma$  case.

The co-adsorption properties of hydrides and tpy ligands on the Ru<sub>55</sub> model could be theoretically evaluated through first-principles thermodynamics,<sup>8</sup> as previously done with Ru NPs in equilibrium with syngas,<sup>6</sup> but it is not under the scope of this present study due to the huge amount of time needed to optimize the systems with different coverages both for H and tpy. Thus, considering the obtained results and the low differences found in  $E_{\text{ads}}$  of the tpy ligand in both the  $\pi\pi\pi$  and  $\pi\sigma\pi$  coordinations (-68.5 kcal/mol vs. -64.5 kcal/mol, respectively), the chosen coordination mode to build a more complex model with more tpy ligands on the surface has been the  $\pi\sigma\pi$  one, owing to its lower steric hindrance compared to the  $\pi\pi\pi$  one. Moreover, the  $\pi\sigma\pi$  coordination allows the coordination of more hydrogen atoms, which will likely stabilize the system. In contrast, the large steric hindrance of the  $\pi\pi\pi$  configuration would push out hydrides placed below the ligand, forcing them to be more crowded in other Ru sites, and thus consequently reducing the number of putative tpy ligands adsorbed at the NP surface. This difference would probably lead to a less stable system if the tpy ligands are only  $\pi\pi\pi$  coordinated, as confirmed in a previous study with 4PP-capped Ru NPs.<sup>3</sup>

In this direction, a model with 5 tpy ligands coordinated in a  $\pi\sigma\pi$ -mode onto the RuNP surface has been constructed, Ru<sub>55</sub>H<sub>35</sub>( $\pi\sigma\pi$ -tpy\*)<sub>5</sub> (Fig. 3). The obtained average  $E_{\text{ads}}$  of the tpy ligands is -21.5 kcal/mol, which has been calculated according to  $E_{\text{ads}} = [E(n\text{tpy}^*) - E(\text{Ru}_{55}\text{H}_{35}\text{NP}) - nE(\text{tpy})]/n$ , where tpy\* designates an adsorbed tpy ligand over the surface of the Ru NP. This lowered  $E_{\text{ads}}$  compared to the value obtained for a single tpy in the same coordination mode (-21.5 vs. -64.5 kcal/mol) is in agreement with the fact that the incorporation of more ligands leads to a decrease in the d-band center of the metal (*i.e.* to a stabilization of the metal) and that the steric hindrance provoked by the saturation of the surface overrides the coordination stabilization effects.

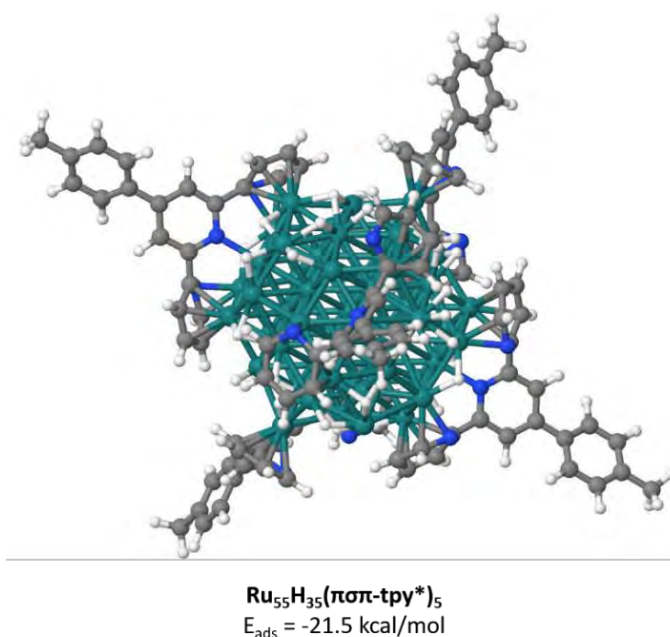


**Figure 3.** Optimized geometry for the 5-tpy-protected 1-nm RuNP ( $\text{Ru}_{55}\text{H}_{35}(\pi\sigma\pi\text{-tpy}^*)_5$ ) and its  $E_{\text{ads}}$ .

### 3.2.2 Standard free energy change calculation

DFT calculations can be used as a tool to have an insight into the electronic structure of a NP surface, which depends on the nature of the species present. It is well-known that there is a relationship between experimental HER exchange current density,  $j_0$ , and the adsorption energy of a single hydrogen atom on a given site ( $\Delta G_{\text{H}^*}$ ), thus being  $\Delta G_{\text{H}^*}$  a well-accepted descriptor for the theoretical prediction of the activity of a nanocatalyst towards HER (Eq. 1):<sup>9</sup>

$$\Delta G_{\text{H}^*} = \Delta E_{\text{H}^*} + \Delta E_{\text{ZPE}} - T\Delta S_{\text{H}} \quad \text{Eq. 1}$$

where  $\Delta E_{\text{H}^*}$  is calculated as  $\Delta E_{\text{H}^*} = E(\text{NP} - \text{H}^*) - E(\text{NP}) - \frac{1}{2} E(\text{H}_2)$ ,  $\Delta E_{\text{ZPE}}$  is the difference in zero-point energy between the adsorbed and the gas phase hydrogen atom and  $\Delta S$  is the entropy change.  $\Delta E_{\text{ZPE}}$  is obtained by a vibrational frequency calculation ( $\Delta E_{\text{ZPE}} = \frac{1}{2} \sum \hbar \nu_i$ , where  $\nu_i$  are the  $3N-6$  computed vibrational harmonic frequencies), and  $\Delta S$  is calculated as  $S = S_{\text{trans}} + S_{\text{vib}} + S_{\text{rot}} + S_{\text{el}}$ , where  $S_{\text{trans}}$ ,  $S_{\text{vib}}$ ,  $S_{\text{rot}}$ , and  $S_{\text{el}}$  are the translational, vibrational, rotational and electronic entropy terms, respectively, and where  $S_{\text{vib}}$  can be derived from frequency calculations. In addition, Nørskov and co-workers<sup>9</sup>

have suggested that 5.5 kcal/mol can be considered a representative value for  $\Delta E_{\text{ZPE}} - T\Delta S_{\text{H}}$  for all metals, being therefore Eq. 1 simplified as follows (Eq. 2):

$$\Delta G_{\text{H}^*} = \Delta E_{\text{H}^*} + 5.5 \text{ kcal/mol} \quad \text{Eq. 2}$$

According to the Sabatier principle, the catalyst-substrate interaction cannot be neither too strong nor too weak ( $\Delta G_{\text{H}^*} < 0$ , relatively strong  $\text{H}^*$  adsorption, and  $\Delta G_{\text{H}^*} > 0$ , relatively weak  $\text{H}^*$  adsorption). Thus, if the interaction between the NPs surface and H is too weak, the hydrogen atom will fail to bind to the catalyst and proton reduction reaction won't take place. On the other hand, if the interaction is too strong, no turnover will occur. Taking into account this principle, for an optimum HER catalyst the hydrogen adsorption Gibbs free energy,  $\Delta G_{\text{H}^*}$ , should lay as close as possible to 0 kcal/mol. However,  $\Delta G_{\text{H}^*}$  depends on global features such as the type of metal, the hydride and ligand coverage, the oxidation state of the surface and, more importantly, on local features such as the coordination mode and environment effects such as other hydrides and/or ligands in the neighbourhood of the coordination sites. It is also noteworthy to mention that this characteristic is not enough to have a good catalyst towards HER, as other parameters have to be taken into account having an effect in the overall HER activity, such as the aggregation of the NPs, the stability and the degree of defects in the real nanomaterial.

The  $\Delta G_{\text{H}^*}$  probing index has been calculated on three different representative adsorption sites that could coexist in the surface of the 5-tpy- $\pi\sigma\pi$  protected model  $\text{Ru}_{55}\text{H}_{35}(\pi\sigma\pi\text{-tpy}^*)_5$ , corresponding to  $\eta$ ,  $\mu$  or  $\mu_3$  bonding. These three hydrides are the top- $\text{H}^{172}$  ( $\eta$  bonding), the edge-capping  $\mu\text{-H}^{57}$  and the face-capping  $\mu_3\text{-H}^{67}$ , respectively, colored in red in Fig. 4.

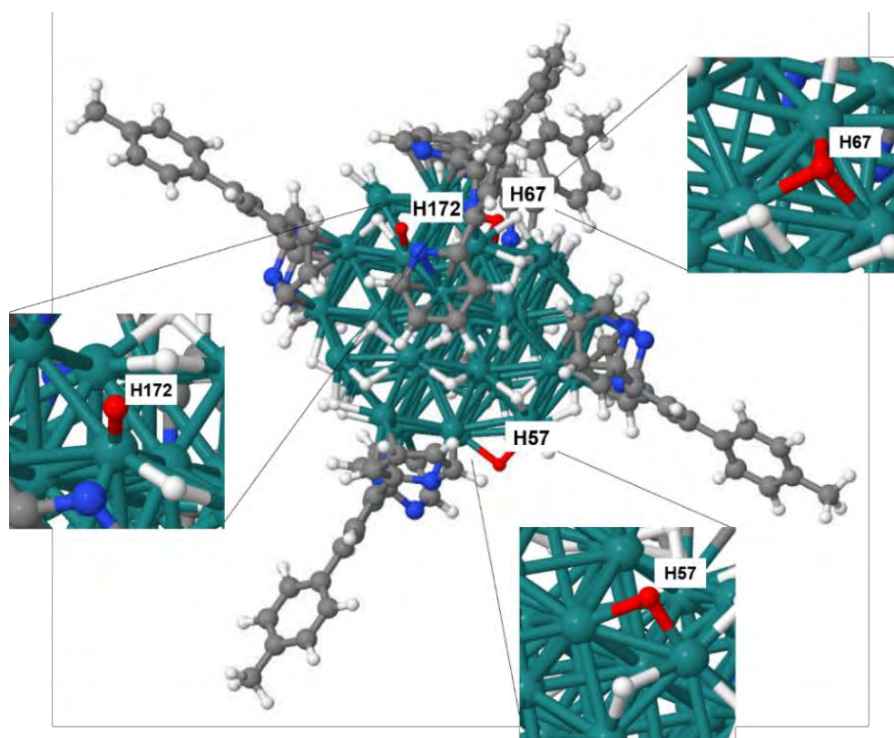


**Figure 4.** Probed adsorption sites for HER on a 5 tpy-protected 1-nm Ru NP ( $\text{Ru}_{55}\text{H}_{35}(\pi\sigma\pi\text{-tpy}^*)_5$ ).

These calculations have been very tricky because of the reorganization of surface hydrides upon adsorption/desorption processes, and thus they may provide artefactual energies. In this sense, it is noticeable that the first adoption Gibbs free energies of these representative hydrides ( $\Delta G_{\text{H}^*}$ ) are positive (*i.e.* weak adsorption), yielding values in between *ca.* 5 and 15 kcal/mol. Thus, a second hydride was removed in the immediate neighbourhood of the 1<sup>st</sup> hydride (*i.e.* the hydrogen atom that migrates after the removal of the 1<sup>st</sup> H) and the  $\Delta G_{\text{H}^*}$  values were again calculated, obtaining values in between *ca.* -9 and 5 kcal/mol (Table 1).

**Table 1.** Summary of the obtained  $\Delta G_{\text{H}^*}$  values for the different H sites of  $\text{Ru}_{55}\text{H}_{35}(\pi\sigma\pi\text{-tpy}^*)_5$ .

Entry	Probed H sites	$\Delta E_{\text{H}^*}$ (kcal/mol)	$\Delta G_{\text{H}^*}$ (kcal/mol)
1	Top- $\text{H}^{172}$	8.6	14.1
2	Top- $\text{H}^{172}$ + 2 <sup>nd</sup> H removal	-0.7	4.8
3	Edge-capping $\mu\text{-H}^{57}$	-0.9	4.6
4	Edge-capping $\mu\text{-H}^{57}$ + 2 <sup>nd</sup> H removal	-14.7	-9.2
5	Face-capping $\mu_3\text{-H}^{67}$	9.2	14.7
6	Face-capping $\mu_3\text{-H}^{67}$ + 2 <sup>nd</sup> H removal	-2.9	2.6

### 3.2.3 DFT vs. experimental data

As explained in the previous sections, a correlation between DFT calculated H adsorption Gibbs free energies,  $\Delta G_{H^*}$ , and the experimental exchange current densities,  $j_0$ , for HER in acidic media leads to a volcano-like behaviour.<sup>5</sup> An optimum catalyst should lie on-top of the volcano plot ( $\Delta G_{H^*} \approx 0$  kcal/mol). The resulting experimental exchange current density,  $j_0$ , for different ligand-capped Ru NPs as well as several other pure metals and MoS<sub>2</sub> are plotted in Fig. 5 as a function of the  $\Delta G_{H^*}$  values obtained from DFT-PBE (Perdew–Burke–Ernzerhof) calculations. The idea of these plots is to have a guide to qualitatively predict the activity of new electrocatalysts.

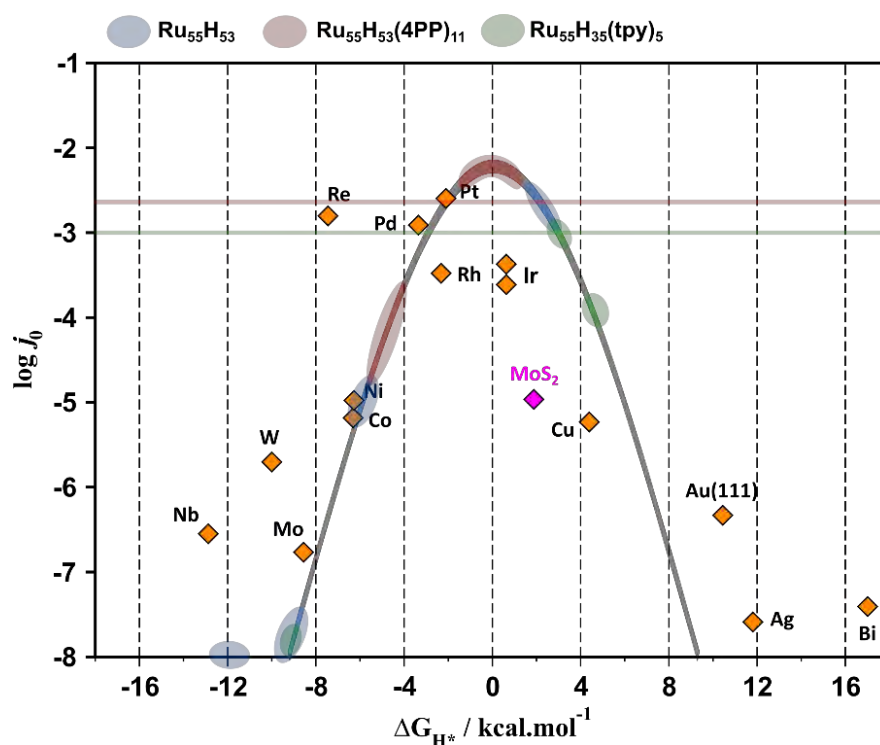


**Figure 5.** Volcano plot of the  $\log$  of the experimental exchange current density  $j_0$  ( $A/cm^2$ ) vs. the DFT-calculated H adsorption Gibbs free energy,  $\Delta G_{H^*}$  (kcal/mol), for pure metals<sup>9</sup> (orange diamonds) and nanoscale MoS<sub>2</sub> (pink diamond).<sup>10</sup> Horizontal lines are the experimental  $\log j_0$  values for Ru-4PP NPs (red) and Ru-tpy (green). The results from our DFT calculations for  $\Delta G_{H^*}$  in the different H probed sites for Ru<sub>55</sub>H<sub>53</sub> (blue), Ru<sub>55</sub>H<sub>53</sub>( $\sigma$ -4PP)<sub>9</sub>( $\pi$ -4PP)<sub>2</sub> (red) and Ru<sub>55</sub>H<sub>35</sub>( $\pi\sigma\sigma$ -tpy)<sub>5</sub> (green) after a 2<sup>nd</sup> hydride removal are shown as oval shapes. Adapted from ref. 7.

Furthermore, a summary of the chemical and electrochemical experimental data obtained for three different ligand-capped Ru NPs is shown in Table 2.

**Table 2.** Summary of the chemical and electrochemical (1 M H<sub>2</sub>SO<sub>4</sub>) experimental data for different ligand-capped Ru NPs.

Entry	Catalyst	$d_{\text{mean}}$ (nm)	H/Ru <sub>surf</sub>	$\eta_{10}$ (mV)	$j_o$ (mA/cm <sup>2</sup> )	$\log j_o$ (A/cm <sup>2</sup> )	Ref.
1	<b>Ru-4PP</b>	1.5 ± 0.3	1.2	20	2.04	-2.69	3
2	<b>Ru-tpy</b>	1.4 ± 0.2	0.7	93	0.99	-3.00	11
3	<b>Ru-2PP</b>	1.8 ± 0.3	1.0	30	1.93	-2.71	11

In previous studies, the  $\Delta G_{\text{H}^*}$  probing index has been calculated on six representative adsorption sites in the Ru<sub>55</sub>H<sub>53</sub>(4PP)<sub>11</sub> model, obtaining  $\Delta G_{\text{H}^*}$  values which can be classified in two groups, those H showing a  $\Delta G_{\text{H}^*}$  in between -5.0 and -4.0 kcal/mol, and those in between -1.0 and 1.5 kcal/mol (red ovals in Fig. 5). These results suggest that some sites in Ru-4PP NPs could be very active towards the HER, showing a  $\Delta G_{\text{H}^*}$  close to 0 kcal/mol (red shapes on-top of the volcano in Fig. 5), supporting their outstanding experimental HER electrocatalytic activity, with an  $\eta_{10}$  value as low as 20 mV (Table 2). The  $\Delta G_{\text{H}^*}$  probing values have also been calculated for the same sites in a ligand-free model (Ru<sub>55</sub>H<sub>53</sub>), obtaining significantly more negative  $\Delta G_{\text{H}^*}$  values (blue ovals in Fig. 5) than for the 4PP ligand-capped model, thus confirming that the 4PP ligand significantly moves the adsorption energies close to *ca.* 0 kcal/mol. Regarding the experimental data for Ru-tpy NPs, it can be noticed that they possess the lowest electrocatalytic activity of all three ligand-capped systems, with a  $\eta_{10}$  value of 93 mV (Table 2). This tendency can be also observed in the probed  $\Delta G_{\text{H}^*}$  values (Table 1), which lie on both branches of the volcano plot, away from its top (green ovals in Fig. 5). This study should be completed with other adsorption energy calculations considering those H that are closer to the tpy ligands in order to check any possible influence of the  $\pi$ -density of the tpy ligand in  $\Delta G_{\text{H}^*}$ . However, it provides up to now interesting trends which are in agreement with our previous experimental results.



### 3.2.4 2PP ligand coordination studies through DFT calculations

As previously exposed, experimental HER electrocatalytic experiments on 2PP-capped Ru NPs (Ru-2PP) in acidic media (1 M H<sub>2</sub>SO<sub>4</sub>) have been performed by a PhD student in our research group (L.I. Álvarez, see Table 2 above)<sup>11</sup> in order to compare their performance with the previously reported 4PP-capped Ru NPs (Ru-4PP).<sup>3</sup> In addition, 3PP-capped Ru NPs (Ru-3PP) are also being evaluated experimentally in our research group. Therefore, the DFT calculations presented in this chapter aims at assessing (1) the effect of the different relative positions of the coordinating N atom and the aromatic substituents in the coordination mode and  $E_{\text{ads}}$  of the set of phenylpyridine ligands, and (2) the changes in the overall HER electrocatalytic activity due to the different electronic and steric effects of each ligand isomer (Fig. 6).

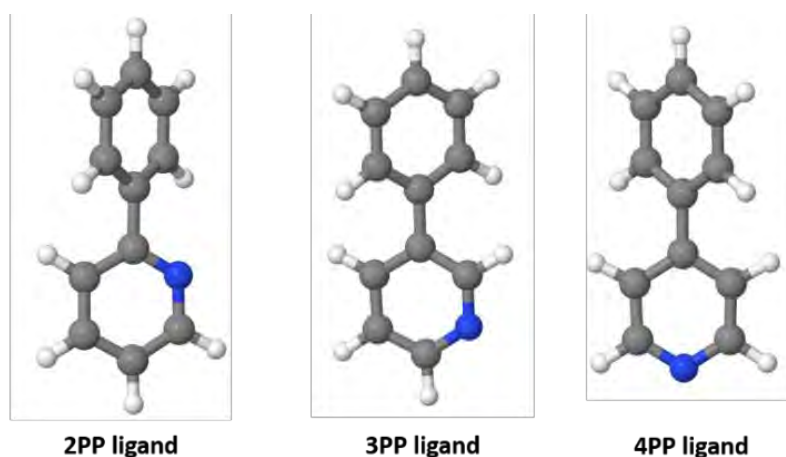


**Figure 6.** DFT-optimized geometry of the 2PP, 3PP and 4PP and ligands.

Thus, the coordination of the 2PP ligand over the surface of a single Ru NP has been also studied, analogously as in the case of the tpy ligand. Previous DFT studies with Ru-4PP confirmed a competition between a vertical  $\sigma$  donation of the N lone pair and an aromatic  $\pi$ -to-metal interaction, being the latest the most stable coordination mode (-32.1 vs. -63.6/-48.8 kcal/mol, respectively).<sup>3</sup> The coordination studies of 2PP have been performed in a Ru<sub>55</sub>H<sub>53</sub> model (1.2 H/Ru<sub>surf</sub>), a reasonable starting model although the last experimental hydride titration revealed the presence of 1.0 H/Ru<sub>surf</sub>. The combination of  $\sigma$  and  $\pi$  coordination modes of the two rings in 2PP allowed to obtain five different adsorption modes (Fig. 7 and Table 3).



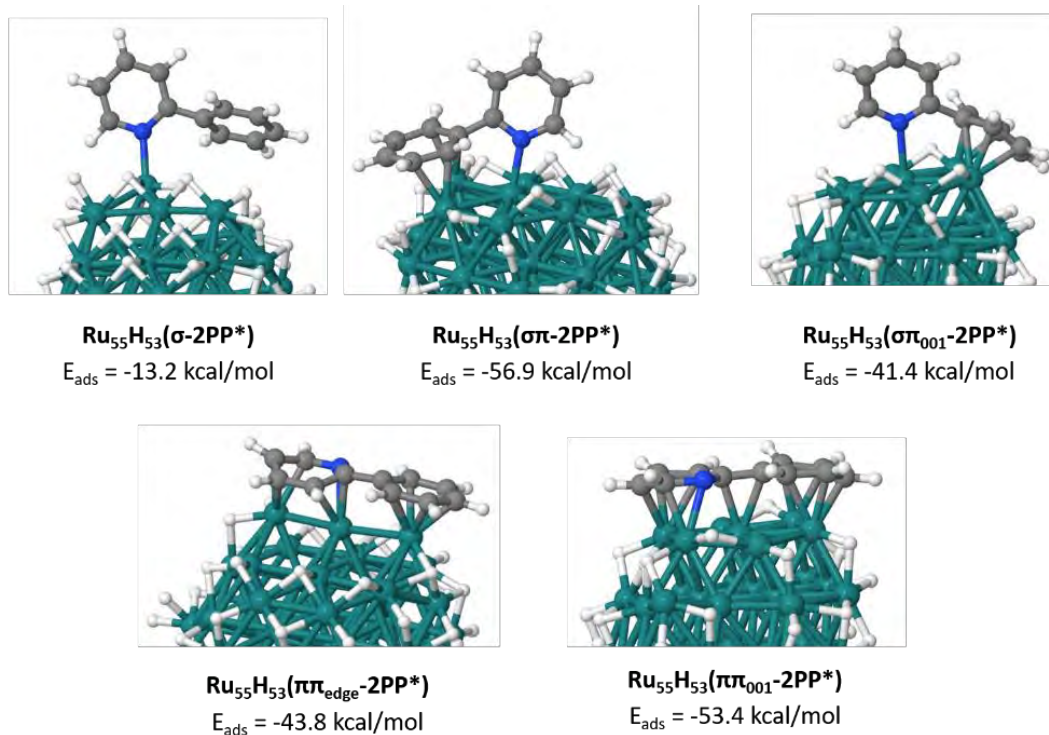


**Figure 7.** Geometry of the five different coordination modes and corresponding  $E_{\text{ads}}$  of 2PP onto the Ru NP model.

The obtained results point again that  $\pi$  coordination is more stable than  $\sigma$  coordination (-43.8/-53.4 kcal/mol vs. -13.2 kcal/mol, respectively). In fact, the  $\sigma$ -coordination is even less stable in 2PP than in 4PP (Table 3, entry 1), which could be probably explained on the basis that 4PP almost maintains its geometry from the free species, while the benzene ring of 2PP needs to twist in order to be able to  $\sigma$ -coordinate through the pyridine ring (Fig. 7).

Furthermore, a new coordination mode could be evaluated now for 2PP, by coordinating each ring in two different modes (*i.e.* the pyridine in  $\sigma$  and the benzene ring in  $\pi$ ). The obtained systems with mixed- $\sigma\pi$  coordination mode show comparable stabilities to the  $\pi\pi$  systems (-41.4/-56.9 kcal/mol vs. -43.8/-53.4 kcal/mol, respectively, Table 3, entries 2 to 5). In this case, the existing twisting of the benzene ring to allow the  $\sigma$  coordination of the pyridine ring can be counterbalanced by the formation of a very stable  $\pi$ -coordination by the benzene ring, leading to a very stable configuration. These results could explain the lower H coverage found experimentally by hydride titration for Ru-2PP compared to Ru-4PP (1.0 H/Ru<sub>surf</sub> vs. 1.2 H/Ru<sub>surf</sub>, respectively), being the

incorporation of hydrides less favoured at the Ru-2PP NPs surface than in the Ru-4PP NPs surface.

**Table 3.**  $E_{\text{ads}}$  per 2PP in the different configuration modes compared to the  $E_{\text{ads}}$  per 4PP in the same configurations.

Entry	System	Number of ligands* ( $n$ )	$E_{\text{ads}}$ per 2PP* (kcal/mol)	$E_{\text{ads}}$ per 4PP* <sup>[ref. 7]</sup> (kcal/mol)
1	Ru <sub>55</sub> H <sub>53</sub> ( $\sigma$ -2PP*)	1	-13.2	-32.1
2	Ru <sub>55</sub> H <sub>53</sub> ( $\sigma\pi$ -2PP*)	1	-56.9	-
3	Ru <sub>55</sub> H <sub>53</sub> ( $\sigma\pi_{001}$ -2PP*)	1	-41.4	-
4	Ru <sub>55</sub> H <sub>53</sub> ( $\pi\pi_{\text{edge}}$ -2PP*)	1	-43.8	-59.0
5	Ru <sub>55</sub> H <sub>53</sub> ( $\pi\pi_{001}$ -2PP*)	1	-53.4	-48.8

Taking into account these results, a more complex model was considered in this case, consisting in two 2PP ligands in  $\pi\pi$  coordination and five ligands  $\sigma\pi$ -coordinated onto a Ru<sub>55</sub>H<sub>44</sub> model (1.0 H/Ru<sub>surf</sub>), simulating now the results obtained from the experimental hydride titration of the Ru-2PP sample. However, the high coverage of the Ru surface with hydrides didn't allow to coordinate the ligands in the  $\sigma\pi$ -coordination, and thus these 5 ligands were coordinated in the  $\sigma$  mode. This behaviour can be explained as for the Ru-tpy case because on the one hand hydrides can be pushed out to form the very stable (and thus energetically compensated)  $\pi$ -coordinated ligand bonds, whereas on the other hand  $\sigma$ -coordination leaves enough room for keeping the hydrides to stabilize the whole system. Thus, a final mode containing two 2PP ligands in  $\pi\pi$ -coordination and five 2PP ligands in  $\sigma$ -coordination has been considered, obtaining an average  $E_{\text{ads}}$  of -29.7 kcal/mol for 2PP (Fig. 8). This model will be considered in the near-future to obtain the  $\Delta G_{\text{H}^*}$  values for different H probed adsorption sites. However, taking into account the hindered hybrid  $\sigma\pi$ -coordination in this model, presenting high surface coverage, we could probably propose a future model with less coordinated ligands in order to be able to favour the  $\sigma\pi$ -coordination and extract more conclusions.

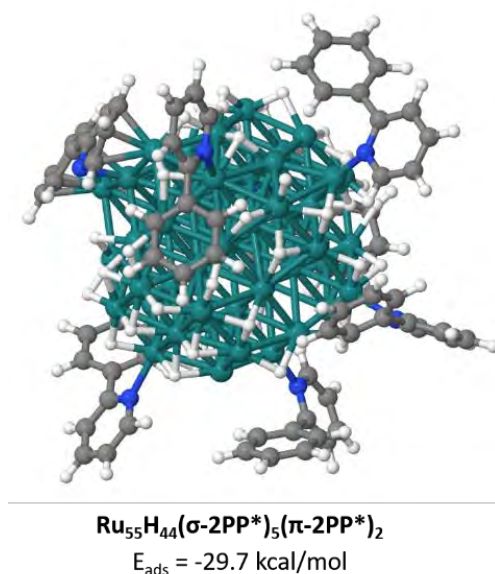


**Figure 8.** Optimized geometry for  $\text{Ru}_{55}\text{H}_{44}(\sigma\text{-2PP}^*)_5(\pi\text{-2PP}^*)_2$  and corresponding  $E_{\text{ads}}$ .

### 3.3 CONCLUSIONS

DFT calculations have allowed to discern the most favourable coordination modes of two different ligands, tpy and 2PP, on the surface of a Ru NP. In general,  $\pi$ -coordination is more stable than the  $\sigma$  one. Final models have been chosen taking into account the  $E_{\text{ads}}$  values obtained from the different ligand coordination modes onto the surface of the Ru NP, choosing the most stable configuration but also putting in balance possible steric effects and hydride push out effects due to high surface coverage with hydrogen atoms. The final proposed models have been  $\text{Ru}_{55}\text{H}_{35}(\pi\sigma\pi\text{-tpy}^*)_5$  for tpy-Ru and  $\text{Ru}_{55}\text{H}_{44}(\sigma\text{-2PP}^*)_5(\pi\text{-2PP}^*)_2$  for 2PP-Ru.

The experimentally lower HER electrocatalytic activity of Ru-tpy compared to Ru-4PP has also been evidenced by the obtained  $\Delta G_{\text{H}^*}$  values, for Ru-tpy lying on the branches of the volcano plot, in contrast to Ru-4PP, placed near the top. Although this study should be completed with other adsorption energy calculations considering those H that are closer to the tpy ligands in order to check any influence of the  $\pi$  density of the ligands in  $\Delta G_{\text{H}^*}$ , it provides up to now interesting trends which are in good agreement with our experimental results.

### **3.4 PERIODIC DFT PARAMETERS**

DFT calculations were done with the Vienna Ab initio Simulation Package, VASP,<sup>12,13</sup> within the framework of density functional theory (DFT). Non-spin polarized calculations have been performed and the exchange-correlation potential has been approximated by the generalized gradient approach proposed by Perdew, Burke, and Ernzerhof (PBE).<sup>14</sup> Projector augmented waves (PAW) full potential reconstruction have been used,<sup>15,16</sup> with a plane-wave kinetic energy cut-off of 525 eV.<sup>6,17,18</sup> PAW data sets for metal atoms treat the (n-1)p, (n-1)d and ns states (*i.e.* Ru atoms treating the 4p, 4d and 5s states; 14 valence electrons).  $\Gamma$ -centered calculations<sup>19</sup> have been performed with a Gaussian smearing of 0.02 eV width. Geometries have been optimized until the criterion of the residual forces on any direction being less than 0.05 eV/Å. The supercell size has been set to ensure a vacuum space of *ca.* 16 Å between periodic images of metal clusters, *i.e.* 41.0 x 35.0 x 43.0 Å for tpy and 31.5 x 31.5 x 32.0 Å for 2PP.

### **3.5 REFERENCES**

- 
- <sup>1</sup> J.R. McKone, E.L. Warren, M.J. Bierman, S.W. Boettcher, B.S. Lewis and H.B. Gray, *Energy Environ. Sci.* **2011**, 4, 3573-3583.
- <sup>2</sup> J. Creus, J. De Tovar, N. Romero, J. García-Antón, K. Philippot, R. Bofill and X. Sala, *ChemSusChem* 2019, 12, 2493-2514.
- <sup>3</sup> J. Creus, S. Drouet, S. Suriñach, P. Lecante, V. Collière, R. Poteau, K. Philippot, J. García-Antón, X. Sala. *ACS Catal.* **2018**, 11094-11102.
- <sup>4</sup> J.K. Nørskov, T. Bligaard, J. Rossmeisl, and C.H. Christensen, *Nat.Chem.* **2009**, 1, 37 – 46;
- <sup>5</sup> Y. Zheng, Y. Jiao, M. Jaroniec and S.Z. Qiao, *Angew. Chem. Int. Ed.* **2015**, 54, 52-65.
- <sup>6</sup> L. Cusinato, L. M. Martinez-Prieto, B. Chaudret, I. del Rosal, R. Poteau, *Nanoscale*, **2016**, 8, 10974-10992.
- <sup>7</sup> I. del Rosal and R. Poteau, Sabatier Principle and Surface Properties of Small Ruthenium Nanoparticles and Clusters: Case Studies **2021**. In *Nanoparticles in Catalysis* (eds K. Philippot and A. Roucoux).
- <sup>8</sup> K. Reuter, C. Stampfl and M. Scheffler, *Handbook of Materials Modeling*, Springer. **2005**, 1, 149-194.
- <sup>9</sup> J.K. Nørskov, T. Bligaard, A. Logadottir, J.R. Kitchin, J.G. Chen, S. Pandalov and U. Stimming, *J. Electrochem. Soc.* **2005**, 152, J23 – J26.
- <sup>10</sup> T.F. Jaramillo, K.P. Jørgensen, J. Bonde, J.H. Nielsen, S. Horch and I. Chorkendorff, *Science* **2007**, 317, 100 – 102.
- <sup>11</sup> L.I. Álvarez, *Ruthenium and Platinum Nanoparticles for Artificial Photosynthesis 2021*, PhD Thesis, UAB.
- <sup>12</sup> G. Kresse and J. Fürthmüller, *Phys. Rev. B: Condens. Matter Mater. Phys.* **1996**, 54, 11169–11186.
- <sup>13</sup> G. Kresse and J. Fürthmüller, *Comput. Mater. Sci* **1996**, 6, 15-50.
- <sup>14</sup> J. P. Perdew, K. Burke and M. Ernzerhof, *Phys. Rev. Lett.* **1996**, 77, 3865–3868.
- <sup>15</sup> P. Blöchl, *Phys. Rev. B: Condens. Matter Mater. Phys.* **1994**, 50, 17953–17979.
- <sup>16</sup> G. Kresse and D. Joubert, *Phys. Rev. B: Condens. Matter Mater. Phys.* **1999**, 59, 1758–1775.
- <sup>17</sup> I. del Rosal, L. Truflandier, R. Poteau and I.C. Gerber, *J. Phys. Chem. C* **2011**, 115, 2169–2178.
- <sup>18</sup> I. del Rosal, M. Mercy, I.C. Gerber and R. Poteau, *ACS Nano* **2013**, 7, 9823–9835.
- <sup>19</sup> H.J. Monkhorst and J.D. Pack, *Phys. Rev. B: Solid State* **1976**, 13, 5188–5192.



# 4

## **Chapter 4. Ruthenium nanoparticles supported on reduced graphene oxide as electrocatalysts towards the hydrogen evolution reaction**

---

*Chapter 4* deals with the synthesis of carbon-supported ruthenium nanoparticles by using the organometallic synthetic methodology. Two related supports have been tested, reduced graphene oxide by following a modified Hummers method (rGO) (*Chapter 4A*) and reduced graphene oxide prepared from the pyrolysis of alginate (G) (*Chapter 4B*). (HR)TEM, EDX, EA, ICP, XPS, XRD, Raman and IR techniques have been used to get information about the structure and composition of the obtained carbon-supported materials. The influence of heteroatom-doping in both the stability and catalytic activity of the two hybrid systems towards the hydrogen evolution reaction (HER) has been studied.

---





## **TABLE OF CONTENTS**

<b>4.1 GENERAL INTRODUCTION</b> .....	71
<b>4.2 REFERENCES</b> .....	78
<b>Chapter 4A. Ru nanoparticles supported on rGO (Hummers) as HER catalysts</b> ..	79
<b>4A.1 INTRODUCTION</b> .....	81
<b>4A.2 SYNTHESIS AND CHARACTERIZATION</b> .....	82
<b>4A.2.1 Synthesis of Ru NPs supported onto rGO</b> .....	82
<b>4A.2.2 Transmission electron microscopy analysis (TEM)</b> .....	83
<b>4A.2.3 X-ray photoelectron spectroscopy (XPS)</b> .....	84
<b>4A.2.4 <sup>15</sup>N and <sup>31</sup>P magic angle spinning solid state NMR spectroscopy analysis (MAS-NMR)</b> .....	86
<b>4A.3 ELECTROCATALYTIC PERFORMANCE</b> .....	87
<b>4A.3.1 Electrocatalytic HER studies in acidic media</b> .....	87
<b>4A.3.2 Fate of the catalyst under catalytic conditions</b> .....	90
<b>4A.3.3 Faradaic efficiencies</b> .....	92
<b>4A.3.4 Electrocatalytic performance benchmarking</b> .....	93
<b>4A.4 CONCLUSIONS &amp; PERSPECTIVES</b> .....	97
<b>4A.5 EXPERIMENTAL SECTION</b> .....	99
<b>4A.6 REFERENCES</b> .....	103
<b>Chapter 4B. Ru nanoparticles supported on rGO (Alginate) as HER catalysts</b> ...	105
<b>4B.1 INTRODUCTION</b> .....	107
<b>4B.2 SYNTHESIS AND CHARACTERIZATION</b> .....	107
<b>4B.2.1 Synthesis of reduced graphene oxide supports</b> .....	107
<b>4B.2.2 Synthesis of Ru NPs supported onto G</b> .....	108

4B.2.3 Transmission electron microscopy analysis (TEM).....	108
4B.2.4 Raman spectroscopy analysis .....	111
4B.2.5 X-ray photoelectron spectroscopy analysis (XPS).....	112
4B.2.6 Fourier-transform infrared spectroscopy analysis (FT-IR).....	114
4B.2.7 <sup>31</sup> P magic angle spinning solid state NMR spectroscopy analysis .....	115
4B.3 ELECTROCATALYTIC PERFORMANCE .....	116
4B.3.1 Electrocatalytic HER studies in 1 M H <sub>2</sub> SO <sub>4</sub> .....	116
4B.3.2 Electrocatalytic performance benchmarking .....	118
4B.3.3 Fate of the catalyst under catalytic conditions.....	122
4B.3.4 Faradaic efficiencies (ε) determination .....	124
4B.4 CONCLUSIONS .....	124
4B.5 EXPERIMENTAL PART .....	126
4B.6 REFERENCES.....	130
ANNEX Chapter 4.....	131

## **4.1 GENERAL INTRODUCTION**

Graphene is a monolayer of hexagonal-packed carbon atoms (Fig. 1), presenting high surface area, high stability and large electrical conductivity. These unique characteristics make this material a suitable support for electrocatalysis.<sup>1</sup> In addition, graphene can be doped both with non-metallic or metallic atoms to modulate its electrocatalytic activity by means of induced electronic changes. Representative literature examples are summarized below.

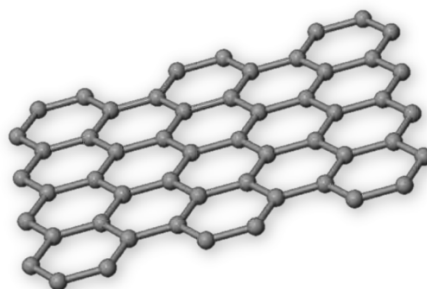


**Figure 1.** Graphene structure

In 2014, Qiao *et al.* presented the first theoretical study on the prediction of the electrocatalytic capacities of graphene-based materials towards HER.<sup>2</sup> The DFT results were also complemented with experimental results, adding a step forward in the design of active carbon-based catalysts for HER. Different heteroatoms with different electronegativity were introduced into the carbon structure (N, B, O, S, P, F), and natural bond orbital (NBO) population analyses showed that while N and O are negatively charged (electron acceptors for adjacent C), the other heteroatoms are positively charged (electron donors) (Fig. 2a). As HER descriptor, Gibbs free-energy for the hydrogen absorption values ( $\Delta G_{H^*}$ ) were calculated, obtaining a highly positive value for pure graphene, confirming its poor electrocatalytic activity (Fig. 2b). Choosing the most different heteroatoms in terms of charge population, *i.e.* P and N, the HER activities of N- and/or P-doped graphene were predicted by DFT studies. Both N and/or P doping help in reducing the  $\Delta G_{H^*}$  value, approaching to the optimum value ( $\Delta G_{H^*} = 0$  kcal/mol), enhancing the  $H^*$  adsorption (Fig. 2c). Later, DFT studies from Ding and co-workers supported also these results.<sup>3</sup>

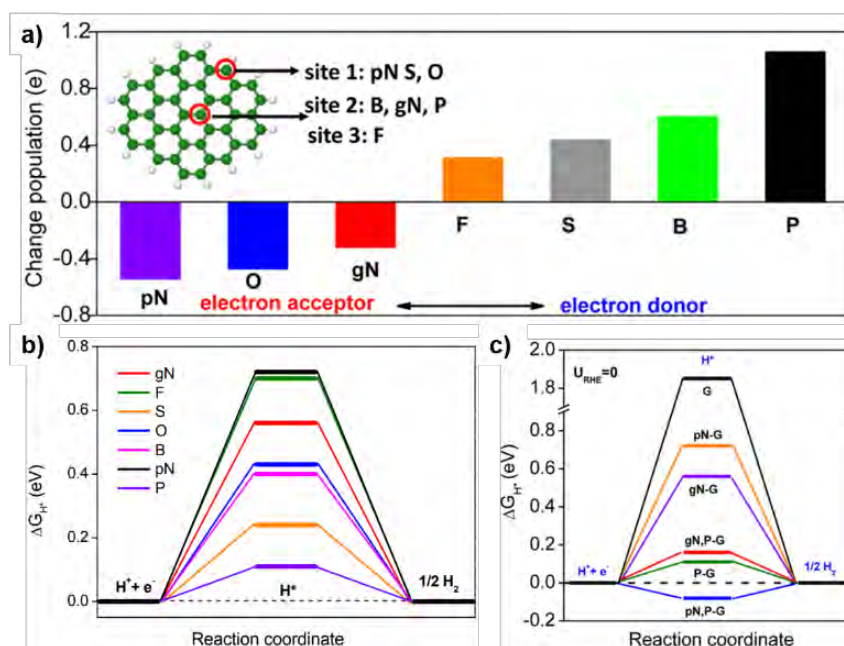


**Figure 2.** NBO population analysis of six different non-metallic heteroatoms in graphene (a). Calculated  $\Delta G_{H^*}$  diagram for HER at the equilibrium potential ( $U_{RHE} = 0V$ ) for various single-doped graphene structures (b). Calculated  $\Delta G_{H^*}$  diagram for HER at the equilibrium potential ( $U_{RHE} = 0V$ ) for N- and/or P-doped graphene (c). Extracted from ref. 2.

Experimental electrocatalytic activities towards HER in acidic media were in good agreement with the theoretical predictions, obtaining a lower overpotential to reach  $10 \text{ mA/cm}^2$  with the dual P-N doped graphene (420 mV) and a lower Tafel slope  $b$  (91 mV/dec), compared to the single doped P- or N-graphene (550 mV and 490 mV and 133 mV/dec and 116 mV/dec, respectively) (Fig. 3). This behaviour was attributed by the authors to the synergistic coupling effect between heteroatoms.

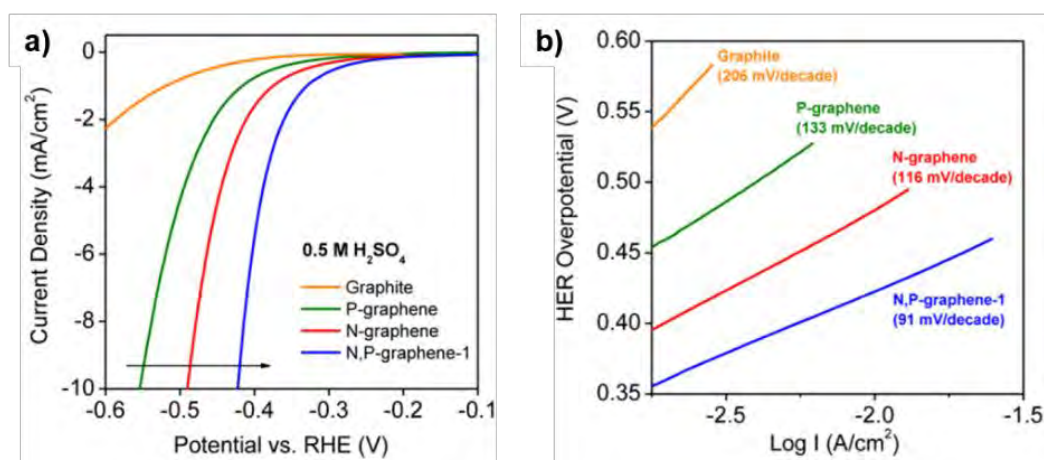


**Figure 3.** HER polarization curves (a) and corresponding Tafel plots (b) of N- and/or P- doped graphene in 0.5 M  $H_2SO_4$ . Graphite is considered as reference. Extracted from ref. 2.

Quiao *et al.* described the promotion of electrocatalytic HER on N-doped carbon nanosheets (CN) with secondary heteroatoms, obtaining in this case the best catalytic activity for N,S-CN ( $\eta_{10} = 290$  mV and  $b = 76.9$  mV/dec).<sup>4</sup> In addition, N,P-CN, N-CN and N,B-CN showed  $\eta_{10}$  of 550 mV, 620 mV and 710 mV and  $b$  of 139.3 mV/dec, 159.3 mV/dec and 198.2 mV/dec, respectively (Fig. 4).

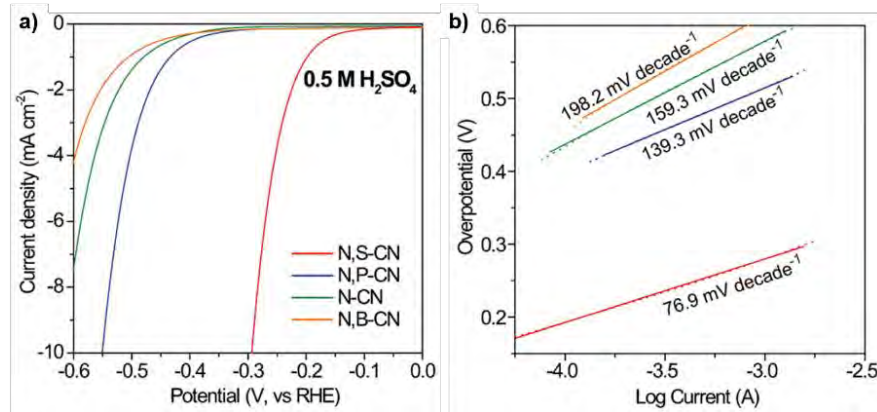


**Figure 4.** HER polarization curves (a) and corresponding Tafel plots (b) for N-CN, N,B-CN, N,P-CN and N,S-CN in 0.5 M H<sub>2</sub>SO<sub>4</sub>. Extracted from ref. 4.

Furthermore, Su *et al.* confirmed the great importance of pyridinic and graphitic nitrogen atoms (pyN/gN) in the final electrocatalytic activity of doped graphene in addition to the P and N-doping.<sup>5,6</sup> While gN in proximity to P-C bonds maintains the electronic conductivity and the distribution of the catalytic sites, pyN helps in generating a large number of electroactive sites. In addition, the best material was the PN-doped graphene (PNG), showing a  $\eta_{10} = 380$  mV and  $b = 125.5$  mV/dec (Fig. 5). DFT studies from Tu *et al.* confirmed also the different contributions of each type of doping atoms (pyridinic, graphitic or pyrrolic N) in vertical graphene (VG) (Fig. 6).<sup>7</sup>

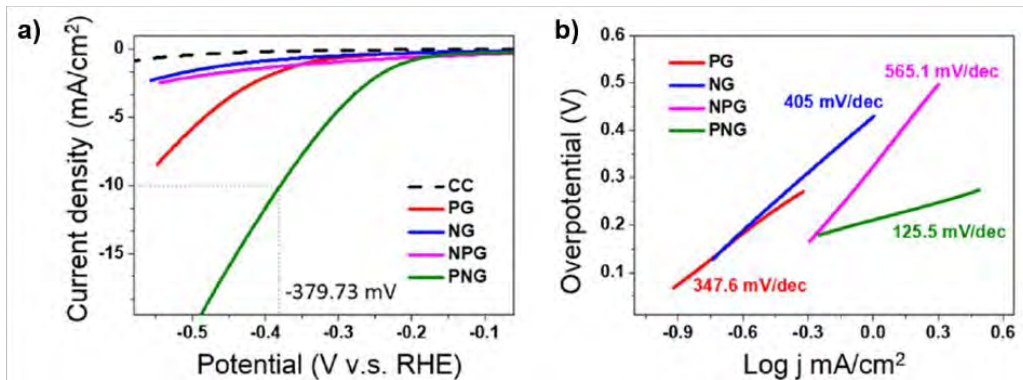


**Figure 5.** HER polarization curves (a) and corresponding Tafel plots (b) of P-, N-, NP- and PN-doped graphene in 0.5 M H<sub>2</sub>SO<sub>4</sub>. Extracted from ref. 5.

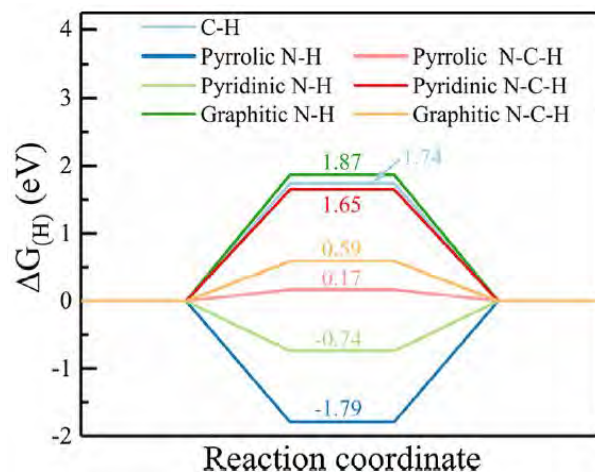


**Figure 6.**  $\Delta G_{H^*}$  on different doping sites of N-VG(c). N-VG = N-doped vertical graphene. Extracted from ref. 7.

Due to the relatively high  $\eta_{10}$  values presented for metal-free graphene materials, doping with metal NPs has also been studied recently to improve their HER catalytic activity. The use of graphene as a supporting material allows attaining improved dispersion and stability of the obtained NPs. Among the different metal atoms to be tested, Pt is the state-of-the-art HER catalyst.<sup>8</sup> However, its scarcity, high price and instability (corrosion) under alkaline catalytic conditions makes the development of alternative catalytic systems a priority in the field, particularly if large-scale applications are envisioned. In the last years Ru has emerged as an alternative metal due to its similar hydrogen bond strength, its higher stability under alkaline conditions and its relative lower price. For some of the developed Ru-based systems, graphene-like materials have been used as conductive supports. Some selected examples are summarized in the following paragraphs.

In 2016, L. Wan *et al.* synthesized well dispersed Ru NPs (2-5 nm) by reduction of  $\text{RuCl}_3$  following a hydrothermal procedure in critical  $\text{H}_2\text{O}$ .<sup>9</sup> The synthesis of those NPs was performed onto a pre-formed graphene-like layered carbon obtained from a graphitization process from a RuB-15 nanoplates and glucose mixture (Ru/GLC) (Fig. 7a). The system showed a low overpotential of 35 mV to reach  $10 \text{ mA/cm}^2$  ( $\eta_{10}$ ) and a Tafel slope of 46 mV/dec in 0.5 M  $\text{H}_2\text{SO}_4$ . In the same direction, M. Tour *et al.* published a study on  $\text{Ru}^0$  nanoclusters (3-7 nm) supported on N-doped graphene (Ru/NG) (Fig. 7b).<sup>10</sup> The materials were obtained with a two-step procedure: initial nucleation of  $\text{Ru}^{\text{III}}$  on GO by hydrolysis of  $[\text{Ru}(\text{NH}_3)_6]\text{Cl}_3$  followed by the reduction of  $\text{Ru}^{\text{III}}$  clusters to  $\text{Ru}^0$



by means of applying a range of high temperatures (350-850 °C) in a NH<sub>3</sub>/Ar environment. Ru/NG-750 was the best system, showing a  $\eta_{10}$  = 53 mV and a Tafel slope of 44 mV/dec.

In 2018, Baek and co-workers presented Ru NPs (2 nm) uniformly distributed on pre-formed graphene nanoplatelets (Ru@GnP).<sup>11</sup> Commercial graphite was ball-milled with dry ice to produce a carbon structure with high content of carboxylic groups at the edges, where Ru ions could be trapped prior to the *in situ* reduction to metal Ru by sodium borohydride (NaBH<sub>4</sub>) (Fig. 7c). A competitive performance compared to Pt was observed, obtaining a  $\eta_{10}$  = 13 mV and a Tafel slope of 30 mV/dec in 0.5 M H<sub>2</sub>SO<sub>4</sub>. In this work, the N-doping of the support was performed after the synthesis of supported Ru NPs, being in this case the HER activity significantly decreased, confirming that N blocks the metal-centred active sites ( $\eta_{10}$  = 45 mV and Tafel slope of 84 mV/dec).

In contrast to the previous examples in which the NPs were synthesized over a pre-formed support, Wang *et al.* presented highly uniform Ru NPs (2-3 nm) over N-doped carbon (Ru@CN) by direct calcination of a solid mixture of D-glucosamine hydrochloride (GAH), melamine and RuCl<sub>3</sub> (Fig. 7d).<sup>12</sup> This system achieved a current density of 10 mA/cm<sup>2</sup> at a higher overpotential than in previous examples,  $\eta_{10}$  = 126 mV in 0.5 M H<sub>2</sub>SO<sub>4</sub>. More recently, in 2020, Chen *et al.* used graphene oxide (GO) obtained according to a modified Hummer method as support for a Ru-hydrogel (Ru-gel) obtained from a Ru-phen complex, which was freeze-dried overnight prior to a pyrolysis treatment, resulting in a Ru-modified N-doped graphene aerogel (Ru-NGA) (3.5 nm) (Fig. 7e).<sup>13</sup> The material showed a  $\eta_{10}$  = 55 mV and a Tafel slope of 32 mV/dec in 0.5 M H<sub>2</sub>SO<sub>4</sub>. Finally, Lau *et al.* developed Ru NPs (*ca.* 2.1 nm) embedded in N-doped carbon (NC), which was synthesized via a thermolysis process using Bu<sub>4</sub>N[Ru(N)Cl<sub>4</sub>] as the metal precursor and ethylenediaminetetraacetic acid tetrasodium (Na<sub>4</sub>EDTA) salt as the ligand and carbon source (Fig. 7f).<sup>14</sup> The authors also tested the effect of different Ru loadings (9, 19, 22, 36<sub>wt.%</sub> Ru), obtaining the best HER activity in 0.5 M H<sub>2</sub>SO<sub>4</sub> with Ru@NC (36<sub>wt.%</sub> Ru), achieving a  $\eta_{10}$  = 62 mV and a Tafel slope of *ca.* 40 mV/dec.

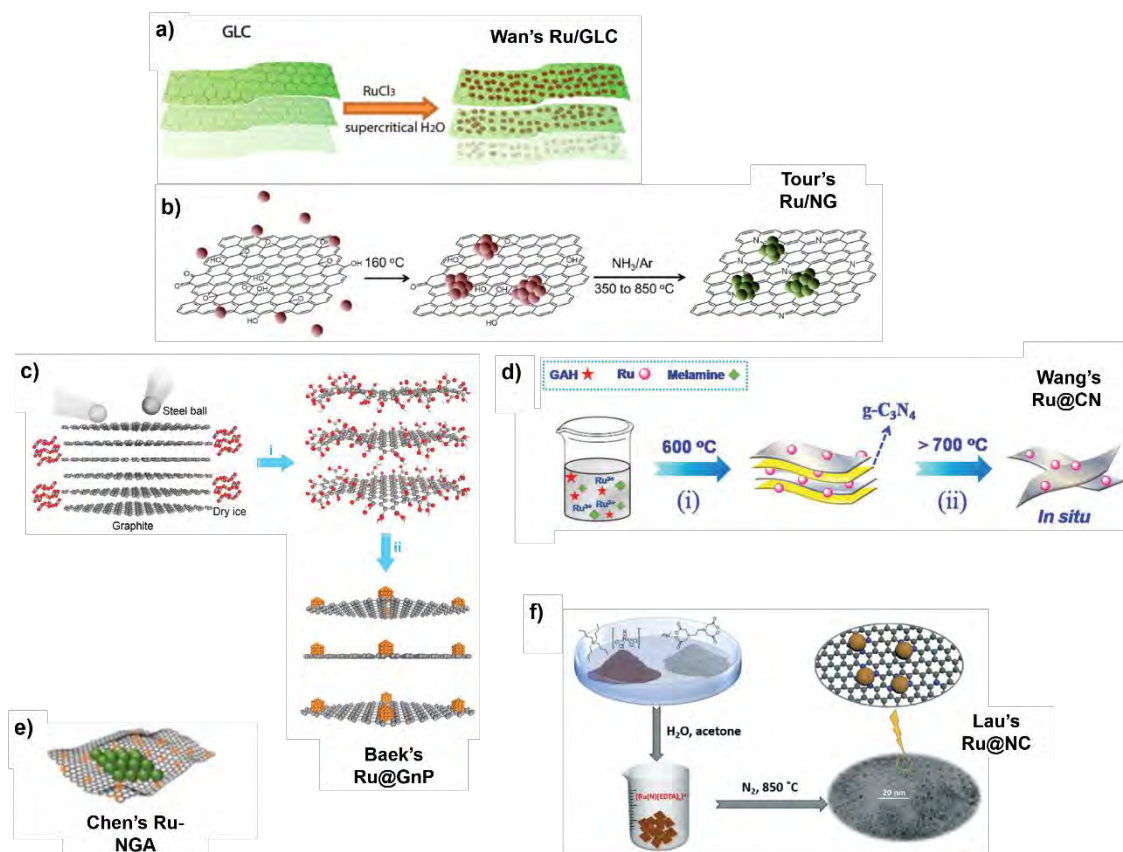


**Figure 7.** Graphene-supported Ru-based HER systems in acidic media. Wan's Ru/GLC (a),<sup>9</sup> Tour's Ru/NG (b),<sup>10</sup> Baik's Ru@GnP (c),<sup>11</sup> Wang's Ru@CN (d),<sup>12</sup> Chen's Ru-NGA (e)<sup>13</sup> and Lau's Ru@NC (f).<sup>14</sup> Adapted from refs. 9-14.

Despite some examples are found in the literature, HER on graphene-based materials has not been highly studied and chemists are thus far to understand them. In addition, the promotional effect of dopants has not been widely studied up to now. Thus, in *Chapter 4*, Ru NPs supported on reduced graphene oxide (rGO) are proposed as electrocatalysts for HER in acidic media. The organometallic approach has allowed to obtain clean-surface Ru NPs deposited onto a pre-formed support by preventing potential surface pollution coming from reducing agents or metal salts (not required in this methodology). rGO was the chosen support instead of GO since the higher concentration of oxygenated functional groups at the surface of GO could block the interaction between the organometallic complex and the graphitic structure, preventing the formation of Ru NPs. In this chapter, two different reduced graphene oxide supports will be used: rGO obtained by a modified Hummers method (rGO) (*Chapter 4A*) and rGO prepared from the pyrolysis of alginate (G) (*Chapter 4B*).



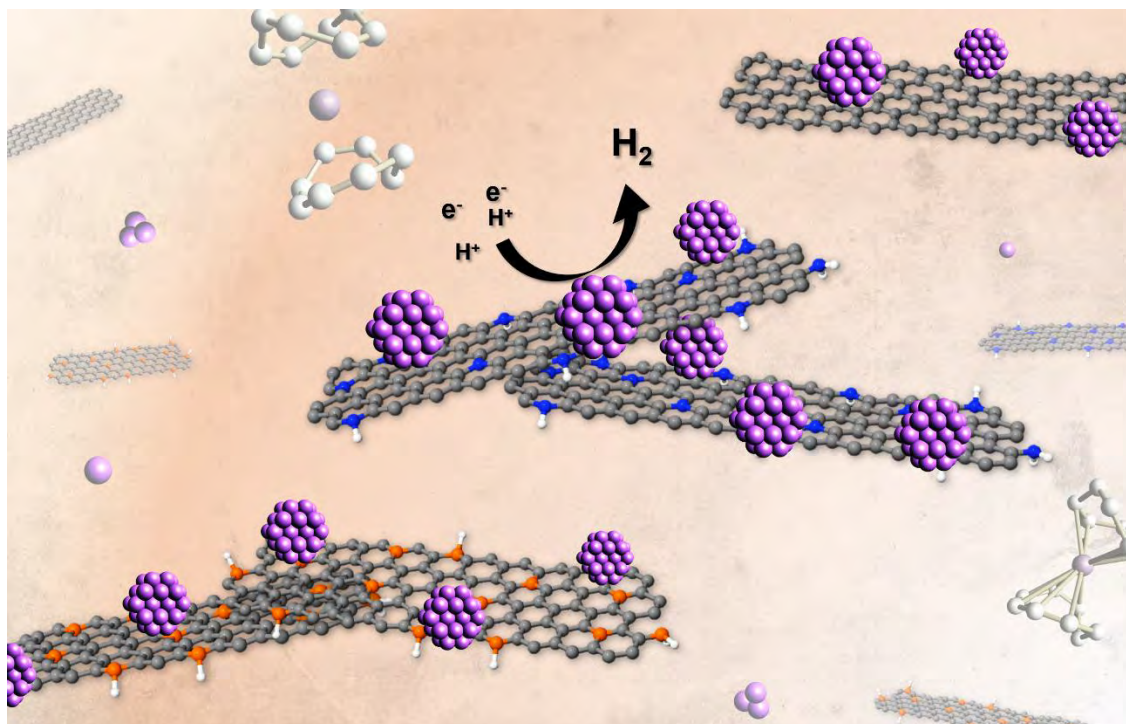
Also, the influence of heteroatom-doping (N and P) in the carbon supports has been studied both in terms of the stability of the NPs during the synthetic procedure and the catalytic activity of the systems towards the HER.

## **4.2 REFERENCES**

- <sup>1</sup> Y. Liang, Y. Li, H. Wang and H. Dai. *J. Am. Chem. Soc.* **2013**, 135, 2013-2036.
- <sup>2</sup> Y. Zheng, Y. Jiao, L. H. Li, T. Xing, Y. Chen, M. Jaroniec and S. Z. Qiao, *ACS Nano* **2014**, 8, 5, 5290-5296.
- <sup>3</sup> C. Ren, L. Wen, S. Magagula, Q. Jiang, W. Lin, Y. Zhang, Z. Chen and K. Ding, *ChemCatChem* **2020**, 12, 536-543.
- <sup>4</sup> K. Qu, Y. Zheng, X. Zhang, K. Davey, S. Dai and S. Z. Qiao, *ACS Nano* **2017**, 11, 7293-7300.
- <sup>5</sup> Y. H. Hung, D. Dutta, Y. J. Tseng, J. K. Chang, A. J. Bhattacharyya and C. Y. Su, *J. Phys. Chem. C* **2019**, 123, 22202-22211.
- <sup>6</sup> W. T. Chen, D. Dutta, Y. H. Hung, Y. Y. Sin, S. M. He, J. K. Chang and C. Y. Su, *J. Phys. Chem. C* **2020**, 124, 25701-25711
- <sup>7</sup> Y. Li, C. Ai, S. Deng, Y. Wang, X. Tong, X. Wang, X. Xia and J. Tu, *Mat. Res. Bull.* **2021**, 134, 111094.
- <sup>8</sup> J.R. McKone, E.L. Warren, M.J. Bierman, S.W. Boettcher, B.S. Lewis and H.B. Gray, *Energy Environ. Sci.* **2011**, 4, 3573-3583.
- <sup>9</sup> Z. Chen, J. Lu, Y. Ai, Y. Ji, T. Adschiri and L. Wan. *ACS Appl. Mater. Interfaces* **2016**, 8, 35132-35137.
- <sup>10</sup> R. Ye, Y. Liu, Z. Peng, T. Wang, A. S. Jalilov, B. I. Yakobson, S. H. Wei and J. M. Tour, *ACS Appl. Mater. Interfaces* **2017**, 9, 3785-3791.
- <sup>11</sup> F. Li, G. F. Han, H. J. Noh, I. Ahmad, I. Y. Jeon and J. B. Baek, *Adv. Mater.* **2018**, 1803676.
- <sup>12</sup> J. Wang, Z. Wei, S. Mao, H. Li and Y. Wang, *Energy Environ. Sci.* **2018**, 11, 800.
- <sup>13</sup> Y. Shi, W. Dai, M. Wang, Y. Xing, X. Xia and W. Chen, *Chem. Res. Chinese Universities* **2020**, 36, 4, 709-714.
- <sup>14</sup> B. Zheng, L. Ma, B. Li, D. Chen, X. Li, J. He, J. Xie, M. Robert and T. C. Lau, *Catal. Sci. Technol.* **2020**, 10, 4405-4411.

## Chapter 4A. Ru nanoparticles supported on rGO (Hummers) as HER catalysts

---



---

Three different cathodes for the hydrogen evolution reaction (HER) based on Ru NPs and reduced graphene oxide (rGO) have been developed. Ru NPs have been synthesized *in situ* in the presence of the carbon support by means of the organometallic approach, being the rGO structure and heteroatom (N or P), when present, the stabilizing agents of the NPs. The addition of heteroatoms into the graphitic structure (*i.e.* N or P) plays a key role in the stability and activity of the hybrid electrodes.

This work has been performed in the frame of a collaboration with Dr. L.M. Martínez (Instituto de Tecnología Química (ITQ) - Universitat Politècnica de València (UPV)), who prepared and characterized the Ru NPs supported on rGO. My contribution has consisted in performing all the electrocatalytic experiments and some characterizations before and after catalysis to explore their catalytic behaviour and understand the catalysts fate under turnover conditions.

---



## **4A.1 INTRODUCTION**

As explained in the the General Introduction section above, the metal-doping of graphene materials leads to improved electrocatalytic HER activity. Among the different metal atoms to be tested, Pt represents the state-of-the-art in HER electrocatalysis.<sup>1</sup> However, its scarcity, high price and relatively fast corrosion under alkaline catalytic conditions motivates the search for alternatives. In this regard, Ru has recently emerged as an alternative metal, given its similar hydrogen absorption energy, higher stability under basic conditions and relative lower price. Also, conductive graphene-structures are known to enhance the electrocatalytic activity of transition-metal based nanomaterials by restraining the aggregation of the nanocatalysts and improving the electron transfer from the metal nanocatalysts to the electrode.<sup>2,3,4,5</sup> In addition, they allow the possibility to use reduced metal precursors, compared to non-supported metal NPs, improving the cost efficiency.

In this *Chapter 4A* Hummers methodology was the chosen one to obtain GO prior to applying a heating process to produce reduced graphene oxide (rGO), which will be used as support for Ru NPs. W. S. Hummers *et al.* developed in 1958 a new methodology to prepare graphene oxide.<sup>6</sup> Until this time, previous methodologies relied on the use of strong oxidizing mixtures containing concentrated acids and oxidizing materials, making this procedure hazardous. The new methodology allowed a faster and safer preparation of GO, becoming a reliable method for producing high quantities of graphite oxide. This methodology consists in the oxidation of powdered flake graphite with sodium nitrate, sulfuric acid and potassium permanganate. Different heteroatoms (N or P) have been also introduced into the carbon structure by using ammonia<sup>7</sup> or triphenylphosphine,<sup>8,9</sup> respectively, following previous studies confirming the positive synergistic effect between the heteroatoms and metal NPs to obtain improved HER activities. In contrast to other methodologies used to obtain carbon-supported Ru NPs, in which the synthesis of the rGO and the NPs is done simultaneously by chemical reduction, in this chapter Ru NPs have been synthesized on-top of a pre-formed rGO. This methodology allows to tune the functional groups and/or heteroatoms doping of the carbon structure prior to its use as a support for the NPs. In addition, the organometallic approach allows to obtain NPs with clean surface, which is normally polluted from the metal salts used in other synthetic pathways.

## **4A.2 SYNTHESIS AND CHARACTERIZATION**

### **4A.2.1 Synthesis of Ru NPs supported onto rGO**

Three different rGO supports were synthesized before their modification with Ru NPs. The different rGOs differ in the heteroatom doping, namely the non-doped **rGO**, rGO doped with N (**NH<sub>2</sub>-rGO**) and rGO doped with P (**P-rGO**). rGO was obtained from GO, which in turn was prepared by a modified Hummers method.<sup>6</sup> Thus, GO was introduced into a quartz reactor and then heated at 400 °C during 15 min in a N<sub>2</sub> atmosphere (5 °C/min). After that, the reactor was cooled down to room temperature in a N<sub>2</sub> atmosphere for 1 h 30 min, obtaining **rGO**. **NH<sub>2</sub>-rGO** was obtained following a modified synthetic method previously reported:<sup>7</sup> 100 mg of GO (prepared by the modified Hummers method) was dispersed in 40 mL of ethylene glycol with the help of an ultrasonicator (3 h). Then, 1 mL of ammonia water (25%) was added to the dark brown dispersion, which was then transferred to a Teflon-lined autoclave and heated at 175 °C for 16 h. Finally, the precipitate was filtered, washed with distilled water until pH 7 and dried at 60 °C for 24 h. Finally, **P-rGO** was obtained following a synthetic method previously reported by using triphenylphosphine (TPP) as phosphorous source.<sup>8,9</sup>

Ru NPs were synthesized directly onto each of the three rGO supports following the organometallic approach.<sup>10</sup> Specifically, [Ru(COD)(COT)] was decomposed under H<sub>2</sub> at room temperature in the presence of each corresponding rGO, previously ultrasonicated in THF, to obtain the three different Ru supported samples, **Ru@rGO**, **Ru@NH<sub>2</sub>-rGO** and **Ru@P-rGO** (Fig. 1).

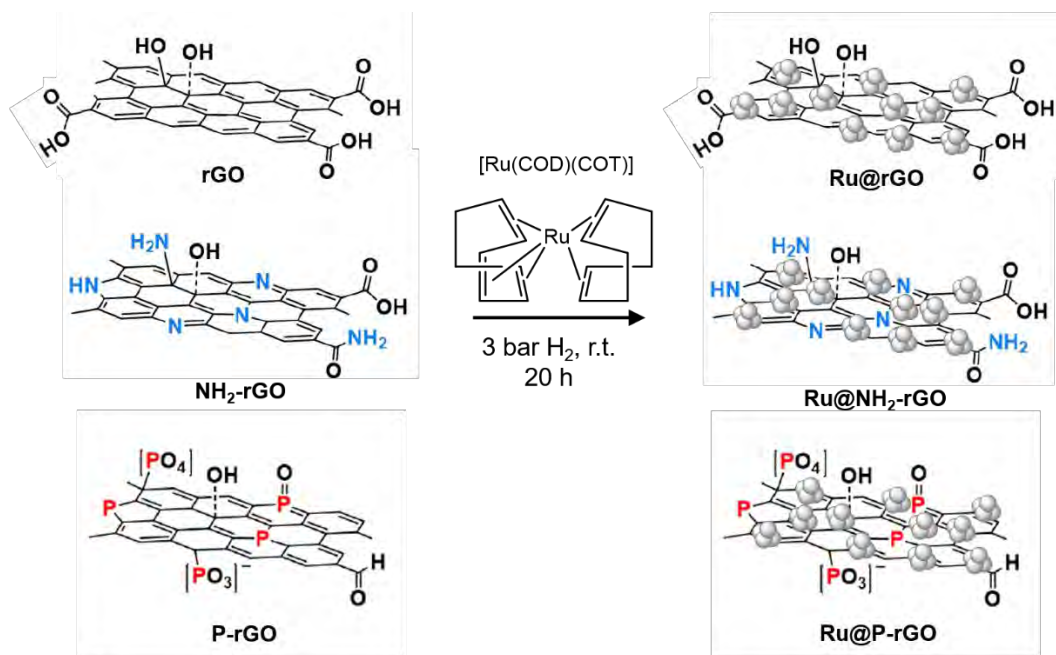


**Figure 1.** Scheme for the preparation of the **Ru@rGO**, **Ru@NH<sub>2</sub>-rGO** and **Ru@P-rGO** samples following the organometallic approach.

#### 4A.2.2 Transmission electron microscopy analysis (TEM)

After synthesis and after removing the remaining hydrogen from the Fischer-Porter reactor under vacuum, each as-prepared sample was analyzed by TEM. A drop of a solution of each of the three isolated **Ru@rGO** samples after dispersion in THF was deposited onto a carbon-coated copper grid. TEM images revealed spherical and isolated NPs on top of all the samples. NPs with similar size and dispersion were found for **Ru@NH<sub>2</sub>-rGO** and **Ru@P-rGO**, being the mean diameters  $1.5 \pm 0.2$  nm and  $1.5 \pm 0.3$  nm, respectively. In contrast, Ru NPs in the non-doped graphene present slightly bigger size and wider size distribution,  $2.0 \pm 0.8$  nm (Fig. 2). These results confirm the positive role of the heteroatom doping in the stabilization of Ru(0) NPs during the synthetic procedure, affecting the nucleation and growth kinetics of the NPs, resulting in smaller mean size and more uniform dispersions.

Inductively coupled plasma atomic emission spectroscopy (ICP-AES) analyses revealed metal contents of 2.4 wt% Ru, 2.5 wt% Ru and 3.1 wt% Ru in **Ru@rGO**, **Ru@NH<sub>2</sub>-rGO** and **Ru@P-rGO**, respectively.



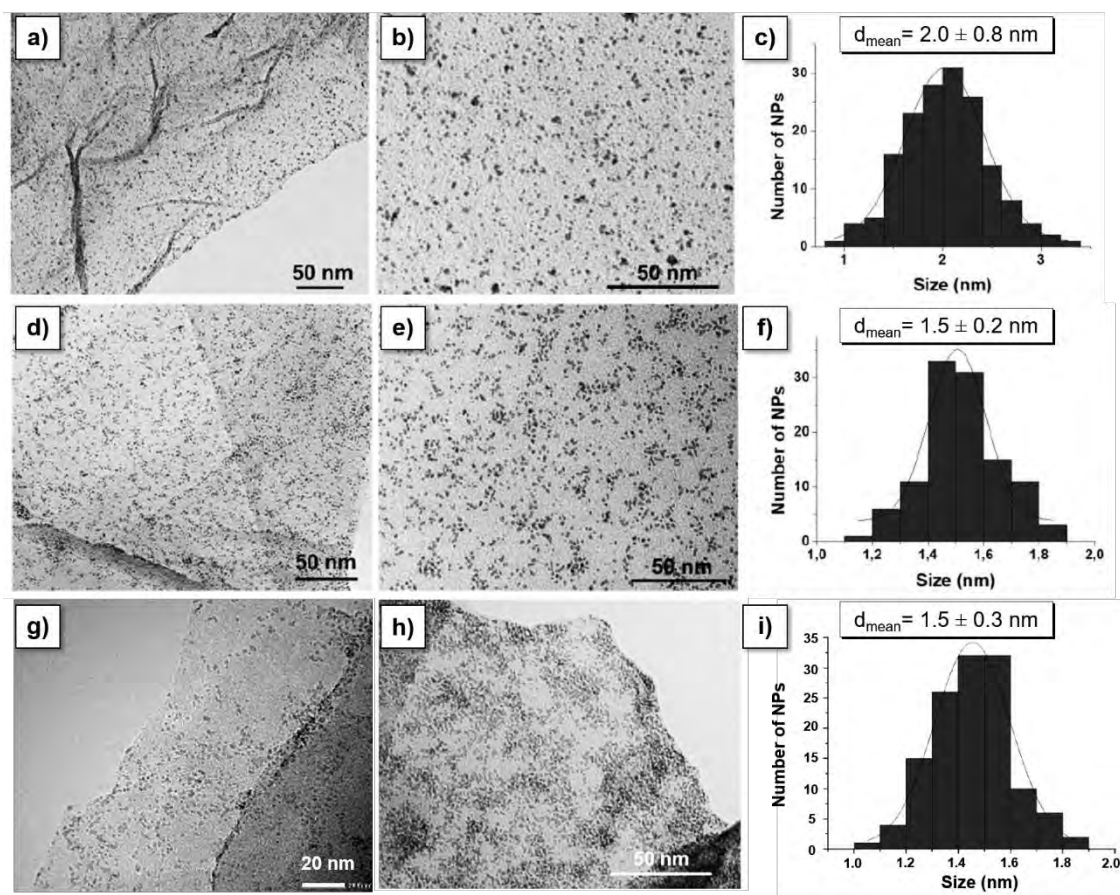


**Figure 2.** TEM images and size distribution histogram of **Ru@rGO** (a-c), **Ru@NH<sub>2</sub>-rGO** (d-f) and **Ru@P-rGO** (g-i).

#### 4A.2.3 X-ray photoelectron spectroscopy (XPS)

In order to confirm the presence of P and N atoms on the doped graphene and unravel their nature, XPS analysis have been performed. The high-resolution spectrum of P 2p shows a broad peak which can be deconvoluted in two components, one peak centred at 133.1 eV, corresponding to P atoms bonded to oxygen, and another one at 130.9 eV, corresponding to P-C bonds (Fig. 3a).<sup>11</sup> These peaks have been previously identified in similar P-doped graphenes.<sup>11</sup> In this case, the percentage of graphitic phosphorous atoms seems higher than in **Ru@P-G** (from alginate, *Chapter 4B*, see below), where P is mainly found in the phosphate form. Analysis of the P 2p signal also allowed to determine the P content in the doped support, **P-rGO**, which appeared to be of 1.26 at.%.



The high-resolution spectrum of N 1s shows a broad peak which can be also deconvoluted in three components, being the most intense peak centred at *ca.* 399.7 eV corresponding to  $-\text{NH}_2$  and  $-\text{NH}$  groups. The peak at 398.6 is attributed to pyridinic N atoms and the other one at 401.2 eV belongs to graphitic N atoms (Fig. 3b).<sup>7</sup>

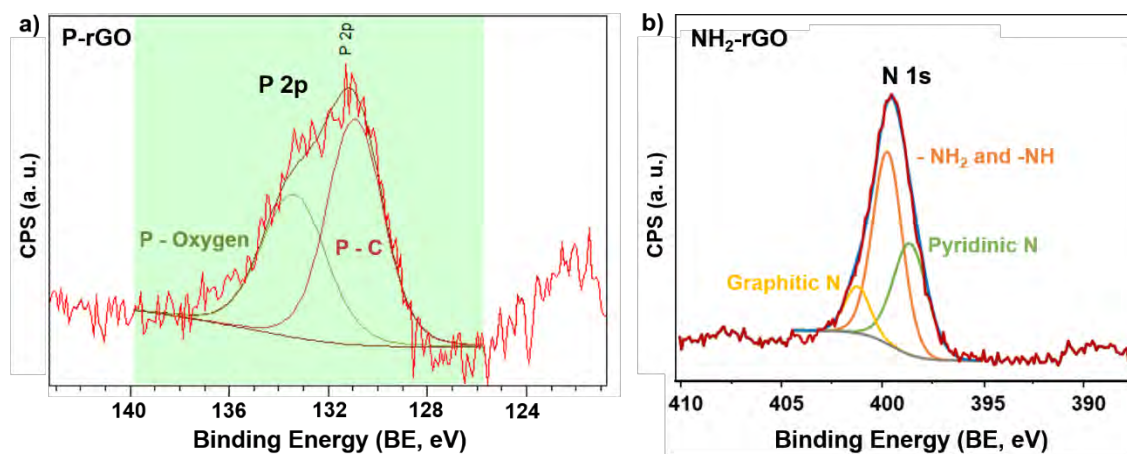


**Figure 3.** High-resolution P 2p XPS spectra of **P-rGO** (a) and high-resolution N 1s XPS spectra of **NH<sub>2</sub>-rGO** (b).

The overlap of the Ru 3d signal with the C 1s peak makes the signal deconvolution and interpretation difficult. Therefore, the different oxidation states of the Ru NPs have been assessed upon analysing the Ru 3p region. Fig. 4 shows the Ru 3p<sub>3/2</sub> signal of the as-synthesized **Ru@NH<sub>2</sub>-rGO**, which displays a binding energy of 462.4 eV. The deconvolution of this peak presents two contributions, one at 463.4 eV that is attributed to Ru(IV), characteristic of RuO<sub>2</sub>, and another one at 461.9 eV, which belongs to Ru(0). These results confirm the formation of a RuO<sub>2</sub> passivation layer around the Ru(0) core after air exposition. Ru 3p XPS analysis from **Ru@rGO** and **Ru@P-rGO** are currently on-going. However, from the obtained results for **Ru@NH<sub>2</sub>-rGO** and previous experience in the group with related Ru NPs,<sup>12</sup> a mixture Ru/RuO<sub>2</sub> is expected in all samples after air exposition.

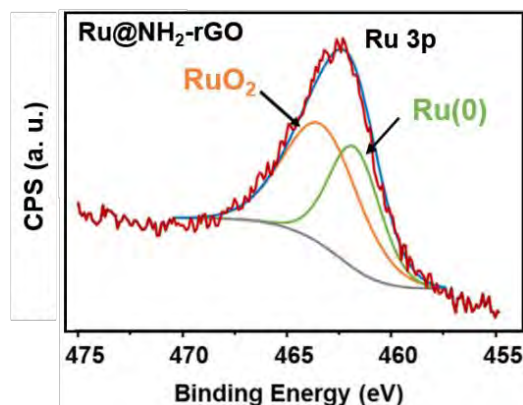


**Figure 4.** High-resolution Ru 3p XPS spectra of the as-synthesized **Ru@NH<sub>2</sub>-rGO**.

#### 4A.2.4 <sup>15</sup>N and <sup>31</sup>P magic angle spinning solid state NMR spectroscopy analysis (MAS-NMR)

The nature of the doping atoms in both **NH<sub>2</sub>-rGO** and **P-rGO** was examined from analogous <sup>15</sup>**NH<sub>2</sub>-rGO** and <sup>31</sup>**P-rGO** materials by <sup>15</sup>N MAS-NMR and <sup>31</sup>P MAS-NMR, respectively. <sup>15</sup>N MAS-NMR spectrum from <sup>15</sup>**NH<sub>2</sub>-rGO** shows a broad band between 330-185 ppm, attributed to N atoms far away from H atoms (*i.e.* pyridinic and graphitic N atoms far from H), and a sharper one around 150 ppm, attributed to N atoms near in space or bonded to H atoms (-NH<sub>2</sub>, -NH and graphitic N atoms close to H) (Fig. 5a, blue). <sup>1</sup>H-<sup>15</sup>N cross-polarization (CP) MAS NMR spectrum supports this assignment as the intensity of the broad signal between 330-185 ppm decreases compared to the one at 150 ppm, meaning that these N groups are not affected by cross polarization from close H atoms (Fig. 5a, khaki).

On the other hand, <sup>31</sup>P MAS NMR spectrum of **P-rGO** displays a broad peak centered at 0 ppm (*ca.* 25 ppm broad) (Fig. 5b). The width of this peak is attributed to a wide array of sites with slightly different isotropic chemical shifts, reflecting the broad array of environments expected to be found in the graphitic sheet, and represents “graphitic” phosphorus or oxidized graphitic phosphorous, bonded to three sp<sup>2</sup>-hybridized carbon atoms.

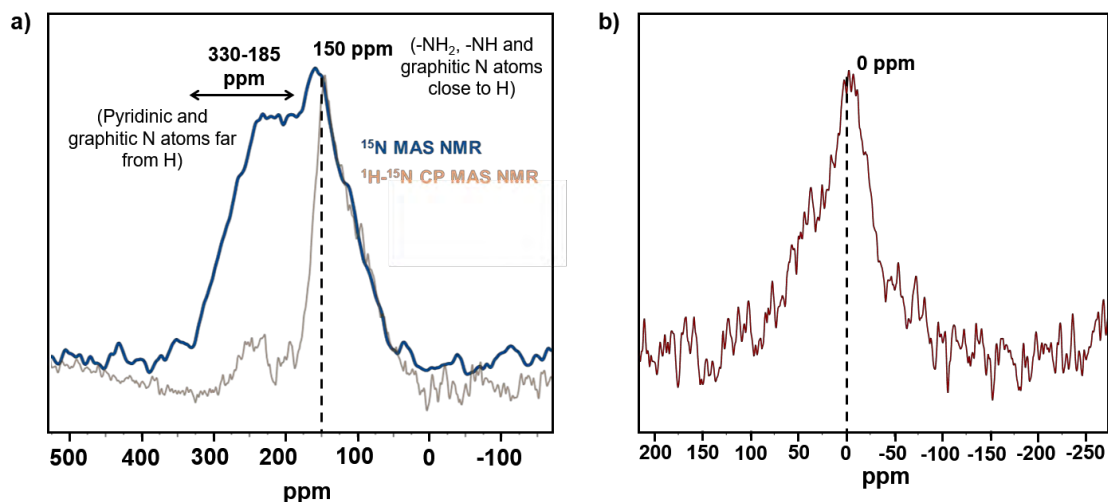


**Figure 5.**  $^{15}\text{N}$  MAS (blue) and CP-MAS (khaki) NMR spectra of  $^{15}\text{NH}_2\text{-rGO}$  (a) and  $^{31}\text{P}$  MAS spectrum of  $^{31}\text{P-rGO}$  (b).

## 4A.3 ELECTROCATALYTIC PERFORMANCE

### 4A.3.1 Electrocatalytic HER studies in acidic media

The HER performance of **Ru@rGO**, **Ru@NH<sub>2</sub>-rGO** and **Ru@P-rGO** was evaluated in 1 M H<sub>2</sub>SO<sub>4</sub> aqueous solution (pH 0). The material was dispersed in THF (2 mg/mL) and drop-casted onto a glassy carbon rotating disk electrode (GC-RDE). A three-electrode configuration was used to study the electrochemical behaviour of the materials, using the drop-casted RDE as working electrode. SCE (Saturated calomel electrode, KCl sat.) and a Pt wire were used as reference (RE) and counter electrodes (CE), respectively. The polarization curves and corresponding Tafel plots of **Ru@rGO**, **Ru@NH<sub>2</sub>-rGO** and **Ru@P-rGO** are shown in Fig. 6 (bold lines). A change in the current density is observed when scanning into reductive potentials, confirming the catalytic reduction of protons into H<sub>2</sub>.

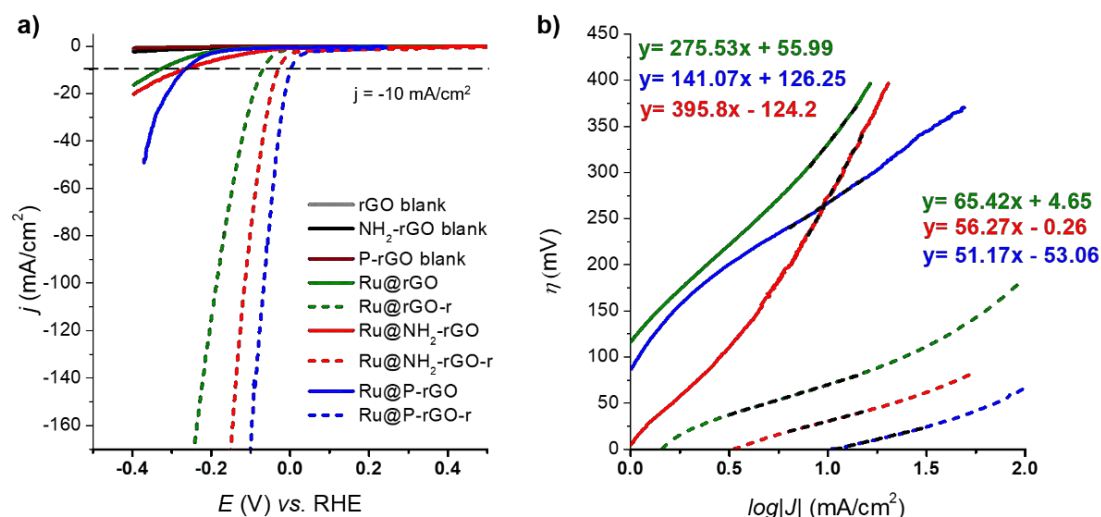


**Figure 6.** Polarization curves of **Ru@rGO** (green line), **Ru@NH<sub>2</sub>-rGO** (red line) and **Ru@P-rGO** (blue line) before (bold) and after (dashed) a reductive process at  $|j| = -10$  mA/cm<sup>2</sup> in 1 M H<sub>2</sub>SO<sub>4</sub>. **rGO** (grey line), **NH<sub>2</sub>-rGO** (black line) and **P-rGO** (wine line) blanks are also shown (a). Tafel plots of **Ru@rGO**, **Ru@rGO-r**, **Ru@NH<sub>2</sub>-rGO**, **Ru@NH<sub>2</sub>-rGO-r**, **Ru@P-rGO** and **Ru@P-rGO-r** in 1 M H<sub>2</sub>SO<sub>4</sub> (b). Same color code as in (a).

The catalytic performance of the systems can be significantly improved when submitted to a current-controlled bulk electrolysis at  $j = -10$  mA/cm<sup>2</sup>. As presented in Fig. 6, whereas **Ru@rGO**, **Ru@NH<sub>2</sub>-rGO** and **Ru@P-rGO** systems show a  $\eta_{10}$  of 331 mV, 274 mV and 268 mV, respectively, a shift on the polarization curves is observed after the reductive process, decreasing the  $\eta_{10}$  down to 71 mV, 30 mV and 2 mV, respectively. This behaviour is attributed to a change in the oxidation state of surface Ru atoms on the NPs. As shown in the XPS Section 4A.2.3 above and for related studies in our research group,<sup>12</sup> the Ru NPs surface gets partially oxidized (passivated) when exposed to air after the synthetic procedure. When applying a reductive potential to this RuO<sub>2</sub> passivated surface it is reduced back to metallic Ru (Fig. 7), and the catalytic current density of the corresponding reduced species, from now on **Ru@rGO-r**, **Ru@NH<sub>2</sub>-rGO-r** and **Ru@P-rGO-r**, radically increases in comparison with the passivated materials (*i.e.* **Ru@rGO**, **Ru@NH<sub>2</sub>-rGO** and **Ru@P-rGO**, Fig. 6a). A deep study of this behaviour was performed previously in our research group with 4PP stabilized Ru NPs (Ru/RuO<sub>2</sub>),<sup>12</sup> confirming a total disappearance of the RuO<sub>2</sub> peak in the XPS, indicating the reduction of the superficial Ru<sup>IV</sup> to metallic Ru under reductive catalytic conditions.

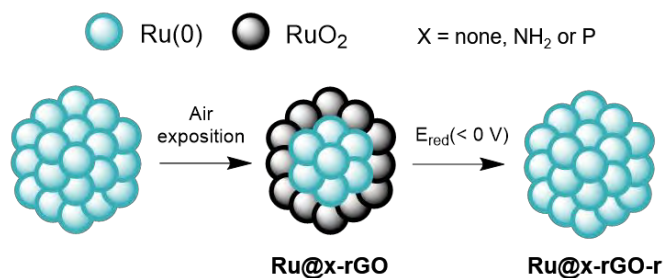


**Figure 7.** Schematic representation of the evolution of Ru species on the surface of NPs under different conditions.

The different nature and catalytic performance of **Ru@rGO/Ru@rGO-r**, **Ru@NH<sub>2</sub>-rGO/Ru@NH<sub>2</sub>-rGO-r** and **Ru@P-rGO/Ru@P-rGO-r** are evidenced through their corresponding Tafel plots as well (Fig. 6b). **Ru@rGO-r** shows a lower Tafel slope of 65 mV/dec compared to 276 mV/dec for **Ru@rGO**. The same tendency is observed with the heteroatom-doped systems, where **Ru@NH<sub>2</sub>-rGO-r** shows a lower Tafel slope of 56 mV/dec compared to 396 mV/dec for **Ru@NH<sub>2</sub>-rGO**, and **Ru@P-rGO-r** has a Tafel slope of 51 mV/dec compared to 141 mV/dec for **Ru@P-rGO**, as expected for the presence of Ru(0) species in the activated forms after bulk electrolysis. A positive effect of the nitrogen and phosphorous incorporated into the carbon support is also observed in the HER catalytic activity. Both **Ru@NH<sub>2</sub>-rGO** and **Ru@P-rGO** materials show better performance than their bare counterpart **Ru@rGO**, with lower overpotentials and Tafel slopes, representing some of the best Ru-based HER electrocatalysts reported so far in the literature (see Table A1 in Annex). Among them, the P-doped system shows the best catalytic activity, with particularly low  $\eta_{10}$  (only 2 mV). The respective electron acceptor and electron donor ability of nitrogen and phosphorous to adjacent carbons in the graphitic structure would affect the electronic structure of the support, with a concomitant effect in the electronic structure of the Ru NPs, improving in this case the synergistic effect between Ru and C, modulating the adsorption of reaction intermediates to enhance the HER catalytic activity.

The Tafel slope ( $b$ ) allows defining the rate determining step (rds) of the catalytic reaction. **Ru@rGO-r**, **Ru@NH<sub>2</sub>-rGO-r** and **Ru@P-rGO-r** show Tafel slopes of 65, 56 and 51 mV/dec, respectively (Fig. 6b), suggesting that the HER follows the Volmer-Heyrovsky mechanism. This value reveals for all electrodes a situation in between the Volmer and Heyrovsky steps as rds (the Heyrovsky step, H<sub>2</sub> electrodesorption with a

proton from the solution, presents values of  $b \approx 40$  mV/dec). In contrast, **Ru@P-rGO** shows a Tafel slope closer to 120 mV, being typically attributed to the Volmer step as rds (adsorption of  $H^+$  to form the M-H species on the NP, typically  $b \approx 120$  mV/dec). In addition, **Ru@rGO** and **Ru@NH<sub>2</sub>-rGO** both show very high Tafel slopes ( $>150$  mV), suggesting that the  $H^+$  adsorption is extremely slow.

#### 4A.3.2 Fate of the catalyst under catalytic conditions

The fate of the heterogeneous systems after short term stability tests (2 h) was assessed by TEM analysis. To do that, after 2 h under catalytic conditions (CP,  $j = -10$  mA/cm<sup>2</sup>), the drop-casted materials were recovered from the RDE with THF and a bit of sonication. Then, a drop of the THF suspension of the recovered material was deposited onto a carbon-coated copper TEM grid. The mean size of the NPs clearly increased for **Ru@rGO**, while the size was maintained for **Ru@NH<sub>2</sub>-rGO** and **Ru@P-rGO** (Fig. 8). These results support the hypothesis that heteroatoms (*i.e.* N or P) stabilize Ru NPs from aggregation/coalescence both during the synthetic process and under catalytic conditions. In addition, fewer NPs are found in TEM images after the catalytic turnover, but due to the difficulties to obtain enough material after catalysis and the heterogeneity of the materials, no hasty conclusions will be taken.



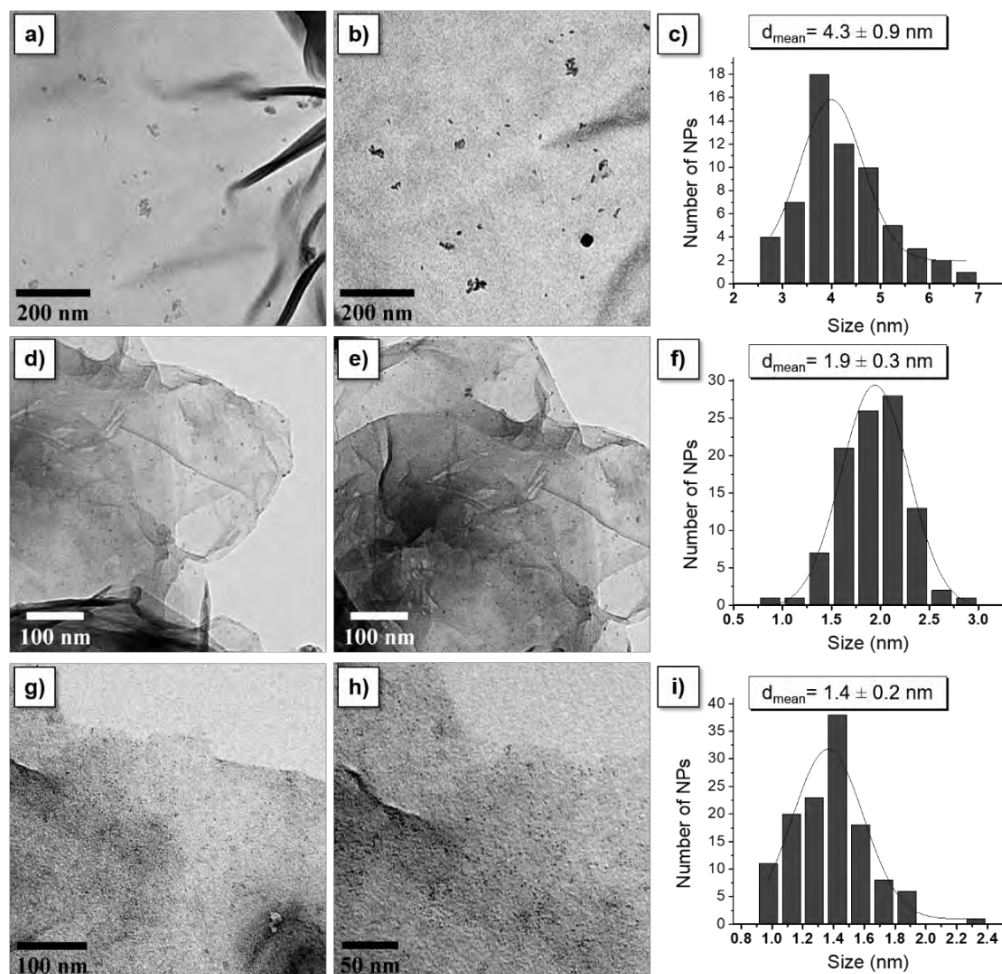


**Figure 8.** TEM images and corresponding histogram of **Ru@rGO** (a-c), **Ru@NH<sub>2</sub>-rGO** (d-f) and **Ru@P-rGO** (g-i) after 2 h under catalytic conditions ( $j = -10 \text{ mA/cm}^2$ ).

In addition, EDX analysis of **Ru@P-rGO** confirmed presence of Ru and P in the sample after 2 h under catalytic conditions (Fig. 9).

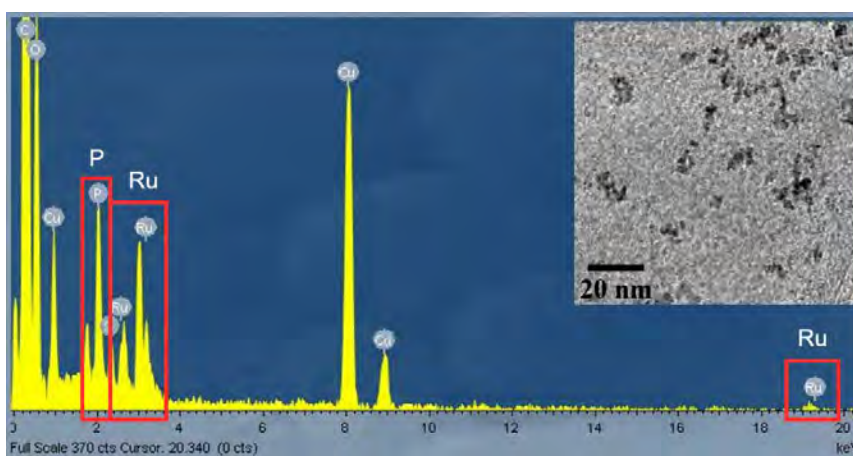


**Figure 9.** TEM (inset) and EDX analysis of **Ru@P-rGO** after 2 h under catalytic conditions ( $j = -10 \text{ mA/cm}^2$ ).

Long-term stability is also a key parameter for a catalyst to be potentially useful in the HER. Thus, **Ru@rGO-r**, **Ru@NH<sub>2</sub>-rGO-r** and **Ru@P-rGO-r** electrodes were held at a constant current density of  $j = -10 \text{ mA/cm}^2$  in a current controlled experiment (*i.e.* chronopotentiometry) for 12 h, monitoring the change in the required overpotential (Fig. 10). LSVs before and after the 12 h experiments are also shown in Fig. 10. The **Ru@NH<sub>2</sub>-rGO-r** and **Ru@P-rGO-r** systems showed almost no change in  $\eta_{10}$  and almost identical LSV polarization curves before and after catalytic turnover (Fig. 10b and 10c). For **Ru@rGO-r**, the stability is also confirmed, obtaining similar catalytic activity after catalytic turnover. A little activation is observed after the 12 h experiment, probably because this experiment started before the complete activation of the system by the previous reductive process (Fig. 10a). Therefore, even though the catalysts suffer from slight changes during the catalytic turnover, as shown in TEM images after 2 h (Fig. 8), their HER activity is preserved for at least 12 h.

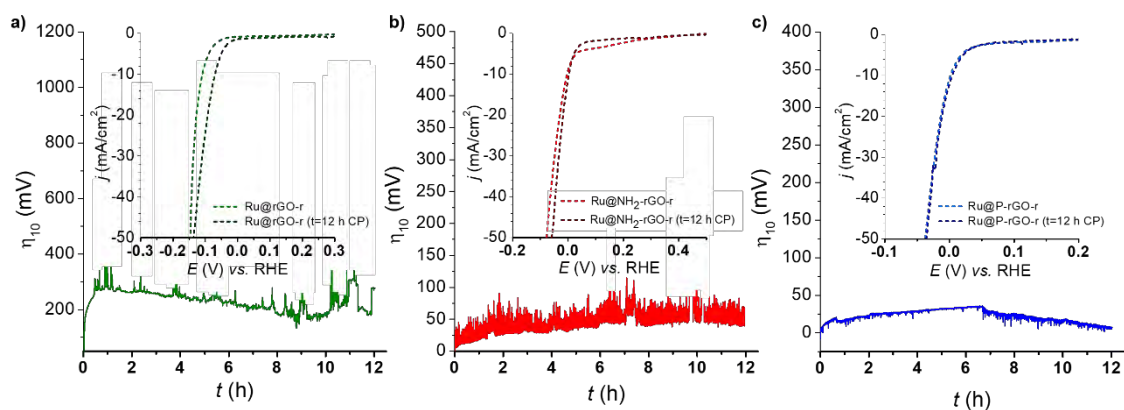


**Figure 10.** LSV of **Ru@rGO-r** (a, green), **Ru@NH<sub>2</sub>-rGO-r** (b, red) and **Ru@P-rGO** (c, blue) before (light color) and after (dark color) a 12-h chronopotentiometry experiment at a  $j = -10 \text{ mA/cm}^2$ .

#### 4A.3.3 Faradaic efficiencies

Faradaic efficiencies of 96-98 % were determined by quantifying the amount of H<sub>2</sub> generated by the systems during a 20-min chronoamperometry using a H<sub>2</sub>-Clark electrode, and comparing it with the maximum theoretical amount of H<sub>2</sub> calculated from the total charge passed through the electrode (Fig. 11). This confirms the production of H<sub>2</sub> as the sole reaction taking place.



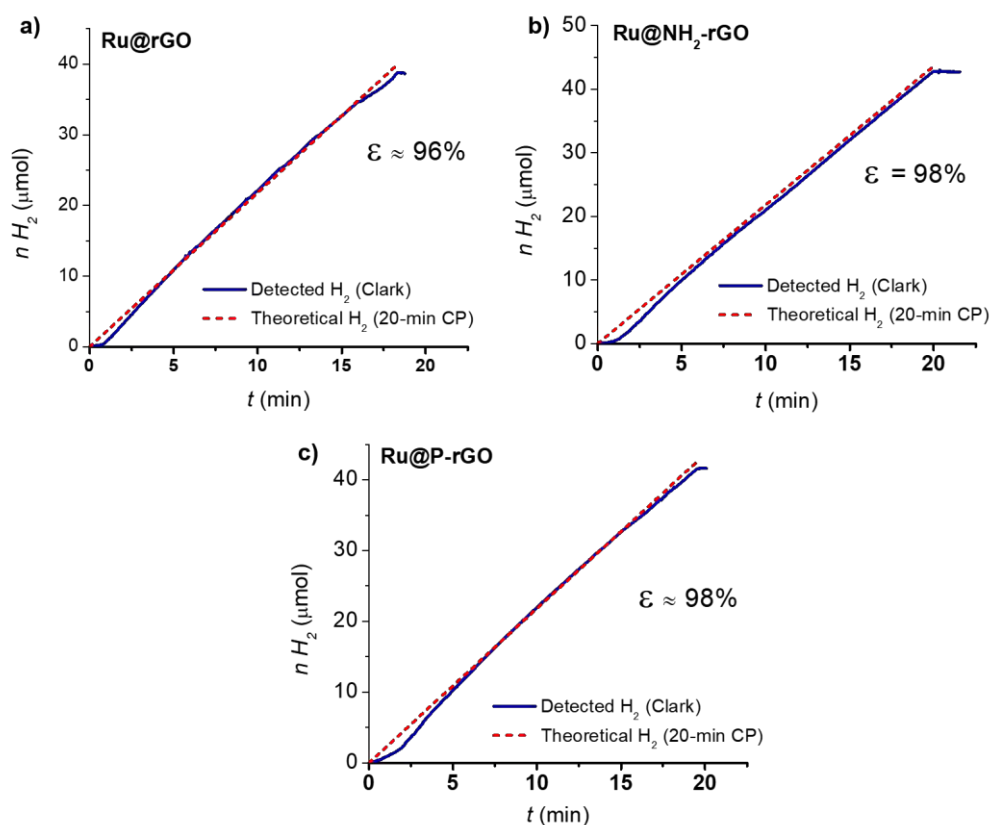


**Figure 11.** H<sub>2</sub>-monitored current-controlled bulk electrolysis of **Ru@rGO** (a), **Ru@NH<sub>2</sub>-rGO** (b) and **Ru@P-rGO** (c) in 1 M H<sub>2</sub>SO<sub>4</sub>. The production of H<sub>2</sub> was detected in the gas phase by the use of a Clark-type electrode.

#### 4A.3.4 Electrocatalytic performance benchmarking

The electrocatalytic performance of all the systems was further compared by following the benchmarking methodology reported by Jaramillo *et al.*<sup>13</sup> Each electrochemically active surface area (ECSA) was calculated from C<sub>DL</sub>, which was estimated by successive scan-rate dependent CVs in a non-faradaic region (Fig. 12, Table 1). In this region no redox process take place and all the measured current is due to double-layer charging. Thus, a plot of *i* as a function of *v* yields a straight line with a slope equal to C<sub>DL</sub> (Eq. 1).

$$i = vC_{DL} \quad \text{Eq. 1}$$

The ECSA was obtained by dividing the calculated capacitance by a tabulated value (C<sub>S</sub> = specific capacitance) that depends on the material used and solution (for C,

in 1 M H<sub>2</sub>SO<sub>4</sub> C<sub>s</sub>=13-17 μF/cm<sup>2</sup>) (Eq. 2). The roughness factor (RF) was calculated by dividing the ECSA by the geometrical surface area (S) (Eq. 3).

$$\text{ECSA [cm}^2\text{]} = \frac{C_{DL}}{C_s} \quad \text{Eq. 2}$$

$$\text{RF} = \frac{\text{ECSA}}{S} \quad \text{Eq. 3}$$

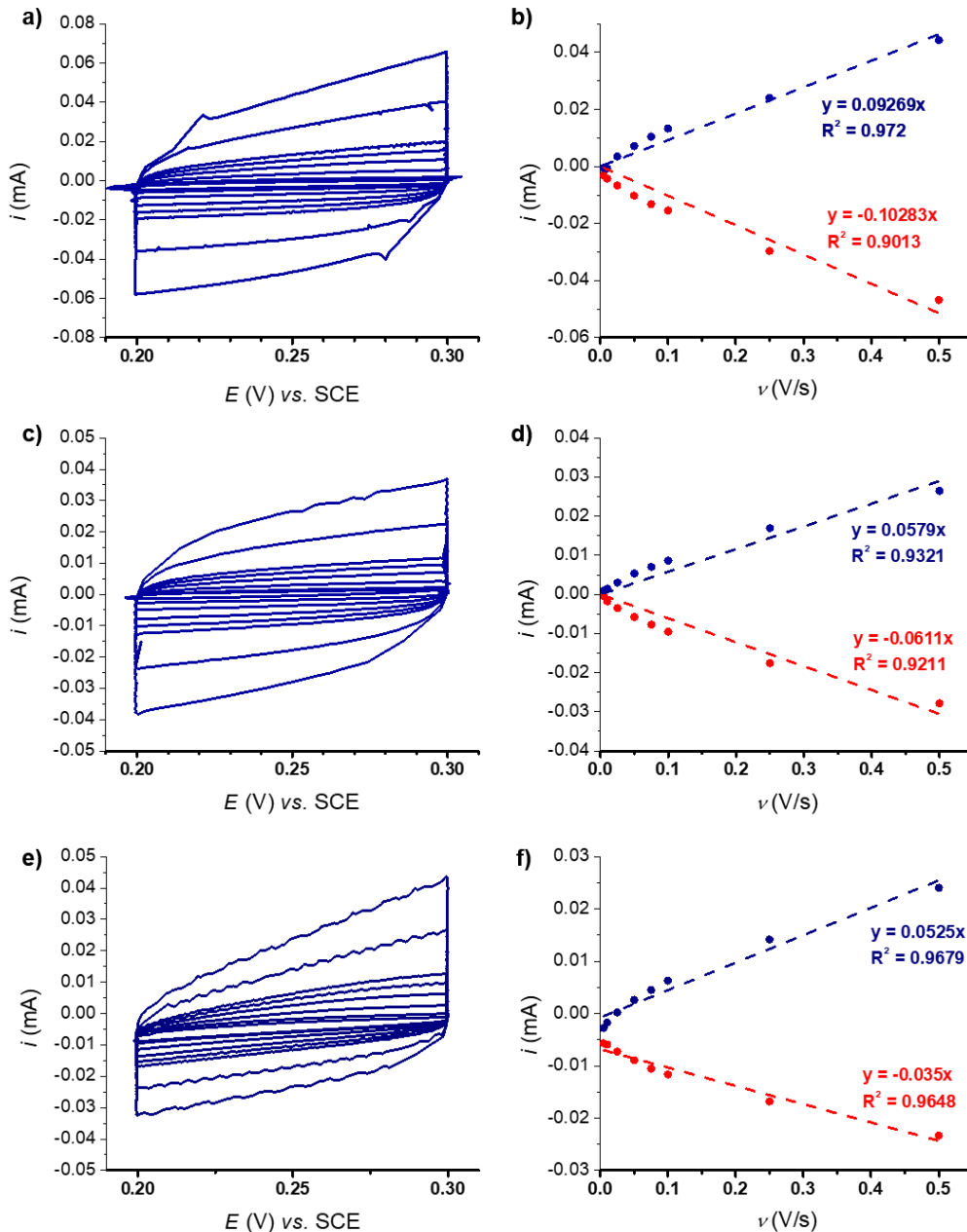


**Figure 12.** Representative multi CV experiments at different scan rates for C<sub>DL</sub> determination of **Ru@rGO** (a), **Ru@NH<sub>2</sub>-rGO** (c) and **Ru@P-rGO** (e). Plot of current values at 0.25 V vs. SCE for the different scan rates in 1 M H<sub>2</sub>SO<sub>4</sub> for **Ru@rGO** (b), **Ru@NH<sub>2</sub>-rGO** (d) and **Ru@P-rGO** (f).

The  $C_{DL}$  values are  $0.07 \pm 0.03$ , 0.0595 and 0.04375 for **Ru@rGO**, **Ru@NH<sub>2</sub>-rGO** and **Ru@P-rGO**, respectively. Having a look at the ECSA values listed in Table 1, the values for **Ru@rGO**, **Ru@NH<sub>2</sub>-rGO** and **Ru@P-rGO** (entries 1, 3 and 5) are comparable, confirming similar RF between supports even if heteroatoms are introduced in the carbon structure, in contrast to results shown in *Chapter 4B* (see below), where the addition of P into the carbon structure made the final material more exfoliated and less rough.

**Table 1.** Summary of physico-chemical and HER electrocatalytic data for the systems studied in this work (1 M H<sub>2</sub>SO<sub>4</sub> aqueous solution). Parameters: mean diameter ( $d_{mean}$ ), onset overpotential at -10 mA/cm<sup>2</sup> ( $\eta_{10}$ ), Tafel slope ( $b$ ), exchange current density ( $j_0$ ), ECSA, RF and specific current density at  $\eta=100$  mV ( $|j_s|$ ).

Entry	System	$d_{mean}$ (nm)	Ru (wt.%)	$\eta_{10}$ (mV)	$b$ (mV/dec)	$j_0$ (mA/cm <sup>2</sup> )	ECSA (cm <sup>2</sup> )	RF	$ j_s $ ( $\eta = 100$ mV) (mA/cm <sup>2</sup> )
1	<b>Ru@rGO</b>	2.0 ± 0.8	2.4	331	276	0.63	5.9 ± 1.4	84.3 ± 20.0	0.01
2	<b>Ru@rGO-r</b>	-	-	71	65	0.85	9.1	130.3	0.19
3	<b>Ru@NH<sub>2</sub>-rGO</b>	1.5 ± 0.2	2.5	274	396	2.06	4.0	56.7	0.05
4	<b>Ru@NH<sub>2</sub>-rGO-r</b>	-	-	30	56	1.01	12.8	183.4	0.42
5	<b>Ru@P-rGO</b>	1.5 ± 0.3	3.1	268	141	0.13	2.9	41.7	0.03
6	<b>Ru@P-rGO-r</b>	-	-	2	51	10.88	26.4	376.9	0.45

The ECSA values allow calculating the specific current density ( $j_s$ ) of the electrode, which represents the real electroactive area of the whole material at a given overpotential. Thus, the current density,  $j_s$ , normalized per ECSA at  $\eta= 100$  mV has been calculated for all the systems (Table 1) as follows:

$$j_s = \frac{j_\eta}{RF} = \frac{\left(\frac{i_\eta}{S}\right)}{\left(\frac{ECSA}{S}\right)} = \frac{i}{ECSA} \quad \text{Eq. 4}$$

The same parameters have been calculated after the activation of the materials (Fig. 13 and Table 1 entries 2, 4 and 6), obtaining higher ECSA, RF and  $j_s$  values in all

cases. As confirmed in *Chapter 4B* (see below), the increase in ECSA values after the reductive process is attributed to changes in the carbon support and the reduction of  $\text{RuO}_2$  into  $\text{Ru}^0$ , as observed in monodispersed RuNPs.<sup>12</sup> In fact, as observed in Table 1, the ECSA increase is emphasized in the doped materials compared to the bare one, following this trend  $\text{rGO} < \text{NH}_2\text{-rGO} < \text{P-rGO}$ . These differences will be studied in near-future by characterizing, by means of XPS, solid NMR, etc. each support and hybrid material after the reductive process, allowing to extract some insights about the evolution of each system under reductive electrocatalytic conditions.

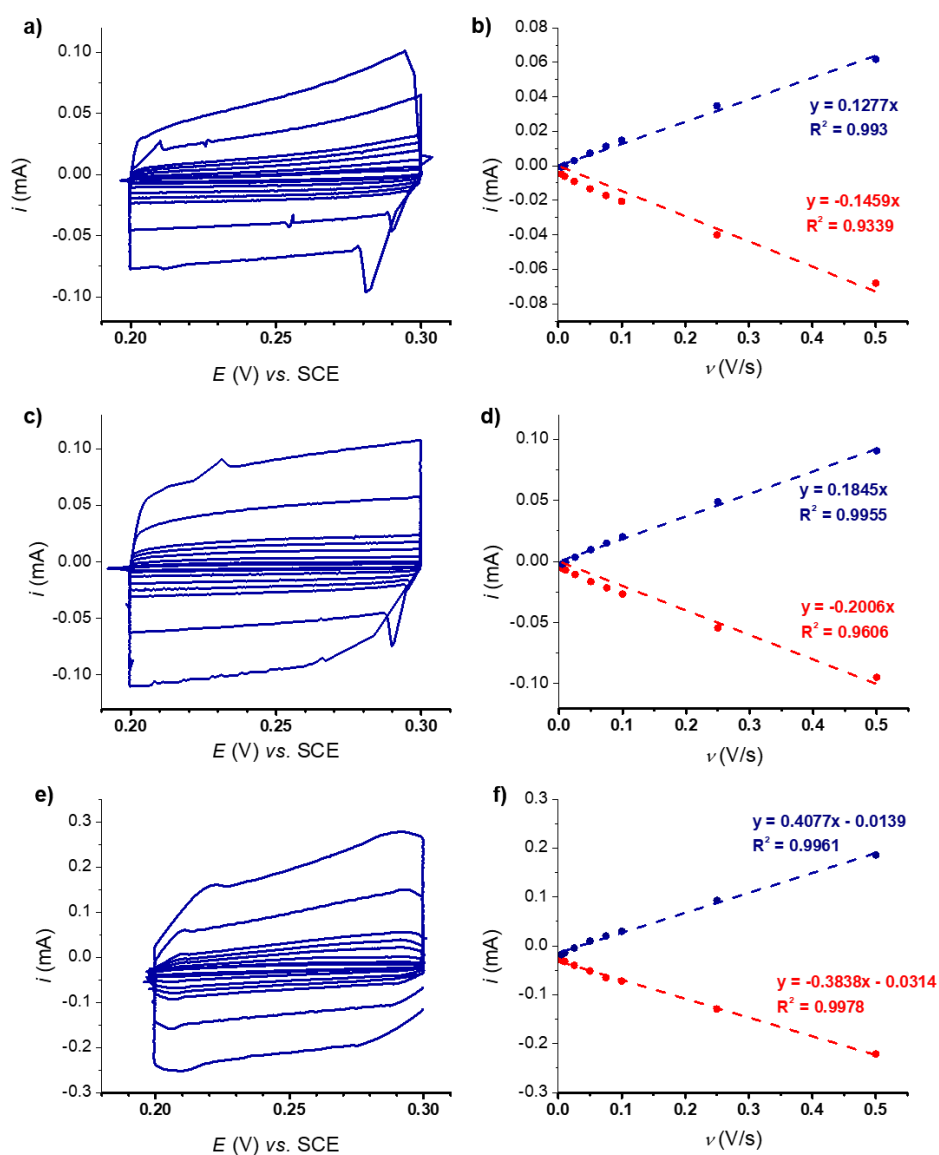


**Figure 13.** Representative multi CV experiment at different scan rates for  $C_{\text{DL}}$  determination of  $\text{Ru@rGO-r}$  (a),  $\text{Ru@NH}_2\text{-rGO-r}$  (c) and  $\text{Ru@P-rGO-r}$  (e). Plot of current values at 0.25 (vs. SCE) for the different scan rates in 1 M  $\text{H}_2\text{SO}_4$  for  $\text{Ru@rGO-r}$  (b),  $\text{Ru@NH}_2\text{-rGO-r}$  (d) and  $\text{Ru@P-rGO-r}$  (f).

#### **4A.4 CONCLUSIONS & PERSPECTIVES**

Well dispersed Ru NPs supported onto three different rGO materials (*i.e.* non-doped (**rGO**), N-doped (**NH<sub>2</sub>-rGO**) and P-doped (**P-rGO**) have been successfully synthesized taking benefit of the organometallic approach, obtaining Ru NPs between 1-3 nm in size. After partial surface oxidation by air exposition after the synthetic procedure, the catalytic activities of the resulting **Ru@rGO**, **Ru@NH<sub>2</sub>-rGO** and **Ru@P-rGO** materials have been studied.

The activity of all materials in 1 M H<sub>2</sub>SO<sub>4</sub> aqueous solution at pH 0 clearly confirms the dependence of the HER catalytic activity on the oxidation state of the NPs surface, being metallic Ru<sup>0</sup> sites more active than RuO<sub>2</sub>. This behaviour has been deduced by comparing the electrocatalytic activity before and after applying reductive conditions to the systems, obtaining better catalytic activities thereafter. All the activated **Ru@rGO-r**, **Ru@NH<sub>2</sub>-rGO-r** and **Ru@P-rGO-r** materials work at low overpotentials ( $\eta_{10} \approx 71$  mV, 30 mV and 2 mV, respectively) and present a Tafel slope of 65, 56 and 51 mV/dec, respectively. It is also noticed a positive effect of the heteroatom (*i.e.* N or P) incorporated into the carbon support in the catalytic HER activity, especially for the P-doped case. This behaviour can be explained by the respective electron acceptor and electron donor ability of N and P atoms adjacent to C atoms in the graphitic structure, affecting the electronic structure of the support, with a concomitant effect in the electronic structure of Ru NPs, improving in this case the synergistic effect between Ru and C, modulating the adsorption of reaction intermediates to enhance the HER activity. Thus, thanks to the high conductivity of rGO, the extremely small Ru NPs size and the synergistic effect between the Ru NPs and the support, high catalytic activities for HER are achieved, especially for **Ru@NH<sub>2</sub>-rGO** and **Ru@P-rGO**, representing some of the best Ru-based HER electrocatalysts reported so far in the literature (see Table A1 in Annex).

Long-term stability studies (12 h) confirmed that all systems are capable to produce a current density of  $j = -10$  mA/cm<sup>2</sup> for at least 12 h without any sign of deactivation. High faradaic efficiency values (*i.e.* 96-98 %) confirmed quantitative H<sub>2</sub> production for all the studied systems.

Since the influence of the doping of different heteroatoms in carbon-supported Ru NPs in their overall HER electrocatalytic activity has not been deeply studied so far,

future DFT calculations by modelling these particular systems could allow to unravel the favourable electronic effects of the different heteroatoms both in the carbon structure and in the Ru catalysts by means of the so-called d-band center calculations.<sup>14</sup> In addition, as a well-accepted HER descriptor in acidic media, the hydrogen adsorption Gibbs free energy ( $\Delta G_{H^*}$ ) could be evaluated by means of DFT calculations, trying to correlate trends between this parameter and the experimental performance (*i.e.* exchange current density values) depending on the used heteroatom doping. In addition, the effect of different doping percentages could be investigated in a future work, trying to find the optimal doping to obtain the best catalytic system.

## **4A.5 EXPERIMENTAL SECTION**

### **Materials and methods**

All procedures concerning the synthesis and preparation of samples were carried out using standard Schlenk tubes, Fisher-Porter glassware and vacuum line techniques or in a glove-box (MBraun) under argon atmosphere. Solvents (THF, hexane, from Sigma-Aldrich) were purified by distillation under Ar atmosphere through filtration in the column of a purification apparatus (MBraun). Solvents were degassed before use via a multi-cycle freeze-pump-thaw process. [Ru(COD)(COT)] was purchased from Nanomeps Toulouse.

### **Characterization techniques**

**Transmission electron microscopy (TEM).** Ru-NPs were observed by TEM after deposition of a drop of a solution of the isolated NPs after dispersion in THF on a copper grid. TEM analyses were performed at the “Servicio de Microscopia Electrónica” of Universitat Politècnica de València (UPV) by using a JEOL JEM 1010 CX-T electron microscope operating at 100 kV with a point resolution of 4.5 Å. Some TEM images have been performed at the “Servei de Microscòpia” of the UAB using a JEOL JEM 1400 electron microscope working at 120 kV with a resolution point of 0.4 nm by re-dispersing the material in THF and adding a drop onto a carbon-coated copper grid just before TEM analysis. Size distributions were determined through manual analysis of enlarged micrographs by measuring > 200 particles on a given grid.

**Energy-dispersive X-ray spectroscopy (EDX):** EDX analysis were performed at “Servei de Microscòpia de la UAB” using a JEOL JEM 2011 electron microscope to analyze the chemical elemental composition of the samples.

**Inductively coupled plasma atomic emission spectroscopy (ICP-AES):** ICP-AES analyses were performed by the ICP technical service of the Instituto de Tecnología Química (ITQ), using a Varian 715-ES ICP-Optical Emission Spectrometer. The samples for ICP-AES were prepared following a modified digestion method reported.<sup>15</sup> In particular, 30 mg of catalyst sample were suspended in 21 mL HCl-HNO<sub>3</sub> (6:1). The solution was then sonicated for 90 minutes and the samples were digested at 180 °C for

15 hours. After that, it was cooled down until room temperature (r.t.), diluted with 100 mL of water and analyzed by ICP-AES.

**Solid-state MAS-NMR spectroscopy.**  $^{15}\text{N}$  and  $^{31}\text{P}$  MAS-NMR analyses were performed at the ITQ on a Bruker Avance 400WB instrument equipped with a 4 mm probe with the sample rotation frequency of 10 kHz. Measurements were carried out in a 4 mm  $\text{ZrO}_2$  rotor.  $^{15}\text{N}$  MAS-NMR analyses have been performed with and without cross-polarization (CP).

**X-ray photoelectron spectroscopy (XPS):** XPS analyses were performed using a SPECS device equipped with a Phoibos 150-9MCD detector using Mg-K $\alpha$  radiation ( $h\nu= 1235.6$  eV) and Al-K $\alpha$  radiation ( $h\nu= 1483.6$  eV) from a dual source. The pressure during the measurements was kept under  $10^{-9}$  Torr. The quantification and titration of the spectra was done with the help of the software CASA, referencing them in base of C1s = 284.5 eV.

## Synthetic procedures

**Synthesis of rGO.** It was obtained from thermal reduction/exfoliation at low temperature of GO prepared by modified Hummers method.<sup>6</sup> GO was introduced into a quartz reactor and then heated at 400 °C during 15 min in a  $\text{N}_2$  atmosphere (5 °C /min). After that, the reactor was cooled down to room temperature in  $\text{N}_2$  atmosphere for 1h 30 min. Elemental analysis: C=83.6 %, H: 0,5 %, S: 0.14 %

**Synthesis of  $\text{NH}_2$ -rGO.** Obtained following a modified synthetic method previously reported elsewhere.<sup>7</sup> 100 mg of GO (prepared by modified Hummers method)<sup>6</sup> was dispersed in 40 mL of ethylene glycol with the help of an ultra-sonicator (3h). After that, 1 mL of ammonia water (25%) was added to the dispersion (dark brown), which was then transferred to a Teflon-lined autoclave and heated at 175 °C for 16h. Finally, the precipitate was filtered, washed with distilled water until pH 7 and dried at 60 °C for 24 h. Elemental analysis: N: 7.91 %, C=75.43 %, H: 1.69 %. XRD: Reduced graphene. IR: (KBr pellet,  $\text{cm}^{-1}$ ), 1580 $\text{cm}^{-1}$  ( $\nu$  N-H) and 1020  $\text{cm}^{-1}$  ( $\nu$  C-N).

**Synthesis of P-rGO.** P-rGO was obtained following a synthetic method previously reported elsewhere.<sup>8,9</sup>



**Synthesis of Ru@x-rGO (X= none, NH<sub>2</sub> or P).** [Ru(COD)(COT)] (10 mg, 0.032 mmol) was introduced in a Schlenk flask and dissolved in 5 mL of THF. Then, the solution was transferred to a Fischer-porter reactor charged with a suspension of x-rGO (100 mg) in 50 mL of THF previously sonicated during 90 min. The Fischer-Porter reactor was then pressurized with 3 bar of H<sub>2</sub> and stirred vigorously. The reaction was kept 20 h at room temperature. After that, the remaining H<sub>2</sub> pressure was released and the Ru@x-rGO material was separated from the suspension by filtration through a polyamide membrane (Whatman ® membrane filters, 47mm x 0.45 µm) and washed with THF (150 mL). The resulting black precipitate was dried overnight at 60 °C. **Ru@rGO:**  $d_{\text{mean}} = 2.0 \pm 0.8$  nm, ICP = 2.4%<sub>wt</sub> Ru. **Ru@NH<sub>2</sub>-rGO:**  $d_{\text{mean}} = 1.5 \pm 0.2$  nm, ICP = 2.5 %<sub>wt</sub> Ru. **Ru@P-rGO:**  $d_{\text{mean}} = 1.5 \pm 0.3$  nm, ICP = 3.1 %<sub>wt</sub> Ru.

## Electrochemical set-up

**Electrode Preparation.** A 2 mg/mL dispersion was prepared by adding 1 mg of hybrid material in 500 µL of THF. Sonication was tried to be avoid to prevent NPs aggregation. Then, an aliquot of 5 µL was drop-casted on the surface of the GC/RDE ( $S = 0.07$  cm<sup>2</sup>) and dried. This procedure was repeated three times. A 5 µL-drop of nafion (0.02 %) was added for the rGO and Ru@rGO systems and dried prior to the electrochemical measurements.

**Electrochemical measurements.** All the electrochemical experiments were performed in a BioLogic SP-150 potentiostat with a rotating GC disk electrode (GC-RDE) at 3000 rpm in order to ensure complete removal of *in situ* formed H<sub>2</sub> bubbles. The solutions were degassed previous to the electrochemical analysis with a N<sub>2</sub> flow. Ohmic potential (IR) drop was automatically corrected at 85 % using the Biologic EC-Lab software for cyclic voltammetry and chronoamperometry. For chronopotentiometry experiments IR drop was manually corrected ( $E_{\text{mod}} = E_{\text{meas}} + E_{\text{IR}}$ , mod=modified and meas=measured) at 85 % by adding the corresponding potential value  $E_{\text{IR}} = i_{\text{exp}} \times (R_{\text{mes}} \times 0.85)$ , where  $i_{\text{exp}}$  is the applied current in A and  $R_{\text{mes}}$  is the measured resistance in Ω. 1 M H<sub>2</sub>SO<sub>4</sub> solution was prepared by mixing 56.1 mL of 95-97 % H<sub>2</sub>SO<sub>4</sub> in 1 L of Mili-Q water. A glassy carbon rotating disk electrode (RDE,  $\phi = 0.3$  cm,  $S = 0.07$  cm<sup>2</sup>) was used as working electrode. A Pt wire was used as counter electrode (CE) and a standard

calomel electrode (SCE, Hg/Hg<sub>2</sub>Cl<sub>2</sub>, KCl sat.) electrode was used as a reference electrode (RE), and electrochemical data transformed to NHE by adding +0.244 V.

A 10 mL two-compartment cell with a proton exchange membrane between the two compartments was used for faradaic efficiency calculation. The CE was placed in one compartment and the WE and RE were placed in the other compartment together with the Clark electrode. Both compartments were filled with 7 mL of 1 M H<sub>2</sub>SO<sub>4</sub> solution and both compartments were equipped with a stirring bar. Prior to each measurement, both compartments were purged with N<sub>2</sub>. The *Unisense* H<sub>2</sub>-NP Clark electrode was used to measure in the gas phase the hydrogen generated by the systems during a chronopotentiometry. The Clark electrode was calibrated by adding different volumes of 99 % pure hydrogen at the end of the experiment.

**Double-layer Capacitance (C<sub>DL</sub>) and Electrochemically active Surface Area (ECSA) determination:** C<sub>DL</sub> was estimated by CV. A non-faradaic region was chosen from the LSV (typically a 0.1 V window about OCP), where no redox process takes place and all the measured current is due to double-layer charging. In this way, 8 different scan rates were used (5, 10, 25, 50, 75, 100, 250 and 500 mV/s), holding the working electrode at each potential vertex for 10 seconds prior to the next step.

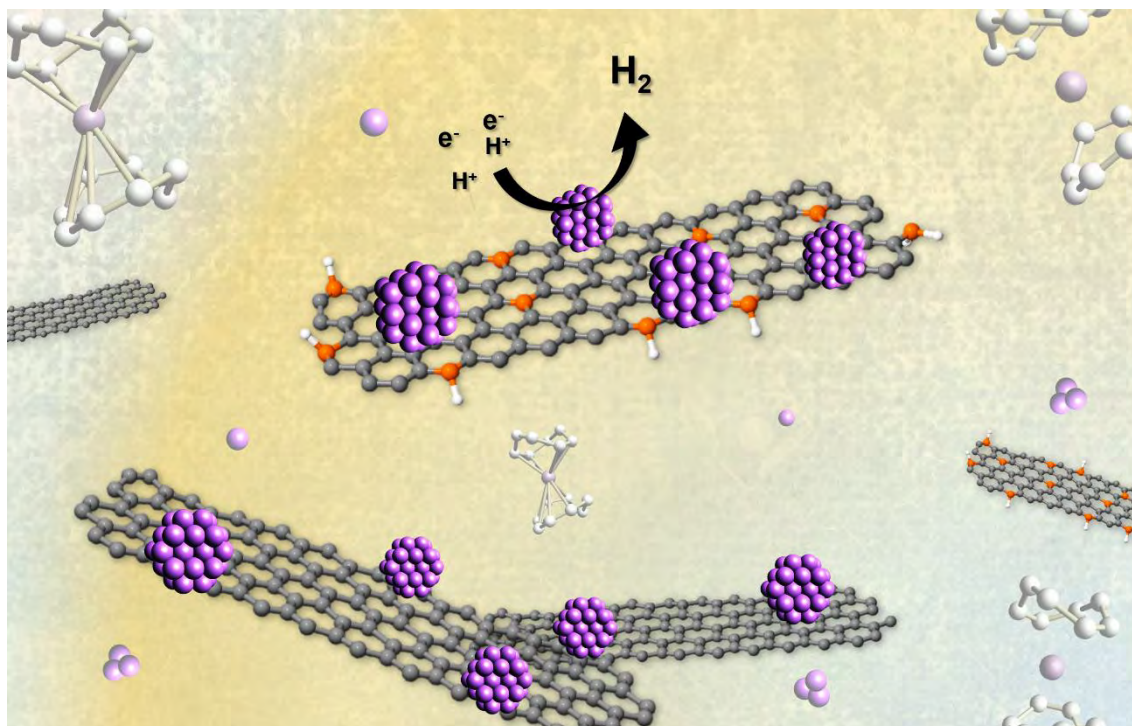
## **4A.6 REFERENCES**

- <sup>1</sup> J.R. McKone, E.L. Warren, M.J. Bierman, S.W. Boettcher, B.S. Lewis and H.B. Gray, *Energy Environ. Sci.* **2011**, 4, 3573-3583.
- <sup>2</sup> D. Yang, W. Hou, Y. Lu, X. Wang, W. Zhang and Y. Chen, *ACS sustainable Chem. Eng.* **2019**, 7, 15, 13031-13040.
- <sup>3</sup> J. Wang W. Yang and J. Liu, *J. Mater. Chem. A* **2016**, 4, 4686.
- <sup>4</sup> M. Liu, F. Hof, M. Moro, G. Valentini, F. Paolucci and A. Pénicaud, *Nanoscale* **2020**, 12, 20165.
- <sup>5</sup> W. Zhang, X. Zhang, L. Chen, J. Dai, Y. Ding, L. Ji, J. Zhao, M. Yan, F. Yang, C.R. Chang and S. Guo, *ACS Catal.* **2018**, 8, 8092-8099.
- <sup>6</sup> W.S. Hummers, R.E. Offeman, *J. Am. Chem. Soc.* **1958**, 80, 1339.
- <sup>7</sup> L. Lai, L. Chen, D. Zhan, L. Sun, J. Liu, S.H. Lim, C.K. Poh, Z. Shen, J. Lin, *Carbon* **2011**, 49, 3250.
- <sup>8</sup> Z. Chenzhen, M. Nasir, Y. Han, L. Fei and H. Yanglong, *Adv. Mat.* **2013**, 25, 4932-4937.
- <sup>9</sup> A.R. MacIntosh, G. Jiang, P. Zamani, Z. Song, A. Riese, K.J. Harris, X. Fu, Z. Chen, X. Sun and G.R. Goward, *J. Phys. Chem. C* **2018**, 122, 6593-6601.
- <sup>10</sup> C. Amiens, B. Chaudret, D. Ciuculescu-Pradines, V. Collière, K. Fajerweg, P. Fau, M. Kahn, A. Maisonnat, K. Soulantica and K. Philippot, *New J. Chem.* **2013**, 37, 3374-3401.
- <sup>11</sup> M. Latorre-Sánchez, A. Primo and H. García, *Angew. Chem. Int. Ed.* **2013**, 52, 11813-1181.
- <sup>12</sup> J. Creus, S. Drouet, S. Suriñach, P. Lecante, V. Collière, R. Poteau, K. Philippot, J. García-Antón and X. Sala. *ACS Catal.* **2018**, 11094-11102.
- <sup>13</sup> C.C.L. McCrory, S. Jung, I.M. Ferrer, S.M. Chatman, J.C. Peters and T.F. Jaramillo, *J. Am. Chem. Soc.* **2015**, 137, 4347-4357.
- <sup>14</sup> B.Hammer, J.K. Nørskov, *Surf. Sci.* **1995**, 243, 211-220.
- <sup>15</sup> T. Suoranta, M. Niemelä, P. Perämäki, *Talanta* **2014**, 119, 425-429.



## Chapter 4B. Ru nanoparticles supported on rGO (Alginate) as HER catalysts

---



---

Two different cathodes for the hydrogen evolution reaction (HER) based on Ru NPs and reduced graphene oxide (G) have been developed. Ru NPs have been synthesized *in situ* in the presence of the carbon support by means of the organometallic approach, being the G structure and phosphorous, when present, the stabilizing agents of the NPs. The addition of P into the graphitic structure plays a key role on the stability and activity of the hybrid electrodes.

This work has been performed in the frame of a collaboration with Dr. L.M. Martínez (Instituto de Tecnología Química (ITQ) – Universitat Politècnica de València (UPV), who prepared and characterized the Ru NPs supported on G. My contribution has been the performance of all the electrocatalytic experiments and some characterization before and after catalysis to explore their catalytic behaviour and understand the catalyst fate under turnover conditions.

---



## **4B.1 INTRODUCTION**

The development of organic-inorganic hybrid materials for redox catalysis is key for the development of new energy conversion schemes and the sustainable production of H<sub>2</sub>. With far higher surface area and charge carrier mobility than related graphitic materials, graphene has emerged in recent years as a paradigmatic 2D carbon-support in electrocatalysis.<sup>1</sup> However, practical application of graphene-based hybrid electrocatalysts relies on the development of scalable and sustainable methods to produce this carbon nanomaterial. In this regard, graphene production through biomass carbonization, a waste-treatment technology, is an attractive valorisation strategy to reduce electrode costs and increase the sustainability of electrode production.<sup>2</sup> In this sense, in *Chapter 4B*, the graphene used as support for Ru NPs has been obtained from pyrolysis of alginate (Fig. 1), refined from alginic acid, which is a widely available natural polysaccharide consisting of unbranched chains extracted in enormous quantities from crustacean skin and algae marine biomass.

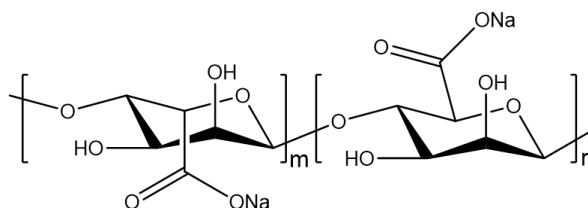


**Figure 1.** Structure of alginate

## **4B.2 SYNTHESIS AND CHARACTERIZATION**

### **4B.2.1 Synthesis of reduced graphene oxide supports**

Preparation of graphene (**G**) and P-doped graphene (**P-G**) supports was accomplished by pyrolysis of alginate according to literature.<sup>3,4</sup> Briefly, **G** was synthesized by alginic acid sodium salt brown algae pyrolysis in argon atmosphere. For **P-G**, alginic acid sodium salt from brown algae was first dissolved in a sodium phosphate dibasic monohydrate aqueous solution before performing the same pyrolysis process as for **G**.

### 4B.2.2 Synthesis of Ru NPs supported onto G

Ru NPs were synthesized from an organometallic Ru precursor in the presence of the corresponding C support (**G** or **P-G**, obtained from pyrolysis of alginate). The graphene-supported Ru NPs were obtained from  $[\text{Ru}(\text{COD})(\text{COT})]$ , which was decomposed by hydrogenation [room temperature (r.t.), 3 bar  $\text{H}_2$ , 20 h] in the presence of the support, previously dispersed in THF by ultra-sonication (Fig. 2). All the samples were exposed to air after drying them under vacuum in order to passivate the surface of the NPs.

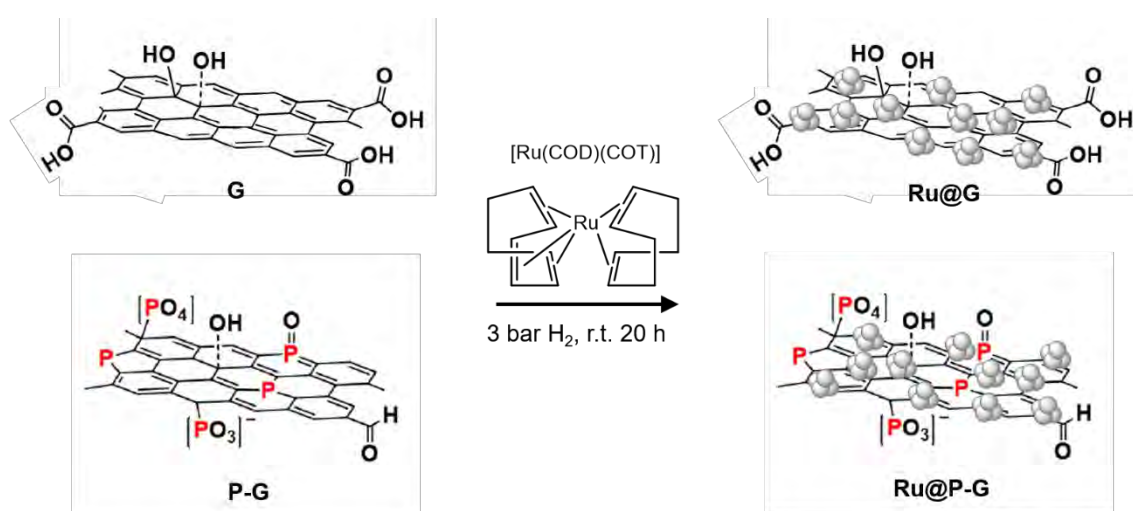


**Figure 2.** Synthesis of **Ru@G** and **Ru@P-G** following the organometallic approach. Grey balls represent Ru atoms forming NPs supported on the graphene.

### 4B.2.3 Transmission electron microscopy analysis (TEM)

Before the decoration of the C support with Ru NPs, the morphology of both supports was assessed by transmission electron microscopy. Typical graphene morphologies and absence of C particles from pyrolyzed alginate residues were observed by TEM for both carbon supports (Fig. 3). Having a look on the TEM images, it is noticed a different degree of exfoliation between **G** and **P-G**. The presence of phosphate and sodium ions during the preparation of **P-G** seems to aid the separation of the C sheets, yielding a more exfoliated C support. The lower roughness of the **P-G** material (*vs.* **G**) was later corroborated by electrochemical measurements (ECSA and RF, see Table 2 in Section 4B.3.2).



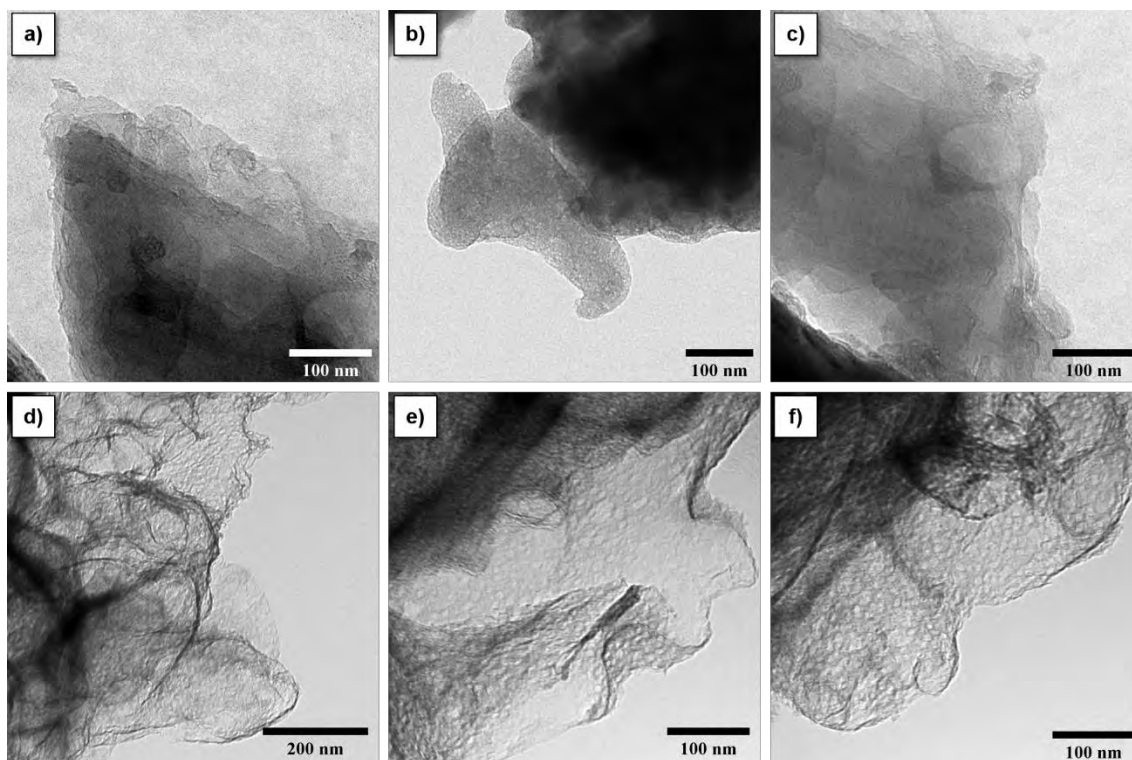


**Figure 3.** TEM images of **G** (a-c) and **P-G** (d-f) supports.

In addition, each Ru-decorated material was analyzed by TEM, which was used as a standard tool of analysis to study the morphology and assure the presence of NPs on-top of the support. After the reaction time, each sample was taken for TEM analysis by removing the remaining hydrogen from the reaction vessel and depositing a drop of colloidal dispersion onto a holey carbon covered copper grid. TEM analysis for **Ru@P-G** revealed spherical, well distributed and monodispersed NPs with a mean diameter of  $1.5 \pm 0.3$  nm (Fig. 4d-f). In contrast, the use of non-doped graphene (**G**) as a support (also prepared by pyrolysis of alginate) yielded slightly bigger ( $1.9 \pm 0.6$  nm) and more aggregated NPs (Fig. 4a-c). This difference in size and dispersion suggests that heteroatoms present in the P-doped graphene assist the generation and the stabilization of the Ru NPs during this synthetic approach.

Inductively-coupled plasma atomic emission spectroscopy (ICP-AES) confirmed the presence of Ru in each sample, obtaining metal contents of 2.6 wt% and 3.3 wt% for **Ru@G** and **Ru@P-G**, respectively.

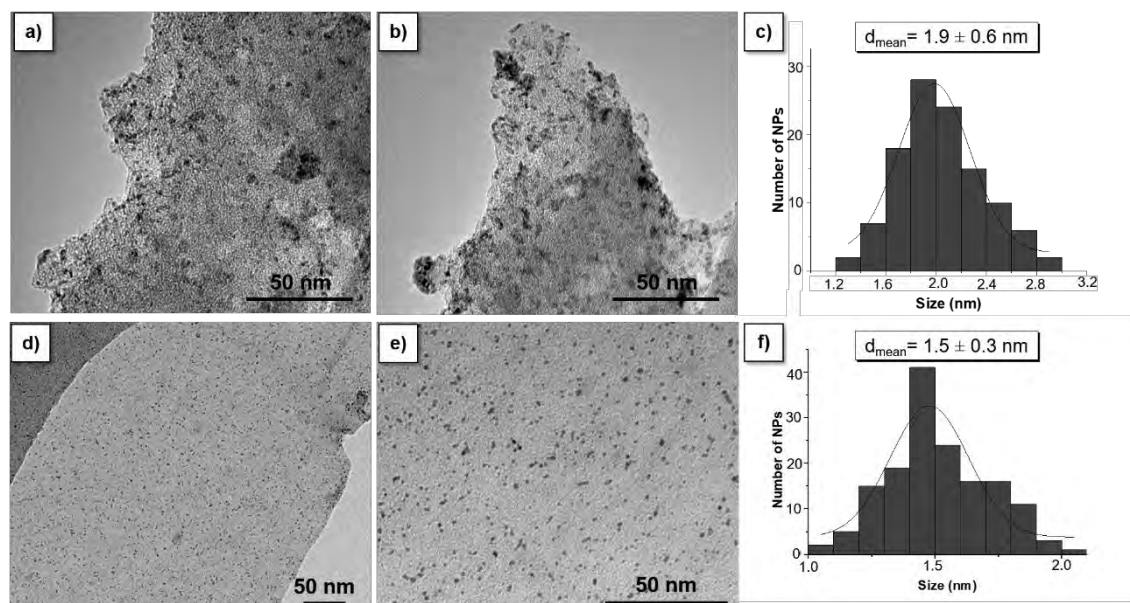


**Figure 4.** TEM images and size distribution histograms of **Ru@G** (a-c) and **Ru@P-G** (d-f).

High-resolution TEM (HRTEM) images confirmed the crystallinity of the NPs present in both **Ru@G** and **Ru@P-G** (Fig. 5). Fourier analyses applied to these images display reflections due to the (002), (200), (100) and (110) atomic planes of the hexagonal compact crystalline (hcp) structure of bulk Ru, attributed to interplanar distances of 0.214, 0.117, 0.234 and 0.135 nm, respectively.

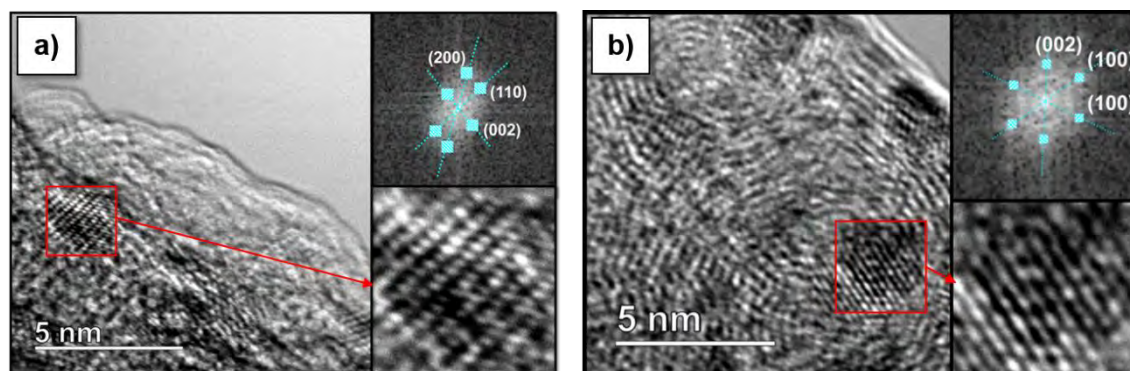


**Figure 5.** HRTEM images, chosen expanded zone and the Fourier transform analysis with planar reflections for **Ru@G** (a) and **Ru@P-G** (b).

#### 4B.2.4 Raman spectroscopy analysis

Raman spectroscopy is a well-known characterization technique to evaluate the quality of graphene.<sup>5</sup> The Raman spectra of **G** and **P-G** display two major bands at 1358  $\text{cm}^{-1}$  (D peak) and 1595  $\text{cm}^{-1}$  (G peak), together with the G' peak at around 2680  $\text{cm}^{-1}$  (Fig. 6a and 6c). These results confirm the graphitized nature of both supports, as the G and G' peaks are characteristic of  $\text{sp}^2$  hybridized carbon-carbon bonds in graphene. In addition, the high intensity of the D peak could confirm the high defect density of the used supports. In addition, introduction of disorder breaks the crystal symmetry, activating other vibrational modes, such as D' band features (D'+G band at *ca.* 3190  $\text{cm}^{-1}$ ), and the appearance of a D+G mode (2930  $\text{cm}^{-1}$ ). These defect sites are exceptional anchoring points for Ru NPs, enhancing the interaction graphene-Ru, which may improve the stability and activity of the catalyst. The incorporation of Ru NPs on these materials did not affect significantly the Raman spectra (Fig. 6b and 6d).

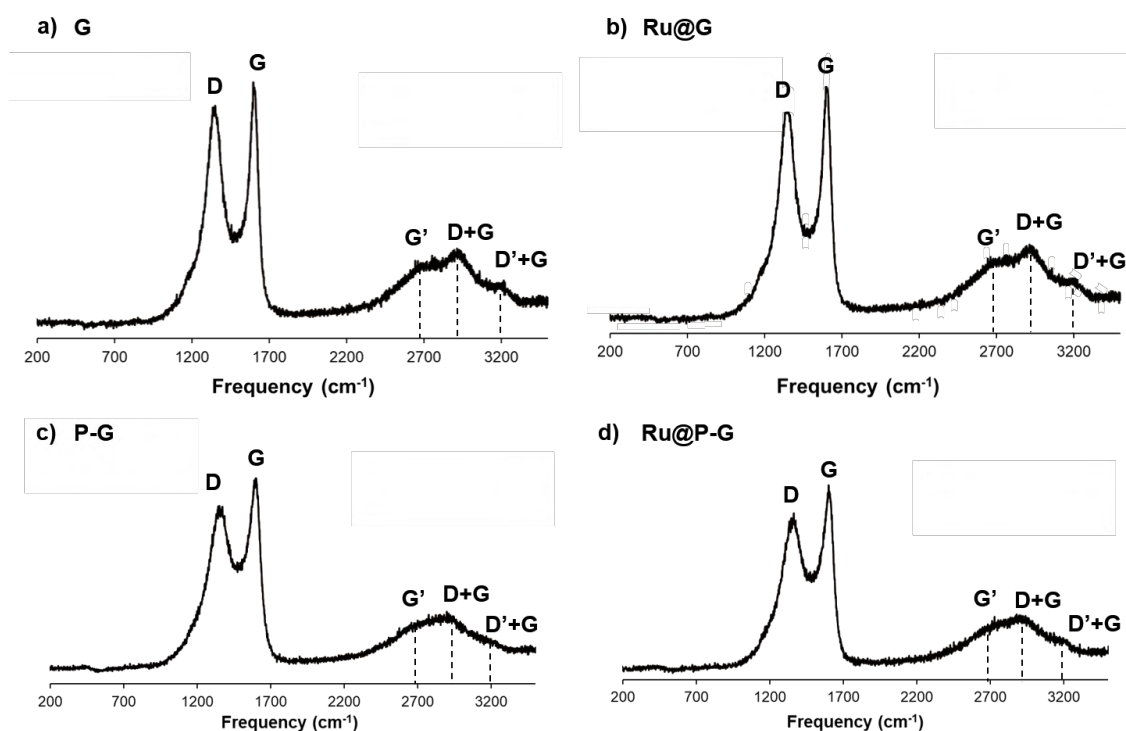


**Figure 6.** Raman spectra of **G** (a), **Ru@G** (b), **P-G** (c) and **Ru@P-G** (d).

### 4B.2.5 X-ray photoelectron spectroscopy analysis (XPS)

XPS analyses were performed on the P-doped support, **P-G**, and both hybrid nanomaterials (*i.e.* **Ru@G** and **Ru@P-G**) to determine the chemical composition and the nature of the C, P and Ru species present.

The high-resolution C 1s XPS spectrum of **P-G** shows a relative broad band at a binding energy (BE) of 284.8 eV, which can be deconvoluted into three components (Fig. 7a). The main peak at 284.8 eV (pink) is attributed to the C atoms of graphitic domains ( $sp^2$ ). The peak at *ca.* 286.9 eV (blue) corresponds to C atoms of epoxides, tertiary alcohols and C atoms connected to P. The third peak centred at *ca.* 289.2 eV (red) belongs to carboxylic groups.<sup>6</sup> Comparable results have been observed at the C 1s region for **Ru@G** (Fig. 7c), confirming that the reductive conditions under  $H_2$  pressure needed to obtain Ru NPs is not affecting considerably the composition of the C support.

Similarly, the P 2p signal of **P-G** is the result of the deconvolution of two components (Fig. 7b), a major peak at 133.1 eV attributed to P atoms bonded to oxygen (pink curve), and a lower intensity one at 131.8 eV (blue curve), which corresponds to P-C bonds. These results confirm the higher percentage of P-O bonds compared to graphitic phosphorous, in contrast with **Ru@P-rGO** (from Hummers, *Chapter 4A*), where the percentage of graphitic phosphorous atoms was found to be higher. These peaks have been previously identified in similar P-doped graphenes<sup>3</sup> and fit well with results obtained by FT-IR (Section 4B.2.6, see below). Analysis of the P 2p signal also allowed to determine the P content in the doped support, **P-G**, which appeared to be of 1.15 at.%.

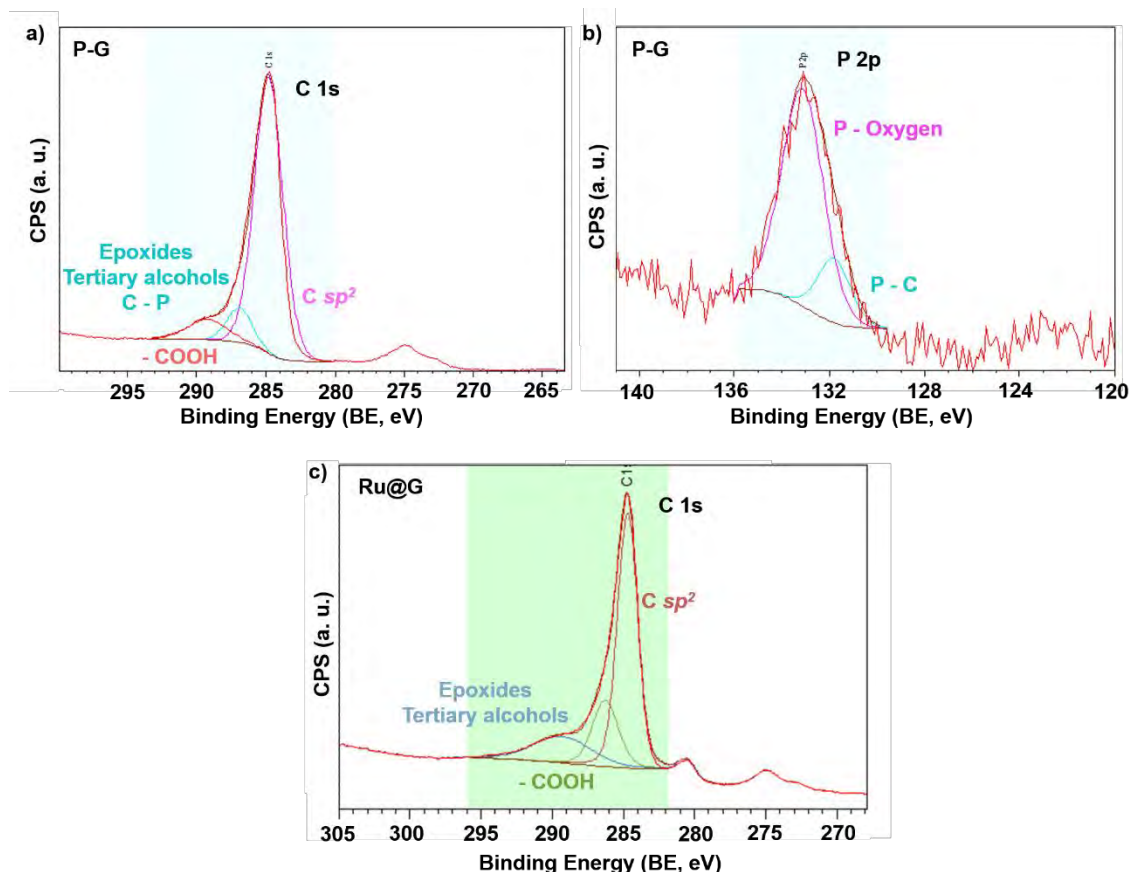


**Figure 7.** High-resolution C 1s XPS spectra of **P-G** (a) and **Ru@G** (c), and high-resolution P 2p XPS spectrum of **P-G** (b).

The overlap of the Ru 3d signal with the C 1s peak makes the signal deconvolution and interpretation difficult. Therefore, the different oxidation states of the Ru NPs in **Ru@G** and **Ru@P-G** were assessed upon analysing the Ru 3p region. Fig. 8a shows the Ru 3p<sub>3/2</sub> signal of the as-synthesized **Ru@G**, which displays a binding energy of 463.0 eV. The deconvolution of this peak presents two contributions, one at 464.5 eV, that is attributed to Ru(IV), characteristic of RuO<sub>2</sub>, and another one at 462.8 eV, which belongs to Ru(0). Specifically, the surface of the as-synthesized sample contains 64 % of Ru(IV) and 36 % of Ru(0). Similarly, the Ru 3p signal of the as-synthesized **Ru@P-G** displays a binding energy of 463.2 eV (Fig. 8b). This peak presents two contributions, one at 464.6, that is attributed to Ru(IV), and another one at 462.5 eV, which belongs to Ru(0). The surface of the as-synthesized **Ru@P-G** sample contains 68 % of Ru(IV) and 32 % of Ru(0).



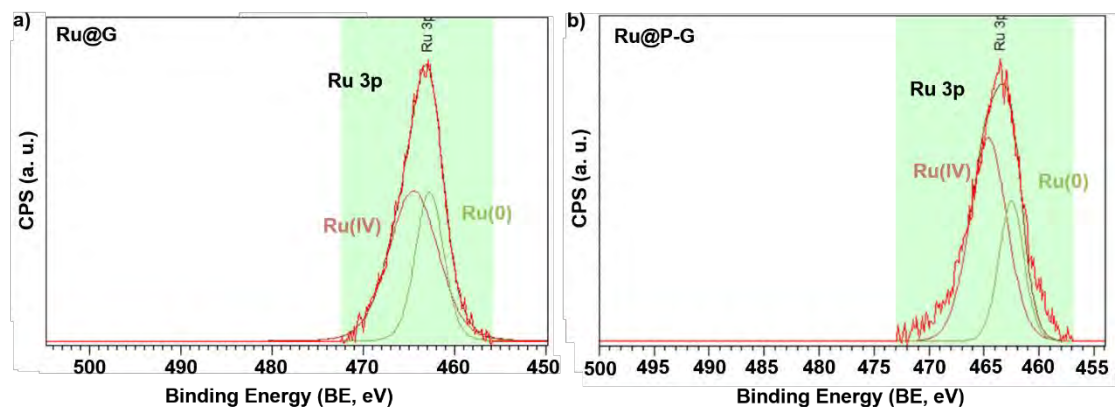


**Figure 8.** High-resolution Ru 3p XPS spectra of the as-synthesized **Ru@G** (a) and **Ru@P-G** (b).

#### 4B.2.6 Fourier-transform infrared spectroscopy analysis (FT-IR)

In order to check any sign of interaction between the phosphorous and Ru NPs, Fourier-transform infrared (FT-IR) spectra of **P-G** and **Ru@P-G** were recorded (Fig. 9). This technique didn't allow to observe any sign of the interaction Ru-phosphorous, as the spectrum from **Ru@P-G** is identical to the one corresponding to the graphene-supported Ru NPs (**Ru@P-G**). However, the characteristic stretching P-O/P=O band can be observed at *ca.* 1160-1252  $\text{cm}^{-1}$ , in agreement with the observed signal from P bonded to oxygen in the P 2p XPS spectrum. In addition, the stretching vibration associated to aromatic C=C bonds from the graphene sheet appears around 1600  $\text{cm}^{-1}$ .

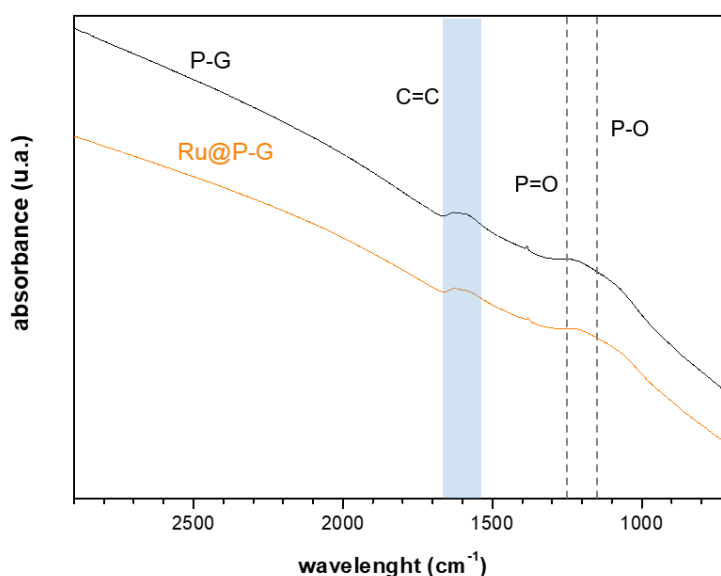


**Figure 9.** FT-IR spectra of **P-G** (black) and **Ru@P-G** (orange).

#### 4B.2.7 $^{31}\text{P}$ magic angle spinning solid state NMR spectroscopy analysis

Finally,  $^{31}\text{P}$  magic angle spinning (MAS) solid state NMR was also employed to double confirm the chemical nature and the presence of the dopant atoms in the graphene materials.  $^{31}\text{P}$  MAS NMR spectra of both **P-G** and **Ru@P-G** display a broad peak between 10 and -30 ppm, which may correspond to the overlapped signals of phosphonate (7 to 10 ppm),<sup>7</sup> phosphate (around 0 ppm),<sup>8</sup> metaphosphate (-3 to -7 ppm),<sup>7</sup> elemental phosphorous (-14 to -17 ppm)<sup>9</sup> and/or polyphosphate (-22 ppm)<sup>10</sup> (Fig. 10). Elemental phosphorous comes from the reduction of the phosphate by carbon at high temperature during the pyrolysis of the P-doped graphene.<sup>7</sup> The presence of metaphosphate and polyphosphate groups could be attributed to the condensation of  $\text{H}_2\text{PO}_4^-$  at 900 °C.<sup>7</sup> In summary, we can confirm that the majority of P-O bonds observed by XPS are due to phosphate-like structures, in contrast with **P-rGO** (Chapter 4A), in which a higher percentage of graphitic phosphorous has been observed.

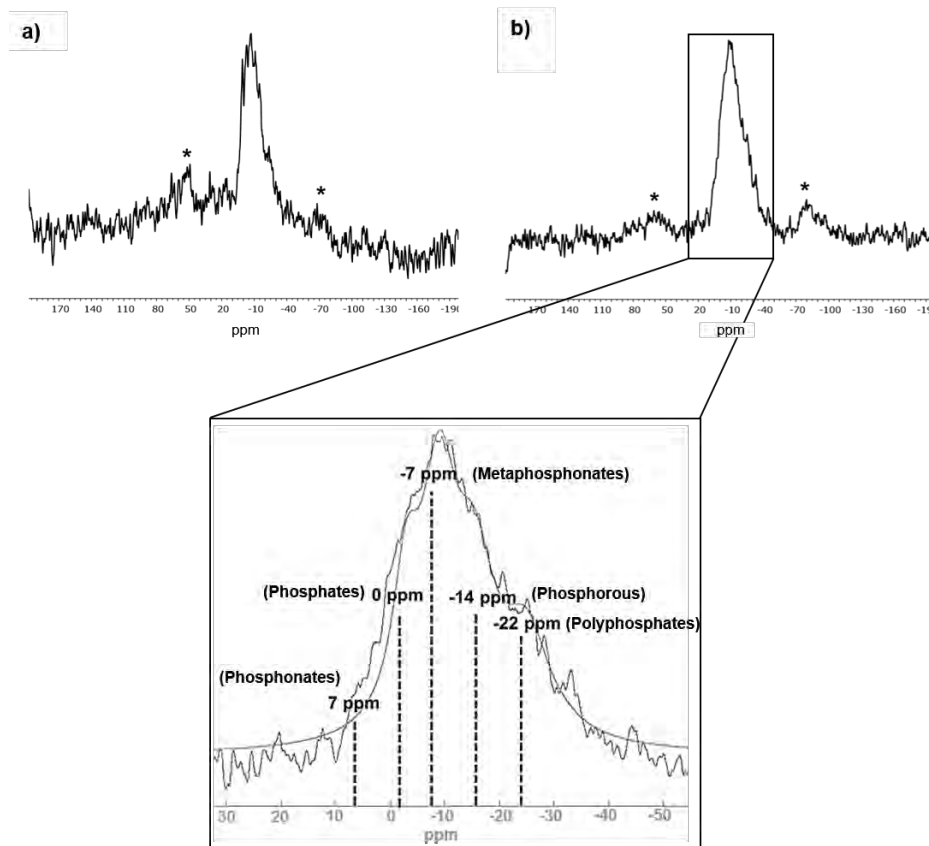


**Figure 10.**  $^{31}\text{P}$  MAS NMR spectra of **P-G** (a) and **Ru@P-G** (b). Asterisks (\*) mark the positions of spinning side bands. The positions of phosphonate (7 ppm), phosphates (0 ppm), metaphosphonates (-7 ppm), phosphorous (-14 ppm) and polyphosphate (-22 ppm) have been highlighted.

## 4B.3 ELECTROCATALYTIC PERFORMANCE

### 4B.3.1 Electrocatalytic HER studies in 1 M H<sub>2</sub>SO<sub>4</sub>

The HER performance of **Ru@G** and **Ru@P-G** was evaluated in 1 M H<sub>2</sub>SO<sub>4</sub> aqueous solution (pH 0). The material was dispersed in THF (2 mg/mL) and drop-casted onto a glassy carbon rotating disk electrode (GC-RDE). A three-electrode configuration was used to study the electrochemical behaviour of the materials, using the drop-casted GC-RDE as working electrode. SCE (saturated calomel electrode, KCl sat.) and a Pt wire were used as reference (RE) and counter (CE) electrodes, respectively.

The polarization curves of **Ru@G** and **Ru@P-G** at  $t=0$  s are shown in Fig. 11 (bold lines). A change in the current density is observed when scanning towards reductive potentials, which is attributed to their catalytic activity when reducing protons to H<sub>2</sub>.

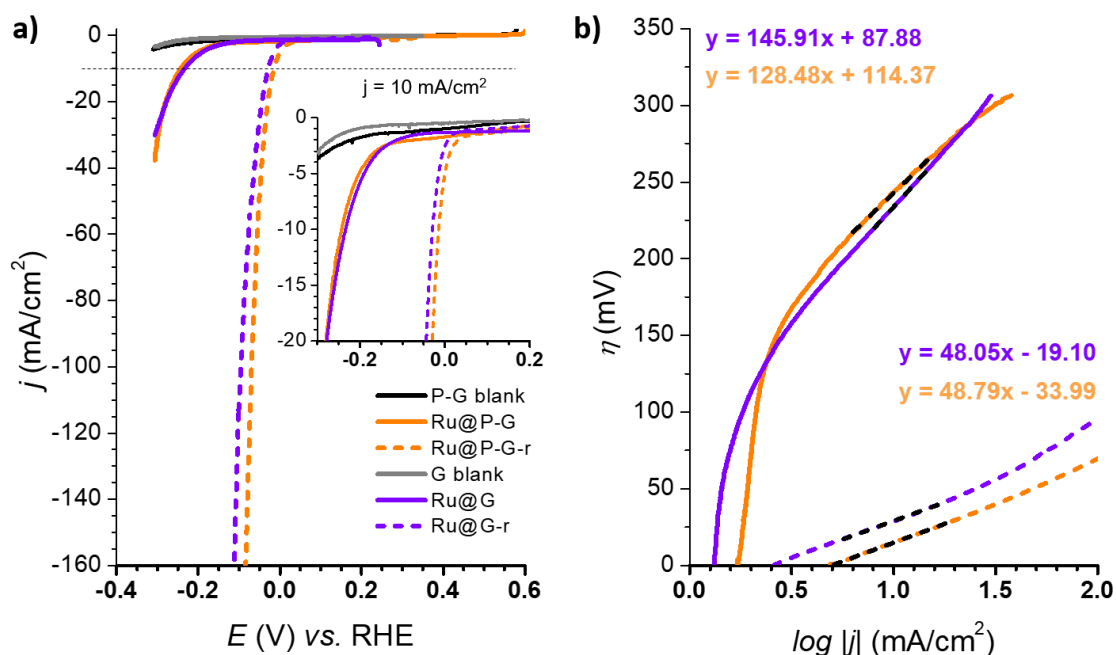


**Figure 11.** Polarization curves of **Ru@G** (purple line), **Ru@P-G** (orange line) before (bold) and after (dashed) a reductive process at  $|j| = -10$  mA/cm<sup>2</sup> in 1 M H<sub>2</sub>SO<sub>4</sub>. **G** (grey line) and **P-G** (black line) blanks are also shown (a). Tafel plots of **Ru@G**, **Ru@G-r**, **Ru@P-G** and **Ru@P-G-r** in 1 M H<sub>2</sub>SO<sub>4</sub> (b). Same code as in (a).

The catalytic performance of the systems can be significantly improved after submitting them to a current-controlled bulk electrolysis at  $j = -10$  mA/cm<sup>2</sup> (Fig. 11a, dashed lines). As presented in Fig. 11 and Table 1, whereas the **Ru@G** and **Ru@P-G**



systems show a  $\eta_{10}$  of 233 mV and 243 mV, respectively, a shift in the polarization curves is observed after the reductive process, improving the  $\eta_{10}$  down to 29 mV and 15 mV, respectively. This behaviour is attributed to a change in the oxidation state of surface Ru atoms on the NPs. The partially oxidized surface of the as-synthesized NPs, confirmed by XPS, gets reduced back to metallic Ru when submitted to this reductive treatment. The obtained reduced species, **Ru@G-r** and **Ru@P-G-r**, are more active in HER than their passivated counterparts, **Ru@G** and **Ru@P-G**, displaying higher current densities and lower  $\eta_{10}$ . A deep study of the proposed RuO<sub>2</sub>/Ru interconversion was performed previously in the group with 4PP stabilized NPs,<sup>11</sup> confirming a total disappearance of the RuO<sub>2</sub> peak in the XPS under reductive catalytic conditions, indicating the reduction of superficial Ru(IV) to metallic Ru.

**Table 1.** Summary of physico-chemical and HER electrocatalytic data (1 M H<sub>2</sub>SO<sub>4</sub>) for the systems studied in this work. Parameters: mean diameter ( $d_{\text{mean}}$ ), onset overpotential at -10 mA/cm<sup>2</sup> ( $\eta_{10}$ ), Tafel slope ( $b$ ) and exchange current density ( $j_0$ ).

Entry	System	$d_{\text{mean}}$ (nm)	Ru (wt%)	$\eta_{10}$ (mV)	$b$ (mV/dec)	$j_0$ (mA/cm <sup>2</sup> )
1	<b>G</b>					
2	<b>Ru@G</b>	1.9 ± 0.6	2.6	233	146	0.25
3	<b>Ru@G-r</b>	-	-	29	48	2.50
4	<b>P-G</b>					
5	<b>P-G-r</b>					
6	<b>Ru@P-G</b>	1.5 ± 0.3	3.3	243	128	0.13
7	<b>Ru@P-G-r</b>	-	-	15	49	4.97

The difference in nature and catalytic performance between each passivated sample and its reduced analogous is evidenced through their corresponding Tafel plots (Fig. 11b), obtaining improved overall kinetics with the reduced systems. The Tafel slope ( $b$ ) allows defining the rate determining step (rds) of the catalytic reaction. Both **Ru@G** and **Ru@P-G** show a Tafel slope close to 120 mV, being typically attributed to the Volmer step as rds (adsorption of H<sup>+</sup> to form the M-H species on the NP, typically  $b \approx 120$  mV/dec). In contrast, **Ru@G-r** and **Ru@P-G-r** show a Tafel slope of 48 mV/dec and 49 mV/dec, respectively, suggesting that the HER follows the Volmer-Heyrovsky mechanism, with the Heyrovsky step (H<sub>2</sub> electrodesorption with a proton from the solution,  $b \approx 40$  mV/dec) as the slowest path in the HER process.

Long-term stability is, together with kinetics, a key parameter for a catalyst to be potentially useful in the HER. Thus, both **Ru@G-r** and **Ru@P-G-r** electrodes were held at a constant current density of  $j = -10 \text{ mA/cm}^2$  in a current controlled experiment (*i.e.* chronopotentiometry) for 12 h, monitoring the change in the required overpotential. LSVs before and after the 12 h experiment are shown in Fig. 12. Both systems show almost no change in  $\eta_{10}$  and almost identical LSV polarization curves before and after catalytic turnover.

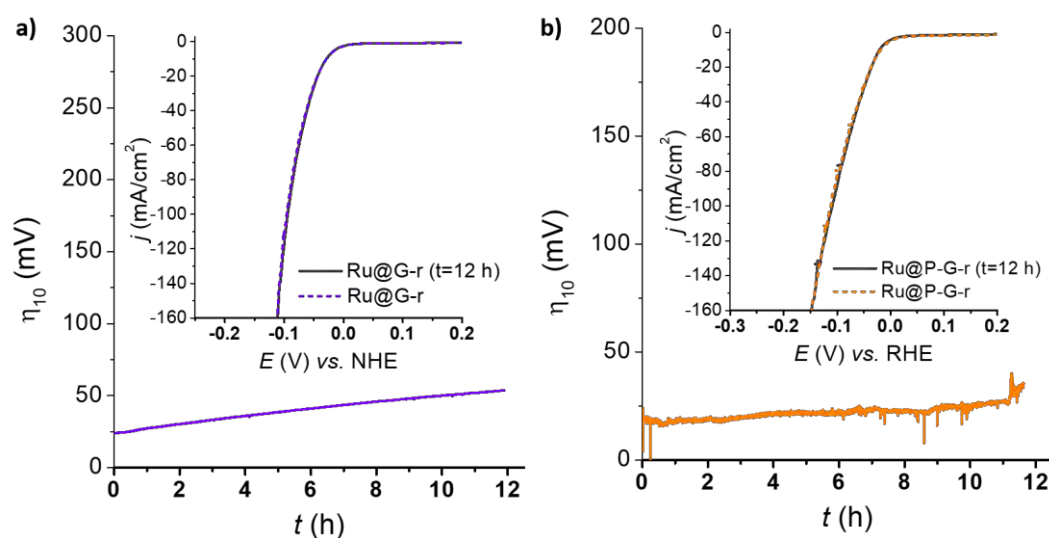


**Figure 12.** LSV of **Ru@G-r** (a) and **Ru@P-G-r** (b) before (dashed lines) and after (solid dark grey lines) a 12 h chronopotentiometry experiment at a  $j = -10 \text{ mA/cm}^2$ .

### 4B.3.2 Electrocatalytic performance benchmarking

The electrocatalytic performance of all the systems was further compared by following the benchmarking methodology reported by Jaramillo *et al.*<sup>12</sup> First, the double-layer capacitance ( $C_{DL}$ ) was estimated from the capacitive current in a non-faradaic region by a multi CV experiment at different scan rates. A plot of  $i$  as a function of  $v$  yields a straight line with a slope equal to  $C_{DL}$  (Eq. 1) (see Figs. 13 and 14 for results before and after activation, respectively).

$$i = vC_{DL} \quad \text{Eq. 1}$$

Then, the electrochemically active surface areas (ECSA) and roughness factor (RF) of all electrodes and supports were calculated from the obtained  $C_{DL}$ , according to equations 2 and 3.

$$ECSA [cm^2] = \frac{C_{DL}}{C_s} \quad \text{Eq. 2}$$

$$RF = \frac{ECSA}{S} \quad \text{Eq. 3}$$

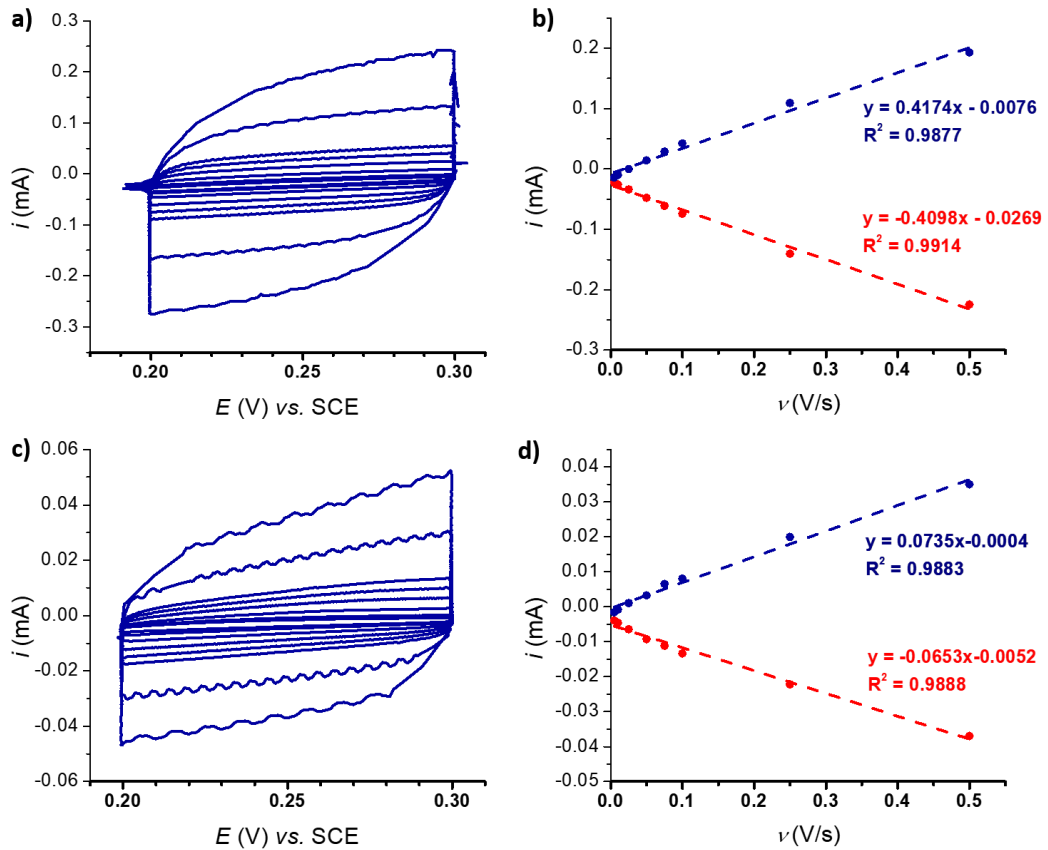


**Figure 13.** Representative multi CV experiment at different scan rates for  $C_{DL}$  determination of **Ru@G** (a) and **Ru@P-G** (c). Plot of current values at 0.25 V (vs. SCE) for the different scan rates in 1 M  $H_2SO_4$  for **Ru@G** (b) and **Ru@P-G** (d).

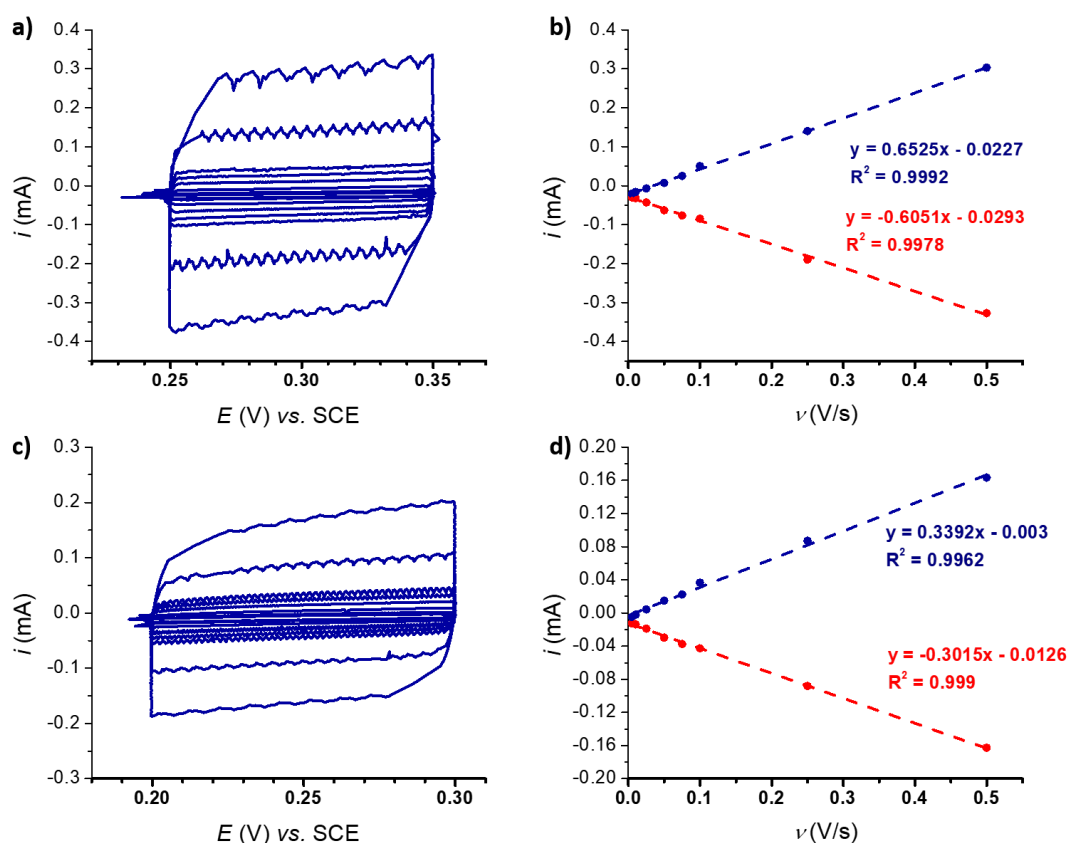


**Figure 14.** Representative multi CV experiment at different scan rates for  $C_{DL}$  determination of **Ru@G-r** (a) and **Ru@P-G-r** (c). Plot of current values at 0.30 V and 0.25 V (vs. SCE) for the different scan rates in 1 M H<sub>2</sub>SO<sub>4</sub> for **Ru@G-r** (b) and **Ru@P-G-r** (d), respectively.

The ECSA value allows calculating the specific current density ( $j_s$ ) of the electrode, which is the current density per “real” electroactive area of each system at a given overpotential. Thus, the current density,  $j_s$ , normalized per ECSA at  $\eta = -100$  mV, has been calculated for all the systems before and after the reductive treatment/activation (Table 2).

In addition, ECSA analyses were also performed on the bare supports (*i.e.* **G** and **P-G**) (Fig. 15). ECSA and RF data support the higher roughness of the non-doped support **G** (RF of 279.4 for **G** vs. 51.8 for **P-G**), as otherwise observed by TEM (Fig. 3). The obtained results are summarized in Table 2.

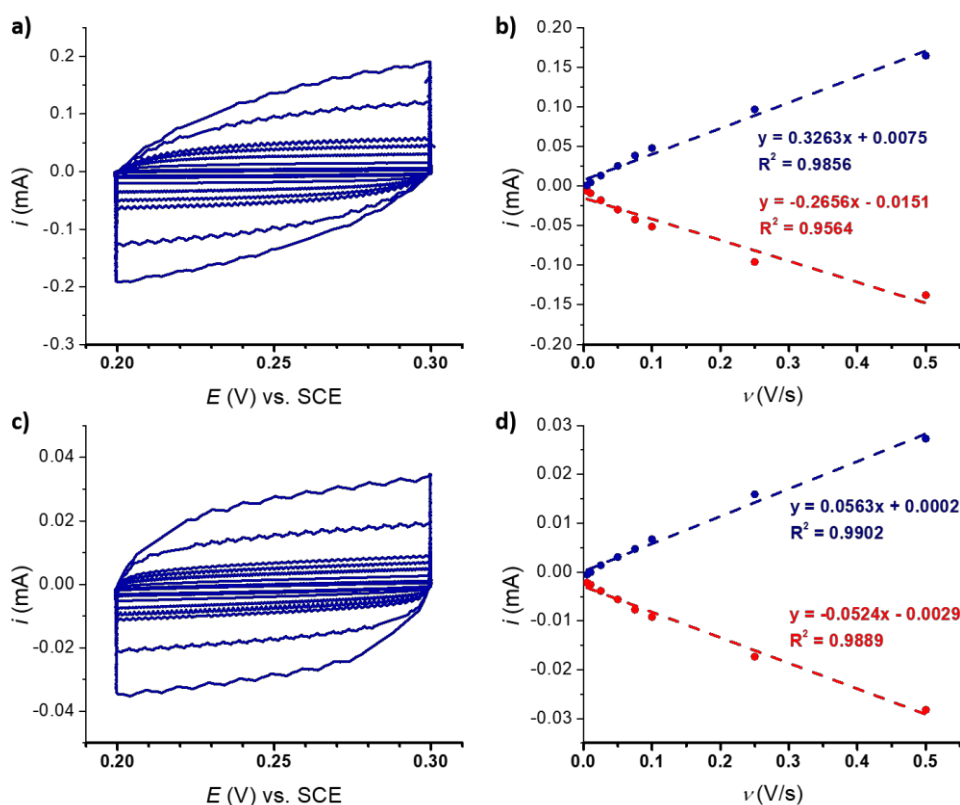


**Figure 15.** Representative multi CV experiment at different scan rates for  $C_{DL}$  determination of **G** (a) and **P-G** (c) Plot of current values at 0.25 V (vs. SCE) for the different scan rates in 1 M  $H_2SO_4$  for **G** (b) and **P-G** (d).

**Table 2.** Summary of physico-chemical and HER electrocatalytic data (1 M  $H_2SO_4$ ) for the systems studied in this work. Parameters: onset overpotential at  $-10$  mA/cm $^2$  ( $\eta_{10}$ ), Tafel slope ( $b$ ), exchange current density ( $j_0$ ), ECSA, RF and specific current density at  $\eta=100$  mV ( $|j_s|$ ).

Entry	System	$\eta_{10}$ (mV)	$b$ (mV/dec)	$j_0$ (mA/cm $^2$ )	ECSA (cm $^2$ )	RF	$ j_s $ ( $\eta = 100$ mV) (mA/cm $^2$ )
1	<b>G</b>				19.6	279.4	
2	<b>Ru@G</b>	233	146	0.25	27.6	393.9	0.005
3	<b>Ru@G-r</b>	29	48	2.50	41.9	598.9	0.184
4	<b>P-G</b>				3.6	51.8	
5	<b>P-G-r</b>				10.4	147.9	
6	<b>Ru@P-G</b>	243	128	0.13	4.6	66.1	0.032
7	<b>Ru@P-G-r</b>	15	49	4.97	21.4	305.1	0.883

The introduction of Ru NPs onto the two carbon materials slightly increases the RF values in both cases (Table 2, entries 2 and 6). Activation of the hybrid electrodes **Ru-G** and **Ru@P-G** under reductive conditions (current-controlled bulk electrolysis at  $j = -10$  mA/cm $^2$  for several hours) substantially increases the ECSA and RF values of

both electrodes (compare entries 2 vs. 3 and 6 vs. 7). This increment seems to be due to surface changes in both the C supports (as confirmed by the increased RF for **P-G-r** vs. **P-G**) and the Ru NPs (reduction process from Ru(IV) to Ru(0)). The activated P-doped electrode **Ru@P-G-r** shows the highest HER activity among the tested electrodes, with a very low  $\eta_{10}$  of 15 mV, the highest exchange current density ( $j_0$ ) and a specific current density 5 times higher than that of its non-doped counterpart **Ru@G-r**. Taking into account these results, **Ru@P-G-r** could be placed among the best Ru-based HER electrocatalysts in acidic media (see Table A1 in the Annex).

### 4B.3.3 Fate of the catalyst under catalytic conditions

In order to know if there is any aggregation or coalescence between individual Ru NPs under catalytic conditions, TEM images were taken after performing a 2h-CP to each system ( $j = -10 \text{ mA/cm}^2$ ). Each material was recovered from the electrode by sonication in THF and drop-casted onto a TEM grid. It is still visible the presence of small NPs onto the support (Figs. 16 and 17). The reductive potential applied for 2 h seems not to change in a significant way the size and morphology of the Ru NPs. However, some of the NPs can be found outside the C support.

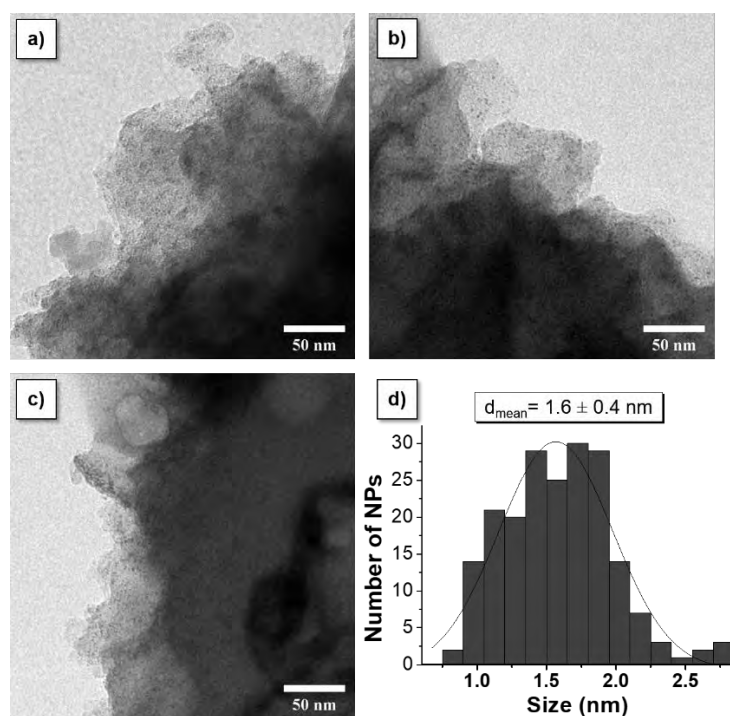


**Figure 16.** TEM images and corresponding histogram of **Ru@G** after 2 h under catalytic conditions ( $j = -10 \text{ mA/cm}^2$ ).



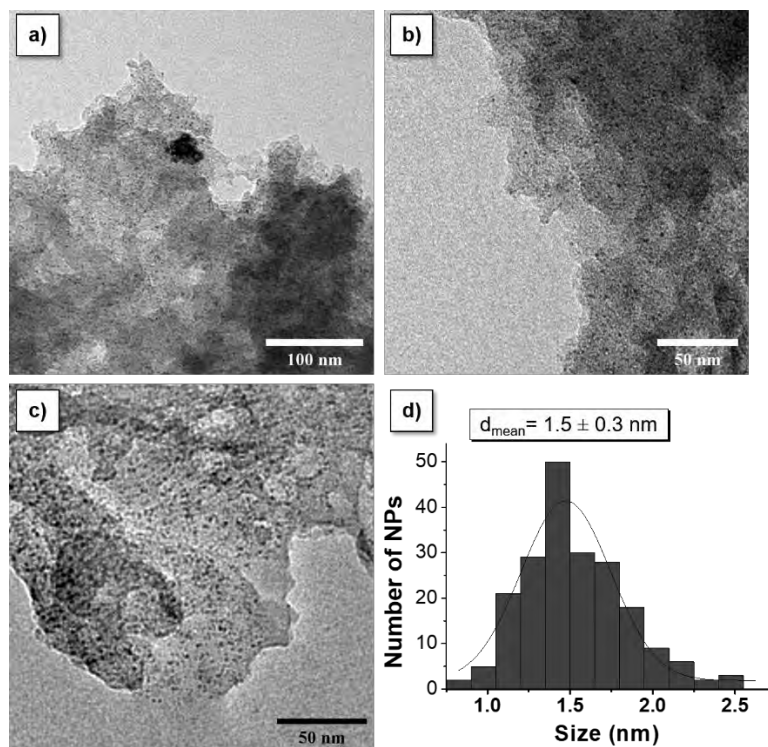


**Figure 17.** TEM images and corresponding histogram of **Ru@P-G** after 2 h under catalytic conditions ( $j = -10 \text{ mA/cm}^2$ ).

In order to verify the presence of Ru NPs on-top of the graphene and no other-metal nano-structures, EDX analysis of **Ru@P-G** was performed after 2 h under catalytic conditions. The results corroborate the presence of Ru in the sample, therefore confirming the presence of supported Ru NPs after short-term catalytic turnover (Fig. 18).

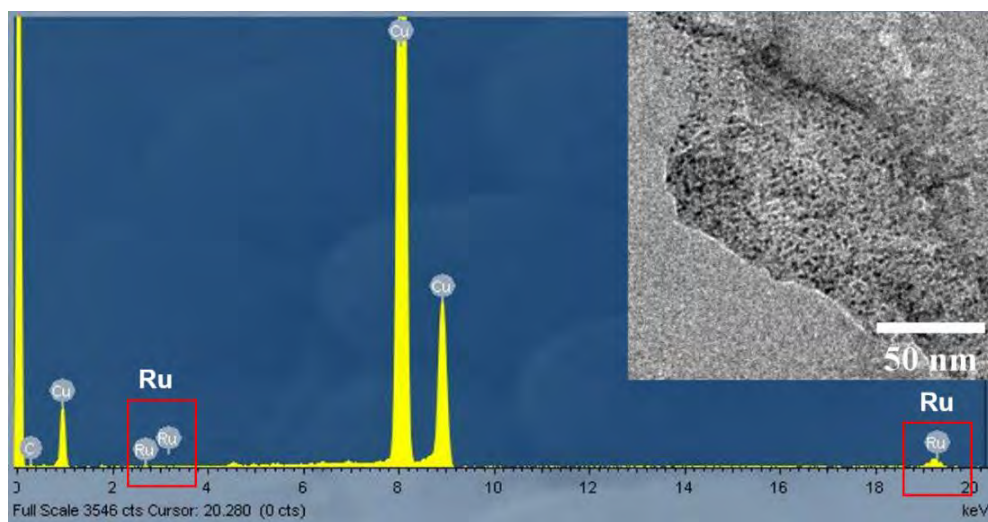


**Figure 18.** TEM/EDX analysis of **Ru@P-G** after 2 h under catalytic conditions ( $j = -10 \text{ mA/cm}^2$ ).

#### 4B.3.4 Faradaic efficiencies ( $\epsilon$ ) determination

Finally, a faradaic efficiency of 97-98 % was determined by quantifying the amount of  $H_2$  generated by the systems during a 20-min chronoamperometry using a  $H_2$ -Clark electrode, and comparing it with the maximum theoretical amount of  $H_2$  calculated from the total charge passed through each respective electrode (Fig. 19). This confirms the production of  $H_2$  as the sole reaction taking place.

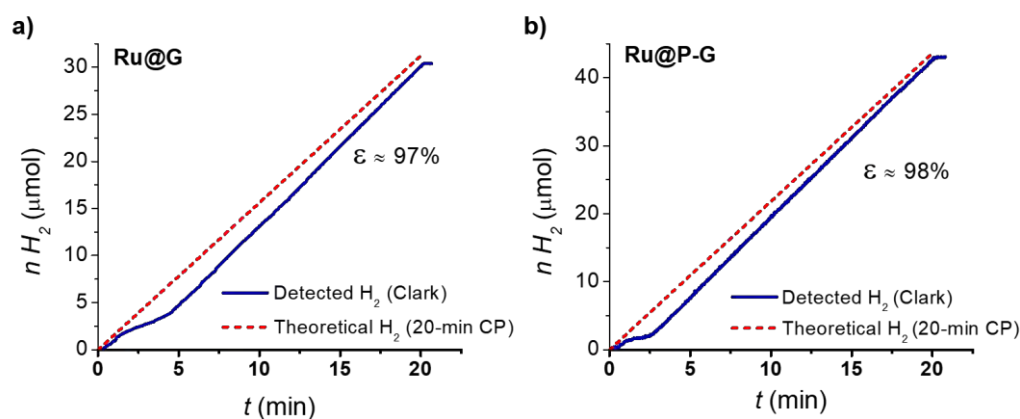


**Figure 19.**  $H_2$ -monitored current-controlled bulk electrolysis of **Ru@G** and **Ru@P-G** in 1 M  $H_2SO_4$ . The production of  $H_2$  was detected in the gas phase by the use of a Clark-type electrode.

#### 4B.4 CONCLUSIONS

Bare and P-doped graphene arising from the pyrolysis of biomass (alginate from marine algae) have been used as a support for the growth and stabilization of ultra-small Ru/RuO<sub>2</sub> NPs through the organometallic synthesis. P-doped graphene allows obtaining smaller and more dispersed NPs ( $1.5 \pm 0.3$  for **Ru@P-G** nm vs.  $1.9 \pm 0.3$  nm in non-doped **Ru@G**) in hybrid electrodes of lower roughness and electroactive surface area. Electrochemical activation of the supported nanocatalysts by reduction of the passivating RuO<sub>2</sub> layer generates excellent HER electrocatalysts under acidic conditions ( $\eta_{10}$  of 29 mV and 15 mV for the bare and P-doped electrodes, respectively). P-doping, identified as surface phosphates by <sup>31</sup>P solid state NMR, induces a general improvement of all the studied HER benchmarking parameters, including overpotential and exchange and specific current densities. All studied systems show excellent long-term stability and selectivity for hydrogen generation, with no sign of deactivation after 12 h under turnover conditions and almost quantitative faradaic efficiencies (97-98 %).



Bearing in mind all the results obtained in *Chapter 4*, graphene materials are confirmed to be suitable supports to obtain small isolated and well-dispersed Ru NPs. In addition, the results confirm the positive role of the heteroatom doping in the stability of Ru NPs during the synthetic procedures, affecting both the nucleation and growth kinetics of the NPs, resulting in smaller mean size and more uniform dispersions. Furthermore, heteroatom doping induces a general improvement in the overall HER electrocatalytic activity of the electrodes, probably due to the respective electron acceptor and electron donor ability of the N and P atoms adjacent to C atoms in the graphitic structures, affecting the electronic properties of the supports. Changes in the supports will be transferred to the Ru NPs, improving in this case the synergistic effect between Ru and C, modulating the adoption of reaction intermediates to enhance the HER electrocatalytic activity. Furthermore, it has been demonstrated that a higher proportion of graphitic phosphorous (*i.e.* **Ru@P-rGO**) contributes more importantly to the enhancement of the HER activity than phosphates (*i.e.* **Ru@P-G**).

## **4B.5 EXPERIMENTAL PART**

### **General considerations and starting materials**

All chemical operations were carried out using standard Schlenk tubes, Fischer–Porter bottle techniques or in a glove-box under argon atmosphere. Solvents (THF and hexane, Sigma-Aldrich) were purified before use by distillation under argon atmosphere through filtration in the column of a purification apparatus (MBraun). [Ru(COD)(COT)] was purchased from Nanomeps Toulouse, alginic acid sodium salt and sodium phosphate dibasic from Sigma Aldrich. All reagents were used without purification.

### **Characterization techniques**

**Transmission electron microscopy (TEM) and high resolution TEM (HRTEM).** Ru-NPs were observed by TEM and HRTEM after deposition of a drop of a solution of the isolated NPs after dispersion in THF on a copper grid. TEM analyses were performed at the “Servicio de Microscopia Electrónica” of Universitat Politècnica de València (UPV) by using a JEOL JEM 1010 CX-T electron microscope operating at 100 kV with a point resolution of 4.5 Å. Some TEM images have been performed at the “Servei de Microscòpia” of the UAB using a JEOL JEM 1400 electron microscope working at 120 kV with a resolution point of 0.4 nm by re-dispersing the material in THF and adding a drop onto a carbon-coated copper grid just before TEM analysis. Size distributions were determined through manual analysis of enlarged micrographs by measuring > 200 particles on a given grid. HRTEM observations were carried out with a JEOL JEM 2010 electron microscope working at 200 kV with a resolution point of 2.35 Å. FFT treatments have been carried out with Digital Micrograph Version 3.7.4.

**Elemental analysis (EA).** EA analyses were performed in Euro EA3000 elemental analyzer (EuroVector) employing sulfanilamide as reference.

**Inductively coupled plasma atomic emission spectroscopy (ICP-AES):** ICP-AES analyses were performed by the ICP technical service of the Instituto de Tecnología Química (ITQ), using a Varian 715-ES ICP-Optical Emission Spectrometer. The samples for ICP-AES were prepared following a modified digestion method reported.<sup>13</sup> In particular, 30 mg of catalyst sample were suspended in 21 mL HCl-HNO<sub>3</sub> (6:1). The

solution was then sonicated for 90 minutes and the samples were digested at 180 °C for 15 hours. After that, it was cooled down until room temperature (r.t.), diluted with 100 mL of water and analyzed by ICP-AES.

**Solid-state MAS-NMR spectroscopy.** <sup>31</sup>P analyses were performed at the ITQ on a Bruker Avance 400WB instrument equipped with a 4 mm probe with the sample rotation frequency of 10 kHz. Measurements were carried out in a 4 mm ZrO<sub>2</sub> rotor.

**Raman spectroscopy:** Raman spectra were recorded using an excitation of 514 and 785 nm in a Renishaw inVia Raman spectrometer equipped with a Lyca microscopy. The samples (powder) were deposited in an Al support, and measured in the region between 0 and 3000 cm<sup>-1</sup> with a resolution of < 4 cm<sup>-1</sup>.

**X-ray photoelectron spectroscopy:** XPS analyses were performed using a SPECS device equipped with a Phoibos 150-9MCD detector using Mg-K $\alpha$  radiation (hv= 1235.6 eV) and Al-K $\alpha$  radiation (hv= 1483.6 eV) from a dual source. The pressure during the measurements was kept under 10<sup>-9</sup> Torr. The quantification and titration of the spectra was done with the help of the software CASA, referencing them in base of C 1s = 284.5 eV.

**Infrared spectroscopy (IR).** FT-IR spectra were recorded on a Nicolet 8700 Thermo spectrometer in the range 4000-600 cm<sup>-1</sup> from samples prepared as KBr pellets.

**X-ray powder diffraction (XRD).** Powder samples were analyzed using a Cubix-Pro PANalytical diffractometer equipped with a detector PANalytical X'Celerator. An X-Ray monochromatic radiation of CuK $\alpha$  ( $\lambda_1=1.5406$  Å,  $\lambda_2=1.5444$  Å, I<sub>2</sub>/I=0.5) was employed

## Synthetic procedures

**G. G** was synthesized by pyrolysis of alginate according to the literature.<sup>3,4</sup>

**P-G. P-G** was synthesized by pyrolysis of alginate according to the literature,<sup>3,14,15</sup> dissolving 0.5 g of alginic acid sodium salt in a sodium phosphate dibasic monohydrate aqueous solution (1.6 g in 50 mL of water). Elemental analysis: C=73.54 %, H: 0.96 %, S: 0.331 %, XPS: P=1.15 %, XRD: reduced graphene. IR: (KBr pellet, cm<sup>-1</sup>), 1160 cm<sup>-1</sup> ( $\nu$  P=O).

**Ru@x-G** ( $x = \text{none or P}$ ): A Schlenk flask was charged with [Ru(COD)(COT)] (10 mg, 0.032 mmol) and dissolved in 5 mL THF. After that the solution was added to a 100 mL Fischer–Porter bottle charged with a suspension of **x-G** (100 mg) in 50 mL of THF previously sonicated during 90 min. The Fischer-Porter was then pressurized with 3 bar of H<sub>2</sub>, and the dispersion was stirred vigorously. The stirring was continued for 20 h at the room temperature. After that, the remaining H<sub>2</sub> pressure was released and **Ru/P-G** was separated from the suspension by filtration through a polyamide membrane (Whatman® membrane filters, 47mm×0.45 μm) and washed with THF (150 mL). The resulting black precipitate was dried overnight at 60 °C. The size of the NPs was measured by TEM on a sample of at least 100 nanoparticles. **Ru@G**: TEM,  $d_{\text{mean}} = 1.9 \pm 0.6$  nm. ICP: 2.6 wt.% Ru. XPS: Ru/RuO<sub>2</sub>. **Ru@P-G**: TEM,  $d_{\text{mean}} = 1.5 \pm 0.3$  nm. ICP: 3.3 wt.% Ru. XPS: Ru/RuO<sub>2</sub>.

## Electrochemical set-up

**Electrochemical measurements:** All the electrochemical experiments were performed in a BioLogic SP-150 potentiostat. The solutions were degassed previous to the electrochemical analysis with an Ar flow. Ohmic potential (IR) drop was automatically corrected at 85 % using the Biologic EC-Lab software for linear sweep voltammetry. 1 M H<sub>2</sub>SO<sub>4</sub> solution was prepared by mixing 56.1 mL of 95-97 % H<sub>2</sub>SO<sub>4</sub> in 1 liter of Milli-Q water. A glassy carbon rotating disk electrode (RDE,  $\phi = 0.3$  cm,  $S = 0.07$  cm<sup>2</sup>) was used as working electrode. The RDE was rotated at 3000 rpm in order to ensure complete removal of *in-situ* formed H<sub>2</sub> bubbles. A Pt wire was used as counter electrode (CE) and a standard calomel electrode (SCE, Hg/Hg<sub>2</sub>Cl<sub>2</sub>, KCl sat.) was used as a reference electrode (RE). The potentials reported versus normal hydrogen electrode were transformed as follows ( $E_{\text{NHE}} = E_{\text{SCE}} + E^0_{\text{SCE}}$ ), where  $E^0_{\text{SCE}} = 0.244$  V.

A 10 mL two-compartment cell with a proton exchange membrane between the two compartments was used for faradaic efficiencies calculation.

The CE was placed in one compartment and the WE and RE were placed in the other compartment together with the Clark electrode. Both compartments were filled with *c.a.* 7 mL of 1 M H<sub>2</sub>SO<sub>4</sub> solution and equipped with a stirring bar. Prior to each measurement, both compartments were purged with Ar. The Unisense H<sub>2</sub>-NP Clark electrode was used to measure in the gas phase the hydrogen generated by the systems during a

chronopotentiometry. The Clark electrode was calibrated by adding different volumes of 99 % pure hydrogen at the end of the experiment.

**Electrode Preparation.** A 2 mg/mL dispersion was prepared by adding 1 mg of Ru material in 0.5 mL of THF. Long-time sonication was tried to be avoided to prevent NPs aggregation over the C support. Then, an aliquot of 5  $\mu\text{L}$  was drop-casted on the surface of the GC/RDE ( $S = 0.07 \text{ cm}^2$ ), and dried. A 5  $\mu\text{L}$ -drop of Nafion (0.02% w/w in water and 1-metanol) was finally added and dried prior to the electrochemical measurements.

**Double-layer capacitance ( $C_{\text{DL}}$ ) and electrochemically active surface area (ECSA) determination:**  $C_{\text{DL}}$  was estimated by performing CV measurements with different scan rates. A non-faradaic region was chosen from the LSV (typically a 0.1 V window about OCP), where no redox process takes place and all the measured current is due to double-layer charging. Based on this assumption, the charging current ( $i_c$ ) can be calculated as the product of the electrochemical double-layer capacitance ( $C_{\text{DL}}$ ) and the scan rate ( $\nu$ ). Plotting  $i_c$  as a function of  $\nu$  yields a straight line with slope equal to  $C_{\text{DL}}$ . In this way, 8 different scan rates were used (5, 10, 25, 50, 75, 100, 250 and 500 mV/s), holding the working electrode at each potential vertex for 10 seconds prior to the next step. The ECSA was obtained by dividing the calculated capacitance by a tabulated value ( $C_s$  = specific capacitance) that depends on the material used and solution (for C, in 1 M  $\text{H}_2\text{SO}_4$   $C_s=13\text{-}17 \mu\text{F}/\text{cm}^2$ ). The Roughness Factor (RF) was calculated by dividing the ECSA by the geometrical surface area ( $S$ ) of the RDE.

## **4B.6 REFERENCES**

- <sup>1</sup> A. Ambrosi, C.K. Chua, A. Bonanni and M. Pumera, *Chem. Rev.* **2014**, 114, 7150-7188.
- <sup>2</sup> D.D. Ouyang, L.B. Hu, G. Wang, B. Dai, F. Yu, L.L. Zhang, *New Carbon Mater.* **2021**, 36, 350-372.
- <sup>3</sup> M. Latorre-Sánchez, A. Primo and H. García, *Angew. Chem. Int. Ed.* **2013**, 52, 11813-1181.
- <sup>4</sup> M.M. Trandafir, M. Florea, F. Neațu, A. Primo, V. I. Parvulescu and H. García, *ChemSusChem* **2016**, 9, 1565–1569
- <sup>5</sup> R. Saito, M. Hofmann, G. Dresselhaus, A. Jorio and M.S. Dresselhaus, *Adv. Phys.* 2011, 60, 413-550.
- <sup>6</sup> A.M. Dimiev and S. Eigler, *Graphene Oxide: Fundamentals and Applications* **2017**, First Edition. Eds: A.M. Dimiev and S. Eigler. John Wiley & Sons, Ltd. Published 2017 by John Wiley & Sons, Ltd.
- <sup>7</sup> A.M. Puziy, O.I. Poddubnaya, R.P. Socha, J. Gurgul and M. Wisniewski, *Carbon* **2008**, 46, 2113-2123.
- <sup>8</sup> D.J. Morgan, *Surf. Interf. Anal.* **2015**, 47, 1072-1079.
- <sup>9</sup> R. Fu, L. Liu, W. Huang and P. Sun, *J. App. Polymer Sci.* **2003**, 87, 2253-2261.
- <sup>10</sup> M. Hupfer, B. Ruübe and P. Schmieder, *Limnol. Oceanogr.* **2004**, 49, 1-10.
- <sup>11</sup> J. Creus, S. Drouet, S. Suriñach, P. Lecante, V. Collière, R. Poteau, K. Philippot, J. García-Antón and X. Sala, *ACS Catal.* **2018**, 11094-11102.
- <sup>12</sup> C.C.L. McCrory, S. Jung, I.M. Ferrer, S.M. Chatman, J. C. Peters, T.F. Jaramillo, *J. Am. Chem. Soc.* **2015**, 137, 4347-4357.
- <sup>13</sup> T. Suoranta, M. Niemelä, P. Perämäki, *Talanta* **2014**, 119, 425-429.
- <sup>14</sup> M.J. McAllister, J.L. Li, D.H. Adamson, H.C. Schniepp, A.A. Abdala, J. Liu, M. Herrera-Alonso, D.L. Milius, R. Car, R.K. Prud'homme, I.A. Aksay, *Chem. Mater.* 2007, 19, 4396-4404.
- <sup>15</sup> J. Meihua, J. Hae-Kyung, K. Tae-Hyung, S. Kang Pyo, C. Yan, Y. Woo Jong, R. Eun Ju and L. Young Hee, *J. Phys. D: Appl. Phys.* **2010**, 43, 275402.

**ANNEX Chapter 4**

**Table A1.** Comparison of the most relevant graphene-derived and Ru/graphene-based HER nanoelectrocatalysts under acidic conditions. Parameters: mean diameter ( $\emptyset$ ), onset overpotential ( $\eta_0$ , mV), overpotential at  $|j| = 10 \text{ mA} \cdot \text{cm}^{-2}$  ( $\eta_{10}$ , mV), Tafel slope ( $b$ , mV/dec), exchange current density ( $|j_0|$ ,  $\text{mA}/\text{cm}^2$ ), specific current density ( $|j_s|$ ,  $\text{mA}/\text{cm}^2$ ) and turnover frequency (TOF,  $\text{s}^{-1}$ ). Unless otherwise stated, electrolyte is 0.5 M  $\text{H}_2\text{SO}_4$ .

Entry	Catalyst	$\emptyset$ (nm)	$\eta_0$ (mV)	$\eta_{10}$ (mV)	$b$ (mV/dec)	$ j_0 $ ( $\text{mA}/\text{cm}^2$ )	Ref.
1	GCE-S-GNs-1000-CB-Ru	30	$\approx 60$	80	61 (Tafel) 71 (EIS)	0.541 0.431	1
2	Ru-GLC	2-5	3	35	46	-	2
3	$\text{Ru}_2\text{P}/\text{RGO}$	$<7$	$\approx 0$	22	29	2.2	3
4	Ru@GnP	2	$\approx 0$	13	30	-	4
5	N-G	-	$\approx 250$	490	116	-	5
6	P-G	-	$\approx 300$	550	133	-	5
7	N,P-G	-	$\approx 240$	420	91	0.00024	5
8	N,B-CN	-	$\approx 410$	710	198	-	6
9	N-CN	-	$\approx 400$	620	159	-	6
10	N,P-CN	-	$\approx 340$	550	139	-	6
11	N,S-CN	-	$\approx 100$	290	77	-	6
12	N-G	-	499	-	405	86	7
13	N,P-G	-	399	-	565	265	7
14	P-G	-	536	-	348	76	7
15	P,N-G	-	247	380	126	21	7
16	VG	-	$\approx 375$	-	158	-	8
17	N-VG	-	$\approx 200$	290	121	-	8
18	Ru/NG-750	3-7	$\approx 0$	53	44	-	9
19	Ru@CN	2.37	$\approx 70$	126	-	-	10
20	Ru-NGA	3.5	$\approx 15$	55	32	-	11
21	Ru@NC	2.1	$\approx 10$	62	40	-	12

Legend: GCE-S-GNs-1000=glassy carbon modified sulfur-doped graphene nanosheets heat treated at 1000 °C, GLC=graphene-layered carbon, RGO=reduced graphene oxide, GnP=graphene nanoplatelets. N-G=N-doped graphene; P-G=P-doped graphene; N,P-G=N,P-doped graphene; N,B-CN=N,B-doped carbon nanosheets, N-CN=N-doped carbon nanosheets, N,P-CN=N,P-doped carbon nanosheets, N,s-CN=N,S-doped carbon nanosheets, P,N-G=P,N-doped graphene, VG=vertical graphene, N-VG=N-doped vertical graphene, Ru/NG-750= Ru nanoclusters on N-doped graphene prepared at 750 °C, Ru@CN=Ru NPs over N-doped carbon, Ru-NGA= Ru-modified N-doped graphene aerogel, Ru@NC= Ru NPs embedded in N-doped carbon.

<sup>1</sup> R. K. Shervedani and A. Amini, *Carbon* **2015**, 93, 762-773.

<sup>2</sup> Z. Chen, J. Lu, Y. Ai, Y. Ji, T. Adschiri and L. Wan, *ACS Appl. Mater. Interfaces* **2016**, 8, 35132-35137.

- <sup>3</sup> T. Liu, S. Wang, Q. Zhang, L. Chen, W. Hu and C.M. Li, *Chem. Commun.* **2018**, 54, 3343-3346.
- <sup>4</sup> F. Li, G.F. Han, H.J. Noh, I. Ahmad, I.Y. Jeon and J.B. Baek, *Adv. Mater.* **2018**, 30, 1803676.
- <sup>5</sup> Y. Zheng, Y. Jiao, L.H. Li, T. Xing, Y. Chen, M. Jaroniec and S.Z. Qiao, *ACS Nano* **2014**, 8, 5, 5290-5296.
- <sup>6</sup> K. Qu, Y. Zheng, X. Zhang, K. Davey, S. Dai and S.Z. Qiao, *ACS Nano* **2017**, 11, 7293-7300.
- <sup>7</sup> Y.H. Hung, D. Dutta, Y.J. Tseng, J.K. Chang, A.J. Bhattacharyya and C.Y. Su, *J. Phys. Chem. C* **2019**, 123, 22202-22211.
- <sup>8</sup> Y. Li, C. Ai, S. Deng, Y. Wang, X. Tong, X. Wang, X. Xia and J. Tu, *Materials Research Bulletin* **2021**, 134, 111094.
- <sup>9</sup> R. Ye, Y. Liu, Z. Peng, T. Wang, A.S. Jalilov, B.I. Yakobson, S.H. Wei and J.M. Tour, *ACS Appl. Mater. Interfaces* **2017**, 9, 3785-3791.
- <sup>10</sup> J. Wang, Z. Wei, S. Mao, H. Li and Y. Wang, *Energy Environ. Sci.* **2018**, 11, 800-806.
- <sup>11</sup> Y. Shi, W. Dai, M. Wang, Y. Xing, X. Xia and W. Chen, *Chem. Res. Chinese Universities*, **2020**, 36 (4), 709-714.
- <sup>12</sup> B. Zheng, L. Ma, B. Li, D. Chen, X. Li, J. He, J. Xie, M. Robert and T.C. Lau, *Catal. Sci. Technol.* **2020**, 10, 4405-4411.



# 5

## **Chapter 5. Metallic nanoparticles supported on carbon microfibers as water splitting catalysts**

---

*Chapter 5* deals with the synthesis of metallic nanoparticles supported on carbon microfibers by using the organometallic synthetic methodology. TEM, EDX, ICP and XPS techniques have been used to get information about the structure and composition of the carbon-supported materials. Two different metals, Ru and Co, have been chosen for this study. Ru-based materials have been electrochemically tested in the HER (*Chapter 5A*) and Co systems evaluated in the OER catalysis (*Chapter 5B*).

---



**TABLE OF CONTENTS**

<b>5.1 GENERAL INTRODUCTION</b> .....	137
<b>5.1.1 Synthesis and characterization of carbon microfibers (CFs) supports</b> .....	138
<b>5.2 REFERENCES</b> .....	142
<b>Chapter 5A. Ru/RuO<sub>2</sub> nanoparticles supported on carbon microfibers for the hydrogen evolution reaction</b> .....	143
<b>5A.1 INTRODUCTION</b> .....	145
<b>5A.2 SYNTHESIS AND CHARACTERIZATION</b> .....	145
<b>5A.3 ELECTROCATALYTIC PERFORMANCE</b> .....	149
<b>5A.4 CONCLUSIONS</b> .....	154
<b>5A.5 EXPERIMENTAL SECTION</b> .....	156
<b>5A.6 REFERENCES</b> .....	159
<b>Chapter 5B. Oxygen evolution anodes based on Co(OH)<sub>2</sub> nanoparticles supported on carbon microfibers</b> .....	161
<b>5B.1 INTRODUCTION</b> .....	163
<b>5B.2 SYNTHESIS AND CHARACTERIZATION</b> .....	164
<b>5B.2.1 Synthesis of Co NPs supported onto carbon microfibers</b> .....	164
<b>5B.2.2 Transmission electron microscopy analysis</b> .....	166
<b>5B.2.2.1 <i>In situ</i> systems</b> .....	166
<b>5B.2.2.2 <i>Ex situ</i> systems</b> .....	168
<b>5B.2.3 Inductively coupled plasma-optical emission spectroscopy</b> .....	170
<b>5B.2.4 X-ray photoelectron spectroscopy</b> .....	171
<b>5B.3 ELECTROCATALYTIC PERFORMANCE</b> .....	176
<b>5B.3.1 Electrocatalytic performance towards the OER</b> .....	176
<b>5B.3.2 Faradaic efficiencies determination</b> .....	186
<b>5B.3.3 Effect of pH in the OER activity</b> .....	188
<b>5B.4 CONCLUSIONS</b> .....	189
<b>5B.5 EXPERIMENTAL SECTION</b> .....	192

**5B.6 REFERENCES**.....197  
**5B.7 ANNEX**.....199

## **5.1 GENERAL INTRODUCTION**

Metal nanoparticles (NPs) stabilized by various molecules such as solvents, ligands, polymers, dendrimers, ionic liquids or inorganic supports are the subject of numerous catalytic studies, lying at the frontier between homogeneous and heterogeneous catalysis. The use of inorganic supports allows to get supported nanoparticles, making them easier to handle and more stable, as observed for other heterogeneous catalysts. The deposition of metal NPs onto a support also allows to take benefit of synergetic effects between the metallic species and the support. In this sense, if the electron transfer in NPs is typically more difficult and slower than in molecular species, the association of appropriate conductive supports with metal NPs is a key point to overcome these limitations.

For example, carbon-based materials (*i.e.* carbon nanotubes (CNTs), graphene, etc.) are excellent supports for electrochemical catalytic applications due to their high electrical conductivity, versatile morphology, surface chemistry and electronic structure<sup>1</sup> and their high stability in both acidic and alkaline environments.<sup>2</sup> Additionally, the integration of heteroatoms (*i.e.* N, P, S, O or B) into the carbon structure has been shown to be a powerful strategy to tune their physicochemical properties, such as electrical conductivity. In this way, doping the carbon skeleton with p-block elements can lead to injection of extra p-electrons to the carbon conjugated systems and then induce electron-donating/accepting sites, depending on the difference in electronegativity and affinity between carbon and dopants, which can facilitate reactions to take place on them.<sup>3,4</sup> As reported for many catalytic processes, the increase of electrical conductivity with modified carbon supports has positive effects on the activity and stability of their corresponding supported-nanocatalysts (due to reduced aggregation under electrocatalytic conditions, obtaining a higher number of exposed active sites).<sup>5,6</sup> The use of low-dimensional carbon supports such as nanotubes or graphene gives major advantages such as high surface areas and feasible tailoring of the electronic structures through functionalization or quantum confinement effects.<sup>7</sup> However, their integration into practical water splitting (WS) electrodes is complex, requiring efficient deposition methods onto macroscopic electrodes (*i.e.* glassy carbon, FTO), which is still a challenge. In this regard, an alternative consists in the use of high-surface area carbon microfibers (CFs) produced by the pyrolysis of polyacrylonitrile (PAN).<sup>8</sup> These CFs present a

graphene-like structure, containing pyridyl moieties that can be easily oxidized by a chemical method to generate carboxylic acid groups on the surface, generating nicotinic fragments in their structure. In contrast to CNTs and graphene, CFs can be easily handled and simply integrated in WS electrolyzers, acting themselves as working electrodes for electrocatalytic transformations.

In this chapter we will describe the use of carbon microfibers as supports for metal nanoparticles in order to access hybrid nanomaterials for their investigation in the water splitting catalysis (*i.e.* HER and OER). CFs-supported systems allowed to treat the overall WS reaction by adapting the nature of the metallic supported NPs (*i.e.* ruthenium or cobalt) for each half-reaction as reflected in the two following sections. *Sub-chapter 5A* reports the use of Ru/RuO<sub>2</sub> NPs supported onto carbon fibers as catalysts for the HER. CFs-supported Co(OH)<sub>2</sub> NPs and their catalytic study towards the OER are described in *sub-chapter 5B*.

### 5.1.1 Synthesis and characterization of carbon microfibers (CFs) supports

The structure of carbon fibers is like that of graphite, which consists of an arrangement of carbon atoms in a regular hexagonal pattern. The main difference between CFs and graphite is how the subsequent carbon layers are disposed. Graphite is a crystalline material in which the different layers are arranged in parallel within a regular disposition.<sup>9,10</sup> The intermolecular forces between them are weak ( $\pi$ - $\pi$  stacking forces), which makes the graphite easily to exfoliate. In CFs, XPS analysis proved that the different carbon atom layers are set in a more irregular manner than the “highly oriented pyrolytic graphite” reference material, leading to a structure with a large number of defects, as described in a previous publication by R. Mas-Ballesté *et al.*<sup>8</sup> The main characteristics of CFs are: high electrical and thermal conductivity, high surface area, easy functionalization thanks to the presence of a high number of structural defects and high N content in the carbon structure. These characteristics make CFs a markedly different support compared to graphene or multi-walled carbon nanotubes (MWCNTs). The electronic properties of the different groups present in CFs supports are expected to influence the electronic structure of the active sites, and to have a potential impact on the overpotential needed to achieve the desired redox process.

Polyacrylonitrile-based carbon microfibers used in this work, were provided by Dr. Rubén Más Ballesté (Inorganic Chemistry Department, Universidad Autónoma de Madrid). They were obtained basically from the pyrolysis process of polyacrylonitrile (PAN).<sup>11,12</sup> Conversion of PAN fibers into carbonized structures requires two heat treatment processes, namely stabilization and carbonization (Fig. 1):

- The stabilization reaction consists of cyclization, dehydrogenation and oxidation steps. Filaments of PAN are subjected to an applied tension to align each fiber prior to their oxidation under air at temperatures between 200 °C-220 °C, with the filaments still subjected to the tension. The PAN macromolecules undergo a transformation from a linear polymer to a rigid, thermally stable ladder structure.
- The carbonization reaction of the stabilized fibers occurs under very little tension at elevated temperatures, typically between 1000-1500 °C, in an inert N<sub>2</sub> environment. During this heating treatment non-carbon elements are released (Fig. 1), thus gradually increasing the carbon content of the material. Consequently, the conversion of the stabilized ladder structure into a graphene-like structure, a more well-ordered structure, occurs.

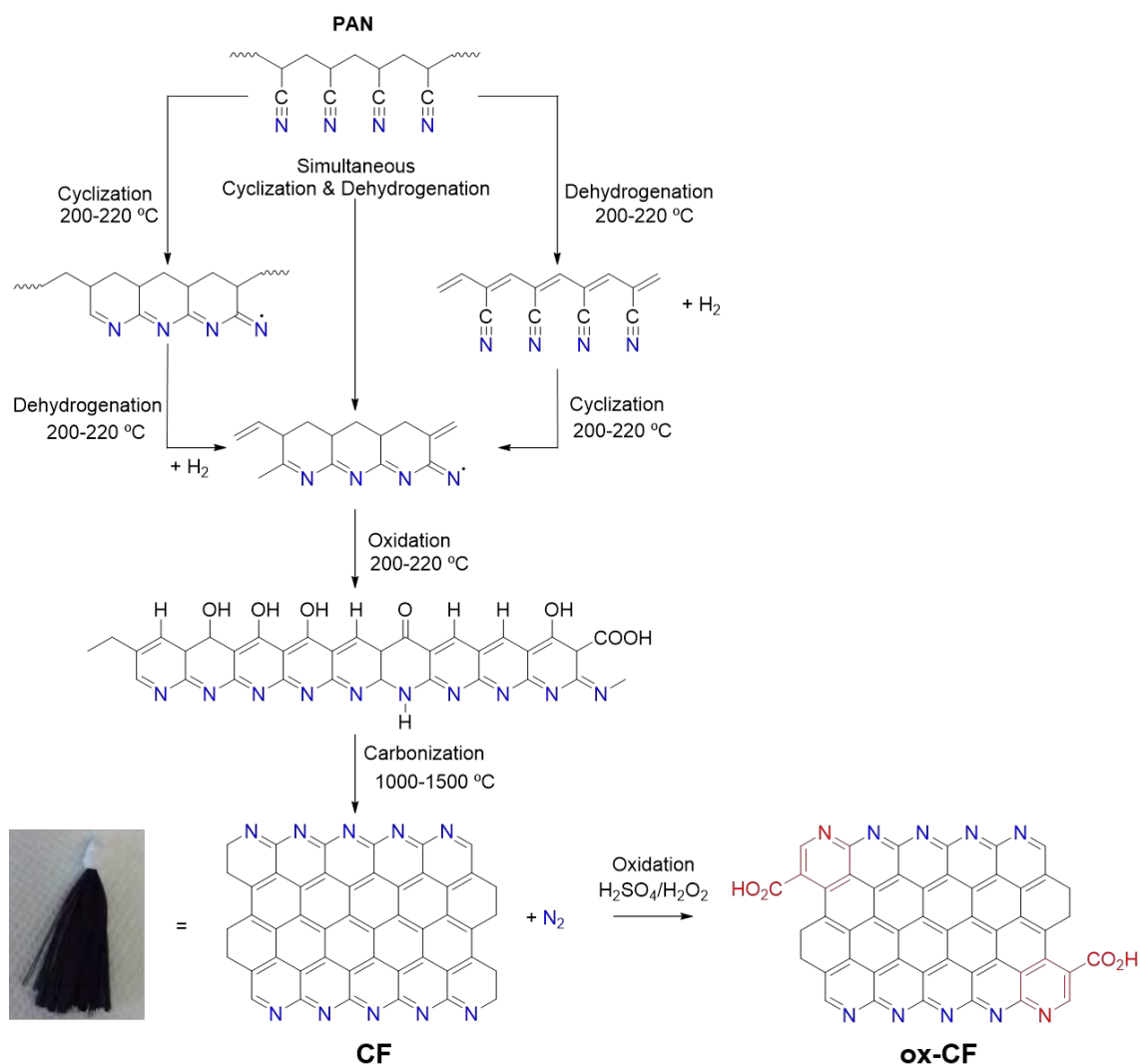


**Figure 1.** Bare-carbon microfibers (**CF**) synthetic pathway and oxidation process to obtain CFs containing carboxylic groups on the surface (**ox-CF**). The picture on the left corresponds to a brush of carbon-microfibers obtained after this synthetic process. Adapted from ref. 12.

Before decoration of the CFs with metal NPs, the CFs filaments were joined in  $\approx 21000$ -fibers bunches and cut in 6-cm long electrodes, each weighting  $\approx 90$  mg (see Experimental Section in sections 5A.5 and 5B.5).

In this work, two different kinds of CFs were used: 1) as prepared carbon microfibers resulting from the direct pyrolysis of polyacrylonitrile (named as **CF**) without any other treatment and 2) functionalized carbon microfibers presenting carboxylic groups on their surface (named as **ox-CF**). The latter material was obtained from the former CFs, after a chemical oxidation process. This process consisted in immersing the CFs brush in a 1:1  $H_2SO_4:H_2O_2$  solution under constant stirring for 1 h at room



temperature (last step in Fig. 1). After this process, the brushes were sonicated 3 times in ethanol to remove the remaining acid. This process allowed to obtain carboxylic groups on the pyridyl moieties under the form of nicotine-like species. XPS analysis showed that approximately 5 % of the carbon atoms on the surface correspond to carboxylic groups.<sup>8</sup> During this oxidative process the graphitic regions of the carbon microfibers were thus not massively altered, preserving their original electrical conductivity. The surface of **CF** and **ox-CF** supports were explored by TEM before any modification with metallic nanoparticles (Fig. 2). For a more detailed characterization of the supports, the reader can refer to ref. 8.

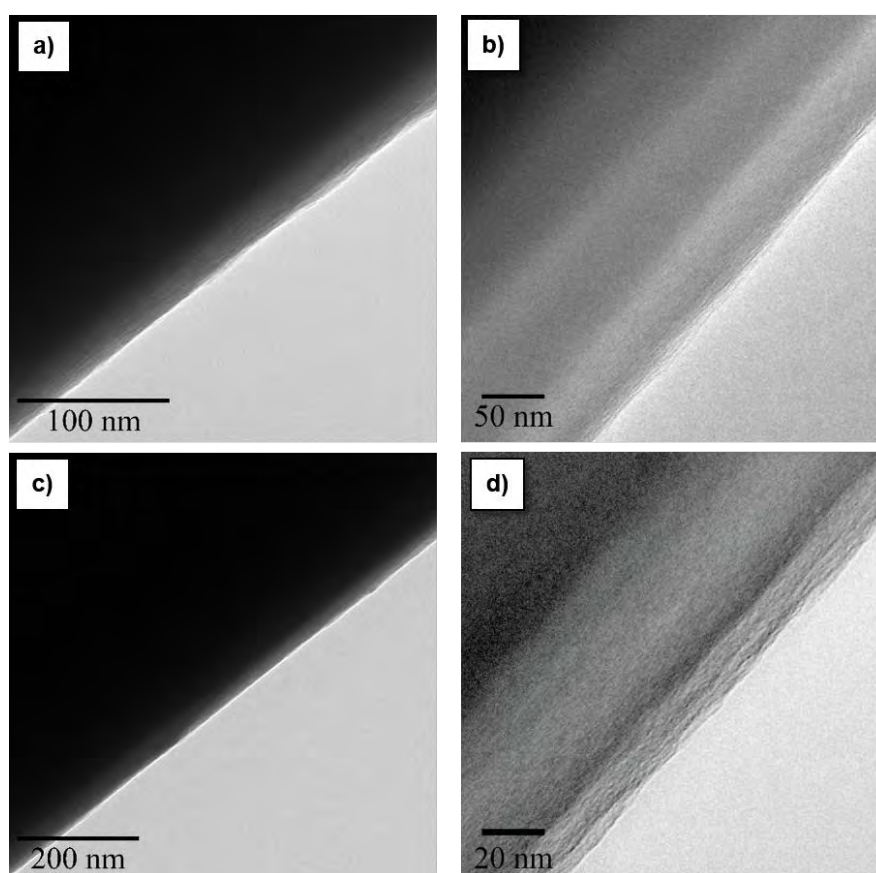


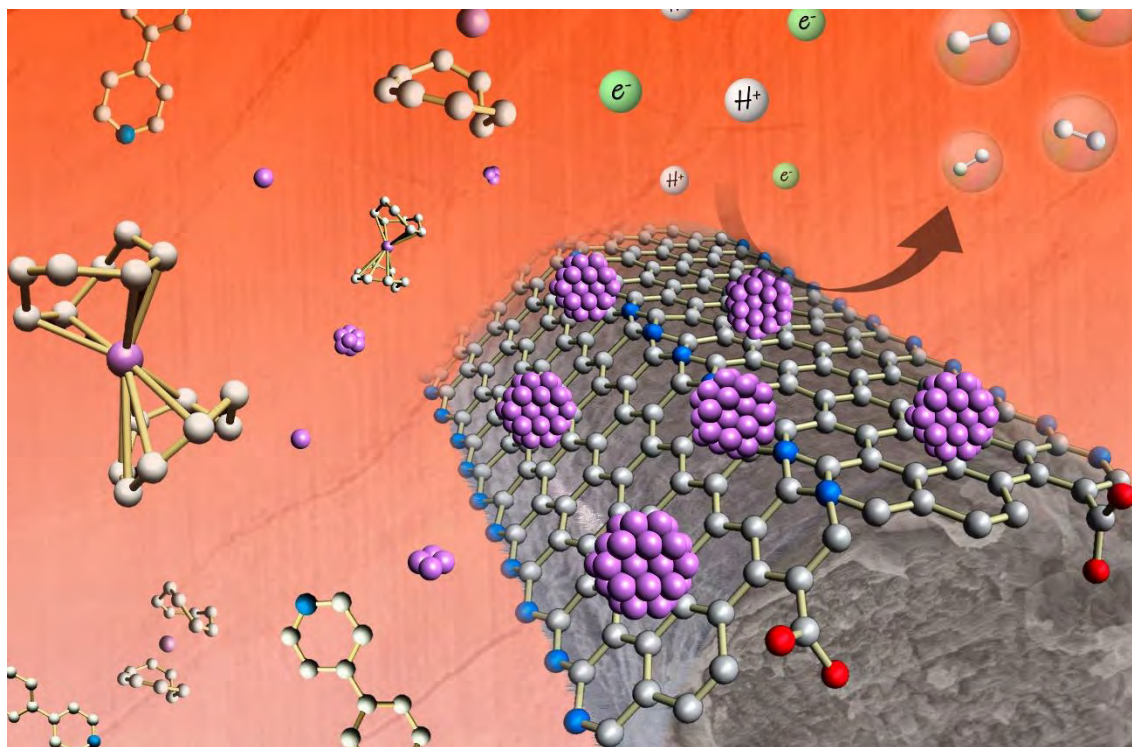
**Figure 2.** TEM pictures of **CF** (a and b) and **ox-CF** (c and d).

## **5.2 REFERENCES**

- <sup>1</sup> J. Zhang, Z. Xia and L. Dai, *Sci. Adv.*, **2015**, 1, e1500564.
- <sup>2</sup> Y. Shen, P. Liu, J. Du, Y. Song, H. Cao, M. Zhao, P. Gao, B. Xu, J. Guo and Y. Wu, *Carbon* **2020**, 166, 388-395.
- <sup>3</sup> K. Qu, Y. Zheng, X. Zhang, K. Davey, S. Dai and S. Z. Qiao, *ACS Nano* **2017**, 11, 7293-7300.
- <sup>4</sup> Z. Zhao, M. Li, L. Zhang, L. Dai and Z. Xia, *Adv. Mater.* **2015**, 27, 6834-6840.
- <sup>5</sup> A. Bähr, G.H. Moon and H. Tüysüz, *ACS Appl. Energy Mater.* **2019**, 2, 6672–6680.
- <sup>6</sup> J. Creus, J. De Tovar, N. Romero, J. García-Antón, K. Philippot, R. Bofill and X. Sala, *ChemSusChem*, **2019**, 12, 2493–2514.
- <sup>7</sup> X. Kong and Z. Peng, *Mater. Today Energy*, **2019**, 11, 119–132.
- <sup>8</sup> O.G. Moral, A. Call, F. Franco, A. Moya, J.A. Nieto-Rodríguez, M. Frias, J.L.G. Fierro, M. Costas, J. Lloret-Fillol, J. Alemán and R. Mas-Ballesté, *Chem. Eur. J.* **2018**, 24, 3305–3313.
- <sup>9</sup> Entegris, inc. Properties and characteristics of graphite **2013**.
- <sup>10</sup> E. Solfiti and F. Berto, *Procedia Structural Integrity* **2020**, 25, 420–429
- <sup>11</sup> A.K. Gupta, D K. Paliwal, P.Bajaj, *J. Macromol. Sci., Rev. Macromol. Chem. Phys.* **1991**, C31(1), 1-89.
- <sup>12</sup> B. A. Newcomb, *Compos. Part A. Appl. Sci. Manuf.* **2016**, 91, 262-282.

## **Chapter 5A. Ru/RuO<sub>2</sub> nanoparticles supported on carbon microfibers for the hydrogen evolution reaction**

---



Four different cathodes for the HER based on Ru NPs and carbon microfibers (CFs) were developed. CFs-supported Ru NPs were synthesized by two different methodologies based on the organometallic approach: direct synthesis of Ru NPs onto the CFs surface (*in situ*) or impregnation of the CFs with a colloidal solution of pre-synthesized Ru NPs stabilized with the 4-phenylpyridine ligand (RuPP NPs, *ex situ*). The electrocatalytic results in acidic conditions showed that both the nature of the NPs and of the CFs play a key role in the stability and activity of the hybrid electrodes towards the HER.

This work was done in close collaboration with Dr. J. Creus, a former PhD student in our groups. My contribution concerned mainly in characterization and electrocatalytic studies.

---



## **5A.1 INTRODUCTION**

As stated in the General Introduction above, hydrogen is exhaustively studied as an efficient energy carrier<sup>1</sup> due to the cleanness of its consumption, obtaining only water as by-product. Pt-based catalysts are considered the state-of-the-art catalysts for the reduction of protons ( $4\text{H}^+ + 4\text{e}^- \rightarrow 2\text{H}_2$ ,  $0\text{ V}_{\text{NHE}}$  at pH 0) because the Pt-H bond is strong enough to be stable but also weak enough to be easily broken and then facilitate  $\text{H}_2$  release.<sup>2,3,4</sup> However, as Pt is a scarce and expensive metal, the scientific community looks for alternative metals. In acidic media, first row transition metals normally show low stability due to corrosion, whereas their activity under alkaline conditions is far away to be competitive with Pt. In contrast, Ru, the chosen metal in this sub-chapter, is a good candidate to replace Pt thanks to its lower price and high stability both in acidic and alkaline conditions as well. Thereby, bare CFs (CF) and oxidized CFs (ox-CFs) were decorated with Ru/RuO<sub>2</sub> NPs following the organometallic approach, yielding four different HER working electrodes.

## **5A.2 SYNTHESIS AND CHARACTERIZATION**

The incorporation of metallic Ru NPs onto CF and ox-CF materials was performed following two different methodologies. The 1<sup>st</sup> methodology is an *in situ* synthesis, in which Ru NPs were prepared by decomposing 10 mg of [Ru(COD)(COT)] (cod: 1,5-cyclooctadiene; cot: 1,3,5-cyclooctatriene) in the presence of CFs (90 mg) in THF, at r.t. and under 3 bar of  $\text{H}_2$  (Fig. 1a, top path). By this method, naked metal atoms released from the decomposition of the Ru precursor nucleated directly onto the CFs. The stabilization of the obtained Ru NPs derives from the different NP-CF (surface C) possible interactions, the surface carboxylic groups (*i.e.* ox-CF) and the presence of solvent molecules (THF). The 2<sup>nd</sup> methodology is an *ex situ* approach. In this case, colloidal Ru nanoparticles (**Ru-4PP NPs**) were pre-synthesized by decomposing [Ru(COD)(COT)] at r.t., under  $\text{H}_2$ , in THF and in the presence of 0.2 eq. of 4-phenylpyridine ligand (4PP) as stabilizer, as previously reported,<sup>5</sup> and then these NPs were used to impregnate the CFs (Fig. 1a, bottom path). These two methodologies thus differed in the presence of 4-phenylpyridine at the NPs surface when deposited on the CF supports.

In addition, the use of two types of CFs (Fig. 1b) allowed obtaining four different hybrid materials, namely **Ru@CF**, **Ru@ox-CF**, **RuPP@CF** and **RuPP@ox-CF** (Fig. 1), which were exposed to air before being characterized by TEM, XPS and ICP. Thus, the combination of these two synthetic methods together with the use of two types of CFs allowed studying the influence of both the presence of a stabilizing agent (*i.e.* 4PP ligand) and the nature of the CFs supports (*i.e.* presence of COOH) in the morphology of the NPs and the catalytic properties of the hybrid materials obtained.

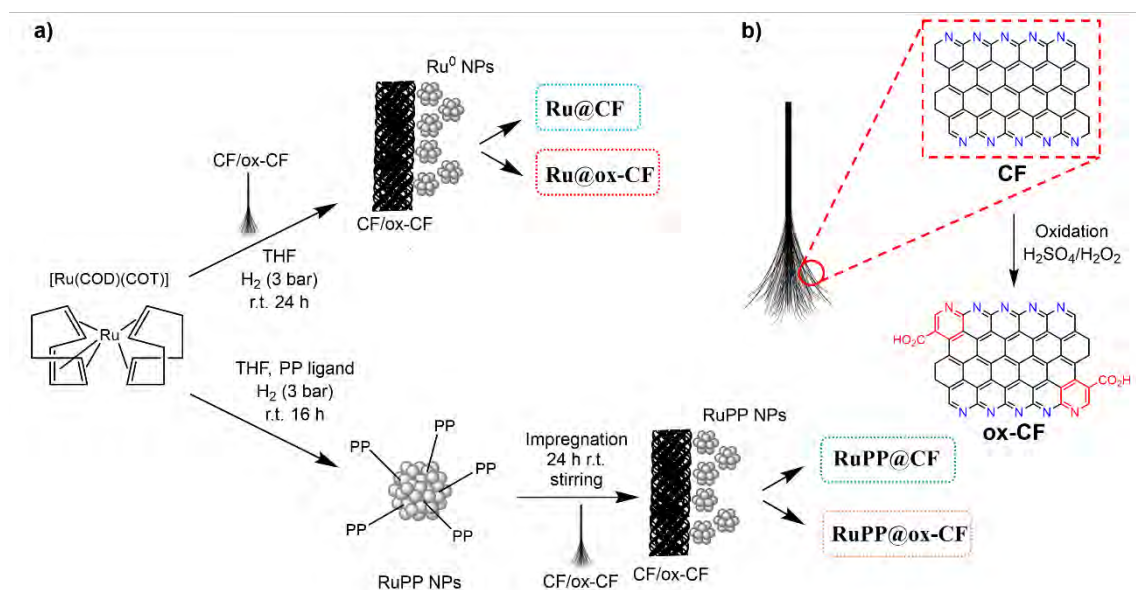


**Figure 1.** Experimental procedure for the preparation of the hybrid RuNPs@CFs materials (a). Schematic representation of the surface chemical composition of CF and ox-CF (b).

TEM proved the successful preparation of supported Ru NPs onto the carbon microfibers, showing the presence of a thin layer of ultra-small Ru NPs onto the surface of CFs both in the *in situ* and *ex situ* systems (Fig. 2 and 3, respectively). In the case of the use of 4PP ligand, a TEM image of Ru-4PP NPs in the absence of support is also given (Fig. 3a) for comparison purpose. These results confirmed that the defects on the C structure, the presence of N atoms (*i.e.* breaking the periodicity and homogeneity of the graphite-like carbon structure) and the addition of carboxylic groups and 4PP ligands, when present, promoted the nucleation and stabilization of Ru atoms to obtain NPs with a narrow size distribution (Table 1).



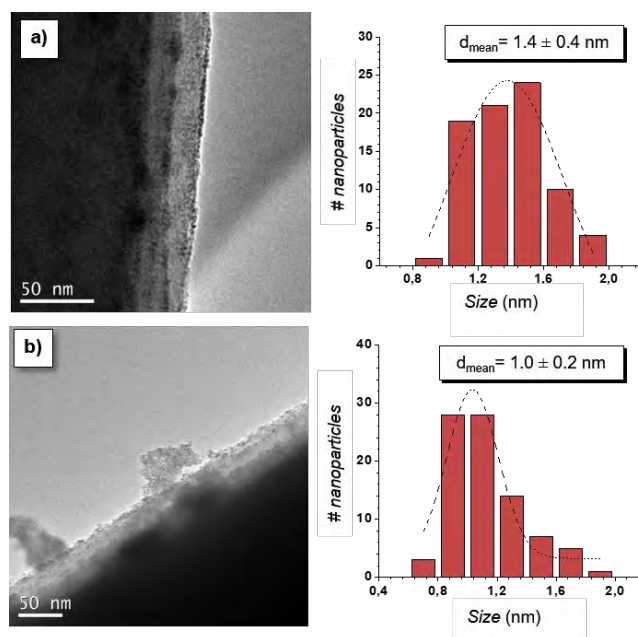


**Figure 2.** Representative TEM images and corresponding size distribution histograms for **Ru@CF** (a) and **Ru@ox-CF** (b).

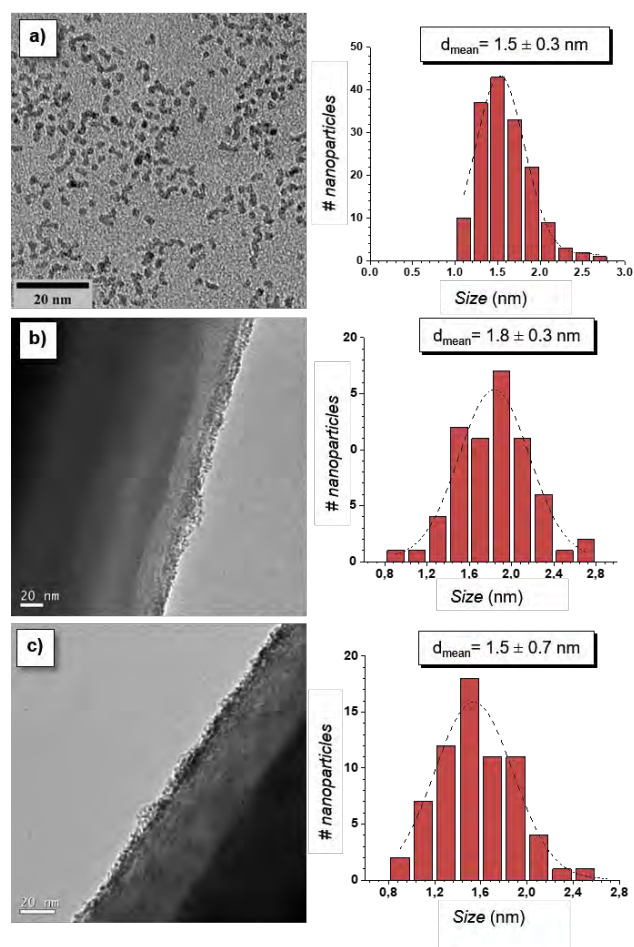


**Figure 3.** Representative TEM image and corresponding size distribution of colloidal Ru NPs stabilized with 4-phenylpyridine (**Ru-4PP NPs**) (a), **RuPP@CF** (b) and **RuPP@ox-CF** (c).

**Table 1.** Main physicochemical data for bare RuPP NPs and all the *in situ* and *ex situ* synthesized hybrid systems (mean size of the NPs ( $d_{\text{mean}}$ ) and state of the NPs layer, Ru content (wt%) by ICP and Ru composition by XPS).

Entry	System	$d_{\text{mean}}$ (nm)	NPs layer	ICP Ru (wt%)	XPS
1	<b>RuPP NPs</b>	$1.5 \pm 0.3$	-	85	Ru/RuO <sub>2</sub>
2	<b>Ru@CF</b>	$1.4 \pm 0.4$	Homogeneous	0.57	Ru/RuO <sub>2</sub>
3	<b>Ru@ox-CF</b>	$1.0 \pm 0.2$	Heterogeneous	0.65	Ru/RuO <sub>2</sub>
4	<b>RuPP@CF</b>	$1.8 \pm 0.3$	Homogeneous	0.47	Ru/RuO <sub>2</sub>
5	<b>RuPP@ox-CF</b>	$1.5 \pm 0.7$	Homogeneous	1.10	Ru/RuO <sub>2</sub>

X-ray photoelectron spectroscopy (XPS) allowed discerning the surrounding chemical environment and oxidation state of Ru in the NPs (Fig. 4). The high-resolution XPS spectra of the Ru 3d region showed a main broad peak, which could be deconvoluted in two different peaks. The one at 280.8 eV is attributed to Ru(IV), characteristic of RuO<sub>2</sub> species, while the other one at 279.8 eV belongs to Ru(0).<sup>6</sup> Thus, XPS analysis confirmed that the Ru NPs in the hybrid systems contain two phases, metallic Ru and RuO<sub>2</sub>, that can be explained by a partial oxidation of the outer shell of the NPs when exposed to air after the synthetic procedure.



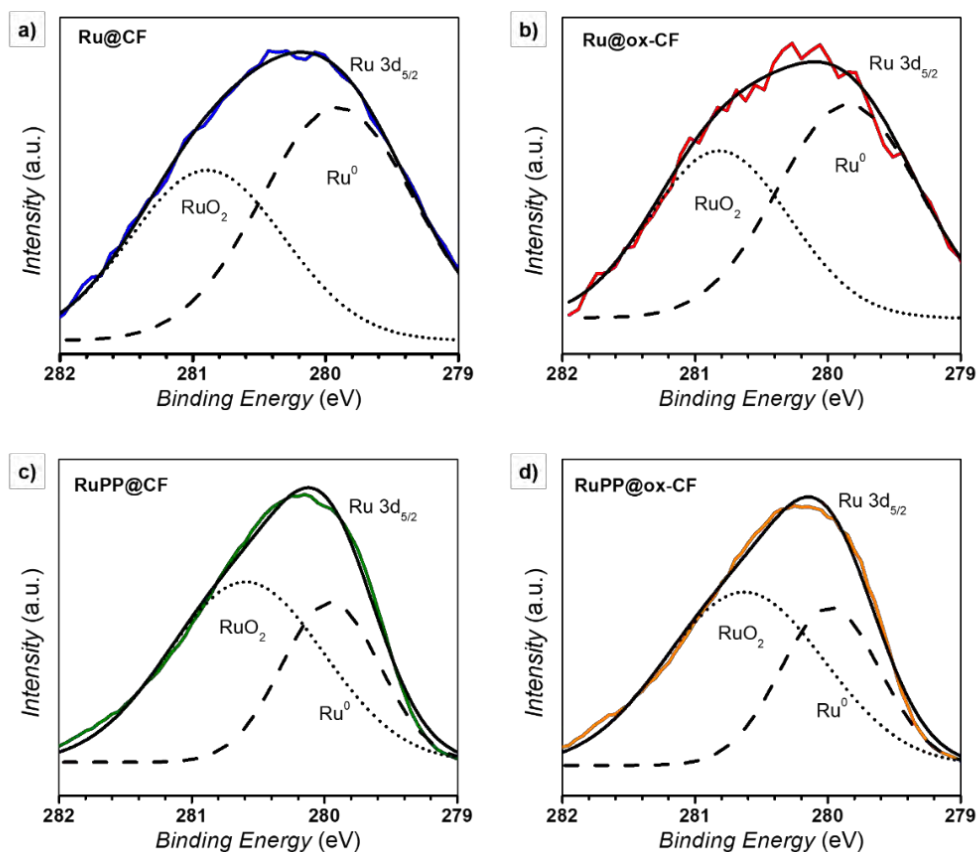


**Figure 4.** High-resolution XPS analysis in the Ru 3d region of **Ru@CF** (a, blue), **Ru@ox-CF** (b, red), **RuPP@CF** (c, green) and **RuPP@ox-CF** (d, orange). Metallic-Ru component (Ru 3d<sub>5/2</sub> 279.8 eV, dashed black), RuO<sub>2</sub>-component (Ru 3d<sub>5/2</sub> 280.8 eV, dotted-black) and envelope (bold).

### **5A.3 ELECTROCATALYTIC PERFORMANCE**

The catalytic activity and stability of the obtained hybrid systems towards the HER was studied by means of linear sweep voltammetry (LSV) and chronoamperometry (CA). The electrodes were built with only 1 mg of each hybrid material to avoid reproducibility issues caused by self-attaching of the microfibers when introduced in the catalytic liquid media, as well as to minimize the accumulation of H<sub>2</sub> bubbles, since the formation of big bubbles could block the electrode surface and diminish its electrochemical response (see the Experimental Section for further details on the electrode preparation). The electrodes were tested under reductive potentials in a two-compartment electrochemical cell containing 1 M H<sub>2</sub>SO<sub>4</sub> (pH 0).

As shown in Fig. 5a, a fast change on the current intensity was observed at potentials below 0 V vs. RHE, which is the thermodynamic potential for the HER ( $E_{\text{therm}}$ ). In order to benchmark the catalytic activity of the four studied electrodes, the intensity of the HER electrocatalytic current observed in the LSVs displayed in Fig. 5a was normalized by the Ru wt% in each case and labelled as  $i_{\text{Ru}} = [\text{mA}/\mu\text{g}_{\text{Ru}}]$ , thus allowing a fair comparison of the electroactivity between samples holding different Ru loadings. Furthermore, stability studies were carried out by the LSV monitoring of  $i_{\text{Cat}}$  after 2 h under chronoamperometric conditions (for the *in situ* and *ex situ*-systems an  $E_{\text{app}}$  of -250 mV and -150 mV vs. RHE was applied, respectively). Table 2 summarizes the electrochemical performance of the four different systems displayed in Fig. 5.

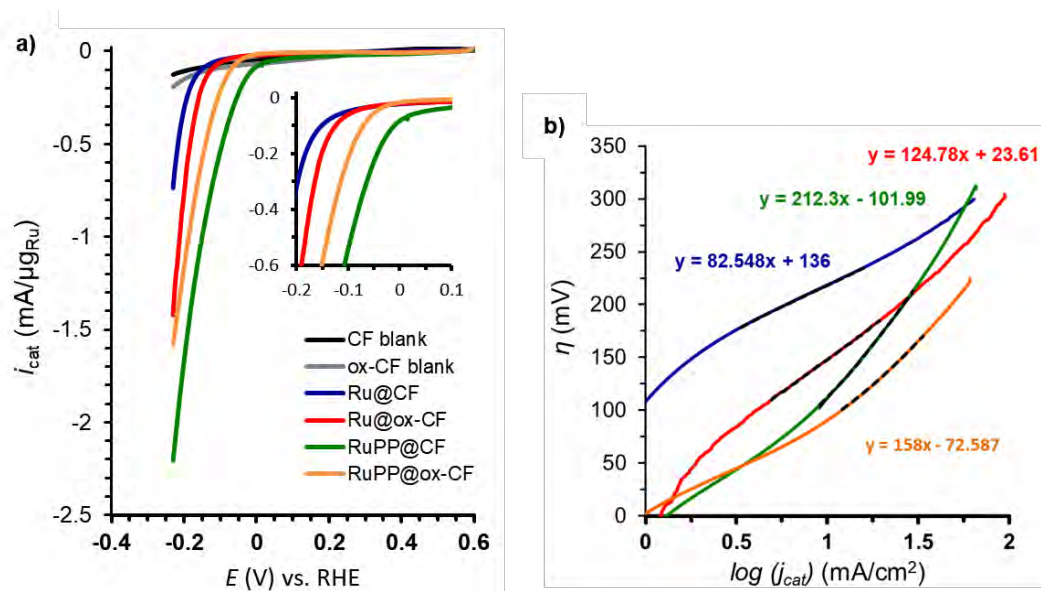


**Figure 5.** Polarization curves of **Ru@CF** (blue), **Ru@ox-CF** (red), **RuPP@CF** (green) and **RuPP@ox-CF** (orange) normalized by mg of material and  $\mu\text{g}$  of Ru in 1 M  $\text{H}_2\text{SO}_4$  (a). A Pt mesh and Ag/AgCl (KCl sat.) electrodes were used as counter (CE) and reference electrodes (RE), respectively. The three-electrode configuration was polarized from 0.6 V to -0.25 V (vs. RHE) at a scan rate of 10 mV/s. Tafel plot of **Ru@CF** (blue), **Ru@ox-CF** (red), **RuPP@CF** (green) and **RuPP@ox-CF** (orange) in 1 M  $\text{H}_2\text{SO}_4$  (b).

**Table 2.** Physico-chemical and OER electrocatalytic data for the anodes studied in this work (1 M H<sub>2</sub>SO<sub>4</sub> aqueous solution, pH 0).

Entry	Sample	$d_{\text{mean}}$ (nm)	Ru (wt%)	$\eta_0^{(a)}$ (mV)	$\eta_{10}^{(b)}$ (mV)	Tafel slope (mV/dec)	% $i_{\text{cat}}^{(c)}$ (%)
1	<b>RuPP NPs<sup>d</sup></b>	1.5 ± 0.3	85	0	20	29	99
2	<b>Ru@CF</b>	1.4 ± 0.4	0.57	70	265	83	34
3	<b>Ru@ox-CF</b>	1.0 ± 0.2	0.65	30	235	125	16
4	<b>RuPP@CF</b>	1.8 ± 0.3	0.47	5	225	212	95
5	<b>RuPP@ox-CF</b>	1.5 ± 0.7	1.10	0	180	158	40

<sup>a</sup>  $\eta_0$  is calculated as  $\eta_0 = E_{\text{Ag}/\text{AgCl}} + 0.20 \text{ V} - (0 - 0.059 \cdot 0)$ , where  $(0 - 0.059 \cdot 0)$  is the theoretical thermodynamic potential at which protons are reduced at pH 0 and  $E_{\text{Ag}/\text{AgCl}}$  is the experimental potential at which an abrupt increase of the current intensity starts in the LSV. <sup>b</sup>  $\eta_{10}$  is the overpotential at  $|i_{\text{cat}}| = 10 \text{ mA/mg}$ . <sup>c</sup> %  $i_{\text{cat}}$  is the percentage of current intensity at  $\eta = 200 \text{ mV}$  after a 2 h electrolysis. <sup>d</sup> Data for RuPP is taken from ref. 5 for  $|j| = 10 \text{ mA/cm}^2$  instead of  $|i_{\text{cat}}| = 10 \text{ mA/mg}$ .

The electrochemical studies confirmed that the nature of the CFs (bare or carboxylic acid-functionalized) and the nature of the Ru NPs (*in situ* or *ex situ*) are key factors affecting the activity and stability of each of the four cathodes for the HER at acidic pH. More specifically, both **RuPP@xCF** electrodes show  $\eta_0$  overpotentials close to 0 mV, similar to  $\eta_0$  for Ru-4PP NPs deposited onto a glassy carbon electrode. In this case, the outstanding catalytic performance of the Ru-4PP NPs makes the nature of the carbon microfibers (*i.e.* CF or ox-CF) irrelevant in the electrocatalytic performance. On the other hand, the nature of the CFs becomes more important in **Ru@xCF** hybrid systems: **Ru@ox-CF** has a lower  $\eta_0$  overpotential (30 mV) than **Ru@CF** (70 mV), being both values comparable to C-supported Ru NPs in the literature.<sup>7,8,9,10,11,12</sup> This indicates that in **Ru@ox-CF** some degree of synergy exists between the Ru NPs and the nicotinic moieties, which were recently suggested to be putative catalytic centers in non-decorated ox-CFs.<sup>8</sup> Furthermore, mechanistic information was obtained from the Tafel plots, where Tafel slopes range in between 83-212 mV/dec, evidencing that the Volmer step is the rds of the HER process (Fig. 5b).

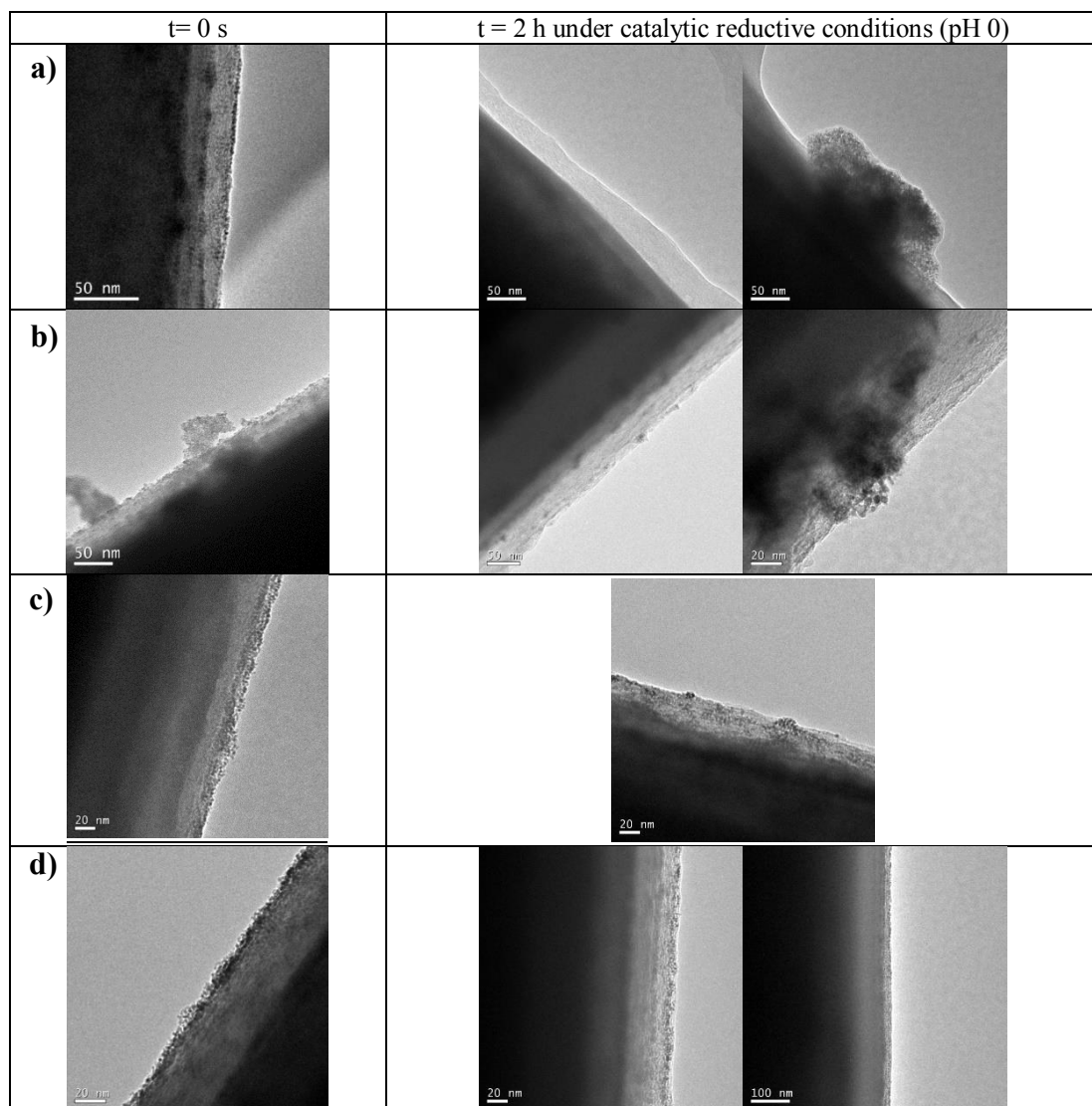
The percentage of current intensity at  $\eta = 200 \text{ mV}$  remaining after a 2 h electrolysis (Table 2) is a quantitative method to compare the stability of the four systems. From these data one can clearly see that the % $i_{\text{cat}}$  values for the *ex situ* systems (**RuPP@CF** and **RuPP@ox-CF**) is higher than for the *in situ* ones (**Ru@CF** and **Ru@ox-CF**). Thus, *ex situ* cathodes are more stable than *in situ* cathodes. These results confirmed the positive effect of the 4PP capping ligand to the Ru NPs, as previously demonstrated,<sup>5</sup> not only acting as a stabilizing agent for the NPs themselves, but also

allowing a potential  $\pi$ - $\pi$  interaction between the pyridilic rings of the ligand and the carbon structure of the CFs, conferring robustness to the hybrid cathode. Thus, the highest intensity observed for **RuPP@CF** (95 %) arises from the formation of  $\pi$ - $\pi$  interactions between the surface carbon structure on the CF and the PP ligand on top of the RuPP NPs. This phenomenon could improve the electronic communication between catalyst and support, thus increasing the catalytic intensity throughout the system. Also, the lower intensity observed for **RuPP@ox-CF** (40 %) makes evident that this stabilizing effect becomes more relevant when no carboxylic groups are present, as these interactions could be hampered by the presence of the -COOH moieties, which could potentially destabilize the resulting electrode through steric interactions with the PP ligands, thus avoiding the optimum  $\pi$ - $\pi$  interactions between catalyst and support. Further, this destabilizing effect of -COOH moieties was also observed for the *in situ*-systems, where  $\%i_{cat}$  decreased from **Ru@CF** (34 %) to **Ru@ox-CF** (16 %).

The same trend in stabilities of the four systems was also revealed by TEM images of the materials after 2 h-CA experiments (Table 3). The *in situ* systems suffered significant leaching during the catalytic process, observing cleaner surfaces of the CFs both for **Ru@CF** and **Ru@ox-CF**. In addition, some agglomerates were found over the surface of the CFs, which were formed during the catalytic reaction, decreasing the number of exposed active sites. This trend was confirmed by the EDX analysis of the surface of **Ru@CF** and **Ru@ox-CF**, showing almost no presence of Ru. In contrast, the two RuPP-based systems (**RuPP@CF** and **RuPP@ox-CF**) presented higher loadings of Ru NPs on the surface of the microfibers after catalysis, with very small NPs along the CFs surface and almost no agglomerates found. EDX analyses confirmed, in this case, the presence of Ru along all the surfaces. In a previous publication of our groups,<sup>5</sup> Ru-4PP NPs deposited onto a GC electrode with no gluing agent added were shown to present no deactivation signs for 12 h under a current-controlled experiment in the same acidic conditions as in the present work (1 M H<sub>2</sub>SO<sub>4</sub>). Thus, taking into consideration that Ru-4PP NPs are stable under the applied catalytic conditions, the deactivation observed for **RuPP@ox-CF** was mostly attributed to a mechanical leaching of the NPs, as confirmed by ICP, observing an unneglectable Ru content (0.41-5.2  $\mu$ g) in the catalytic media after the 2-h CA. In fact, this hypothesis supported the fact that the formation of  $\pi$ - $\pi$  interactions between the surface carbon structure on the CFs and the PP ligands on top of

Ru NPs could be hampered when carboxylic groups are added on top of the CFs (ox-CF), leading to more pronounced NPs leaching and deactivation of the systems.

**Table 3.** Representative TEM images of **Ru@CF** (a), **Ru@ox-CF** (b), **RuPP@CF** (c) and **RuPP@ox-CF** (d) after 2 h of chronoamperometry at  $E_{app}$  -250 mV for **Ru@CF/Ru@ox-CF** and -150 mV for **RuPP@CF/RuPP@ox-CF**.



Finally, faradaic efficiencies in all cases were above 90 % (Fig. 6), confirming that almost all electrons were devoted to proton reduction and not to other side reactions.

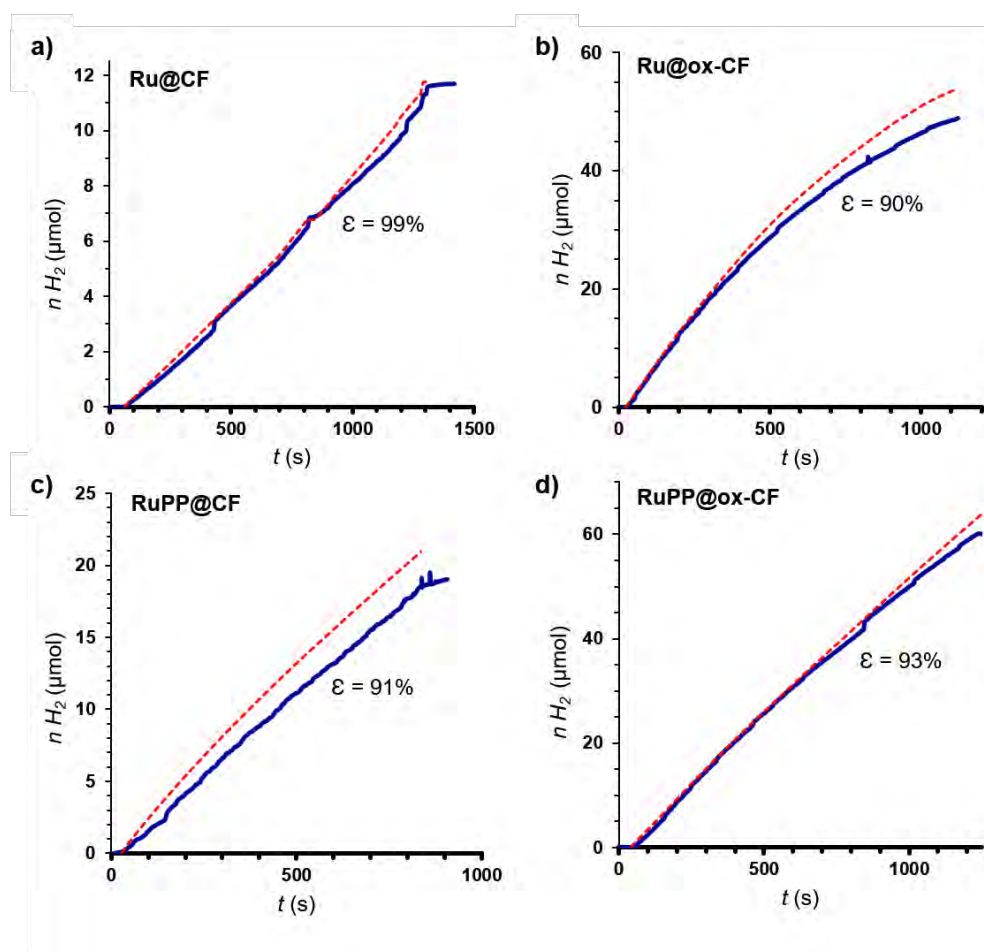


**Figure 6.** H<sub>2</sub>-monitored chronoamperometry experiments for faradaic efficiency determination for Ru@CF (a), Ru@ox-CF (b), RuPP@CF (c) and RuPP@ox-CF (d). An E<sub>app</sub> of -250 and -150 mV were respectively applied for Ru@CF/Ru@ox-CF and RuPP@CF/RuPP@ox-CF.

## 5A.4 CONCLUSIONS

The organometallic approach allowed to prepare Ru-decorated high surface area carbon electrodes with a low metal content (< 1.1 wt%). The used carbon-based supports constitute a macroscopic cheap substrate, allowing thus to build a step further towards a massive and economic production of hydrogen under benign conditions. The importance of the nature of the support and of the ligand used to stabilize the NPs was also assessed.

An increased catalytic intensity was found for the *ex situ* systems where the Ru NPs were first stabilized with 4-phenylpyridine (4PP) ligands and then deposited onto



the CF supports, confirming the importance of a proper electronic interaction between the NPs and the support, in this case achieved by potential  $\pi$ - $\pi$  interactions between the pyridilic rings of the 4PP ligand and the carbon structure of the support. The importance of these interactions was also confirmed in stability experiments, where *ex situ* cathodes (**RuPP@CF** and **RuPP@ox-CF**) presented much higher stabilities than those obtained with Ru NPs synthesized *in situ* (**Ru@CF** and **Ru@ox-CF**). In addition, a synergistic effect between -COOH moieties and Ru NPs was observed in the *in situ* systems, where  $\eta_0$  decreased for **Ru@ox-CF** in comparison to **Ru@CF**. Finally, even if some of the materials were partially deactivated during the catalytic experiments, almost quantitative faradaic efficiencies were achieved, confirming hydrogen evolution as the only redox reaction occurring at their surface.

*This work has been published in European Journal of Inorganic Chemistry in 2019 (Ruthenium nanoparticles supported on carbon microfibers for hydrogen evolution electrocatalysis. J. Creus, L. Mallón, N. Romero, R. Bofill, A. Moya, J.L.G. Fierro, R. Más-Ballesté, X. Sala, K. Philippot, J. García-Antón, Eur. J. Inorg. Chem. 2019, 2071–2077).*

## **5A.5 EXPERIMENTAL SECTION**

### **Materials and methods**

All operations for the synthesis of the CF-supported Ru NPs were carried out using standard Schlenk tubes, Fisher-Porter reactor techniques or in a glove-box (MBraun) under argon atmosphere. Solvents (THF and pentane) were purified before use by filtration through adequate columns in a purification apparatus (MBraun) and handled under argon atmosphere. Solvents were degassed before use according to a freeze-pump-thaw process. The ruthenium precursor, [Ru(COD)(COT)], was purchased from Nanomeps-Toulouse. Hydrogen gas (Alphagaz) was purchased from Air Liquide. 4-Phenylpyridine used as stabilizer was purchased from Sigma-Aldrich and used as received. High purity deionized water was obtained by passing distilled water through a nanopore Milli-Q water purification system. Pristine carbon microfibers were purchased from ClipCarbono.

### **Synthetic procedures**

**Ru@CF** and **Ru@ox-CF**: 2 cm of CFs were soaked in a 10 mL of THF solution containing [Ru(COD)(COT)] (10 mg, 0.026 mmol) inside a Fisher-Porter reactor. 3 bar of H<sub>2</sub> were introduced and the reaction mixture was stirred at r.t. overnight. After depressurization, the hydrogen was evacuated under vacuum and the solvent was removed through a cannula. The resulting CF materials were rinsed with pentane and dried under vacuum. **Ru@CF**. TEM:  $d_{\text{mean}} = 1.4 \pm 0.4$  nm. ICP (Ru %) = 0.57%. **Ru@ox-CF**. TEM:  $d_{\text{mean}} = 1.0 \pm 0.2$  nm. ICP (Ru %) = 0.65%.

**RuPP@CF** and **RuPP@ox-CF**: 2 cm of CFs electrodes were soaked overnight in a THF (10 mL) crude dispersion of Ru-4PP NPs<sup>5</sup> inside a Fisher-Porter reactor. Then, the supernatant was removed through cannula and the resulting CF materials were rinsed with pentane (3 × 10 mL) and dried under vacuum. **RuPP@CF**. TEM:  $d_{\text{mean}} = 1.8 \pm 0.3$  nm. ICP (Ru %): 0.47%. **RuPP@ox-CF**. TEM:  $d_{\text{mean}} = 1.5 \pm 0.7$  nm. ICP (Ru %): 1.10%.



## **Characterization techniques**

**Transmission electron microscopy (TEM) and high-resolution electron microscopy (HREM):** TEM and HREM observations were performed at the “Centre de Microcaractérisation Raymond Castaing” in Toulouse (UMS-CNRS 3623) and at the “Servei de Microscòpia Electrònica” of the UAB. Samples for TEM and HREM analyses were prepared by deposition of several CFs onto a holey carbon covered copper grid. TEM and HREM analyses were performed on a MET JEOL JEM 1011 microscope operating at 100 kV with a resolution point of 0.45 nm and a JEOL JEM-ARM 200F microscope working at 200 kV with a resolution point lower of 0.19 nm, respectively. TEM allowed the evaluation of the particle size, size distribution and morphology. Enlarged micrographs were used for treatment with *ImageJ* software to obtain a statistical size distribution and the NP mean diameter. The analyses were done by assuming that the NPs were spherical. NP sizes are quoted as the mean diameter  $\pm$  the standard deviation.

**Inductive-coupled plasma optical emission spectroscopy (ICP-OES):** ICP-OES measurements were performed at the “Servei d'Anàlisi Química” (SAQ) in the UAB, on an Optima 4300DV Perkin-Elmer system. Solid samples were prepared by digesting 1 mg of the hybrid CFs with aqua regia under microwave conditions followed by a dilution of the mixture with HCl 1% (v/v). Liquid samples were directly diluted with HCl 1% (v/v).

**X-ray photoelectron spectroscopy (XPS):** Measurements were performed at the Catalan Institute of Nanoscience and Nanotechnology (ICN2) in Barcelona with a Phoibos 150 analyzer (SPECS GmbH, Berlin, Germany) in ultra-high vacuum conditions (base pressure  $5 \times 10^{-10}$  mbar) with a monochromatic aluminium K $\alpha$  X-ray source (1486.74 eV). The energy resolution was measured by the FWHM of the Ag 3d $_{5/2}$  peak which for a sputtered silver foil was 0.62 eV.

## **Electrochemical set-up**

**CF electrode preparation:** CFs electrodes were prepared as stated in ref. 13. For a more detailed preparation of the electrodes, see the Experimental Part of *sub-chapter 5B*.

**Electrochemical measurements:** All the electrochemical experiments were performed using a BioLogic SP-150 potentiostat. Solutions were degassed before the electrochemical analysis with a N<sub>2</sub> flow. IR drop was automatically corrected at 85% using the Biologic EC-Lab software for cyclic voltammetry and chronoamperometry. 1 M H<sub>2</sub>SO<sub>4</sub> solution was prepared by mixing 56.1 mL of 95–97% H<sub>2</sub>SO<sub>4</sub> in 1 L of Milli-Q water. A Pt grid was used as a counter electrode (CE) and an Ag/AgCl (KCl sat.) electrode was used as a reference electrode (RE).

All data were transformed to RHE by adding +0.20 V. A 10 mL two-compartment cell with a separation membrane between the two compartments was used. Both compartments were filled with 8 mL of 1 M H<sub>2</sub>SO<sub>4</sub> solution and were equipped with a stirring bar. Prior to each measurement, they were purged with N<sub>2</sub> for 15 min. For H<sub>2</sub>-monitored bulk electrolysis an Unisense H<sub>2</sub>-NP Clark electrode was used to measure hydrogen evolution in the gas phase and to calculate the faradaic efficiency. The Clark electrode was calibrated by adding different volumes of 99 % pure hydrogen at the end of the experiment. The CE was placed in one compartment and the other was provided with the WE, the RE and the Clark electrode.

**Linear sweep voltammetry (LSV):** The system was scanned from  $E_i = 0.6$  V to  $E_f = -0.4$  V at 10 mV/s scan rate unless otherwise stated.

**Chronoamperometry:** Controlled potential chronoamperometric experiments were performed at  $E_{app} = -0.25$  V and  $-0.15$  V for *in situ* (**Ru@CF** and **Ru@ox-CF**) and *ex situ* (**RuPP@CF** and **RuPP@ox-CF**) based systems, respectively.

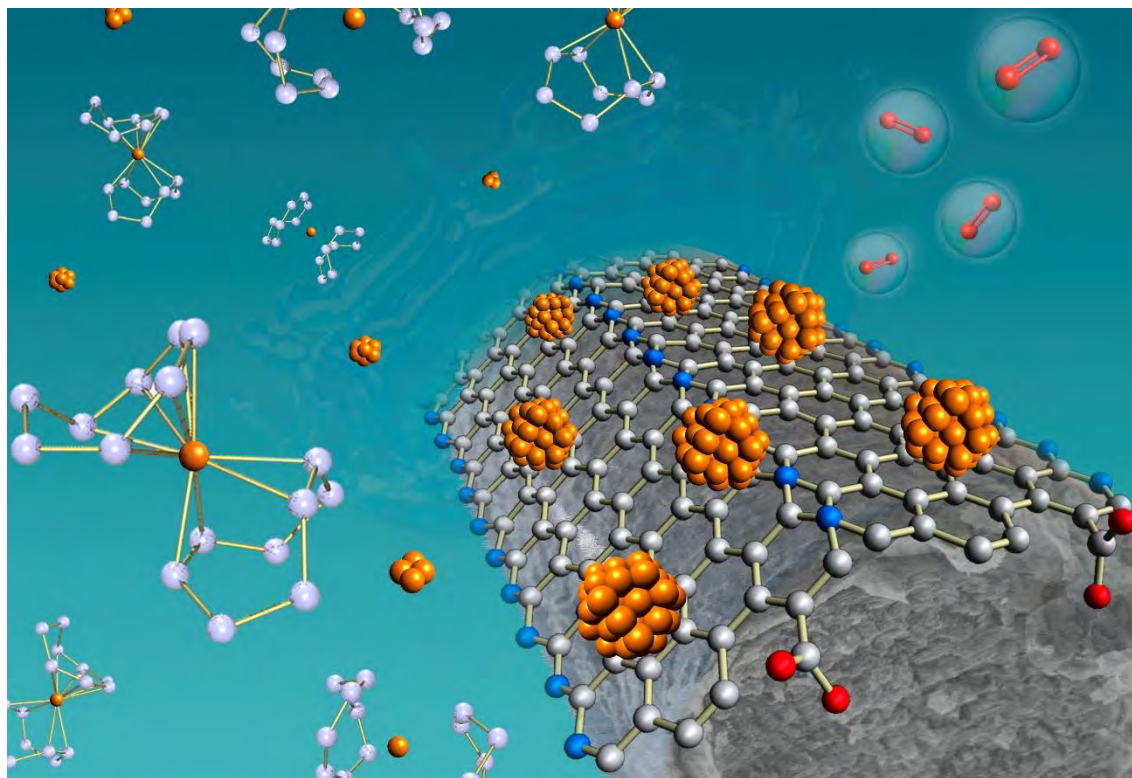
## **5A.6 REFERENCES**

- <sup>1</sup> N. S. Lewis, *Nature* **2001**, 414, 589–590.
- <sup>2</sup> S. Trasatti, *J. Electroanal. Chem.* **1972**, 39, 163–184
- <sup>3</sup> C.C.L. McCrory, S. Jung, I.M. Ferrer, S.M. Chatman, J.C. Peters and T.F. Jaramillo, *J. Am. Chem. Soc.* **2015**, 137, 4347–4357
- <sup>4</sup> J.K. Norskov, T. Bligaard, A. Logadottir, J.R. Kitchin, J.G. Chen, S. Pandalov and U. Stimming, *J. Electrochem. Soc.* **2005**, 152, J23–J26.
- <sup>5</sup> J. Creus, S. Drouet, S. Suriñach, P. Lecante, V. Colliere, R. Poteau, K. Philippot, J. García-Antón and X. Sala, *ACS Catal.* **2018**, 8, 11094–11102.
- <sup>6</sup> D.J. Morgan, *Surf. Interface Anal.* **2015**, 47, 1072-1079.
- <sup>7</sup> J. Mahmood, F. Li, S. Jung, M.S. Okyay, I. Ahmad, S. Kim, N. Park, H.Y. Jeong and J. Baek, *Nat. Nanotechnol.* **2017**, 12, 441–446;
- <sup>8</sup> T. Bhowmik, M.K. Kundu and S. Barman, *ACS Appl. Mater. Interfaces* **2016**, 8, 28678–28688;
- <sup>9</sup> J. Cheng, H. Zhang, H. Ma, H. Zhong and Y. Zou, *Electrochim. Acta* **2010**, 55, 1855–1861;
- <sup>10</sup> X. Kong, K. Xu, C. Zhang, J. Dai, S.N. Oliaee, L. Li, X. Zeng, C. Wu and Z. Peng, *ACS Catal.* **2016**, 6, 1487–1492;
- <sup>11</sup> Y. Zheng, Y. Jiao, Y. Zhu, L.H. Li, Y. Han, Y. Chen, M. Jaroniec and S. Qiao, *J. Am. Chem. Soc.* **2016**, 138, 16174–16181;
- <sup>12</sup> Z. Chen, J. Lu, Y. Ai, Y. Ji, T. Adschiri and L. Wan, *ACS Appl. Mater. Interfaces* **2016**, 8, 35132–35137.
- <sup>13</sup> O.G. Moral, A. Call, F. Franco, A. Moya, J.A. Nieto-Rodríguez, M. Frias, J.L.G. Fierro, M. Costas, J. Lloret-Fillol, J. Alemán and R. Mas-Ballesté, *Chem. Eur. J.* **2018**, 24, 3305–3313.



## **Chapter 5B. Oxygen evolution anodes based on $\text{Co}(\text{OH})_2$ nanoparticles supported on carbon microfibers**

---



The performance of OER anodes based on supported nanocatalysts is highly dependent on the interactions taking place at the interface between the nanocatalyst and the employed conductive support. A set of OER working electrodes based on  $\text{Co}(\text{OH})_2$  NPs and carbon microfibers (CFs) have been prepared. The so-obtained systems differ in either the stabilizer present at the surface of the NPs (THF or 1-heptanol), the surface functionalization of the used CFs (bare CFs or oxidized-CFs) or the growth of the NPs in the presence (*in situ*) or the absence (*ex situ*) of the carbonaceous support. Correlation of a detailed structural and compositional analysis with the electroactivity of the tested nanomaterials allowed extracting valuable insights about the influence of the metal-support interface on the OER performance of the studied anodes.

---



## **5B.1 INTRODUCTION**

As stated in the General Introduction, the OER ( $2 \text{ H}_2\text{O} \rightarrow \text{O}_2 + 4 \text{ H}^+ + 4 \text{ e}^-$ , 1.23  $V_{\text{NHE}}$  at pH 0) is particularly demanding from both the thermodynamic and kinetic points of view. Consequently, the development of efficient, robust and easy to engineer electrodes based on earth-abundant metals for this reaction is a key challenge. Currently, highly active but scarce noble-metal based electrocatalysts (typically  $\text{IrO}_x$  and  $\text{RuO}_2$ ) are still the state-of-the-art anodic materials in commercial devices, which hampers the upgrading of the WS technology to practical large-scale applications. As a result, first-row transition metal based oxides and hydroxides have been the target materials in the last decade.<sup>1</sup> Among them, Co-containing nanocatalysts and their corresponding composite materials arise as promising alternatives to noble-metal based OER anodes owing to their good balance between intrinsic activity, stability against corrosion and suitable morphology-tailoring through well-established synthetic methodologies.<sup>2</sup> In this regard, our research group reported in 2018 the preparation of ligand/photoabsorber-capped  $\text{Co}_3\text{O}_4$  nanoparticles (NPs) through the so-called organometallic approach followed by air oxidation and their successful application as catalysts for the OER.<sup>3</sup> However, non-supported cobalt oxide/hydroxide nanocatalysts normally suffer from low conductivity (typically in the  $10^{-2}$ - $10^{-3}$  S/m range)<sup>4</sup> and fast agglomeration under OER turnover conditions.<sup>3,5</sup> Therefore, the use of appropriate conductive supports (*i.e.* carbon microfibers) is critical to overcome these weaknesses.

The study of the interactions taking place at the metal-support interface is a doorway to understand the catalytic performance and long-term stability of OER electro-anodes made of supported-nanocatalysts,<sup>6,7,8</sup> but in-depth studies covering the effect of systematic variations on the surface characteristics of both nanocatalysts and supports are scarce.<sup>9</sup> This part of my PhD work arises in this direction. Similarly to *sub-chapter 5A* for Ru systems, the modularity of the organometallic approach for the synthesis of metal-based NPs was also exploited in order to prepare a set of OER working electrodes based on  $\text{Co}(\text{OH})_2$  NPs and CFs for comparative purposes. The prepared electro-anodes differed in either the stabilizer present at the surface of the NPs (THF or 1-heptanol), the use of bare or functionalized CFs as a support (CF or ox-CF) and the growth of the NPs in the presence (*in situ*) or the absence (*ex situ*) of the carbonaceous support.

Correlation between detailed structural and compositional analyses with the observed electroactivity of the tested nanomaterials allowed extracting helpful insights about the influence of the metal-support interface on the OER performance of the studied anodes.

## **5B.2 SYNTHESIS AND CHARACTERIZATION**

### **5B.2.1 Synthesis of Co NPs supported onto carbon microfibers**

Supported Co(0) NPs were synthesized following the organometallic approach (Fig. 1a).<sup>10</sup> The incorporation of metallic Co NPs onto the **CF** and **ox-CF** supports was performed by two different methods (*in situ* and *ex situ*). The *in situ* method consists in the direct growth of the metallic Co NPs onto the CF surface through the reductive decomposition of 10 mg of the (cyclooctadienyl)(1,5-cyclooctadiene)cobalt(I) complex, [Co(COD)(COE)], acting as a metal precursor, either in THF (10 mL) or 1-heptanol (10 mL), under 3 bar of H<sub>2</sub> at r.t. (Fig. 1a, top and middle for THF and 1-heptanol, respectively). Both **CF** and **ox-CF** ( $\approx 90$  mg each) were simultaneously placed in the reaction vessel to ensure the same reaction conditions for the two different CF-supported materials, with a Co/CFs ratio of  $\approx 1.2$  wt%. The initial yellow solution due to the cobalt precursor turned into an almost transparent solution after the reaction time, indicating the precursor was decomposed to form Co(0) NPs onto the CFs surface (Fig. 2a). By this method, the internal carbon structure of the CFs, the surface carboxylic groups when present (*i.e.* **ox-CF**, Fig. 1b) and the solvent (*i.e.* THF or 1-heptanol) can all contribute to the stabilization of the metallic Co NPs due to their direct growth onto the CF surface.

The *ex situ* method required two steps. First, the pre-synthesis of Co NPs was performed, and then the obtained colloidal suspension was used to impregnate the CFs. As THF is not able to stabilize Co NPs by itself, only 1-heptanol was used as solvent in this case. Co<sup>heptOH</sup> NPs<sup>3</sup> were thus first obtained by decomposing 10 mg of [Co(COD)(COE)] at r.t. under 3 bar of H<sub>2</sub> in 10 mL of 1-heptanol for 24 h. The yellow color solution of [Co(COD)(COE)] turned into a dark brown-black solution, indicating the formation of NPs (Fig. 2b). Then, CFs (either **CF** or **ox-CF**) were immersed in the obtained colloidal suspension of metallic Co NPs for the impregnation step (vigorous stirring under inert conditions, 24h, r.t.) (Fig. 1a, bottom), leading to the attachment of



the NPs onto the CFs surface. This method allowed studying the influence of the presence of both a previous stabilizing agent (*i.e.* 1-heptanol) and the nature of the CFs supports (*i.e.* presence of COOH) on the morphology of the NPs and the catalytic properties of the hybrid materials.

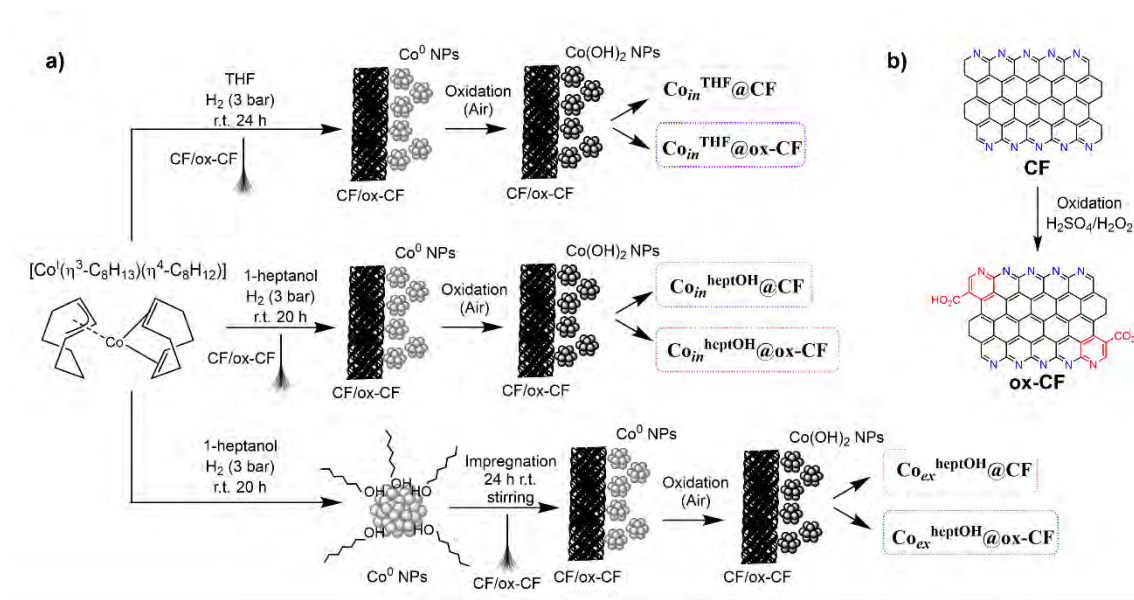


**Figure 1.** Experimental procedure for the preparation of the hybrid anodes described in this work (a). Schematic representation of the surface chemical composition of CF and ox-CF (b).

Finally, all systems were washed with pentane and dried under vacuum before being exposed to air to achieve the oxidation of the metal before their characterization and their use in electrocatalysis. Thus, the combination of two synthetic methods, two types of CFs and two solvents allowed to obtain six different electrodes, that will be hereafter labelled as indicated in Fig. 1a.

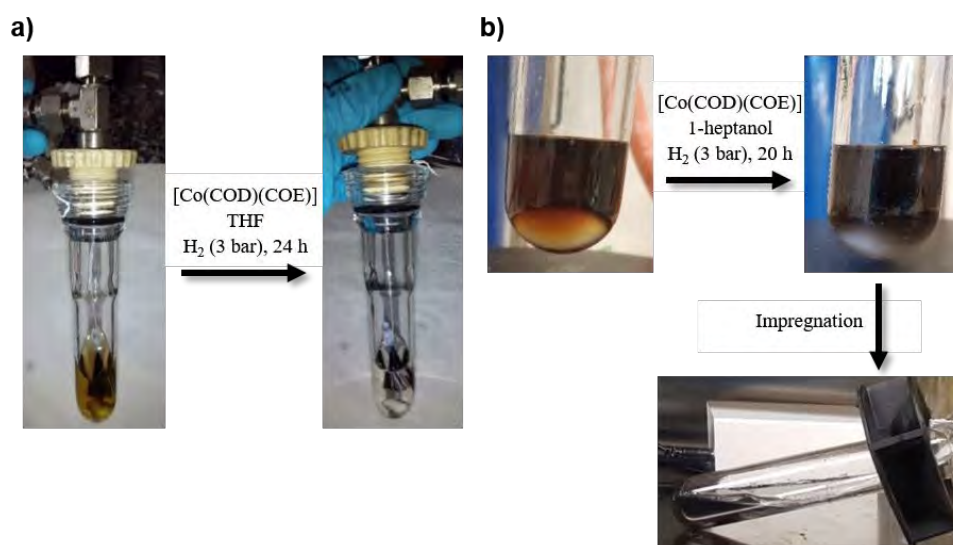


**Figure 2.** Pictures of the reaction medium before (left) and after (right) the hydrogenation of [Co(COD)(COE)] during the *in situ* synthesis of CF-supported Co NPs in THF (a). Pictures of the starting reaction medium before hydrogenation (left) and crude colloidal suspension of Co<sup>heptOH</sup> NPs after the hydrogenation reaction (right), and set-up for the impregnation process of CFs with Co<sup>heptOH</sup> NPs (*ex situ* synthesis) (bottom) (b).

### 5B.2.2 Transmission electron microscopy analysis

After the reaction time, each as-prepared sample was analyzed by transmission electron microscopy (TEM). For this purpose, the remaining hydrogen was removed from the Fisher-porter reactor under vacuum before cleaning and drying the CFs brushes. A very small amount of CFs was deposited onto a carbon covered copper grid under air. Size distributions were determined through manual analysis of enlarged micrographs with *ImageJ* software to obtain statistical size distribution and a mean diameter. For each system, the mean size was calculated by assuming a spherical form. Size distributions are quoted as the mean diameter  $\pm$  the standard deviation. In all size distributions over than 200 particles were counted.

#### 5B.2.2.1 *In situ* systems

For the *in situ* systems, TEM images evidenced the presence of a thin homogeneous layer of small NPs over the surface of the CFs (Fig. 3). The precise mean size of the Co NPs was difficult to determine due to their ultra-small nature ( $\approx 2$  nm) and

their location at the surface of the bulky CFs ( $\approx 8 \mu\text{m}$  of diameter), which made highly challenging to get well-focused TEM images. However, the NPs diameter were found to be *ca.*  $2.6 \pm 0.7 \text{ nm}$ ,  $1.8 \pm 0.4$ ,  $2.8 \pm 0.6 \text{ nm}$  and  $2.1 \pm 0.4 \text{ nm}$  for  $\text{Co}_{in}^{\text{THF}}@CF$ ,  $\text{Co}_{in}^{\text{THF}}@ox\text{-CF}$ ,  $\text{Co}_{in}^{\text{heptOH}}@CF$ ,  $\text{Co}_{in}^{\text{heptOH}}@ox\text{-CFs}$ , respectively.

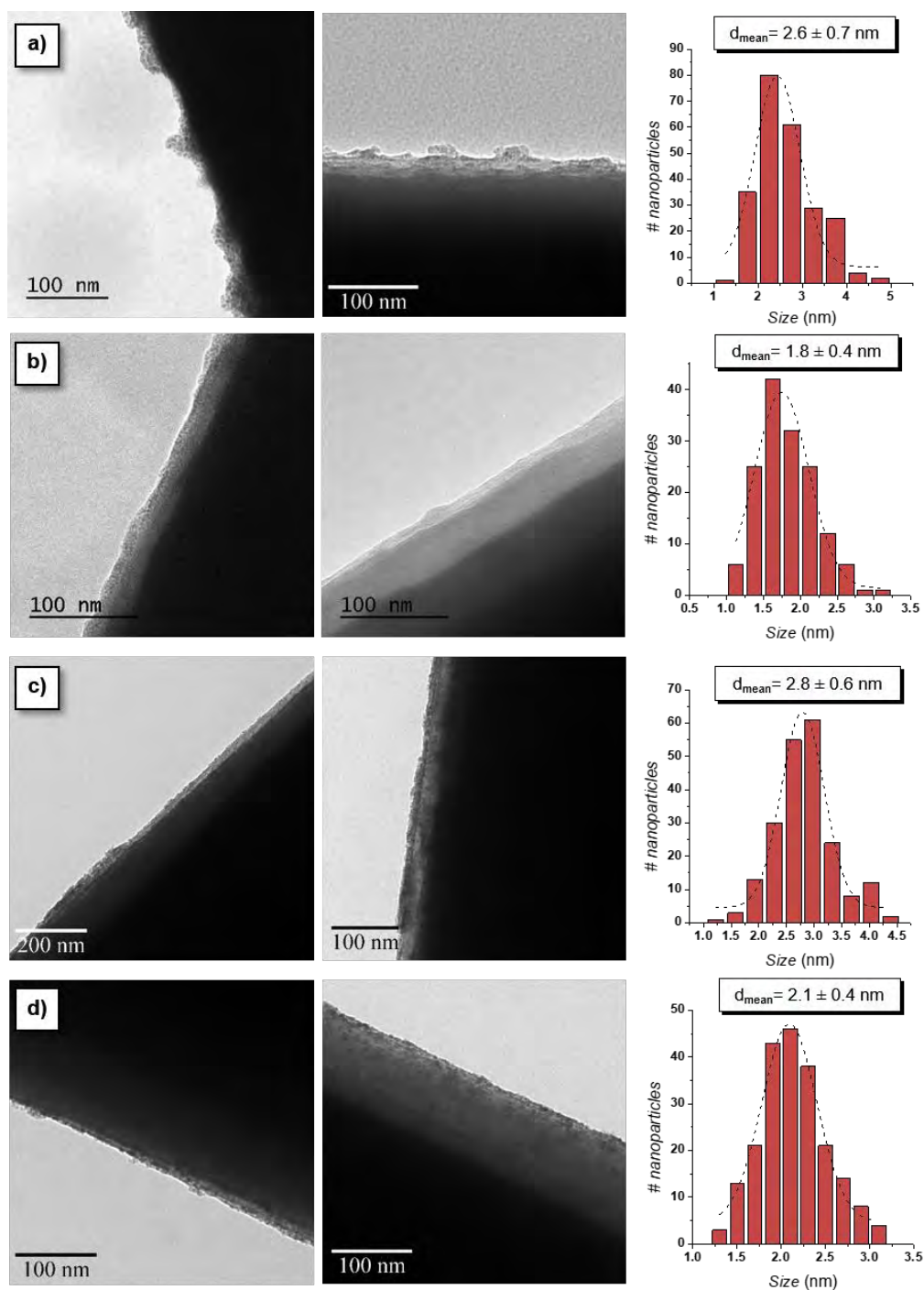


**Figure 3.** Representative TEM images and corresponding size distribution of *in situ* supported CoNPs:  $\text{Co}_{in}^{\text{THF}}@CF$  (a),  $\text{Co}_{in}^{\text{THF}}@ox\text{-CF}$  (b),  $\text{Co}_{in}^{\text{heptOH}}@CF$  (c) and  $\text{Co}_{in}^{\text{heptOH}}@ox\text{-CF}$  (d).

5B.2.2.2 *Ex situ* systems

TEM analysis from the  $\text{Co}^{\text{heptOH}}\text{NPs}$  crude colloidal suspension was performed after depositing a drop onto a carbon covered copper grid. It revealed the presence of isolated small and spherical NPs, with an average diameter of  $3.0 \pm 0.4$  nm (Fig. 4).

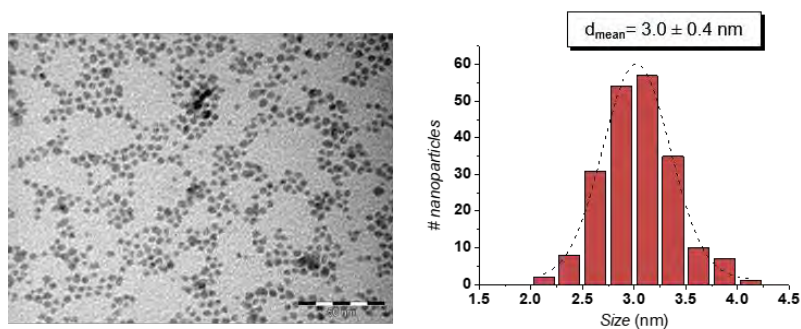


**Figure 4.** TEM images of Co NPs synthesized in 1-heptanol ( $\text{Co}^{\text{heptOH}}\text{NPs}$ ) and corresponding size distribution.

After the impregnation of CF and ox-CF with the suspension of pre-synthesized Co NPs, TEM images were recorded. A homogeneous layer of small NPs over the surface of CFs was observed in both *ex situ* systems in the presence of 1-heptanol,  $\text{Co}_{\text{ex}}^{\text{heptOH}}\text{NPs}@CF$  and  $\text{Co}_{\text{ex}}^{\text{heptOH}}\text{NPs}@ox\text{-CF}$  (Fig. 5). The obtained Co NPs had a mean diameter of *ca.*  $2.0 \pm 0.5$  nm and  $2.3 \pm 0.5$  nm, respectively.

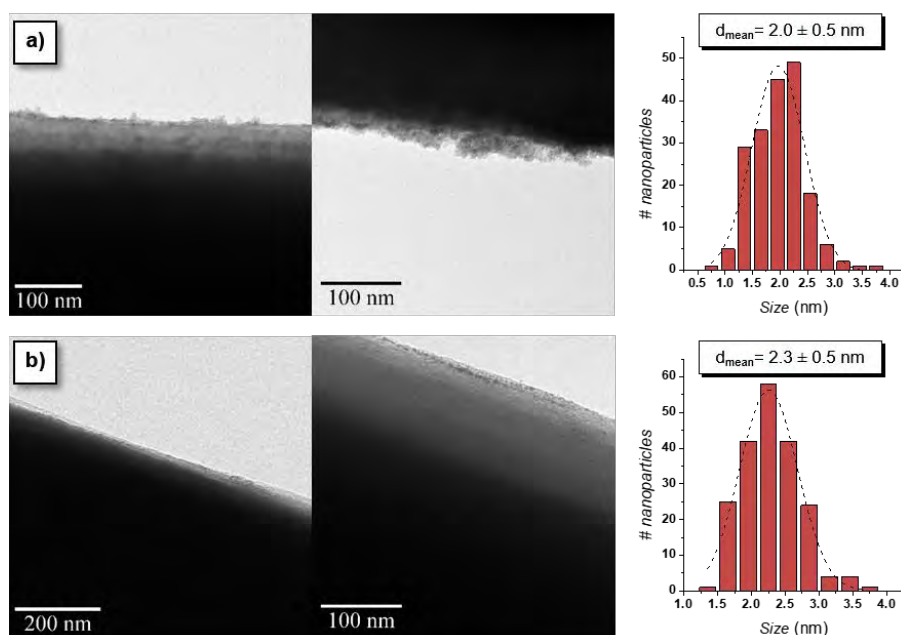


**Figure 5.** Representative TEM images and corresponding size distribution histogram of *ex situ* supported CoNPs:  $\text{Co}_{\text{ex}}^{\text{heptOH}}\text{NPs}@CF$  (a) and  $\text{Co}_{\text{ex}}^{\text{heptOH}}\text{NPs}@ox\text{-CF}$  (b).

Thus, TEM proved the successful synthesis of supported Co NPs onto carbon microfibers, showing the presence of a thin layer of small Co NPs onto the surface of CFs in all systems (*in situ* and *ex situ*). This confirmed that the defects on the C structure, the presence of N atoms (*i.e.* breaking the periodicity and homogeneity of the graphite-like carbon structure) and the addition of carboxylic groups, if applicable, promote the nucleation and stabilization of Co atoms to obtain NPs with a narrow size distribution (Table 3). Though some aggregates can be observed in some regions, in general the NPs are homogeneously distributed onto the CFs surface, where they form a continuous layer. However, for the  $\text{Co}_{in}^{\text{THF}}@CF$  and  $\text{Co}_{ex}^{\text{heptOH}}@CF$  systems (Fig. 3a and 5a, respectively), more agglomerates together with more naked zones (*i.e.* without NPs) were repeatedly observed, indicating a more heterogeneous distribution of the Co nanocatalyst in these cases. This characteristic could be key regarding their electrocatalytic performance towards the OER.

The comparison of the four *in situ* systems (Table 1) shows that the use of CFs with surface carboxylic groups (**ox-CF** systems) led to smaller NPs than the bare support (**CF** systems), which can be explained by a better stabilization of Co NPs by the  $-\text{COOH}$  functionality. In addition, the synthesis solvent (*i.e.* THF or 1-heptanol) did not seem to play a key role in the Co NP stabilization during the synthetic process, as comparable NPs sizes and morphologies were observed between analogous *in situ* systems ( $\text{Co}_{in}^{\text{THF}}@CF/\text{Co}_{in}^{\text{heptOH}}@CF$  and  $\text{Co}_{in}^{\text{THF}}@ox-CF/\text{Co}_{in}^{\text{heptOH}}@ox-CF$ ).

For the impregnated systems (*ex situ* systems), a tendency towards a decrease in the NPs mean size was observed from the *ca.* 3 nm pre-synthesized  $\text{Co}^{\text{heptOH}}$  NPs. Different reasons could explain this behaviour: i) smaller NPs have better interaction with the CFs surface, being the only ones that remained attached to the support; ii) as the impregnation process was performed in solution under stirring conditions, when adding the CFs, the environment for Co atoms may have changed, yielding for instance to a reorganization of Co atoms to reach a new energy minimum, obtaining smaller NPs.

**Table 1.** Mean size of the NPs ( $d_{\text{mean}}$ ) and homogeneity of the NPs layer determined from the TEM analysis for all synthesized Co@CF systems (*in situ* and *ex situ*).

Entry	System	$d_{\text{mean}}$ (nm)	NPs layer
1	Co <sup>heptOH</sup> NPs	3.0 ± 0.4	-
2	Co <sub>in</sub> <sup>THF</sup> @CF	2.6 ± 0.7	Heterogeneous
3	Co <sub>in</sub> <sup>THF</sup> @ox-CF	1.8 ± 0.4	Homogeneous
4	Co <sub>in</sub> <sup>heptOH</sup> @CF	2.8 ± 0.6	Homogeneous
5	Co <sub>in</sub> <sup>heptOH</sup> @ox-CF	2.1 ± 0.4	Homogeneous
6	Co <sub>ex</sub> <sup>heptOH</sup> @CF	2.0 ± 0.5	Heterogeneous
7	Co <sub>ex</sub> <sup>heptOH</sup> @ox-CF	2.3 ± 0.5	Homogeneous

### 5B.2.3 Inductively coupled plasma-optical emission spectroscopy

To determine the Co content of all hybrid systems, inductively coupled plasma-optical emission spectrometry (ICP-OES) analyses were performed after digestion of the solid samples in a HNO<sub>3</sub>/HCl concentrated mixture. The analyses revealed Co contents ≤ 0.23 wt% for all six hybrid samples (*vs.* 1.2 % expected to the synthetic conditions) (Table 2).

**Table 2.** Wt% of Co determined by ICP-OES in CFs hybrid systems

Entry	System	Co (wt.%)
1	Co <sup>heptOH</sup> NPs	30.7
2	Co <sub>in</sub> <sup>THF</sup> @CF	0.13
3	Co <sub>in</sub> <sup>THF</sup> @ox-CF	0.23
4	Co <sub>in</sub> <sup>heptOH</sup> @CF	0.14
5	Co <sub>in</sub> <sup>heptOH</sup> @ox-CF	0.13
6	Co <sub>ex</sub> <sup>heptOH</sup> @CF	0.039
7	Co <sub>ex</sub> <sup>heptOH</sup> @ox-CF	0.055

Data in Table 2 reveal that the *in situ* systems (entries 2-5) display higher Co loadings than their *ex situ* counterparts (entries 6-7). This observation points to the detrimental effect of the *ex situ* synthetic method, where 1-heptanol acted as Co NPs stabilizer that could limit the deposition of the Co NPs during the impregnation step. This can be the result of steric effects between heptanol carbon chains or weak interactions of the latter with the carbon structure of the CFs.

#### **5B.2.4 X-ray photoelectron spectroscopy**

X-ray photoelectron spectroscopy (XPS) allows identifying elements and discerning their surrounding chemical environment and oxidation state. The complete XPS survey spectra of all the as-synthesized hybrid nanomaterials is displayed in Fig. 6. The main peaks observed can be clearly indexed to O 1s, N 1s and C 1s regions, indicating that no other metallic or inorganic contaminants are present. Slightly significant signals are found also at the Co region.



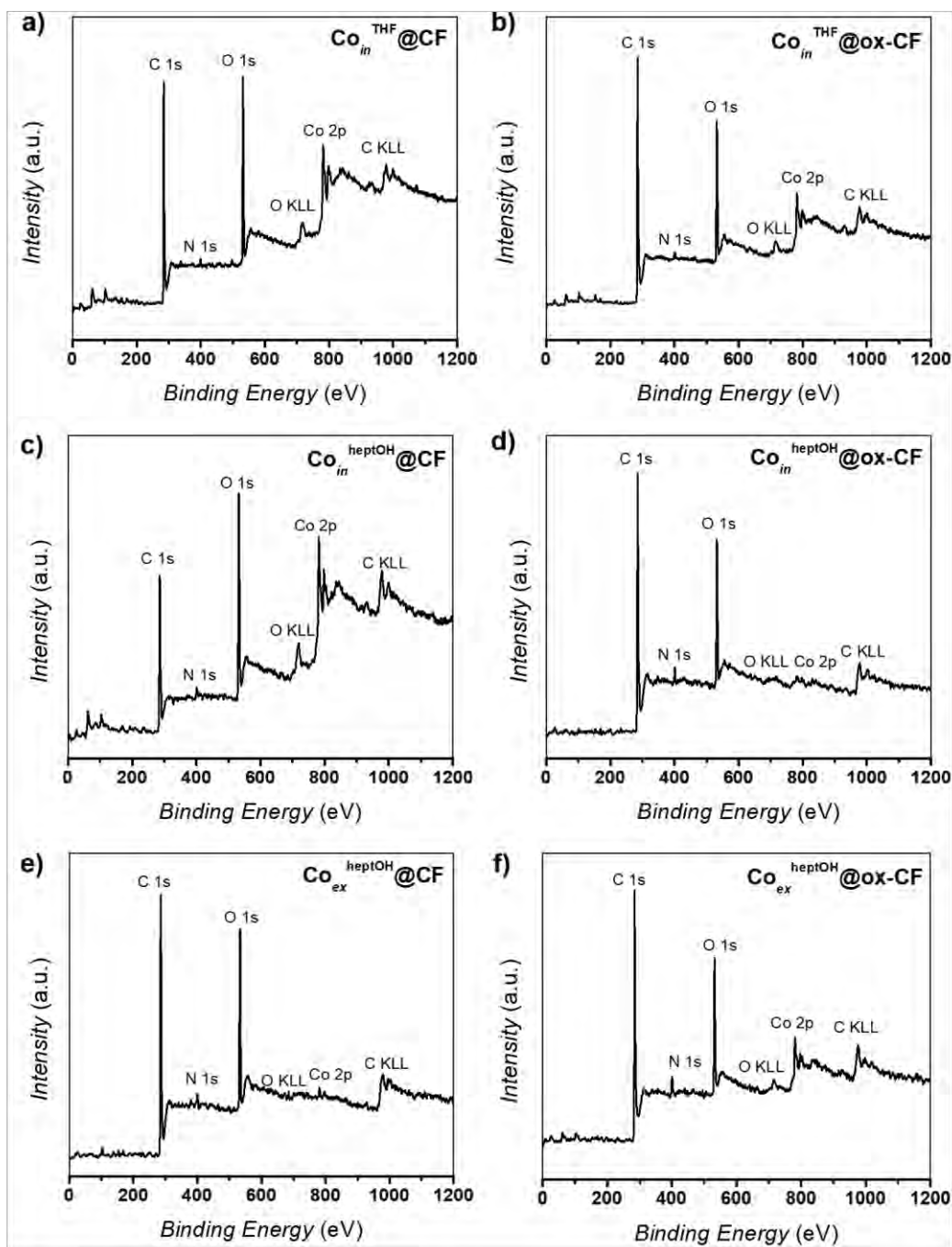


**Figure 6.** XPS data of all the synthesized hybrid materials,  $\text{Co}_{\text{in}}^{\text{THF}}@CF$  (a),  $\text{Co}_{\text{in}}^{\text{THF}}@ox-CF$  (b),  $\text{Co}_{\text{in}}^{\text{heptOH}}@CF$  (c),  $\text{Co}_{\text{in}}^{\text{heptOH}}@ox-CF$  (d),  $\text{Co}_{\text{ex}}^{\text{heptOH}}@CF$  (e) and  $\text{Co}_{\text{ex}}^{\text{heptOH}}@ox-CF$  (f). The main peaks are indexed to O 1s, N 1s and C 1s regions (O KLL represents the energy of the electrons ejected from the atoms due to the filling of the O 1s state (K shell) by an electron from the L shell coupled with the ejection of an electron from an L shell).



The high-resolution XPS spectra of Co 2p, performed at r.t. in ultra-high vacuum conditions using a monochromatic aluminum K $\alpha$  x-ray source (1486.74 eV) as the excitation X-ray source, are compared in Fig. 7 and a summary of the most relevant data is presented in Table 3. All the spectra were referenced to the aliphatic carbon at a binding energy (BE) of 284.8 eV. The XPS Co 2p spectra show two main peaks at a binding energy of  $\approx$  781-782 eV and  $\approx$  796-797.5 eV, corresponding to the Co 2p<sub>3/2</sub> and 2p<sub>1/2</sub> levels, respectively. Besides the normal core photoelectron lines, strong satellite peaks at *c.a.* 3.9-7.4 eV higher energy than the main peaks are also observed. These additional spectral lines were related either to a coupling between unpaired electrons in the atom (multiplet splitting) or to a multiple electron excitation (shake-up). It is well-known that high spin cobalt(II) compounds have intense satellite bands, while satellite lines for the low spin cobalt(III) compounds are either weak or missing.<sup>11,12</sup> The peaks observed in the Co 2p region thus indicate the presence of high spin cobalt(II) species in the six prepared materials.

**Table 3.** Binding energies (eV) of core electrons and satellites of CFs-supported Co-based NPs.

Entry	Sample	Co 2p <sub>3/2</sub>	Satellites	Co 2p <sub>1/2</sub>	Satellites
1	Co <sub>in</sub> <sup>THF</sup> @CF	781.4 eV	785.4 eV	797.3 eV	800.8 eV
2	Co <sub>in</sub> <sup>THF</sup> @ox-CF	781.5 eV	785.4 eV	797.3 eV	802.9 eV
3	Co <sub>in</sub> <sup>heptOH</sup> @CF	781.7 eV	785.6 eV	797.4 eV	803.0 eV
4	Co <sub>in</sub> <sup>heptOH</sup> @ox-CF	781.6 eV	786.9 eV	796.9 eV	804.3 eV
5	Co <sub>ex</sub> <sup>heptOH</sup> @CF	781.2 eV	785.9eV	797.4 eV	804.2 eV
6	Co <sub>ex</sub> <sup>heptOH</sup> @ox-CF	781.0 eV	785.5 eV	797.1 eV	803.1 eV

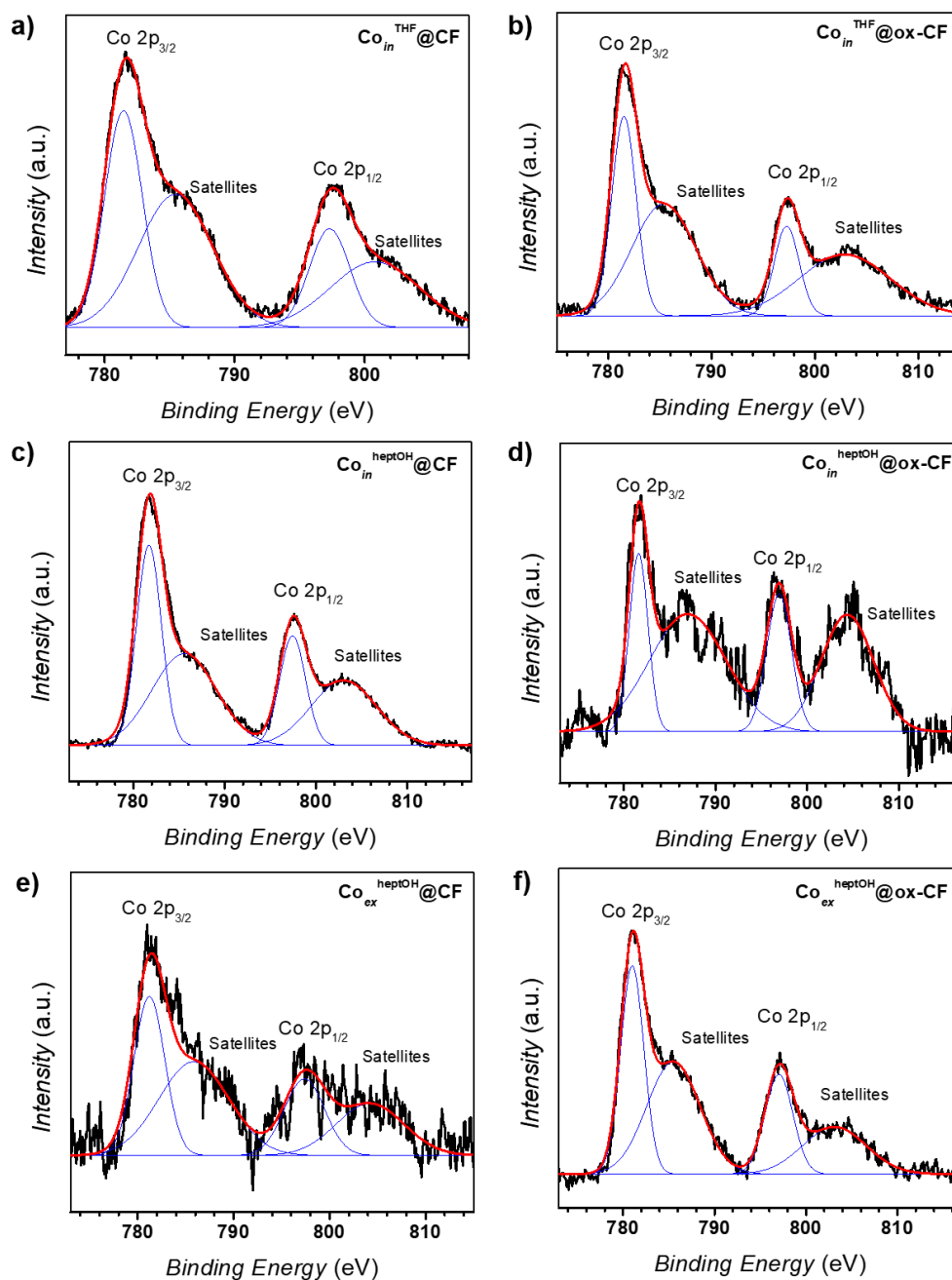


**Figure 7.** High-resolution XPS analysis in the Co 2p region of  $\text{Co}_{in}^{\text{THF}}@\text{CF}$  (a),  $\text{Co}_{in}^{\text{THF}}@\text{ox-CF}$  (b),  $\text{Co}_{in}^{\text{heptOH}}@\text{CF}$  (c),  $\text{Co}_{in}^{\text{heptOH}}@\text{ox-CF}$  (d),  $\text{Co}_{ex}^{\text{heptOH}}@\text{CF}$  (e) and  $\text{Co}_{ex}^{\text{heptOH}}@\text{ox-CF}$  (f).

Moreover, the O 1s spectra reported in Fig. 8 show strong peaks at relatively high BE (531-533 eV) for all samples. According to literature data,<sup>12,13</sup> O from hydroxides appears on the higher BE side of the spectrum (531 - 533 eV), whereas O from oxides appears at lower BE (529 - 530 eV). Thus, our results indicate the presence of -OH moieties bonded to Co(II). Taken all together, XPS data evidenced the presence of supported  $\text{Co}(\text{OH})_2$  NPs in all the prepared systems.

The low oxidation state of Co here found for  $\text{Co}_{\text{ex}}^{\text{heptOH}}@\text{CF}$  and  $\text{Co}_{\text{ex}}^{\text{heptOH}}@\text{ox-CF}$  contrasts with that recently reported by our research group for the corresponding non-supported Co NPs prepared under similar reaction conditions, where a mixed  $\text{Co}^{\text{II}}\text{Co}^{\text{III}}_2\text{O}_4$  ( $\text{Co}_3\text{O}_4$ ) species was detected. This fact highlights the reductive nature of the carbonaceous support here employed and its decisive role in the final oxidation state of the Co nanocatalysts when oxidized from metallic Co on its surface.

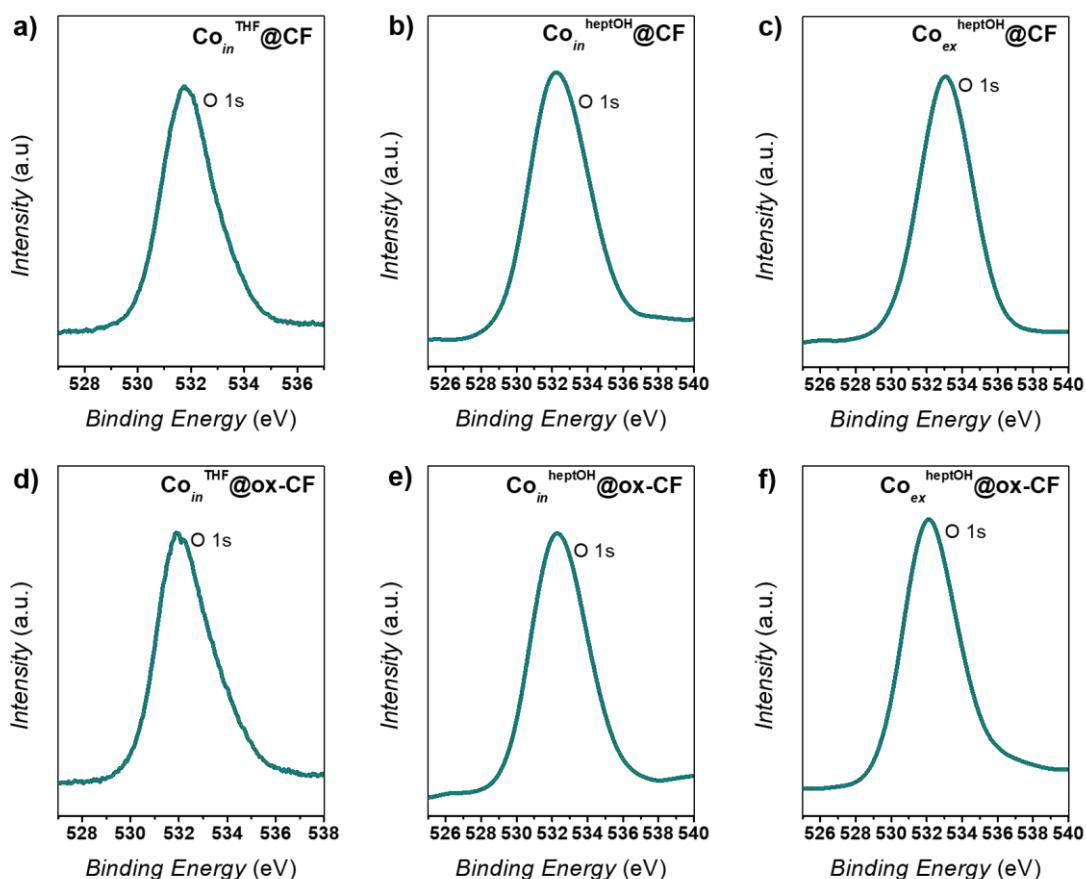


**Figure 8.** XPS high-resolution spectra in the O 1s region of  $\text{Co}_{\text{in}}^{\text{THF}}@\text{CF}$  (a),  $\text{Co}_{\text{in}}^{\text{THF}}@\text{ox-CF}$  (b),  $\text{Co}_{\text{in}}^{\text{heptOH}}@\text{CF}$  (c),  $\text{Co}_{\text{in}}^{\text{heptOH}}@\text{ox-CF}$  (d),  $\text{Co}_{\text{ex}}^{\text{heptOH}}@\text{CF}$  (e) and  $\text{Co}_{\text{ex}}^{\text{heptOH}}@\text{ox-CF}$  (f).

In addition, an XPS analysis of  $\text{ox-CF}$  after the *in situ* formation of Co NPs onto the surface was performed to assure that no changes in the oxidized C structure had occurred during its exposure to reductive conditions under  $\text{H}_2$ . Thus, the high resolution XPS of the C 1s region for  $\text{Co}_{\text{in}}^{\text{heptOH}}@\text{ox-CF}$  is shown in Fig. 9.

According to the literature,<sup>14</sup> it can be clearly seen that all the initial C 1s signals present in the as-synthesized **ox-CF** (C-C signal (284-285 eV), C-O signal (286.2 eV), C=O signal (287.7 eV) and highly oxidized carbon atoms (O-C=O) signal at 289.1 eV) are still visible in the XPS spectrum of **ox-CF** treated under reductive conditions for obtaining the Co NPs, thus confirming the robustness of **ox-CF** during the whole synthetic procedure.

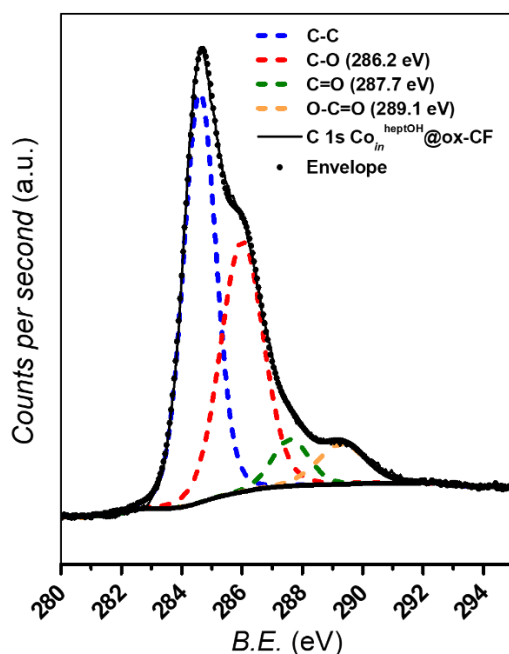


**Figure 9.** High-resolution XPS analysis in the C 1s region of  $\text{Co}_{in}^{\text{heptOH}}@ox\text{-CF}$  after submission to the reductive synthetic conditions for the synthesis of Co NPs.

## **5B.3 ELECTROCATALYTIC PERFORMANCE**

### **5B.3.1 Electrocatalytic performance towards the OER**

To study the catalytic activity and stability of the obtained systems towards the OER, cyclic voltammetry (CVs) and chronoamperometry (CA) experiments were performed, respectively. CVs were performed from  $E_i = -0.25$  V to  $E_f = 1.25$  V ( $E$  vs. NHE) at pH 13 (0.1 M NaOH) and a potential of 1.00 V vs. NHE was fixed for CA experiments. In order to solve electrochemical irreproducibility issues caused by microfibers self-attaching when introduced in the reaction media, working electrodes for electrocatalytic evaluation were built using a small amount of each hybrid material (*i.e.* 1-mg CFs electrode, see the Experimental Section for further details).

As shown in Fig. 10a and 10b, when scanned anodically up to 1.25 V vs. NHE all electrodes showed two anodic peaks in the oxidative forward scan prior to a sharp current increase assigned to the electrocatalytic oxidation of water to dioxygen. According to literature data,<sup>15,16</sup> the first faradaic process observed in the voltammogram ( $E_{ap}=0.36$  V vs. NHE) could be attributed to the oxidation of Co(II) to Co(III). The second one, appearing at a higher anodic potential ( $E_{ap} = 0.76$  V vs NHE) and partially masked with the OER electrocatalytic current, is characteristic of the subsequent oxidation of Co(III) to Co(IV). Interestingly, the Co(IV) species is usually proposed as the active species towards the OER in related Co-based systems.<sup>17,18,19</sup> The two cathodic waves in the backward scan correspond to the complementary reduction processes.

The intensity of the OER electrocatalytic current observed in the CVs displayed in Fig. 10a was normalized by the Co wt% in each case and labelled as  $i_{Co}=[\text{mA}/\mu\text{g}_{Co}]$ , thus allowing a fair comparison of the electroactivity between samples holding different Co loadings. A summary of the most relevant figures of merit defining the electrocatalytic activity of the studied anodes for the OER is given in Table 4.

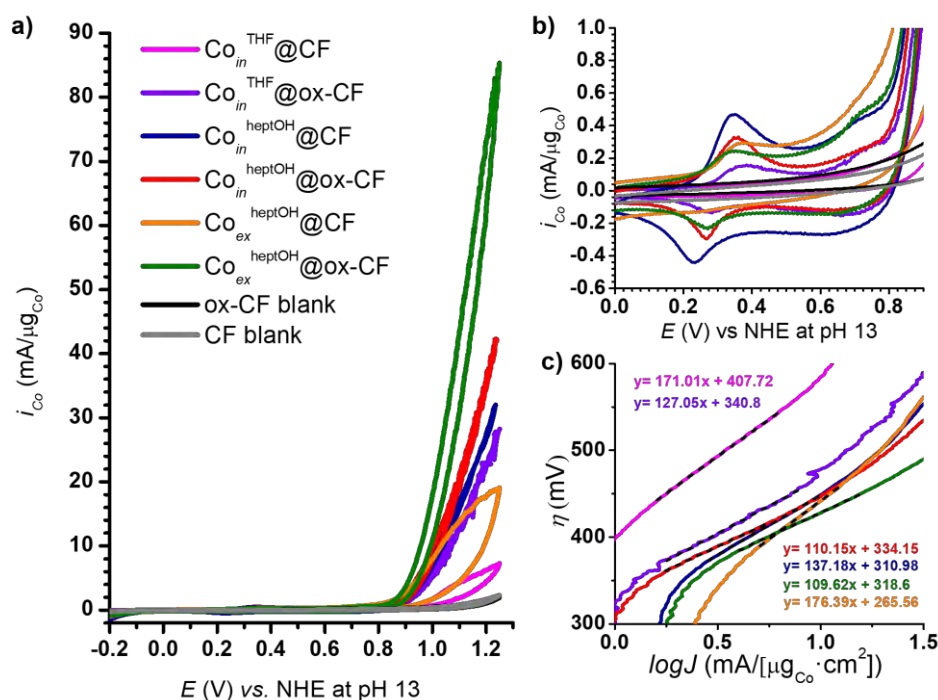


**Figure 10.** Cyclic voltammograms in a 0.1 M NaOH aqueous solution of 1 mg CFs brush of  $\text{Co}_{in}^{\text{THF}}@CF$  (pink),  $\text{Co}_{in}^{\text{THF}}@ox-CF$  (purple),  $\text{Co}_{in}^{\text{heptOH}}@CF$  (blue),  $\text{Co}_{in}^{\text{heptOH}}@ox-CF$  (red),  $\text{Co}_{ex}^{\text{heptOH}}@CF$  (orange) and  $\text{Co}_{ex}^{\text{heptOH}}@ox-CF$  (green); ox-CF (black) and CF (grey) blanks are also shown (a). Zoom in the potential range at which the Co(III/II) and Co(IV/III) redox events occur (b). Tafel plots of all materials studied in this work (c) (same color code as in (a)).

**Table 4.** Physico-chemical and OER electrocatalytic data for the anodes studied in this work (0.1 M NaOH aqueous solution, pH 13).

Entry	Sample	$d_{\text{mean}}$ (nm)	Co (wt%)	$\eta_0^{(a)}$ (mV)	Tafel slope (mV/dec)
1	$\text{Co}_{\text{in}}^{\text{THF}}@CF$	$2.6 \pm 0.7$	0.13	342	171
2	$\text{Co}_{\text{in}}^{\text{THF}}@ox-CF$	$1.8 \pm 0.4$	0.23	327	127
3	$\text{Co}_{\text{in}}^{\text{heptOH}}@CF$	$2.8 \pm 0.6$	0.14	307	137
4	$\text{Co}_{\text{in}}^{\text{heptOH}}@ox-CF$	$2.1 \pm 0.4$	0.13	307	110
5	$\text{Co}_{\text{ex}}^{\text{heptOH}}@CF$	$2.0 \pm 0.5$	0.039	322	176
6	$\text{Co}_{\text{ex}}^{\text{heptOH}}@ox-CF$	$2.3 \pm 0.5$	0.055	312	110

<sup>a</sup>  $\eta_0$  is calculated as  $\eta_0 = E_{\text{Hg}/\text{Hg}_2\text{SO}_4, \text{K}_2\text{SO}_4(\text{sat'd})} + 0.65 \text{ V} - (1.23 - 0.059 \cdot 13)$ , where  $(1.23 - 0.059 \times 13)$  is the theoretical thermodynamic potential at which water is oxidized at pH 13 and  $E_{\text{Hg}/\text{Hg}_2\text{SO}_4, \text{K}_2\text{SO}_4(\text{sat'd})}$  is the experimental potential at which an abrupt increase of the current intensity starts in the CV.

The recorded onset overpotentials ( $\eta_0$ , 307-342 mV range) and Tafel slopes (110-176 mV/dec, Fig. 10c) are comparable to those reported for related carbon-supported Co-based OER electrocatalysts under alkaline conditions (see Table A1 in Annex). However, a deep examination of all the data summarized in Table 4 allowed extracting valuable information about how the different catalyst-support interfaces influence the resulting OER performances. The presence of carboxylic acid groups at the surface of the CFs (*i.e.* **ox-CF**) has a remarkable positive effect in the electrocatalytic performance of the studied systems, promoting higher normalized current intensities, lower Tafel slopes (*i.e.* more favourable reaction kinetics) and slightly lower onset overpotentials (Table 4). Even if this trend appeared general for all the CF/ox-CF pairs studied, CF surface oxidation presented maximum benefits in the THF stabilized (entries 1 and 2) and the *ex situ* (entries 5 and 6) systems, where normalized current intensities increased by a factor of 4 and Tafel slopes (Table 4) decrease nearly 35 % in both cases. This improved behaviour in **ox-CF** electrodes could arise from potential coordinative or/and H-bond interaction between the surface carboxylate groups of the support and the  $\text{Co}(\text{OH})_2$  NPs, improving the electronic communication between catalyst and support and easing the attainment of high oxidation states through the anionic nature of the  $-\text{COO}^-$  scaffolds.

The tendency to obtain slightly smaller NPs with **ox-CF** material (entry 1 vs. 2 and entry 3 vs. 4 in Table 4) also supports the stabilizing role of surface carboxylates and thus their interaction with the Co-based species. The higher surface/volume ratio in the smaller in size  $\text{Co}(\text{OH})_2$  NPs present in **ox-CF-based** systems can also contribute to the observed enhanced OER activity for these electrodes due to higher number of active sites.

Additionally, as recently described for molecular complexes,<sup>20</sup> the potential role of dangling carboxylates from the **ox-CF** support as proton acceptor moieties (internal bases) lowering the activation free energies that lead to O-O bond formation during the OER, cannot be discarded. Furthermore, the absence of stabilizing groups at the surface of bare CF electrodes leads to Co(OH)<sub>2</sub> NPs less dispersed on the support, which probably reduces the number of exposed active sites (*i.e.* some of the active centres are blocked due to agglomerates) and contributes to the lower intensities found for these electrodes. Thus, it is confirmed that an homogeneous dispersion of NPs onto the surface of the CFs is a key point for a good electrocatalytic activity.

In contrast, the less amount of Co in the *ex situ* materials could help to obtain a thinner and more homogeneous film of Co(OH)<sub>2</sub> NPs, thus obtaining a material with higher exposed active sites. This fact also leads to a better interaction between the Co(OH)<sub>2</sub> nanoparticulated catalyst and the support C surface, obtaining higher catalytic activities per  $\mu\text{g}$  of Co ( $i_{\text{Co}}$ , Fig. 10a, *i.e.* higher intensities).

In addition, stability studies were carried out by the CV monitoring of  $i_{\text{Co}}$  after different exposure times of the samples to chronoamperometric conditions (1 V vs. NHE at pH 13,  $\eta = 537$  mV, Fig. 11). The evolution of the normalized electrocatalytic current intensities ( $i_{\text{Co}}$ ) measured by CV after a certain time (0, 10, 30, 60 and 120 min) under chronoamperometric OER conditions reveal again a distinct behaviour between **CF** and **ox-CF** electrodes. As can be observed in Fig. 11 and Table 5, while the  $i_{\text{Co}}$  of **ox-CF** electrodes progressively decreases with time ( $i_{\text{Co } t=0} > i_{\text{Co } t>0}$ ), in all cases (entries 2, 4 and 6 in Table 5) due to deactivation pathways (see below for more details), CF anodes firstly activate ( $i_{\text{Co } t=0} < i_{\text{Co } t=10}$ , entries 1, 3 and 5 in Table 5) prior to progressively deactivate after longer time under turnover conditions. Again, this behaviour could be explained by the different catalyst-support interactions inherent to each case. Therefore, the electronic communication between the bare CF electrodes and Co(OH)<sub>2</sub> NPs seems to be initially weak and its improvement (and concomitant activation) under OER conditions could be related to the partial removal of the stabilizer. Contrarily, the electronic communication (through coordinative COO-Co(OH)<sub>2</sub> bonds and/or H-bonds) seems optimum in the **ox-CF** anodes, where no activation is observed.



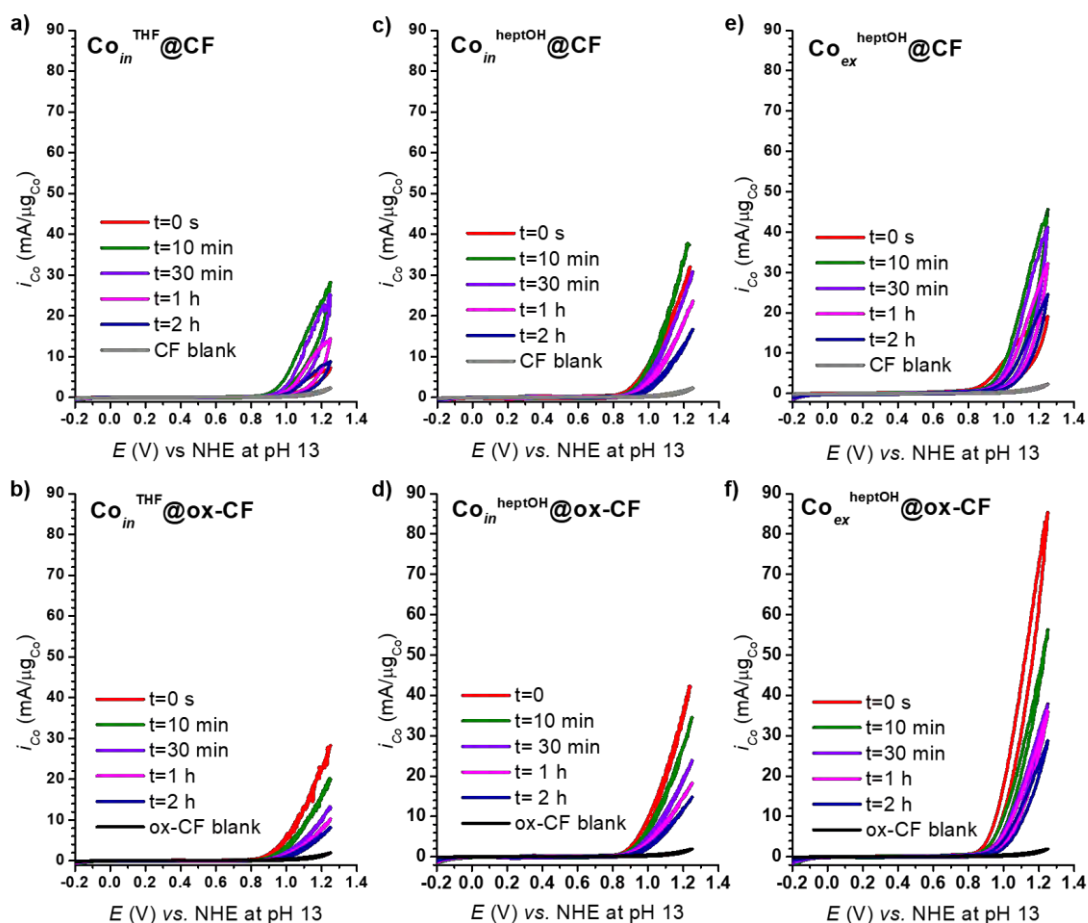


**Figure 11.** Cyclic voltammeteries in a 0.1 M NaOH aqueous solution (pH 13) of  $\text{Co}_{in}^{\text{THF}}@CF$ ,  $\text{Co}_{in}^{\text{THF}}@ox-CF$ ,  $\text{Co}_{in}^{\text{heptOH}}@CF$ ,  $\text{Co}_{in}^{\text{heptOH}}@ox-CF$ ,  $\text{Co}_{ex}^{\text{heptOH}}@CF$  and  $\text{Co}_{ex}^{\text{heptOH}}@ox-CF$ . CF blanks in grey, ox-CF blanks in black, CV at  $t=0$  s in red, CV after 10 min CA in green, CV after 30 min CA in purple, CV after 1 h CA in pink and CV after 2 h CA in blue.

**Table 5.** Main data of the progressive deactivation of the systems when successive CAs at a fixed potential of 1 V vs. NHE at pH 13 are applied to each system.

Entry	System	$i_{Co}$	$i_{Co}$	$i_{Co}$	$i_{Co}$	$i_{Co}$	$i_{Co}$	$i_{Co}$
		$t=0$ s	$t=10$ min	$t=30$ min	$t=1$ h	$t=2$ h	$t=2h^*$ (a)	REM (b)
		(mA/ $\mu\text{g}_{Co}$ )						(%)
1	$\text{Co}_{in}^{\text{THF}}@CF$	7.2	28.2	25.2	14.4	8.8	8.9	32
2	$\text{Co}_{in}^{\text{THF}}@ox-CF$	28.3	20.1	13.3	10.3	8.2	14.1	50
3	$\text{Co}_{in}^{\text{heptOH}}@CF$	32.9	39.3	30.7	23.6	16.8	25	64
4	$\text{Co}_{in}^{\text{heptOH}}@ox-CF$	42.3	34.6	23.8	18.5	15.4	26.2	62
5	$\text{Co}_{ex}^{\text{heptOH}}@CF$	19.2	46.15	41.0	33.3	25.6	25.6	55
6	$\text{Co}_{ex}^{\text{heptOH}}@ox-CF$	85.5	56.4	38.2	36.4	29.1	37.0	43

<sup>a</sup>  $i_{Co}$   $t=2h^*$  measured after removing all the bubbles formed and performing an IR drop correction at 85% again. <sup>b</sup> %  $i_{Co}$  REM calculated by dividing  $i_{Co}$   $t=2h$  by  $i_{Co}$   $t=0$  s as short-term stability data for ox-CF systems and by dividing  $i_{Co}$   $t=2h$  by  $i_{Co}$   $t=10$  min (value after activation) as short-term stability data for CF systems.



Irrespective of the presence or not of an initial activation process, the  $i_{Co}$  values progressively decreased in all systems and only a percentage of the initial electrocatalytic current was maintained after 2 h under chronoamperometric OER conditions ( $i_{Co\ REM}$  in Table 5 and Fig. 12). Comparing the systems synthesized in 1-heptanol, irrespective of the CF/ox-CF nature of the support, when  $i_{Co\ REM}$  is compared for *in situ* and *ex situ* systems, the former tends to be slightly more robust than the latter. This observation highlights the stronger catalyst-support interaction attained when the NPs are directly grown onto the supports.

Among the *in situ* electrodes, the surface functionalization of the support (**ox-CF**) is only beneficial when THF, a weak stabilizer, is used as solvent for the electrode synthetic process (compare  $i_{Co\ REM}$  in THF, entries 1 and 2 in Table 5, vs.  $i_{Co\ REM}$  in entries 3 and 4, where 1-heptanol is used). Therefore, when the support becomes the main stabilizing agent for  $Co(OH)_2$  NPs, the role of surface carboxylic acid groups in **ox-CF** is clearly emphasized. Contrarily, when comparing the stability of the two *ex situ* anodes ( $i_{Co\ REM}$  in entries 5 and 6, Table 5), it appears that the presence of carboxylic acid groups in the support (**ox-CF**) is not beneficial but even detrimental. Therefore, the presence of surface carboxylate groups in **ox-CF** seems to destabilize the resulting electrodes, potentially through steric interactions of the carboxylate moieties with the 1-heptanol molecules stabilizing the preformed NPs.

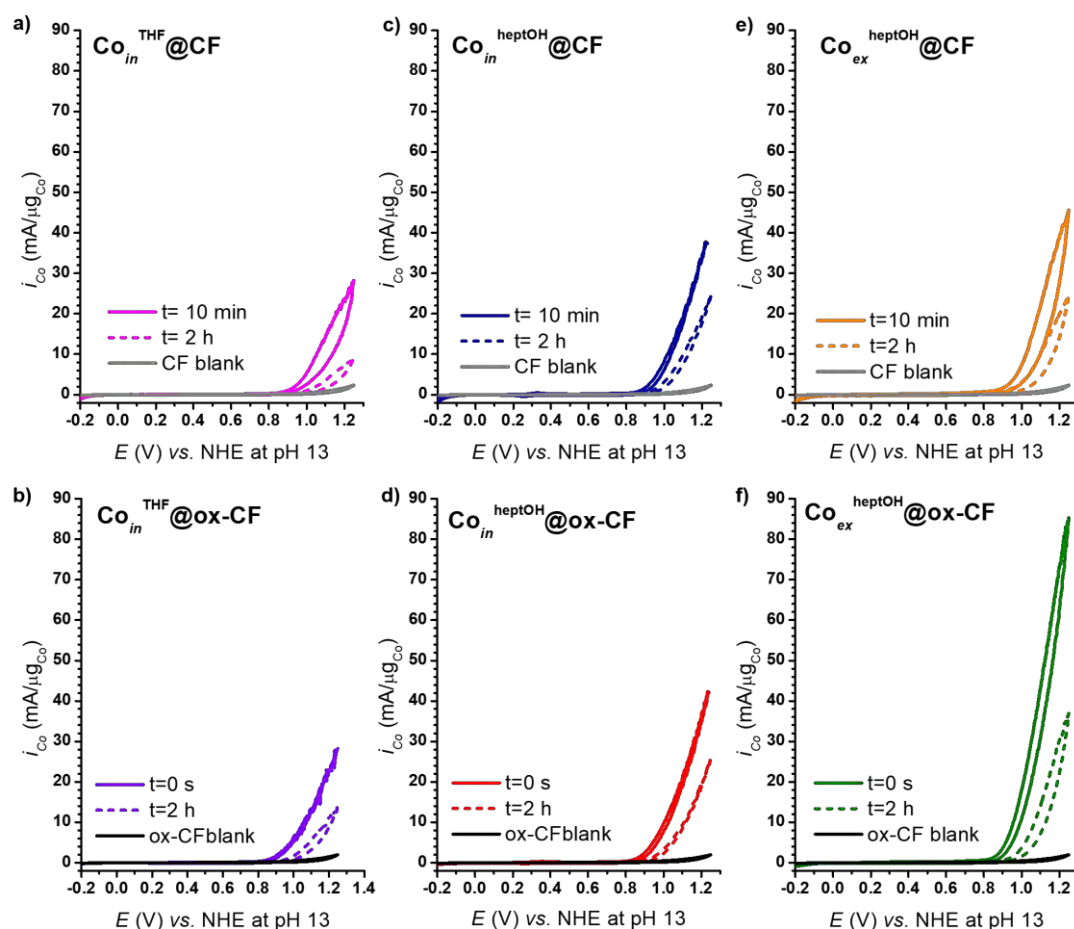
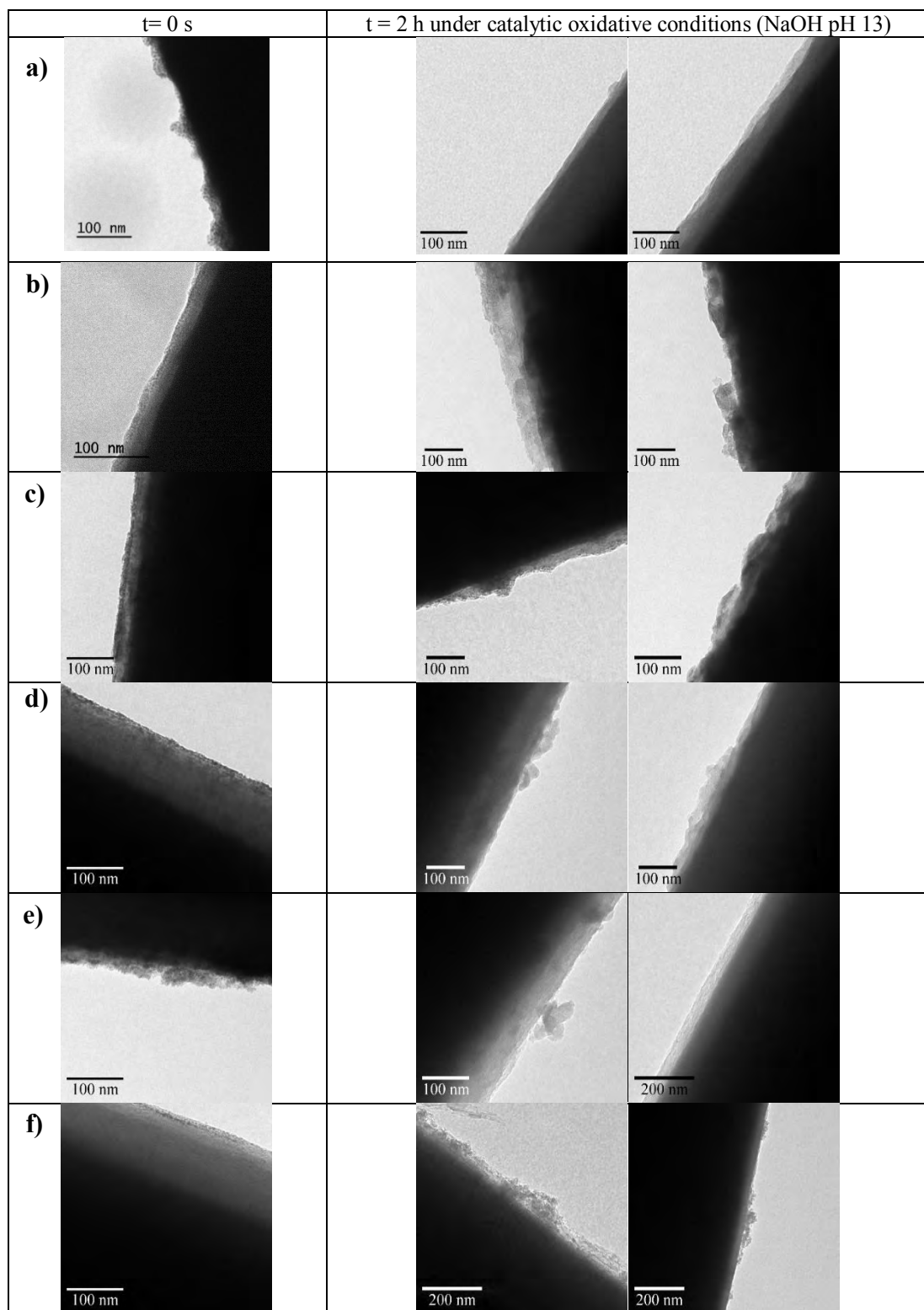


**Figure 12.** Cyclic voltammeteries for  $\text{Co}_{in}^{\text{THF}}@CF$  (pink),  $\text{Co}_{in}^{\text{THF}}@ox-CF$  (purple),  $\text{Co}_{in}^{\text{heptOH}}@CF$  (blue),  $\text{Co}_{in}^{\text{heptOH}}@ox-CF$  (red),  $\text{Co}_{ex}^{\text{heptOH}}@CF$  (orange) and  $\text{Co}_{ex}^{\text{heptOH}}@ox-CF$  (green) recorded before (at  $t=0$  for the  $ox-CF$  systems and at  $t=10$  min for the  $CF$  systems, when the  $i_{Co}$  is maximum) and after a 2 h CA experiment in a 0.1 M NaOH aqueous solution (pH 13).  $i_{Co}$   $t=2$  h was measured after removing all the bubbles formed on the system and performing an IR drop correction at 85% again. Ox-CF (black) and CF (grey) blanks are also displayed. CAs were performed at a fixed potential of 1 V vs NHE at pH 13 ( $\eta = 537$  mV) for 2 h.

In order to study the deactivation pathways occurring in the prepared anodes under OER conditions, a set of complementary analyses were carried out after catalytic experiments. TEM images together with EDX analysis (Table 6 and Fig. A1-A6) of the full set of working electrodes were recorded after a 2 h chronoamperometric experiment (1 V vs. NHE, 0.1 M NaOH). Post-catalysis TEM images revealed a more heterogeneous distribution of the Co NPs onto the surface of the CFs, showing regions with big aggregates together with naked areas in the supports (Table 6).

**Table 6.** Representative TEM images of  $\text{Co}_{in}^{\text{THF}}@CF$  (a),  $\text{Co}_{in}^{\text{THF}}@ox-CF$  (b),  $\text{Co}_{in}^{\text{heptOH}}@CF$  (c),  $\text{Co}_{in}^{\text{heptOH}}@ox-CF$  (d),  $\text{Co}_{ex}^{\text{heptOH}}@CF$  (e) and  $\text{Co}_{ex}^{\text{heptOH}}@ox-CF$  (f) at  $t=0$  s (left column) and after 2 h of CA (right column) at 1 V vs. NHE (*i.e.*  $\eta=537$  mV) in 0.1 M NaOH.



Together with their aggregation under turnover conditions, which decreases the number of exposed active sites, the mechanical leaching of the NPs and/or the evolution of  $\text{Co}(\text{OH})_2$  to other phases presenting reduced OER activity could also be at the origin of the observed decrease in activity over time. Thus, selecting  $\text{Co}_{in}^{\text{heptOH}}@ox\text{-CF}$  as a representative anode, XPS and ICP-OES analyses were carried out after 2 h under electrocatalytic conditions. The complete XPS survey spectra in Fig. 13a shows, as before catalysis, O 1s, C 1s and N 1s as main peaks. In addition of a slightly significant signal for Co, some other peaks are found, such as sodium, attributable to physisorbed sodium cations coming from the NaOH used as catalytic alkaline media (Na 1s  $\approx$  1071 eV, Na KLL  $\approx$  497 eV). Some other impurities can be attributed to  $\text{CaCO}_3$  species from the degradation of the glass of the catalytic cell (Ca  $2p_{3/2}$   $\approx$  347 eV). XPS analysis revealed comparable Co 2p and O 1s binding energies before and after catalysis (Fig. 13b, 13c and Table 7), thus confirming  $\text{Co}(\text{OH})_2$  as the Co species present at the electrode surface after catalytic turnover. Additionally, ICP data indicated both a clear decrease in the Co content at the electrode surface (from 0.13 wt% to 0.05 wt%) and the presence of Co in the resulting 0.1 M NaOH solution (0.4 mg/L). Thus, both the aggregation and partial leaching of the  $\text{Co}(\text{OH})_2$  NPs under OER electrocatalytic conditions seem to be at the origin of the observed deactivation.

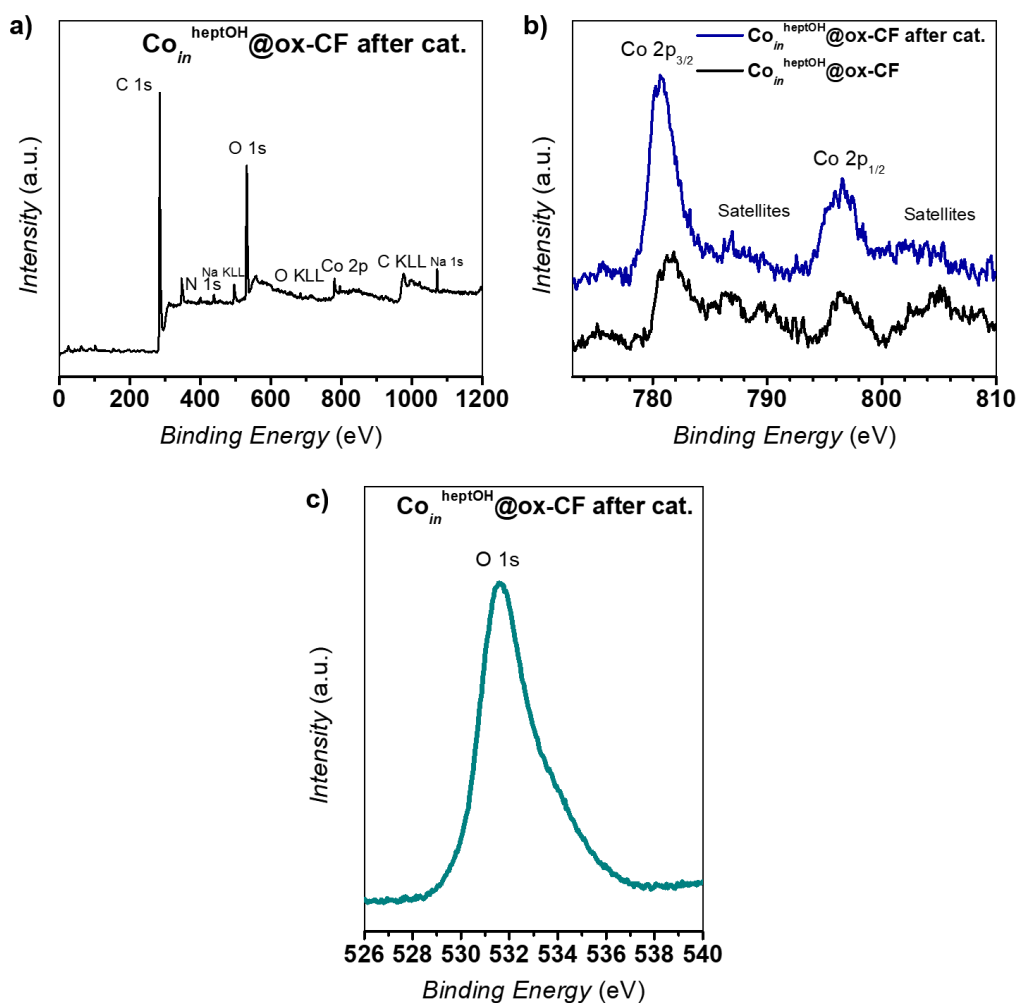


**Figure 13.** XPS survey of  $\text{Co}_{in}^{\text{heptOH}}@ox\text{-CF}$  after a 2 h CA (1V vs. NHE, 0.1 M NaOH) (a). The main peaks can be clearly indexed to O 1s, N 1s and C 1s regions (O KLL represents the energy of the electrons ejected from the atoms due to the filling of the O 1s state (K shell) by an electron from the L shell coupled with the ejection of an electron from an L shell). Comparison of high-resolution XPS analysis in the Co 2p region for  $\text{Co}_{in}^{\text{heptOH}}@ox\text{-CF}$  before (black line) and after (blue line) a 2-h CA (b). O 1s XPS high-resolution spectra for  $\text{Co}_{in}^{\text{heptOH}}@ox\text{-CF}$  after a 2-h CA (c).

**Table 7.** High-resolution XPS analysis in the Co 2p region of  $\text{Co}_{in}^{\text{heptOH}}@ox\text{-CF}$  after a 2 h CA.

Sample	Co 2p <sub>3/2</sub>	Satellites	Co 2p <sub>1/2</sub>	Satellites
$\text{Co}_{in}^{\text{heptOH}}@ox\text{-CFs}$ after catalysis	780.9 eV	786.2eV	796.4 eV	802.6 eV
$\text{Co}_{in}^{\text{heptOH}}@ox\text{-CF}$	781.6 eV	786.9 eV	796.9 eV	804.3 eV

### 5B.3.2 Faradaic efficiencies determination

The faradaic efficiency ( $\epsilon$ , %) of all hybrid materials was evaluated by a 20-minute  $O_2$ -monitored CA at a fixed potential of 1 V vs. NHE at pH 13. These experiments were carried out in a two-compartment cell by placing the counter electrode in the cathodic part and the reference and working electrodes (*i.e.* 1-mg CFs brush) in the anodic part (Fig. 14). These experiments were carried out in conjunction with a  $O_2$ -Clark-type electrode able to *in situ* detect and measure the  $O_2$  generated by the system in the gas phase of the anodic compartment. The charge passed through the system was transformed first into moles of electrons by using the Faradaic constant ( $96485 \text{ C/mol e}^-$ ) and then into theoretical  $O_2$  moles considering that the formation of each oxygen molecule requires four electrons ( $2H_2O \rightarrow O_2 + 4H^+ + 4e^-$ ). All the experimental data were extracted from the Clark sensor and the obtained values (mV) were transformed to oxygen moles by calibrating the electrochemical signal with different amounts of 99 % pure  $O_2$  and extrapolating the obtained data. The faradaic efficiency was obtained by dividing the sensor-coming data (experimental  $\mu\text{mol } O_2$ ) by the charge-coming data (theoretical  $\mu\text{mol } O_2$ ) at the end of the experiment.

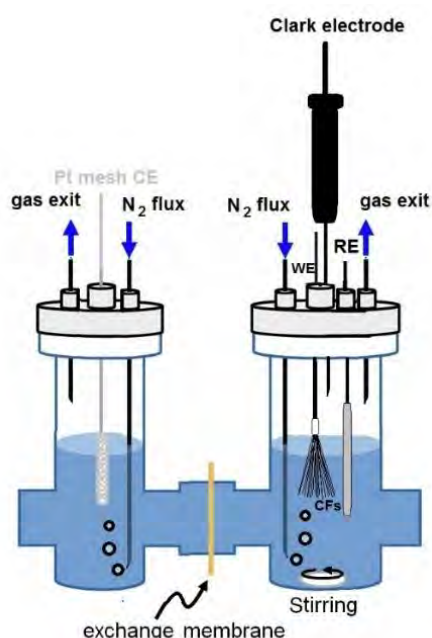


**Figure 14.** Two-compartment cell set-up for oxygen detection experiments. The counter electrode is placed in the cathodic part of the cell and the reference electrode and the working electrodes in the anodic part. The  $O_2$ -Clark electrode is placed also in the anodic part of the cell to detect the generated oxygen in the gas phase.

As shown in Fig. 15, the observed  $O_2$  signal has some delay after initiation of CA as some time is needed to saturate first the solution with  $O_2$  before starting to fill the headspace with  $O_2$  gas, which will be detected by the Clark sensor. Oxygen level continues rising after the CA is off as a lot of  $O_2$  bubbles are still trapped in the CFs surface, which are slowly released with the continuous magnetic stirring. The faradaic efficiency was calculated when the  $O_2$  level was stabilized, obtaining  $\epsilon > 90\%$  in all cases. Thus, even if partial deactivation due to aggregation and leaching may take place under the applied OER conditions, the high faradaic efficiency confirms oxygen evolution as the sole reaction happening in the studied anodes.

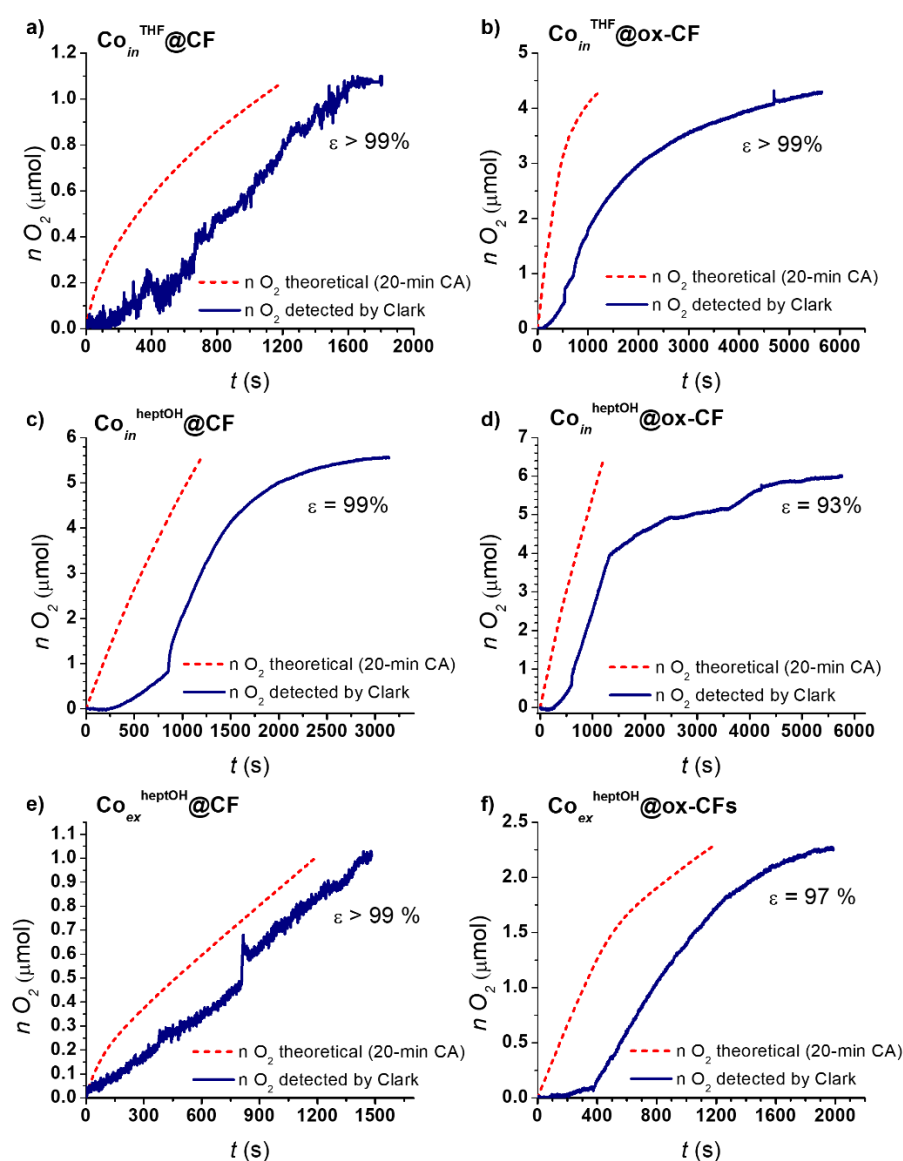


**Figure 15.**  $O_2$ -monitored CA experiments for faradaic efficiency determination for all 6 synthesized anodic systems. A fixed potential of 1 V vs NHE (pH 13) was applied for 20 min in the CA experiments.

### 5B.3.3 Effect of pH in the OER activity

The OER reaction is obviously favored under alkaline conditions due to the first-row transition metal oxides susceptibility to corrosion in acidic environments. Protons produced by the OER can dramatically lower the pH near the working electrode, and at some critical pH,  $\text{H}_3\text{O}^+$  could protonate the oxidic framework of the metal oxide, making the metal-oxygen bonds weaker, leading to dissolution of metal ions. In addition, from an engineering point of view, the presence of hydroxide anions ( $\text{OH}^-$ ) helps to increase the conductivity of the solution, lowering ohmic losses that become larger when operating at higher current densities.

However, a neutral pH offers non-corrosive and technologically friendly environment for stable and safe devices (e.g. popular photovoltaic materials such as silicon degrade quickly as passivated silicon dioxide in alkaline conditions).<sup>21</sup> Furthermore, one major class of electrolyzers, based on a proton exchange membrane (PEM) as a key element, operate at high current and power densities and achieve low gas crossover in comparison with alkaline electrolyzers.<sup>22</sup>

In view of this,  $\text{Co}(\text{OH})_2@\text{CFs}$  systems were tested at different pHs to study the effect of this parameter in their catalytic performance (Fig. 16). Polarization curves at pH 0, 7, 9 and 13 for  $\text{Co}_{\text{in}}^{\text{THF}}@\text{ox-CF}$  (as a model system) show that current densities decrease in medium-range pHs, with the worst results displayed at pH 0. The highest intensity is achieved at pH 13, in agreement with the fact that the basic environment aids in “accepting” the protons generated during the OER and thus avoiding catalyst corrosion (Fig. 16a). This corrosion effect was confirmed by performing CVs at pH 13 before and after performing CVs at pH 7, 9 and 0. It can be noticed in Fig. 16b that the activity at pH 13 was preserved after catalytic experiments at medium-range pH (i.e. pH 7 and 9). However, at pH 0, an oxidation wave was observed in the first scan, followed by a second scan showing no activity (Fig. 16c inset). The following CV at pH 13 showed a deactivation of the system, as seen in Fig. 16c, confirming the corrosive and irreversible action of acidic media onto the metal catalyst.



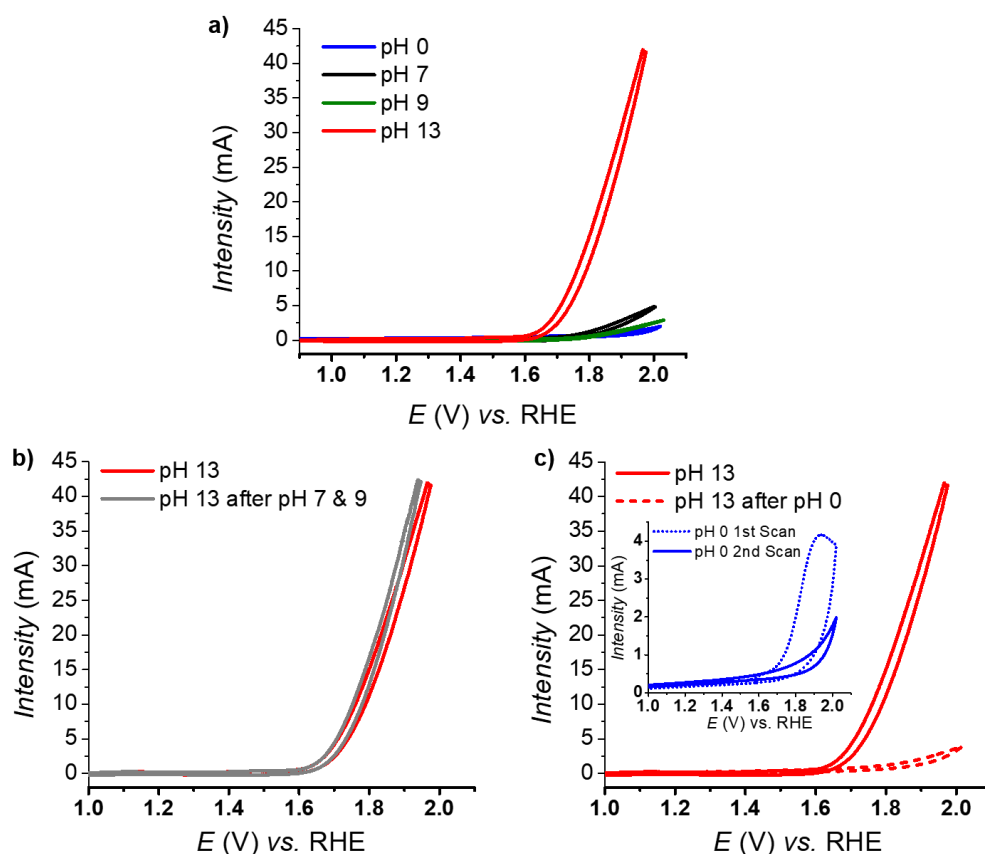


**Figure 16.** Cyclic voltammograms of  $\text{Co}_{in}^{\text{THF}}@ox\text{-CFs}$  at different pH conditions: 1 M  $\text{H}_2\text{SO}_4$  pH 0 (blue), PBS pH 7 (black), BBS pH 9 (green) and 0.1 M NaOH pH 13 (red) (a). Comparison of the OER activity at pH 13 before and after CVs at pH 7 and 9 (b). Comparison of OER activity at pH 13 before and after CVs at pH 0. Inset: CVs at pH 0, 1<sup>st</sup> CV (dotted blue) and 2<sup>nd</sup> CV (blue) (c).

## **5B.4 CONCLUSIONS**

This work highlights the applicability of the organometallic approach for the synthesis of nanostructures to systematically tailor the interface between nanocatalysts and carbon-based supports in OER electro-anodes. Hence, the use of bare (CF) and surface-functionalized (ox-CF) carbon microfibers as cheap, easy to engineer and high-surface area supports combined with the versatility of the synthetic method, which allows adding different NP stabilizers and perform the synthesis both in the presence *-in situ-* or absence *-ex situ-* of the carbonaceous support, permitted obtaining a set of six  $\text{Co}(\text{OH})_2@CF/ox\text{-CF}$  electrodes presenting different interfacial nature.

Several meaningful conclusions about the role of the catalyst-support interactions in the electrocatalytic performances were extracted from the morphological (TEM) and compositional (XPS, ICP-OES, EDX) characterization of the series of prepared electrodes together with their evaluation as OER electrocatalysts under alkaline conditions. First, the presence of carboxylic groups at the surface of the CFs support (**ox-CF** electrodes) showed to play an important role in both the morphology, by systematically reducing the NPs size and increasing their dispersion at the electrode surface, and the OER performance, by improving the activity and stability of the prepared electrodes during the OER, particularly when the weak stabilizer THF is employed. These observations point to the likely formation of COO-Co(OH)<sub>2</sub> coordinative bonds and/or H-bonds improving both the electronic communication between catalyst and support, and the dispersibility and stability of the former on top of the latter. Second, the formation of stronger catalyst-support interactions happened when the nanocatalysts were directly grown at the surface of the CFs, as evidenced by observing higher Co loadings and higher stabilities under electrocatalytic OER conditions in *in situ* systems compared to their corresponding counterparts prepared *ex situ* by an impregnation step, thus evidencing the formation of stronger catalyst-support interactions when the nanocatalysts are directly grown at the surface of the CFs.

It was also confirmed that the anodes maintain Co(OH)<sub>2</sub> as the catalytic species after 2 h of electrocatalytic turnover and, even if partially deactivated due to both aggregation and leaching of the NPs from the electrode surface, almost quantitative faradaic efficiencies show oxygen evolution as the only redox reaction occurring at their surface.

All in all, the results reported in this *sub-chapter* evidence how subtle surface modifications of either the catalyst or the support in OER anodes can lead to significantly different catalytic outputs, and thus highlight the importance of new research focused on exploring the nature of catalyst-support interfaces.

Putting altogether the results obtained both in *Chapter 5A* and *Chapter 5B*, it can be concluded that a proper interaction between the NPs and the support surface is a key factor for an improved catalytic activity of the hybrid systems, confirmed by means of potential  $\pi$ - $\pi$  interactions between Ru4PP NPs/carbon structures or by coordinative H-bonds between Co(OH)<sub>2</sub> and COOH moieties in the microfibers. In addition, it is also

important to avoid steric hindrance between moieties, which could lead to a bad stabilization of the systems.

*This work has been published in Catalysis Science & Technology in 2020 (The role of catalyst-support interactions in oxygen evolution anodes based on Co(OH)<sub>2</sub> nanoparticles and carbon microfibers. L. Mallón, N. Romero, A. Jiménez, E. Martín Morales, J. Alemán, R. Más-Ballesté, R. Bofill, K. Philippot, J. García-Antón, X. Sala, Catal. Sci. Technol. 2020, 10, 4513).*

## **5B.5 EXPERIMENTAL SECTION**

### **Materials and methods**

All procedures concerning the synthesis and preparation of samples were carried out using standard Schlenk tubes, Fisher-Porter glassware and vacuum line techniques or in a glove-box (MBraun) under argon atmosphere. Solvents (THF, pentane) were purified before use by filtration on adequate alumina columns in a purification apparatus (MBraun) and handled under argon atmosphere. Reagents and solvents were degassed before use via a multi-cycle freeze-pump-thaw process. The (cyclooctadienyl)(1,5-cyclooctadiene)cobalt(I) complex,  $[\text{Co}^{\text{I}}(\eta^3\text{-C}_8\text{H}_{13})(\eta^4\text{-C}_8\text{H}_{12})]$ , was purchased from Nanomeps-Toulouse. Dihydrogen and argon were purchased from Alphagaz. 1-Heptanol was acquired from Sigma-Aldrich and dried over activated molecular sieves (4Å) prior to use. Other reagents were employed as received unless otherwise specified. Carbon microfibers (CFs) (Twill 2x2 3K weight 200 g/m<sup>2</sup> width 1200 mm, Model HA2301) were purchased from ClipCarbono.

### **Synthetic procedures**

**Synthesis of  $\text{Co}_{in}^{\text{THF}}@CF$  and  $\text{Co}_{in}^{\text{THF}}@ox\text{-CF}$ .** Under argon atmosphere, one brush of each type of CFs (~90 mg) was introduced into a Fisher-Porter reactor containing 10 mL of THF and  $[\text{Co}^{\text{I}}(\eta^3\text{-C}_8\text{H}_{13})(\eta^4\text{-C}_8\text{H}_{12})]$  (10 mg, 0.036 mmol), leading the two ends of each brush to be soaked in the reaction media. The Fischer-Porter was then pressurized with 3 bar of dihydrogen and the reaction mixture kept at r. t. under vigorous stirring for 24 h. After the reaction time, the remaining H<sub>2</sub> was removed under vacuum. The obtained materials were washed by soaking them in degassed anhydrous pentane (x3) and dried under vacuum. Both CFs brushes were exposed to air to achieve the oxidation of the as-synthesized metallic Co NPs.  **$\text{Co}_{in}^{\text{THF}}@CF$ :** TEM:  $d_{\text{mean}} = 2.6 \pm 0.7$  nm, ICP(Co wt%): 0.13%, XPS: Co(OH)<sub>2</sub> 2p<sub>3/2</sub> (781.4 eV) satellites (785.4 eV) 2p<sub>1/2</sub> (797.3 eV) satellites (800.8 eV).  **$\text{Co}_{in}^{\text{THF}}@ox\text{-CF}$ :** TEM:  $d_{\text{mean}} = 1.8 \pm 0.4$  nm, ICP-OES (Co wt%): 0.23%, XPS: Co(OH)<sub>2</sub> 2p<sub>3/2</sub> (781.5 eV) satellites (785.4 eV) 2p<sub>1/2</sub> (797.3 eV) satellites (802.9 eV).

**Synthesis of  $\text{Co}_{in}^{\text{heptOH}}@CF$  and  $\text{Co}_{in}^{\text{heptOH}}@ox-CF$ .** Under argon atmosphere, one brush of each type of CFs (~90 mg) was introduced into a Fisher-Porter reactor containing 10 mL of 1-heptanol and  $[\text{Co}^I(\eta^3\text{-C}_8\text{H}_{13})(\eta^4\text{-C}_8\text{H}_{12})]$  (10 mg, 0.036 mmol), leading the two ends of each brush to be soaked in the reaction media. The Fischer-Porter was then pressurized with 3 bar of dihydrogen and the reaction mixture kept at r. t. under vigorous stirring for 20 h. After the reaction time, the remaining  $\text{H}_2$  was removed under vacuum. The obtained materials were washed by soaking them in degassed anhydrous pentane (x3) and dried under vacuum. Both CFs brushes were exposed to air to achieve the oxidation of the as-synthesized metallic Co NPs.  $\text{Co}_{in}^{\text{heptOH}}@CF$ : TEM:  $d_{\text{mean}} = 2.8 \pm 0.6$  nm, ICP-OES (Co wt%): 0.14%, XPS:  $\text{Co}(\text{OH})_2$   $2p_{3/2}$  (781.7 eV) satellites (785.6 eV)  $2p_{1/2}$  (797.4 eV) satellites (803.0 eV).  $\text{Co}_{in}^{\text{heptOH}}@ox-CF$ : TEM:  $d_{\text{mean}} = 2.1 \pm 0.4$  nm, ICP-OES (Co wt%): 0.13%, XPS:  $\text{Co}(\text{OH})_2$   $2p_{3/2}$  (781.6 eV) satellites (786.9 eV)  $2p_{1/2}$  (796.9 eV) satellites (804.3 eV).

**Synthesis of  $\text{Co}_{ex}^{\text{heptOH}}@CF$  and  $\text{Co}_{ex}^{\text{heptOH}}@ox-CF$ .** Under Ar atmosphere,  $[\text{Co}^I(\eta^3\text{-C}_8\text{H}_{13})(\eta^4\text{-C}_8\text{H}_{12})]$  (10 mg, 0.036 mmol) was introduced into a Fischer-Porter reactor. Next, anhydrous 1-heptanol (10 mL) was transferred to the reactor vessel *via cannulae*. The Fischer-Porter was then pressurized with dihydrogen (3 bar) and the reaction mixture kept at r. t. under vigorous stirring for 20 h. After the reaction time, the remaining  $\text{H}_2$  was removed under vacuum and one brush (~90 mg) of each type of CFs (CF/ox-CF) were introduced into the reactor leading the two ends of each brush soaked in the reaction media. They were left impregnating for 24 h under Ar atmosphere, at r. t. and under vigorous stirring. Finally, both brushes were washed by soaking them in degassed anhydrous pentane (x3) and dried under vacuum. Both CFs brushes were finally exposed to air to achieve the oxidation of the as-synthesized metallic Co NPs.  $\text{Co}_{ex}^{\text{heptOH}}@CF$ : TEM:  $d_{\text{mean}} = 2.0 \pm 0.5$  nm, ICP-OES (Co wt%): 0.039%, XPS:  $\text{Co}(\text{OH})_2$   $2p_{3/2}$  (781.2 eV) satellites (785.9 eV)  $2p_{1/2}$  (797.4 eV) satellites (804.2 eV).  $\text{Co}_{ex}^{\text{heptOH}}@ox-CF$ : TEM:  $d_{\text{mean}} = 2.3 \pm 0.5$  nm, ICP-OES (Co wt%): 0.055%, XPS:  $\text{Co}(\text{OH})_2$   $2p_{3/2}$  (781.0 eV) satellites (785.5 eV)  $2p_{1/2}$  (797.1 eV) satellites (803.1 eV).

## Characterization techniques

**Transmission electron microscopy (TEM):** Observations for the colloidal system were performed at the “UMS 3623 – Centre de microcaractérisation Raimond Castaing” using a MET JEOL JEM 1011 electron microscope operating at 100 kV with resolution point of 4.5 Å. TEM grids were prepared by drop-casting of the crude 1-heptanol NPs colloidal solution into a carbon-coated copper grid. Pumping with a Gatan turbo pumping station model 655 was carried out before analysis in the TEM. Supported systems were analyzed at the “Servei de Microscòpia” of the UAB using a using a JEOL JEM 1400 electron microscope working at 120 kV with a resolution point of 0.4 nm by depositing a small amount of CFs onto a carbon-coated copper grid just before TEM analysis. Size distributions were determined through manual analysis of enlarger micrographs with *ImageJ* software to obtain statistical size distribution and a mean diameter. For each system, the mean size was calculated by assuming spherical form. In all size distributions, over than 200 particles were counted. Size distributions are quoted as the mean diameter  $\pm$  the standard deviation ( $\sigma$ ).

**Energy-dispersive X-ray spectroscopy (EDX):** EDX analysis were performed at “Servei de Microscòpia de la UAB” using a JEOL JEM 2011 electron microscope to analyze the chemical elemental composition of the samples.

**X-ray photoelectron spectroscopy (XPS):** Measurements were performed by Dr. Guillaume Sauthier at the Catalan Institute of Nanoscience and Nanotechnology (ICN2) using a Phoibos 150 analyzer (SPECS GmbH, Berlin, Germany) in ultra-high vacuum conditions (base pressure  $5 \cdot 10^{-10}$  mbar) with a monochromatic aluminium  $K\alpha$  x-ray source (1486.74 eV). The energy resolution was measured by the Full Width at Half Maximum (FWHM) of the Ag  $3d_{5/2}$  peak for a sputtered silver foil which was 0.62 eV and all data were corrected using the C1s peak at 284.8 eV as an internal standard.

**Inductively coupled plasma optic emission spectroscopy (ICP-OES):** Analysis were performed at “Servei d’Anàlisi Químic” (SAQ) in the UAB, on a Perkin Elmer Optima 4300 DV system. Solid samples were prepared by wheightening 1 mg with an analytic balance XPE205DR (Mettler Toledo) and digested in a Milestone UltraWave in a mixture of concentrate  $HNO_3$  and HCl (Merck) prior to the analysis (two replicates were

performed for each sample). For liquid samples, 1 mL was digested following the same procedure as for solid samples.

## Electrochemical set-up

**CFs electrode preparation:** CFs electrodes were prepared as stated in ref. 14. Commercial carbon microfibers consist of bundles of around 3000 filaments of 5-8  $\mu\text{m}$  of diameter. The CFs electrodes contain 7 bundles of 3000 filaments (21000 filaments) making a 6 cm long bunch of fibers (1). Then, this 6 cm long bunch was folded in half (2), obtaining electrodes ( $\approx 90$  mg) containing the double of filaments (42000) but only with 2 cm exposed for NPs synthesis and electrode usage (3) (Fig. 17). The ready-made electrodes (CF) were treated 30 minutes into commercial sulfuric acid (98%) at r.t. with stirring and later introduced into a 1:1  $\text{H}_2\text{SO}_4/\text{H}_2\text{O}_2$  mixture for 1 h to obtain the oxidized CFs (**ox-CF**). The  $\text{H}_2\text{O}_2$  should be fresh and the mixture with  $\text{H}_2\text{SO}_4$  must be prepared few minutes before use. Later, the electrodes were washed and sonicated in distilled water to remove all the acid traces among microfibers. It required several washing cycles until the pH of the water kept almost constant. The electrodes were sonicated 10-15 minutes in isopropanol or ethanol and then dried with a heat gun.

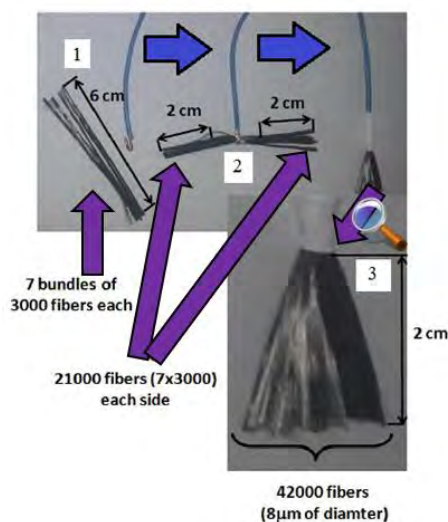


**Figure 17.** Steps to prepare CFs brush. Figure adapted from ref. 14 (R. Mas-Ballesté *et al.*).

After the synthesis of the NPs onto CFs electrodes and before the catalytic evaluation, these brushes were cut in 3-cm-long filaments (half fiber). 1 mg of those filaments was attached to a Cu tape together with a Cu-wire and everything was tight with a Teflon tape, still ensuring 2 cm length for the catalytic experiments.

**Electrochemical measurements:** Electrocatalytic OER experiments were performed in a 10 mL two-compartment cell with a proton exchange membrane between them, at room temperature in a three-electrode configuration using Hg/Hg<sub>2</sub>SO<sub>4</sub>, K<sub>2</sub>SO<sub>4</sub>(sat'd) and Pt as reference and counter electrode, respectively. Working electrodes (WE) were hand-made prepared using a short copper wire, 1-mg CFs brush and some Teflon tape to tight everything together. Both compartments were filled with 6 mL of 0.1 M NaOH aqueous solution and equipped with a stirring bar, being the CE placed in one compartment and the WE and RE in the other one. The potential was controlled using a BioLogic SP-150 potentiostat using the EC-Lab software for data acquisition and data handling. IR drop was automatically corrected at 85% for cyclic voltammetry and chronoamperometry. All catalytic experiments were measured with a sweep rate of 100 mV·s<sup>-1</sup>. Potentials are reported vs NHE (adding +0.65 V) and overpotentials are calculated as  $\eta_0 = E_{\text{Hg}/\text{Hg}_2\text{SO}_4, \text{K}_2\text{SO}_4(\text{sat'd})} + 0.65 \text{ V} - (1.23 - 0.059 \times \text{pH})$ .

A Clark type electrode (Unisense OX-NP needle microsensor) was used to measure the produced oxygen in the gas phase during the chronoamperometry experiment by placing it together with the WE and RE in the same compartment. Prior to Faradaic Efficiencies experiments, both cell compartments were purged with Ar. The instrument was kept polarizing at -800 mV overnight before use. The sensor was calibrated by adding different known volumes of 99 % pure oxygen at the end of the experiment.

**Cyclic Voltammetry (CV):** The system was scanned from  $E_i = -0.25 \text{ V}$  to  $E_f = 1.25 \text{ V}$  vs. NHE at 100 mV/s.

**Chronoamperometry (CA).** Controlled potential chronoamperometric experiments were performed at  $E_{\text{app}} = 1 \text{ V}$  vs. NHE.



## **5B.6 REFERENCES**

- <sup>1</sup> I. Roger, M.A. Shipman and M.D. Symes, *Nat. Rev. Chem.* **2017**, 1, 0003.
- <sup>2</sup> S. Li, X. Hao, A. Abudula and G. Guan, *J. Mater. Chem. A* **2019**, 7, 18674–18797.
- <sup>3</sup> J. De Tovar, N. Romero, S.A. Denisov, R. Bofill, C. Gimbert-Suriñach, D. Ciuculescu-Pradines, S. Drouet, A. Llobet, P. Lecante, V. Colliere, Z. Freixa, N. McClenaghan, C. Amiens, J. García-Antón, K. Philippot and X. Sala, *Mater. Today Energy* **2018**, 9, 506–515.
- <sup>4</sup> K.M. Shaju, L. Guerlou-Demourgues, G. Godillot, W. Weill and C. Delmas, *J. Electrochem. Soc.* **2012**, 159, A1934–A1940.
- <sup>5</sup> M. S. Burke, L.J. Enman, A.S. Batchellor, S. Zhou and S.W. Boettcher, *Chem. Mater.* **2015**, 27, 7549–7558.
- <sup>6</sup> H. Li, C. Chen, D. Yan, Y. Wang, R. Chen, Y. Zou and S. Wang, *J. Mater. Chem. A* **2019**, 7, 23432–23450.
- <sup>7</sup> H.S. Oh, H. N. Nong, T. Reier, A. Bergmann, M. Gliech, J.G. de Araújo, E. Willinger, R. Schlogl, D. Teschner and P. Strasser, *J. Am. Chem. Soc.* **2016**, 138, 12552–12563.
- <sup>8</sup> H. He, J. Chen, D. Zhang, F. Li, X. Chen, Y. Chen, L. Bian, Q.O.G. Moral, A. Call, F. Franco, A. Moya, J.A. Nieto-Rodríguez, M. Frias, J.L.G. Fierro, M. Costas, J. Lloret-Fillol, J. Alemán and R. Mas-Ballesté, *Chem. Eur. J.* **2018**, 24, 3305–3313. Wang, P. Duan, Z. Wen and X. Lv, *ACS Catal.*, 2018, 8, 6617–6626.
- <sup>9</sup> T.W. Van Deelen, C. Hernández-Mejía and K.P. De Jong, *Nat. Catal.* **2019**, 2, 955–970.
- <sup>10</sup> C. Amiens, D. Ciuculescu-Pradines and K. Philippot, *Coord. Chem. Rev.* **2016**, 308, 409–432.
- <sup>11</sup> M.C. Biesinger, B.P. Payne, A.P. Grosvenor, L.W.M. Lau, A.R. Gerson and R.St.C. Smart, *Appl. Surf. Sci.* **2011**, 257, 2717–2730.
- <sup>12</sup> J. Yang, H. Liu, W.N. Martens and R L. Frost, *J. Phys. Chem. C* **2010**, 114, 111–119.
- <sup>13</sup> J. Stoch and J. Gablankowska-Kukucz, *Surf. Interface Anal.* **1991**, 17, 165–167.
- <sup>14</sup> O.G. Moral, A. Call, F. Franco, A. Moya, J.A. Nieto-Rodríguez, M. Frias, J.L.G. Fierro, M. Costas, J. Lloret-Fillol, J. Alemán and R. Mas-Ballesté, *Chem. Eur. J.* **2018**, 24, 3305–3313.
- <sup>15</sup> Y.C. Liu, J.A. Koza and J. A. Switzer, *Electrochim. Acta* **2014**, 140, 359–365.
- <sup>16</sup> Y.Q. Gao, H.B. Li and G.W. Yang, *J. Appl. Phys.* **2016**, 119, 034902.
- <sup>17</sup> N.H. Chou, P.N. Ross, A.T. Bell and T.D. Tilley, *ChemSusChem* **2011**, 4, 1566–1569.
- <sup>18</sup> B.S. Yeo and A.T. Bell, *J. Am. Chem. Soc.* **2011**, 133, 5587–5593.
- <sup>19</sup> M.E.G. Lyons and M.P. Brandon, *J. Electroanal. Chem.* **2010**, 641, 119–130.
- <sup>20</sup> R. Matheu, M.Z. Ertem, J. Benet-Buchholz, E. Coronado, V.S. Batista, X. Sala and A. Llobet, *J. Am. Chem. Soc.* **2015**, 137, 10786–10795.

---

<sup>21</sup> Gerischer, H. In *Solar Energy Conversion: Solid-State Physics Aspects*; Seraphin, B. O., Ed.; Topics in Applied Physics; Springer Berlin Heidelberg: Berlin, 1979; Vol. 31, pp. 115-172.

<sup>22</sup> M. Carmo, D.L. Fritz, J. Mergel and D. Stolten, *Int. J. Hydrogen Energy* **2013**, 38, 4901-4934.

## **5B.7 ANNEX**

**Table A1.** Summary of electrocatalytic data for relevant carbon-supported Co-based OER electrocatalysts in alkaline media.

Entry	Catalyst	Ø (nm)	$\eta_0$ (mV)	Tafel slope (mV·dec <sup>-1</sup> )
1 <sup>1</sup>	Co <sub>3</sub> O <sub>4</sub> /BCNO	20	295	57.58
	Co <sub>3</sub> O <sub>4</sub> + BCNO		390	93.91
	Co <sub>3</sub> O <sub>4</sub>		380	98.81
2 <sup>2</sup>	Co@C	100-400	295 <sup>b</sup>	58
3 <sup>3</sup>	CoP NP/C	25	320 <sup>b</sup>	99
	CoP NR/C		270 <sup>b</sup>	71
4 <sup>4</sup>	Amorphous Co(OH) <sub>2</sub> Nanosheet	-	320 <sup>c</sup>	68
	Crystalline Co(OH) <sub>2</sub>		330 <sup>c</sup>	102
	Co <sub>3</sub> O <sub>4</sub>		400 <sup>c</sup>	84
5 <sup>5</sup>	Co <sub>3</sub> O <sub>4</sub> -NC/Gr-12h	50-80 ± 3	220 <sup>b</sup>	95
	Co <sub>3</sub> O <sub>4</sub> -NC/NGr-12h	50 ± 3	200 <sup>b</sup>	69
6 <sup>6</sup>	CG-CoO	10-30	320 <sup>b</sup>	75
	N-CG-CoO	10-30	270 <sup>b</sup>	71
7 <sup>7</sup>	Co <sub>3</sub> O <sub>4</sub> /N-rmGO	4-8	295 <sup>c</sup> 270 <sup>b</sup>	67 <sup>b</sup>
	Co <sub>3</sub> O <sub>4</sub> /rmGO	12-25	270 <sup>b</sup>	68
8 <sup>8</sup>	CoP NPs	1.5-2	350 <sup>d</sup>	80
	CoP-CNT		290 <sup>d</sup>	50
9 <sup>9</sup>	Co(TCNQ) <sub>2</sub> /CFs		295 <sup>b</sup>	188
	Co(OH) <sub>2</sub> -TCNQ/CFs		280 <sup>b</sup>	101
10 <sup>10</sup>	Co <sub>3</sub> O <sub>4</sub> /N-p-MCNTs 1	<10	295 <sup>c</sup>	98
	Co <sub>3</sub> O <sub>4</sub> /N-p-MCNTs 2		245 <sup>c</sup>	78
	Co <sub>3</sub> O <sub>4</sub> /p-MCNTs		370 <sup>c</sup>	114
11 <sup>11</sup>	Yolk-Shell Co-CoO/BC	74	280 <sup>b</sup>	73.3
	Solid Co-CoO/BC		380 <sup>b</sup>	93.1
12 <sup>12</sup>	Co@NC-G-500		390 <sup>b</sup>	125.6
	Co@NC-G-600		340 <sup>b</sup>	116.4
	Co@NC-G-700		270 <sup>b</sup>	73.7
	Co@NC-G-800		290 <sup>b</sup>	82.5
13 <sup>13</sup>	Co@GDY/Co	<10	300 <sup>c</sup>	148
	Co@GDY		400 <sup>c</sup>	222

Electrolyte: (<sup>a</sup>) 0.1 M potassium phosphate pH 7, (<sup>b</sup>) 1 M KOH pH 14, (<sup>c</sup>) 0.1 M KOH pH 13 and (<sup>d</sup>) 0.1 M NaOH pH 13.

- <sup>1</sup> X. Ji, Y. Li, X. Jia, X. Yang, L. Li, Y. Yao, Y. Cheng, X. Zhang, Z. Lu and H. Liu, *J. Electrochem. Soc.* **2019**, 166, H177-H181.
- <sup>2</sup> Q. Xiao, Y. Zhang, X. Guo, L. Jing, Z. Yang, Y. Xue, Y.M Yan and K. Sun, *Chem. Commun.* **2014**, 50, 13019-13022.
- <sup>3</sup> J. Chang, Y. Xiao, M. Xiao, J. Ge, C. Liu, and W. Xing, *ACS. Catal.* **2015**, 5, 6874-6878.
- <sup>4</sup> Y.Q. Gao, H.B. Li and G.W. Yang, *J. Appl. Phys.* **2016**, 119, 034902.
- <sup>5</sup> S.K. Singh, V.M. Dhavale and S. Kurungot, *ACS Appl. Mater. Interfaces* **2015**, 7, 442-451.
- <sup>6</sup> S. Mao, Z. Wen, T. Huang, Y. Hou and J. Chen, *Energy Environ. Sci.* **2014**, 7, 609-616.
- <sup>7</sup> Y. Liang, Y. Li, H. Wang, J. Zhou, J. Wang, T. Regier and H. Dai, *Nature Materials* **2011**, 10, 780- 786.
- <sup>8</sup> C.C. Hou, S. Cao, W.F. Fu and Y. Chen, *ACS Appl. Mater. Interfaces* **2015**, 7, 2412-28419.
- <sup>9</sup> D. Wu, Y. Wei, X. Ren, X. Li, Y. Liu, X. Guo, Z. Liu, A. M. Asiri, Q. Wei and X. Sun, *Adv. Mater.* **2018**, 1705366.
- <sup>10</sup> Z. Huang, X. Qin, G. Li, W. Yao, J. Liu, N. Wang, K. Ithisuphalp, G. Wu, M. Shao and Z. Shi, *ACS Appl. Energy Mater.* **2019**, 2, 4428-4438.
- <sup>11</sup> M. Yang, D. Wu and D. Cheng, *Int. J. Hydrog. Energy* **2019**, 44, 6525-6534.
- <sup>12</sup> X. Wen, X. Yang, M. Li, L. Bai and J. Guan, *Electrochim Acta* **2019**, 296, 830-841
- <sup>13</sup> J. Li, X. Gao, X. Jiang, X.B. Li, Z. Liu, J. Zhang, C.H. Tung and L Z. Wu, *ACS Catal.* **2017**, 7, 5209-5213.

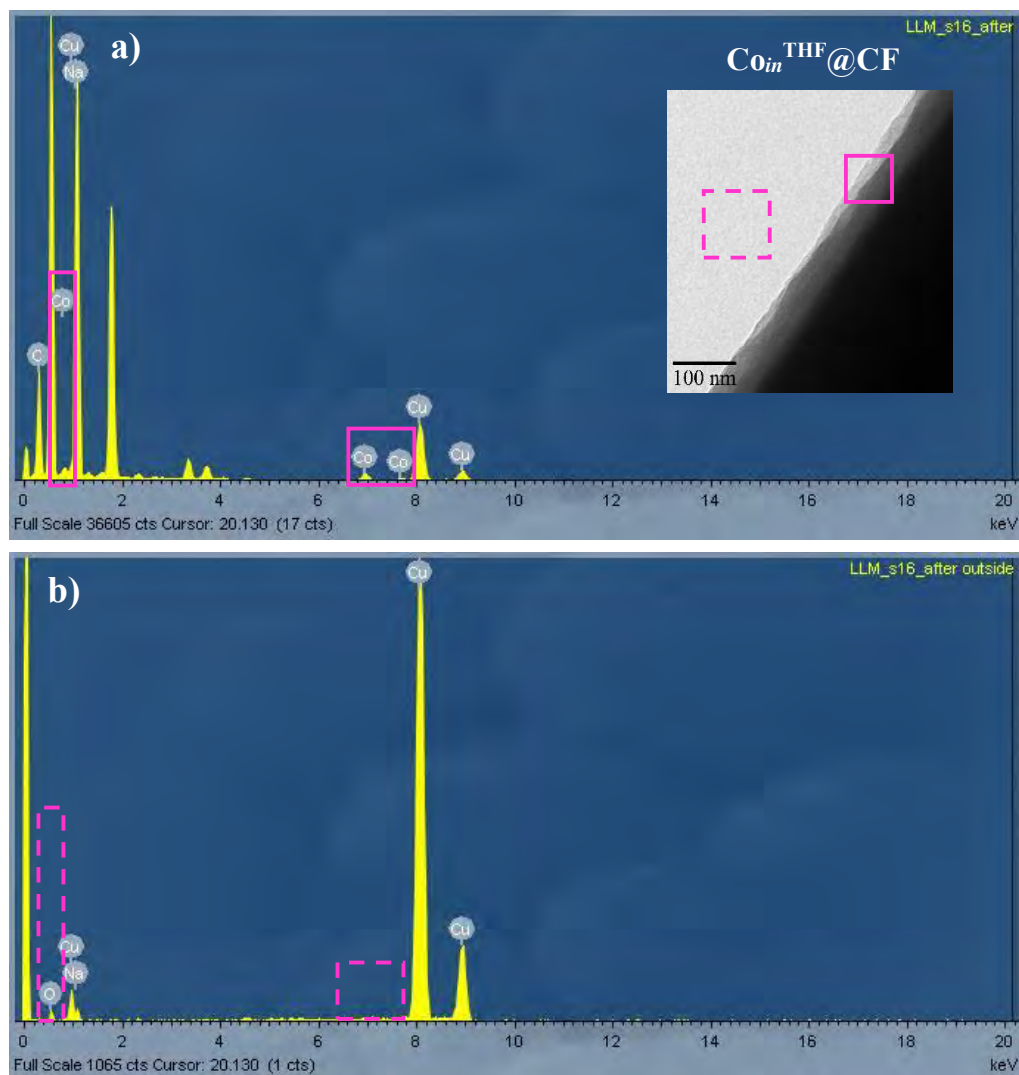


**Figure A1.** TEM/EDX analysis of  $\text{Co}_{in}^{\text{THF}}@CF$  after a 2 h chronoamperometry at 1 V vs. NHE (*i.e.*  $\eta=537$  mV) in 0.1 M NaOH (pH 13). EDX analysis a) over the CF and b) outside the CF.

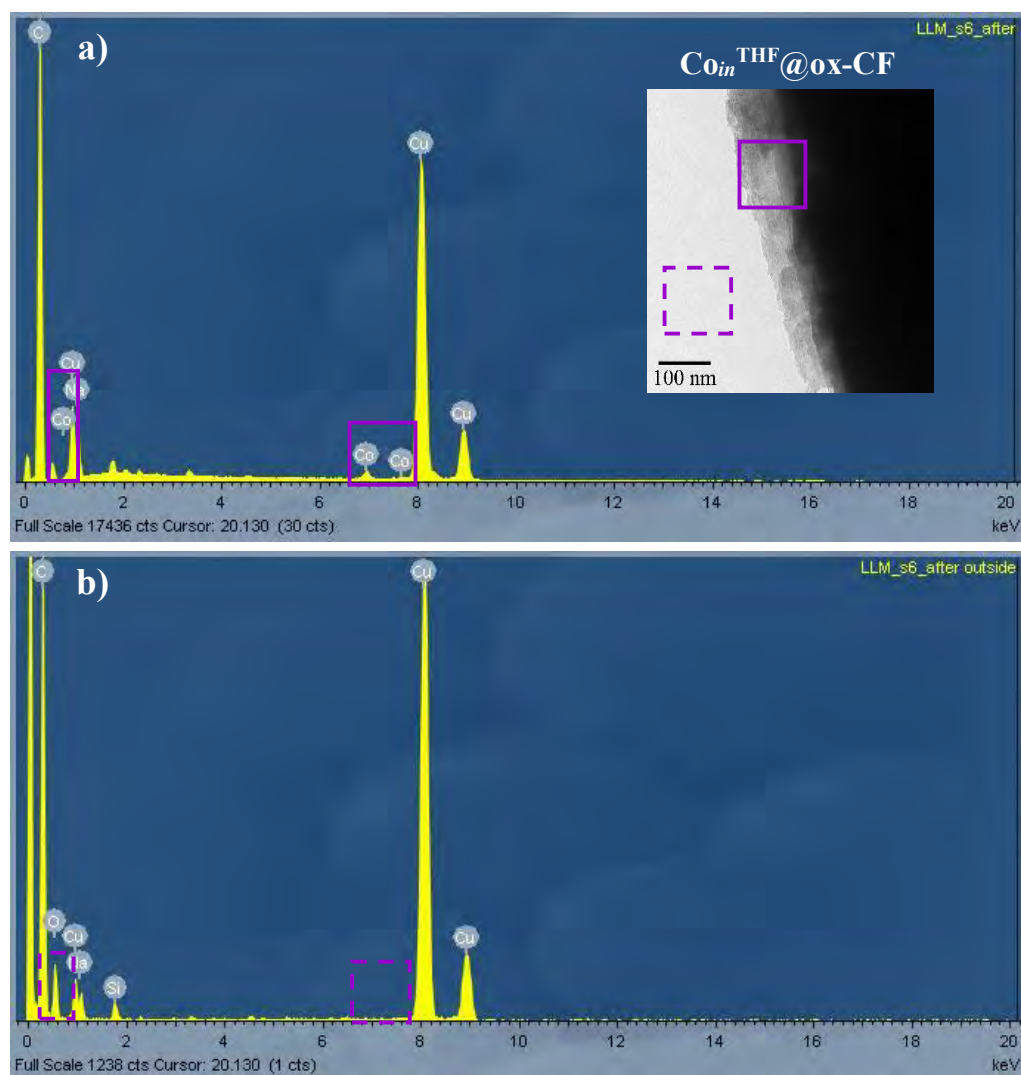


**Figure A2.** TEM/EDX analysis of  $\text{Co}_{in}^{\text{THF}}@ox\text{-CF}$  after a 2 h chronoamperometry at 1 V vs. NHE (*i.e.*  $\eta = 537$  mV) in 0.1 M NaOH (pH 13). EDX analysis a) over the CF and b) outside the CF.

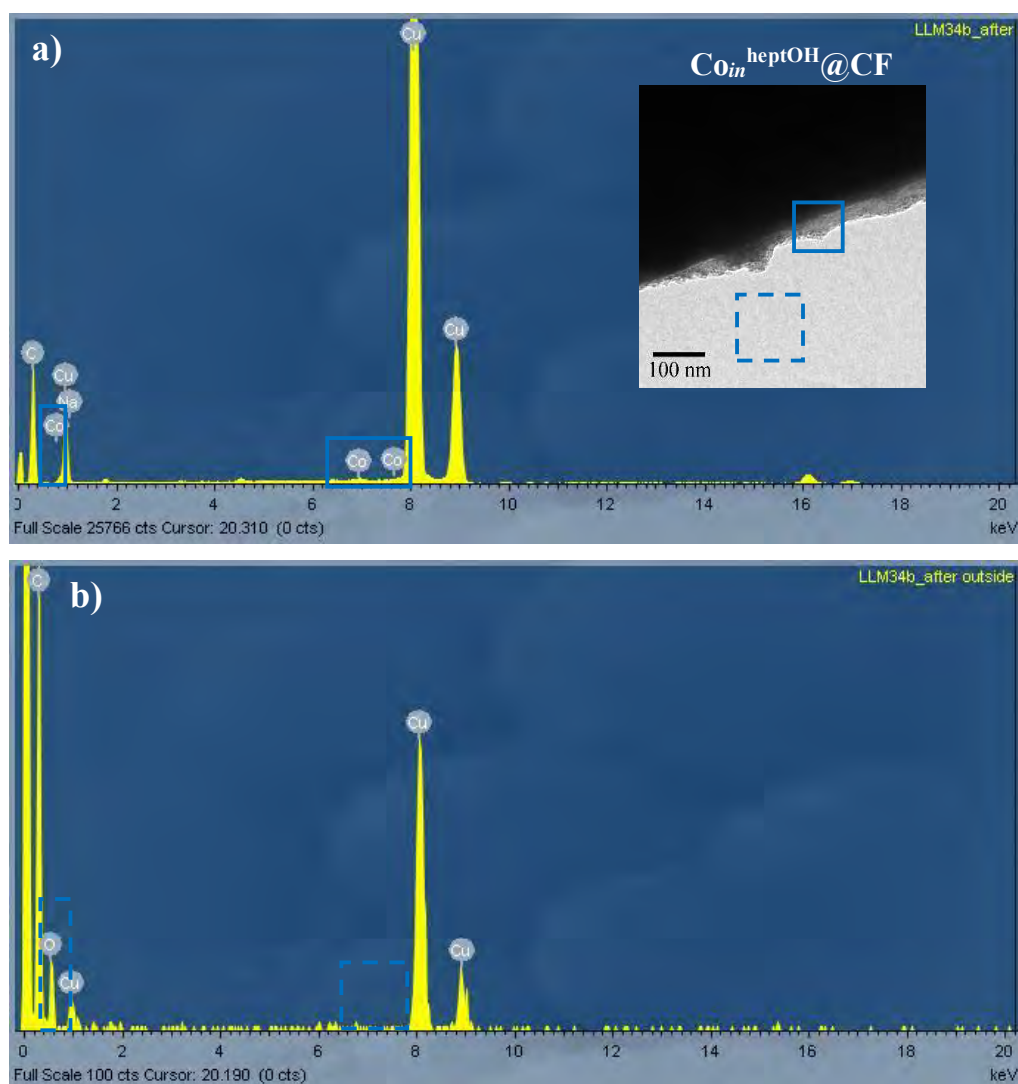


**Figure A3.** TEM/EDX analysis of  $\text{CoIn}^{\text{heptOH}}\text{@CF}$  after a 2 h chronoamperometry at 1 V vs. NHE (*i.e.*  $\eta = 537$  mV) in 0.1 M NaOH (pH 13). EDX analysis a) over the CF and b) outside the CF.

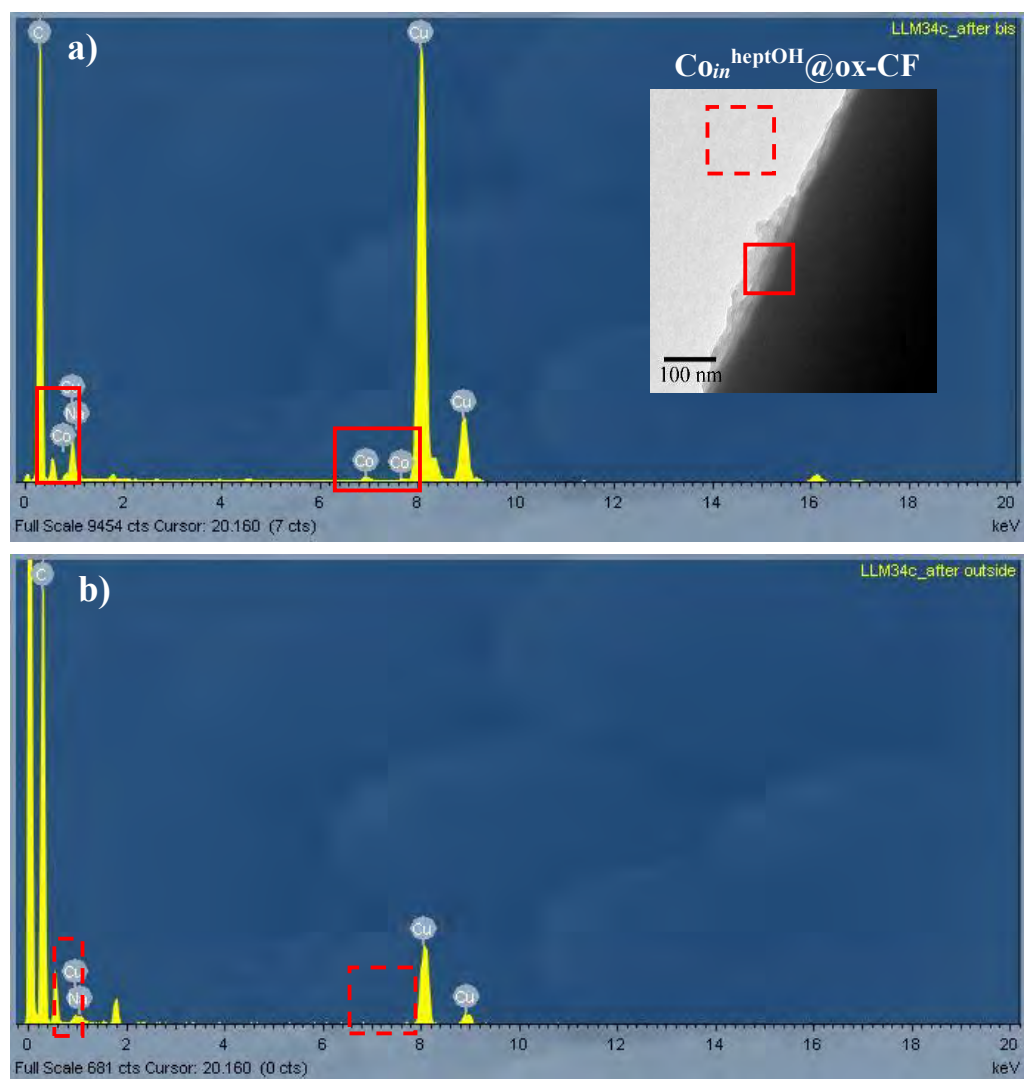


**Figure A4.** TEM/EDX analysis of  $\text{Co}_{in}^{\text{heptOH}}@ox\text{-CF}$  after a 2 h chronoamperometry at 1 V vs. NHE (*i.e.*  $\eta = 537$  mV) in 0.1 M NaOH (pH 13). EDX analysis a) over the CF and b) outside the CF.



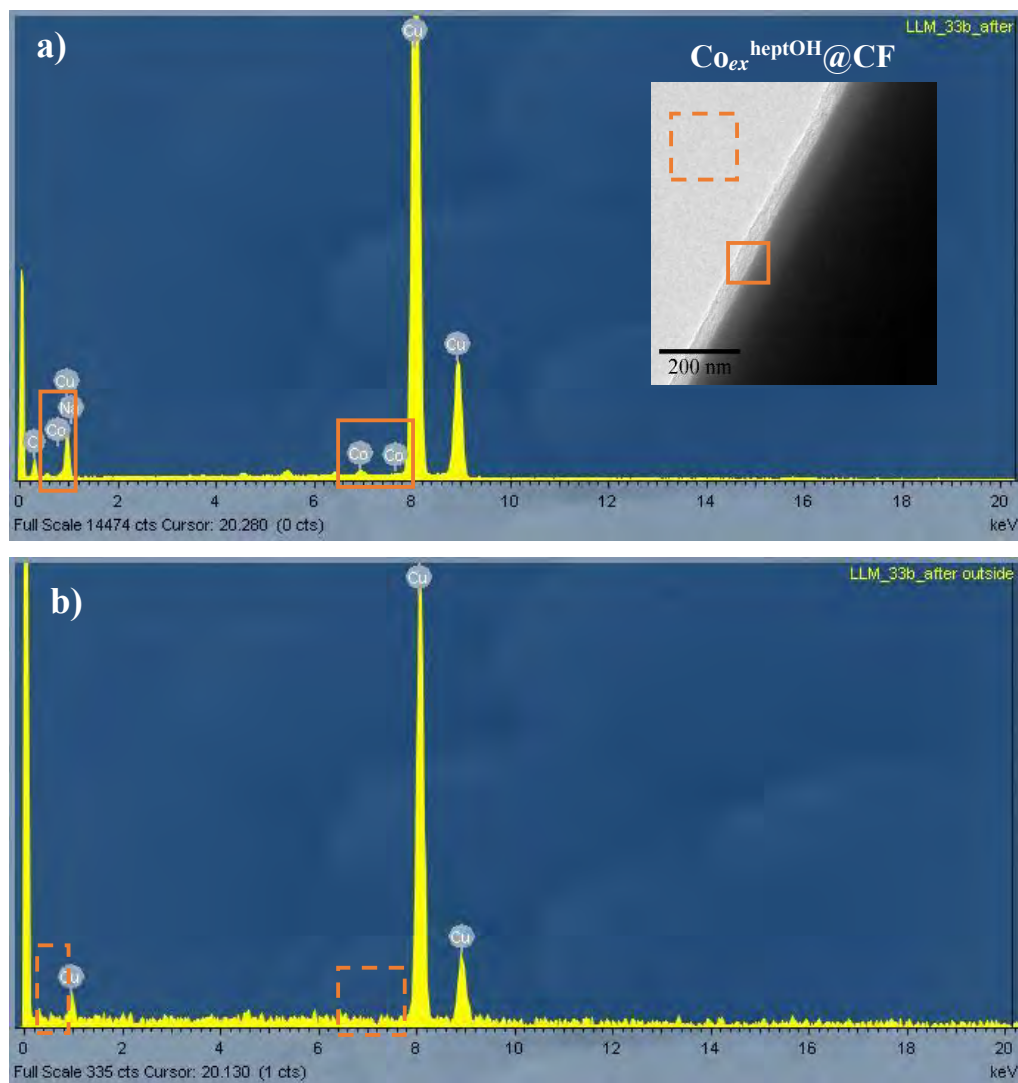


**Figure A5.** TEM/EDX analysis of  $\text{Co}_{\text{ex}}^{\text{heptOH}}\text{@CF}$  after a 2 h chronoamperometry at 1 V vs. NHE (*i.e.*  $\eta = 537$  mV) in 0.1 M NaOH (pH 13). EDX analysis a) over the CF and b) outside the CF.

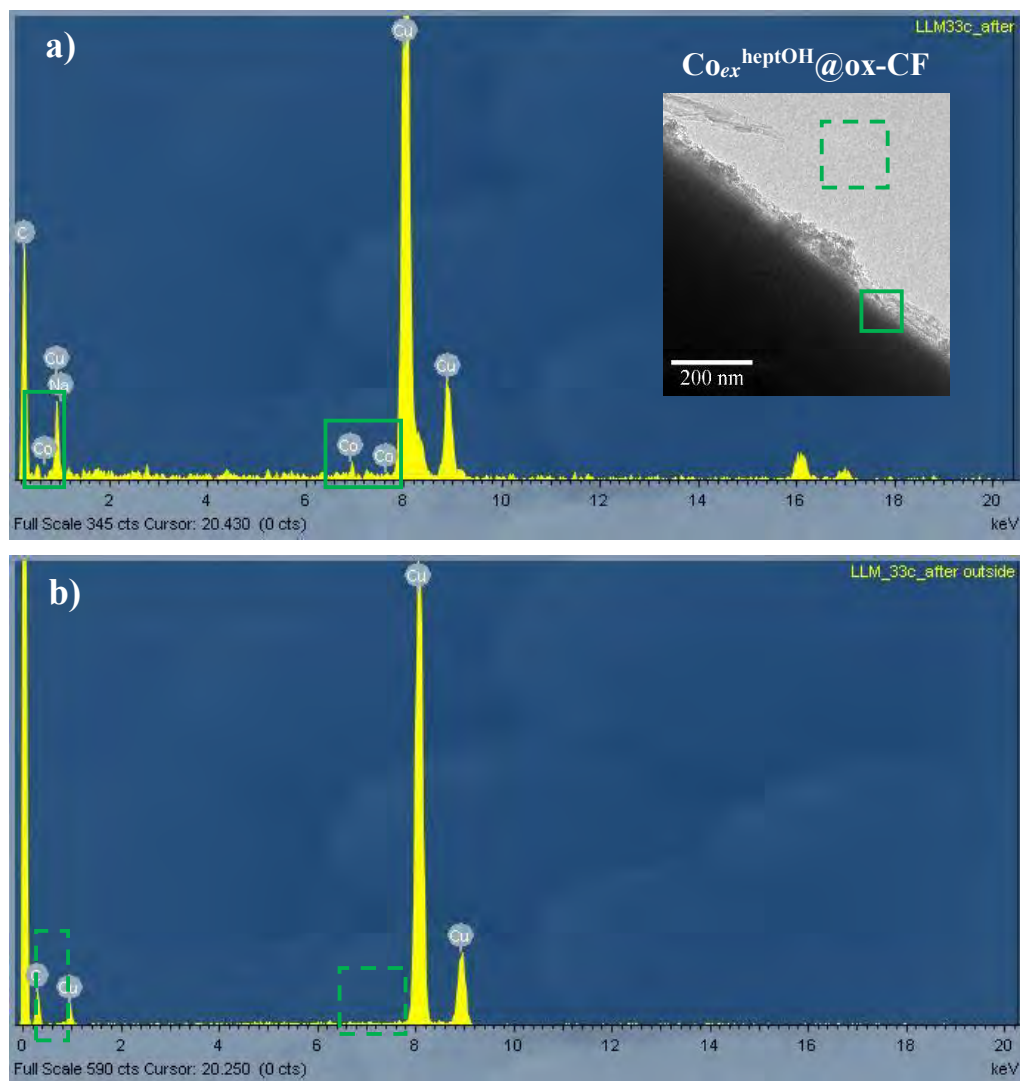


**Figure A6.** TEM/EDX analysis of  $\text{Co}_{ex}^{\text{heptOH}}@ox\text{-CF}$  after a 2 h chronoamperometry at 1 V vs. NHE (*i.e.*  $\eta = 537$  mV) in 0.1 M NaOH (pH 13). EDX analysis a) over the CF and b) outside the CF.

# 6

## **Chapter 6. Bimetallic nanomaterials for electrocatalytic water splitting**

---

*Chapter 6* deals with the electrocatalytic activity of bimetallic nanomaterials in water-splitting. As for the previous monometallic counterparts, these nanomaterials have been prepared by the organometallic approach and characterized by TEM, SEM, XRD, EDX, ICP and XPS techniques to determine their structure and composition. Two different types of bimetallic systems have been studied. In a first part, the results obtained when Ru@Ni-foam materials are tested as electrocatalysts for the OER (and HER to a minor extent) will be described (*Chapter 6A*). The second part will report the synthesis of ligand-capped RuCo NPs (*Chapter 6B*).

---



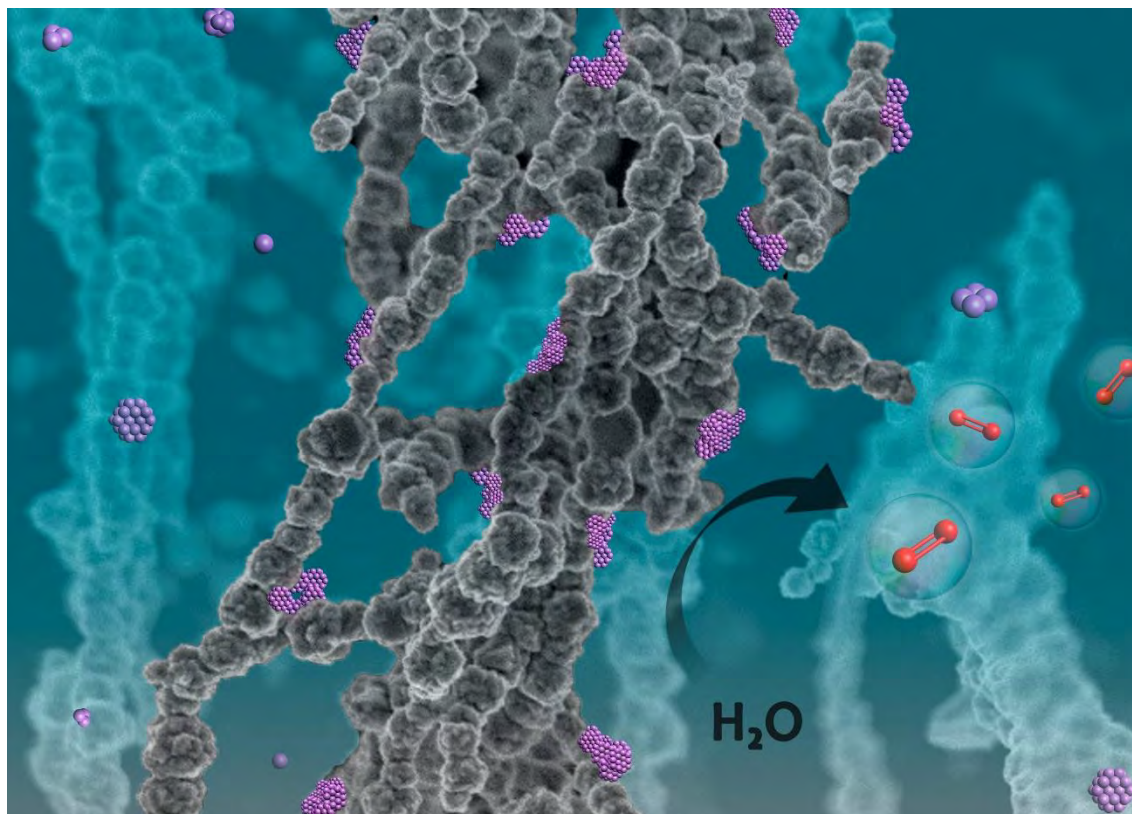
## **TABLE OF CONTENTS**

<b>Chapter 6A. Ru@Ni-foam samples for electrocatalytic water splitting</b> .....	211
<b>6A.1 INTRODUCTION</b> .....	213
<b>6A.2 SYNTHESIS AND CHARACTERIZATION</b> .....	223
<b>6A.2.1 Synthesis of Ni foam-based nanomaterials</b> .....	223
<b>6A.2.2 Transmission electron microscopy (TEM), scanning electron microscopy (SEM) and energy-dispersive X-ray (XRD) analysis</b> .....	224
<b>6A.2.3 X-ray diffraction (XRD) analysis</b> .....	226
<b>6A.2.4 Inductively-coupled plasma (ICP) analysis</b> .....	227
<b>6A.2.5 X-ray photoelectron spectroscopy (XPS) analysis</b> .....	228
<b>6A.3 ELECTROCATALYTIC PERFORMANCE</b> .....	231
<b>6A.3.1 Electrocatalytic performance towards the HER in acidic media</b> .....	231
<b>6A.3.2 Electrocatalytic performance towards the HER in alkaline media</b> .....	234
<b>6A.3.3 Electrocatalytic performance towards the OER in alkaline media</b> .....	235
<b>6A.3.3.1 Fe-incorporation studies</b> .....	237
<b>6A.3.4 Electrocatalytic performance towards the OER in neutral/near-neutral media</b> .....	239
<b>6A.3.5 Spectroelectrochemistry</b> .....	242
<b>6A.4 CONCLUSIONS AND PERSPECTIVES</b> .....	248
<b>6A.5 EXPERIMENTAL SECTION</b> .....	250
<b>6A.6. REFERENCES</b> .....	253
<b>Chapter 6B. Ligand-capped RuCo bimetallic nanoparticles</b> .....	255
<b>6B.1 INTRODUCTION</b> .....	257
<b>6B.2 SYNTHESIS AND CHARACTERIZATION OF RuCo NPs</b> .....	260
<b>6B.2.1 Synthesis of RuCo bimetallic NPs</b> .....	260

<b>6B.2.2 TEM, STEM-HAADF and EDX analysis</b> .....	262
<b>6B.2.2.1 Pyridine-based ligands as stabilizers</b> .....	262
<b>6B.2.2.2 1-heptanol as stabilizer</b> .....	271
<b>6B.2.3 Wide angle X-ray spectroscopy (WAXS)</b> .....	275
<b>6B.3 CONCLUSIONS &amp; PERSPECTIVES</b> .....	277
<b>6B.4 EXPERIMENTAL PART</b> .....	279
<b>6B.5 REFERENCES</b> .....	284

## Chapter 6A. Ru@Ni-foam samples for electrocatalytic water splitting

---



---

Production of oxygen *via* WS using cost-effective metal-based heterogeneous catalysts is highly attractive. In this chapter the organometallic synthesis of a pure Ni-based foam-like nanomaterial and Ru-doped counterparts with different Ru loadings will be reported. The effect of the Ru-doping has been mostly studied in electrocatalytic OER but some insights into the HER will be also assessed. A detailed structural and compositional analysis of these nanomaterials allow to draw a correlation with their OER electrocatalytic activity and thus to extract valuable information about the influence of the metal–metal interface interactions in bimetallic systems.

This work was done in collaboration with Dr. L. Peres (Postdoctoral researcher, LCC-CNRS), who synthesized and characterized the Ni-foam based nanomaterials. My contribution has consisted in their electrocatalytic assessment by carrying out electrochemical and spectroelectrochemical studies.

---





## **6A.1 INTRODUCTION**

The OER is a kinetically unfavorable process as  $4\text{H}^+$  and  $4\text{e}^-$  have to be extracted from two water molecules in addition to the formation of an oxygen-oxygen double bond. Highly active and efficient electrocatalysts are thus needed. Ru and Ir oxides are the state-of-the-art OER electrocatalysts in acid media,<sup>1,2</sup> but their scarcity and high cost prevent their use in practical large-scale  $\text{H}_2$  production devices based on WS. First row transition metal Ni and its oxides have been used alternatively as active electrocatalysts towards OER in alkaline media, increasing the cost-effectivity of the  $\text{H}_2$  production due to their high abundance on Earth and lower price.

The high electrocatalytic activity of Ni-based anodes has been attributed to Fe incorporation into the Ni structure. The close position of Ni and Fe in the periodic table makes easy the formation of NiFe alloys. The role of Fe incorporation has been widely studied during last decades. Corrigan *et al.* first studied the effect towards the OER of intentional incorporation of Fe into thin nickel oxide film electrodes in KOH electrolytes (Fig. 1a).<sup>3</sup> Even 1 ppm iron caused an increase in the oxygen evolution current of the nickel electrodes. In addition, the effect of the presence of iron in the electrolyte was evidenced by a decrease in the oxygen evolution overpotential during successive potential cycling (Fig. 1b). The incorporation of iron onto the Ni thin film was revealed by atomic adsorption spectrometry. In contrast, in the absence of iron in the electrolyte, the overpotential increased during the process (Fig. 1b). The same authors also confirmed a higher effect of iron in thinner films, in which the fraction of incorporated Fe with respect to the Ni content was higher, obtaining in this case a decrease in the overpotential over 100 mV. It appears that the key variable is the fraction of iron in the active material. Two different hypotheses were given: Fe could provide more favorable sites for the adsorption of intermediate species or Fe could improve the conductivity of the semiconducting oxide.

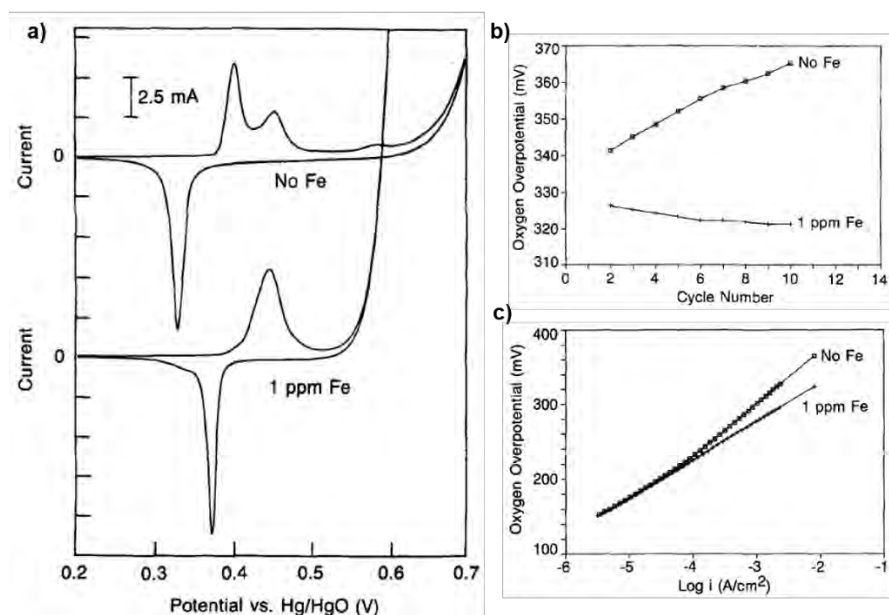


**Figure 1.** CVs of the effect of iron in the electrolyte onto a Ni electrode (a), effect of iron in the electrolyte on the OER overpotential of Ni oxide electrodes (b) and effect of iron in the electrolyte on the Tafel plots for OER in Ni oxide thin films (c). Extracted from ref. 3.

In that direction, several studies on the effect of Fe into Ni-based thin films have been reported. In 2010, D. Pletcher and co-workers tested the catalytic activity of different mixed electrodeposited films of Ni hydroxide with other transition metals, observing that the OER activity increases with the series  $\text{Cu(II)} < \text{Mn(II)} < \text{Cr(II)} < \text{Co(II)} < \text{Fe(II)}$ , therefore with the  $\text{NiFe(OH)}_2$  material showing the best performance.<sup>4</sup> Also, Boettcher *et al.* reported a  $\text{Ni}_{0.9}\text{Fe}_{0.1}\text{O}_x$  thin film, which was found to be the most active WO catalyst in basic media among  $\text{NiO}_x$ ,  $\text{CoO}_x$ ,  $\text{Ni}_y\text{Co}_{2-y}\text{O}_x$ ,  $\text{IrO}_x$ ,  $\text{MnO}_x$  and  $\text{FeO}_x$ , yielding  $\eta_{10} = 336$  mV and a Tafel slope of 30 mV/dec.<sup>5</sup> However, some studies revealed that while a small amount of Fe on the Ni oxide enhanced the OER activity, larger additions reduced the activity, obtaining lower activities for those systems containing mostly Fe than those containing Ni alone, confirming the detrimental role of Fe in large quantities (Fig. 2).<sup>4,6</sup>

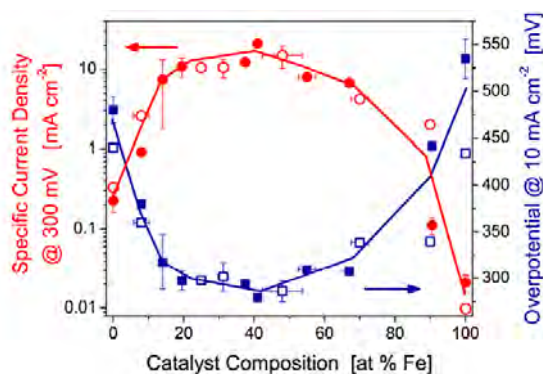


**Figure 2.** Specific current density at 300 mV overpotential and overpotential at 10 mA/cm<sup>2</sup> towards the OER in 0.1 M KOH as a function of composition of the Ni-Fe films. Extracted from ref. 6.

In addition to mixed Ni-Fe nanocatalysts to obtain improved OER, S. H. Boettcher *et al.* presented also a layered Ni(OH)<sub>2</sub> film deposited on a GC-RDE that showed also increasing activities with each CV cycle (Fig. 3a),<sup>7</sup> confirming by XPS the Fe incorporation from the electrolyte into the Ni(OH)<sub>2</sub> film after only 5 CV cycles (Fig. 3b, purple line). In this work it was proved that Fe incorporation also takes place in the absence of applied potential, even if to a lower extent (Fig. 3b, blue line). In contrast, after 300 CV cycles in Fe-free electrolyte, the film shows no detectable Fe 2p XPS peak (Fig. 3b, green line) and even decreased OER activity.

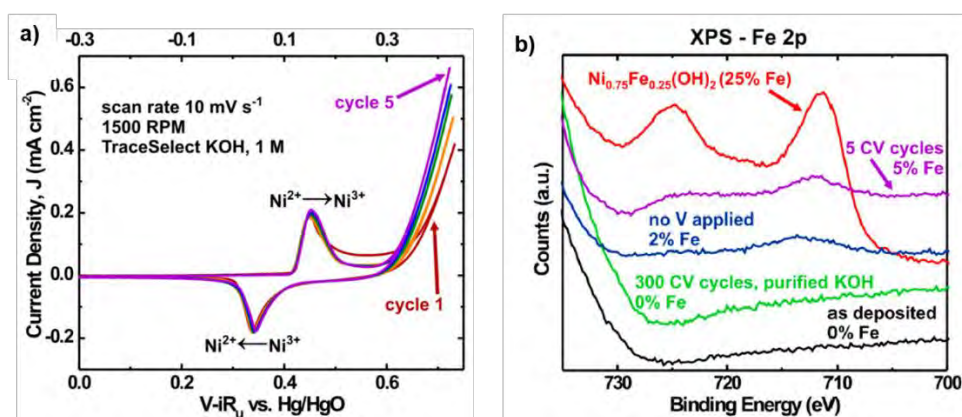


**Figure 3.** Successive cyclic voltammogram of Ni(OH)<sub>2</sub> film deposited on a GC-RDE (a). XPS Fe 2p spectra for Ni(OH)<sub>2</sub>/NiOOH thin films after 5 CV cycles in non-purified KOH (purple), 12 min in non-purified KOH (*i.e.* containing traces of iron) without applied potential (blue), and 300 CV cycles in purified KOH (green), and a film containing no Fe (black) and a film with 25 % co-deposited Fe (red) are used as references (b). Extracted from ref. 7.

Supporting the hypothesis from Corrigan *et al.*, T. Bell and co-workers supported experimental results on electrodeposited NiFe oxyhydroxides ( $\text{Ni}_{1-x}\text{Fe}_x\text{OOH}$ ) by DFT+U calculations, obtaining that Fe(III) in  $\gamma\text{-Ni}_{1-x}\text{Fe}_x\text{OOH}$  exhibits a significantly lower overpotential than  $\text{Ni}^{3+}$  cations in either  $\gamma\text{-Ni}_{1-x}\text{Fe}_x\text{OOH}$  or  $\gamma\text{-NiOOH}$ , confirming that Fe rather than Ni constitutes the active site for OER in mixed Fe-Ni oxyhydroxides.<sup>8</sup>

In addition to increasing OER intensities with Fe incorporation, iron could also change the Ni environment.<sup>7</sup> The usually observed redox waves before the onset of the OER in Ni-based catalysts are attributed to the oxidation from  $\text{Ni(OH)}_2$  to  $\text{NiOOH}$ , being well accepted that  $\text{NiOOH}$  is the active species towards OER. Differences in the  $\text{Ni(OH)}_2/\text{NiOOH}$  redox potentials are also observed with different Fe content, observing a shift to higher potentials as more Fe is incorporated, following a linear correlation.<sup>6</sup> This means that a higher potential is needed to form the  $\text{NiOOH}$  active species, being the electrochemical oxidation of  $\text{Ni(OH)}_2$  diffculted by the presence of Fe (Fig. 4). A similar behaviour was found by X. Duan *et al.* in a 3D film of vertically aligned NiFe-layered double hydroxide (NiFe-LDH) NPs loaded on Ni-foam synthesized by a hydrothermal method using Ni and Fe nitrates as metal sources and urea as precipitant.<sup>9</sup>

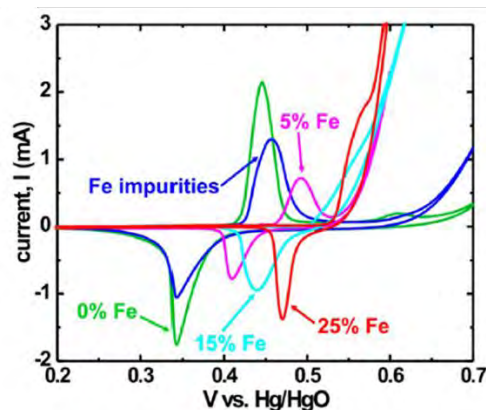


**Figure 4.** CV scans of  $\text{Ni-Fe(OH)}_2/\text{Ni-FeOOH}$  films with different Ni-Fe composition deposited on IDA (interdigitated arrays) electrodes. Extracted from ref. 7.

The catalytic behaviour of Ni-based films can also depend on the presence of different Ni-phases. T. Bell *et al.* studied the aging of Ni electrodes in alkaline electrolytes (*i.e.* electrode soaked into the electrolyte without an applied potential), observing also an anodic shift in the  $\text{Ni(II)}/\text{Ni(III)}$  redox wave and an increase in the OER activity (Fig. 5).<sup>6</sup>

Contrary to Boettcher *et al.*,<sup>7</sup> T. Bell and co-workers attributed these changes to the transformation of the  $\alpha$ -Ni(OH)<sub>2</sub>/ $\gamma$ -NiOOH couple to the ordered and compact  $\beta$ -Ni(OH)<sub>2</sub>/ $\beta$ -NiOOH pair, as they obtained comparable Fe concentrations in freshly and aged Ni films.<sup>6</sup> They confirmed that although Fe incorporation cannot be disregarded, the dramatic change in CV parameters during aging cannot be due only to a change in Fe content. In fact, Raman spectroscopy confirmed a change from  $\gamma$ -NiOOH to  $\beta$ -NiOOH as a consequence of Fe incorporation, being the  $\beta$ -phase the preferred one for the OER catalysis. In contrast to these results, Y. Yan *et al.* demonstrated the utilization of highly nanostructured  $\alpha$ -Ni(OH)<sub>2</sub> hollow spheres with better OER performance than  $\beta$ -Ni(OH)<sub>2</sub>.<sup>10</sup>

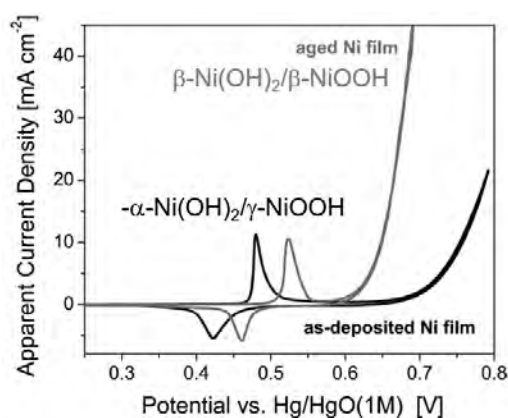


**Figure 5.** Comparison of CVs for as-deposited and aged Ni films in 0.1 M KOH attributed to Ni phase changes. Extracted from ref. 6.

On the other hand, some studies on the changes in conductivity of Ni-based thin films due to Fe incorporation have been performed. Conductivity experiments done by Boettcher and co-workers<sup>7</sup> confirmed the hypothesis of Corrigan *et al.*,<sup>3</sup> obtaining improved conductivity upon Fe incorporation (Fig. 6). Low conductivities for reduced films were found, independently of Fe concentration, which increased upon Ni oxidation. NiOOH under Fe-free has  $\sigma \approx 0.1$ - $0.2$  mS/cm, whereas samples with 5%-25% Fe have more than one order of magnitude higher conductivity,  $\sigma \approx 3.5$ - $6.5$  mS/cm. Fe incorporation at normal impurity level in KOH leads to  $\sigma \approx 2.5$  mS/cm (Fig. 6).<sup>7</sup>

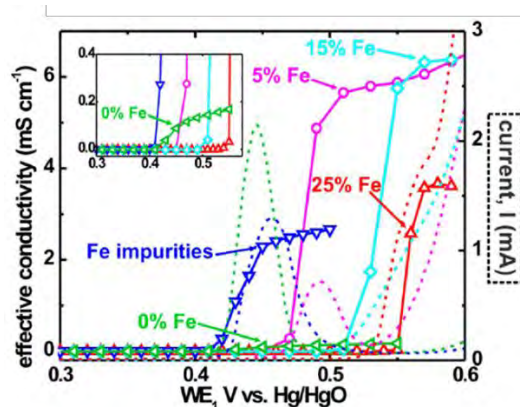


**Figure 6.** Conductivity experiments for  $\text{Ni}_{1-x}\text{Fe}_x(\text{OH})_2/\text{Ni}_{1-x}\text{Fe}_x\text{OOH}$  films with different Fe contents. Extracted from ref. 7.

As described above, most of the studies on the effect of the activation of Ni-based electrocatalysts have been performed using thin films. More recently, Ni-based NPs have also been explored. Given their high surface area and number of available active sites some highly active OER electrocatalysts have also been reported. In 2019, A. J. Wang *et al.* synthesized mesoporous spinel NiFe oxide cubes (60 nm) following the coprecipitation methodology followed by a pyrolysis treatment from NiHCF at different temperatures (Fig. 7a and 7b).<sup>11</sup> The optimum pyrolysis temperature for obtaining the NiFeO NCs in air was 400 °C, obtaining the lowest  $\eta_{10}$  of 240 mV in 1 M KOH, compared to other pyrolysis temperatures, NiO and  $\text{Fe}_3\text{O}_4$  NPs (See table in Fig 7c). The Tafel slopes follow a decreasing order as follows: NiO >  $\text{Fe}_3\text{O}_4$  > NiFeO-300 > NiFeO-500 > NiFeO-400 (Fig. 7c), confirming the improved kinetics for NiFeO-400.

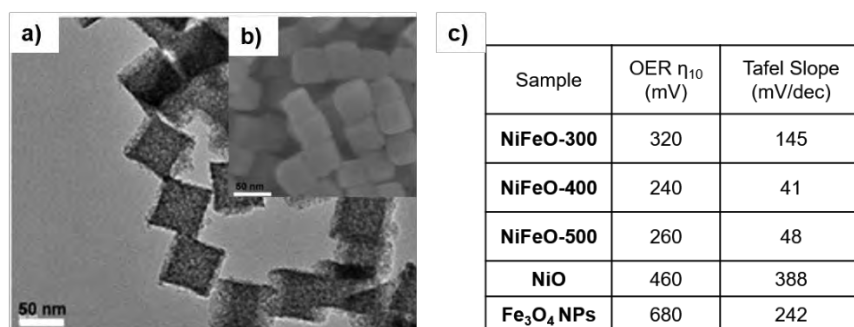


**Figure 7.** TEM (a) and SEM (b) images of NiFeO-400. Electrochemical data of different NiFe NC in 1.0 M KOH (c). Extracted from ref. 11.



J. Chen and co-workers reported the synthesis of different 3D Ni-Fe based nanocatalysts from thermal decomposition of organometallic complexes, namely NiO<sub>x</sub>-NiO<sub>x</sub>/FeO<sub>x</sub> core-mixed shell NPs (16.8 ± 2.0 nm) (Fig. 8a), NiO<sub>x</sub>/FeO<sub>x</sub> alloy NPs (9.4 ± 1.7 nm) (Fig. 8b) and FeO<sub>x</sub>-NiO<sub>x</sub> core-shell NPs (9.8 ± 1.6 nm) (Fig. 8c).<sup>12</sup> The NiO<sub>x</sub>-NiO<sub>x</sub>/FeO<sub>x</sub> core-mixed shell NPs exhibited the best performance with  $\eta_{10} = 320$  mV. The Ni redox peaks also differ from one sample to another, obtaining the oxidation wave of Ni(OH)<sub>2</sub> to NiOOH at the lowest potential for NiO<sub>x</sub> NPs, whereas NiO<sub>x</sub>-NiO<sub>x</sub>/FeO<sub>x</sub> core-mixed shell NPs show the highest potential to achieve this conversion, in agreement with previous studies stating that incorporation of Fe into NiO<sub>x</sub> thin films hampers the transformation of Ni(OH)<sub>2</sub> to NiOOH (Fig. 8d).

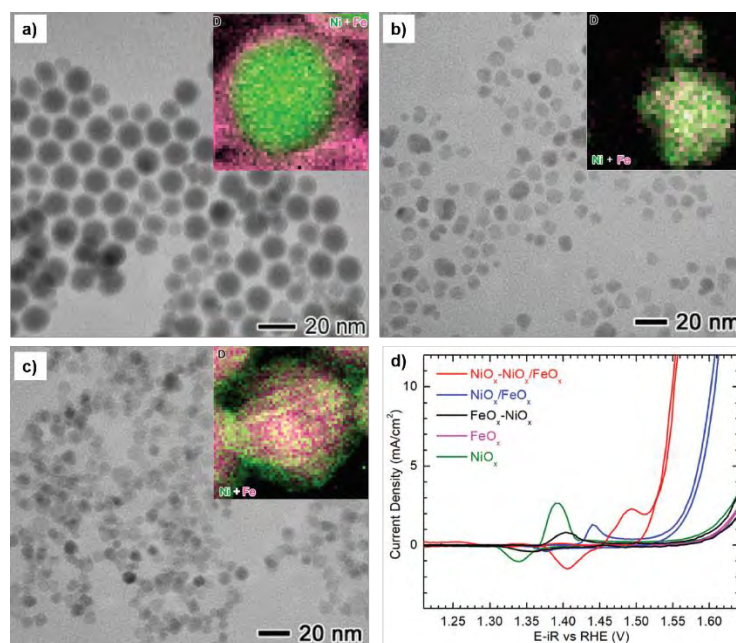


**Figure 8.** TEM image and EELS (electron energy loss spectrometry) mapping of NiO<sub>x</sub>-NiO<sub>x</sub>/FeO<sub>x</sub> core-mixed shell NPs (a), NiO<sub>x</sub>/FeO<sub>x</sub> alloy NPs (b) and FeO<sub>x</sub>-NiO<sub>x</sub> core-shell NPs (c). CV profiles of the different catalysts in 1 M KOH at a scan rate of 10 mV/s (d). Extracted from ref. 12.

Despite all the efforts described above, highly active Ni(Fe)-based OER electrocatalysts presenting higher current densities, lower overpotentials and stability in neutral/acid mediums are still missing. One strategy could be to introduce other elements into the Ni(Fe) materials. Having in mind that and the fact that Ru is, together with Ir, the state-of-the-art OER catalyst, Ru-doping onto Ni(Fe) materials with the purpose of enhancing their OER activity has emerged in recent years. The addition of low amounts

of Ru into these materials would allow obtaining more economic materials than the existing pure  $\text{RuO}_2$  ones. Several studies confirmed the improvement of the electrocatalytic activity of Ni-based nanomaterials by Ru-doping.

The high OER and HER activities have been widely attributed to synergistic effects between Ru and Ni. For alkaline OER, Qiao *et al.*<sup>13</sup> attributed this improvement due to the coupling between  $\text{NiOOH}$ , which favours the dissociation of water molecules,<sup>14</sup> and  $\text{RuO}_2$ , which can dissociate  $\text{OH}^-$  due to the strong affinity of the bridging oxygen for H and of the neighbouring coordinative unsaturated Ru for O.<sup>15,16</sup> Thus, in a  $\text{RuO}_2/\text{NiOOH}$  interface, dissociation of  $\text{H}_2\text{O}$  (Fig. 9a, i) and dissociation of  $\text{OH}^-$  (Fig. 9a, ii) can be coupled to produce the  $\text{OOH}^*$  intermediate, which can be further deprotonated to release molecular  $\text{O}_2$  (Fig. 9a, iii). In addition, X. Lu and co-workers hypothesized that Ru can transfer electrons between the substrate and the intermediate species and facilitate the O-O bond formation in OER at basic pH.<sup>17</sup>

For HER in alkaline conditions, Qiao *et al.*<sup>13</sup> proposed the formation of an *in situ* Ru/NiO interface considering  $\text{RuO}_2$  reduction under reductive conditions. Due to the strong affinity of  $\text{OH}^-$  for the NiO surface,<sup>14</sup> NiO can promote the dissociation of water into  $\text{OH}^-$  and  $\text{H}^*$ , being the latest rapidly adsorbed by nearby Ru atoms and recombined into  $\text{H}_2$  (Fig. 9b). This synergistic mechanism was also supported by X. Lu and co-workers.<sup>17</sup>

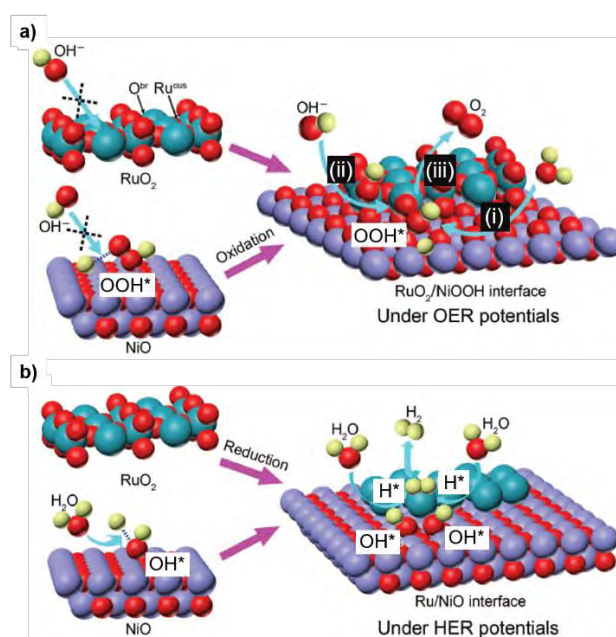


**Figure 9.** Schematic illustration of potential-induced synergy between  $\text{RuO}_2$  and NiO for enhanced OER (a) and HER (b) in alkaline conditions. Extracted from ref. 13.



Finally, Z. Tang *et al.*<sup>18</sup> and Lu *et al.*<sup>17</sup> attributed the improved HER electrocatalytic activity of mixed Ru/Ni nanoparticulate systems to the chemical coupling of Ru with Ni, resulting in a down-shift of the d-band center, leading to a lowered adsorption energy of the reaction substrates and/or intermediates. These studies were supported by a previous work from Liu *et al.* in which they discovered that a Ru modulation can facilitate the desorption of H<sub>2</sub> to achieve a moderate hydrogen adoption energy ( $\Delta G_{H^*}$ ), boosting HER.<sup>19</sup>

All the studies presented above agree with the fact that the Ru-doping of Ni-based nanocatalysts lead to lower charge-transfer resistance than their monometallic counterparts, obtaining faster electron transfer processes in bimetallic systems. In addition, higher ECSA values are also observed for Ru-Ni systems, confirming the increased intrinsic activity of these nanomaterials. These results are also supported by L. Feng *et al.*<sup>20</sup> and Y. Gong *et al.*<sup>21</sup> A summary table containing the most relevant HER and OER electrocatalytic activity data for these systems is presented below (Table 1).

**Table 1.** Summary of HER and OER electrocatalytic performance of different Ni-Ru based catalysts.

Ref.	Catalyst	HER $\eta_{10}$ (mV)	HER Tafel slope (mV/dec)	OER $\eta_{10}$ (mV)	OER Tafel slope (mV/dec)
13 <sup>a</sup>	RuO <sub>2</sub> /NiO/NF	22	31.7	250	50.5
	RuO <sub>2</sub> /NF	43	55.4	283	53.4
	IrO <sub>2</sub> /NF	-	-	311	55.6
	NiO/NF	189	82.8	333	61
	Bare NF	281	103.2	384	65.5
	PtC/NF	-	30.1	-	-
17	Ru <sub>1</sub> Ni <sub>1</sub> -NCNF	35 <sup>a</sup> /23 <sup>b</sup>	30 <sup>a</sup> /29 <sup>b</sup>	290 <sup>a</sup>	-
	Ru <sub>1</sub> Ni <sub>1</sub> -NCNF-700	48 <sup>a</sup>	30 <sup>a</sup>	406 <sup>a</sup>	-
	Ru <sub>1</sub> Ni <sub>1</sub> -NCNF-800	-	-	-	-
	Ru <sub>1</sub> Ni <sub>1</sub> -NCNF-900	83 <sup>a</sup>	-	327 <sup>a</sup>	-
	Ru <sub>2</sub> Ni <sub>1</sub> -NCNF	49 <sup>a</sup>	-	380 <sup>a</sup>	-
	Ni <sub>2</sub> Ru <sub>1</sub> -NCNF	186 <sup>a</sup>	-	320 <sup>a</sup>	-
	Ru-NCNF	45 <sup>a</sup> /50 <sup>b</sup>	35 <sup>a</sup> /41 <sup>b</sup>	-	-
	Ni-NCNF	233 <sup>a</sup> /389 <sup>b</sup>	79 <sup>a</sup> /175 <sup>b</sup>	340 <sup>a</sup>	-
Pt/C	37 <sup>a</sup> /17 <sup>b</sup>	30 <sup>a</sup> /28 <sup>b</sup>	-	-	
18 <sup>a</sup>	Ni/CNS	204.2	114.2	451	166.8
	Ni@Ru/CNS-5%	65	107.2	391	155.6
	Ni@Ru/CNS-10%	20.1	87.3	356	89.6
	Ni@Ru/CNS-15%	23.5	93.8	365	123.5
	RuO <sub>2</sub>	-	-	316	78.9
	Pt/C	13.3	75.8	-	-
20 <sup>d</sup>	Ru/Ni <sub>3</sub> N-Ni	53	32.4	200	56.4
	Ni <sub>3</sub> N/Ni	180	178	330	70.4
	RuO <sub>2</sub>	110	88.1	315	68.2
	Ru	96	71.7	364	76.5
21 <sup>a</sup>	Ru-NiFe-MOF/NF	-	-	205	50
	NiFe-MOF/NF	-	-	232	61
	Ru-Ni <sub>1</sub> Fe <sub>3</sub> -MOF/NF	-	-	217	55
	Ru-Ni <sub>3</sub> Fe <sub>1</sub> -MOF/NF	-	-	209	54

Electrolyte: <sup>a</sup> 1.0 M KOH, <sup>b</sup> 0.5 M H<sub>2</sub>SO<sub>4</sub> and <sup>d</sup> non-specified alkaline electrolyte.

In summary, the real role of Fe in Ni-based OER catalysts is still a matter of controversy. Also, most of the Fe incorporation studies have been performed on thin films and not on Ni-based NPs. In addition, studies on bimetallic Ni-Ru nanocatalysts for WS are still scarce. Thus, in *Chapter 6A* we propose the synthesis of Ru NPs onto a Ni-foam-like structure. The effect of different percentages of Ru-doping onto their HER and OER electrocatalytic activity will be analysed.

## 6A.2 SYNTHESIS AND CHARACTERIZATION

### 6A.2.1 Synthesis of Ni foam-based nanomaterials

The Ru-doped Ni-based nanomaterials were synthesized by the organometallic approach<sup>22</sup> following a two-step procedure. First, a Ni foam was produced by hydrogenation of the  $[\text{Ni}(\text{COD})_2]$  complex (COD = 1,5-cyclooctadiene), in ethanol/THF (10 % v/v), under 3 bar of  $\text{H}_2$  at 70 °C.<sup>23</sup> Second, Ru NPs were grown on-top of the pre-synthesized Ni foam by reduction of the  $[\text{Ru}(\text{Me-allyl})_2(\text{COD})]$  (Me-allyl = 2-methylallyl, COD = 1,5-cyclooctadiene) complex as a Ru source. First, the Ni foam was mixed with a THF solution of the Ru precursor for 3 days at room temperature under stirring. Then, the growth of the metallic Ru NPs directly onto the surface of the Ni foam was induced by the reductive decomposition of the impregnated Ru precursor under 3 bar of  $\text{H}_2$  at 50 °C (Fig. 11). For comparative purposes, this second step was performed at different Ru loadings (1, 5 and 10 wt%, theoretical values) in order to get a series of samples of different composition, named as **Ni-foam**, **Ru1@Ni-foam**, **Ru5@Ni-foam** and **Ru10@Ni-foam**, respectively.

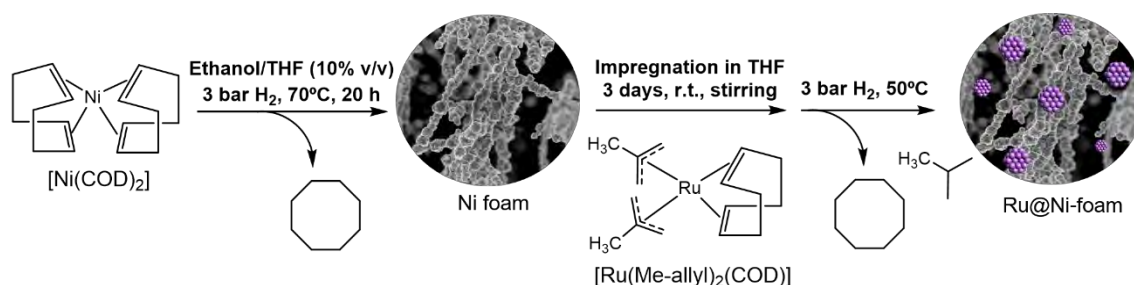


**Figure 11.** Organometallic synthesis of the Ru@Ni-foam nanomaterials.

The materials were passivated under air exposure before the electrocatalytic tests. A detailed structural (TEM, SEM) and compositional (XRD, ICP, XPS) analysis allowed to draw a correlation with the observed electrocatalytic activity and spectroelectrochemical data of the tested nanomaterials, and then to extract valuable insights about the influence of the Ru loading on the electrocatalytic activity towards the HER/OER.

### 6A.2.2 Transmission electron microscopy (TEM), scanning electron microscopy (SEM) and energy-dispersive X-ray (EDX) analysis

The as-prepared nanomaterials were dispersed in isopropyl alcohol before deposition onto a carbon-covered copper TEM grid. TEM and SEM images of **Ni-foam** revealed the presence of particles of *ca.* 100 nm of thickness that result from the alignment of smaller particles (Fig. 12a and 12b). These images also show the foam-like character of this nanomaterial, indicating it is porous, which is of interest for catalysis due to higher surface area. In the Ru-doped Ni-foam samples, the presence of worm-like superstructures made of smaller particles was also assessed by TEM and SEM analysis. In these cases, the **Ni-foam** nanomaterial serves as support for the Ru NPs. In the TEM images recorded for **Ru1@Ni-foam**, if we can suspect the presence of a few ones, there is no clear evidence of the deposition of Ru NPs over the Ni-foam probably as the result of their ultra-small size due to the very low Ru loading in this case (Fig. 2c, red arrows). However, EDX analysis (Fig. 12e) confirmed the presence of both Ni and Ru in the nanomaterial, attesting that the Ru deposition happened well onto the Ni-foam. If NPs are present, they are probably too small (<1 nm) to be visible in the TEM images. Another explanation could be that the Ru is present under the form of small Ru islands or as a thin layer over the Ni foam. In contrast, TEM images of **Ru5@Ni-foam** and **Ru10@Ni-foam** samples reveal the presence of sponge-like nanostructures that can be explained by the aggregation of small Ru NPs onto the Ni foam (Fig. 12f and 12i, red arrows). This was confirmed by EDX mapping that shows for both samples the presence of well-dispersed Ru over the Ni foam surface (Fig. 12h and 12k).

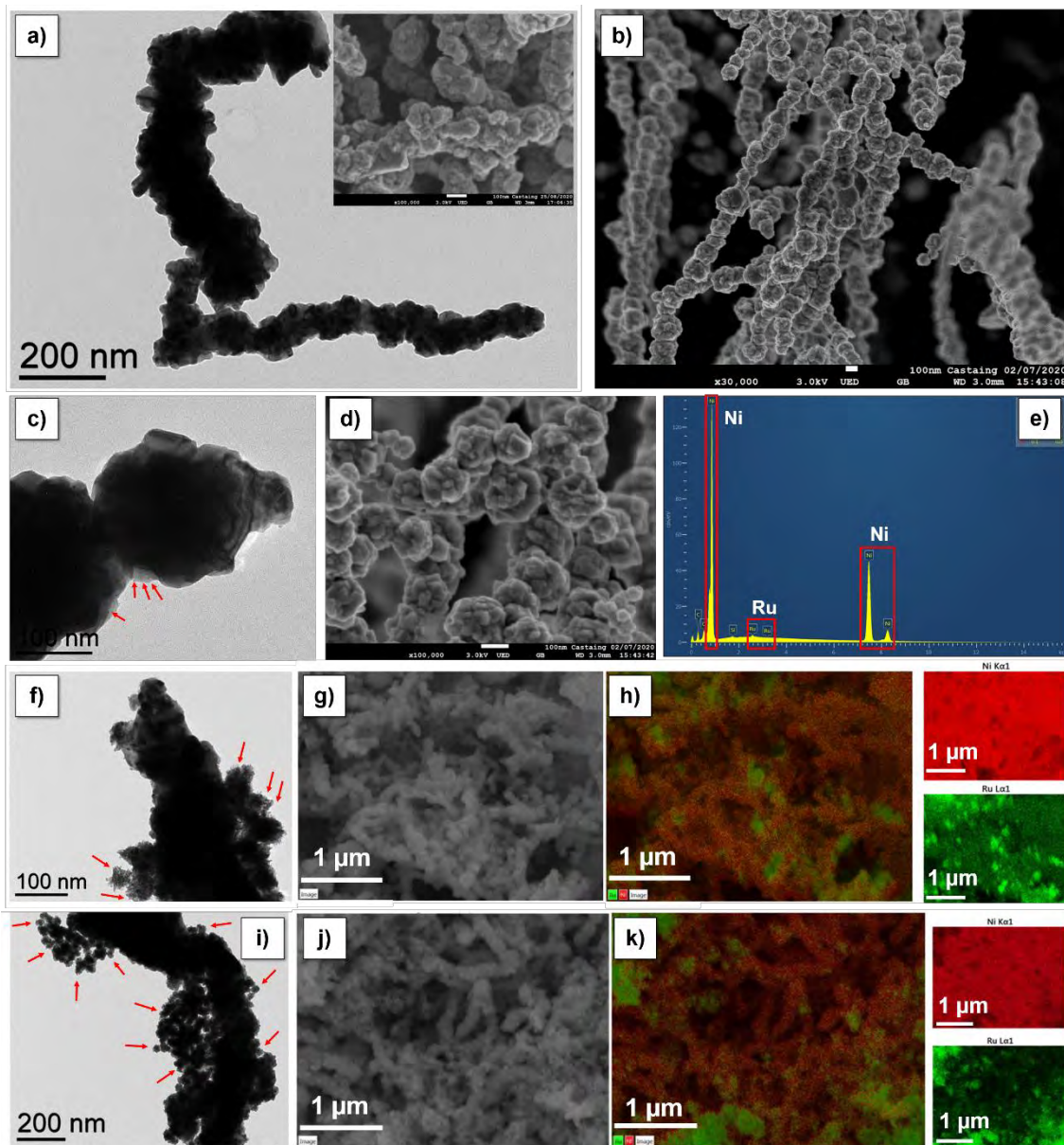


**Figure 12.** From top to bottom: Ni-foam characterization by TEM (a) and SEM (b); **Ru1@Ni-foam** characterization by TEM (c), SEM (d) and EDX analysis (e); **Ru5@Ni-foam** characterization by TEM (f), SEM (g) and EDX mapping of Ni K $\alpha$ 1 (red) and Ru L $\alpha$ 1 (green) (h); **Ru10@Ni-foam** characterization by TEM (i), SEM (j) and EDX mapping of Ni K $\alpha$ 1 (red) and Ru L $\alpha$ 1 (green) (k). The arrows show the presence of small Ru NPs.

### 6A.2.3 X-ray diffraction (XRD) analysis

The crystallinity and phase purity of the nanomaterials were examined by XRD for all samples (Fig. 13). XRD patterns indicated the presence of Ni(111), Ni(002) and Ni(022) peaks, attributed to the Ni fcc structure (Ni-ICDD: 96-901-2978), thus confirming the presence of metallic Ni in all samples. The size of individual Ni crystallites was determined by using the Scherrer equation and was found to be *ca.* 22.4 nm, 28.6 nm, 20.2 nm and 19.3 nm for **Ni-foam**, **Ru1@Ni-foam**, **Ru5@Ni-foam** and **Ru10@Ni-foam**, respectively. XRD patterns of **Ru1@Ni-foam** and **Ru10@Ni-foam** samples revealed the presence of only very broad shoulders that can be attributed to Ru under the form of a poorly crystallized or even amorphous phase (Fig. 13b and 13d). The XRD pattern of **Ru5@Ni-foam** revealed the presence of better-defined peaks corresponding to the Ru(010), Ru(002), Ru(012), Ru(110), Ru(013) and Ru(112) peaks of Ru hcp structure (Ru-ICDD-96-900-8514) (Fig. 13c). In addition, the size of individual Ru crystallites in this sample was calculated (Scherrer equation) as *ca.* 7.6 nm.



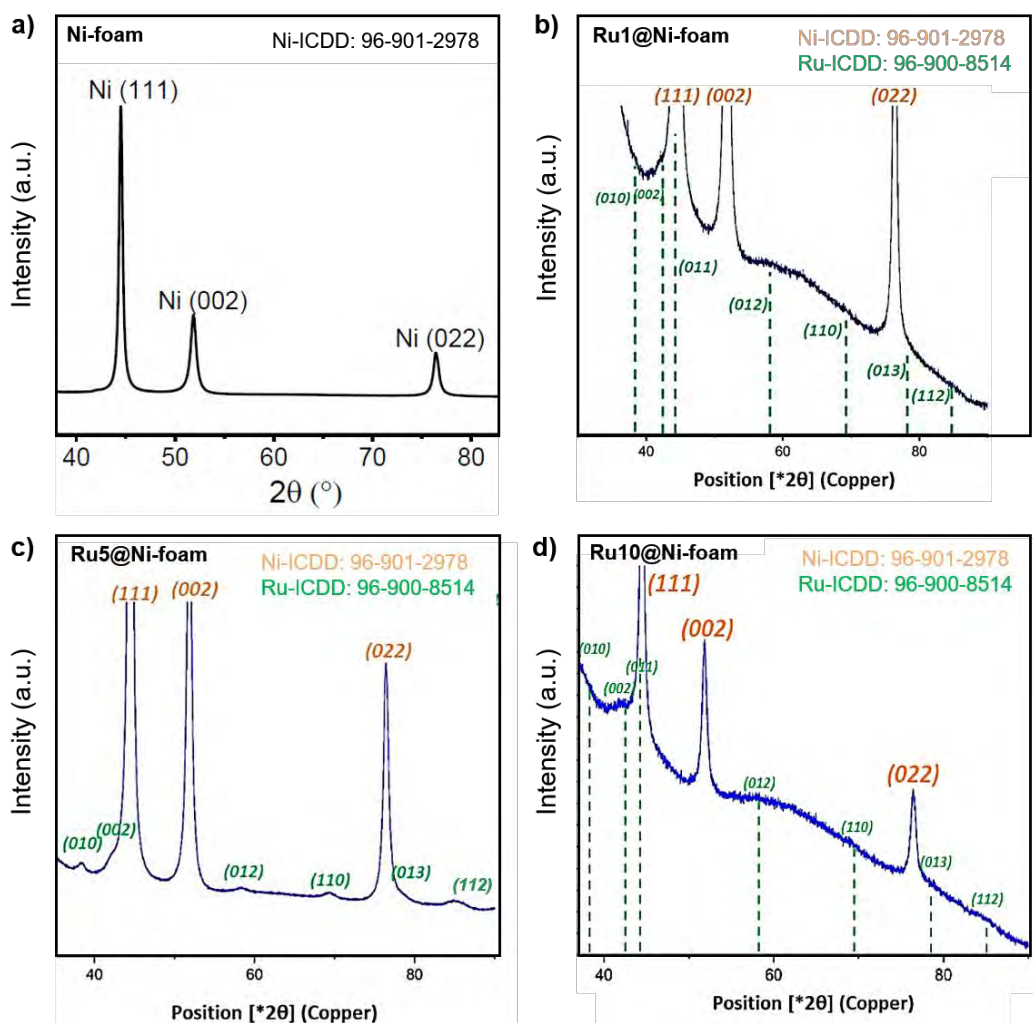


Figure 13. XRD patterns for Ni-foam (a), Ru1@Ni-foam (b), Ru5@Ni-foam (c) and Ru10@Ni-foam (d).

#### 6A.2.4 Inductively-coupled plasma (ICP) analysis

ICP analyses provided a Ni content of 96.7 wt% and 95.0 wt% for the fresh and air passivated **Ni-foam**, respectively. For the air passivated **Ru1@Ni-foam**, **Ru5@Ni-foam** and **Ru10@Ni-foam**, ICP revealed Ni contents of 95.6 wt%, 91.5 wt% and 88.7 wt%, respectively. The Ru content was also determined by ICP, with 0.43 wt%, 3.2 wt% and 6.4 wt% values for **Ru1@Ni-foam**, **Ru5@Ni-foam** and **Ru10@Ni-foam**, respectively. For an easier comparison, all these experimental data are reported in Table 2.

**Table 2.** ICP results for **Ni-foam**, **Ru1@Ni-foam**, **Ru5@Ni-foam** and **Ru10@Ni-foam** samples.

Entry	System	Ni (wt%)	Ru (wt%)
		Fresh/passivated	
1	<b>Ni-foam</b>	96.7/95.0	-
2	<b>Ru1@Ni-foam</b>	/95.6	0.43
3	<b>Ru5@Ni-foam</b>	/91.5	3.20
4	<b>Ru10@Ni-foam</b>	/88.7	6.40

### 6A.2.5 X-ray photoelectron spectroscopy (XPS) analysis

XPS analysis allowed discerning the surrounding chemical environment and oxidation state of the different elements present in the samples. The XPS spectrum of the **Ni-foam** revealed two distinguishable regions in the Ni 2p part, namely the Ni 2p<sub>3/2</sub> (850-650 eV) and Ni 2p<sub>1/2</sub> (650- 880 eV) regions (Fig. 14a, khaki trace). Focusing on the Ni 2p<sub>3/2</sub> region, two sharp peaks are observed at 852.6 eV and 855.6 eV, attributed to metallic Ni and Ni(OH)<sub>2</sub>, respectively. These results indicate the co-presence of metallic and hydroxide nickel species in the nanomaterial.<sup>24,25</sup> Given these results, the Ni-foam can be described as a layered structure where a metallic Ni phase is surrounded by a Ni(OH)<sub>2</sub> shell. The absence of any Ni(OH)<sub>2</sub> fingerprint in the XRD pattern in Fig. 13a can be explained by the fineness/thinness/lightness ( $\leq 1$  nm) and/or amorphousness of this outer shell. As expected after air passivation, the XPS spectrum of the passivated Ni foam shows a decreased Ni(0) peak but an increased Ni(OH)<sub>2</sub> component (Fig. 13a, light blue trace). An additional small peak is also visible at 853.7 eV that can be attributed to NiO.

The XPS spectra for **Ru1@Ni-foam** (Fig. 14b, blue) and **Ru10@Ni-foam** (Fig. 14c, blue trace) revealed two sharp peaks in the Ni 2p<sub>3/2</sub> region. The one centered at 852.6 eV is attributed to Ni(0) and the other peak could be deconvoluted in two peaks centered at 855.6 eV and  $\approx 856$  eV, attributed to Ni(OH)<sub>2</sub> and NiOOH, respectively.<sup>26,27</sup> As it can be expected due to reaction with air in passivated samples, the Ni(0) contribution is reduced and part of the Ni(OH)<sub>2</sub> shell seems to have been partially converted to oxo-hydroxo nickel species (NiOOH) (Fig. 14b and 14c, khaki traces). Given that no NiOOH signal was visible in the XPS spectrum of the passivated Ni foam sample, its appearance in the Ru@Ni foam nanomaterials can arise from the presence of Ru that may help the stabilization of higher oxidation states of Ni (*i.e.* NiOOH) in the passivated samples.



The Ni XPS data of the **Ru5@Ni-foam** sample are not available yet, but due to the similarities observed between the other Ru-containing samples, the same Ni composition can be assumed.

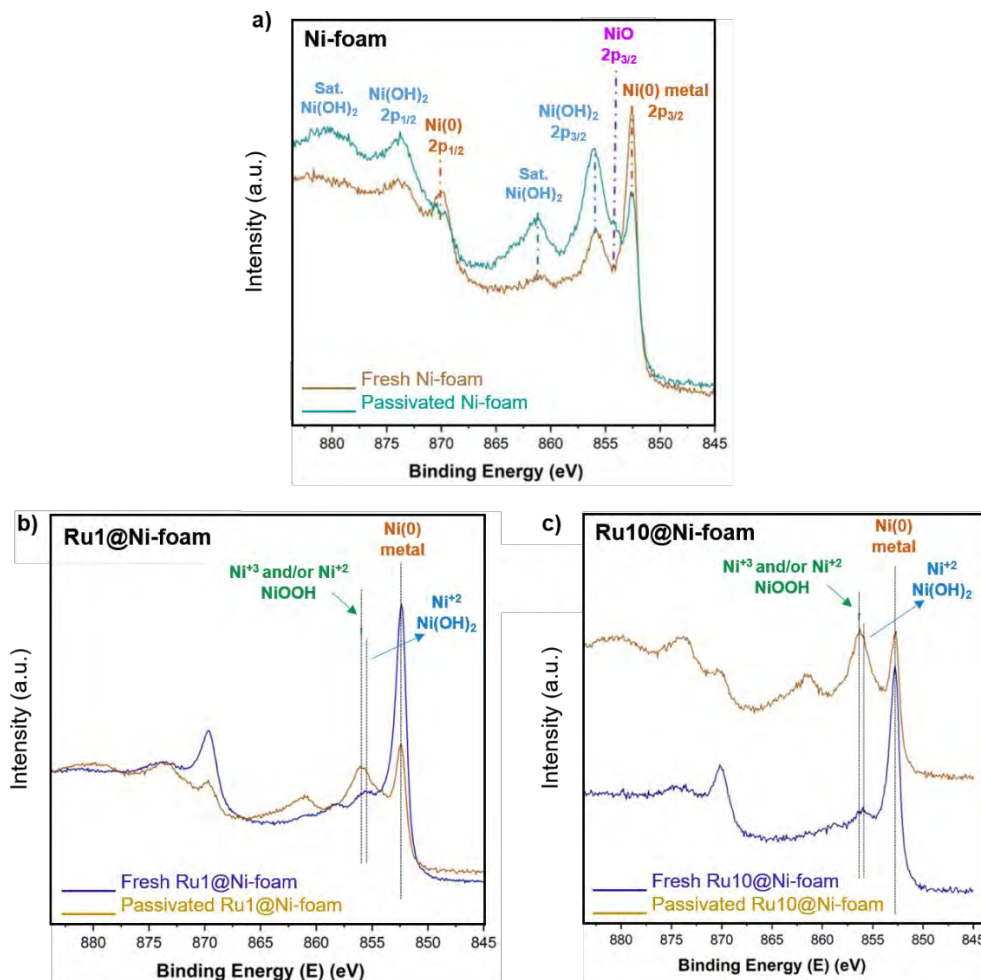


**Figure 14.** Ni 2p XPS spectra for **Ni-foam** (a), **Ru1@Ni-foam** (b) and **Ru10@Ni-foam** (c).

XPS analysis in the Ru 3d<sub>5/2</sub> region allowed to confirm the presence of Ru(0) as the main Ru species in the fresh **Ru1@Ni-foam** and **Ru10@Ni-foam** samples (Fig. 15a and 15c). After air passivation, XPS analysis in the same region indicated that Ru is present in two different phases, namely metallic Ru and RuO<sub>2</sub>. Indeed, the intense peak can be deconvoluted in one component centred between 279.7 - 280.3 eV (metallic Ru) and another one at 280.8 eV (RuO<sub>2</sub>) (Fig. 15b and 15d).<sup>28</sup> In fact, and as expected after air exposure, the RuO<sub>2</sub> contribution increase can be attributed to the formation of a RuO<sub>2</sub> layer over the Ru(0) NPs. This possibly leads to a Ru@RuO<sub>2</sub> core@shell type structure, at least for the RuNP region in contact with air. In this regard, the Ru/RuO<sub>2</sub> ratio was found to be 1.4 and 2.3 for **Ru1@Ni-foam** and **Ru@Ni-foam**, respectively.

These results are in agreement with the fact that, hypothesised by TEM images, more dispersed and smaller NPs are present in the **Ru1@Ni-foam** sample (*i.e.* easier oxidation). Again, the Ru XPS data for **Ru5@Ni-foam** is not available yet, but a mixture of Ru/RuO<sub>2</sub> is also expected to be present after exposure under air.

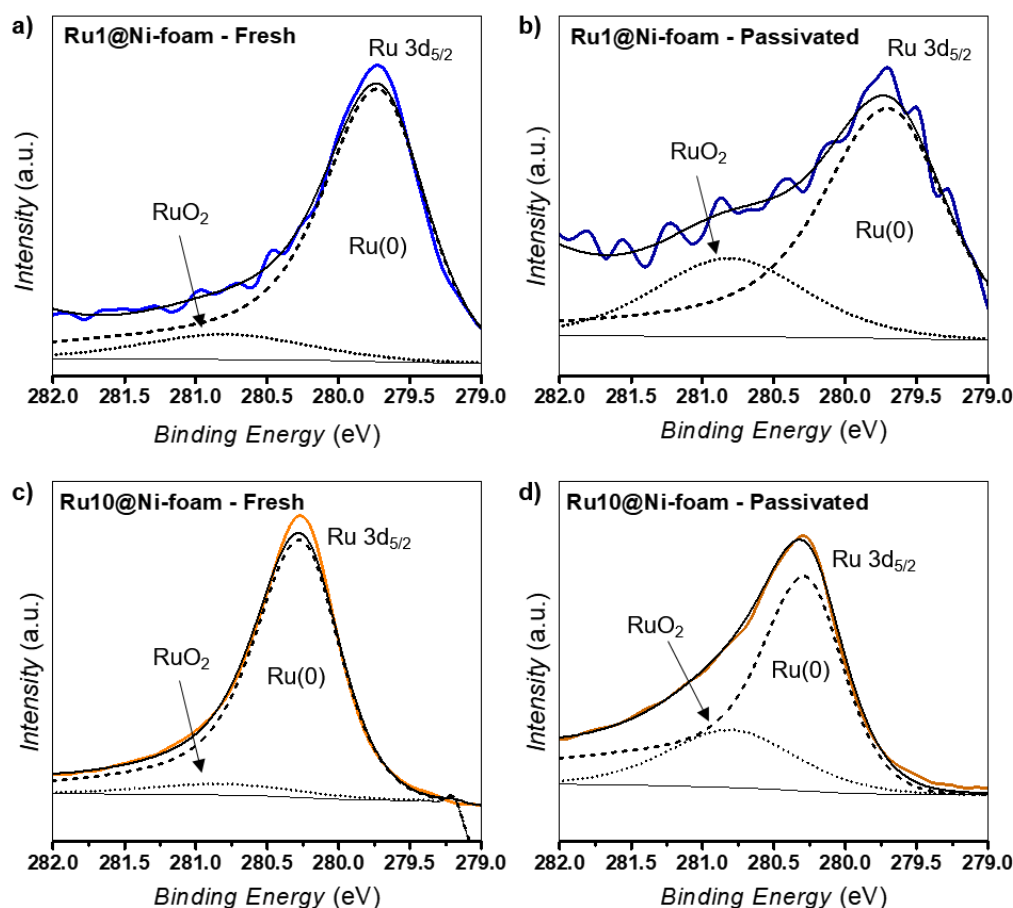


**Figure 15.** Ru 3d<sub>5/2</sub> XPS spectra for fresh **Ru1@Ni-foam** (a), passivated **Ru1@Ni-foam** (b), fresh **Ru10@Ni-foam** (c) and passivated **Ru10@Ni-foam** (d). Metallic-Ru component (Ru 3d<sub>5/2</sub> 279.7 - 280.3 eV, dashed black), RuO<sub>2</sub>-component (Ru 3d<sub>5/2</sub> 280.8 eV, dotted black), envelope (bold black).

The characterization data of the foam-like Ni nanomaterial (**Ni-foam**) and the Ru-doped derived nanomaterials with different Ru loadings (**Ru1@Ni-foam**, **Ru5@Ni-foam** and **Ru10@Ni-foam**) are summarized in Table 3. In the Ru@Ni foam nanomaterials, the Ni foam served as a support for the growth of Ru NPs in the absence of any other stabilizer, leading to Ru/Ni bimetallic nanomaterials.

**Table 3.** Summary of the characterization data of all the Ni foam-based samples

	<b>Ni-foam</b>	<b>Ru1@Ni-foam</b>	<b>Ru5@Ni-foam</b>	<b>Ru10@Ni-foam</b>
<b>XRD</b>	Worm-like superstructures ( <i>ca.</i> 100 nm of thickness) composed of individual Ni(0) crystallites ( <i>ca.</i> 22.4 nm)	Ni(0) crystallites ( <i>ca.</i> 28.6 nm) with possibly: small Ru NPs (<1 nm) or small Ru islands or thin Ru layer over the Ni foam	Ni(0) crystallites ( <i>ca.</i> 20.2 nm) with aggregates of Ru NPs ( <i>ca.</i> 7.6 nm)	Ni(0) crystallites ( <i>ca.</i> 19.3 nm) with aggregates of Ru NPs
<b>ICP</b>	-	0.4 wt% Ru	3.2 wt% Ru	6.4 wt% Ru
<b>XPS Ni</b>	<u>Fresh:</u> Mainly Ni(0) and Ni(OH) <sub>2</sub>  <u>Passivated:</u> Mainly Ni(OH) <sub>2</sub> , Ni(0) and a bit of NiO	<u>Fresh:</u> Mainly Ni <sup>0</sup> and Ni(OH) <sub>2</sub> /Ni(OOH)  <u>Passivated:</u> More Ni(OH) <sub>2</sub> /NiOOH + less Ni(0)	-	<u>Fresh:</u> Mainly Ni(0) and Ni(OH) <sub>2</sub> /NiOOH  <u>Passivated:</u> More Ni(OH) <sub>2</sub> /NiOOH + less Ni(0)
<b>XPS Ru</b>	-	<u>Fresh:</u> Mainly Ru(0)  <u>Passivated:</u> Ru/RuO <sub>2</sub> mixture (ratio 1.4)	-	<u>Fresh:</u> Mainly Ru(0)  <u>Passivated:</u> Ru/RuO <sub>2</sub> mixture (ratio 2.3)

## **6A.3 ELECTROCATALYTIC PERFORMANCE**

### **6A.3.1 Electrocatalytic performance towards the HER in acidic media**

Ni-based materials are usually studied at basic pH due to their instability under acidic conditions. However, given Ru NPs are more active at acidic pH, the HER performance of the **Ni-foam** and Ru@Ni-foam nanomaterials were first studied in acidic conditions, namely in 1 M H<sub>2</sub>SO<sub>4</sub> aqueous solution (pH 0). Each sample was dispersed in THF (2 mg/mL) and drop-casted onto a glassy carbon rotating disk electrode (GC-RDE).

The electrochemical performance was determined using a three-electrode configuration with the GC-RDE being the working electrode and a SCE (KCl sat'd) and a Pt wire as reference (RE) and counter (CE) electrodes, respectively. A change in the current density, compared to the signal from RDE blank, was observed when scanning into reductive potentials for all the samples, thus confirming a catalytic activity towards the reduction of protons to H<sub>2</sub>. From the TEM analysis, two different sample sets can be considered *versus* the Ru doping: in the one hand the **Ni-foam** (no Ru deposition) and **Ru1@Ni-foam** (no visible RuNPs on TEM images); and in the second hand **Ru5@Ni-foam** and **Ru10@Ni-foam** (both displaying visible RuNPs).

From the polarization curves (Fig. 16), it can be noticed that higher catalytic current densities are observed with the samples containing a higher amount of Ru (5 wt% Ru and 10 wt% Ru *vs.* 1 wt% Ru). However, the best catalytic activity was obtained with **Ru5@Ni-foam**. This result can derive from a higher degree of crystallinity<sup>29</sup> of the Ru NPs in this sample since a well-defined XRD pattern was obtained in this case (Fig. 13c), contrarily to the other systems. Another hypothesis can be that a different Ru/RuO<sub>2</sub> ratio or even an optimum Ru-doping content is present for the 5 wt% Ru sample, providing a good interface between the Ni/Ni(OH)<sub>2</sub>-NiOOH and the Ru dopant. Even though the obtained  $\eta_{10}$  values (>195 mV, Table 4) are far from state-of-the-art literature data, these results allow to study the influence of Ru-doping onto a noble-metal free electrode for the HER electrocatalysis. The Tafel slope of **Ru5@Ni-foam** is around 78 mV/dec (Fig. 16b and Table 4), confirming a catalytic behavior in between the Volmer and Heyrovsky steps as rds (Heyrovskyy: H<sub>2</sub> electrodesorption with a proton from the solution,  $b \approx 40$  mV/dec, and Volmer: adsorption of H<sup>+</sup> to form the M-H species on the NP, typically  $b \approx 120$  mV/dec). This is in contrast with the catalytic behavior of the **Ni-foam** alone, where a Tafel slope >150 mV/dec suggests an extremely slow H<sup>+</sup> adsorption (Fig. 16b and Table 4). This evidences the positive role of Ru-doping in changing the HER mechanism, enhancing the adsorption of H<sup>+</sup> and thus facilitating the HER.

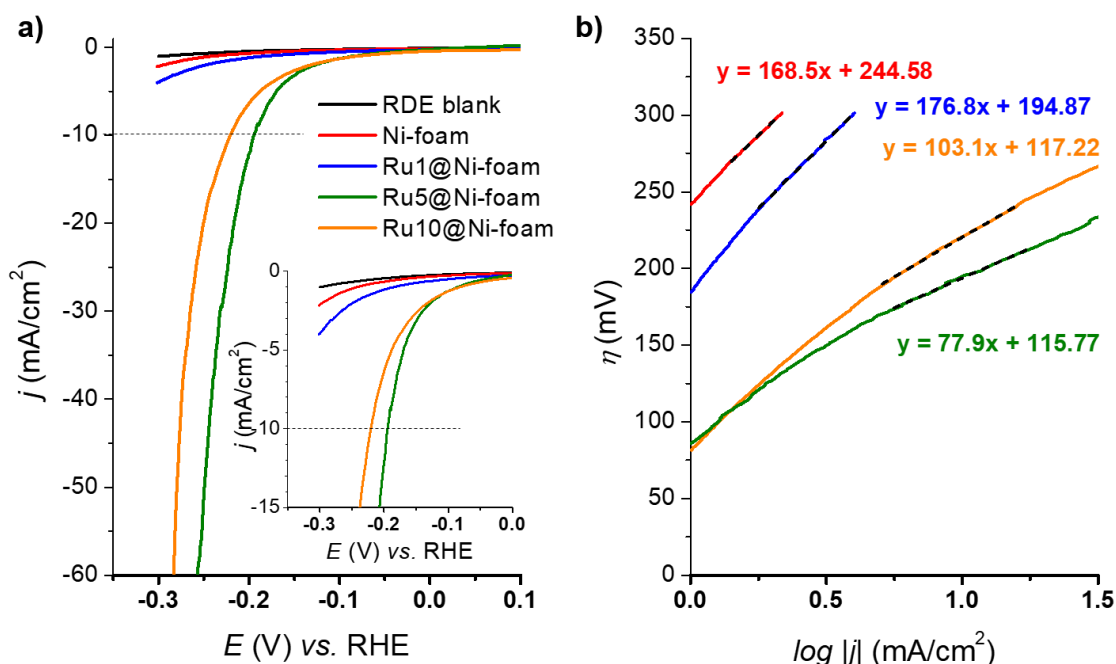


**Figure 16.** Polarization curves of **Ni-foam** (red), **Ru1@Ni-foam** (blue), **Ru5@Ni-foam** (green) and **Ru10@Ni-foam** (orange) in 1 M H<sub>2</sub>SO<sub>4</sub>. Blank LSV from bare RDE is also shown (black) (a). Corresponding Tafel plots (b).

**Table 4.** Summary of the HER electrocatalytic data for the four samples studied (1 M H<sub>2</sub>SO<sub>4</sub>). Parameters: onset overpotential at -10 mA/cm<sup>2</sup> ( $\eta_{10}$ ), Tafel slope ( $b$ ) and exchange current density ( $j_0$ ).

Entry	System	$\eta_{10}$ (mV)	Tafel Slope ( $b$ ) (mV/dec)	$j_0$ (mA/cm <sup>2</sup> )
1	<b>Ni-foam</b>	-	169	0.035
2	<b>Ru1@Ni-foam</b>	-	177	0.079
3	<b>Ru5@Ni-foam</b>	195	78	0.033
4	<b>Ru10@Ni-foam</b>	221	103	0.073

Finally, a stability study was performed with the most active catalyst, **Ru5@Ni-foam** (Fig. 17). The progressive decrease in intensity observed along the consecutive LSV curves evidences the poor stability of the system. This behavior could be explained by the corrosion of Ni in acid media.<sup>30</sup>

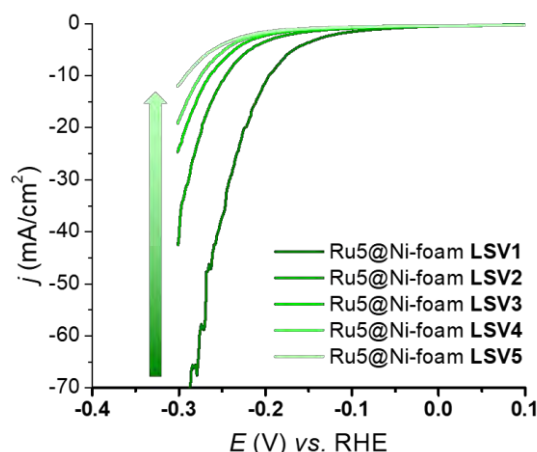


**Figure 17.** Stability study towards HER at pH 0 after registering consecutive LSV curves for **Ru5@Ni-foam**.

### 6A.3.2 Electrocatalytic performance towards the HER in alkaline media

A fast screening of the activity of the **Ni-foam** and **Ru@Ni-foam** materials towards the HER was performed at pH ~14 (1 M NaOH) (Fig. 18). In all cases the activity was found to be very low, obtaining high  $\eta_{10}$  values (Table 5). However, interestingly, again the best performances were observed for **Ru5@Ni-foam** and **Ru10@Ni-foam** compared to **Ni-foam**, showing lower  $\eta_{10}$  and Tafel slopes and confirming their improved kinetics.

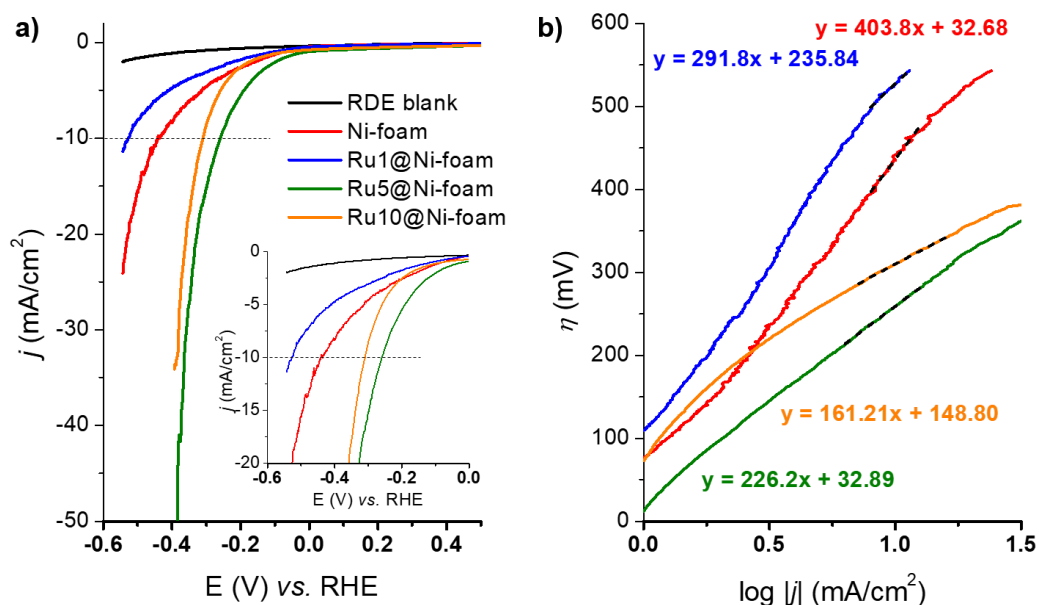


**Figure 18.** Polarization curves of **Ni-foam** (red), **Ru1@Ni-foam** (blue), **Ru5@Ni-foam** (green) and **Ru10@Ni-foam** (orange) in 1 M NaOH. Blank LSV from bare RDE is also shown (black) (a). Corresponding Tafel plots (b).

**Table 5.** Summary of HER electrocatalytic data for the four samples studied (1 M NaOH). Parameters: onset overpotential at -10 mA/cm<sup>2</sup> ( $\eta_{10}$ ), Tafel slope ( $b$ ) and exchange current density ( $j_0$ ).

Entry	System	$\eta_{10}$ (mV)	Tafel Slope ( $b$ ) (mV/dec)	$j_0$ (mA/cm <sup>2</sup> )
1	Ni-foam	442	404	0.83
2	Ru1@Ni-foam	527	292	0.16
3	Ru5@Ni-foam	259	226	0.72
4	Ru10@Ni-foam	310	161	0.12

Consecutive LSVs were performed with the most active material, **Ru5@Ni-foam**, to study its stability (Fig. 19). This study shows again a decrease in intensity along the CVs, although to a lower extent than under acidic conditions. This difference could be attributed to a better stability of Ni-based materials under basic conditions, as already reported in the literature.<sup>30</sup>

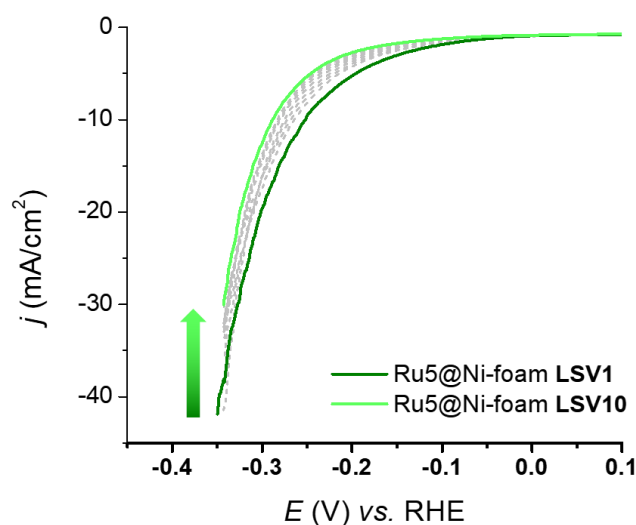


**Figure 19.** Stability study towards HER at pH ~14 after registering consecutive LSVs for **Ru5@Ni-foam**.

### 6A.3.3 Electrocatalytic performance towards the OER in alkaline media

To study the catalytic activity of the obtained systems towards the OER, cyclic voltammeteries (CVs) have been performed. CVs were conducted from  $E_i = 1.05$  V to  $E_f = 1.75$  V ( $E$  vs. SCE) at pH ~14 (1 M NaOH).

As shown in Fig. 20, when scanned anodically up to 1.75 V vs. RHE, all electrodes showed one anodic peak in the oxidative forward scan prior to a sharp current increase assigned to the electrocatalytic oxidation of water to dioxygen. According to literature data,<sup>6,31</sup> the first faradaic process observed in the voltammogram ( $E_{ap} = ca. 1.5$  V vs. RHE) could be attributed to the oxidation of Ni(II) to Ni(III), following Eq. 1. Interestingly, the NiOOH species is usually proposed as the active species towards the OER in related Ni-based systems.<sup>5</sup> The cathodic wave in the backward scan corresponds to the respective inverse reduction process of this Ni species.



It is well known that the catalytic intensity and the potentials of the redox couples depend on the sample deposition on the electrode. They can also depend on the Ni/Ru environment, which is very heterogeneous in the samples here studied. Thus, correlation of any differences in the aforementioned parameters between samples, with the Ru loading, has been infeasible due to intrinsic internal differences between the electrodes prepared from the same sample. In addition, an increase in  $j$  after 10 progressive CVs is observed in all samples, which could be attributed to Fe incorporation into the Ni structure, a common process observed in Ni-based electrocatalysts under OER conditions in alkaline media, or due to hydration of the sample.<sup>32</sup> Due to this activation process, only the  $\eta_0$  value has been considered in the 10<sup>th</sup> CV, being the obtained values 334 mV, 310 mV, 330 mV and 335 mV for **Ni-foam**, **Ru1@Ni-foam**, **Ru5@Ni-foam** and **Ru10@Ni-foam**, respectively.



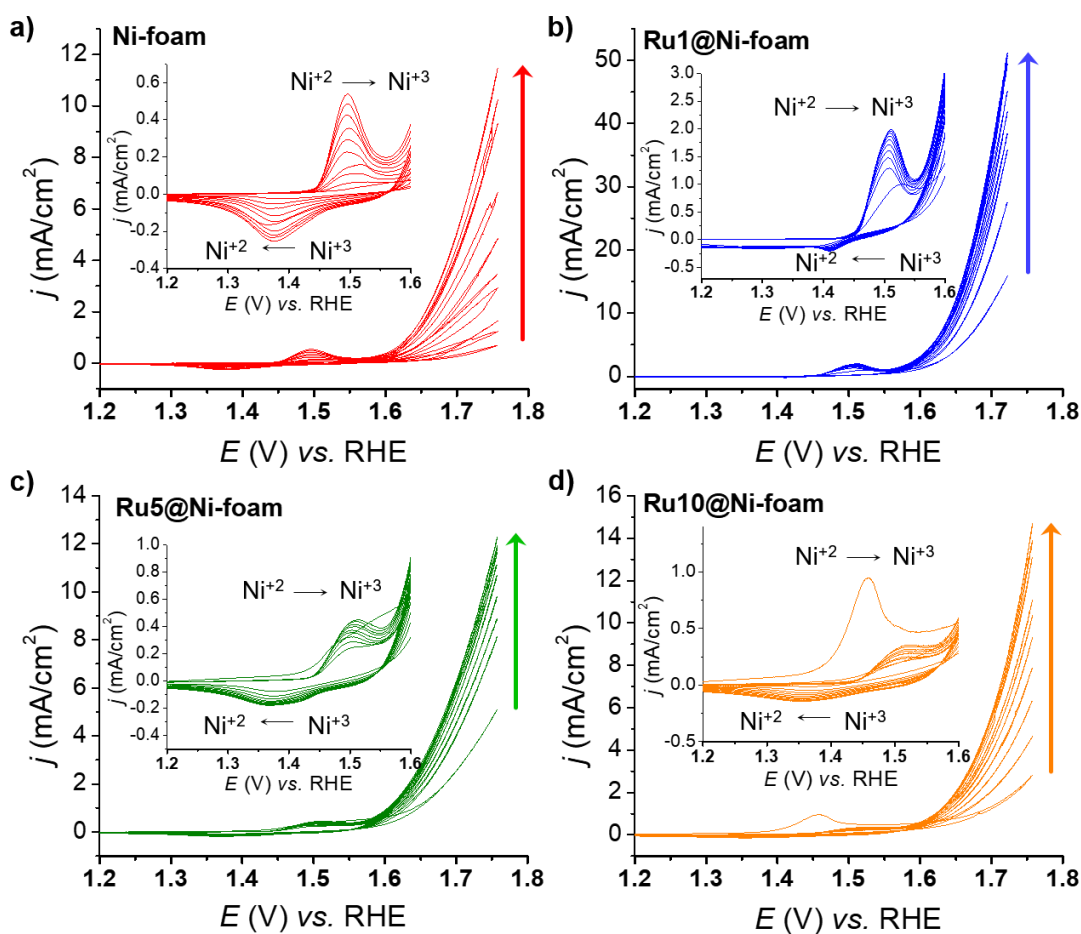


**Figure 20.** 10 progressive CVs studies of OER catalytic activity in non-purified NaOH aqueous solution for Ni-foam (a), Ru1@Ni-foam (b), Ru5@Ni-foam (c) and Ru10@Ni-foam (d).

### 6A.3.3.1 Fe-incorporation studies

As explained in the Introduction, and observed in the previous section, the incorporation of Fe traces/impurities from commonly used alkaline solutions and/or hydration of the sample can strongly improve the OER activity of Ni-based electrocatalysts. In this way, catalytic studies performed in Fe-free alkaline solutions are critical to understand the effect of Fe incorporation in the Ni-foam nanomaterials studied in this work. Furthermore, Ru-doping could have also an influence on the OER performance and/or in Fe incorporation. Given that Ni(OH)<sub>2</sub> readily absorbs Fe without applying any potential, suspended high purity Ni(OH)<sub>2</sub> powder prepared by precipitation in the alkaline electrolyte was used to absorb all Fe impurities from the commercial base used (NaOH) prior to electrochemical testing.<sup>33</sup>

All the Ni foam nanomaterials have been electrocatalytically tested in Fe-free alkaline solutions, observing lower activities and lower activation processes compared to the studies performed in non-purified alkaline solutions. As the CV intensity is dependent on the amount of material deposited onto the electrode and also on the way the material is distributed on it, the same prepared electrodes have been used both in Fe-free and non-purified alkaline solutions. Each sample was first tested in a Fe-free solution by performing 10 consecutive CVs, and then the same electrode was tested in a non-purified solution performing other 10 CVs. In all cases an increase in activity was observed when the electrode was submerged in the non-purified electrolyte. Furthermore, the OER current further increased progressively in subsequent CV cycles due to Fe incorporation (Fig. 21). However, in order to check that this increase in intensity is due to Fe incorporation and not due to other changes in the alkaline solution during the purification procedure, the same electrode was tested again in the Fe-free electrolyte. This led to an increased activity compared with that obtained in the Fe-free solution before exposing the electrode to Fe-containing electrolyte (Fig. 21). These results confirm that incorporation of Fe into the Ni structure has a crucial influence on the OER catalytic activity of these materials, which is maintained when introduced again in Fe-free solutions. Interestingly, when the materials were introduced in the Fe-free solution after the experiments in the non-purified medium, the intensity of CVs progressively decreased (Fig. 21). This process could be explained as no more Fe can be incorporated and some incorporated Fe could get free from the Ni structure. All the Ni-based materials presented the same catalytic behavior except **Ru1@Ni-foam**, in which a progressive activation (*i.e.* progressive intensity increase) was also observed in Fe-free electrolyte (Fig. 21b). In addition, the intensities obtained with this catalyst are higher both in Fe-free and non-purified electrolyte compared with the other ones. It seems that a low Ru loading can contribute to a higher Fe incorporation into the Ni structure and also to a better hydration of the sample,<sup>32</sup> as confirmed by the activation process in Fe-free electrolyte.

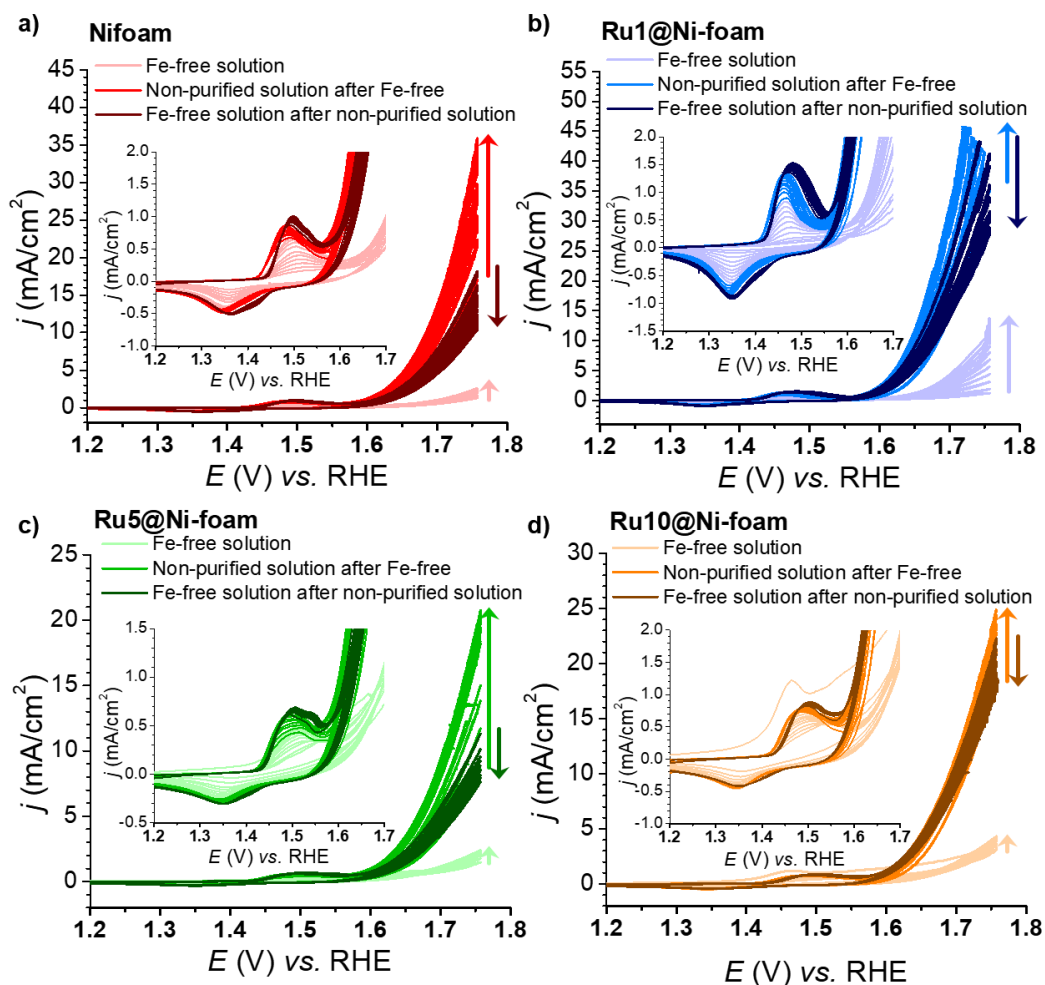


**Figure 21.** Comparative studies of the OER catalytic activity in Fe-free, non-purified NaOH aqueous solution after Fe-free and Fe-free solution after non-purified solution for **Ni-foam** (a), **Ru1@Ni-foam** (b), **Ru5@Ni-foam** (c) and **Ru10@Ni-foam** (d).

#### 6A.3.4 Electrocatalytic performance towards the OER in neutral/near-neutral media

Looking to a future implementation of Ni-based catalysts with semiconductors in photochemical WS devices, the development of active and stable materials in neutral/near-neutral conditions would offer more technological flexibility as semiconductors are more stable in neutral electrolyte.<sup>34</sup> In this regard, Nocera and co-workers reported high activities of Ni-(oxy)hydroxide/borate ( $\text{NiO}_x\text{-B}_i$ ) catalysts at near-neutral pH of  $\sim 9$ , which they attributed to changes in Ni oxidation state and film structure.<sup>35,36,37</sup>

However, kinetic studies demonstrated the antagonistic effects of borate in OER activity: an inhibitor effect due to its ability to adsorb/coordinate onto oxide surfaces in aqueous media and a favoring effect for proton transfer, thus improving the OER kinetics.<sup>37</sup> The effect of pH and the role of borate on the OER activity of Fe-containing Ni-based catalysts has also been studied by W. A. Smith *et al.*<sup>38</sup> At similar Fe content, this work shows that the measured catalytic activity at pH 9.2 is approximately half than that at pH 13, demonstrating the role of borate to hinder the catalytic activity of Ni-Fe systems below pH 10. Considering the existing literature and the interest in developing catalytic systems able to work under near-neutral conditions, the OER performance of the four Ni-based nanomaterials studied in this chapter was assessed at pH 7 and pH 9.

The series of Ni-foam materials was thus first studied at pH 7 phosphate buffer (1 M ionic strength). The effect of Ru incorporation on the catalytic performance at this pH has not yet been reported. CVs were performed from  $E_i = 0.86$  V to  $E_f = 1.96$  V ( $E$  vs. RHE). All the catalysts showed a low activity together with moderate deactivation (Fig. 22, pink curves). In addition, only a slight increase of the current intensity was observed for the Ru-containing samples compared to the **Ni-foam**. In comparison with the results obtained in alkaline conditions, the  $\text{Ni}^{+3}/\text{Ni}^{+2}$  redox waves are not observed with the **Ni-foam** and only slightly observed in the Ru-doped samples (Fig. 22, blue arrows in pink curves).

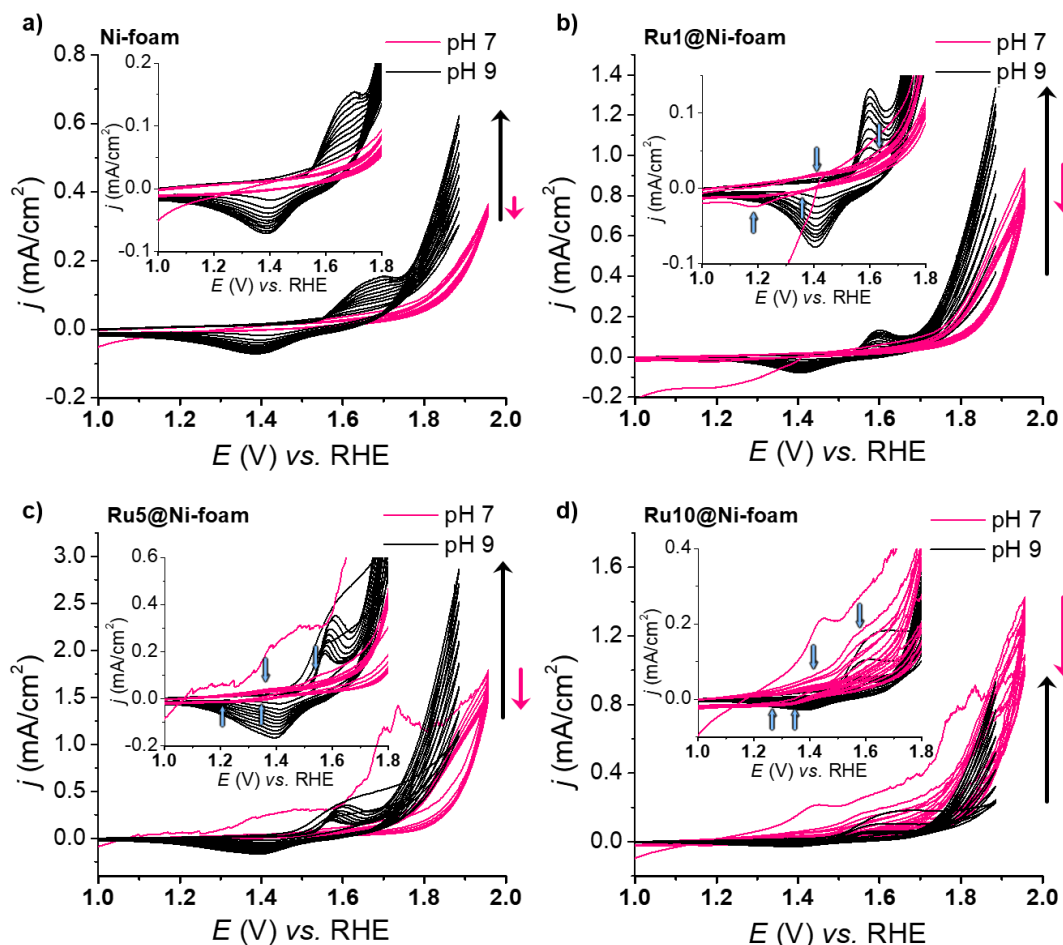


**Figure 22.** OER Polarization curves measured in phosphate buffer (pH 7, pink curves) and borate buffer (pH 9, black curves) for **Ni-foam** (a), **Ru1@Ni-foam** (b), **Ru5@Ni-foam** (c) and **Ru10@Ni-foam** (d).

OER studies were also carried out in a pH 9 borate buffer to determine any positive effect of the Ru-loadings over the Ni-foam structure at this pH. CVs were performed from  $E_i = 0.88$  V to  $E_f = 1.88$  V ( $E$  vs. RHE). The obtained results evidenced a shift of the potential of the  $\text{Ni}(\text{OH})_2/\text{NiOOH}$  oxidation to higher potentials compared to the ones observed in NaOH solution (Table 6 and Fig. 22, black curves).

**Table 6.** Potentials for the  $\text{Ni}^{+2} \rightarrow \text{Ni}^{+3}$  oxidation wave from CV at pH 9 and pH ~14.

Sample	E pH 9 ( $V_{\text{RHE}}$ )	E pH ~14 ( $V_{\text{RHE}}$ )	$\Delta E$ (V)
<b>Ni-foam</b>	1.67	1.49	0.18
<b>Ru1@Ni-foam</b>	1.60	1.47	0.13
<b>Ru5@Ni-foam</b>	1.60	1.51	0.09
<b>Ru10@Ni-foam</b>	1.57	1.49	0.08

From these results, a plausible conclusion is that the formation of “active oxygen” species (*i.e.* NiOO<sup>-</sup>),<sup>38</sup> which provides a more favorable pathway for efficient water oxidation (*i.e.* lower overpotentials), occurs only in strong alkaline media, pointing to a clear structure/functionality relationship between the catalyst and the electrolyte in which it is tested (*i.e.* importance of catalyst-electrolyte coupling). Thus, the low activity observed at pH 9 compared to pH ~14 under similar Fe content in solution points that catalyst deprotonation toward formation of activated oxygen species has a real effect on the overall catalytic activity, which in turn is not related to Fe impurities in the electrolyte.

In addition, the activity towards the OER was seriously inhibited when compared with the activity observed in a NaOH solution, under comparable content of Fe in solution (Fig. 22, black curves). Since the isoelectric point of Ni(OH)<sub>2</sub> lies in between pH 10-11, the active species formed before the OER (*i.e.* NiOOH) should be negatively charged at pH ~14, but cannot be deprotonated at pH 9, thus observing the Ni<sup>+2</sup>/Ni<sup>+3</sup> process but a decreased OER activity at pH 9 (Fig. 22, black curves).

### 6A.3.5 Spectroelectrochemistry

*In situ* UV-vis spectroelectrochemistry has been used to track the metal oxidation states along different potentials of the studied Ni-based materials.<sup>39,40</sup> These experiments have been performed with the **Ru1@Ni-foam** and **Ru5@Ni-foam** samples towards OER at pH ~14. The results have been compared with **Ni-foam** with the aim to extract valuable insights about the influence of Ru-doping. The samples were deposited onto the transparent FTO conductive electrode in order to enable their transmittance in UV-Vis spectroscopic measurements.

As explained in Section 6A.3.3, all the Ni-foam based samples show a progressive activation (*i.e.* increase of *j*) when successive CVs on the sample deposited on a RDE are performed in non-purified 1 M NaOH. This activation is attributed to Fe incorporation into the Ni-foam structure. In fact, an activation is also observed when the sample drop-casted onto FTO is kept soaking overnight inside the electrolyte without any applied potential (Fig. 23).

For **Ni-foam**, the oxidation and reduction waves for the Ni species after the soaking are clearly displaced to more anodic potentials compared to the initial CV. This displacement is normally observed when Fe incorporation is taking place in the sample.<sup>6,9</sup> Thus, we state that Fe incorporation difficult the oxidation of the Ni centers (*i.e.* stabilising the Ni(II) species), shifting the onset of  $\text{Ni}^{2+} \rightarrow \text{Ni}^{3+}$  closer to the OER onset potential (Fig. 23a). In contrast, for **Ru1@Ni-foam** and **Ru5@Ni-foam**, this shift is not clearly observed (Fig. 23b and 23c). In addition, the  $\text{Ni}^{2+} \rightarrow \text{Ni}^{3+}$  oxidation wave is wider than in the case of **Ni-foam** and the  $\text{Ni}^{3+} \rightarrow \text{Ni}^{2+}$  reduction wave is clearly split into two waves in **Ru1@Ni-foam** (Fig. 23b, inset). This behaviour could be attributed to the Ru-doping, masking the Ni oxidation/reduction processes by changing the Ni environment (making it more locally complex), obtaining wider and split waves.

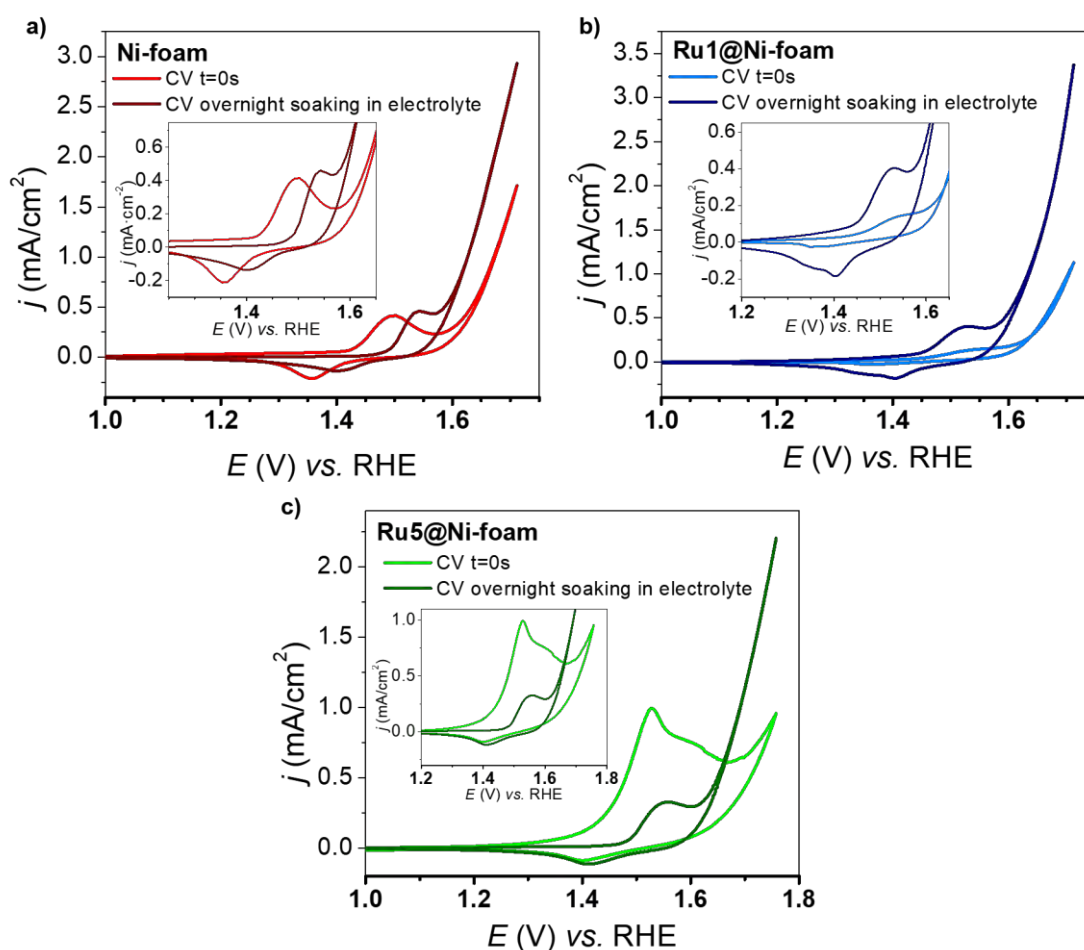


**Figure 23.** CV at  $t=0\text{s}$  and CV after overnight soaking for **Ni-foam** (light and dark red) (a), **Ru1@Ni-foam** (light and dark blue) (b) and **Ru5@Ni-foam** (light and dark green) (c).

Once the samples have been activated, *in situ* UV-vis spectroelectrochemistry was used to track the metal oxidation process from Ni(OH)<sub>2</sub> to NiOOH taking place under potential stress. Chronoamperometries at different potentials (before and after the Ni<sup>+2</sup> → Ni<sup>+3</sup> oxidation wave) were performed and, after stabilization of the current, a UV-vis spectrum was recorded. When a potential after the 1<sup>st</sup> oxidative redox wave is applied an absorbance increase was observed in all samples. The difference in absorbance when applying a potential before and after the oxidative Ni wave is shown in Figs. 24b, 24d and 24f. As can be observed, the obtained spectra show two different shapes. In the **Ni-foam** and **Ru5@Ni-foam** samples, the resulting spectra are similar to those previously reported in the literature and assigned to the NiOOH species with a characteristic broad band centred at 450 nm (Fig. 24b and 24f).<sup>40</sup> On the other hand, the sample **Ru1@Ni-foam** presents a very different shape with an increasing absorption towards the NIR peaking at 650 nm (Fig. 24d). This observation suggests that the low Ru incorporation changes the NiOOH species, supporting the different behaviour found for this system towards the OER in section 6A.3.3.1, compared to **Ni-foam**, **Ru5@Ni-foam** and **Ru10@Ni-foam**.



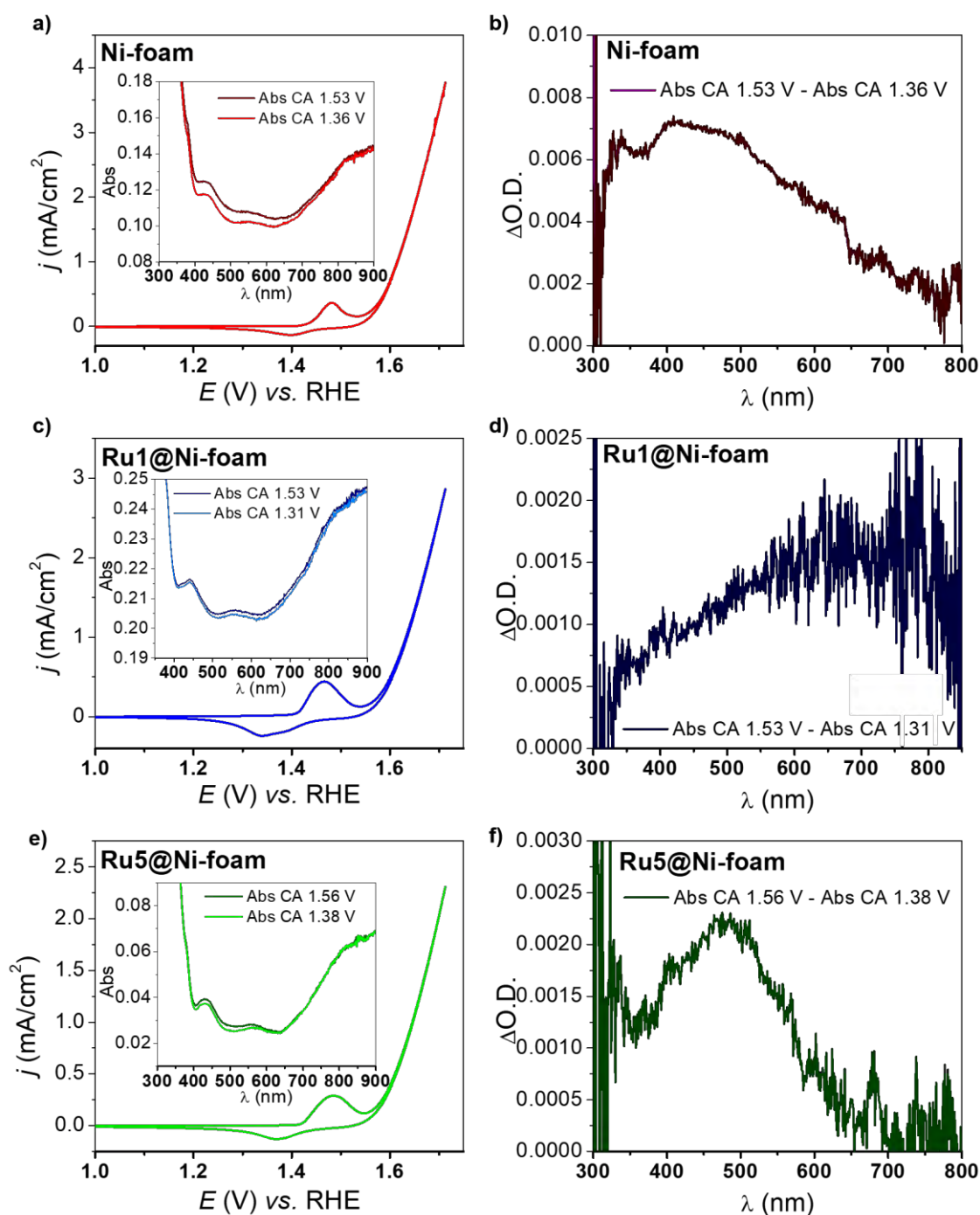


**Figure 24.** Initial CV and UV-vis spectrum during CA at a potential before the redox oxidative wave (light colour) and UV-vis spectrum during CA at a potential after the redox oxidative wave (dark colour) for **Ni-foam** (a), **Ru1@Ni-foam** (c) and **Ru5@Ni-foam** (e). Subtraction of the spectrum of  $\text{CA}_{E_{\text{after ox}}} - \text{CA}_{E_{\text{before ox}}}$  for **Ni-foam** (b), **Ru1@Ni-foam** (d) and **Ru5@Ni-foam** (f).

Considering the observed increase in absorbance in all the studied samples around 350-700 nm, 500 nm was chosen as the wavelength to follow the evolution of the formed species along a CV at 1 mV/s scan rate.

Potential cycling reveals that the absorption band of the Ni catalyst rises right after the onset of the  $\text{Ni}(\text{OH})_2 \rightarrow \text{NiOOH}$  redox wave, and finishes before the catalytic OER starts (Fig. 25). The NiOOH species can be considered as the preferential oxidation state previous the OER, facilitating a more favourable (*i.e.* with lower overpotential) pathway for OER. According to these results, once the NiOOH species is formed on the sample, even though the applied potential increases, and also the current density, the signal from this species seems not to scale with potential. This observation confirms that the formation of the NiOOH species occurs entirely during the Ni oxidation reaction, suggesting that it is not the species accumulated during the catalysis. Therefore, in agreement with the literature, NiOOH needs to be further oxidized to be able to oxidize water.<sup>39</sup>

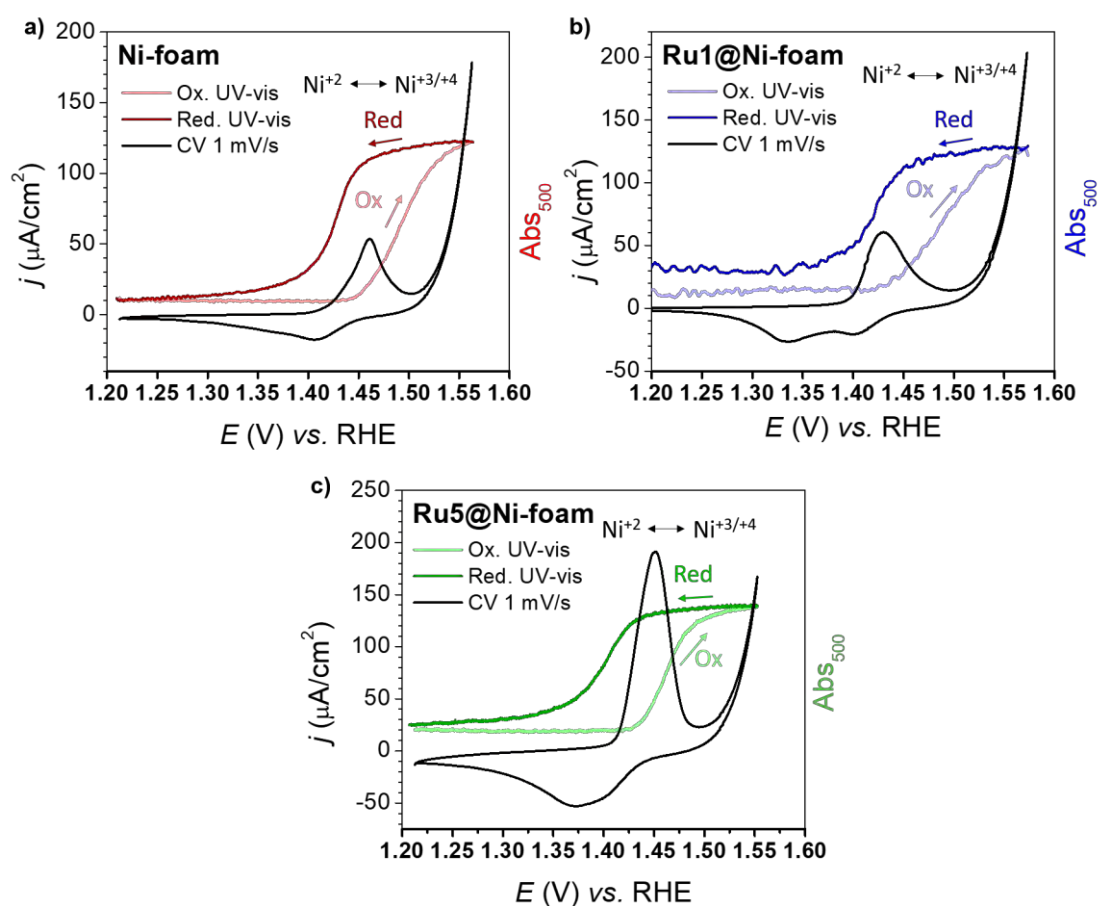


**Figure 25.** *In situ* UV-vis spectra monitored at  $\text{Abs}_{500}$  ( $\lambda_{500\text{nm}}$ ) during potential cycling of **Ni-foam** (a), **Ru1@Ni-foam** (b) and **Ru5@Ni-foam** (c). The black solid line shows the faradaic current (CV), light colour lines show the absorption at the oxidative scan and dark colour lines the absorption at the reductive scan.

After all the spectroelectrochemical studies, the stability of **Ru1@Ni-foam** has been checked by performing successive CVs. It is observed in Fig. 26 that the current density decreases progressively as more cycles are performed. In addition, the redox wave of Ni(OH)<sub>2</sub> oxidation to NiOOH is shifted to higher potentials after each CV, which can be attributed to more Fe incorporation. At CV > 500, the oxidation peak is shifted to potentials at which OER takes place, being masked with the rapid increase due to the OER catalysis. An hypothesis of the progressive decrease in  $j$  could be the high Fe incorporation, suppressing the OER, as demonstrated in other reported studies.<sup>4,6</sup>

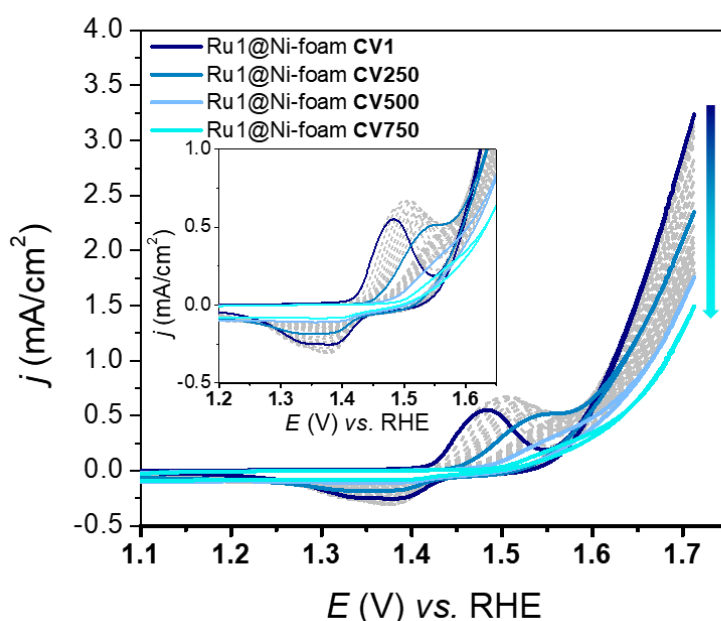


**Figure 26.** Stability study of **Ru1@Ni-foam** by 750 successive CVs in 1 M NaOH electrolyte. Dashed grey lines indicate CVs each 25 cycles until CV500. Intermediate CVs between CV500-CV750 are not shown.

## **6A.4 CONCLUSIONS**

In collaboration with Dr. L. Peres (LCC-CNRS, Toulouse), pure Ni-based Ni-foam nanomaterials and their corresponding Ru-doped counterparts with different Ru loadings have been successfully synthesized following the organometallic approach in a two-step procedure. First, a foam-like Ni structure has been obtained composed of particles of *ca.* 100 nm of thickness that result from the alignment of smaller particles. Ru NPs have been synthesized on-top of the Ni nanomaterial, obtaining three different Ru loadings (0.43 wt% in **Ru1@Ni-foam**, 3.2 wt% in **Ru5@Ni-foam** and 6.4 wt% in **Ru10@Ni-foam**). While the samples with higher Ru content show aggregated Ru NPs, no clear definition of the morphology of the one containing less Ru have been achieved yet. Passivation of the materials under air exposition allowed to obtain a Ni(0)/Ni(OH)<sub>2</sub>-NiOOH core@shell Ni-based structure with supported Ru/RuO<sub>2</sub> (core/shell) NPs.

HER electrocatalytic studies in acidic media showed higher catalytic current densities with the samples containing a higher amount of Ru. However, the best catalytic activity was achieved for **Ru5@Ni-foam**, which can derive from its higher degree of crystallinity, as observed in the corresponding XRD pattern, or even from its different Ru/RuO<sub>2</sub> ratio or its optimum Ru-doping content, providing a good interface between the Ni/Ni(OH)<sub>2</sub>-NiOOH species and the Ru dopant. HER electrocatalytic studies in alkaline media have shown again the same tendencies as in acidic media.

Anodic scanning under alkaline OER conditions has confirmed the appearance of one anodic peak in the oxidative forward scan prior to a sharp current increase, assigned to the electrocatalytic oxidation of water to dioxygen. This redox wave has been attributed to the oxidation of Ni(II) to Ni(III), confirming NiOOH species as the real active species towards the OER. The electrocatalytic studies in Fe-free solutions point to lower activities and activations than in non-purified alkaline solutions, confirming the crucial role of Fe incorporation in the overall OER catalytic activity of Ni-based materials. The reduced OER catalytic performances at pH 7 and pH 9 compared to pH ~14 allow to conclude that even though the presence of iron is crucial for an efficient catalysis, the deprotonating effect of hydroxyl anions under strong alkaline conditions also plays a key role assisting the formation of the active oxygen species (NiOO<sup>-</sup>).

Finally, *in situ* UV-vis spectroelectrochemistry was used to track the metal oxidation process from Ni(OH)<sub>2</sub> to NiOOH taking place under potential stress. When a potential after the 1<sup>st</sup> oxidative redox wave is applied, an absorbance increase was observed in all samples. The difference in absorbance when applying a potential before and after the oxidative Ni wave revealed two different spectrum shapes. In the **Ni-foam** and **Ru5@Ni-foam** samples, the resulting spectra are similar to those previously reported in the literature and assigned to the NiOOH species with a characteristic broad band centered at 450 nm. On the other hand, the sample **Ru1@Ni-foam** presents a very different shape, with an increasing absorption towards the NIR peaking at 650 nm, suggesting that the low Ru incorporation changes the NiOOH species, supporting the different behaviour found for this system towards the OER, compared to **Ni-foam**, **Ru5@Ni-foam** and **Ru10@Ni-foam**. The formed species and their evolution were followed along a potential cycling, revealing that the absorption band ( $\lambda=500$  nm) of the Ni catalyst was rising right after the onset of the Ni(OH)<sub>2</sub>  $\rightarrow$  NiOOH redox wave, and finished before the catalytic OER starts. This later confirms NiOOH species as the preferential oxidation state previous the OER, facilitating a more favourable (*i.e.* with lower overpotential) pathway for the OER. These results suggest that the formation of NiOOH species occurs entirely during the Ni oxidation reaction, so it is not directly the species accumulated during catalysis, as a further oxidation of the species is needed to oxidize water.

## **6A.5 EXPERIMENTAL SECTION**

### **Materials and methods**

All procedures concerning the synthesis and preparation of samples were carried out using standard Schlenk tubes, Fisher-Porter glassware and vacuum line techniques or in a glove-box (MBraun) under argon atmosphere. Tetrahydrofuran (THF) was obtained from CarloErba, purified using a purification MBraun SPS-800 equipment and degassed with three freeze–pump–thaw cycles before use. Absolute anhydrous ethanol (CarloErba, ACS reagent) was dried over molecular sieve and degassed by Ar bubbling before use. Bis(1,5-cyclooctadiene)nickel(0)  $[\text{Ni}(\text{COD})_2]$  (>98%, Strem Chemicals) was stored under argon inside the glovebox (MBraun).  $[\text{Ru}(\text{Me-allyl})_2(\text{COD})]$  was purchased from Sigma-Aldrich. Deionized water was obtained from Millipore (MilliQ, 18.2 M $\Omega$ /cm; Millipore, Bedford, MA). Ar and H<sub>2</sub> were purchased from Air Liquide (Alphagaz).

### **Synthetic procedures**

**Synthesis of Ni foam.** Under argon atmosphere,  $[\text{Ni}(\text{COD})_2]$  (4.0 mmol, 1.1 g) was added into a Fischer-Porter and solubilized in THF (180 mL). Then, outside the glovebox, ethanol (20 mL, 10% v/v) was added with a syringe under Ar. The Fischer-Porter was then pressurized with 3 bar of dihydrogen and the reaction mixture kept at 70 °C under vigorous stirring for 20 h. After the reaction time, excess H<sub>2</sub> was evacuated and the solvent evaporated under vacuum. The product was collected inside the glovebox using a magnet and scraping with a spatula and stored under inert atmosphere.

**Synthesis of x wt% Ru over Ni foam.** Under argon atmosphere,  $[\text{Ru}(\text{Me-allyl})_2(\text{COD})]$  was added to a Fischer-Porter containing a dispersion of the pre-synthesized Ni foam in THF and kept impregnating for 3 days at room temperature under agitation. Next, the reaction vessel was pressurized with 3 bar of H<sub>2</sub> at 50 °C for 18 h.

## **Characterization techniques**

All the analyses on the samples before catalysis have been conducted under inert gas except for XPS.

**Transmission electron microscopy (TEM)** and high resolution transmission electron microscopy (HRTEM) analyses were performed at the “Centre de microcaracterisation Raimond Castaing, UMS 3623, Toulouse” by using a JEOL JEM 1400 operating at 120 kV with a point resolution of 2.0 Å. High resolution analyses were conducted using a JEOL JEM 2100F equipped with a Field Emission Gun (FEG) operating at 200 kV with a point resolution of 2.3 Å and a JEOL JEM-ARM200F Cold FEG (cold field emission gun) operating at 200 kV with a point resolution of >1.9 Å and coupled to an EDX spectrometer and an energy loss spectrometer (EELS).

**Scanning electron microscopy (SEM):** SEM observations were conducted on a JEOL 6700F microscope.

**X-ray photoelectron spectroscopy (XPS).** The XPS spectra were collected by a Thermo Scientific K-Alpha system via using a monochromatised Al K $\alpha$  ( $h\nu = 1486.6$  eV) source. The size of the X-ray Spot was about 400  $\mu\text{m}$ . The Pass energy was respectively fixed at 30 eV for core levels (step 0.1 eV) and 160 eV for surveys (step 1eV). The Au 4f $_{7/2}$  ( $83.9 \pm 0.1$  eV) and Cu 2p $_{3/2}$  ( $932.8 \pm 0.1$  eV) photoelectron lines were used to calibrate the spectrometer energy. All the XPS spectra were collected in direct mode N (Ec), coupling with subtraction of background signal via Shirley method. The charge effect was neutralized by using flood Gun on the top surface.

**X-ray diffraction (XRD).** The crystallinity and phase purity were investigated by XRD on a Panalytical MPDPro diffractometer using Cu K $\alpha$  radiation ( $\lambda = 1.5418$  Å).

**Inductively coupled plasma optic emission spectroscopy (ICP-OES).** Ru contents were determined by ICP-OES using a PerkinElmer, Optima 2100 DV instrument at LCC-CNRS Toulouse.

**Electrochemical measurements.** Electrocatalytic experiments were performed at room temperature in a three-electrode configuration using Saturated Calomel Electrode (SCE, KCl sat'd) and Pt as reference and counter electrodes, respectively. RDE ( $\varnothing=0.3$  cm,  $S=0.07$  cm<sup>2</sup>) was used as working electrode (WE) after drop-casting each sample from a THF suspension (2 mg/mL). The potential was controlled using a BioLogic SP-150 potentiostat using the EC-Lab software for data acquisition and data handling. IR drop was automatically corrected at 85% for cyclic voltammetry and chronoamperometry. All catalytic experiments were measured with a sweep rate of 10 mV·s<sup>-1</sup>. Potentials are reported vs. RHE ( $E_{\text{RHE}} = E_{\text{SCE}} + 0.244 \text{ V} + (0.059 \times \text{pH})$ ) and overpotentials are calculated as  $\eta_0 = E_{\text{SCE}} + 0.244 \text{ V} - (1.23 - 0.059 \times \text{pH})$  or  $\eta_0 = E_{\text{SCE}} + 0.244 \text{ V} - (0 - 0.059 \times \text{pH})$  for OER and HER, respectively.

Purified electrolyte (*i.e.* Fe-free) was prepared following a procedure reported by Trotochaud *et al.*<sup>33</sup>

**In situ UV-vis Spectroelectrochemistry.** UV-vis spectra were collected using a Cary 60 UV-vis spectrometer (Agilent Technologies). Spectra were collected between 290 and 900 nm with a medium scan rate. Electrochemical experiments were carried out using a PalmSens4 potentiostat and a typical three-electrode configuration by using Ag/AgCl (KCl sat'd) and a Pt mesh as reference and counter electrodes, respectively. WE were prepared by drop-casting 2 drops of 25  $\mu\text{L}$  of a suspension of the material in THF (2 mg/mL) onto a FTO electrode. All potentials are reported versus the reversible hydrogen electrode ( $E_{\text{RHE}} = E_{\text{Ag/AgCl}} + E^0_{\text{Ag/AgCl}} + 0.059 \text{ V} \times \text{pH}$ ), where  $E^0_{\text{Ag/AgCl}} = 0.199$  V. Fluorine doped tin oxide (FTO) electrodes (Xop Física) ( $S=1$  cm<sup>2</sup>) were used as working electrodes. The electrodes were cleaned prior to the measurements in high purity ethanol and afterward rinsed with Milli-Q water using sonication. A 1 M NaOH aqueous solution (pH  $\sim 14$ ) was used as the electrolyte in all this experiments, unless stated.

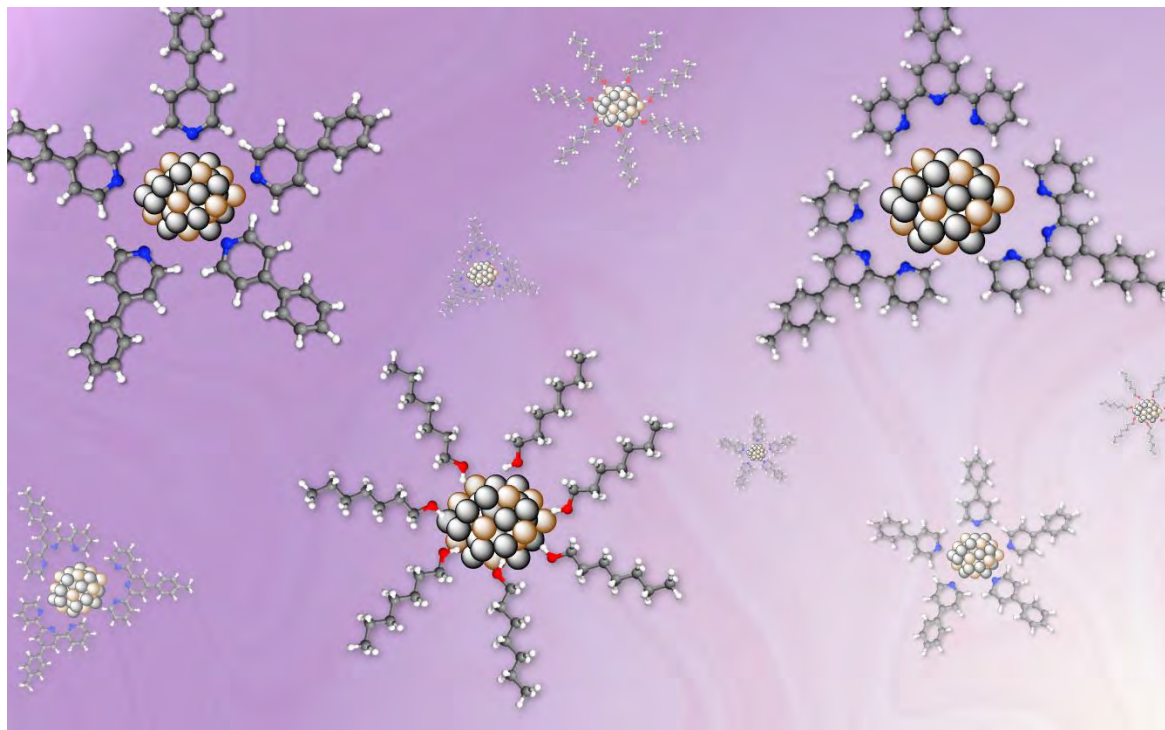


## 6A.6. REFERENCES

- <sup>1</sup> Y. Lee, J. Suntivich, K. J. May, E. E. Perry and Y. Shao-Horn. *J. Phys. Chem. Lett.* **2012**, 3, 399-404.
- <sup>2</sup> T. Reier, M. Oezaslan and P. Strasser. *ACS Catal.* **2012**, 2, 1765-1772.
- <sup>3</sup> D. A. Corrigan, *J. Electrochem. Soc.* **1987**, 134, 2, 377-384
- <sup>4</sup> X. Li, F. C. Walsh and D. Pletcher, *Phys. Chem. Chem. Phys.* **2011**, 13, 1162-1167.
- <sup>5</sup> L. Trotochaud, J.K. Ranney, K.N. Williams and S.W. Boettcher, *J. Am. Chem. Soc.* **2012**, 134, 17253-17261.
- <sup>6</sup> M.W. Louie and A. T. Bell. *J. Am. Chem. Soc.* **2013**, 135, 12329-12337.
- <sup>7</sup> L. Trotochaud, S.L. Young, J.K. Ranney and S.W. Boettcher, *J. Am. Chem. Soc.* **2014**, 136, 6744-6753
- <sup>8</sup> D. Friebel, M.W. Louie, M. Bajdich, K.E. Sanwald, Y. Cai, A. M. Wise, M.J. Cheng, D. Sokaras, T. C. Weng, R. Alonso-Mori, R. C. Davis, J.R. Bargar, J.K. Norskov, A. Nilsson and A.T. Bell, *J. Am. Chem. Soc.* **2015**, 137, 1305-1313.
- <sup>9</sup> Z. Lu, W. Xu, W. Zhu, Q. Yang, X. Lei, J. Liu, Y. Li, X. Sun and X. Duan, *Chem. Commun.* **2014**, 50, 6479.
- <sup>10</sup> M. Gao, W. Shen, Z. Zhuang, Q. Fang, S. Gu, J. Jiang and Y. Yan. *J. Am. Chem. Soc.* **2014**, 136, 7077-7084.
- <sup>11</sup> J. Qiao, F. Song, J. Hu, D. Huo, J. Yuan, J. Shen, L. Niu and A.J. Wang, *Int. J. Hydrogen Energy* **2019**, 44, 16368-16377.
- <sup>12</sup> R.H. Manso, P. Acharya, S. Deng, C.C. Crane, B. Reinhart, S. Lee, X. Tong, D. Nykypanchuk, J. Zhu, Y. Zhu, L.F. Greenlee and J. Chen, *Nanoscale* **2019**, 11, 8170.
- <sup>13</sup> J. Liu, Y. Zheng, Y. Jiao, Z. Wang, Z. Lu, A. Vasileff and S. Z. Qiao, *Small* **2018**, 14, 1704073.
- <sup>14</sup> I.C. Man, H.Y. Su, F. Calle-Vallejo, H.A. Hansen, J.I. Martínez, N.G. Inoglu, J. Kitchin, T.F. Jaramillo, J.K. Norskov and J. Rossmeisl, *ChemCatChem* **2011**, 3, 1159-1165.
- <sup>15</sup> Q. Sun, K. Reuter and M. Scheffler, *Phys. Rev. B* **2004**, 70, 235402
- <sup>16</sup> Y.D. Kim, A.P. Seitsonen, S. Wendt, J. Wang, C. Fan, K. Jacobi, H. Over and G. Ertl, *J. Phys. Chem. B* **2001**, 3752-3758.
- <sup>17</sup> M. Li, H. Wang, W. Zhu, W. Li, C. Wang and X. Lu, *Adv. Sci.* **2020**, 7, 1901833.
- <sup>18</sup> W. Wu, Y. Wu, D. Zheng, K. Wang and Z. Tang, *Electrochim. Acta* **2019**, 320, 134568.
- <sup>19</sup> Y. Liu, S. Liu, Y. Wang, Q. Zhang, L. Gu, S. Zhao, D. Xu, Y. Li, J. Bao and X. Dai, *J. Am. Chem. Soc.* **2018**, 140, 2731-2734.
- <sup>20</sup> Z. Liu, M. Zha, Q. Wang, G. Hu and L. Feng, *Chem. Commun.* **2020**, 56, 2352.
- <sup>21</sup> Y. Lin, L. Zhao, L. Wang and Y. Gong, *Dalton Trans.* **2021**, 50, 4280.

- <sup>22</sup> C. Amiens, B. Chaudret, D. Ciuculescu-Pradines, V. Collière, K. Fajerweg, P. Fau, M. Kahn, A. Maisonnat, K. Soulantica and K. Philippot, *New J. Chem.* **2013**, 37, 3374-3401.
- <sup>23</sup> X.P. Fu, L. Peres, J. Esvan, C. Amiens, K. Philippot, N. Yan. *Nanoscale*, 2021, 13, 8931–8939.
- <sup>24</sup> Y. Gao, H. Li and G. Yang, *Cryst. Growth Des.* **2015**, 15, 4475-4483.
- <sup>25</sup> Hao Lei, Zhen Song, Dali Tan, Xinhe Bao, Xuhong Mu, Baoning Zong and E. Min, *Appl. Catal. A: General* **2001**, 214, 69-76.
- <sup>26</sup> M. C. Biesinger, B.P. Payne, L.W.M. Lau, A. Gerson and R. St. C. Smart. *Surf. Interface Anal.* **2009**, 41, 324-332.
- <sup>27</sup> N. Weidler, J. Schuch, F. Knaus, P. Stenner, S. Hoch, A. Maljusch, R. Schäfer, B. Kaiser and W. Jaegermann, *J. Phys. Chem. C* **2017**, 121, 6455-6463
- <sup>28</sup> D.J. Morgan, *Surf. Interface Anal.* **2015**, 47, 1072-1079.
- <sup>29</sup> Y. Li, L.A. Zhang, Y. Qin, F. Chu, Y. Kong, Y. Tao, Y. Li, Y. Bu, D. Ding and M. Liu. *ACS Catal.* **2018**, 8, 5714-5720.
- <sup>30</sup> L.F. Huang, M.J. Hutchison, R.J. Santucci, J.R. Scully and J.M. Rondinelli, *J. Phys. Chem. C* **2017**, 121, 9782-9789
- <sup>31</sup> Y.Q. Gao, H.B. Li and G.W. Yang, *Cryst. Growth Des.* **2015**, 15, 4475-4483.
- <sup>32</sup> S. Corby, M.G. Tecedor, S. Tengeler, C. Steinert, B. Moss, C.A. Mesa, H.F. Heiba, A.A. Wilson, B. Kaiser, W. Jaegermann, L. Francàs, S. Gimenez and J.R. Durrant, *Sustainable Energy Fuels* **2020**, 4, 5024-5030.
- <sup>33</sup> L. Trotochaud, S.L. Young, J.K. Ranney and S.W. Boetcher, *J. Am. Chem. Soc.* **2014**, 136, 6744-6753.
- <sup>34</sup> Gerischer, H. In *Solar Energy Conversion: Solid-State Physics Aspects*; B.O. Seraphin, Ed.; Topics in Applied Physics; Springer Berlin Heidelberg: Berlin, **1979**, Vol. 31, pp. 115-172.
- <sup>35</sup> M. Dinca, Y. Surendranath and D.G. Nocera, *Proc. Natl. Acad. Sci. U. S. A.* **2010**, 107, 10337–10341.
- <sup>36</sup> D.K. Bediako, B. Lassalle-Kaiser, Y. Surendranath, J. Yano, V.K. Yachandra and D.G. Nocera, *J. Am. Chem. Soc.* **2012**, 134, 6801–6809.
- <sup>37</sup> D.K. Bediako, Y. Surendranath and D.G. Nocera, *J. Am. Chem. Soc.* **2013**, 135, 3662–3674.
- <sup>38</sup> B.J. Trzesniewski, O. Diaz-Morales, D.A. Vermaas, A. Longo, W. Bras, M.T.M. Koper and W.A. Smith, *J. Am. Chem. Soc.* **2015**, 137, 15112–15121.
- <sup>39</sup> L. Francàs, S. Corby, S. Selim, D. Lee, C.A. Mesa, R. Godin, E. Pastor, I.E.L Stephens, K.S. Choi and J.R. Durrant, *Nat. Commun.* **2019**, 10, 5208.
- <sup>40</sup> L. Francàs, S. Selim, S. Corby, D. Lee, C.A. Mesa, E. Pastor, K.S. Choi and J. R. Durrant, *Chem. Sci.* **2021**, 12, 7442-7452.

## Chapter 6B. Ligand-capped RuCo bimetallic nanoparticles



WS catalysis using cost-effective metal-based heterogeneous catalysts is highly attractive for economical and sustainable concerns. In this chapter the organometallic synthesis of bimetallic RuCo NPs will be reported. The effect of different stabilizing agents and of the Ru/Co ratio on the morphology of the obtained NPs has been assessed by TEM and STEM-HAADF. Other techniques such as EDX and WAXS have allowed to extract more information about the structure of the obtained materials.



## **6B.1 INTRODUCTION**

As stated in the introduction of Section 6.A.1, a well-known strategy to improve the catalytic activity of monometallic nanomaterials relies on the incorporation of a second metal in order to modulate the electronic properties of the final material. The synergistic effect between metal atoms, which modulates the electronic properties of the final material and, consequently, the adsorption energy of reaction intermediates, may end up improving the catalytic activity. In addition to synergistic effects, several works have shown that alloyed materials (*i.e.* RuCo systems related to those developed in this work) present much higher ECSA and lower charge-transfer resistance (*i.e.* improved kinetics) than the corresponding monometallic counterparts, boosting both the HER and OER catalytic activities.<sup>1,2,3,4,5</sup>

Accordingly, the improvement of the catalytic activity of monometallic Ru and Co nanomaterials by combining both metals in bimetallic systems has been reported in the literature. For instance, DFT studies from J. Rossmeisl and co-workers indicated that the outstanding OER activity of RuCo systems may result from the activation of the proton donor-acceptor functionality on the conventionally inactive bridge Ru surface sites, when Co is incorporated into Ru-based materials.<sup>6</sup> In addition, some studies reported the positive effect of Co addition to obtain higher oxidation state Ru species, which are more prone to catalyze the OER. In this regard, S. Kang and collaborators demonstrated that in CoRu-MoS<sub>2</sub> systems, Co-doping favors the oxidation of Ru into RuO<sub>2</sub>, which is a well-known active OER catalyst due to its adsorption affinity for OH<sup>-</sup> and OOH intermediates.<sup>1</sup> This was confirmed by the poor activity towards OER obtained with Ru-MoS<sub>2</sub> ( $\eta_{10} = 800$  mV *vs.*  $\eta_{10} = 308$  mV for Ru-MoS<sub>2</sub> and Co/Ru-MoS<sub>2</sub>, respectively), where negligible oxidation to RuO<sub>2</sub> was observed. Also, F. Yang and collaborators evidenced a correlation between the obtained lower overpotential towards OER ( $\eta_{10} = 240$  mV for Ru<sub>1</sub>Co<sub>2</sub> *vs.*  $\eta_{10} = 301$  mV for RuO<sub>2</sub>) and the increased content of Ru<sup>+4</sup> in the catalyst, confirming that the Ru<sup>+4</sup> species are the predominant active species favoring OH<sup>-</sup> adsorption.<sup>2</sup> In fact, the addition of Co into the Ru-based nanomaterial allowed to shift the Ru 3d XPS peak to higher binding energies, indicating that Co regulates the electronic structure of Ru, favoring the formation of Ru<sup>+4</sup>, and thus improving its OER catalytic activity.

Furthermore, C. Wang and L. Qi reported an inter-doped bimetallic heterostructure ((Ru-Co)O<sub>x</sub>) formed by Co-doped RuO<sub>2</sub> (Co-RuO<sub>2</sub>) nanocrystals and Ru-doped Co<sub>3</sub>O<sub>4</sub> (Ru-Co<sub>3</sub>O<sub>4</sub>) nanocrystals.<sup>3</sup> They attributed the observed increased catalytic activity for the bimetallic system to the transformation, under OER conditions, of Ru-Co<sub>3</sub>O<sub>4</sub> to Ru-CoOOH species which, jointly with the Co sites in the as-synthesized Co-RuO<sub>2</sub> species, could improve the oxygen binding energy of the Ru sites, leading to improved OER performance ( $\eta_{10} = 171.2$  mV for (Ru-Co)O<sub>x</sub> vs.  $\eta_{10} = 333.6$  and 311.4 mV for Co<sub>3</sub>O<sub>4</sub> and RuO<sub>2</sub>, respectively).

Regarding HER, L. Qi and co-workers attributed the increase in HER activity of bimetallic Co-RuO<sub>2</sub>/Ru-Co<sub>3</sub>O<sub>4</sub> nanocrystals to the formation of Co(OH)<sub>2</sub> species and the reduction of RuO<sub>2</sub> to Ru(0) under alkaline reductive conditions.<sup>3</sup> In addition, synergistic effects between the Co sites in the as-synthesized Ru-Co<sub>3</sub>O<sub>4</sub> nanocrystals and the generated Co(OH)<sub>2</sub> species could improve water dissociation on the Ru(0) sites during HER catalysis ( $\eta_{10} = 44.1$  mV for (RuCo)O<sub>x</sub> vs.  $\eta_{10} = 268.6$  and 87.7 mV for Co<sub>3</sub>O<sub>4</sub> and RuO<sub>2</sub>, respectively). Finally, F. Yang and co-workers found a correlation between the HER activity and the content of Co(0) species in the catalyst, related to the fact that metallic Co possesses an adsorption energy of H close to that of Pt and thus promotes rapid H adsorption and recombination to form H<sub>2</sub> molecules.<sup>2</sup> XPS analysis confirmed that the simultaneous presence of Ru and Co modulates the electronic structure of the material, shifting the Co 2p peak to lower energies, thus indicating that Co is reduced and prone to be in the metallic state, which leads to improved HER catalytic activity ( $\eta_{10} = 188$  mV for Ru<sub>1</sub>Co<sub>2</sub>).

A summary of the most relevant electrocatalytic HER and OER parameters for the catalytic systems reported above can be found in Table 1.

**Table 1.** Summary of the electrocatalytic parameters towards HER and OER from Co/Ru bimetallic nanocatalytic systems.

Reference	Catalyst	HER		OER	
		$\eta_{10}$ (mV)	Tafel slope (mV/dec)	$\eta_{10}$ (mV)	Tafel slope (mV/dec)
1	Co/Ru-MoS <sub>2</sub>	52	55	308	50
	Co-MoS <sub>2</sub>	139	89	353	74
	Ru-MoS <sub>2</sub>	90	58	800	61
	MoS <sub>2</sub>	287	74	-	-
2	Ru <sub>1</sub> Co <sub>2</sub>	188	66.5	240	54.4
	Ru <sub>1</sub> Co <sub>0.5</sub>	329	-	308	70.1
	Ru <sub>1</sub> Co <sub>1</sub>	295	-	278	59.7
	Ru <sub>1</sub> Co <sub>3</sub>	229	-	283	63.3
	RuO <sub>2</sub>	-	-	301	66.4
3	(Ru-Co)O <sub>x</sub>	44.1	23.5	171.2	60.8
	Co <sub>3</sub> O <sub>4</sub>	268.6	124.4	333.6	61.6
	RuO <sub>2</sub>	87.5	59.6	311.4	78.7

Used electrolyte: 1 M KOH, G = graphene, NG=nitrogen doped graphene.

In view of the interest in combining Ru and Co to develop cost-efficient catalysts for electrocatalytic WS, the organometallic synthesis of new bimetallic RuCo NPs will be described in the following subsections. Special emphasis will be put in extracting valuable insights on the influence of the nature of the stabilizing ligands and of the metal molar ratio on the morphology of the obtained NPs. Unfortunately, due to lack of time electrocatalytic WS tests will be performed in a future work.

## 6B.2 SYNTHESIS AND CHARACTERIZATION OF RuCo NPs

### 6B.2.1 Synthesis of RuCo bimetallic NPs

Bimetallic RuCo NPs were synthesized following the organometallic approach,<sup>7</sup> taking inspiration from a previous work in our group where alloyed RuCo NPs of low size (< 2 nm) embedded in a polymeric matrix (polyvinylpyrrolidone) were easily prepared.<sup>8</sup> This synthesis protocol is based on the simultaneous hydrogenation (3 bar H<sub>2</sub>; r.t., THF) of the [Co<sup>I</sup>(η<sup>3</sup>-C<sub>8</sub>H<sub>13</sub>)(η<sup>4</sup>-C<sub>8</sub>H<sub>12</sub>)] and [Ru(η<sup>4</sup>-C<sub>8</sub>H<sub>12</sub>)(η<sup>6</sup>-C<sub>8</sub>H<sub>10</sub>)] (also named [Co(COD)(COE)] [Ru(COD)(COT)], respectively) complexes. Given the similar kinetics of decomposition of these two precursors, these synthesis conditions tend to favor the formation of alloyed NPs.

As previously explained in the Introduction part, the nature of the stabilizer can influence the NPs properties, *i.e.* mean size, shape, dispersion, solubility, stability, etc. In the present study, three different stabilizing agents, namely 4-phenylpyridine (**4PP**), 4'-(4-methylphenyl)-2,2':6',2''-terpyridine (**tpy**), and 1-heptanol (**heptOH**) were used to synthesize RuCo NPs, the last one being as well the synthetic reaction solvent (Fig. 1). The effect of this parameter on the characteristics of the NPs was followed by transmission electron microscopy (TEM). Monometallic Ru and Co NPs were also synthesized for comparison purposes by following previously reported procedures.<sup>9,10,11</sup>

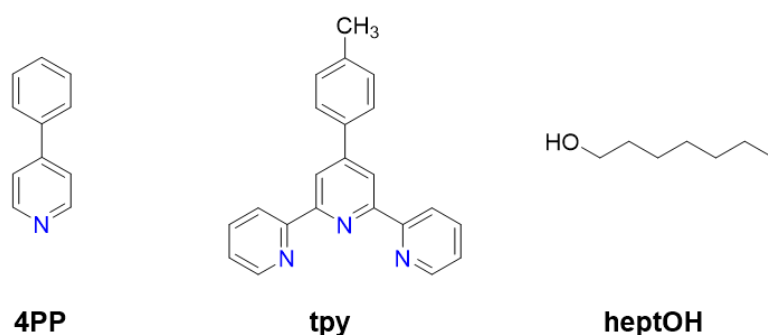


**Figure 1.** Stabilizing agents used in the synthesis of RuCo NPs: 4-Phenylpyridine (4PP), 4'-(4-methylphenyl)-2,2':6',2''-terpyridine (tpy) and 1-heptanol (heptOH).

The RuCo NPs were prepared following a one-step procedure under typical decomposition reaction conditions (3 bar of H<sub>2</sub>, r.t., 24 h) using [Ru(COD)(COT)] and [Co(COD)(COE)] as metal sources (Fig. 2). For each stabilizer, the synthesis was



performed with different RuCo molar ratios, [Ru:Co, 1:1, 2:1 and 1:2], in order to have different RuCo compositions and study the influence of the metal ratio. Concerning the ligand concentration, 0.2 molar eq. of 4PP or tpy ligands with respect to the total metal content were used. A solution of each ligand in THF (or a volume of pure 1-heptanol for the heptOH-stabilized NPs) was added into the Fisher-Porter reactor that contained the two organometallic precursors. The reactor was maintained at low temperature to prevent any intermediate complex formation, followed by pressurizing the reactor with 3 bar of H<sub>2</sub> before leaving the reaction under constant stirring at r.t. for 24 h (or 18 h for the heptOH systems) (Fig. 2). A fast change of color from brown to dark black indicated the NPs formation (Fig. 3). After removing the excess H<sub>2</sub>, the formed RuCo NPs were isolated either by magnetic precipitation when applying a magnet onto the reactor walls (4PP systems), through addition of pentane after reducing the solution volume under vacuum (tpy systems) or by evaporation under vacuum at 70 °C (heptOH systems). Three washings were then performed with pentane under Ar in order to eliminate any rest of free ligand/cyclooctane and get a purified black solid. All RuCo NPs could be obtained as a solid powder after drying under vacuum.

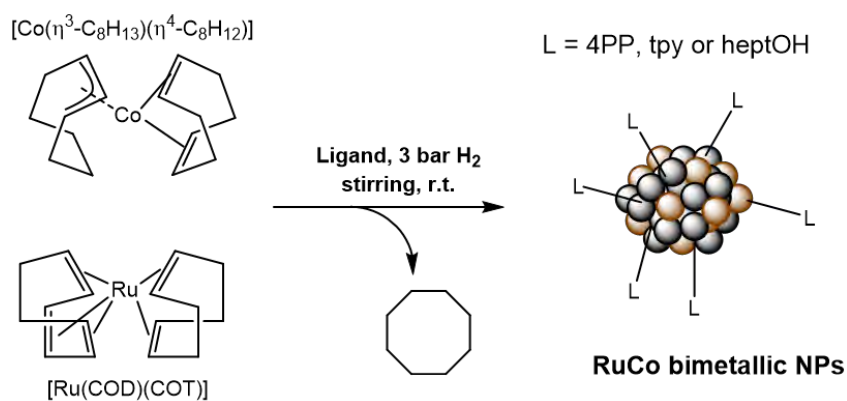


**Figure 2.** Schematic synthesis of bimetallic RuCo NPs stabilized with 4PP, tpy or heptOH ligands (L).

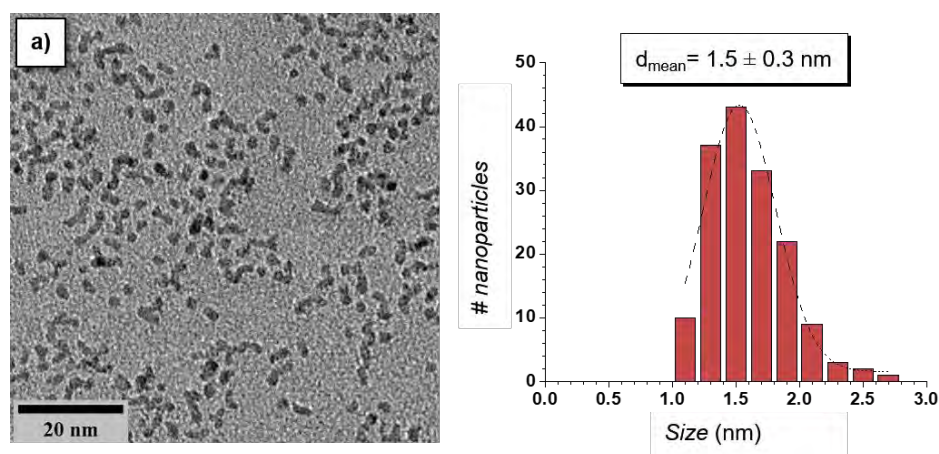


**Figure 3.** Picture of the starting reaction medium before hydrogenation (left) and crude colloidal suspension of bimetallic RuCo NPs obtained after hydrogenation (right).

## 6B.2.2 TEM, STEM-HAADF and EDX analysis

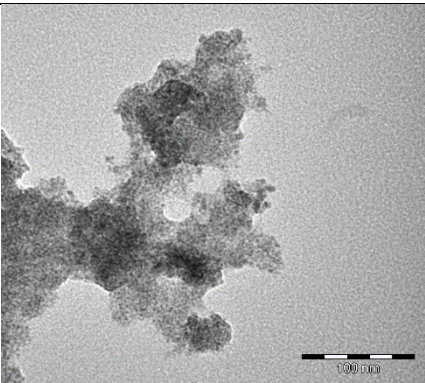
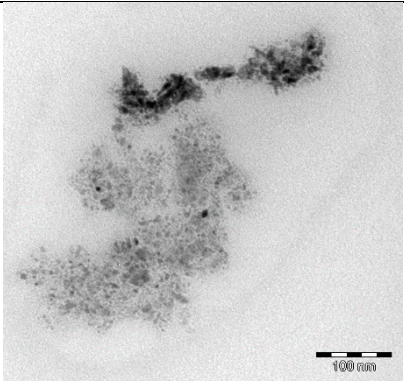
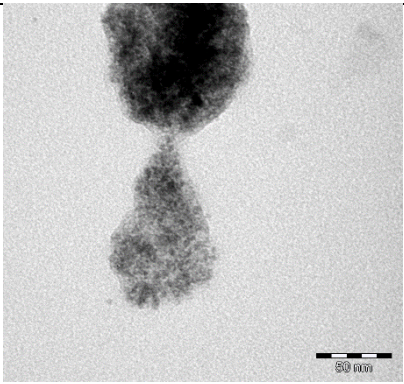
### 6B.2.2.1 Pyridine-based ligands as stabilizers

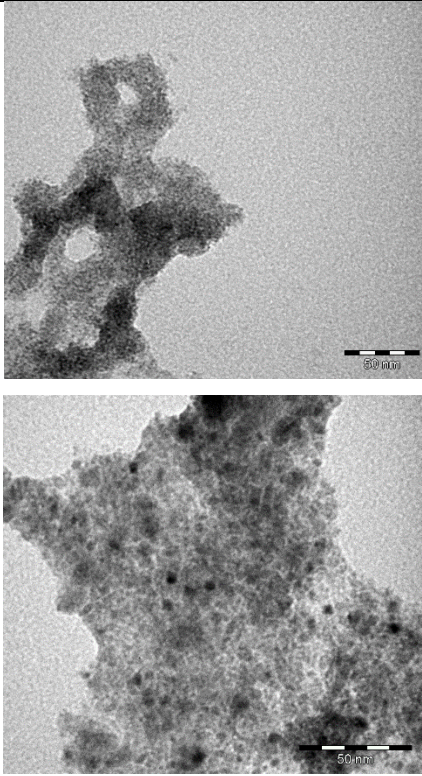
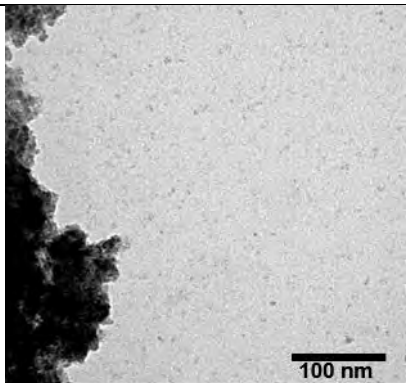
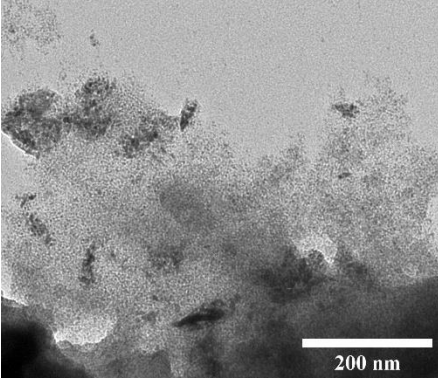
Monometallic Ru and Co NPs stabilized with the 4-phenylpyridine ligand, Ru-4PP and Co-4PP, have been prepared for comparative purposes with the bimetallic systems. For Ru-4PP NPs (0.2 eq. 4PP), a previously reported procedure was followed,<sup>9</sup> that allows to access elongated and well-dispersed NPs ( $1.5 \pm 0.3$  nm), thus indicating that 4PP is a good stabilizer for Ru NPs even at a low quantity (Fig. 4). In contrast, when applying a similar procedure to synthesize Co NPs, heterogenous samples have been obtained for all Co-4PP NPs prepared using different quantities of 4PP ligand (Table 2), presenting large nanostructures that look like agglomerates of small individual NPs. The addition of a very high quantity of ligand (*i.e.* 10 and 20 eq.) allowed to obtain some isolated and well dispersed NPs, although a lot of agglomerates are still found. The use of toluene as a solvent instead of THF seemed to provide a less heterogeneous system, but with only one result in this solvent it is not possible to conclude on the real role of the solvent. Altogether, the TEM results indicate that 4PP ligand does not allow to access well dispersed NPs contrarily to what is obtained with ruthenium. This difference would merit to be studied in depth in the future, for example by comparing the coordination mode of the ligand at the metal surface and its strength through DFT calculations.



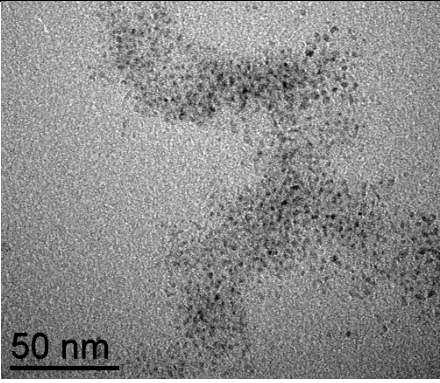
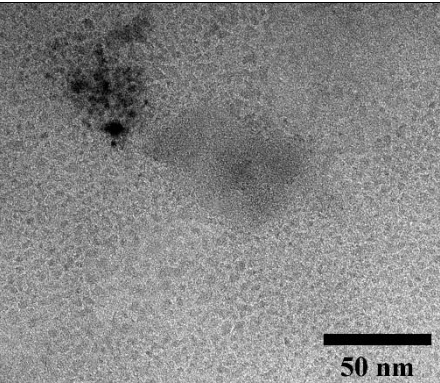
**Figure 4.** TEM image and corresponding size histogram for Ru-4PP (0.2 eq. 4PP).

**Table 2.** Summary of the evolution of synthesis colour, TEM images and visual observations for Co-4PP NPs obtained with different 4PP ligand quantities. Solvent used was THF unless otherwise stated.

Sample	Reaction colours	TEM images	Observations
Co-4PP 0.2 eq.	Bright brown/orange → translucent brown with black solid attached to stirring bar		Agglomerates of small NPs (≈ 1.5 – 2.0 nm)
Co-4PP 0.5 eq.	Bright brown/orange → dark brown clouds with black solid attached to stirring bar		Some agglomerated NPs (1.5 – 3.0 nm) with large nanostructures. Heterogeneous sample.
Co-4PP 2 eq.	Bright brown/orange → brown solution with black solid attached to stirring bar		Agglomerated NPs (1.0 - 5.0 nm). Heterogeneous sample.

<p><b>Co-4PP</b> <b>5 eq.</b></p>	<p>Bright brown/orange → dark brown/black</p>		<p>Agglomeration of NPs with two different sizes (1.0 - 2.0 nm and 3.0 - 4.0 nm)</p>
<p><b>Co-4PP</b> <b>10 eq.</b></p>	<p>Bright brown/orange → black</p>		<p>Some isolated NPs together with large agglomerates. NPs around 2.0 - 3.0 nm. Heterogeneous sample.</p>
<p><b>Co-4PP</b> <b>20 eq.</b></p>	<p>Bright brown/orange → dark brown</p>		<p>Agglomerated NPs (2.0-3.0 nm) with large nanostructures. Less heterogeneous sample.</p>



			
<b>Co-4PP</b> <b>10 eq.</b> <b>in</b> <b>toluene</b>	Bright brown/orange → dark brown (NPs attached to magnet, solution with a lot of colour)		Isolated NPs (2.0- 4.0 nm) with large nanostructures. Less heterogeneous sample.

Despite the poor ability of the 4PP ligand to provide well-dispersed Co NPs, bimetallic, RuCo NPs have been synthesized with this ligand, expecting that the presence of formed Ru clusters may favor Co stabilization to obtain bimetallic NPs. TEM analysis from the crude colloidal solution was performed after depositing a drop onto a carbon covered copper grid. It revealed the presence of isolated, small and spherical NPs together with some aggregates made of individual small NPs for **Ru<sub>1</sub>Co<sub>1</sub>-4PP** and **Ru<sub>2</sub>Co<sub>1</sub>-4PP**. In contrast, for **Ru<sub>1</sub>Co<sub>2</sub>-4PP** small and spherical aggregated NPs were observed but no isolated NPs. The average diameter of these bimetallic NPs was found to be  $2.0 \pm 0.3$  nm,  $1.9 \pm 0.3$  nm and  $1.8 \pm 0.3$  nm for **Ru<sub>1</sub>Co<sub>1</sub>-4PP**, **Ru<sub>2</sub>Co<sub>1</sub>-4PP** and **Ru<sub>1</sub>Co<sub>2</sub>-4PP**, respectively (Figs. 5, 6 and 7, respectively).

Even though no significant effect is observed on the size of the obtained NPs depending on the Ru:Co ratio employed, this parameter has a clear effect on NPs dispersion. This result can be explained by the fact that upon increasing Co content, the stabilization ability of the 4PP ligand decreases, leading to less stable NPs. They may thus tend to agglomerate in order to minimize their surface energy, as already observed for monometallic Co systems. However, the formation of agglomerates of NPs may also result from  $\pi$ - $\pi$  interactions between the aromatic rings of the ligands in adjacent NPs.

Concerning the presence of isolated NPs in samples **Ru<sub>1</sub>Co<sub>1</sub>-4PP** and **Ru<sub>2</sub>Co<sub>1</sub>-4PP** it can result from the high ability of the ligand to stabilize Ru, capping more the NPs when they are more Ru-rich and avoiding their agglomeration. Finally, the formation of Ru clusters may have facilitated the nucleation of Co atoms to form the bimetallic systems, even though the 4PP ligand is not a good stabilizer for Co.

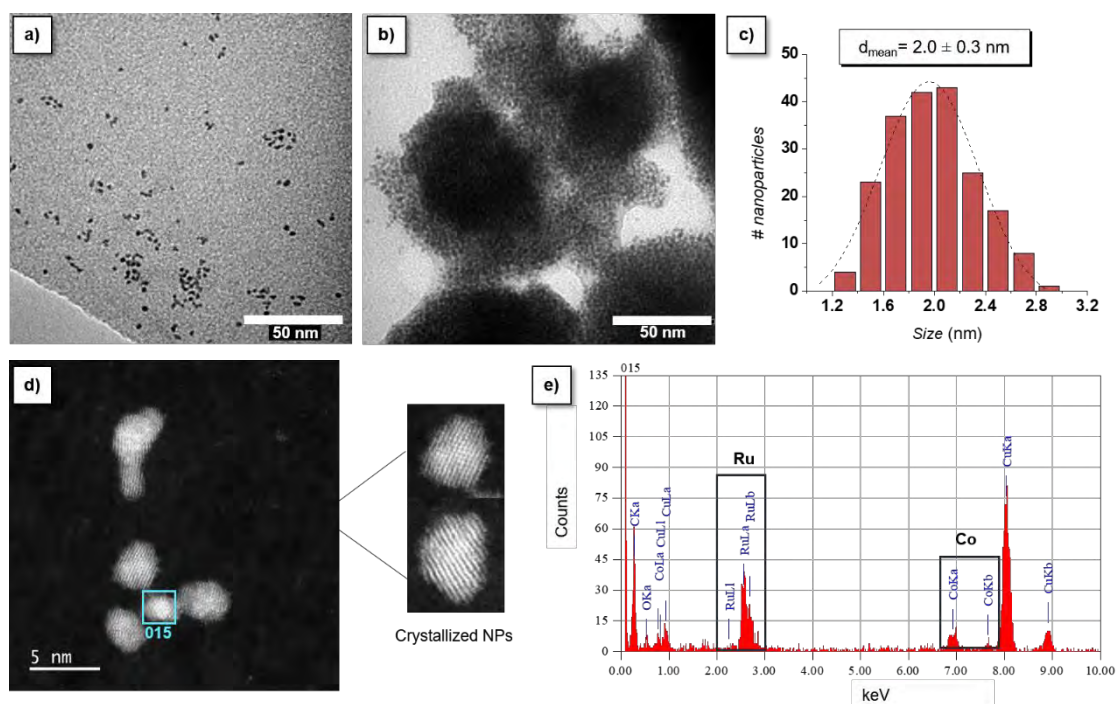


**Figure 5.** TEM images (a-b), size distribution histogram (c), STEM-HAADF image (d) and EDX analysis of a single NP (e) of **Ru<sub>1</sub>Co<sub>1</sub>-4PP**.

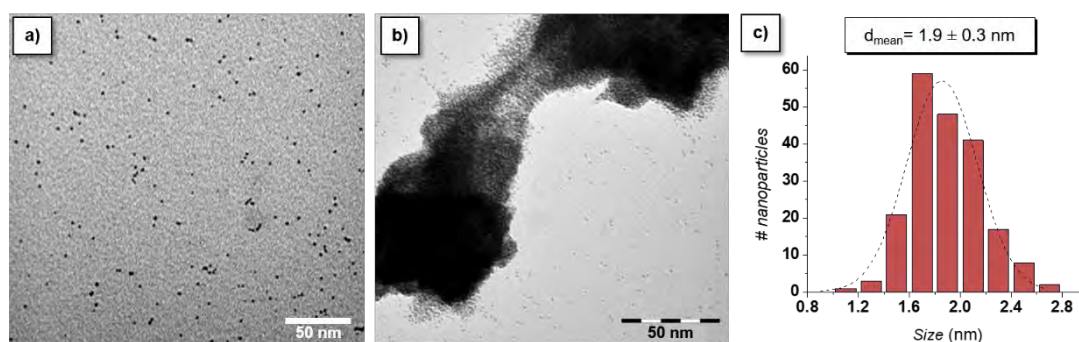


**Figure 6.** TEM images (a-b) and size distribution histogram (c) of **Ru<sub>2</sub>Co<sub>1</sub>-4PP**.

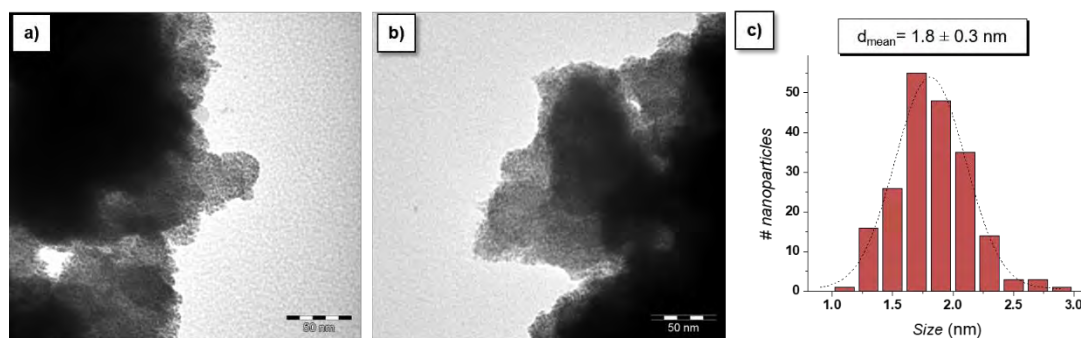


**Figure 7.** TEM images (a-b) and size distribution histogram (c) of **Ru<sub>1</sub>Co<sub>2</sub>-4PP**.

STEM-HAADF images for **Ru<sub>1</sub>Co<sub>1</sub>-4PP** showed well crystallized NPs (Fig. 5d), and EDX analysis revealed the presence of both Ru and Co in a single NP, confirming their bimetallic nature (Fig. 5e). The Ru<sub>at</sub>/Co<sub>at</sub> ratio found by quantitative EDX considering the average results from different isolated NPs is 88%Ru<sub>at</sub>/12%Co<sub>at</sub>. However, when analyzing a set of agglomerated NPs, the Co content increases, obtaining a 56%Ru<sub>at</sub>/44%Co<sub>at</sub> ratio which is in good accordance with the theoretical ratio. In Fig. 8 we can see the evolution of Ru and Co composition along a zone of agglomerated NPs, indicating an increase of Co within the interior of these agglomerates while the content of Ru seems similar along the agglomerate. These results indicate a certain inhomogeneity in the agglomerates that can be explained by the poorer affinity of 4PP ligand for Co compared to Ru, being Co more prone to be placed in the internal part of the agglomerates.

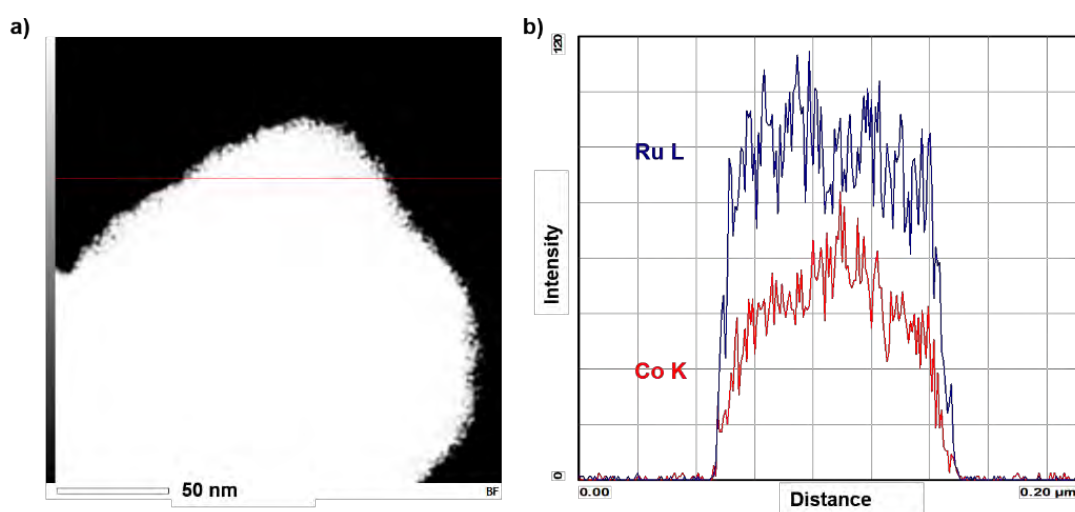


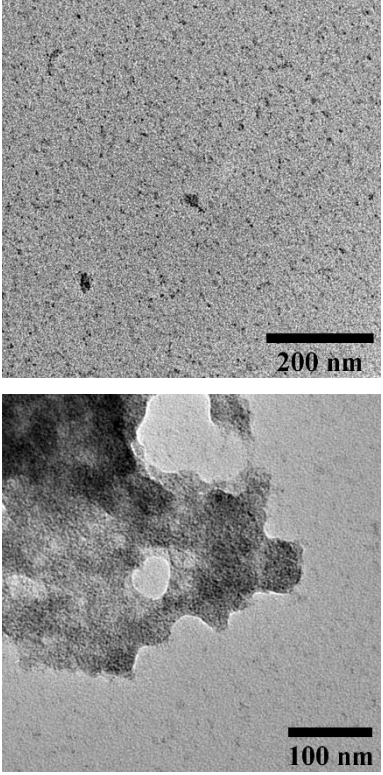
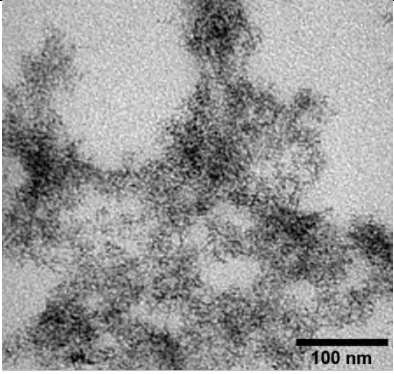
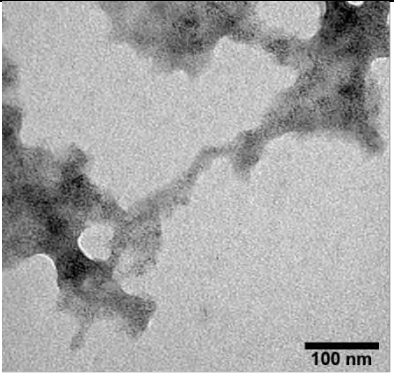
**Figure 8.** STEM-HAADF image of an agglomerated zone from **Ru<sub>1</sub>Co<sub>1</sub>-4PP** (a) and evolution of the Ru and Co composition vs. the distance from the surface (b).

The 4'-(4-methylphenyl)-2,2':6',2''-terpyridine (tpy) ligand has been used as another stabilizing agent. Previous work in the group on the synthesis of Ru NPs in the presence of tpy ligand provided ultrasmall and well dispersed NPs with a mean size depending on the metal/ligand ratio as follows:  $1.4 \pm 0.2$  nm (0.05 eq. tpy),  $1.1 \pm 0.2$  nm (0.1 eq. tpy),  $0.8 \pm 0.3$  nm (0.2 eq. tpy) and  $0.6 \pm 0.3$  nm (0.5 eq. tpy).<sup>12</sup> On the basis of the very NP small sizes observed even at very low ligand content, tpy is considered as a very efficient stabilizing agent for Ru NPs. This can be explained by a strong coordination of the tpy at the NPs surface due to the hard Lewis acid nature of Ru and the hard Lewis base nature of N as well as the chelating nature of this ligand. Before preparing RuCo NPs using tpy as stabilizer, Co-tpy NPs were synthesized in the presence of three different amounts of ligand (Table 3). First, when using 1 eq., a network of agglomerated small NPs ( $2.2 \pm 0.4$  nm) was observed by TEM together with a high quantity of organic matter surrounding them. In addition, the obtained colloidal solution was dark purple but became green after air exposition. This could be explained by the formation of an air-sensitive complex between the organometallic precursor and the ligand under excessive ligand content. Then, we decided to add lower amounts of the tpy ligand (0.2 eq.). In this case, after 24 h, the solution became dark brown although a purple colour was also observed at some point of the reaction. Small NPs with a mean size of  $2.3 \pm 0.3$  nm were obtained. If these NPs were also agglomerated, no organic matter was visible mean time.

When adding 0.1 eq., the colloidal suspension was still a bit purple after 24 h of reaction, indicating again the possible formation of a complex between the ligand and the organometallic precursor. Therefore, the reaction was pursued up to 52 h, obtaining finally a dark brown solution. TEM images of this sample showed again agglomerated NPs but also some isolated and well-dispersed NPs ( $2.2 \pm 0.4$  nm) (Table 3, top row). From these results, tpy appears to be a better ligand than 4PP, providing better dispersed CoNPs than 4PP. As discussed above for 4PP, the agglomeration of the NPs can be favored by  $\pi$ - $\pi$  interactions between the aromatic rings of the surface-coordinated tpy ligands of adjacent NPs, obtaining a network-like structure.



**Table 3.** Summary of the evolution of synthesis colour, TEM images and visual observations for Co-tpy NPs obtained with different ligand equivalents.

Sample	Reaction colours	TEM images	Observations
Co-tpy 0.1 eq.	Bright brown/orange → dark purple → dark brown		Isolated and well-dispersed NPs ( $2.2 \pm 0.4$ nm) and some agglomerates.
Co-tpy 0.2 eq.	Bright brown/orange → dark purple → dark brown		Agglomerated NPs ( $2.3 \pm 0.3$ nm). No organic matter observable.
Co-tpy 1 eq.	Bright brown/orange → black/dark purple		Agglomerated small NPs ( $2.2 \pm 0.4$ nm). Organic matter observable.

Thereafter, bimetallic RuCo-tpy NPs (0.2 eq. tpy) have been synthesized using three different Ru:Co molar ratios as previously with 4PP ligand, samples named as **Ru<sub>1</sub>Co<sub>1</sub>-tpy**, **Ru<sub>2</sub>Co<sub>1</sub>-tpy** and **Ru<sub>1</sub>Co<sub>2</sub>-tpy**. Very small, isolated and well-dispersed NPs have been observed on TEM images for all the samples, even if some aggregates are also present. The average diameter of these NPs was found to be  $1.3 \pm 0.2$  nm,  $1.3 \pm 0.2$  nm and  $1.5 \pm 0.3$  nm for **Ru<sub>1</sub>Co<sub>1</sub>-tpy**, **Ru<sub>2</sub>Co<sub>1</sub>-tpy** and **Ru<sub>1</sub>Co<sub>2</sub>-tpy**, respectively (Figs. 9, 10 and 11, respectively). These results confirm the higher stabilization ability of tpy towards RuCo NPs compared to 4PP, obtaining smaller and better dispersed NPs with tpy than with 4PP for all Ru:Co molar ratios. These results also agree with those obtained for monometallic Ru and Co NPs where tpy allowed to get better controlled NPs than 4PP.

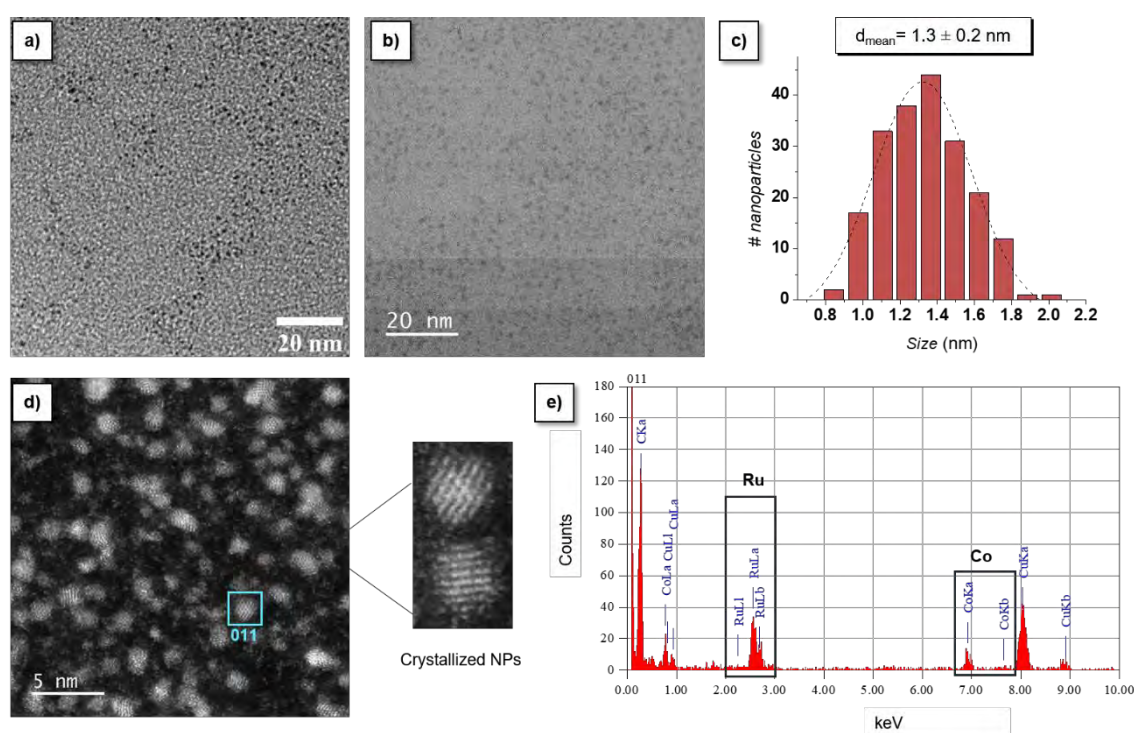


**Figure 9.** TEM images (a-b), size distribution histogram (c), STEM-HAADF image (d) and EDX analysis of a single NP (e) of **Ru<sub>1</sub>Co<sub>1</sub>-tpy**.

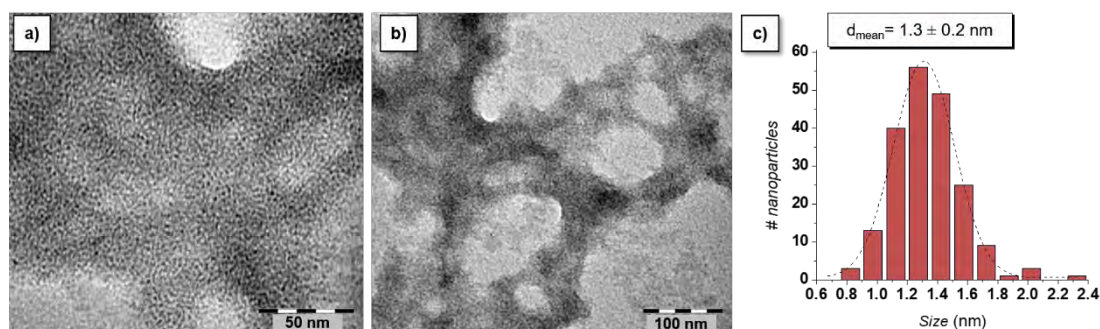


**Figure 10.** TEM images (a-b) and size distribution histogram (c) of **Ru<sub>2</sub>Co<sub>1</sub>-tpy**.

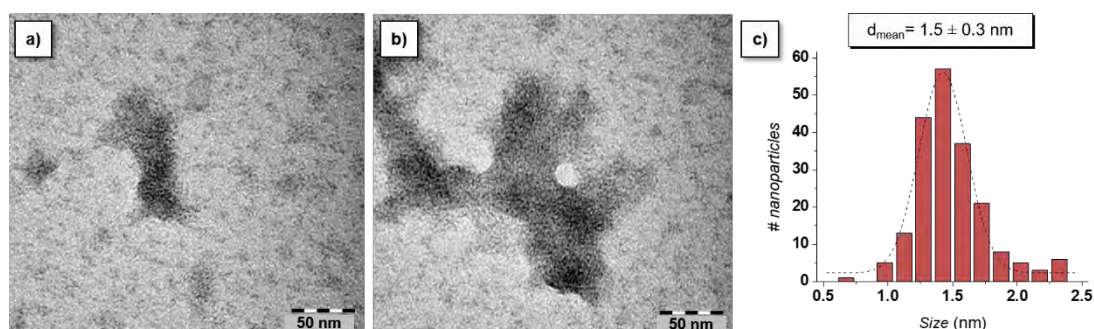


**Figure 11.** TEM images (a-b) and size distribution histogram (c) of **Ru<sub>1</sub>Co<sub>2</sub>-tpy**.

STEM-HAADF images for **Ru<sub>1</sub>Co<sub>1</sub>-tpy** indicated the presence of well crystallized NPs (Fig. 9d), and EDX analysis revealed the presence of both Ru and Co in a single NP, confirming their bimetallic nature (Fig. 9e). The Ru<sub>at</sub>/Co<sub>at</sub> ratio found by quantitative EDX considering the average results from different isolated NPs is 77%Ru<sub>at</sub>/23%Co<sub>at</sub>. Again, when analyzing a set of agglomerated NPs, we observed a Co content increase, but to a lower extent than for **Ru<sub>1</sub>Co<sub>1</sub>-4PP**, obtaining 65%Ru<sub>at</sub>/35%Co<sub>at</sub>. This lower difference in Co content between single NPs and agglomerated NPs points again to the better stabilization of the Co NPs with the tpy ligand compared to 4PP.

#### 6B.2.2.2 1-heptanol as stabilizer

For comparison purpose with RuCo NPs systems, both monometallic Ru and Co NPs were first prepared in heptanol, namely Ru-heptOH and Co-heptOH, following previously reported procedures.<sup>10,11</sup> Spherical and well-dispersed NPs have been obtained in both cases, presenting a mean size of  $2.5 \pm 0.4 \text{ nm}$  for Ru-heptOH<sup>10</sup> (Fig. 12a) and of  $3.0 \pm 0.4 \text{ nm}$  for Co-heptOH (Fig. 12b).<sup>11</sup> These results confirm the dual stabilization ability of 1-heptanol towards both Ru and Co NPs.

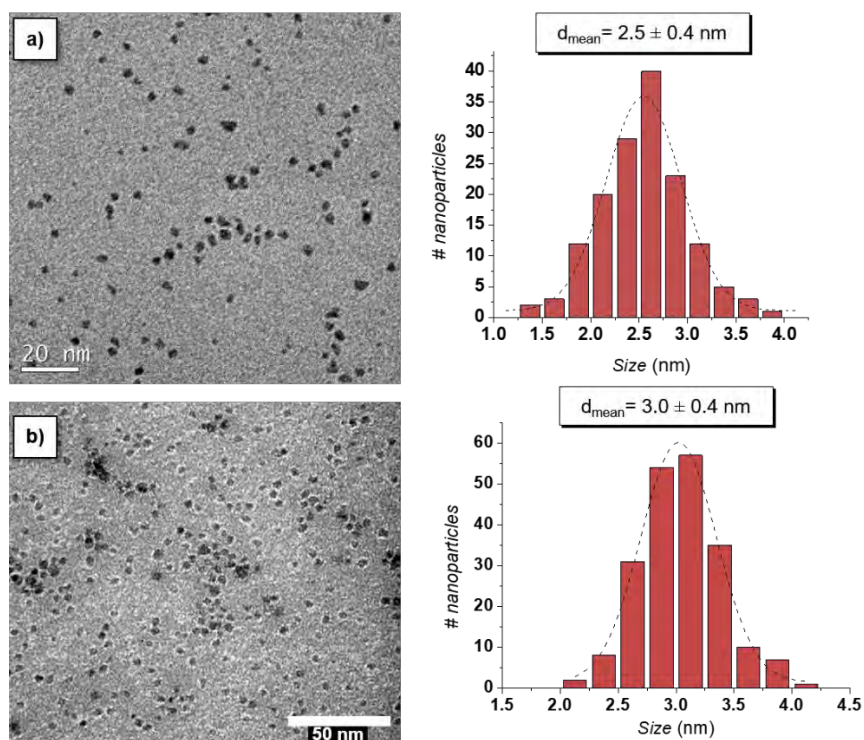


**Figure 12.** TEM images and corresponding histograms of monometallic Ru-heptOH NPs (a) and Co-heptOH NPs (b).

Then, RuCo NPs were synthesized at three different metal ratios as for the previous series of bimetallic NPs ([Ru:Co] : 1:1, 2:1 and 1:2). TEM analysis from the crude colloidal solutions after depositing a drop onto a carbon covered copper grid revealed the presence of isolated, small and spherical NPs for all the systems prepared with 1-heptanol, namely **Ru<sub>1</sub>Co<sub>1</sub>-heptOH**, **Ru<sub>2</sub>Co<sub>1</sub>-heptOH** and **Ru<sub>1</sub>Co<sub>2</sub>-heptOH**. The average diameter of these NPs is smaller than for their monometallic counterparts, being now  $1.1 \pm 0.2$  nm,  $1.3 \pm 0.3$  nm and  $1.1 \pm 0.2$  nm, respectively (Figs. 13, 14 and 15, respectively). The small and similar sizes obtained for the three Ru:Co ratios can be explained by the good stabilizing properties of 1-heptanol towards both Ru and Co. Also, as heptanol is not prone to induce  $\pi$ - $\pi$  interactions between adjacent NPs, well dispersed NPs are produced.



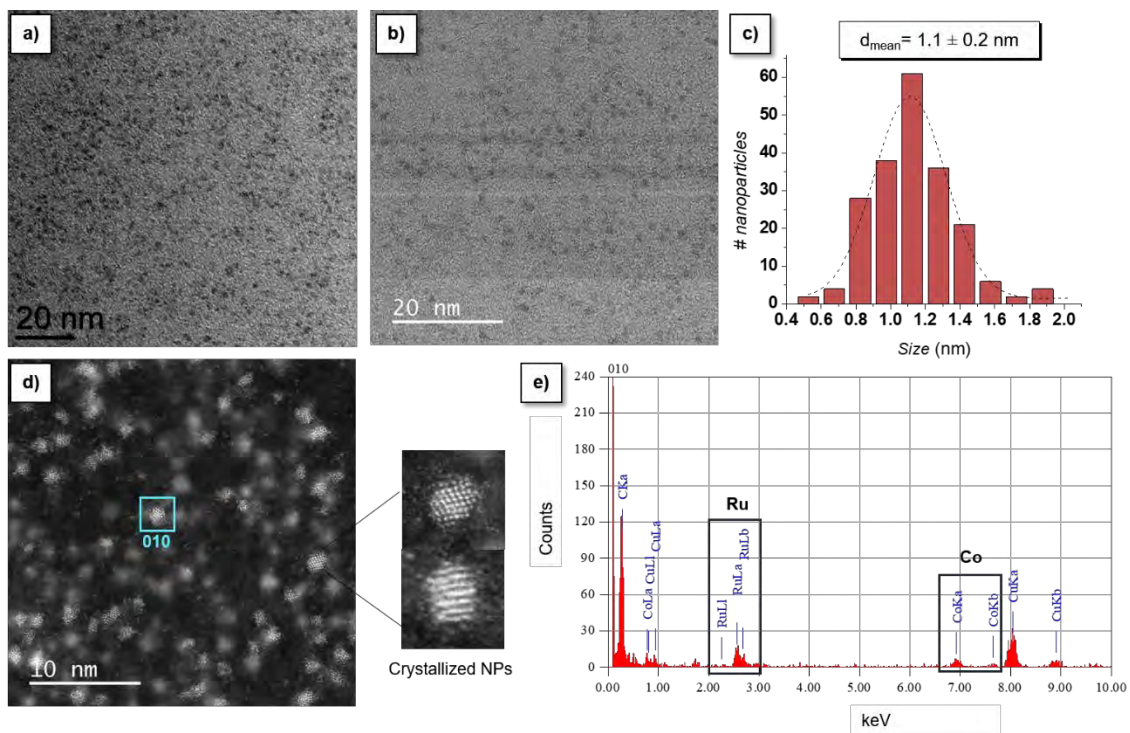


**Figure 13.** TEM images (a-b), size distribution histogram (c), STEM-HAADF image (d) and EDX analysis of a single NP (e) of **Ru<sub>1</sub>Co<sub>1</sub>-heptOH**.

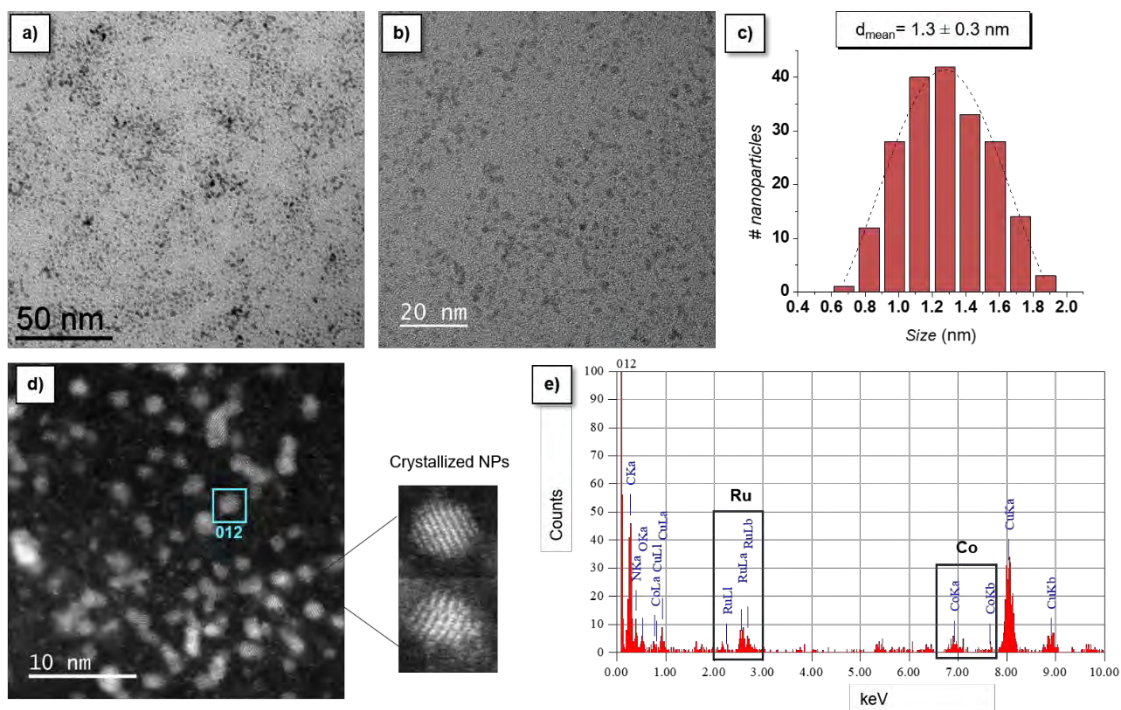


**Figure 14.** TEM images (a-b), size distribution histogram (c), STEM-HAADF image (d) and EDX analysis of a single NP (e) of **Ru<sub>2</sub>Co<sub>1</sub>-heptOH**.

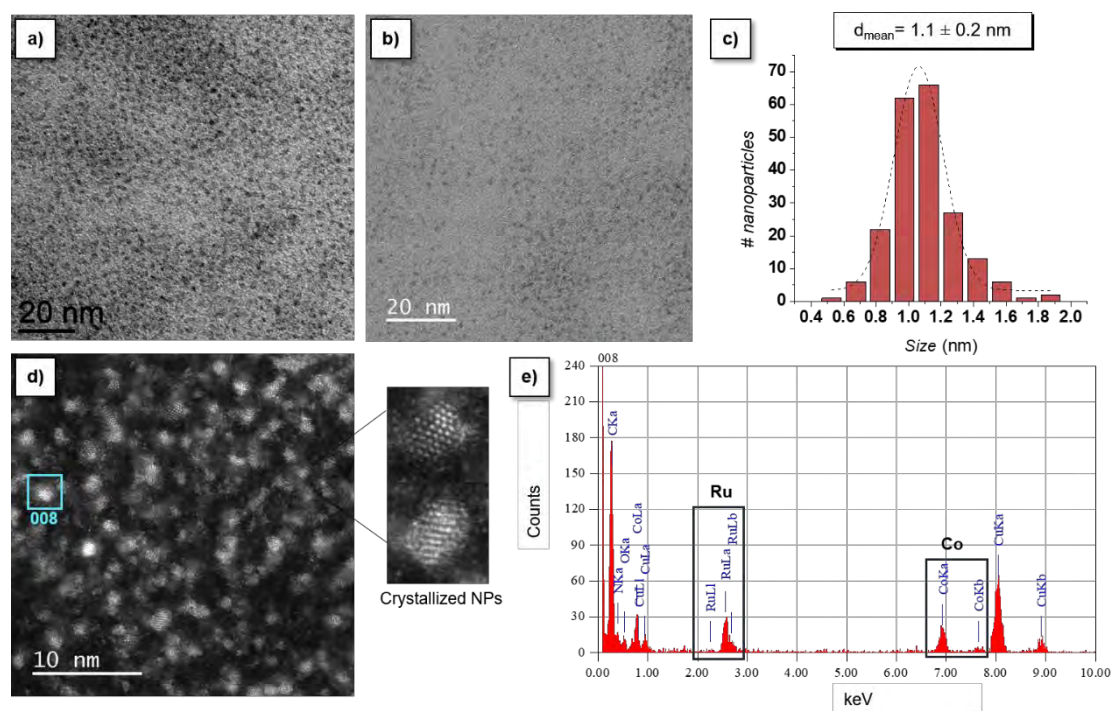


**Figure 15.** TEM images (a-b), size distribution histogram (c), STEM-HAADF image (d) and EDX analysis of a single NP (e) of **Ru<sub>1</sub>Co<sub>2</sub>-heptOH**.

STEM-HAADF images revealed the presence of well crystallized NPs in all samples (Figs. 13d, 14d and 15d), and EDX analyses revealed both Ru and Co in a single NP, confirming their bimetallic nature in all cases (Figs. 13e, 14e and 15e). The Ru<sub>at</sub>/Co<sub>at</sub> ratios found by quantitative EDX considering the average results from different isolated NPs are 70%Ru<sub>at</sub>/30%Co<sub>at</sub>, 77%Ru<sub>at</sub>/23%Co<sub>at</sub> and 56%Ru<sub>at</sub>/44%Co<sub>at</sub> for **Ru<sub>1</sub>Co<sub>1</sub>-heptOH**, **Ru<sub>2</sub>Co<sub>1</sub>-heptOH** and **Ru<sub>1</sub>Co<sub>2</sub>-heptOH**, respectively.

From the results above, it can be concluded that the three used stabilizing agents allow to obtain homogeneous and well-dispersed Ru NPs. In the case of Co NPs, the stabilizing effect is lower for tpy and 4PP ligands than for Ru and the stabilization abilities of the three ligands towards follows the order: heptOH > tpy > 4PP. This tendency is confirmed by the attainment of well dispersed Co NPs in the presence of heptOH and the higher amount of 4PP ligand required to access well dispersed Co-4PP NPs (*i.e.* 10 or 20 eq.) compared to the 0.1 eq. needed when using the tpy ligand. These differences could be explained by the differential Lewis acid-base interactions in each case. The intermediate Lewis acid nature of Co and the hard Lewis base nature of N makes more difficult the stabilization of the NPs, in contrast to Ru NPs, where its hard Lewis acid nature yields stronger interactions between the pyridine-based ligands and the Ru NPs

surfaces. Also, the higher N content of tpy compared to 4PP (3 vs. 1) as well as the chelating nature of the former can account for the improved stability of the Co-tpy NPs compared to the Co-4PP NPs. With respect to the results obtained with the RuCo NPs series, their mean size follows the order RuCo-4PP > RuCo-tpy  $\approx$  RuCo-heptOH. The poorer stabilization abilities of 4PP and tpy (vs. heptOH) towards Co leads to some isolated and well dispersed NPs but also to the formation of agglomerates. In addition, the better stabilization effect of tpy compared to 4PP for both metals may have induced the slightly smaller size observed for the RuCo-tpy NPs. Also, heptOH allowed to obtain well dispersed RuCo bimetallic NPs owing to its dual ability to stabilize well both Ru NPs and Co NPs. Comparison of the %Ru<sub>at</sub>/%Co<sub>at</sub> ratios obtained from EDX analysis using RuCo [1:1] ratios for RuCo-4PP (88%Ru<sub>at</sub>/12%Co<sub>at</sub>), RuCo-tpy (77%Ru<sub>at</sub>/23%Co<sub>at</sub>) and RuCo-heptOH (70%Ru<sub>at</sub>/30%Co<sub>at</sub>) also confirms the tendency in stabilization of each compound towards Co, obtaining higher Co content in a single NP in the heptOH system, coinciding with the fact that this is the best stabilizing agent for Co.

### **6B.2.3 Wide angle X-ray spectroscopy (WAXS)**

Although pending questions remain, WAXS analysis allowed to have an insight on the structure of the obtained bimetallic NPs. As expected, the obtained WAXS spectra don't match either with the monometallic Ru nor Co NPs, thus confirming the formation of bimetallic systems (Table 4). Interestingly, coherence lengths obtained by WAXS analysis agree with the NPs sizes measured from the TEM images.

**Table 4.** Summary of information extracted from WAXS analysis and comparison with average NPs sizes obtained from the TEM images.

Sample	TEM	WAXS	
		Coherence length	Structure
<b>Ru<sub>1</sub>Co<sub>1</sub>-4PP</b>	2.0 ± 0.3 nm	2.2 nm	hcp structure but neither pure Ru nor Co. Ru hcp contracted 3-4%/ Mn beta + octahedral peak alloy dilated 4% respect Co-Co
<b>Ru<sub>2</sub>Co<sub>1</sub>-4PP</b>	1.9 ± 0.3 nm	1.6 nm	Mn beta & non-compact. Mn beta + octahedral peak alloy dilated 5% respect Co-Co. Evolving to hcp
<b>Ru<sub>1</sub>Co<sub>2</sub>-4PP</b>	1.8 ± 0.3 nm	1.5-1.6 nm	Mn beta. Mn beta alloy dilated 3-4% respect Co-Co
<b>Ru<sub>1</sub>Co<sub>1</sub>-tpy</b>	1.3 ± 0.2 nm	1.5 nm	Less crystallized and disordered (glassy). Mn beta alloy dilated 5% respect Co-Co
<b>Ru<sub>2</sub>Co<sub>1</sub>-tpy</b>	1.3 ± 0.3 nm	1.3 nm	More amorphous. Mn beta alloy dilated 6% respect Co-Co
<b>Ru<sub>1</sub>Co<sub>2</sub>-tpy</b>	1.5 ± 0.2 nm	-	Mn beta alloy dilated 5% respect Co-Co
<b>Ru<sub>1</sub>Co<sub>1</sub>-heptOH</b>	1.1 ± 0.2 nm	1.5-1.6 nm	Non-pure but closer to Mn beta. Mn beta alloy 6% respect Co-Co
<b>Ru<sub>2</sub>Co<sub>1</sub>-heptOH</b>	1.3 ± 0.3 nm	1.7 nm	Non-compact structure/more amorphous. Mn beta alloy 6% respect Co-Co. Evolving to hcp
<b>Ru<sub>1</sub>Co<sub>2</sub>-heptOH</b>	1.1 ± 0.2 nm	1.5 nm	Mn beta alloy, bond length dilated 5% respect pure Co-Co

In general terms, all WAXS spectra have been difficult to interpret, therefore making it difficult to extract final conclusions about the effect of the different ligands and Ru:Co ratios in the composition and structure of the different obtained bimetallic NPs. However, the following general tendencies could be proposed from WAXS analysis:

- The Co-rich samples possess an invariant dilated Mn beta structure with a bond length dilated between 3-5% respect the pure Co-Co, attributed to a RuCo alloy with a fixed core composition and maybe the rest of Ru in an invisible shell.
- The binding distance doesn't change for intermediate samples (*i.e.* similar Ru/Co content) but Mn beta signature becomes blurred.
- The Ru-rich samples are closer to compact structures (hcp).



All these data suggest a structure dominated by a Co-rich core with invariant organization and probably composition, with the excess of Ru situated in a shell, almost invisible except for a large proportion of Ru, whose hcp signature is beginning to appear.

### **6B.3 CONCLUSIONS & PERSPECTIVES**

The successful synthesis of RuCo bimetallic NPs by the simultaneous hydrogenation of Ru and Co organometallic precursors has been confirmed by EDX and WAXS analysis. WAXS analysis has allowed to propose a general trend on the structure, with a dilated Mn beta structure for the Co-rich samples and an evolution towards hcp in Ru-rich samples. In addition, special emphasis has been put in extracting valuable insights on the influence of the nature of the stabilizing ligands (4PP, tpy and heptOH) and of the metal molar ratio (Ru:Co, 1:1, 2:1 and 1:2) on the morphology of the obtained NPs. Monometallic NPs have been also synthesized for comparison purposes. TEM images indicate that the 4PP ligand does not allow to obtain well dispersed Co NPs, contrarily to what is observed with Ru. Regarding the RuCo-4PP samples, even though no significant effect is observed on the size (*ca.* 2 nm) of the obtained NPs depending on the Ru:Co ratio employed, this parameter has a clear effect on the NPs dispersion. This result can be explained by the fact that upon increasing the Co content, the stabilization ability of the 4PP ligand decreases, leading to less stable NPs. They may thus tend to agglomerate in order to minimize their surface energy, as already observed for monometallic Co systems.

However, the formation of agglomerates of NPs may also result, to a minor extent, from  $\pi$ - $\pi$  interactions between the aromatic rings of the ligands in adjacent NPs. In contrast, the high ability of the ligand to stabilize Ru allowed a more intense capping of the NPs when they are more Ru-rich, avoiding their agglomeration.

Furthermore, the tpy ligand has been found to be a very efficient stabilizing agent for the Ru NPs due to the strong coordination of tpy to the NPs surface due to the hard Lewis acid nature of Ru and the hard Lewis base nature of N, as well as the chelating nature of this ligand. In this sense, the higher N content of tpy compared to 4PP (3 vs. 1) as well as the chelating nature of the former can account for the improved stability of the Co-tpy NPs compared to the Co-4PP NPs. TEM images for the RuCo-tpy samples, obtained under the different Ru:Co proportions assayed, reveal a more intense stabilizing

ability of tpy towards both metals than 4PP, obtaining smaller NPs (ca. 1.5 nm) for the former.

Finally, isolated, small (ca. 1 nm), spherical and well-dispersed RuCo NPs have been obtained when 1-heptanol is used as stabilizing agent, owing to its dual ability to stabilize well both Ru and Co NPs. In conclusion, the mean size of the RuCo NPs series follows the order RuCo-4PP > RuCo-tpy  $\approx$  RuCo-heptOH, being the stabilizing ability of each ligand inversely proportional to the size of the obtained NPs.

The effect of the ligand and the RuCo ratio in the overall WS electrocatalytic activity will be assessed in the future.

## **6B.4 EXPERIMENTAL PART**

### **Materials and methods**

All operations were carried out using Standard Schlenk tubes, Fisher-Porter reactors and vacuum lines techniques or in a glove box (Mbraun) under argon atmosphere. Metal precursors,  $[\text{Co}^{\text{I}}(\eta^3\text{-C}_8\text{H}_{13})(\eta^4\text{-C}_8\text{H}_{12})]$  (also named  $[\text{Co}(\text{COD})(\text{COE})]$ ) and  $[\text{Ru}(\eta^4\text{-C}_8\text{H}_{12})(\eta^6\text{-C}_8\text{H}_{10})]$  (also named  $[\text{Ru}(\text{COD})(\text{COT})]$ ), were purchased from NanoMePS (NanoMatériaux et Poudres et Solutions, Toulouse). Hydrogen gas (Alphagaz) was purchased from Air Liquide. 4-Phenylpyridine (4PP), 4'-(4-methylphenyl)-2,2':6',2''-terpyridine (tpy) ligands and 1-heptanol were purchased from Sigma-Aldrich. 1-heptanol was dried over activated molecular sieves (4 Å) prior to use and other chemicals were employed as received unless otherwise specified. Solvents (THF, pentane) were purified before use through filtration on a column in a purification apparatus (Braun) and degassed before use by a freeze-pump process (x3).

### **Synthetic protocols**

**Synthesis of Ru-4PP and Ru-tpy NPs (0.2 eq.).** 120 mg of  $[\text{Ru}(\text{COD})(\text{COT})]$  (0.38 mmol) were introduced under argon atmosphere in a Fischer-Porter reactor. 12 mg (0.2 eq., 0.08 mmol) of 4-phenylpyridine or 26 mg of 4'-(4-methylphenyl)-2,2':6',2''-terpyridine (0.2 eq., 0.08 mmol) were dissolved in 120 mL of anhydrous THF in a schlenk tube and the obtained THF solution was cooled down to 193 K with an ethanol/liquid  $\text{N}_2$  bath. Thereafter, outside the glovebox, the ligand solution was transferred to the Fischer-porter *via cannulae*. Finally, the Fischer porter was pressurized with dihydrogen (3 bar) and the reaction mixture was left at r.t. under vigorous stirring for 16 h (Ru-4PP) or 24 h (Ru-tpy). The solution colour turned from yellow (Ru-4PP) or dark purple (Ru-tpy) to homogeneous black (Ru-4PP) or dark brown (Ru-tpy). The remaining  $\text{H}_2$  was removed under vacuum and the THF evaporated one half before adding pentane to precipitate the NPs. A black powder was obtained after evaporation to dryness under vacuum. **Ru-4PP (0.2 eq.):** TEM:  $d_{\text{mean}} = 1.5 \pm 0.3$  nm NPs; **Ru-tpy:** TEM:  $d_{\text{mean}} = 1.4 \pm 0.2$  nm NPs (0.05 eq.),  $1.1 \pm 0.2$  nm NPs (0.1 eq.),  $0.8 \pm 0.3$  nm NPs (0.2 eq.) and  $0.6 \pm 0.3$  nm NPs (0.5 eq.).

**Synthesis of Co-4PP (10 eq.) and Co-tpy (0.1 eq) NPs.** 10 mg of [Co(COD)(COE)] (0.036 mmol) were introduced under argon atmosphere in a Fischer-Porter reactor. 56.23 mg (0.36 mmol) of 4-phenylpyridine or 1.17 mg (3.6  $\mu\text{mol}$ ) of 4'-(4-methylphenyl)-2,2':6',2''-terpyridine were dissolved in 10 mL of anhydrous THF in a schlenk tube and the THF solution was cooled down to 193 K with an ethanol/liquid N<sub>2</sub> bath. Thereafter, outside the glovebox, the ligand solution was transferred to the Fischer-porter *via cannulae*. Finally, the Fischer porter was pressurized with dihydrogen (3 bar) and the reaction mixture was left at r.t. under vigorous stirring for 24 h. The solution colour turned from bright brown/orange to black. The remaining H<sub>2</sub> was removed under vacuum, and NPs were recovered from the THF colloidal solution by application of a magnet on the reactor walls (magnetic filtration) and removing the supernatant *via cannulae* (Co-4PP) or by evaporating one half of the THF before adding pentane to precipitate the NPs (Co-tpy). A black powder was obtained after evaporation to dryness under vacuum. The obtained black powder was washed with THF (3x10 mL) and pentane (3x10 mL) and dried under vacuum before collecting it in a vial. **Co-4PP:** TEM:  $d_{\text{mean}} \approx 1.5 - 2.0$  nm NPs (0.2 eq.),  $\approx 1.5 - 3.0$  nm NPs (0.5 eq.),  $\approx 1.0 - 5.0$  nm NPs (2 eq.),  $\approx 1.0 - 2.0$  nm and  $\approx 3.0 - 4.0$  nm NPs (5 eq.),  $\approx 2.0 - 3.0$  nm NPs (10 eq.),  $d_{\text{mean}} \approx 2.0 - 3.0$  nm NPs (20 eq.) and  $\approx 2.0 - 4.0$  nm NPs (10 eq. in toluene.). **Co-tpy:** TEM:  $d_{\text{mean}} = 2.2 \pm 0.4$  nm NPs (0.1 eq.),  $2.3 \pm 0.3$  nm NPs (0.2 eq.) and  $2.2 \pm 0.4$  nm NPs (1 eq.).

**Synthesis of RuCo NPs stabilized with 4PP (RuCo-4PP) and tpy (RuCo-tpy).**  
**Detailed synthesis for [1:1], [1:2] and [2:1] RuCo NPs.** The synthesis of bimetallic NPs was performed in one pot conditions with a similar procedure as for the monometallic NPs, by introducing simultaneously the two metal precursors into the Fisher-Porter reactor. Under Ar atmosphere, anhydrous THF (90 mL) was introduced in a pre-dried Fisher-Porter reactor containing a stirring bar. Next, [Ru(COD)(COT)] (100.0 mg, 0.32 mmol, 66.7 mg, 0.21 mmol, or 133.3 mg, 0.43 mmol) and [Co<sup>I</sup>( $\eta^3$ -C<sub>8</sub>H<sub>13</sub>)( $\eta^4$ -C<sub>8</sub>H<sub>12</sub>)] (87.6 mg, 0.32 mmol, 116.8 mg, 0.43 mmol, or 58.4 mg, 0.21 mmol) were also introduced into the reactor for obtaining the [1:1], [1:2] and [2:1] RuCo NPs, respectively. The metal precursor solution was cooled down to 193 K with an ethanol/liquid nitrogen bath before transferring the ligand solution (10 mL THF + 19.87 mg 4PP, 0.12 mmol, for RuCo-4PP or 10 mL THF + 41.39 mg tpy, 0.128 mmol, for RuCo-tpy) into the Fisher-Porter reactor with a syringe. Finally, the Fisher-Porter was pressurized with dihydrogen (3 bar) and let it warm until r.t. under vigorous stirring. The reaction mixture was left at r.t. under

vigorous stirring for 24 h. After this reaction time, a homogeneous black colloidal solution was obtained. The remaining H<sub>2</sub> was removed under vacuum and the application of a magnet on the reactor walls allowed to separate a black powder that was washed with THF (x3) and pentane (x3). The resulting black powder was dried under vacuum and collected in a vial. **Ru<sub>1</sub>Co<sub>1</sub>-4PP**: TEM:  $d_{\text{mean}} = 2.0 \pm 0.3$  nm, **Ru<sub>2</sub>Co<sub>1</sub>-4PP**: TEM:  $d_{\text{mean}} = 1.9 \pm 0.3$  nm, **Ru<sub>1</sub>Co<sub>2</sub>-4PP**: TEM:  $d_{\text{mean}} = 1.8 \pm 0.3$  nm, **Ru<sub>1</sub>Co<sub>1</sub>-tpy**: TEM:  $d_{\text{mean}} = 1.3 \pm 0.2$  nm, **Ru<sub>2</sub>Co<sub>1</sub>-tpy**: TEM:  $d_{\text{mean}} = 1.3 \pm 0.2$  nm. **Ru<sub>1</sub>Co<sub>1</sub>-tpy**: TEM:  $d_{\text{mean}} = 1.5 \pm 0.3$  nm.

**Synthesis of Ru-heptOH NPs:** 77 mg of [Ru(COD)(COT)] (0.245 mmol) were introduced under argon atmosphere in a Fischer-Porter reactor. Thereafter, outside the glovebox, 30 mL of 1-heptanol were added to the reactor with a *cannulae*. Finally, the reactor was pressurized with dihydrogen (3 bar) and the reaction mixture was left at r.t. under vigorous stirring for 18 h. The solution colour turned from yellow to homogeneous black. The remaining H<sub>2</sub> was removed under vacuum. The nanoparticles were precipitated by methanol addition and centrifugation at 2500 rpm for 30 min. The obtained solid was washed with pentane and transferred into a vial prior to be dried until obtaining a dry black powder. **Ru-heptOH**: TEM:  $d_{\text{mean}} = 2.5 \pm 0.4$  nm.

**Synthesis of Co-heptOH NPs:** 300 mg of Co(COD)(COE) (1.09 mmol) were introduced under argon atmosphere in a Fischer-Porter reactor. Thereafter, outside the glovebox, 50 mL of 1-heptanol were added to the reactor with a *cannulae*. Finally, the reactor was pressurized with dihydrogen (3 bar) and the reaction mixture was left at r.t. under vigorous stirring for 20 h. The reaction medium turned from a brownish to a dark-brown/black colloidal solution. The remaining H<sub>2</sub> was removed under vacuum. NPs were recovered from the 1-heptanol colloidal solution by application of a magnet on the reactor walls (magnetic filtration) and removing the supernatant *via cannulae*. The obtained black powder was washed with pentane (5 x 20 mL) and dried under vacuum before collecting it in a vial. **Co-heptOH**: TEM:  $d_{\text{mean}} = 3.0 \pm 0.4$  nm.

**Synthesis of RuCo NPs stabilized in 1-heptanol (RuCo-heptOH). Detailed synthesis for [1:1] , [1:2] and [2:1] RuCo NPs.** Under Ar atmosphere, anhydrous 1-heptanol (50 mL) was introduced in a pre-dried Fisher-Porter reactor containing a stirring bar. Next, [Ru(COD)(COT)] (100.0 mg, 0.32 mmol, 66.7 mg, 0.21 mmol, or 133.3 mg, 0.43 mmol) and [Co<sup>I</sup>( $\eta^3$ -C<sub>8</sub>H<sub>13</sub>)( $\eta^4$ -C<sub>8</sub>H<sub>12</sub>)] (87.6 mg, 0.32 mmol, 116.8 mg, 0.43 mmol,

or 58.4 mg, 0.21 mmol) were added into the reactor for obtaining the [1:1], [1:2] and [2:1] RuCo NPs, respectively. Thereafter, the Fisher-Porter was pressurized with dihydrogen (3 bar) and left under vigorous stirring at r. t. for 24 h. After this reaction time, a homogeneous black colloidal solution was obtained. After releasing H<sub>2</sub> pressure, the as-synthesized NPs were isolated by 1-heptanol evaporation under vacuum at 70 °C. Finally, the obtained black material was washed with pentane and finally dried under vacuum to get a black powder that was collected in a vial. **Ru<sub>1</sub>Co<sub>1</sub>-heptOH**: TEM:  $d_{\text{mean}} = 1.1 \pm 0.2$  nm, **Ru<sub>2</sub>Co<sub>1</sub>-heptOH**: TEM:  $d_{\text{mean}} = 1.3 \pm 0.3$  nm. **Ru<sub>1</sub>Co<sub>2</sub>-heptOH**: TEM:  $d_{\text{mean}} = 1.1 \pm 0.2$  nm.

## Characterization Techniques

**Transmission Electron Microscopy (TEM)** analyses were performed at “Servei de Microscopia de la UAB” using a JEOL JEM 2011 electron microscope working at 200 kV with a resolution point of 0.18 nm and at the “UMS 3623 – Centre de microcaractérisation Raimond Castaing” using a MET JEOL JEM 1011 electron microscope operating at 100 kV with resolution point of 4.5 Å or a MET JEOL JEM-ARM200F operating at 200 kV with a resolution point of 1.9 Å. TEM images were taken after the deposition of 1 drop of each crude colloidal suspension onto a carbon covered copper grid. Size distributions of bimetallic NPs were determined through manual analysis of enlarged micrographs with ImageJ software to obtain statistical size distributions and mean diameters. For each system of nanoparticles, the mean size was calculated by assuming spherical forms. Size distributions are quoted as the mean diameter  $\pm$  the standard deviation ( $\sigma$ ) by counting over than 200 particles.

**Scanning transmission electron microscopy coupled with high angle annular dark field detector (STEM-HAADF)** analyses were performed at the “UMS 3623 – Centre de microcaractérisation Raimond Castaing” using a MET JEOL JEM-ARM200F electron microscope operating at 200 kV with resolution point of 0.78 Å coupled to a HAADF detector. Samples for STEM-HAADF have been prepared as for TEM analysis. **Energy dispersive X-ray spectroscopy (EDX)** is typically integrated into electron microscopy instruments. EDX analyses were performed at the “UMS 3623 – Centre de microcaractérisation Raimond Castaing” with a using a MET JEOL JEM-ARM200F electron microscope operating at 200 kV with resolution point of 0.78 Å. The electron

microscope is equipped with a EDX SDD CENTURIO-X detector, allowing the analysis of the chemical elemental composition of the samples.

**Wide-angle X-ray scattering (WAXS)** measurements were performed at CEMES-CNRS in Toulouse. Samples were measured in 1.0 mm diameter Lindemann glass capillaries. The samples were irradiated with graphite monochromatized molybdenum  $K\alpha$  (0.071069 nm) radiation and the X-ray scattering intensity measurements were performed using a dedicated two-axis diffractometer. Radial distribution functions (RDF) were obtained after Fourier transformation of the corrected and reduced data.

## **6B.5 REFERENCES**

- <sup>1</sup> I. S. Kwon, T.T. Debela, I.H. Kwak, Y.C. Park, J. Seo, J.Y. Shim, S.J. Yoo, J.G. Kim, J. Park and H.S. Kang, *Small* **2020**, 2000081.
- <sup>2</sup> Y. Bao, J. Dai, J. Zhao, Y. Wu, C. Li, L. Ji, X. Zhang and F. Yang, *ACS. Appl. Energy Mater.* **2020**, 3, 1869-1874.
- <sup>3</sup> C. Wang and L. Qi, *Angew. Chem. Int. Ed.* **2020**, 59, 39, 17219-17224
- <sup>4</sup> L. An, W. Zhang, W. Ma, S. Wang, L. Ma, Q. Liu, J. Guo and X. Zhang, *J. Taiwan Inst. Chem. Eng.* **2019**, 104, 75-81.
- <sup>5</sup> T. He, Y. Peng, Q. Li, J.E. Lu, Q. Liu, R. Mercado, Y. Chen, F. Nichols, Y. Zhang and S. Chen, *ACS Appl. Mater. Interfaces* **2019**, 11, 46912-46919.
- <sup>6</sup> N.B. Halck, V. Petrykin, P. Krtil and J. Rossmeisl, *Phys. Chem. Chem. Phys.* **2014**, 16, 13682-13688.
- <sup>7</sup> C. Amiens, D. Ciuculescu-Pradines and K. Philippot, *Coord. Chem. Rev.* **2016**, 308, 409-432.
- <sup>8</sup> D. Zitoun, M. Respaud, M.C. Fromen, P. Lecante, M.J. Casanove, C. Amiens and B. Chaudret, *J. Magn. Magn. Mater.* **2004**, 272-276, 1536-1537.
- <sup>9</sup> J. Creus, S. Drouet, S. Suriñach, P. Lecante, V. Collière, R. Poteau, K. Philippot, J. García-Antón and X. Sala, *ACS Catal.* **2018**, 11094-11102.
- <sup>10</sup> K. Pelzer, K. Philippot and B. Chaudret, *Z. Phys. Chem.* **2003**, 217, 1539-1547.
- <sup>11</sup> J. De Tovar, N. Romero, S.A. Denisov, R. Bofill, C. Gimbert-Suriñach, D. Ciuculescu-Pradines, S. Drouet, A. Llobet, P. Lecante, V. Colliere, Z. Freixa, N. McClenaghan, Catherine Amiens, J. García-Antón, K. Philippot and Xavier Sala, *Mater. Today Energy* **2018**, 9, 506-515.
- <sup>12</sup> L.I. Álvarez, **2021**, Ruthenium and Platinum Nanoparticles for Artificial Photosynthesis, *PhD Thesis*, UAB.



# 7

## Chapter 7. General conclusions

---

As a final overview, *Chapter 7* will list the main results and conclusions obtained from the synthesis, characterization and catalytic performance of all nanoparticulate systems studied along this PhD thesis.

---



## **7. CONCLUSIONS**

In this PhD thesis, the design of new metal-based nanomaterials as electrocatalysts for both the HER and the OER has been accomplished. (HR)TEM, SEM, STEM-HAADF, WAXS, XRD, MAS NMR and ICP-AES/OES, XPS, FT-IR and Raman spectroscopies have allowed to extract valuable insights correlating structure with catalytic activity. To obtain improved nanocatalysts, the following strategies have been employed:

- Chapter 3 – The use of DFT calculations as a tool to explain trends in the experimental HER performances observed for a series of ligand-capped NPs in acidic media.
- Chapter 4 – The use of graphene-like conductive supports to improve the performance and stability of NPs in the HER electrocatalysis and unravel the effect of support P/N-doping in the final catalytic output.
- Chapter 5 – The use of a conductive, cheap and easy to handle macroscopic carbon support to improve the conductivity and stability of NPs.
- Chapter 6 – The combination of two different metals in bimetallic systems.

The main conclusions of each chapter will be overviewed thereafter:

In *Chapter 3*, DFT calculations have allowed to discern the most favourable coordination modes of two different ligands, tpy and 2PP, on the surface of a Ru NP. In general,  $\pi$ -coordination is more stable than the  $\sigma$  one. Thus, final models have been chosen taking into account the  $E_{\text{ads}}$  values obtained from the different ligand coordination modes onto the surface of the Ru NP, choosing the most stable configuration but also putting in balance possible steric effects and hydride push out effects due to high surface coverage with hydrogen atoms.

The experimentally lower HER electrocatalytic activity of Ru-tpy compared to Ru-4PP has been also demonstrated by the obtained  $\Delta G_{\text{H}^*}$  values, lying for Ru-tpy on the branches of the volcano plot, in contrast to Ru-4PP, placed near the top. Although this study should be completed with other adsorption energy calculations considering those H that are closer to the tpy ligands in order to check any possible influence of the  $\pi$  density of the ligands in  $\Delta G_{\text{H}^*}$ , it provides up to now interesting trends which are in good agreement with our experimental results.

Bearing in mind all the results obtained in Chapter 4, graphene materials are confirmed to be suitable supports to obtain small isolated and well-dispersed Ru NPs. In chapter 4A, rGO obtained from the Hummers method has been used as the carbon support for Ru/RuO<sub>2</sub> NPs. In addition, N and P heteroatoms have been introduced into the carbon structure, allowing to obtain smaller and well dispersed NPs, presenting a mean size of  $1.5 \pm 0.2/0.3$  nm. Contrastingly, the use of the non-doped graphene leads to bigger NPs, with a more heterogeneous size distribution. These results confirm the positive role of the heteroatom doping in the stabilization of the Ru(0) NPs during the synthetic procedure, affecting their nucleation and growth kinetics. Similar results have been obtained in Chapter 4B when using rGO from the pyrolysis of alginate, generating small and well-dispersed NPs with a mean size of  $1.9 \pm 0.6$  nm and  $1.5 \pm 0.3$  nm when using the bare and the P-doped rGO, respectively.

After partial surface oxidation by air exposition, the catalytic activities of the as-synthesized materials have been studied. The activity of all materials in 1 M H<sub>2</sub>SO<sub>4</sub> aqueous solution clearly confirms the dependence of the HER catalytic activity on the oxidation state of the NPs surface, being metallic Ru<sup>0</sup> sites more active than RuO<sub>2</sub>, as confirmed by the improved HER activity after submitting the systems to reductive treatment.

Furthermore, heteroatom doping induces a general improvement of the overall HER activity, especially for the P-doped cases. This improvement could be probably attributed to the respective electron acceptor and electron donor ability of the adjacent N and P atoms to C atoms in the graphitic structure, affecting the electronic properties of the support. Changes in the support will be transferred to the Ru NPs, improving in this case the synergistic effects between Ru and C, modulating the adoption of reaction intermediates to enhance its HER catalytic activity. Furthermore, it has been also demonstrated that a higher proportion of graphitic phosphorous (*i.e.* **Ru@P-rGO**) contributes more importantly to the enhancement of the HER activity than phosphates (*i.e.* **Ru@P-G**). In this sense, **Ru@P-rGO** has been found to be the best electrocatalyst, showing a  $\eta_{10}$  as low as 2 mV and a Tafel slope of 49 mV/dec.

*Chapter 5* highlights the applicability of the organometallic approach for the synthesis of nanostructures to systematically tailor the interface between nanocatalysts and carbon-based supports in HER and OER electrodes. The use of two different carbon microfibers, bare (CF) and carboxylic-group containing (ox-CF) fibers as cheap, easy to engineer and high surface area supports, combined with the versatility of the synthetic method, which allows adding different NP stabilizers and perform the synthesis both in the presence *-in situ-* or absence *-ex situ-* of the carbonaceous support, has permitted obtaining different electrodes with diverse interfacial nature.

In *Chapter 5A*, we obtained small Ru NPs (*ca.* 1-1.8 nm) supported on CFs. Increased HER catalytic intensities and decreased overpotentials were found for the *ex situ* systems, where the Ru NPs were first stabilized with 4-phenylpyridine (4PP) ligands and then deposited onto the CF supports, confirming the importance of a proper electronic interaction between the NPs and the support, in this case achieved by potential  $\pi$ - $\pi$  interactions between the pyridylic rings of 4PP and the carbon structure. In addition, a synergistic effect between the -COOH moieties and Ru NPs has been observed in the *in situ* systems, where  $\eta_0$  decreases for **Ru@ox-CF** (30 mV) in comparison to **Ru@CF** (70 mV).

In addition, in *Chapter 5B*, Co(OH)<sub>2</sub> NPs have been also successfully synthesized on-top of CFs, observing a positive role of the carboxylic groups at the surface of the CFs by the systematic reduction of the size of the NPs and increase of their dispersion at the electrode surface during the *in situ* syntheses. In addition, this functional group has also improved the activity and stability of the systems during the OER, particularly when the weak stabilizer THF is employed. These observations point to the likely formation of COO-Co(OH)<sub>2</sub> coordinative bonds and/or H-bonds, both improving the electronic communication between the catalyst and the support as well as the dispersibility and stability of the former on top of the latter. Furthermore, the potential role of dangling carboxylates from the **ox-CF** support as proton acceptor moieties (internal bases) lowering the activation free energies that lead to O-O bond formation during the OER cannot be discarded.

Putting altogether the results obtained in *Chapter 5*, it can be concluded that a proper interaction between the NPs and the support surface is crucial for an improved catalytic activity of the hybrid systems, as hypothesized by means of potential  $\pi$ - $\pi$  interactions between the Ru4PP NPs and the carbon structures or by coordinative H-bonds between the Co(OH)<sub>2</sub> NPs and the COOH moieties in the microfibers. In addition, it is also important to avoid steric hindrance between moieties, which could lead to a bad stabilization of the systems.

*Chapter 6* expands the scope of this PhD thesis to bimetallic systems, and highlights the usefulness of the employed synthetic methodology also in this regard. In *Chapter 6A*, in collaboration with Dr. L. Peres (LCC-CNRS, Toulouse), Ni-foam nanomaterials and their corresponding Ru-doped counterparts with different Ru loadings (*i.e.* 1, 5 and 10 wt.% Ru) have been successfully synthesized following a two-step procedure. Interestingly, XPS has revealed that the NiOOH species is only present in the Ru-containing samples (*vs.* Ni(OH)<sub>2</sub> in the Ni-foam), suggesting that Ru may help the stabilization of higher oxidation states of Ni in the passivated samples.

The different Ru deposition in **Ru1@Ni-foam** compared to **Ru5@Ni-foam** and **Ru10@Ni-foam** (thin layer of small clusters <1 nm or single atoms *vs.* sponge-like nanostructures of small aggregated NPs) was translated in a slightly different behaviour of this sample towards the OER in complementary studies performed in non-purified and Fe-free alkaline electrolyte. In contrast with the other samples, a progressive activation of **Ru1@Ni-foam** has been also observed in a Fe-free electrolyte, jointly with a higher activation in a non-purified electrolyte, pointing to the fact that a low Ru doping can contribute to a higher Fe incorporation or to a better hydration of the sample. Despite these differences, it was generally confirmed that Fe-incorporation and/or, to a minor extent, hydration of the samples is a key point to achieve high electrocatalytic OER performances in Ni-based nanomaterials. In addition, reduced OER catalytic performances in phosphate and borate buffers confirmed that even though the presence of iron is crucial for an efficient catalysis, the deprotonating effect of hydroxyl anions under strong alkaline conditions plays a prominent role, aiding the formation of the active oxygen species (NiOO<sup>-</sup>).

Finally, *in situ* UV-vis spectroelectrochemistry allowed to track the Ni(II) → Ni(III) oxidation process prior to the sharp current increase assigned to the

electrocatalytic OER. The results suggested that the low Ru doping in **Ru1@Ni-foam** could lead to changes in the NiOOH species, which is in agreement with the different Ru-deposition observed and different behaviour of this sample under alkaline OER conditions. In addition, it was confirmed that the formation of the NiOOH species occurs entirely during the Ni oxidation reaction, suggesting that it is not the species accumulated during the catalysis. Therefore, in agreement with the literature, NiOOH needs to be further oxidized to be able to oxidize water.

Polarization curves of all the samples towards the HER in acidic media have revealed higher catalytic current densities in those samples containing a higher amount of Ru. However, the best catalytic activity has been achieved by **Ru5@Ni-foam**, which could be driven by a higher degree of crystallinity, as confirmed by XRD, or even from its different Ru/RuO<sub>2</sub> ratio or its optimum Ru-doping content, providing in this sample a good interface between the Ni/Ni(OH)<sub>2</sub>-NiOOH species and the Ru dopant. A similar tendency has been observed for HER in alkaline media, along with better stabilities.

In *Chapter 6B*, the successful synthesis of RuCo bimetallic NPs by the simultaneous hydrogenation of Ru and Co organometallic precursors has been confirmed by EDX and WAXS analysis by using three different ligands (4PP, tpy and heptOH) and three Ru:Co ratios (1:1, 2:1 and 1:2). The mean size of the RuCo NPs series follows the order RuCo-4PP > RuCo-tpy  $\approx$  RuCo-heptOH, being the stabilization ability of each ligand inversely proportional to the size of the obtained NPs. The hard Lewis base nature of N and the hard Lewis acid nature of Ru, compared to the intermediate Lewis acid nature of Co could explain the obtained differences in affinity (*i.e.* stabilization) towards both metals, translated in more agglomerated NPs in high Co-content samples. In addition, the improved stability achieved with tpy ligand could be attributed to its chelating nature, in contrast to 4PP. Finally, the dual ability of heptOH to stabilize both Ru NPs and Co NPs contributed to the attainment of well-dispersed RuCo NPs.

All in all, this PhD work has aimed to enlarge the limited understanding about the key factors that control the performance of WS (OER and HER) electrocatalysts at the nanoparticle scale. Therefore, with the flexible organometallic approach as synthetic ally, this work has explored a wide range of strategies to fine-tune and rationalize the activity and stability of metal-based NPs, including the ligand-capping, the doping/functionalization of carbon-based conducting supports and the combination of

two different metals in different proportions and dispositions. With the conclusions exposed above, this work opens new doors in the rational design of new highly active and efficient WS nanoelectrocatalysts.



## **Résumé de Thèse**

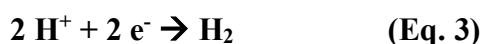
---



L'augmentation de la population mondiale, conjuguée à l'accroissement de l'activité humaine, perturbe l'équilibre énergétique de la Terre, principalement en brûlant des quantités excessives de combustibles fossiles (charbon, gaz naturel et pétrole) pour obtenir de l'énergie, ce qui augmente la libération de dioxyde de carbone dans l'atmosphère (la concentration de CO<sub>2</sub> a augmenté de 47 % depuis le début de la révolution industrielle).<sup>1</sup> L'augmentation de la quantité de CO<sub>2</sub> dans l'atmosphère terrestre piège la chaleur supplémentaire près de la surface de la Terre, la libérant progressivement au fil du temps et provoquant une élévation de la température globale.<sup>2</sup> Une solution pour obtenir une source d'énergie décarbonée est la photoproduction d'H<sub>2</sub> par fractionnement catalytique de l'eau (WS, Eq. 1) en utilisant l'énergie solaire.



Le fractionnement de l'eau est un processus en deux étapes: à l'anode l'eau est oxydée en O<sub>2</sub> (réaction d'évolution de l'oxygène, OER, Eq. 2), libérant des électrons permettant la réduction des protons en H<sub>2</sub> à la cathode (réaction d'évolution de l'hydrogène, HER, Eq. 3).



Le développement de catalyseurs OER et HER performants est essentiel pour avoir une cinétique adéquate entre ces deux réactions intimement liées. Les nanoparticules (NPs) sont des catalyseurs intéressants en raison de leur stabilité et du rapport surface/volume élevé qu'elles présentent, exposant un grand nombre de sites actifs. Dans cette thèse, différents électrocatalyseurs nanométriques (Ru, Co et systèmes bimétalliques) ont été synthétisés via l'approche organométallique.<sup>3</sup> Cette méthode permet de disposer de NPs de surface propre comparativement à d'autres méthodologies (Fig. 1).

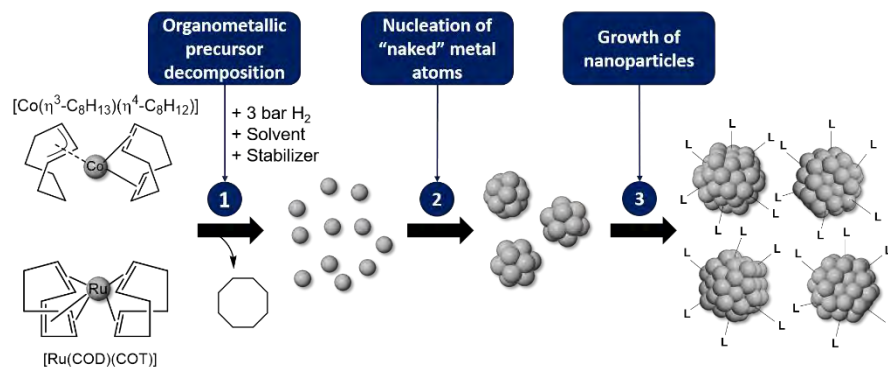


**Figure 1.** Représentation schématique de l'approche organométallique pour la synthèse de nanoparticules métalliques. Le stabilisant peut être un ligand, un polymère, un dendrimère, un support, etc. Les précurseurs de ruthénium et cobalt représentés sont ceux utilisés dans ce travail. Ils peuvent conduire indépendamment à des NP monométalliques ou lorsqu'ils sont associés à des NP bimétalliques.

Un ensemble de techniques d'analyses telles que (HR)TEM, SEM, STEM-HAADF, WAXS, XRD, MAS NMR et ICP-AES/OES, XPS, FT-IR et Raman ont permis d'extraire des informations précieuses corrélant la structure avec l'activité catalytique. Pour obtenir de meilleurs nanocatalyseurs, les stratégies suivantes ont été employées :

- Chapitre 3 - L'utilisation de calculs DFT a permis d'expliquer les tendances observées dans les performances HER obtenues en milieu acide pour une série de NPs fonctionnalisées par des ligands.
- Chapitre 4 - L'utilisation de supports conducteurs de type graphène a permis d'améliorer les performances et la stabilité des NPs dans l'électrocatalyse HER et de comprendre l'effet du dopage P/N du support sur le résultat catalytique final.
- Chapitre 5 - L'utilisation d'un support de carbone macroscopique conducteur, bon marché et facile à manipuler, a permis d'améliorer la conductivité et la stabilité des NPs.
- Chapitre 6 - La combinaison de deux métaux différents pour bénéficier d'une synergie dans des systèmes bimétalliques.

Les nanomatériaux à base de Ru sont apparus ces dernières années comme des catalyseurs prometteurs pour la catalyse HER en raison de leur grande stabilité en milieu acide et alcalin et de la force de liaison Ru-H similaire à celle de la liaison Pt-H.<sup>4</sup> À cet

égard, des NPs de Ru stabilisées par la 4-phénylpyridine (Ru-4PP) précédemment synthétisées et étudiées dans notre groupe. Se sont révélées des systèmes particulièrement intéressants<sup>5</sup> Cependant, l'élucidation des mécanismes catalytiques avec des catalyseurs nanoparticulaires demeure une tâche difficile malgré les avancées récentes dans les techniques de caractérisation des matériaux à l'échelle nanométrique. Dans ce sens, la combinaison de calculs théoriques avec les résultats expérimentaux est extrêmement intéressante pour prédire et/ou rationaliser certaines tendances dans l'activité électrocatalytique HER des nanocatalyseurs. Certains concepts théoriques tels que l'énergie libre d'adsorption, les modèles microcinétiques, les diagrammes de volcan et les centres de bande d sont largement acceptés pour l'évaluation (semi-)quantitative de la performance des électrocatalyseurs HER en milieu acide.<sup>6</sup> L'activité catalytique d'un nanomatériau dépend de son énergie de surface, et donc de la nature/couverture des espèces de surface. La théorie de la fonctionnelle de la densité (DFT) permet d'élucider les propriétés chimiques/électroniques de clusters métalliques modélisés construits sur la base de la caractérisation expérimentale des nanocatalyseurs (structure, état de surface, titrage des hydrures de surface, etc.).

Les études DFT menées pour les NPs de Ru stabilisées par 4PP ont permis d'évaluer le mode de coordination du ligand sur un modèle  $\text{Ru}_{55}\text{H}_{53}$ , modèle établi à partir du titrage expérimental des hydrures de surface d'un nanocatalyseur réel. Les résultats ont indiqué une compétition entre la  $\sigma$ -donation de la paire solitaire N et une interaction  $\pi$ -métal aromatique, le dernier mode de coordination le plus stable. Un modèle avec ligands a donc pu être construit,  $\text{Ru}_{55}\text{H}_{53}(\sigma\text{-4PP}^*)_9(\pi\text{-4PP}^*)_2$ , et les énergies Gibbs d'adsorption de l'hydrogène correspondantes,  $\Delta G_{\text{H}^*}$ , calculées sur différents sites d'adsorption représentatifs.<sup>7</sup> Les valeurs  $\Delta G_{\text{H}^*}$  obtenues ont montré que certains sites dans les NPs de Ru protégés par 4PP pouvaient être très actifs envers le HER, avec une  $\Delta G_{\text{H}^*} \approx 0$  kcal/mol. Ces résultats théoriques sont en accord avec l'activité HER exceptionnelle observées pour les NPs Ru-4PP, présentant un surpotentiel à  $10 \text{ mA} \cdot \text{cm}^{-2}$  ( $\eta_{10}$ ) faible de 20 mV.<sup>5</sup> Deux autres types de Ru NPs fonctionnalisées par d'autres ligands ont fait l'objet de calculs DFT ( *chapitre 3* ), à savoir des NPs de Ru fonctionnalisées par la 4'-(4-méthylphényl)-2,2':6',2''-terpyridine (Ru-tpy) et la 2-phénylpyridine (Ru-2PP).

La coordination du ligand tpy sur la surface d'une NP de Ru a été étudiée par DFT afin de définir ses modes de coordination les plus favorisés sur le plan énergétique. Les

calculs ont été effectués sur un modèle de NP de Ru hydrogénée de 1 nm ( $\text{Ru}_{55}\text{H}_{35}$ , 0,8 H/Rusurf), simulant les résultats expérimentaux de titration des hydrures (voir Fig. 2 pour les géométries de  $\text{Ru}_{55}\text{H}_{35}$  et du ligand tpy).

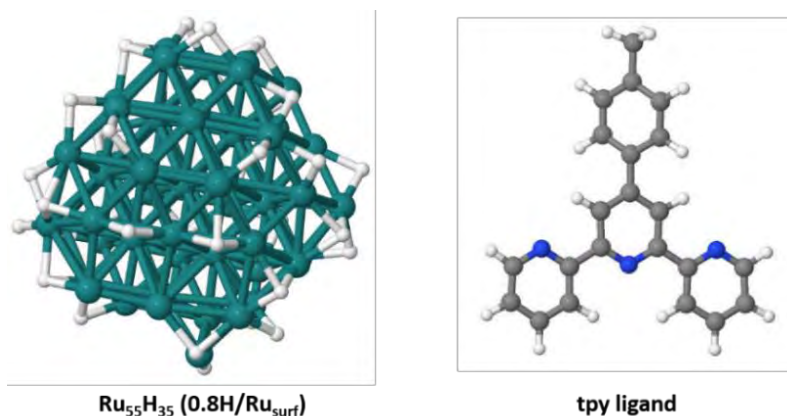


**Figure 2.** Géométrie du modèle de NP  $\text{Ru}_{55}\text{H}_{35}$  (0,8 H/Rusurf) et du ligand 4'-(4-méthylphényl)-2,2':6',2''-terpyridine (tpy) utilisés pour les calculs DFT. L'énergie moyenne d'adsorption des 35 hydrures dans  $\text{Ru}_{55}\text{H}_{35}$  est d'environ -14,0 kcal/mol.

Les trois différents cycles pyridine du ligand tpy peuvent être coordonnés aux atomes de Ru de surface par deux modes de coordination différents:  $\sigma$ -donation de la paire libre de l'azote ou interaction  $\pi$ -métal aromatique avec une configuration plate du cycle. En combinant ces deux possibilités pour tous les cycles pyridine, il en découle cinq géométries différentes avec différents modes de coordination du ligand (Fig. 3). Les énergies d'adsorption pour le tpy dans chaque mode de coordination sont également résumées dans la Fig. 3.

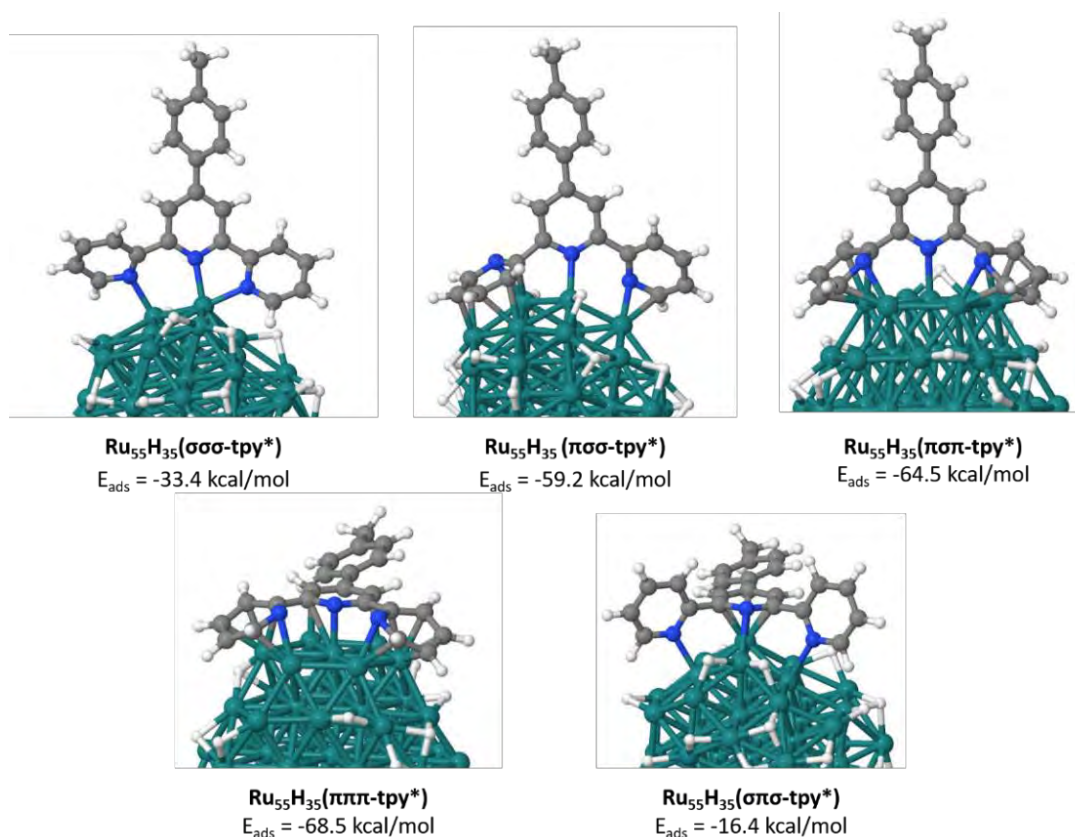


**Figure 3.** Géométrie des cinq structures possibles pour tpy sur Ru<sub>55</sub>H<sub>35</sub> NP (0.8 H/Rusurf) selon différents modes de coordination et énergies d'adsorption correspondantes ( $E_{\text{ads}}$ ).

Lorsque les trois cycles pyridine sont tous coordonnés par une interaction  $\pi$ -métal, le système est stable de -68,5 kcal/mol, alors que lorsque tous les cycles sont coordonnés par  $\sigma$ -donation, le ligand l'est moins (-33,4 kcal/mol). Alors que la géométrie des atomes de carbone dans les cycles aromatiques coordonnés dans  $\sigma\sigma\sigma$ -tpy est proche de celle d'un ligand libre, elle est significativement déformée dans la configuration  $\pi\pi\pi$ . De plus, dans les situations intermédiaires (coordination hybride  $\sigma$  et  $\pi$ ), une torsion d'un ou deux des cycles aromatiques terpyridiniques est induite, ce qui pourrait conduire à la déstabilisation du système final. La coordination  $\pi\sigma\pi$  est la plus stable (-64,5 kcal/mol), puisque les deux anneaux distordus sont coordonnés en  $\pi$ , proportionnant la stabilité du système et contrebalançant les changements structurels, alors que la coordination  $\sigma\pi\sigma$  (-16,4 kcal/mol) est la moins stable, avec une torsion élevée et un seul anneau coordonné en  $\pi$ . D'énergie intermédiaire, la géométrie  $\pi\sigma\sigma$  (-59,2 kcal/mol), bien qu'elle ne contienne qu'un seul anneau  $\pi$ -coordonné, présente une distorsion globale plus faible que dans le cas  $\sigma\pi\sigma$ . Au vu de ces résultats et en considérant les faibles différences d' $E_{\text{ads}}$  du ligand tpy dans les deux coordinations  $\pi\pi\pi$  et  $\pi\sigma\pi$  (-68,5 kcal/mol contre -64,5 kcal/mol,

respectivement), la géométrie choisie pour construire un modèle avec plus de ligands tpy sur la surface a été la  $\pi\sigma\pi$ , en raison de son encombrement stérique plus faible par rapport à celui de  $\pi\pi\pi$ . De plus, la coordination  $\pi\sigma\pi$  permet la coordination de plus d'atomes d'hydrogène, ce qui stabilise probablement le système. En revanche, l'important encombrement stérique de la configuration  $\pi\pi\pi$  repousse les hydrures placés sous le ligand, les forçant à s'entasser sur d'autres sites de Ru, et par conséquent à réduire le nombre de ligands tpy putatifs adsorbés à la surface de la NP. Cette différence conduirait probablement à un système moins stable avec des ligands tpy seulement coordonnés  $\pi\pi\pi$ , comme le confirme une étude précédente avec des NP de Ru fonctionnalisées par 4PP.<sup>5</sup>

Un modèle avec 5 ligands tpy coordonnés en mode  $\pi\sigma\pi$  sur la surface du RuNP a donc été construit,  $\text{Ru}_{55}\text{H}_{35}(\pi\sigma\pi\text{-tpy}^*)_5$  (Fig. 4). L' $E_{\text{ads}}$  moyenne obtenue des ligands tpy est de -21,5 kcal/mol, calculée selon  $E_{\text{ads}} = [E(\text{n tpy}^*) - E(\text{Ru}_{55}\text{H}_{35}\text{NP}) - nE(\text{tpy})]/n$ , où  $\text{tpy}^*$  désigne un ligand tpy adsorbé sur la surface de la NP de Ru. Cette diminution de  $E_{\text{ads}}$  par rapport à la valeur obtenue pour un seul tpy dans le même mode de coordination (-21,5 contre -64,5 kcal/mol) est en accord avec le fait que l'incorporation de plus de ligands conduit à une diminution du centre de la bande d du métal (c'est-à-dire à une stabilisation du métal) et que l'encombrement stérique provoqué par la saturation de la surface supplante les effets de stabilisation de la coordination.

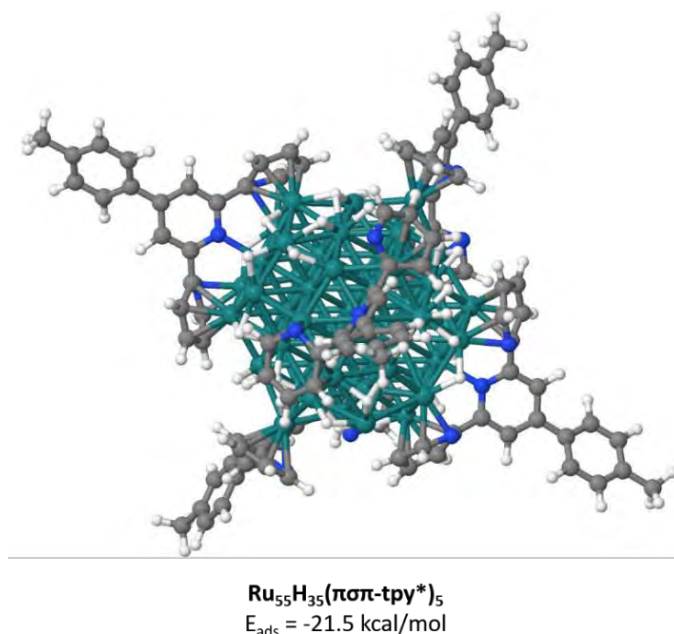


**Figure 4.** Géométrie optimisée pour le RuNP 1 nm protégée par 5-tpy ( $\text{Ru}_{55}\text{H}_{35}(\pi\sigma\pi\text{-tpy}^*)_5$ ) et son  $E_{\text{ads}}$ .



En catalyse HER, une bonne corrélation entre les valeurs expérimentales de la densité de courant d'échange ( $j_0$ , qui reflète le taux intrinsèque de transfert d'électrons entre l'analyte et l'électrode) et l'énergie libre d'adsorption de Gibbs de l'hydrogène ( $\Delta G_{H^*}$ ) a été établie, obtenant des dépendances de type volcan.<sup>8</sup> Un catalyseur optimal doit se trouver au sommet du diagramme volcan ( $\Delta G_{H^*} \approx 0$  kcal/mol). Selon le principe de Sabatier, l'interaction catalyseur-substrat ne peut être ni trop forte ni trop faible ( $\Delta G_{H^*} < 0$ , adsorption de  $H^*$  relativement forte, et  $\Delta G_{H^*} > 0$ , adsorption de  $H^*$  relativement faible). Ainsi, si l'interaction entre la surface des NPs et H est trop faible, l'atome d'hydrogène ne parviendra pas à se lier au catalyseur et la réaction de réduction des protons n'aura pas lieu. D'autre part, si l'interaction est trop forte, le produit ne peut pas être libéré.

L'énergie libre d'adsorption de Gibbs de l'hydrogène  $\Delta G_{H^*}$  ( $\Delta G_{H^*} = \Delta E_{H^*} + 5,5$  kcal/mol) a été calculée sur trois sites d'adsorption différents représentatifs et pouvant coexister à la surface du modèle 5-tpy- $\pi\sigma\pi$  ( $Ru_{55}H_{35}(\pi\sigma\pi\text{-tpy}^*)_5$ ), correspondant à une liaison  $\eta$ ,  $\mu$  ou  $\mu^3$ . Ces trois hydrures sont respectivement le  $H^{172}$  (liaison  $\eta$ ), le  $\mu\text{-H}^{57}$  et le  $\mu^3\text{-H}^{67}$ , en rouge sur la Fig. 5.

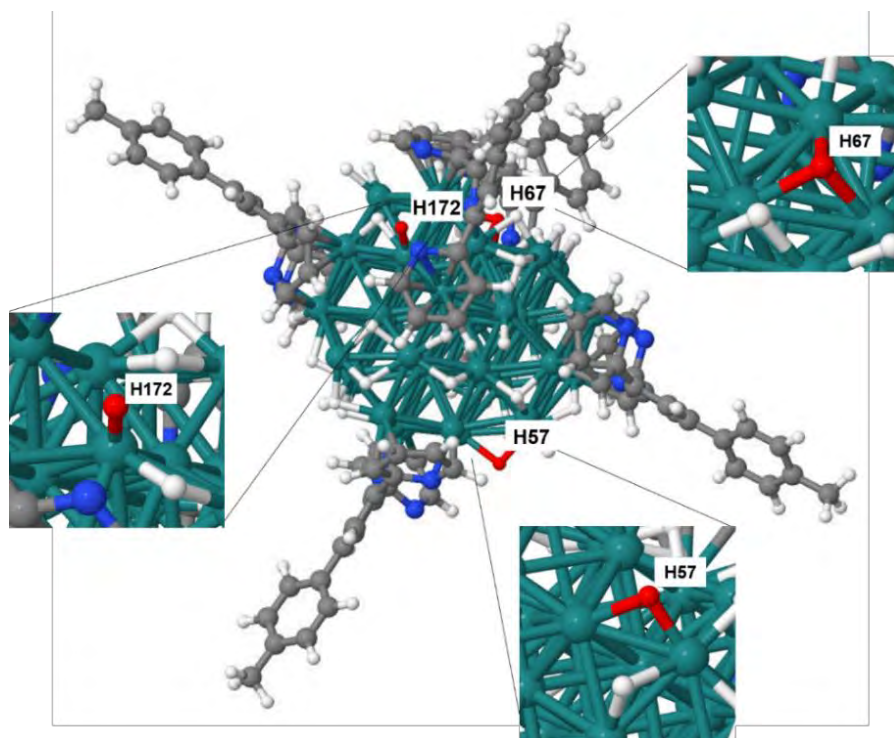


**Figure 5.** Sites d'adsorption étudiés pour HER sur une NP de Ru de 1 nm protégée par 5-tpy ( $Ru_{55}H_{35}(\pi\sigma\pi\text{-tpy}^*)_5$ ).

Ces calculs, très délicats en raison de la réorganisation des hydrures de surface lors des processus d'adsorption/désorption, peuvent donc fournir des énergies artefactuelles. Il est à noter que les énergies libres de Gibbs de première adoption de ces hydrures représentatifs ( $\Delta G_{H^*}$ ) sont positives (c'est-à-dire une faible adsorption), avec des valeurs comprises entre 5 et 15 kcal/mol. Après retrait d'un deuxième hydrure dans le voisinage immédiat du premier hydrure (c'est-à-dire l'atome d'hydrogène qui migre après le retrait du premier H) les valeurs  $\Delta G_{H^*}$  ont été à nouveau calculées, avec des valeurs comprises entre -9 et 5 kcal/mol (Tableau 1).

**Tableau 1.** Valeurs  $\Delta G_{H^*}$  obtenues pour les différents sites H de Ru<sub>55</sub>H<sub>35</sub>( $\pi\sigma\pi$ -tpy\*)<sub>5</sub>.

Entry	Probed H sites	$\Delta E_{H^*}$ (kcal/mol)	$\Delta G_{H^*}$ (kcal/mol)
1	Top-H <sup>172</sup>	8.60	14.10
2	Top-H <sup>172</sup> + 2 <sup>nd</sup> H removal	-0.68	4.82
3	Edge-capping $\mu$ -H <sup>57</sup>	-0.86	4.64
4	Edge-capping $\mu$ -H <sup>57</sup> + 2 <sup>nd</sup> H removal	-14.68	-9.18
5	Face-capping $\mu_3$ -H <sup>67</sup>	9.19	14.69
6	Face-capping $\mu_3$ -H <sup>67</sup> + 2 <sup>nd</sup> H removal	-2.88	2.62

La densité de courant d'échange expérimentale résultante,  $j_0$ , pour différentes NPs de Ru fonctionnalisées par ligand ainsi que pour plusieurs autres métaux purs et MoS<sub>2</sub> est représentée sur la Fig. 6 en fonction des valeurs  $\Delta G_{H^*}$  obtenues à partir des calculs DFT-PBE (Perdew-Burke-Ernzerhof). L'objectif de ces graphiques est de disposer d'un guide pour prédire qualitativement l'activité de nouveaux électrocatalyseurs.

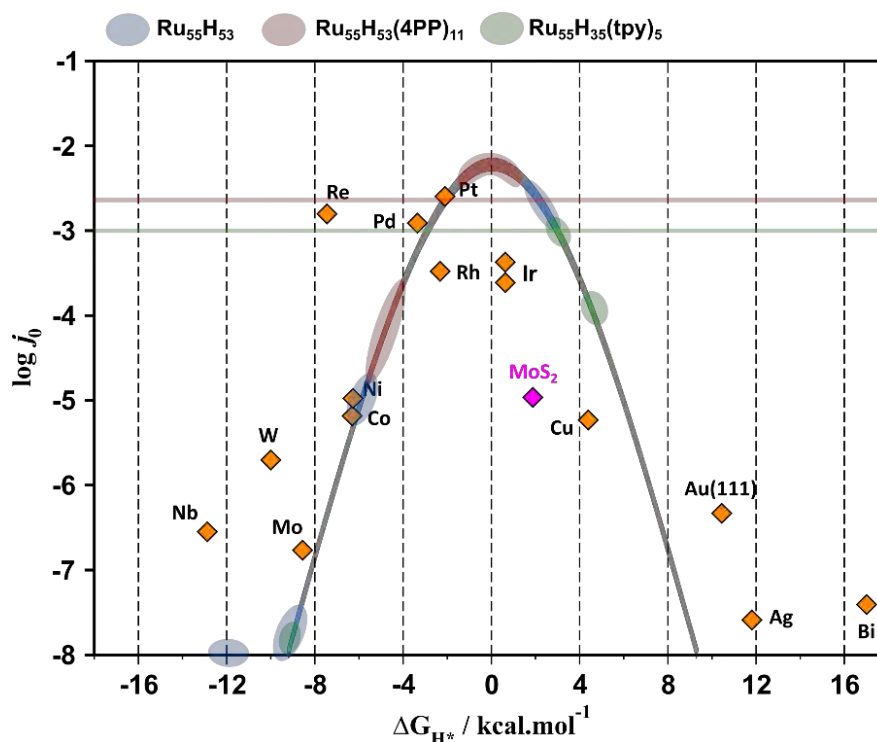


**Figure 6.** Diagramme en volcan du logarithme de la densité de courant d'échange expérimentale  $j_0$  ( $A/cm^2$ ) en fonction de l'énergie libre de Gibbs d'adsorption de H calculée par DFT,  $\Delta G_{H^*}$  (kcal/mol), pour les métaux purs<sup>9</sup> (diamants orange) et le  $MoS_2$  nanométrique<sup>10</sup> (diamant rose). Les lignes horizontales représentent les valeurs expérimentales du  $\log j_0$  pour les NPs Ru-4PP (rouge) et Ru-tpy (vert). Les résultats de nos calculs DFT pour  $\Delta G_{H^*}$  dans les différents sites sondés par H pour  $Ru_{55}H_{53}$  (ovales bleus),  $Ru_{55}H_{53}(\sigma-4PP)_9(\pi-4PP)_2$  (ovales rouges) et  $Ru_{55}H_{35}(\pi\sigma\sigma-tpy)_5$  (ovales verts) après une 2ème élimination d'hydrure sont présentés sous forme d'ovales. Adapté de la réf. 6.

En outre, le tableau 2 présente les données expérimentales chimiques et électrochimiques obtenues pour les NPs de Ru fonctionnalisées par les ligands 4PP, tpy et 2PP.

**Tableau 2.** Données expérimentales chimiques et électrochimiques (1 M  $H_2SO_4$ ) pour différentes NP de Ru fonctionnalisées par les ligands 4PP, tpy et 2PP.

Entry	Catalyst	$d_{mean}$ (nm)	H/Ru <sub>surf</sub>	$\eta_{10}$ (mV)	$j_0$ (mA/cm <sup>2</sup> )	$\log j_0$ (A/cm <sup>2</sup> )	Ref.
1	Ru-4PP	$1.5 \pm 0.3$	1.2	20	2.04	-2.69	5
2	Ru-tpy	$1.4 \pm 0.2$	0.7	93	0.99	-3.00	11
3	Ru-2PP	$1.8 \pm 0.3$	1.0	30	1.93	-2.71	11

Dans des études précédentes,  $\Delta G_{H^*}$  a été calculée sur six sites d'adsorption représentatifs dans le modèle  $Ru_{55}H_{53}(4PP^*)_{11}$ , obtenant des valeurs  $\Delta G_{H^*}$  se répartissant en deux groupes,  $\Delta G_{H^*}$  entre -5,0 et -4,0 kcal/mol, et  $\Delta G_{H^*}$  entre -1,0 et 1,5 kcal/mol (ovales rouges dans la Fig. 6). Ces résultats suggèrent que certains sites dans les NPs Ru-4PP pourraient être très actifs envers le HER, montrant un  $\Delta G_{H^*}$  proche de 0 kcal/mol (formes rouges au sommet du volcan dans la Fig. 6), corroborant leur remarquable activité électrocatalytique HER observée expérimentalement, avec une valeur  $\eta_{10}$  faible de 20 mV (Tableau 2). Les valeurs de  $\Delta G_{H^*}$  ont également été calculées pour les mêmes sites dans un modèle sans ligand ( $Ru_{55}H_{53}$ ), obtenant des valeurs  $\Delta G_{H^*}$  significativement plus négatives (ovales bleus dans la Fig. 6) que pour le modèle fonctionnalisé avec le ligand 4PP, confirmant ainsi que ce ligand déplace significativement les énergies d'adsorption près de ca. 0 kcal/mol. En ce qui concerne les données expérimentales pour les NPs Ru-tpy, on peut remarquer qu'elles possèdent l'activité électrocatalytique la plus faible des trois systèmes étudiés, avec une valeur  $\eta_{10}$  de 93 mV (Tableau 2). Cette tendance est également observée dans les valeurs  $\Delta G_{H^*}$  (Tableau 1), qui se situent sur les deux branches du graphique en forme de volcan, loin de son sommet (ovales verts sur la Fig. 6). Cette étude devrait être complétée par d'autres calculs d'énergie d'adsorption considérant les H les plus proches des ligands tpy afin de vérifier une éventuelle influence de la densité  $\pi$  du ligand tpy dans  $\Delta G_{H^*}$ . Cependant, elle fournit jusqu'à présent des tendances intéressantes qui sont en accord avec nos résultats expérimentaux précédents.

Des études similaires ont été réalisées avec le ligand 2PP, montrant à nouveau que la coordination  $\pi$  est plus stable que la coordination  $\sigma$  (-43,8/-53,4 kcal/mol contre -13,2 kcal/mol, respectivement). En fait, la coordination  $\sigma$  est encore moins stable avec 2PP qu'avec 4PP, ce qui pourrait s'expliquer par le fait que le ligand 4PP maintient presque sa géométrie par rapport à l'espèce libre, alors que le cycle benzénique du 2PP doit se tordre pour se coordonner en mode  $\sigma$  par le cycle pyridine (Fig. 7). En outre, un nouveau mode de coordination a pu être évalué avec 2PP, en coordonnant chaque cycle différemment (c'est-à-dire la pyridine en  $\sigma$  et le cycle benzénique en  $\pi$ ). Les systèmes obtenus avec un mode de coordination mixte- $\sigma\pi$  présentent des stabilités comparables à celles des systèmes  $\pi\pi$  (-41,4/-56,9 kcal/mol contre -43,8/-53,4 kcal/mol, respectivement, Fig. 7). Dans ce cas, la torsion du cycle benzénique nécessaire à la coordination  $\sigma$  du cycle

pyridine peut être contrebalancée par une coordination  $\pi$  par du cycle benzénique, conduisant à une configuration très stable.

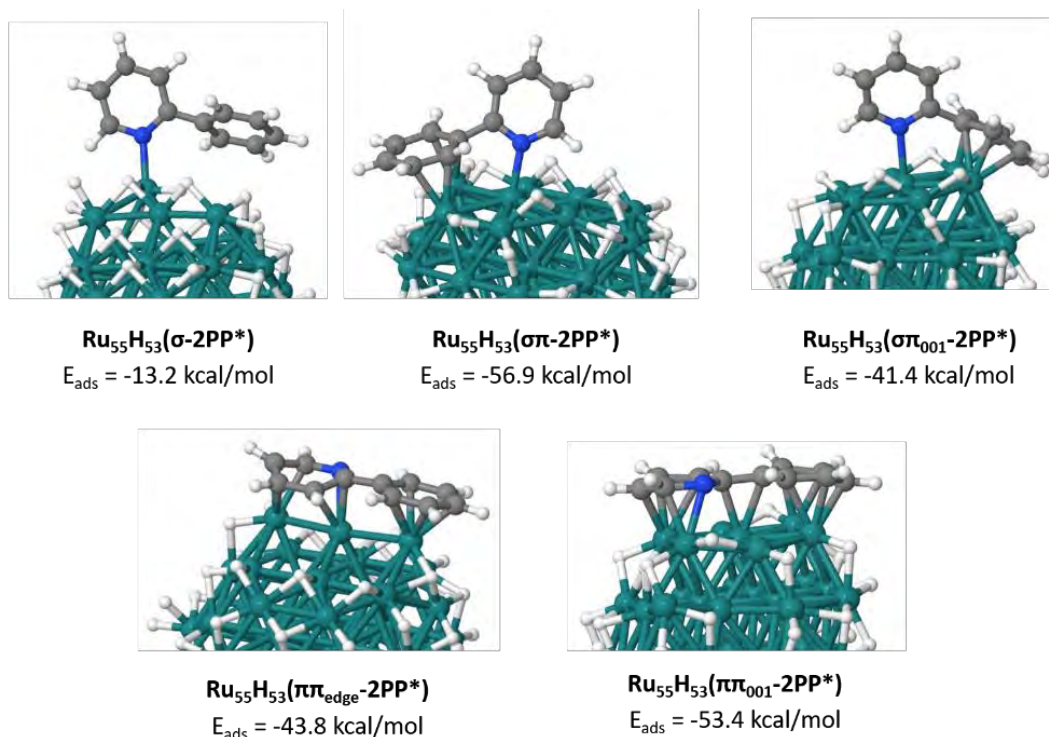


**Figure 7.** Géométrie des cinq différents modes de coordination et E<sub>ads</sub> correspondantes avec 2PP sur le modèle Ru<sub>55</sub>H<sub>53</sub>.

En tenant compte de ces résultats, un modèle plus complexe a été proposé, en considérant cinq ligands 2PP en  $\sigma$  et deux autres en  $\pi$ , nommé Ru<sub>55</sub>H<sub>44</sub>(σ-2PP\*)<sub>5</sub>(π-2PP\*)<sub>2</sub> (Fig. 8). Ce modèle sera utilisé prochainement pour calculer les valeurs de  $\Delta G_{H^*}$  pour les différents sites d'adsorption d'hydrogène. Cependant, en tenant compte de la coordination hybride  $\sigma\pi$  entravée dans ce modèle, présentant une couverture de surface élevée, nous pourrions considérer un autre modèle avec moins ligands coordonnés afin de pouvoir favoriser la coordination  $\sigma\pi$  et extraire plus de conclusions.

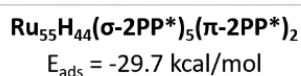
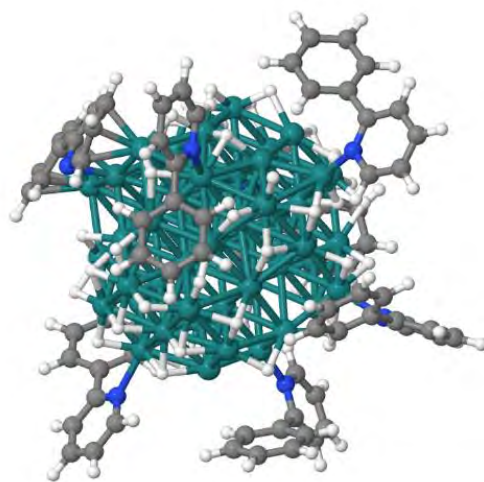


**Figure 8.** Géométrie optimisée pour  $\text{Ru}_{55}\text{H}_{44}(\sigma\text{-2PP}^*)_5(\pi\text{-2PP}^*)_2$  et  $E_{\text{ads}}$  correspondante.

Dans le *chapitre 4*, nous avons montré que les matériaux de type graphène sont des supports appropriés pour obtenir de petites NPs de Ru bien dispersées. Les techniques (HR)TEM, EDX, EA, ICP, XPS, XRD, Raman et IR ont livré des informations sur la structure et la composition des nanomatériaux supportés obtenus.

Dans le *chapitre 4A*, l'oxyde de graphène réduit (rGO) préparé par la méthode Hummers a été utilisé comme support pour des NPs Ru/RuO<sub>2</sub>. L'introduction d'hétéroatomes N et P dans la structure carbonée, a permis d'obtenir des NPs plus petites et bien dispersées, présentant une taille moyenne de  $1,5 \pm 0,2/0,3$  nm, comparativement à l'utilisation de graphène non dopé qui a conduit à des NPs plus grandes ( $2,0 \pm 0,8$  nm) et avec une distribution de taille plus hétérogène (Fig. 9). Ces résultats confirment le rôle positif du dopage hétéroatomique dans la stabilisation des NPs de Ru(0) pendant la procédure de synthèse, affectant leur nucléation et leur cinétique de croissance. Les analyses ICP-AES ont révélé des teneurs en métal de 2,4 %wt. Ru, 2,5 %wt. Ru et 3,1 %wt. Ru dans **Ru@rGO**, **Ru@NH<sub>2</sub>-rGO** et **Ru@P-rGO**, respectivement. L'analyse XPS du signal P 2p a également permis de déterminer la teneur en P dans le support dopé, **P-rGO**, qui s'est avérée être de 1,26 at.%. Enfin, le signal Ru 3p<sub>3/2</sub> a confirmé la présence d'un mélange de Ru(0) et de Ru(IV), confirmant la formation d'une couche de passivation de RuO<sub>2</sub> autour du cœur de Ru(0) après exposition à l'air. La RMN <sup>31</sup>P à l'état solide, a confirmé la présence d'atomes de P liés à l'oxygène et de liaisons P-C, avec un

pourcentage d'atomes de phosphore graphitique plus élevé que dans le **Ru@P-G** (à partir d'alginate, *chapitre 4B*, voir ci-dessous).

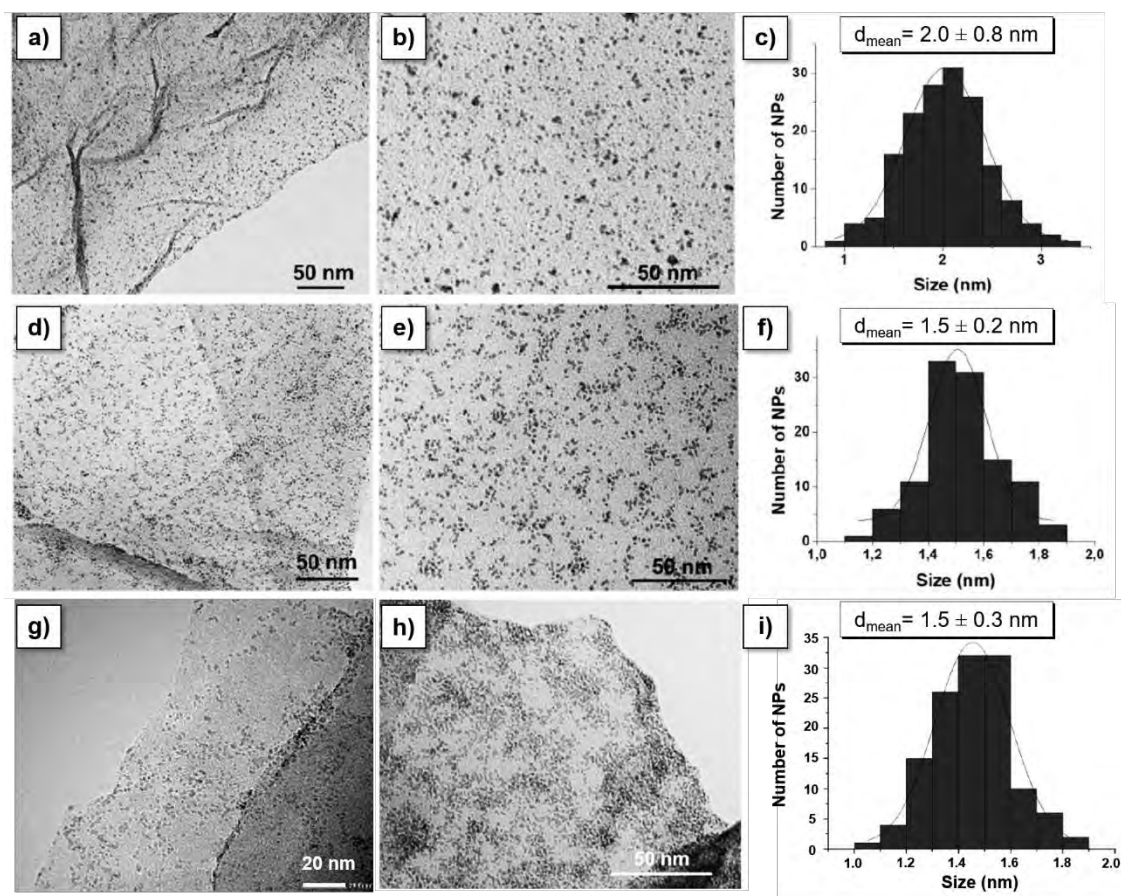


**Figure 9.** Images TEM et histogrammes de distribution de taille de **Ru@rGO** (a-c), **Ru@NH<sub>2</sub>-rGO** (d-f) et **Ru@P-rGO** (g-i).

Après oxydation partielle de la surface par exposition à l'air, les activités catalytiques des matériaux ont été étudiées en HER. L'activité de tous les matériaux dans une solution aqueuse de H<sub>2</sub>SO<sub>4</sub> 1 M montre clairement la dépendance de l'activité catalytique HER en fonction de l'état d'oxydation de la surface des NPs, les sites métalliques Ru(0) étant plus actifs que RuO<sub>2</sub>. Ceci est confirmée par l'amélioration de l'activité HER observée après avoir soumis les systèmes à un traitement réducteur (Fig. 10). Tous les matériaux **Ru@rGO-r**, **Ru@NH<sub>2</sub>-rGO-r** et **Ru@P-rGO-r** activés fonctionnent à de faibles surtensions ( $\eta_{10} \approx 71$  mV, 30 mV et 2 mV, respectivement, Fig. 10a) et présentent une pente de Tafel (b) dans les tracés de Tafel correspondants de 65, 56 et 51 mV/dec, respectivement (Fig. 10b). On remarque également un effet positif de l'hétéroatome (c'est-à-dire N ou P) incorporé dans le support de carbone sur l'activité



catalytique HER, en particulier pour le matériau dopé au P. Ce comportement peut être expliqué par la capacité respective d'accepteur et de donneur d'électrons des atomes de N et de P adjacents aux atomes de C dans la structure graphitique, affectant la structure électronique du support, avec un effet concomitant dans la structure électronique des NPs de Ru, améliorant dans ce cas l'effet synergique entre Ru et C, modulant l'adsorption des intermédiaires de réaction pour augmenter l'activité HER.

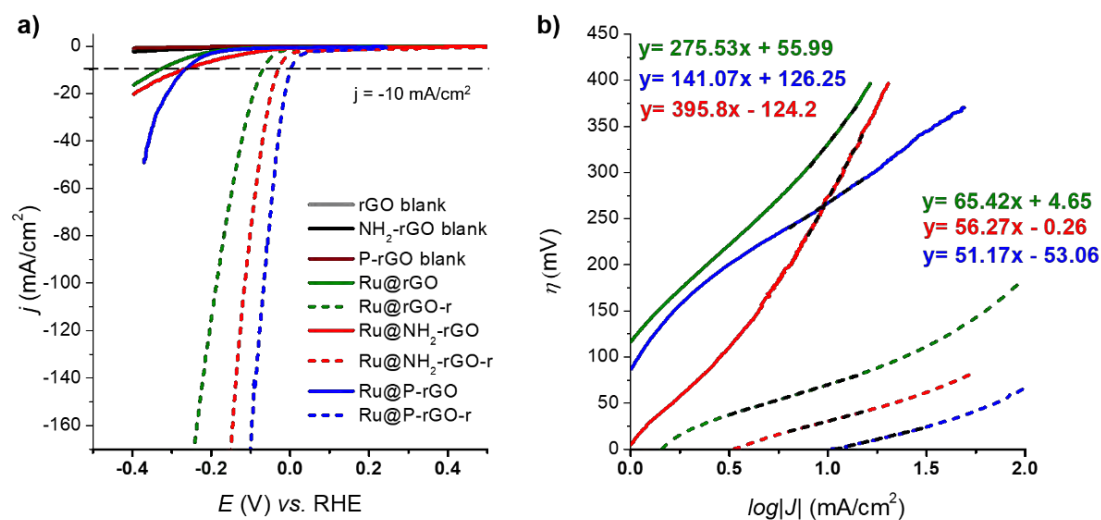


**Figure 10.** Courbes de polarisation de **Ru@rGO** (ligne verte), **Ru@NH<sub>2</sub>-rGO** (ligne rouge) et **Ru@P-rGO** (ligne bleue) avant (en gras) et après (en pointillés) un processus de réduction à  $|j| = -10$  mA/cm<sup>2</sup> dans 1 M H<sub>2</sub>SO<sub>4</sub>. Les blancs de **rGO** (ligne grise), **NH<sub>2</sub>-rGO** (ligne noire) et **P-rGO** (ligne vin) sont également représentés (a). Diagrammes de Tafel de **Ru@rGO**, **Ru@rGO-r**, **Ru@NH<sub>2</sub>-rGO**, **Ru@NH<sub>2</sub>-rGO-r**, **Ru@P-rGO** et **Ru@P-rGO-r** dans 1 M H<sub>2</sub>SO<sub>4</sub> (b). Même code couleur que dans (a).

Des études de stabilité à long terme ont mis en évidence que tous les systèmes sont capables de produire une densité de courant de  $j = -10$  mA/cm<sup>2</sup> pendant au moins 12 h sans aucun signe de désactivation. Des valeurs élevées d'efficacité faradique (i.e. 96-98%) ont confirmé la production quantitative de H<sub>2</sub> pour tous les systèmes étudiés.

Des résultats similaires ont été obtenus dans le *chapitre 4B* en utilisant des rGO préparés par la pyrolyse de l'alginate, générant de petites NPs bien dispersées avec une taille moyenne de  $1,9 \pm 0,6$  nm et  $1,5 \pm 0,3$  nm en utilisant les rGO nus et dopés P, respectivement (Fig. 11). La spectroscopie d'émission atomique à plasma à couplage inductif (ICP-AES) a confirmé la présence de Ru dans chaque échantillon, obtenant des teneurs en métal de 2,6 % en poids et 3,3 % en poids pour **Ru@G** et **Ru@P-G**,



respectivement. Là encore, l'analyse XPS du signal Ru 3p<sub>3/2</sub> a confirmé la présence d'un mélange d'espèces Ru(0) et Ru(IV) après exposition des échantillons à l'air.

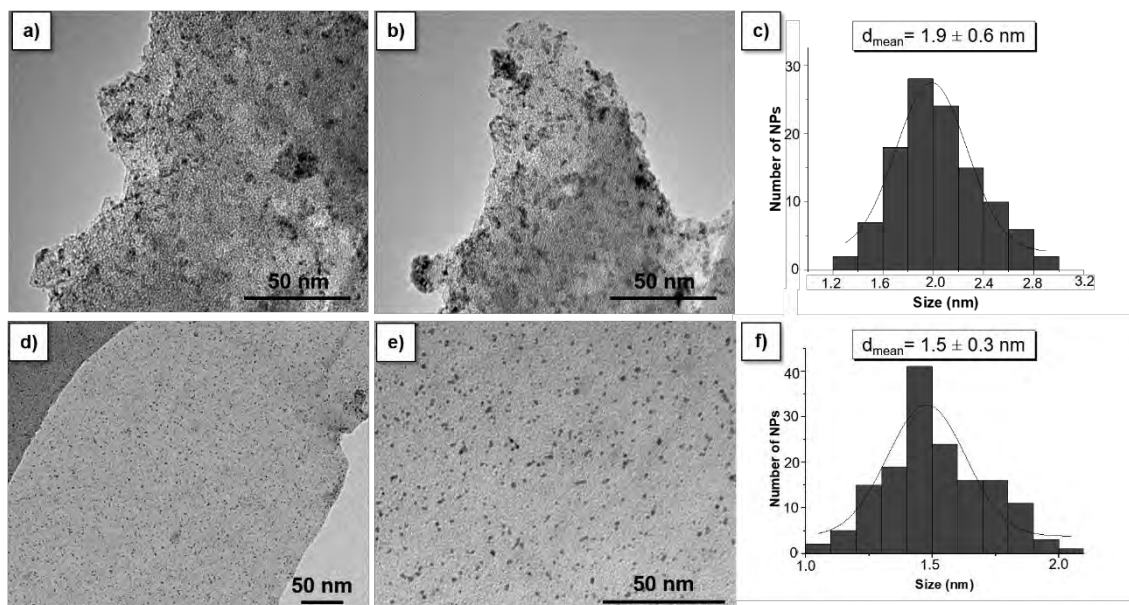


**Figure 11.** Images TEM et histogrammes de distribution de taille de Ru@G (a-c) et Ru@P-G (d-f).

Les courbes de polarisation de **Ru@G** et **Ru@P-G** à  $t=0$  s sont présentées dans la Fig. 12 (lignes en gras). Un changement de la densité de courant est observé lors du balayage vers les potentiels réducteurs, ce qui est attribué à leur activité catalytique lors de la réduction des protons en  $H_2$ .

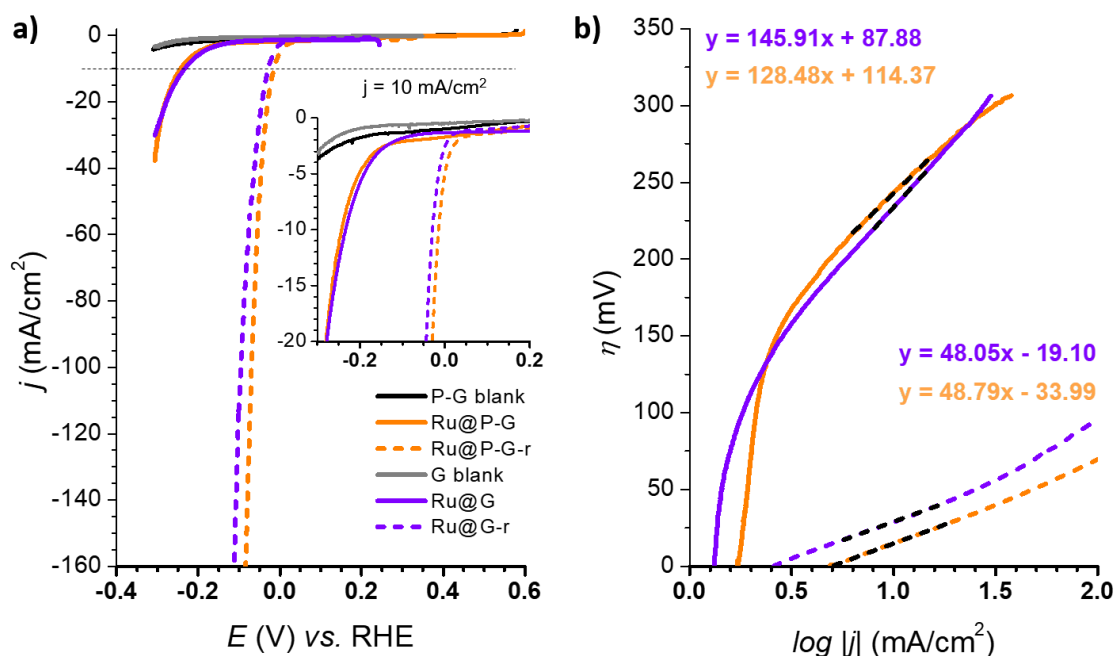


**Figure 12.** Courbes de polarisation de **Ru@G** (ligne violette), **Ru@P-G** (ligne orange) avant (en gras) et après (en pointillés) un processus de réduction à  $|j| = -10$  mA/cm<sup>2</sup> dans 1 M H<sub>2</sub>SO<sub>4</sub>. Les blancs **G** (ligne grise) et **P-G** (ligne noire) sont également représentés (a). Diagrammes de Tafel de **Ru@G**, **Ru@G-r**, **Ru@P-G** et **Ru@P-G-r** dans 1 M H<sub>2</sub>SO<sub>4</sub> (b). Même code que dans (a).

La performance catalytique des systèmes peut être améliorée de manière significative après les avoir soumis à une électrolyse en masse contrôlée par le courant à  $j = -10$  mA/cm<sup>2</sup> (Fig. 12a, lignes pointillées). Alors que les systèmes **Ru@G** et **Ru@P-G** présentent un  $\eta_{10}$  de 233 mV et 243 mV, respectivement, un déplacement des courbes de polarisation est observé après le processus de réduction, améliorant l' $\eta_{10}$  jusqu'à 29 mV et 15 mV, respectivement. Ce comportement est attribué à un changement de l'état d'oxydation des atomes de Ru en surface des NPs. La surface partiellement oxydée des NPs après synthèse, confirmée par XPS, est réduite en Ru métallique lorsqu'elle est soumise à ce traitement réducteur.

La différence de nature et de performance catalytique entre chaque échantillon passivé et son analogue réduit est mise en évidence par les diagrammes de Tafel

correspondants (Fig. 12b), la cinétique globale étant améliorée avec les systèmes réduits. **Ru@G** et **Ru@P-G** montrent tous deux une pente de Tafel proche de 120 mV, étant typiquement attribuée à l'étape de Volmer comme rds (adsorption de H<sup>+</sup> pour former l'espèce M-H sur la NP, typiquement  $b \approx 120$  mV/dec). En revanche, **Ru@G-r** et **Ru@P-G-r** présentent une pente de Tafel de 48 mV/dec et 49 mV/dec, respectivement, suggérant que le HER suit le mécanisme de Volmer-Heyrovsky, l'étape de Heyrovsky (électrodésorption de H<sub>2</sub> avec un proton de la solution,  $b \approx 40$  mV/dec) étant le chemin le plus lent du processus HER.

Le dopage P, identifié comme correspondant à des phosphates de surface par RMN <sup>31</sup>P à l'état solide, induit une amélioration de tous les paramètres de référence HER étudiés, y compris le surpotentiel et les densités d'échange et de courant spécifique. Tous les systèmes étudiés présentent une stabilité à long terme et une sélectivité excellentes pour la génération d'hydrogène, sans aucun signe de désactivation après 12 h dans des conditions électrocatalytiques et des efficacités faradiques presque quantitatives (97-98 %).

Une comparaison de l'ensemble des résultats du *chapitre 4*, montrent qu'une proportion plus élevée de phosphore graphitique (c'est-à-dire **Ru@P-rGO**) contribue de manière plus importante à l'amélioration de l'activité HER que les phosphates (c'est-à-dire **Ru@P-G**). En effet, **Ru@P-rGO** s'est avéré être le meilleur électrocatalyseur, montrant un  $\eta_{10}$  aussi bas que 2 mV et une pente de Tafel de 49 mV/dec.

Le *chapitre 5* met en évidence l'applicabilité de l'approche organométallique à la synthèse de nanostructures pour adapter l'interface entre les nanocatalyseurs et les supports carbonés dans les électrodes HER et OER. L'utilisation de deux types de microfibrilles de carbone différents, des fibres nues (CF) et des fibres fonctionnalisées par des groupes carboxyliques (ox-CF), en tant que supports bon marché, faciles à fabriquer et de surface spécifique élevée, combinée à la polyvalence de la synthèse organométallique, qui permet d'ajouter différents stabilisants de NPs et d'effectuer la synthèse en présence *-in situ-* ou en l'absence *-ex situ-* du support carboné, a permis d'obtenir différentes électrodes avec des interfaces de différentes natures.

Dans le *chapitre 5A*, nous avons obtenu une fine couche de NP de Ru ultra-petites (1-1,8 nm) sur la surface des CFs dans les systèmes *in situ* et *ex situ* (Fig. 13 et 14,

respectivement). Ces résultats ont confirmé que les défauts de la structure C, la présence d'atomes N (c'est-à-dire la rupture de la périodicité et de l'homogénéité de la structure carbonée de type graphite) et l'ajout de groupes carboxyliques et de ligands PP, lorsqu'ils sont présents, ont favorisé la nucléation et la stabilisation des atomes de Ru pour obtenir des NPs avec une distribution de taille étroite.

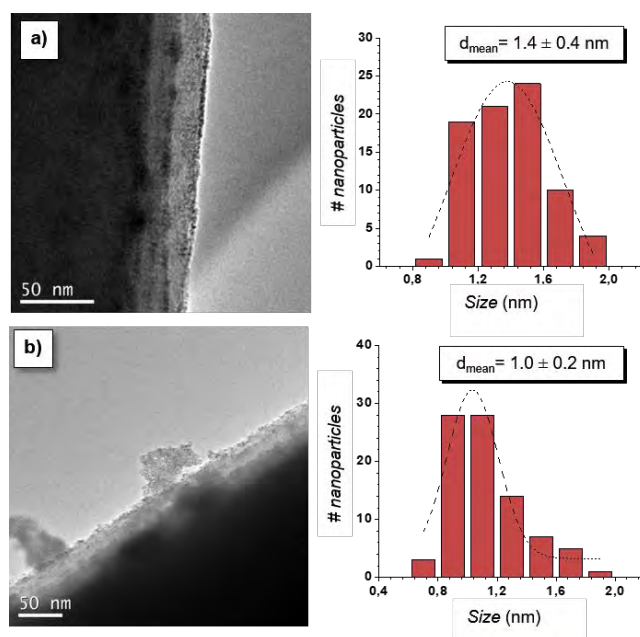


**Figure 13.** Images TEM représentatives et histogrammes de distribution de taille correspondants pour les NP de Ru supportées in situ sur CF (**Ru@CF**, a) et ox-CF (**Ru@ox-CF**, b).

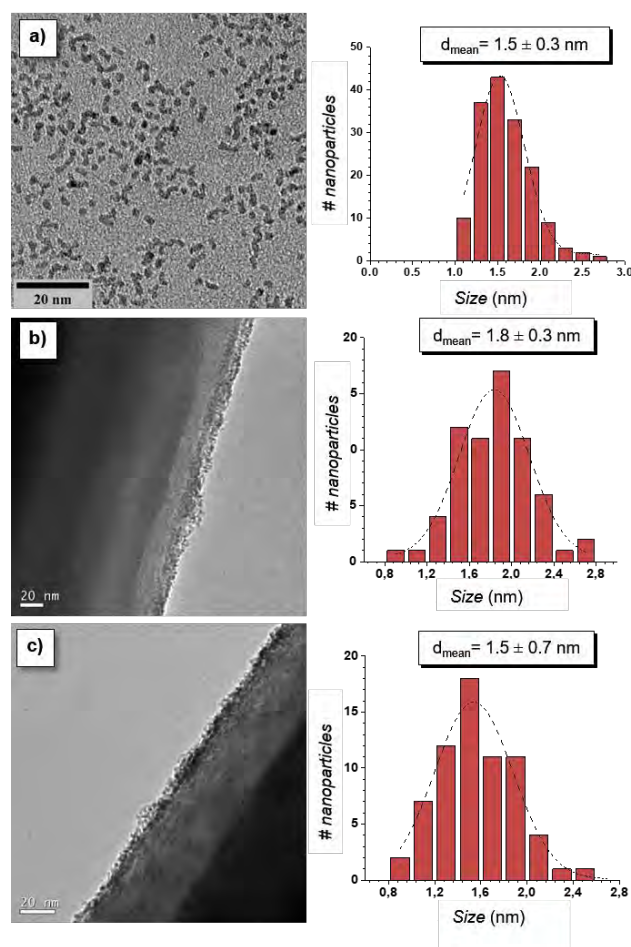


**Figure 14.** Image TEM représentative et distribution de taille correspondante des NPs de Ru colloïdales stabilisées avec de la 4-phénylpyridine (RuPP NPs) (a), des NPs de Ru supportées *ex situ* sur CF (**RuPP@CF**) (b) et ox-CF (**RuPP@ox-CF**) (c).

Des intensités catalytiques HER accrues et des surtensions réduites ont été constatées pour les systèmes *ex situ* (Fig. 15), où les NPs de Ru ont d'abord été stabilisées avec de la 4-phénylpyridine (4PP) et ensuite déposées sur les supports CF, confirmant l'importance d'une interaction électronique appropriée entre les NPs et le support, dans ce cas probablement via des interactions  $\pi$ - $\pi$  entre les cycles pyridyliques de 4PP et la structure carbonée du support. L'importance de ces interactions a également été confirmée dans des expériences de stabilité, où les cathodes *ex situ* (**RuPP@CF** et **RuPP@ox-CF**) ont présenté des stabilités beaucoup plus élevées que celles obtenues avec des NPs de Ru synthétisées *in situ* (**Ru@CF** et **Ru@ox-CF**). En outre, un effet synergique entre les fragments -COOH et les NPs de Ru a été observé dans les systèmes *in situ*, où  $\eta_0$  diminue pour **Ru@ox-CF** (30 mV) par rapport à **Ru@CF** (70 mV) (Fig. 15). Enfin, même si certains des matériaux ont été partiellement désactivés au cours des expériences

catalytiques, des efficacités faradiques presque quantitatives ont été atteintes (> 90%), confirmant l'évolution de l'hydrogène comme la seule réaction redox se produisant à leur surface.

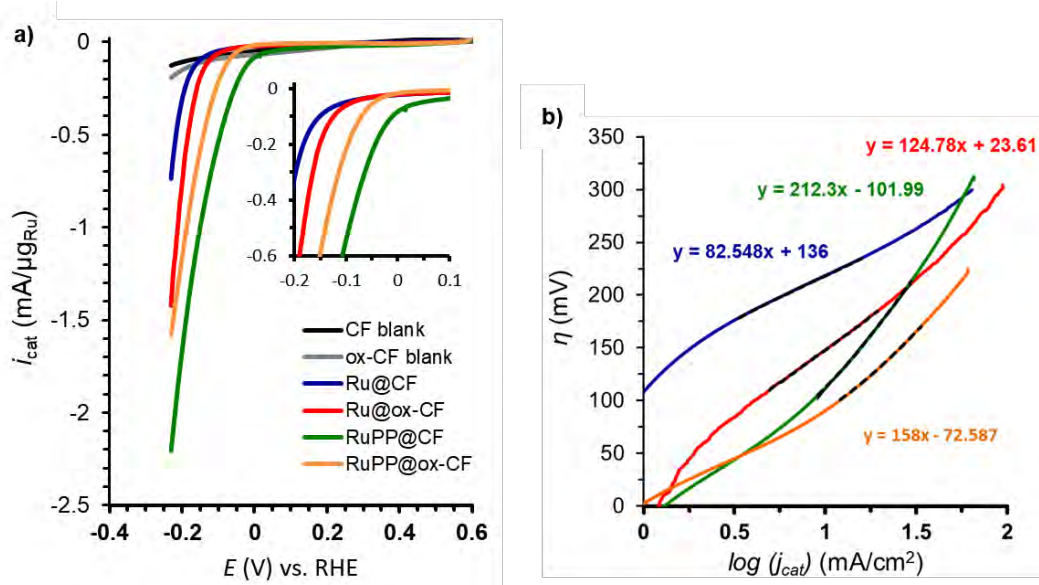


**Figure 15.** Courbes de polarisation de **Ru@CF** (bleu), **Ru@ox-CF** (rouge), **RuPP@CF** (vert) et **RuPP@ox-CF** (orange) normalisées par mg de matériau et  $\mu$ g de Ru dans 1 M H<sub>2</sub>SO<sub>4</sub> (a). Une maille de Pt et des électrodes Ag/AgCl (KCl sat.) ont été utilisées comme contre-électrodes (CE) et électrodes de référence (RE), respectivement. La configuration à trois électrodes a été polarisée de 0,6 V à -0,25 V (par rapport à RHE) à une vitesse de balayage de 10 mV/s. Tracé Tafel de **Ru@CF** (bleu), **Ru@ox-CF** (rouge), **RuPP@CF** (vert) et **RuPP@ox-CF** (orange) dans 1 M H<sub>2</sub>SO<sub>4</sub> (b).

De plus, dans le *chapitre 5B*, des NPs à base de Co ont également été synthétisées avec succès sur des CFs suivant l'approche organométallique (0,039 – 0,23 % en poids de Co) en présence de THF ou de 1-heptanol, observant un rôle positif des groupes carboxyliques à la surface des CFs par la réduction systématique de la taille des NPs et l'augmentation de leur dispersion à la surface de l'électrode pendant les synthèses *in situ*. Le diamètre des NPs s'est avéré être ca.  $2,6 \pm 0,7$  nm,  $1,8 \pm 0,4$ ,  $2,8 \pm 0,6$  nm et  $2,1 \pm 0,4$  nm pour **Co<sub>in</sub><sup>THF</sup>@CF**, **Co<sub>in</sub><sup>THF</sup>@ox-CF**, **Co<sub>in</sub><sup>heptOH</sup>@CF**, **Co<sub>in</sub><sup>heptOH</sup>@ox-CFs**, respectivement (Fig. 16). Après l'imprégnation des CF et ox-CF avec la suspension de NPs de Co présynthétisées, une couche homogène de petites NPs sur la surface des CF a été observée dans les deux systèmes *ex situ* en présence d'heptanol, **Co<sub>ex</sub><sup>heptOH</sup>@CF** et **Co<sub>ex</sub><sup>heptOH</sup>@ox-CF** (Fig. 17). Les NPs de Co obtenues avaient un diamètre moyen

d'environ  $2,0 \pm 0,5$  nm et  $2,3 \pm 0,5$  nm, respectivement. De plus, les spectres XPS haute résolution de Co 2p et O 1s ont confirmé la présence de NPs de  $\text{Co}(\text{OH})_2$  supportées dans tous les systèmes préparés.

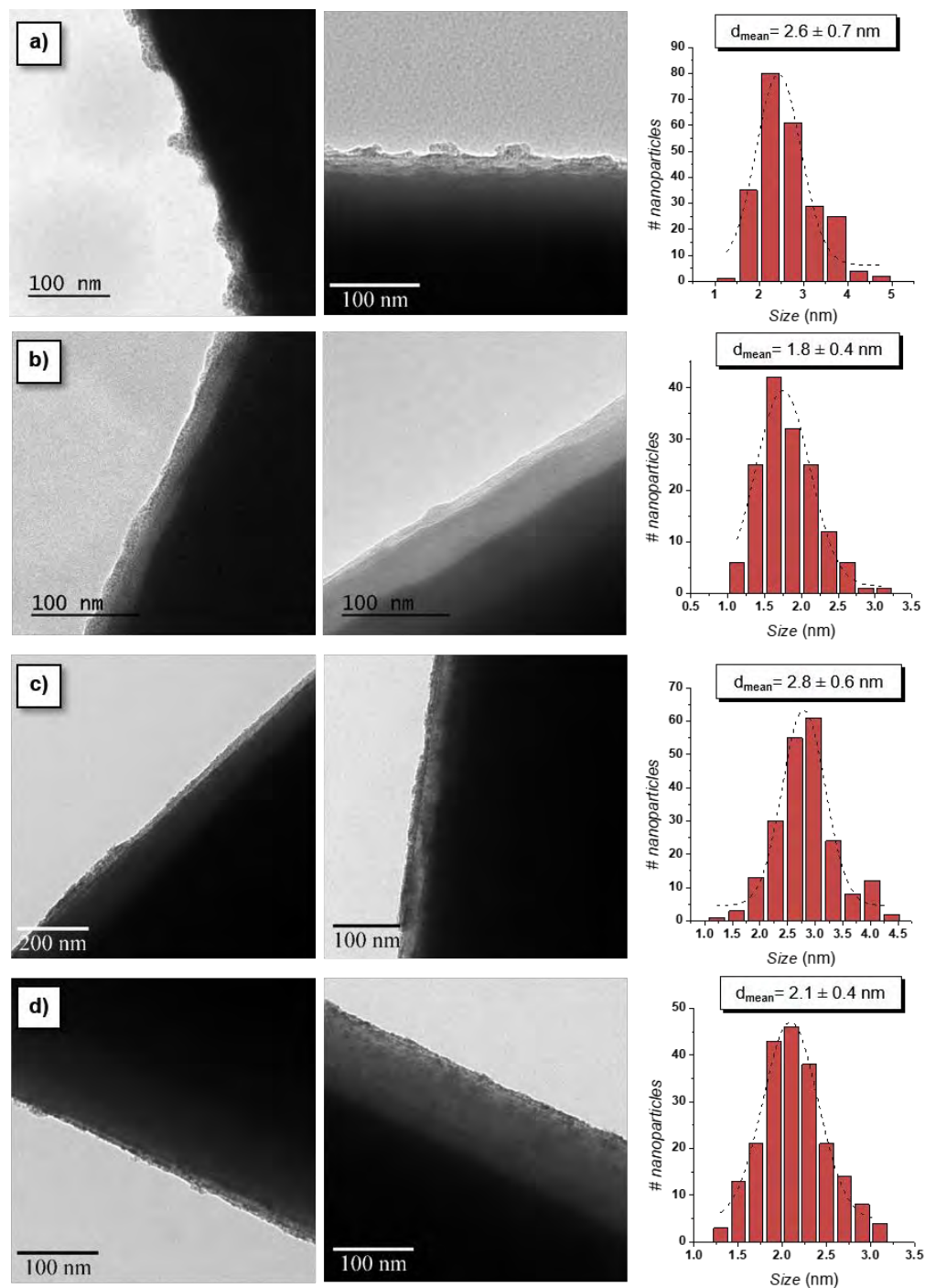


**Figure 16.** Images TEM représentatives et distribution de taille correspondante des CoNPs supportées *in situ*:  $\text{Co}_{\text{in}}^{\text{THF}}@CF$  (a),  $\text{Co}_{\text{in}}^{\text{THF}}@ox-CF$  (b),  $\text{Co}_{\text{in}}^{\text{heptOH}}@CF$  (c) et  $\text{Co}_{\text{in}}^{\text{heptOH}}@ox-CF$  (d).



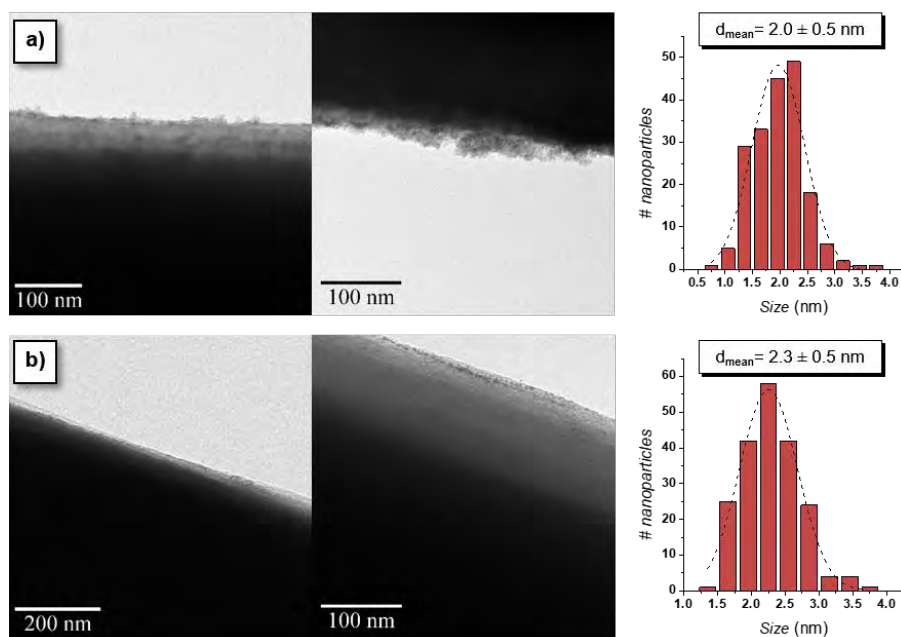


**Figure 17.** Images TEM représentatives et histogramme de distribution de taille correspondant des CoNPs supportées *ex situ*:  $\text{Co}_{\text{ex}}^{\text{heptOH}}@\text{CF}$  (a) et  $\text{Co}_{\text{ex}}^{\text{heptOH}}@\text{ox-CF}$  (b).

Des études d'OER électrocatalytique en milieu NaOH 0.1 M ont été réalisées. Comme le montrent les figures 18a et 18b, lors d'un balayage anodique jusqu'à 1,25 V contre NHE, toutes les électrodes ont montré deux pics anodiques dans le balayage avant une forte augmentation de courant attribuée à l'oxydation électrocatalytique de l'eau en dioxygène. Selon les données de la littérature,<sup>12,13</sup> le premier processus faradique observé dans le voltammogramme ( $E_{\text{ap}}=0.36$  V vs NHE) pourrait être attribué à l'oxydation de Co(II) en Co(III). Le second, apparaissant à un potentiel anodique plus élevé ( $E_{\text{ap}} = 0,76$  V vs NHE) et partiellement masqué par le courant électrocatalytique de l'OER, est caractéristique de l'oxydation ultérieure du Co(III) en Co(IV). Il est intéressant de noter que l'espèce Co(IV) est généralement proposée comme l'espèce active pour l'OER dans les systèmes connexes à base de Co.<sup>14,15,16</sup> Les deux ondes cathodiques dans le balayage cathodique correspondent aux processus de réduction complémentaires.

Les surtensions d'amorçage enregistrées ( $\eta_0$ , plage de 307 à 342 mV) et les pentes de Tafel (110 à 176 mV/dec, figure 18c) sont comparables à celles rapportées pour des électrocatalyseurs OER à base de Co supportés par du carbone dans des conditions alcalines.



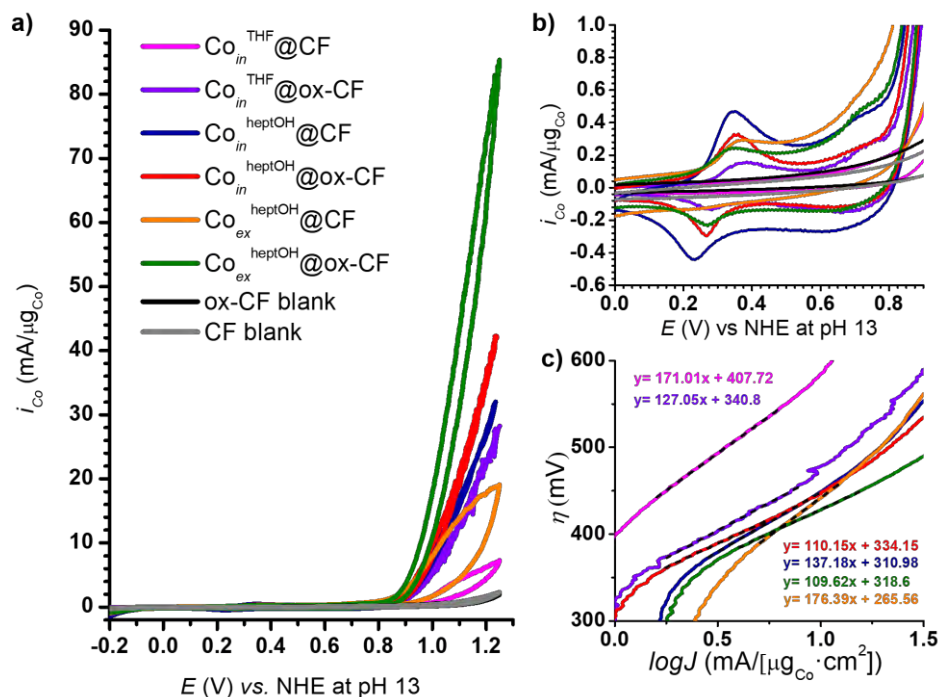


**Figure 18.** Voltampérométries cycliques dans une solution aqueuse de NaOH 0,1 M (pH 13) pour  $Co_{in}^{THF}@CF$  (rose),  $Co_{in}^{THF}@ox-CF$  (violet),  $Co_{in}^{heptOH}@CF$  (bleu),  $Co_{in}^{heptOH}@ox-CF$  (rouge),  $Co_{ex}^{heptOH}@CF$  (orange) et  $Co_{ex}^{heptOH}@ox-CF$  (vert); les blancs ox-CF (noir) et CF (gris) sont également représentés (a). Zoom sur la gamme de potentiel à laquelle les événements redox Co(III/II) et Co(IV/III) se produisent (b). Graphiques de Tafel de tous les matériaux étudiés dans ce travail (c) (même code couleur que dans (a)).

La présence de groupements acides carboxyliques à la surface des CF (c'est-à-dire ox-CF) a un effet positif remarquable sur les performances électrocatalytiques des systèmes étudiés, en favorisant des intensités de courant normalisées plus élevées, des pentes de Tafel plus faibles (c'est-à-dire une cinétique de réaction plus favorable) et des surtensions d'amorçage légèrement plus faibles. Même si cette tendance semble générale pour tous les couples CF/ox-CF étudiés, l'oxydation de la surface du CF a présenté des avantages maximaux dans les systèmes stabilisés au THF et *ex situ*, où les intensités de courant normalisées ont augmenté d'un facteur 4 et les pentes de Tafel ont diminué de près de 35 % dans les deux cas. Ce meilleur comportement des électrodes ox-CF pourrait provenir d'une interaction potentielle de coordination ou/et de liaison H entre les carboxylates de surface du support et les NPs de  $Co(OH)_2$ , améliorant la communication électronique entre le catalyseur et le support et facilitant l'atteinte d'états d'oxydation élevés grâce à la nature anionique des groupes  $-COO^-$ .

De plus, le rapport surface/volume plus élevé des NP de  $\text{Co(OH)}_2$  de plus petite taille présentes dans les systèmes supportés sur ox-CF peut également contribuer à l'amélioration observée de l'activité OER pour ces électrodes, en raison du nombre plus élevé de sites actifs. Comme récemment décrit pour les complexes moléculaires,<sup>17</sup> le rôle potentiel des carboxylates pendants du support ox-CF en tant qu'espèces acceptrices de protons (bases internes) et diminuant les énergies libres d'activation qui mènent à la formation de liaisons O-O pendant l'OER ne peut être écarté. L'absence de groupes stabilisants à la surface des électrodes CF nues conduit à des NP de  $\text{Co(OH)}_2$  moins dispersées sur le support, ce qui réduit probablement le nombre de sites actifs exposés (c'est-à-dire que certains des centres actifs sont bloqués à cause des agglomérats) et contribue aux intensités plus faibles trouvées pour ces électrodes (Fig. 18 a-b). Ainsi, il est confirmé qu'une dispersion homogène des NPs sur la surface des CFs est un point clé pour une bonne activité électrocatalytique.

En revanche, la quantité moindre de Co dans les matériaux *ex situ* pourrait permettre d'obtenir un film plus fin et plus homogène de NPs de  $\text{Co(OH)}_2$ , et donc un matériau avec des sites actifs plus exposés. Ce fait conduit également à une meilleure interaction entre les catalyseurs nanoparticulés de  $\text{Co(OH)}_2$  et la surface du support C, obtenant ainsi des activités catalytiques plus élevées par  $\mu\text{g}$  de Co ( $i_{\text{Co}}$ , Fig. 18 a-b, c'est-à-dire des intensités plus élevées).

L'évolution des intensités de courant électrocatalytique normalisées ( $i_{\text{Co}}$ ) mesurées par CV après un certain temps (0, 10, 30, 60 et 120 min) dans des conditions chronoampérométriques d'OER révèle à nouveau un comportement distinct entre les électrodes CF et ox-CF. Comme on peut l'observer sur la Fig. 19, alors que le  $i_{\text{Co}}$  des électrodes ox-CF diminue progressivement avec le temps ( $i_{\text{Co}} t=0 > i_{\text{Co}} t>0$ ), dans tous les cas en raison des voies de désactivation (Fig. 19b, 19d et 19f), les anodes CF s'activent d'abord ( $i_{\text{Co}} t=0 < i_{\text{Co}} t=10'$ ) avant de se désactiver progressivement après un temps plus long dans des conditions électrocatalytiques (Fig. 19a, 19c et 19e). Encore une fois, ce comportement pourrait être expliqué par les différentes interactions catalyseur-support inhérentes à chaque cas. Par conséquent, la communication électronique entre les électrodes CF nues et les NPs de  $\text{Co(OH)}_2$  semble être initialement faible et son amélioration (et l'activation concomitante) dans les conditions OER pourrait être liée à l'élimination partielle du stabilisateur. Au contraire, la communication électronique (par

des liaisons coordinatives COO-Co(OH)<sub>2</sub> et/ou des liaisons H) semble optimale dans les anodes d'ox-CF, où aucune activation n'est observée.

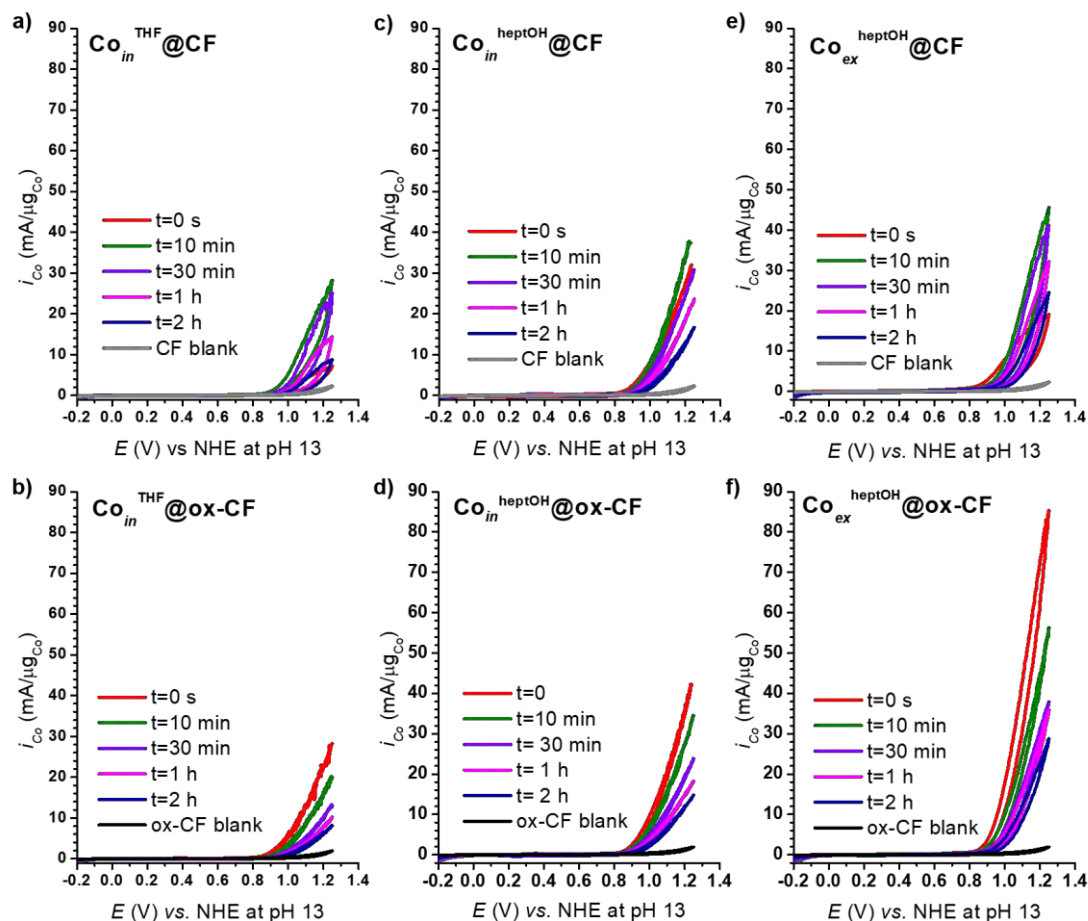


**Figure 19.** Voltampérométries cycliques dans une solution aqueuse de NaOH 0,1 M (pH 13) de  $\text{Co}_{in}^{\text{THF}}@CF$ ,  $\text{Co}_{in}^{\text{THF}}@ox-CF$ ,  $\text{Co}_{in}^{\text{heptOH}}@CF$ ,  $\text{Co}_{in}^{\text{heptOH}}@ox-CF$ ,  $\text{Co}_{ex}^{\text{heptOH}}@CF$  et  $\text{Co}_{ex}^{\text{heptOH}}@ox-CF$ . Blancs CF en gris, blancs ox-CF en noir, CV à  $t=0$  s en rouge, CV après 10 min CA en vert, CV après 30 min CA en violet, CV après 1 h CA en rose et CV après 2 h CA en bleu.

En outre, la formation d'interactions catalyseur-support plus fortes se produit lorsque les nanocatalyseurs sont directement synthétisés à la surface des CF, comme le montre l'observation de charges de Co et la stabilité plus élevées dans des conditions d'OER électrocatalytique pour les systèmes *in situ* par rapport à leurs homologues préparés *ex situ* par imprégnation.

Parmi les électrodes *in situ*, la fonctionnalisation de la surface du support (ox-CF) n'est bénéfique que lorsque le THF, un faible stabilisant, est utilisé comme solvant pour

la préparation de l'électrode (comparez les  $i_{Co}$  REM dans le THF, entrées 1 et 2 du tableau 3, par rapport aux  $i_{Co}$  REM dans les entrées 3 et 4, où le 1-heptanol est utilisé). Par conséquent, lorsque le support devient le principal agent stabilisant des NPs de  $Co(OH)_2$ , l'influence des groupements d'acides carboxyliques à la surface des ox-CF est importantes. Au contraire, lorsque l'on compare la stabilité des deux anodes **ex situ** ( $i_{Co}$  REM dans les entrées 5 et 6, Tableau 3), la présence d'acides carboxyliques dans le support (ox-CF) n'est pas bénéfique mais même préjudiciable. La présence de carboxylates en surface des ox-CF semble déstabiliser les électrodes résultantes, potentiellement par des interactions stériques des carboxylates avec les molécules de 1-heptanol stabilisant les NPs préformées.

**Tableau 3.** Données principales de la désactivation progressive des systèmes lorsque des AC successifs à un potentiel fixe de 1 V par rapport au NHE à pH 13 sont appliqués à chaque système.

Entry	System	$i_{Co\text{ REM}}^{(a)}$ (%)
1	$Co_{in}^{THF}@CF$	32
2	$Co_{in}^{THF}@ox-CF$	50
3	$Co_{in}^{heptOH}@CF$	64
4	$Co_{in}^{heptOH}@ox-CF$	62
5	$Co_{ex}^{heptOH}@CF$	55
6	$Co_{ex}^{heptOH}@ox-CF$	43

(a) %  $i_{Co}$  REM calculé en divisant  $i_{Co}$  t=2 h par  $i_{Co}$  t=0 s comme données de stabilité à court terme pour les systèmes ox-CF et en divisant  $i_{Co}$  t=2 h par  $i_{Co}$  t=10 min (valeur après activation) comme données de stabilité à court terme pour les systèmes CF.

Il a également été confirmé par XPS que les anodes conservent le  $Co(OH)_2$  comme espèce catalytique après 2 h en conditions électrocatalytiques et, même si elles sont partiellement désactivées en raison de l'agrégation (TEM) et de la lixiviation des NPs de la surface de l'électrode (ICP), les efficacités faradiques presque quantitatives (environ 93 - 99%) montrant l'évolution de l'oxygène comme la seule réaction redox se produisant à leur surface.

Le *chapitre 6* étend le champ d'application de cette thèse de doctorat aux systèmes bimétalliques, et souligne l'utilité de la méthodologie de synthèse employée à cet égard. Dans le *chapitre 6A*, des nanomatériaux de Ni de type mousse et leurs homologues dopés avec différentes charges de Ru (1, 5 et 10 % en poids de Ru) ont été synthétisés suivant une procédure en deux étapes. Tout d'abord, un matériau de Ni de type mousse a été obtenu, composé de particules d'environ 100 nm constituées d'agglomérats de particules

plus petites (22 nm). Des nanoparticules de Ru ont ensuite été synthétisées sur ce nanomatériau de Ni, avec trois charges de Ru différentes (0,43 % en poids dans la mousse de **Ru1@Ni-foam**, 3,2 % en poids dans la mousse de **Ru5@Ni-foam** et 6,4 % en poids dans la mousse de **Ru10@Ni-foam**). Les échantillons de plus forte teneur en Ru présentent des NPs de Ru agrégées, mais la morphologie de celui contenant moins de Ru n'a encore été obtenue (Fig. 20). La passivation de ces matériaux par exposition à l'air a conduit à une structure composite Ni(0)/Ni(OH)<sub>2</sub>-NiOOH core@shell décorées de NPs Ru/RuO<sub>2</sub> (core/shell), comme confirmé par XPS. Il est à noter que l'XPS a révélé que l'espèce NiOOH n'est présente que dans les échantillons contenant du Ru (par opposition au Ni(OH)<sub>2</sub> dans la mousse de Ni initiale), suggérant ainsi que le Ru peut contribuer à la stabilisation des états d'oxydation supérieurs du Ni dans les échantillons passivés.

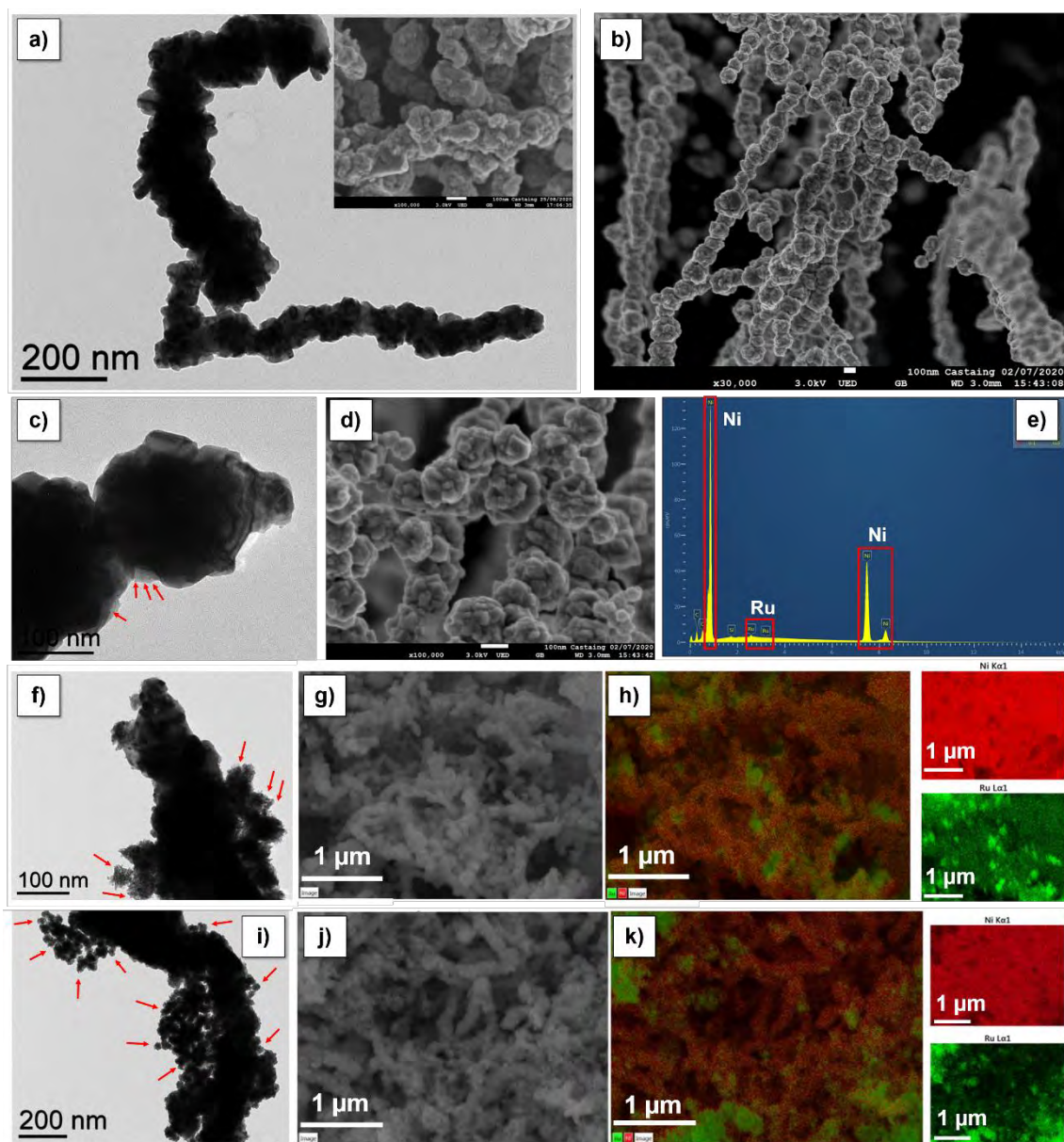


**Figure 20.** De haut en bas: Caractérisation de la **mousse de Ni** par TEM (a) et SEM (b); caractérisation de la **Ru1@Ni-foam** par TEM (c), SEM (d) et analyse EDX (e); Caractérisation de la **Ru5@Ni-foam** par TEM (f), SEM (g) et cartographie EDX de Ni K $\alpha$ 1 (rouge) et Ru L $\alpha$ 1 (vert) (h); Caractérisation de la **Ru10@Ni-foam** par TEM (i), SEM (j) et cartographie EDX de Ni K $\alpha$ 1 (rouge) et Ru L $\alpha$ 1 (vert) (k). Les flèches montrent la présence de petites NPs de Ru.

Les courbes de polarisation de ces nanomatériaux vis-à-vis de la production d' $H_2$  en milieu acide ont montré des densités de courant catalytique plus élevées pour les systèmes contenant une plus grande quantité de Ru. Cependant, la meilleure activité catalytique a été obtenue pour la mousse de **Ru5@Ni-foam**, ce qui peut s'expliquer par son degré de cristallinité plus élevé, comme observé par XRD, ou même de son rapport

Ru/RuO<sub>2</sub> différent ou de sa teneur optimale en dopant Ru, fournissant une bonne interface entre les espèces Ni/Ni(OH)<sub>2</sub>-NiOOH et le dopant Ru. Les études électrocatalytiques HER en milieu alcalin ont montré les mêmes tendances qu'en milieu acide.

Le balayage anodique OER en conditions alcalines a montré l'apparition d'un pic anodique avant une forte augmentation du courant, attribué à l'oxydation électrocatalytique de l'eau en dioxygène (Fig. 21). Cette onde redox a été attribuée à l'oxydation de Ni(II) en Ni(III), indiquant que l'espèce NiOOH est la véritable espèce active dans les conditions OER.<sup>18</sup>

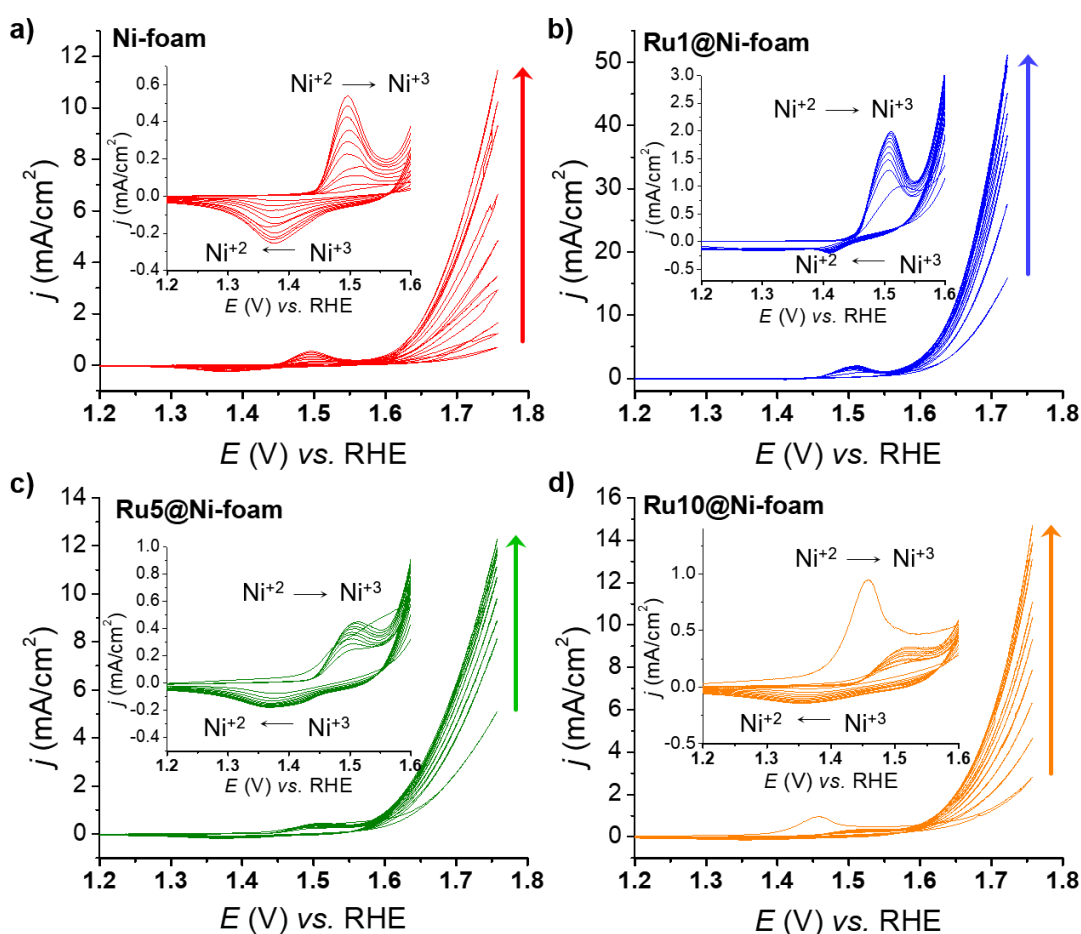


**Figure 21.** 10 CVs progressives pour l'étude de l'activité catalytique du OER dans une solution aqueuse de NaOH non purifiée pour la mousse de Ni (a), Ru1@Ni-foam (b), Ru5@Ni-foam (c) et Ru10@Ni-foam (d).

Le système Ru1@Ni-foam comparativement aux matériaux Ru5@Ni-foam et Ru10@Ni-foam (couche mince de petits clusters <1 nm ou d'atomes uniques par rapport à des nanostructures spongieuses de petites NP agrégées) a montré un comportement



légèrement différent en OER lors d'études complémentaires dans un électrolyte alcalin non purifié et sans Fe (Fig. 22). Une activation progressive de **Ru1@Ni-foam** a également été observée dans un électrolyte sans Fe, conjointement avec une activation plus élevée dans un électrolyte non purifié, ce qui indique qu'un faible dopage en Ru peut contribuer à une incorporation plus importante de Fe ou à une meilleure hydratation de l'échantillon. Malgré ces différences, il a été confirmé que l'incorporation de Fe et/ou, dans une moindre mesure, l'hydratation des échantillons est un point clé pour atteindre des performances électrocatalytiques élevées en OER avec ces nanomatériaux à base de Ni.<sup>19</sup>

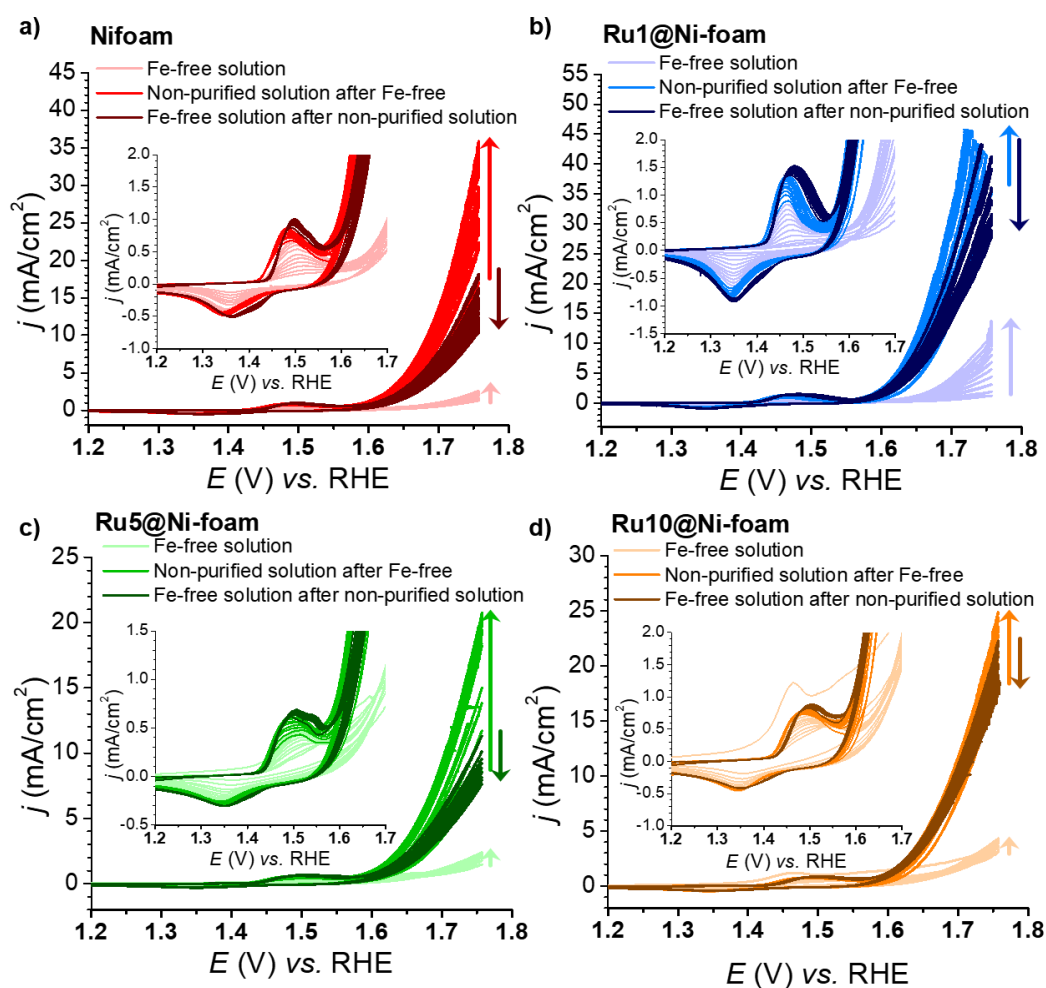


**Figure 22.** Études comparatives de l'activité catalytique en OER dans une solution aqueuse de NaOH sans Fe, non purifiée après Fe et non purifiée pour la **mousse de Ni** (a), la mousse de **Ru1@Ni-foam** (b), la mousse de **Ru5@Ni-foam** (c) et la mousse de **Ru10@Ni-foam** (d).



Dans l'optique d'une mise en œuvre de catalyseurs de Ni avec des semi-conducteurs dans des dispositifs photochimiques de WS, le développement de matériaux actifs et stables dans des conditions neutres offrirait une plus grande flexibilité technologique, car les semi-conducteurs sont plus stables en milieu neutre.<sup>20</sup> En outre, les performances catalytiques réduites d'OER dans des tampons de phosphate et de borate ont confirmé que, même si la présence de Fer est cruciale pour une catalyse efficace, l'effet déprotonant des anions hydroxyles dans des conditions fortement alcalines joue un rôle prépondérant, favorisant la formation des espèces d'oxygène actif (NiOO<sup>-</sup>).<sup>21</sup>

La spectroélectrochimie UV-vis *in situ* a été utilisée pour suivre les états d'oxydation des métaux à différents potentiels des matériaux nickel étudiés.<sup>22,23</sup> Ces expériences ont été réalisées avec les systèmes **Ru1@Ni-foam** et **Ru5@Ni-foam** vers l'OER à pH ~14 (Fig. 23). Les résultats ont été comparés à ceux obtenus avec la mousse de nickel sans Ru afin d'obtenir de déterminer l'influence du dopage au Ru. Les échantillons ont été déposés sur une électrode conductrice transparente de FTO pour réaliser les mesures spectroscopiques UV-Vis de transmittance. La spectroélectrochimie UV-vis *in situ* a permis de suivre le processus d'oxydation Ni(II)→Ni(III) avant la forte augmentation de courant attribuée à l'OER électrocatalytique. Des chronoampérométries à différents potentiels (avant et après la vague d'oxydation Ni<sup>+2</sup> → Ni<sup>+3</sup>) ont été réalisées et, après stabilisation du courant, un spectre UV-vis a été enregistré. Lorsqu'un potentiel postérieur à la 1ère vague d'oxydation redox est appliqué, une augmentation de l'absorbance est observée dans tous les cas. La différence d'absorbance lors de l'application d'un potentiel avant et après l'onde oxydative de Ni est représentée sur les figures 23b, 23d et 23f. Comme on peut l'observer, les spectres obtenus présentent deux formes différentes. Avec les échantillons de Ni et **Ru5@Ni-foam**, les spectres obtenus sont similaires à ceux précédemment rapportés dans la littérature et attribués à l'espèce NiOOH avec une large bande caractéristique centrée à 450 nm (Fig. 23b et 23f).<sup>23</sup> D'autre part, l'échantillon **Ru1@Ni-foam** présente un spectre très différent, avec une absorption croissante vers le NIR culminant à 650 nm (Figure 23d). Cette observation suggère que la faible incorporation de Ru modifie l'espèce NiOOH, soutenant le comportement différent trouvé pour ce système en OER, par rapport au système de Ni non dopé Ni et les systèmes **Ru5@Ni-foam** et **Ru10@Ni-foam**.

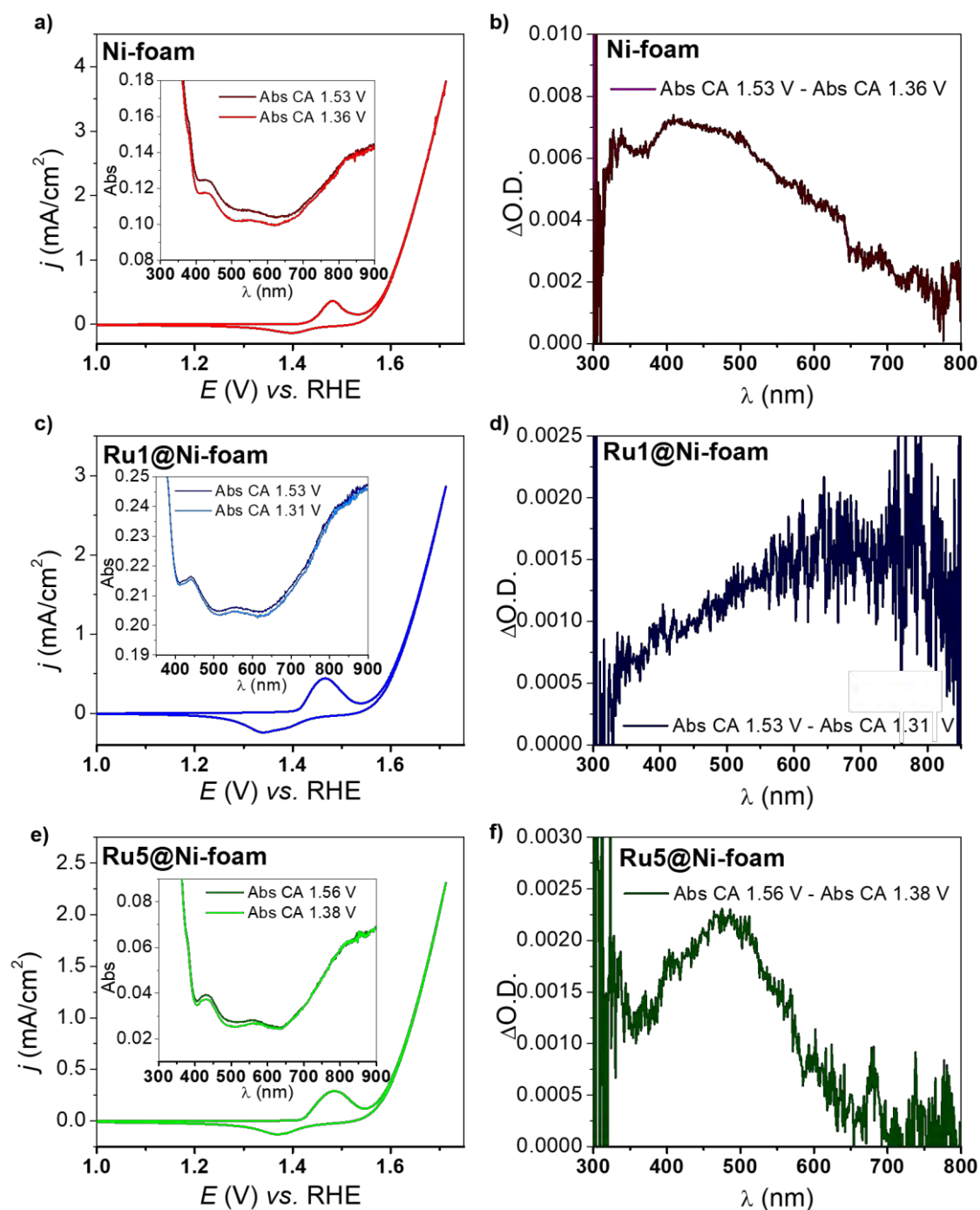


**Figure 23.** CV initial et spectre UV-vis pendant l'AC à un potentiel avant l'onde oxydative redox (couleur claire) et spectre UV-vis pendant l'AC à un potentiel après l'onde oxydative redox (couleur sombre) pour la mousse de Ni (a), la mousse de **Ru1@Ni-foam** (c) et la mousse de **Ru5@Ni-foam** (e). Soustraction du spectre du  $CA_E$  after ox. -  $CA_E$  before ox. pour Ni-foam (b), **Ru1@Ni-foam** (d) et **Ru5@Ni-foam** (f).

Considérant l'augmentation de l'absorbance observée dans tous les échantillons étudiés autour de 350-700 nm, 500 nm a été choisi comme longueur d'onde pour suivre

l'évolution des espèces formées par CV à un taux de balayage de 1 mV/s. Le cycle de potentiel révèle que la bande d'absorption du catalyseur Ni augmente juste après le début de l'onde redox  $\text{Ni}(\text{OH})_2 \rightarrow \text{NiOOH}$ , et se termine avant le début de l'OER catalytique (Fig. 24). L'espèce NiOOH peut être considérée comme l'état d'oxydation préférentiel précédent l'OER, une voie plus favorable (c'est-à-dire avec un surpotentiel plus faible) pour l'OER. Selon ces résultats, une fois que l'espèce NiOOH est formée, même si le potentiel appliqué augmente, ainsi que la densité de courant, le signal de cette espèce ne semble pas augmenter avec le potentiel. Cette observation confirme que la formation de l'espèce NiOOH se produit entièrement pendant la réaction d'oxydation du Ni, suggérant qu'il ne s'agit pas de l'espèce accumulée pendant la catalyse. Par conséquent, en accord avec la littérature, NiOOH doit être davantage oxydé pour pouvoir oxyder l'eau.<sup>22</sup>

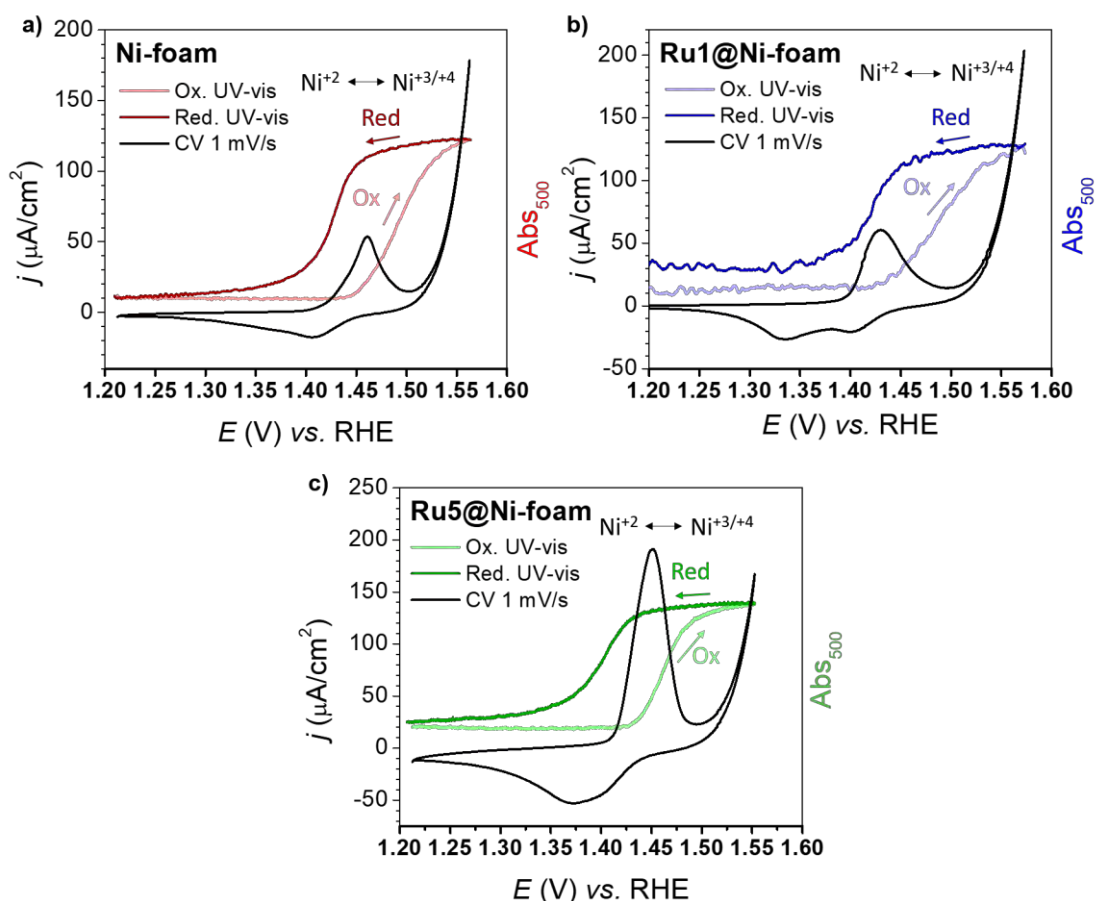


**Figure 24.** Spectres UV-vis in situ suivis à Abs500 ( $\lambda_{500\text{nm}}$ ) pendant le cycle de potentiel de la mousse de Ni (a), de la mousse de **Ru1@Ni-foam** (b) et de la mousse de **Ru5@Ni-foam** (c). La ligne solide noire montre le courant faradique (CV), les lignes de couleur claire montrent l'absorption lors du balayage oxydatif et les lignes de couleur sombre l'absorption lors du balayage réducteur.

Dans le *chapitre 6B*, en s'inspirant d'un travail antérieur où des NPs de RuCo alliées de faible taille ( $< 2$  nm) dispersées dans une matrice polymère (polyvinylpyrrolidone),<sup>24</sup> la synthèse de NPs bimétalliques RuCo par l'hydrogénation simultanée de précurseurs organométalliques Ru et Co a été confirmée par des analyses EDX et WAXS. L'analyse WAXS indique une tendance générale sur la structure, avec une structure bêta Mn dilatée pour les échantillons riches en Co et une évolution vers le hcp dans les échantillons riches en Ru. En outre, un effort particulier a été mis sur l'extraction d'informations sur l'influence de la nature des ligands stabilisants 4PP, tpy et 1-heptanol (heptOH) et du rapport molaire des métaux (Ru:Co, 1:1, 2:1 et 1:2) sur la morphologie des NPs obtenues. Des NPs monométalliques ont également été synthétisées à des fins de comparaison. Les images TEM indiquent que le ligand 4PP ne permet pas d'obtenir des NPs de Co bien dispersées, contrairement à ce qui est observé avec le Ru. En ce qui concerne les échantillons RuCo-4PP, même si aucun effet significatif n'est observé sur la taille ( $2,0 \pm 0,3$  nm,  $1,9 \pm 0,3$  nm et  $1,8 \pm 0,3$  nm pour **Ru<sub>1</sub>Co<sub>1</sub>-4PP**, **Ru<sub>2</sub>Co<sub>1</sub>-4PP** et **Ru<sub>1</sub>Co<sub>2</sub>-4PP**, respectivement) des NPs obtenues en fonction du ratio Ru:Co employé, ce paramètre a un effet clair sur la dispersion des NPs (voir Figs. 25, 26 et 27). Ce résultat peut être expliqué par le fait qu'en augmentant la teneur en Co, la capacité de stabilisation du ligand 4PP diminue, conduisant à des NPs moins stables. Elles peuvent donc avoir tendance à s'agglomérer afin de minimiser leur énergie de surface, comme déjà observé pour les systèmes monométalliques de Co. Cependant, la formation d'agglomérats de NPs peut également résulter, dans une moindre mesure, d'interactions  $\pi$ - $\pi$  entre les cycles aromatiques des ligands dans les NPs adjacentes. En revanche, la forte capacité de la 4PP à stabiliser le Ru a permis une couverture plus intense des NPs lorsqu'elles sont plus riches en Ru, évitant leur agglomération.

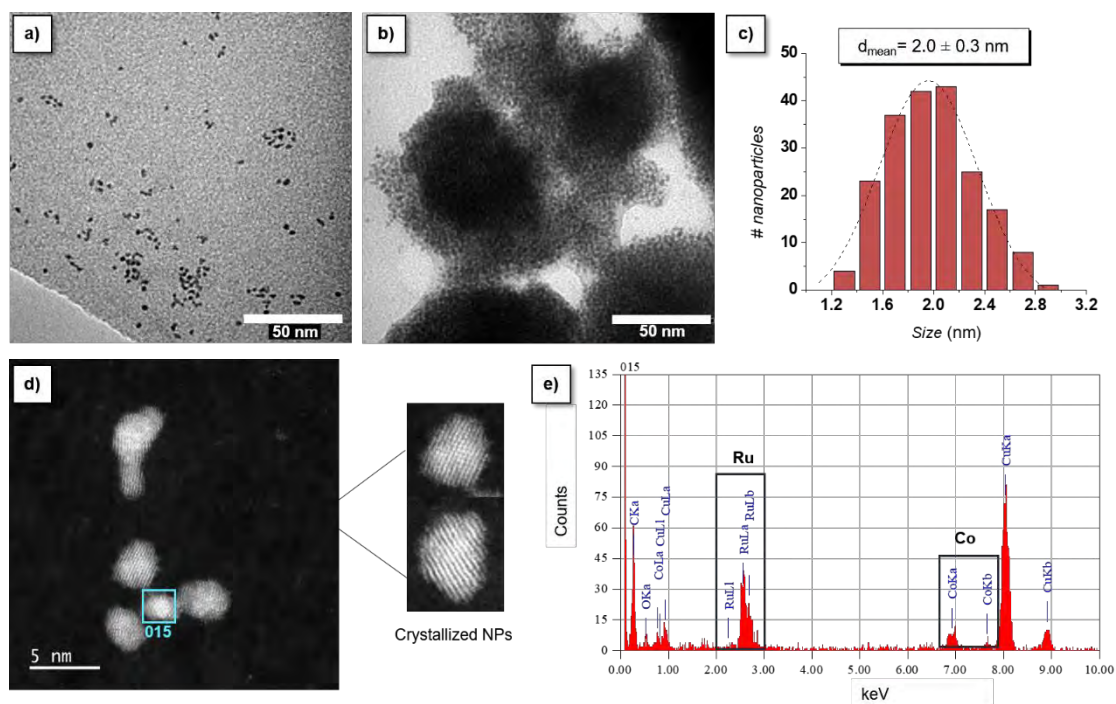


**Figure 25.** Images TEM (a-b), histogramme de distribution de taille (c), image STEM-HAADF (d) et analyse EDX d'une seule NP (e) de **Ru<sub>1</sub>Co<sub>1</sub>-4PP**.

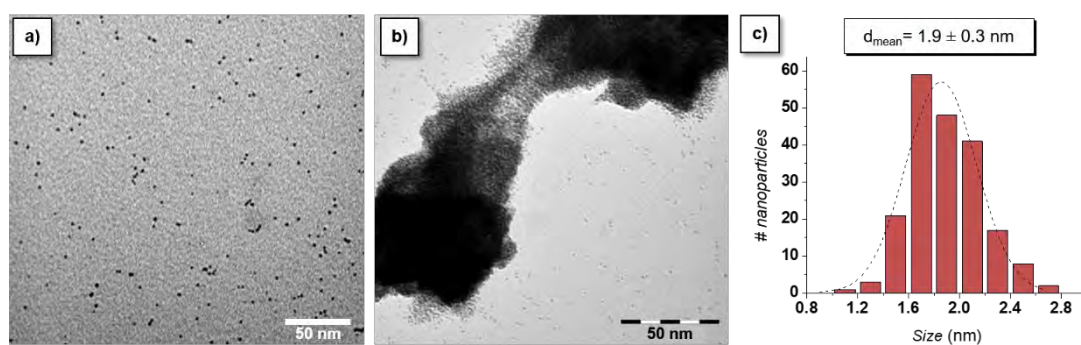


**Figure 26.** Images TEM (a-b) et histogramme de distribution de taille (c) de **Ru<sub>2</sub>Co<sub>1</sub>-4PP**.

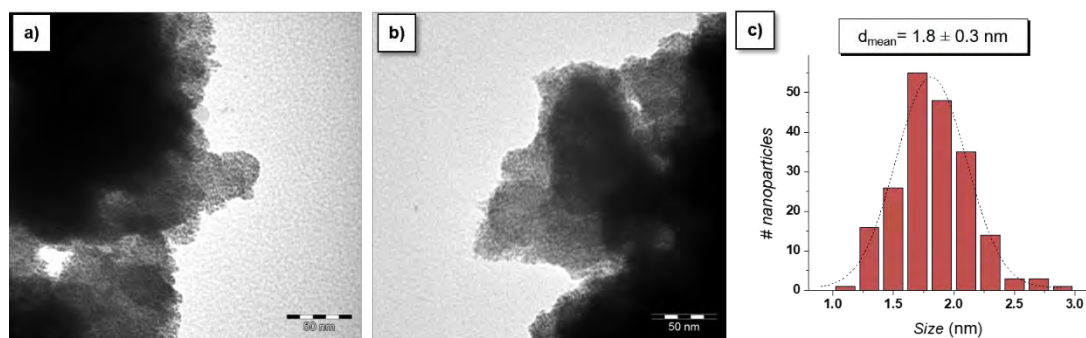


**Figure 27.** Images TEM (a-b) et histogramme de distribution de taille (c) de **Ru<sub>1</sub>Co<sub>2</sub>-4PP**.

De plus, le ligand tpy s'est avéré être un agent stabilisant très efficace pour les NPs de Ru de par la forte coordination du tpy à la surface des NPs due au caractère acide de Lewis dur du Ru et à celui de base de Lewis dure de l'N, ainsi qu'à la nature chélatrice de ce ligand. La teneur plus élevée en N du tpy par rapport au 4PP (3 contre 1) ainsi que la nature chélatrice du premier peuvent expliquer la meilleure stabilité des NPs de Co-tpy par rapport aux NPs de Co-4PP. Les images TEM des échantillons de RuCo-tpy obtenus avec différentes proportions de Ru:Co (Figs. 28, 29 et 30) révèlent une capacité de stabilisation plus intense du tpy envers les deux métaux que le 4PP, obtenant des NPs plus petites ( $1,3 \pm 0,2$  nm,  $1,3 \pm 0,2$  nm et  $1,5 \pm 0,3$  nm pour **Ru<sub>1</sub>Co<sub>1</sub>-tpy**, **Ru<sub>2</sub>Co<sub>1</sub>-tpy** et **Ru<sub>1</sub>Co<sub>2</sub>-tpy**, respectivement) pour le premier.

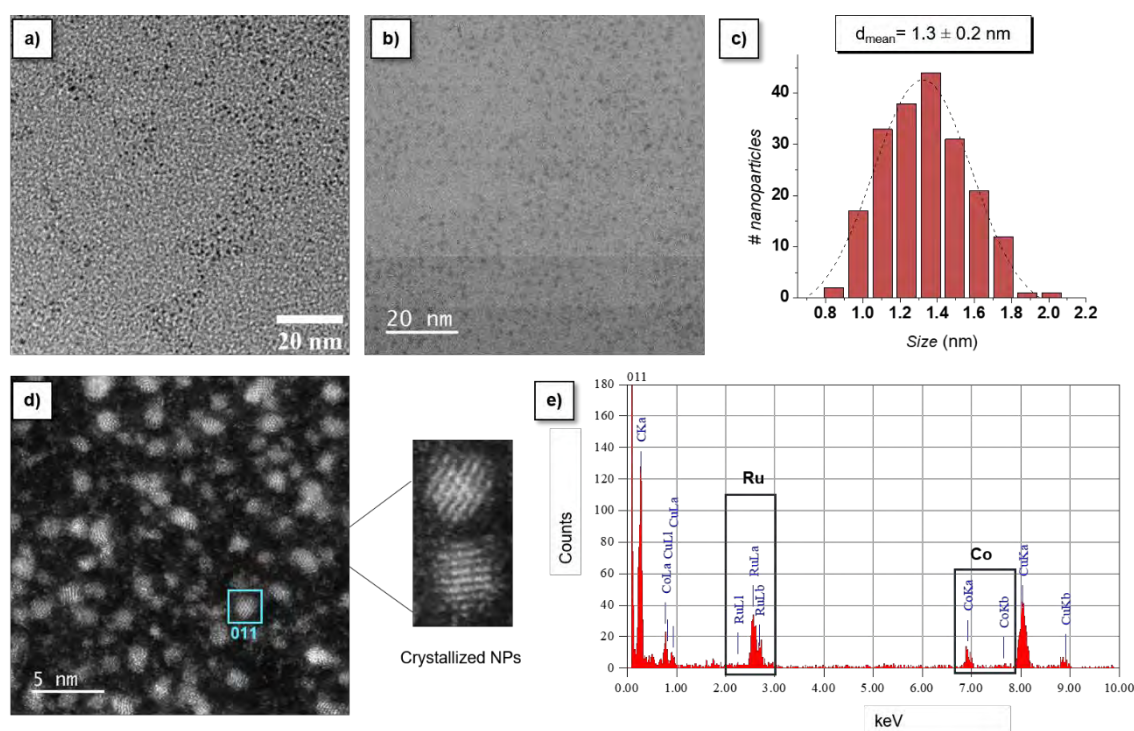


**Figure 28.** Images TEM (a-b), histogramme de distribution de taille (c), image STEM-HAADF (d) et analyse EDX d'une seule NP (e) de **Ru<sub>1</sub>Co<sub>1</sub>-tpy**.

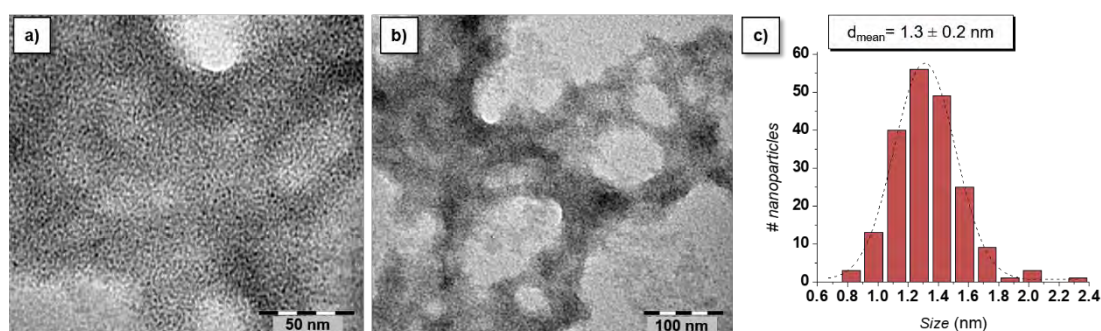


**Figure 29.** Images TEM (a-b) et histogramme de distribution de taille (c) de **Ru<sub>2</sub>Co<sub>1</sub>-tpy**.



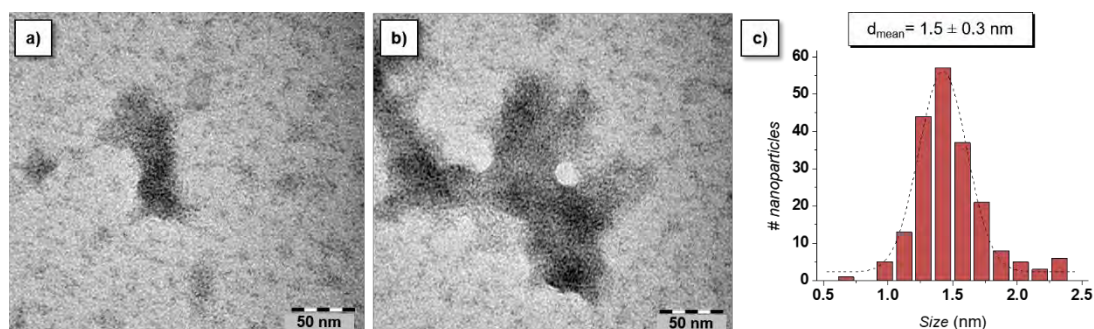


**Figure 30.** Images TEM (a-b) et histogramme de distribution de taille (c) de **Ru<sub>1</sub>Co<sub>2</sub>-tpy**.

Enfin, des NPs RuCo isolées, petites (ca. 1 nm), sphériques et bien dispersées ont été obtenues avec le 1-heptanol comme agent stabilisant, en raison de sa double capacité à bien stabiliser les NPs de Ru et de Co. Le diamètre moyen de ces NPs est plus petit que pour leurs homologues monométalliques, étant  $1,1 \pm 0,2$  nm,  $1,3 \pm 0,3$  nm et  $1,1 \pm 0,2$  nm pour **Ru<sub>1</sub>Co<sub>1</sub>-heptOH**, **Ru<sub>2</sub>Co<sub>1</sub>-heptOH** et **Ru<sub>1</sub>Co<sub>2</sub>-heptOH**, respectivement (voir Figs. 31, 32 et 33). Les tailles petites et similaires obtenues pour les trois rapports Ru:Co peuvent être expliquées par les bonnes propriétés stabilisantes du 1-heptanol envers le Ru et le Co. De plus, comme l'heptanol n'est pas enclin à induire des interactions  $\pi$ - $\pi$  entre les NPs adjacentes, ces NPs sont bien dispersées.

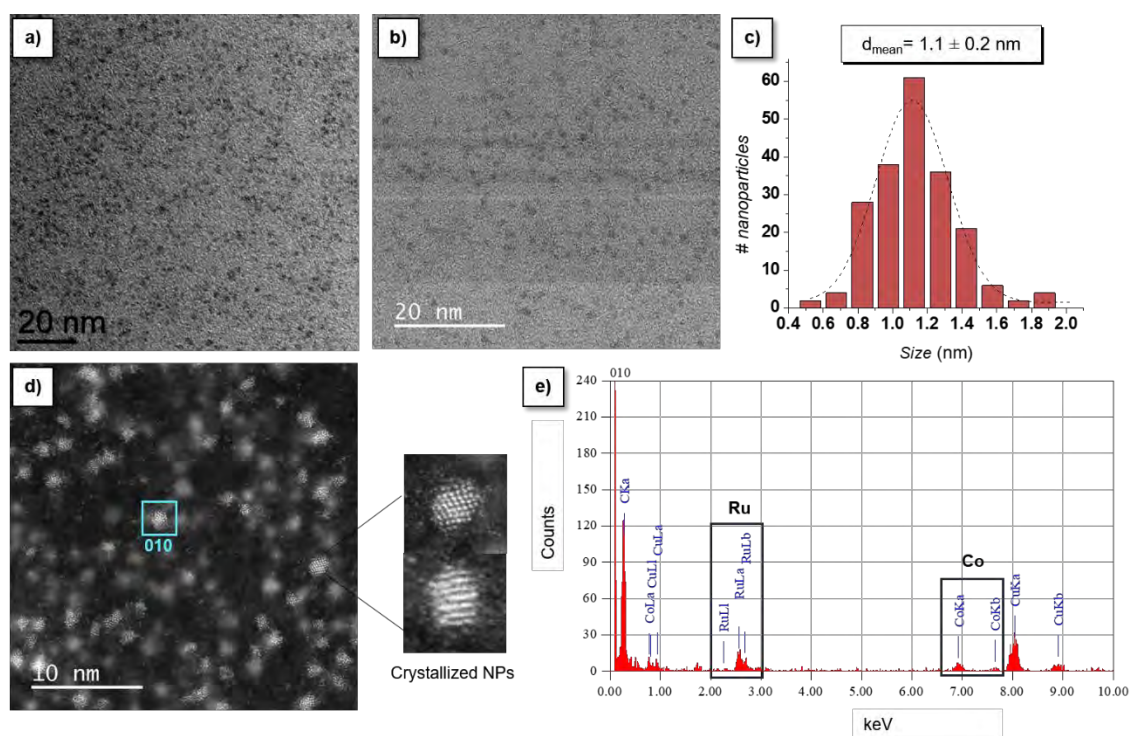


**Figure 31.** Images TEM (a-b), histogramme de distribution de taille (c), image STEM-HAADF (d) et analyse EDX d'une seule NP (e) de **Ru<sub>1</sub>Co<sub>1</sub>-heptOH**.

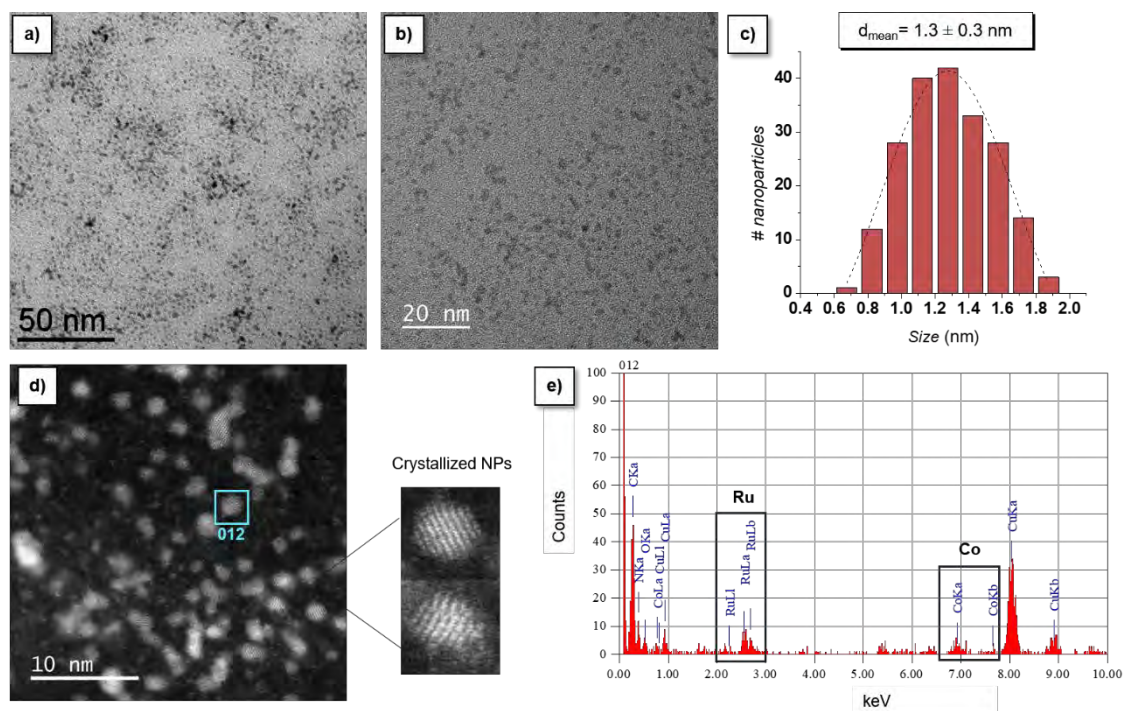


**Figure 32.** Images TEM (a-b), histogramme de distribution de taille (c), image STEM-HAADF (d) et analyse EDX d'une seule NP (e) de  $\text{Ru}_2\text{Co}_1\text{-heptOH}$ .

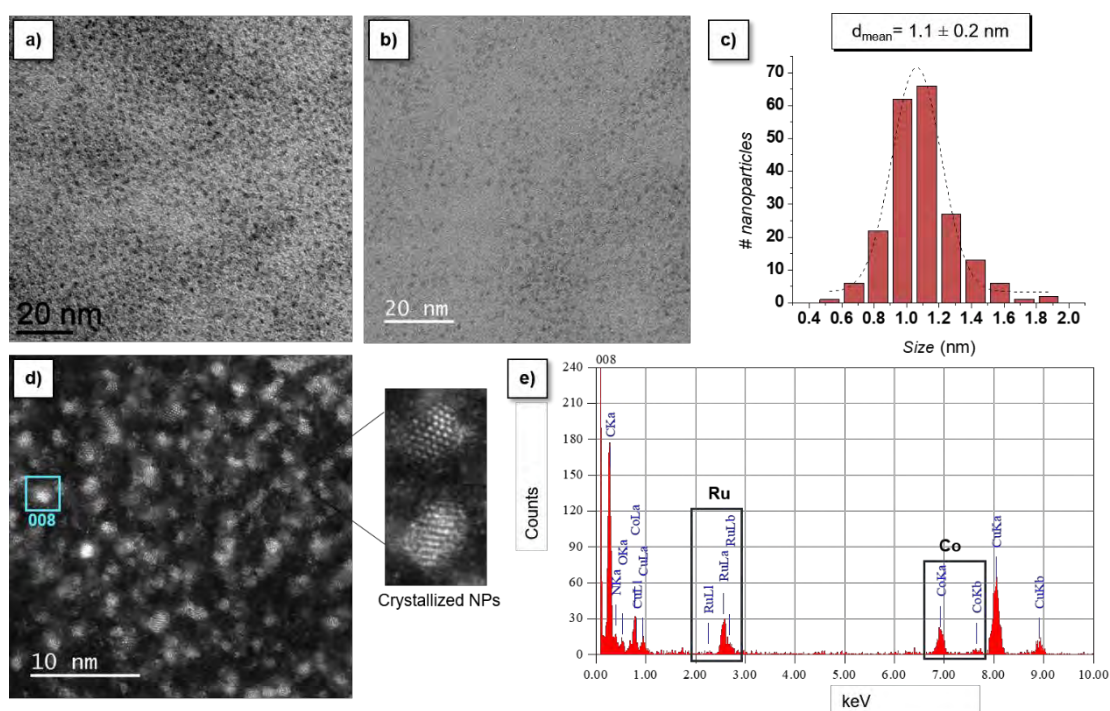


**Figure 33.** Images TEM (a-b), histogramme de distribution de taille (c), image STEM-HAADF (d) et analyse EDX d'une seule NP (e) de  $\text{Ru}_1\text{Co}_2\text{-heptOH}$ .



En conclusion, la taille moyenne des NPs dans la série de NPs RuCo étudiée suit l'ordre RuCo-4PP > RuCo-tpy  $\approx$  RuCo-heptOH, la capacité de stabilisation de chaque ligand étant inversement proportionnelle à la taille des NPs obtenues.

En conclusion, ce travail de thèse visait à mieux cerner les facteurs clés qui contrôlent la performance des électrocatalyseurs WS (OER et HER) à l'échelle nanométrique. En tirant parti de l'approche organométallique, une méthode de synthèse flexible, ce travail a pu explorer un large éventail de stratégies pour affiner et rationaliser l'activité et la stabilité de NPs métalliques, y compris en présence de ligands stabilisants, le dopage/fonctionnalisation des supports carbonés conducteurs et la combinaison de deux métaux dans des proportions et ordres chimiques différents. Au vu des résultats résumés ci-dessus, ce travail ouvre de nouvelles perspectives pour la conception rationnelle de nouveaux nanoélectrocatalyseurs WS hautement actifs et efficaces.

- <sup>1</sup> Global Climate Change: Vital signs of the planet. Retrieved May, **2021**, from <https://climate.nasa.gov/causes/>
- <sup>2</sup> NOAA Climate.gov
- <sup>3</sup> C. Amiens, B. Chaudret, D. Ciuculescu-Pradines, V. Collière, K. Fajerweg, P. Fau, M. Kahn, A. Maisonnat, K. Soulantica and K. Philippot, *New J. Chem.* **2013**, 37, 3374-3401.
- <sup>4</sup> J. Creus, J. De Tovar, N. Romero, J. García-Antón, K. Philippot, R. Bofill and X. Sala, *ChemSusChem* **2019**, 12, 2493-2514.
- <sup>5</sup> J. Creus, S. Drouet, S. Suriñach, P. Lecante, V. Collière, R. Poteau, K. Philippot, J. García-Antón, X. Sala, *ACS Catal.* **2018**, 11094-11102.
- <sup>6</sup> J.K. Nørskov, T. Bligaard, J. Rossmeisl, and C.H. Christensen, *Nat. Chem.* **2009**, 1, 37 – 46.
- <sup>7</sup> I. del Rosal and R. Poteau, Sabatier Principle and Surface Properties of Small Ruthenium Nanoparticles and Clusters: Case Studies **2021**. In *Nanoparticles in Catalysis* (eds K. Philippot and A. Roucoux).
- <sup>8</sup> Y. Zheng, Y. Jiao, M. Jaroniec and S.Z. Qiao, *Angew. Chem. Int. Ed.* **2015**, 54, 52-65.
- <sup>9</sup> J.K. Nørskov, T. Bligaard, A. Logadottir, J.R. Kitchin, J.G. Chen, S. Pandelov and U. Stimming, *J. Electrochem. Soc.* **2005**, 152, J23 – J26.
- <sup>10</sup> T.F. Jaramillo, K.P. Jørgensen, J. Bonde, J.H. Nielsen, S. Hørch and I. Chorkendorff, *Science* **2007**, 317, 100 – 102.
- <sup>11</sup> L.I. Álvarez, Ruthenium and Platinum Nanoparticles for Artificial Photosynthesis **2021**, PhD Thesis, UAB.
- <sup>12</sup> Y.C. Liu, J.A. Koza and J. A. Switzer, *Electrochim. Acta* **2014**, 140, 359–365.
- <sup>13</sup> Y.Q. Gao, H.B. Li and G.W. Yang, *J. Appl. Phys.* **2016**, 119, 034902.
- <sup>14</sup> N.H. Chou, P.N. Ross, A.T. Bell and T.D. Tilley, *ChemSusChem* **2011**, 4, 1566–1569.
- <sup>15</sup> B.S. Yeo and A.T. Bell, *J. Am. Chem. Soc.* **2011**, 133, 5587–5593.
- <sup>16</sup> M.E.G. Lyons and M.P. Brandon, *J. Electroanal. Chem.* **2010**, 641, 119–130.
- <sup>17</sup> R. Matheu, M.Z. Ertem, J. Benet-Buchholz, E. Coronado, V.S. Batista, X. Sala and A. Llobet, *J. Am. Chem. Soc.* **2015**, 137, 10786–10795.
- <sup>18</sup> L. Trotochaud, J.K. Ranney, K.N. Williams and S.W. Boettcher, *J. Am. Chem. Soc.* **2012**, 134, 17253-17261.
- <sup>19</sup> S. Corby, M.G. Tecedor, S. Tengeler, C. Steinert, B. Moss, C.A. Mesa, H.F. Heiba, A.A. Wilson, B. Kaiser, W. Jaegermann, L. Francàs, S. Gimenez and J.R. Durrant, *Sustainable Energy Fuels* **2020**, 4, 5024-5030.
- <sup>20</sup> Gerischer, H. In *Solar Energy Conversion: Solid-State Physics Aspects*; B. O. Seraphin, Ed.; Topics in Applied Physics; Springer Berlin Heidelberg: Berlin, **1979**; Vol. 31, pp. 115-172.

- <sup>21</sup> B.J. Trzesniewski, O. Diaz-Morales, D.A. Vermaas, A. Longo, W. Bras, M.T.M. Koper and W.A. Smith, *J. Am. Chem. Soc.* **2015**, 137, 15112–15121
- <sup>22</sup> L. Francàs, S. Corby, S. Selim, D. Lee, C.A. Mesa, R. Godin, E. Pastor, I.E.L Stephens, K.S. Choi and J.R. Durrant, *Nat. Commun.* **2019**, 10, 5208.
- <sup>23</sup> L. Francàs, S. Selim, S. Corby, D. Lee, C.A. Mesa, E. Pastor, K.S. Choi and J. R. Durrant, *Chem. Sci.* **2021**, 12, 7442-7452.
- <sup>24</sup> D. Zitoun, M. Respaud, M.C. Fromen, P. Lecante, M.J. Casanove, C. Amiens and B. Chaudret, *J. Magn. Magn. Mater.* **2004**, 272-276, 1536-1537.





